David Taylor Research Center
Bethesda, MD 20084-5000

DTRC-91/002 January 1991
Technical Conference Proceedings

Proceedings of the Sixth International Cryocoolers Conference

Plymouth, Massachusetts
October 25-26, 1990

Volume II

Edited by
Geoffrey Green and
Margaret Knox

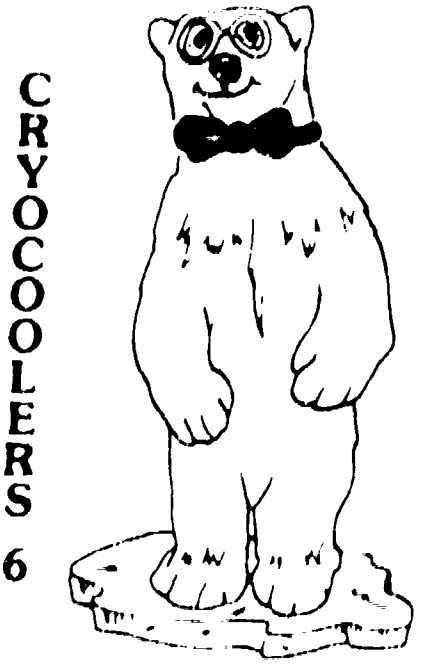

CONFERENCE COMMITTEE

Chairman

Peter J. Kerney
CTI-CRYOGENICS
Waltham, MA 02254–9171
(617) 622–5391

Program Committee

Geoffrey Green, Chairman
David Taylor Research Center
Annapolis, MD 21402–5067
(301) 267–3632

Ronald White, WRDC/FIVEA

Jill Ludwigsen, Nichols Research Corp

Walter Swift, CREARE R&D Inc.

Frank Kadi, Leybold Vacuum Products, Inc.

Local Arrangements

George Y. Robinson, Nichols Research Corp.

Advisory Board

John Barclay
Astronautics

Stephen Castles
NASA/Goddard

Gordon Davey
University of Oxford, U.K.

Alfred Johnson
Aerospace Corp.

Hiroshi Nagano
Toyama University, Japan

Ralph Longsworth
APD-Cryogenics

Martin Nisenoff
Naval Research Laboratory

Joseph L. Smith
MIT

Michael Superczynski
DTRC

Klaus Timmerhaus
University of Colorado

Paul Schelhing
DOE

William Shields
Janis Research Inc.

David Taylor Research Center
Bethesda, MD 20084–5000

DTRC–91/002 January 1991
Technical Conference Proceedings

Proceedings of the Sixth International Cryocoolers Conference

Plymouth, Massachusetts
October 25–26,1990

Volume II

Edited by Geoffrey Green and Margaret Knox
David Taylor Research Center

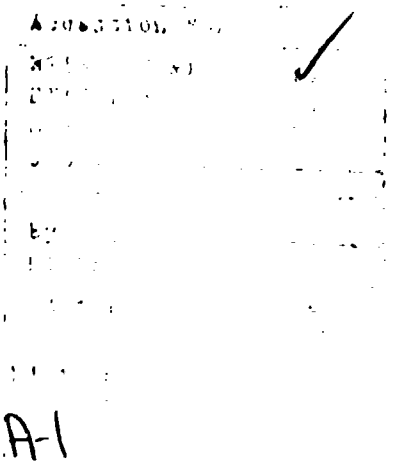

A-1

CONTENTS—VOLUME I

SESSION I: APPLICATIONS

SESSION II: PULSE TUBE AND SORPTION COOLERS

SESSION IIIA—SPACE COOLERS AND SESSION IIIB—REGENERATOR TECHNOLOGY

CONTENTS—VOLUME I (continued)

CONTENTS—VOLUME II (continued)

SESSION VIIA—MAGNETIC COOLERS AND SESSION VIIB—SPACE COOLERS II

Session V — Regenerator/Rare Earth

Chairperson: Hiroshi Nagano, Toyama University

Co-Chairperson: Klaus Timmerhaus, University of Colorado

TWO-STAGE GM REFRIGERATOR WITH Er_3Ni REGENERATOR FOR HELIUM LIQUEFACTION

Toru Kuriyama, Masahiko Takahashi, and Hideki Nakagome
Energy Science & Technology Laboratory
Toshiba Research and Development Center
4-1, Ukishima-cho, Kawasaki-ku, Kawasaki, 210, Japan

Hikaru Seshake, Tatsuji Eda, and Takasu Hashimoto
Department of Applied Physics
Tokyo Institute of Technology
2-12-1, Oh-Okayama, Meguro, Tokyo, 152, Japan

ABSTRACT

This paper describes experimental results obtained from a two-stage Gifford-McMahon (GM) refrigerator which uses Erbium 3 Nickel (Er_3Ni) as the 2nd regenerator matrix. Er_3Ni has a much larger volumetric specific heat than lead (Pb) below about 15 K and has almost the same specific heat as Pb at higher temperature. The purpose of this study was to obtain high refrigeration capacity in the liquid helium temperature region and to confirm the Er_3Ni regenerator reliability. The technical point was to use Er_3Ni spheres. The 0.28 W refrigeration capacity at 4.2 K was obtained and helium was liquefied at the 2nd refrigeration stage. A continuous running test was operated for more than 3,000 hours. Since Er_3Ni spheres were used as the regenerator matrix, no minute Er_3Ni grains, which cause refrigerator performance degradation, were generated and the Er_3Ni regenerator reliability was confirmed. The refrigeration loss mechanism in the liquid helium temperature region is also discussed.

INTRODUCTION

Two-stage GM refrigerators are commonly used in many cryogenic systems, such as cryopumps and shield cooling for MRI (Magnetic Resonance Imaging) magnets. Usually, Pb is preferred as a 2nd regenerator matrix, because of its high heat capacity below about 80 K.

The specific heat for Pb, however, decreases rapidly with decreasing temperature and the heat capacity for a regenerator matrix is no longer much larger than that for helium gas in the liquid helium temperature region. This is why the lowest temperature achieved by a conventional two-stage GM refrigerator is mostly limited to the 8 K level.

To obtain a lower temperature for regenerative cycle refrigerators, utilizing the magnetic specific heat of rare earth compounds has been proposed[1-5]. The authors adopted Er_3Ni[6] as a 2nd regenerator matrix for a two-stage GM refrigerator. The refrigeration performance was extremely improved below 10 K[7].

In this research, Er_3Ni was used as a 2nd regenerator matrix. Displacer reciprocating speed was optimized to obtain high refrigeration capacity in the liquid helium temperature region and Er_3Ni spheres were used to improve the Er_3Ni regenerator reliability. The refrigeration loss mechanism in the low temperature region is also discussed.

EXPERIMENTAL APPARATUS AND RESULTS FOR CONVENTIONAL SIZE TWO-STAGE GM REFRIGERATOR

EXPERIMENTAL APPARATUS

Figure 1 shows the volumetric specific heat for Er_3Ni and Pb. Below about 15 K, the volumetric specific heat for Er_3Ni is much larger than that for Pb. At higher temperature, Er_3Ni has almost the same specific

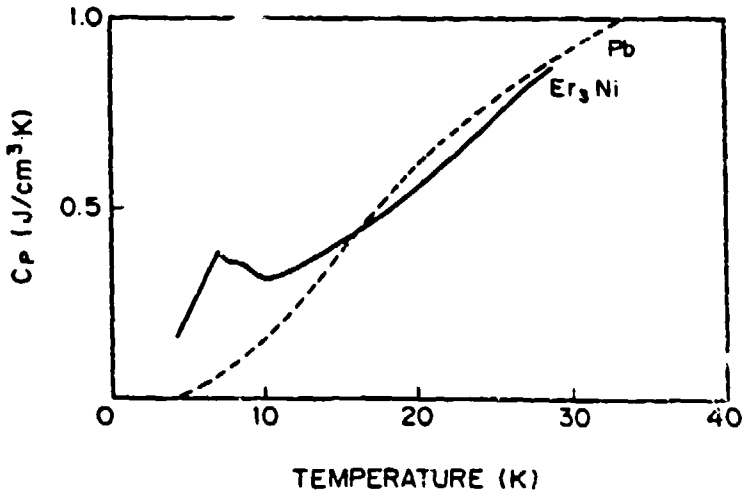

Fig. 1. Volumetric specific heat for Er_3Ni and Pb.

heat as Pb. Though a hybrid structure with Er_3Ni grains and Pb spheres was adopted for the 2nd regenerator in reference 7, in the present work, only Er_3Ni spheres (0.2 to 0.3 mm in diameter, 295 g) were used as the 2nd regenerator matrix. Figure 2 shows a photograph of Er_3Ni spheres[9].

The two stage GM refrigerator used in this paper was the same size as that for a conventional GM refrigerator, which was originally produced by CVI Incorporated. The 2nd cylinder size was 32 mm in diameter and 180 mm in length. The 1st cylinder size was 70 mm in diameter and 220 mm in length. The 1st and the 2nd expansion volumes were 97.4 cm^3 and 25.4 cm^3, respectively.

Figure 3 shows the experimental apparatus layout diagram. The 1st and the 2nd displacers, which included the 1st and the 2nd regenerators, were driven by an AC induction motor. Since a power supply to a driving motor was connected to an electric frequency inverter, the reciprocating speed for the displacer could be varied from 18 to 60 rpm (revolutions per minute). Carbon glass resistance thermometers were placed in contact with the cylinder at both refrigeration stages. An electric heater was also mounted on the 2nd stage, to aid in measuring the refrigeration capacity. Displacement and pressure transducer were mounted, to obtain Pressure-Volume (P-V) diagrams.

To confirm helium liquefaction and condensation by a two-stage GM refrigerator with Er_3Ni regenerator, a small helium chamber was attached to the 2nd refrigeration stage (not shown in Fig. 3). Helium gas was supplied to a helium chamber through a stainless-steel tube, which was thermally anchored to the 1st refrigeration stage.

The compressor unit supplies 2.0 to 2.2 MPa helium gas. Return pressure was 0.6 to 1.0 MPa. The pressure range and helium gas flow rate depended on the operating conditions for a GM refrigerator, such as reciprocating speed and operating temperature. Electric input power to the compressor unit was 3.1 to 3.4 kW.

REFRIGERATION CAPACITY IN THE LIQUID HELIUM TEMPERATURE REGION

First, the authors determined the refrigeration performance in the liquid helium temperature region without a helium chamber. Figure 4 shows the relation between no load temperature and reciprocating speed. Since 2nd stage temperature changes periodically synchronized with reciprocation, 2nd stage temperature in this paper is defined as an

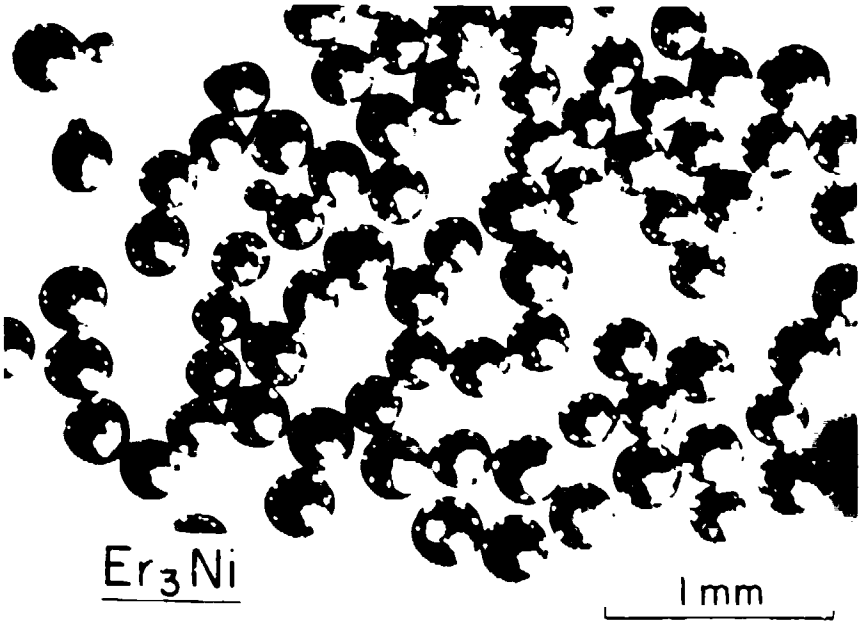

Fig. 2. Er_3Ni spheres used in this study.

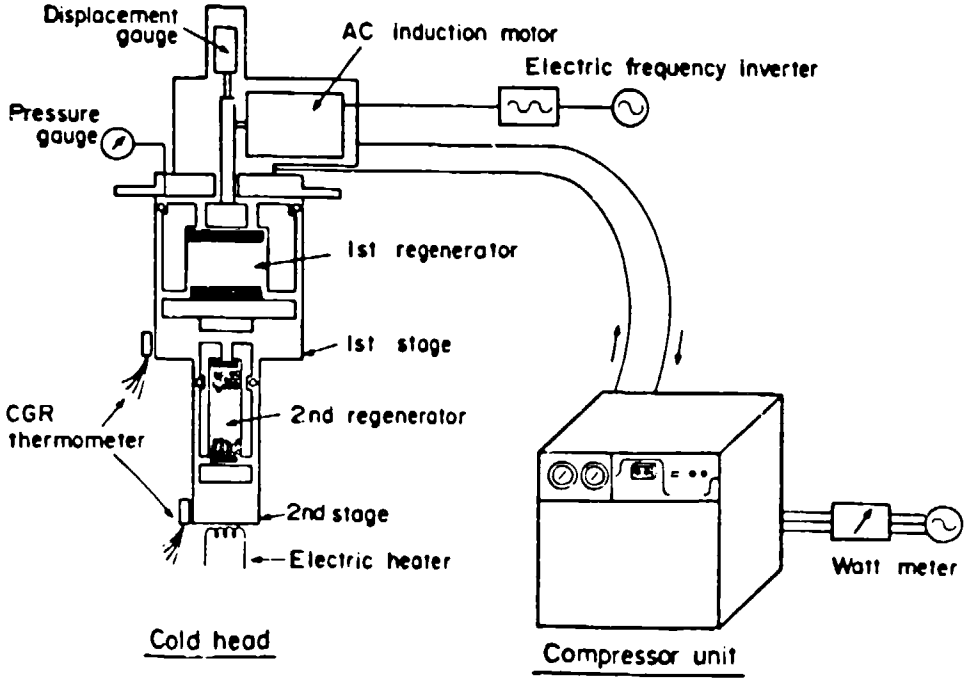

Fig. 3. Experimental apparatus diagram.

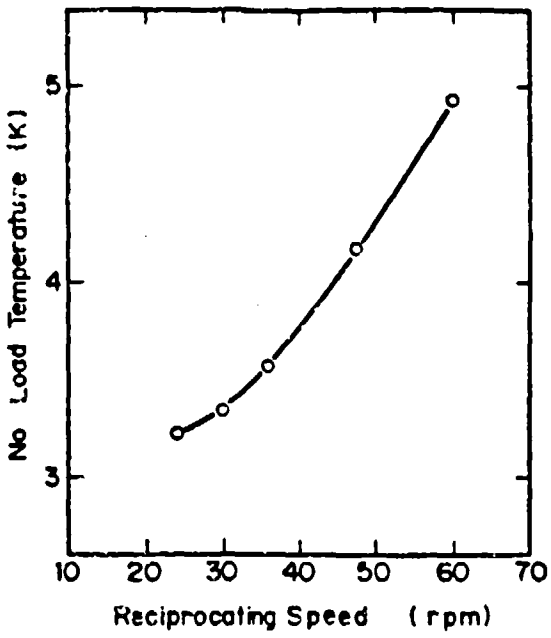

Fig. 4. Relation between no load temperature and reciprocating speed.

average temperature of the highest and the lowest temperatures in one stage refrigeration temperature was between 25 and 30 K. No load temperature, 4.96 K, was achieved by 60 rpm reciprocating speed. The 60 rpm reciprocating speed is a normal operating speed for a conventional GM refrigerator with Pb regenerator (50 Hz) and its no load temperature has been limited to an about 8 K level. The Er_3Ni high heat capacity effect on lowering the refrigeration temperature is shown clearly. The slower reciprocating speed gave the lower no load temperature. The lowest no load temperature, 3.22 K, was achieved by 24 rpm reciprocating speed. In this condition, the temperature change in a cycle was between 3.05 K and 3.39 K.

Figure 5 shows refrigeration capacities for the 2nd stage, obtained by 24, 36, 48, and 60 rpm reciprocating speeds. In the liquid helium temperature region, lower reciprocating speeds, such as 24 or 36 rpm, gave higher refrigeration capacity. At 24 rpm reciprocating speed, the 0.28 W refrigeration capacity was obtained at 4.2 K.

HELIUM LIQUEFACTION AND CONDENSATION

Since high refrigeration capacity at 4.2 K had been obtained, a helium chamber was attached to the 2nd refrigeration stage, to confirm

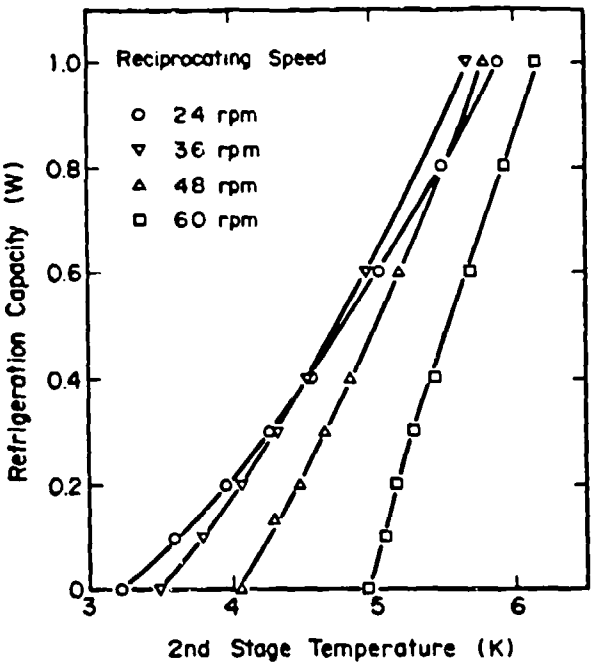

Fig. 5. Refrigeration capacities at the 2nd stage.

the helium liquefaction and condensation by a two-stage GM refrigerator with Er_3Ni regenerator. After cooling down below 4.2 K by 24 rpm reciprocating speed, with vacuum condition in a helium chamber, helium gas was supplied to a helium chamber at about 0.02 MPa. Then, the 2nd stage temperature kept the saturation temperature for the supplied helium gas pressure and the helium liquefaction was confirmed. The calculated helium liquefaction ratio was about 50 cm^3/hr.

When half of a helium chamber was filled with liquid helium, helium gas supply was stopped and the helium chamber inlet valve was closed. In this condition, 2nd stage temperature was equal to saturation temperature for the pressure in a helium chamber. Then, the 2nd stage temperature went down and 3.15 K no load temperature was achieved. Temperature change in a cycle was between 3.10 K and 3.20 K. Due to the high heat capacity of helium in a helium chamber, 2nd stage temperature fluctuation was reduced. Heat load was added to the 2nd refrigeration stage by an electric heater and helium condensation occurred in a helium chamber. Figure 6 shows refrigeration capacity values, obtained with liquid helium and without liquid helium at 24 rpm reciprocating speed. Triangle symbols indicate the refrigeration capacity, obtained with liquid helium. The dotted line indicates the refrigeration capacity for without liquid

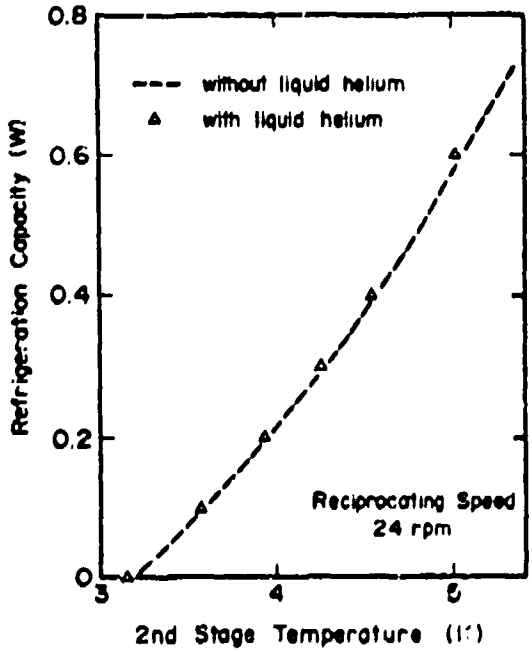

Fig. 6. Refrigeration capacities at the 2nd stage, with liquid helium and without liquid helium.

helium shown in Fig. 5. No marked differences in refrigeration capacity were observed. The 0.28 W refrigeration capacity at 4.2 K has the ability to condense liquid helium at the rate of 390 cm3/hr. This is the first time helium liquefaction and condensation by a two-stage GM refrigerator has been confirmed.

LONG TIME RUNNING TEST

When rare earth compounds are used as regenerator matrices, minute particles are generated, which affect refrigeration performance. In this study, Er_3Ni spheres were used and no minute particles were generated from their surfaces. The authors had carried out a continuous running test at 60 rpm reciprocating speed. During operation, the 2nd stage temperature fluctuation was within 0.3 K. After continuous operation for 3,000 hours, no degradation in refrigeration performance and chemical or physical changes for Er_3Ni spheres were observed. The Er_3Ni regenerator reliability was confirmed.

REFRIGERATION LOSS ANALYSIS AND EXPERIMENTAL RESULTS FOR LONG CYLINDER OF TWO-STAGE GM REFRIGERATOR

REFRIGERATION LOSS ANALYSIS IN THE LIQUID HELIUM TEMPERATURE REGION

The refrigeration loss (Q_{Loss}) was analyzed in the liquid helium temperature region. Q_{Loss} is described with the net refrigeration capacity (Q_{Net}) and the useful refrigeration capacity (Q_{Useful}) as

$$Q_{Loss} = Q_{Net} - Q_{Useful}. \qquad (1)$$

Q_{Useful} is obtained from the heat load added to the 2nd refrigeration stage by an electric heater shown in Fig. 5. Though Q_{Net} is usually calculated from a P-V diagram, helium gas cannot be regarded as an ideal gas in the liquid helium temperature region and helium gas properties must be considered for Q_{Net} calculation[7-9]. Then, Q_{Net} is calculated from a P-V diagram, obtained from a GM refrigerator, and helium gas properties.

The calculated results of Q_{Net} and Q_{Loss} for 24 rpm reciprocating speed are shown in Fig. 7. In this temperature region, Q_{Net} decreases rapidly with decreasing temperature, because of helium gas non-ideality. However Q_{Loss} also decreases with decreasing temperature. Since the calculated losses for heat conduction and shuttle heat transfer are so small, the domestic loss is regenerator loss and the regenerator loss decreases with decreasing temperature. Decrease in the regenerator loss means that the regenerator efficiency increases with decreasing temperature.

To confirm the increase in regenerator efficiency in the low temperature region, the regenerator efficiency was calculated, considering both the specific heat values for the regenerator matrix and for helium gas. Figure 8 shows the calculated results of Er_3Ni regenerator and Pb regenerator efficiencies. The warm end temperature (T_H) is fixed to 32 K and the cold end temperature was changed as a parameter. High and low pressure helium gas flow values were 20 atm and 0 atm, respectively. The regenerator efficiency for Er_3Ni regenerator increases with decreasing cold end temperature below about 7 K. This tendency is caused by an enthalpy imbalance for high and low pressure helium gas flow in the regenerator and explains the Q_{Loss} decreasing in the low temperature region as shown in Fig. 7.

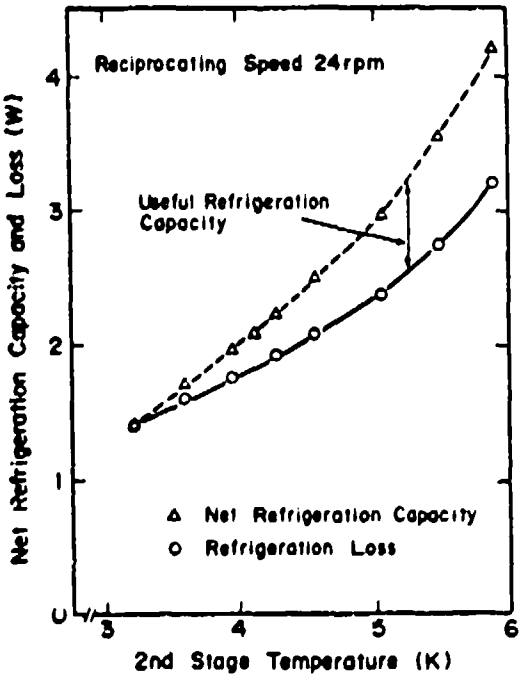

Fig. 7. Calculated results showing net refrigeration capacity and refrigeration loss.

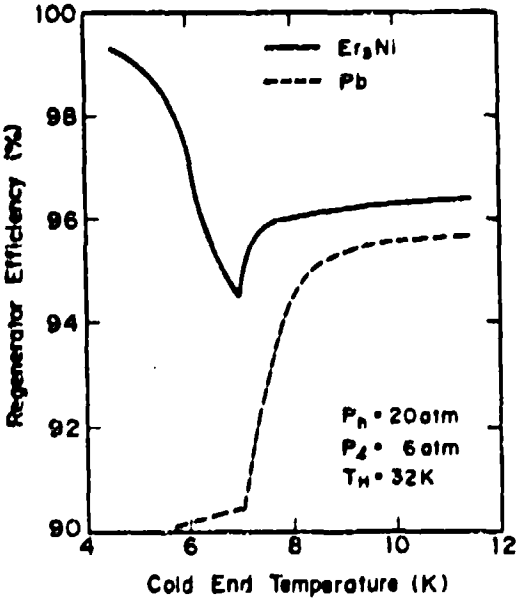

Fig. 8. regenerator efficiencies calculated for Er_3Ni regenerator and Pb regenerator.

EXPERIMENTAL RESULTS FOR LONG CYLINDER

According to the refrigeration loss analysis mentioned above, it had been expected that the higher regenerator efficiency would improve the refrigeration performance in the liquid helium temperature region. The regenerator efficiency was calculated as a parameter of Er_3Ni amount. Calculation results show that increase in Er_3Ni amount improve regenerator efficiency. Then, another 2nd cylinder and regenerator pair was made and investigated. The 2nd cylinder was 260 mm in length, which was 80 mm longer than that for conventional cylinder (180 mm) investigated before. However other dimensions, such as 1st cylinder length or diameter, and expansion volumes were the same as for a conventional cylinder. The new regenerator was also 80 mm longer and filled with 565 g Er_3Ni spheres, which was about twice as much as that for conventional regenerator (295 g). Figure 9 shows the relations between no load temperature and reciprocating speed. The circle symbols indicate no load temperatures for conventional cylinder (180 mm), shown in Fig. 4. The triangle symbols indicate no load temperatures for the new cylinder (260 mm). The 1st refrigeration stage temperature was between 30 and 43 K. No

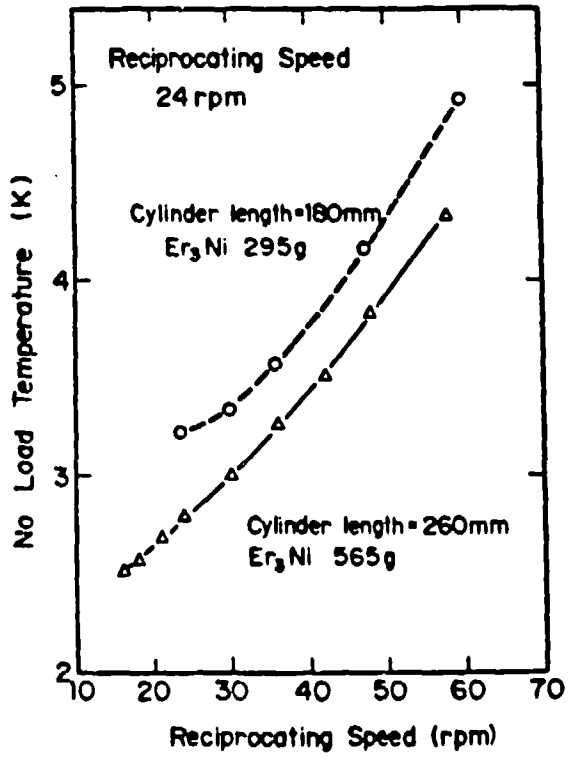

Fig. 9. Relation between no load temperature and reciprocating speed.

load temperature for the new cylinder was lower than that for a conventional cylinder, at the same reciprocating speed. For the new cylinder, the lowest temperature, 2.52 K, was achieved at 18 rpm reciprocating speed. The regenerator matrix quantity effect on the refrigeration performance was shown clearly in the liquid helium temperature region.

CONCLUSIONS

A two-stage GM refrigerator, which used Er_3Ni spheres as the 2nd regenerator matrix, was investigated. The following conclusions were drawn from the investigation results.

(1) High refrigeration capacity in the liquid helium temperature region, such as 0.28 W at 4.2 K, was obtained by 24 rpm reciprocating speed. Helium liquefaction and condensation were also confirmed.

(2) After continuous running test for 3,000 hours, no refrigeration capacity degradation was observed and the reliability for Er_3Ni regenerator was confirmed.

(3) In the liquid helium temperature region, the refrigeration loss decreased with decreasing temperature. This phenomena was explained by the increase in regenerator efficiency, which was caused by an enthalpy imbalance between high and low pressure helium gas flow in the regenerator.

(4) Domestic refrigeration loss in the liquid helium temperature region was regenerator loss. An increase in regenerator efficiency improved refrigerator performance. For example, the lowest temperature went from 3.22 K to 2.56 K by increasing the amount for the regenerator matrix.

REFERENCES

1. A. Daniels et al., "Triple-expansion Stirling-cycle refrigerator," Adv. Cryog. Eng. vol.16, (1971), pp. 178-184.
2. Y. Matsubara et al., "Vuilleumier cycle cryocooler operating below 8 K," in: Proc. 3rd Cryocooler Conf., National Bureau of Standards, (1985), pp. 234-239.
3. H. Nakashima et al., "Development of a 4-5 K cooling Stirling cycle refrigerator," Proc. 4th Cryocooler Conf., David Taylor Naval Ship, pp. 263-271.

4. T. Kuriyama et al., "Development of a 5K refrigerator using rare earth compounds as a regenerator matrix," in: Proc. Intl. Conf. on Cryogenics and Refrigeration, Beijing, China (May 1989), pp. 91-96.
5. M. Nagao et al., "Helium liquefaction by a Gifford-McMahon cycle cryocooler," Adv. Cryog. Eng. vol.35, (1989), pp. 1251-1260.
6. M. Sahashi et al., "New magnetic material R_3T system with extremely large heat capacities used as heat regenerators," Adv. Cryog. Eng. vol.35, (1989), pp. 1175-1182.
7. T. Kuriyama et al., "High efficient two-stage GM refrigerator with magnetic material in the liquid helium temperature region," Adv. Cryog. Eng. vol.35, (1989), pp. 1261-1269.
8. R. Radebaugh, "Prospect for small cryocoolers," Proc. ICEC-9, Kobe, Japan (May 1982), pp.761-765.
9. G. Chen, et al. "The influence of non-ideal effects of actuating medium on the performance of a plastic cryocooler," Proc. ICEC-12, Southampton, UK (July 1984), pp.571-575.

HIGH EFFICIENT 4 K REFRIGERATOR (GM REFRIGERATOR WITH JT CIRCUIT) USING Er_3Ni REGENERATOR

Hideki Nakagome, Ryuichi Hakamada,
Masahiko Takahashi, and Toru Kuriyama
Energy Science & Technology Lab.
Research and Development Center
TOSHIBA CORPORATION
4-1,Ukishima-cho,Kawasaki-ku,Kawasaki,210,Japan

ABSTRACT

A highly efficient 4 K GM/JT refrigerator has been developed. The technical point of the refrigerator is that Erbium 3 Nickel (Er_3Ni) spheres are used as the 2nd regenerator matrix for the GM refrigerator, to obtain a lower pre-cooling temperature for the JT circuit.

The thermodynamic cycle analysis for the JT circuit shows that the lower pre-cooling temperature of the GM 2nd stage and the lower inlet pressure for the JT circuit give a higher 3rd stage refrigeration capacity. For example, if the GM 2nd stage temperature goes down, from 16 K to 11 K, and the inlet pressure for the JT circuit is reduced from 1.8 MPa to 1.4 MPa, the 3rd stage refrigeration capacity per unit mass flow increases by about 30 % and the JT compressor reliability will be significantly improved by lowering the compression ratio.

The authors have examined the performance of the GM/JT refrigerator with Er_3Ni regenerator by changing the inlet pressure and the mass flow rate for the JT circuit. A maximum refrigeration capacity of 5.6 W at 4.5 K and a calculated figure of merit (FOM) of 1025 has been achieved.

INTRODUCTION

This paper presents the experimental results determined for a 4 K GM/JT refrigerator, which uses Er_3Ni for the GM 2nd regenerator matrix. The thermodynamic cycle analysis shows that the refrigeration capacity of the GM/JT refrigerator increases, when the JT circuit pre-cooling

temperature at the GM 2nd stage decreases.

The Er_3Ni regenerator GM refrigerator has a lower refrigeration temperature at the 2nd stage, compared with the lead (Pb) regenerator GM refrigerator. Therefore, the GM/JT refrigerator with Er_3Ni regenerator is expected to have a larger cooling capacity and a higher refrigeration efficiency than the conventional GM/JT refrigerator with Pb regenerator.

Recently, development efforts on a GM refrigerator with magnetic material for the regenerator matrix are growing[1-5]. By using a two stage GM refrigerator with Er_3Ni regenerator, the lowest temperature, 2 Kelvin level, and the 0.28 W refrigeration power at 4.2 K were accomplished[6]. The spherical particles for the Er_3Ni regenerator matrix were also fabricated. By using the spheres, more than 3000 hours continuous operation has been successfully achieved, with no refrigeration performance degradation.

The GM/JT refrigerator is used for cooling cryogenic systems, for example MRI system, SQUID system, and SIS mixer[7-10]. The less than 5 W refrigeration capacity is usual for the presently commercially available GM/JT refrigerator. Recently, however, the need for a larger capacity refrigerator is growing. This paper presents the first experimental results of the development program for the large capacity GM/JT refrigerator.

THERMODYNAMIC CYCLE ANALYSIS

Figure 1 shows the flow diagram for the GM/JT refrigerator. In the JT circuit, high pressure helium gas (about 1.8 MPa) is cooled by 3 counter flow heat exchangers and 2 heat exchangers at stages in the GM refrigerator. Then, the high pressure helium gas expands to about 0.1 MPa at the Joule-Thomson valve. After absorbing heat at the 3rd stage, the low pressure helium gas returns to the compressor through 3 counter flow heat exchangers. When the 3rd stage heat load is 5 W, the heat load to the GM refrigerator is estimated as 6 to 8 W for the 2nd stage and as 20 to 25 W for the 1st stage, respectively.

Figure 2 shows a lower part of the flow diagram for the JT circuit and the temperature-entropy (T-S) diagram for helium. High pressure helium gas flows through the 3rd heat exchanger (Ta-Tb), and then expands, according to the iso-enthalpy curve at the JT valve (Tb-Tc). After that, heat (Q_3) is absorbed at the 3rd stage (Tc-Td). Then, the low pres-

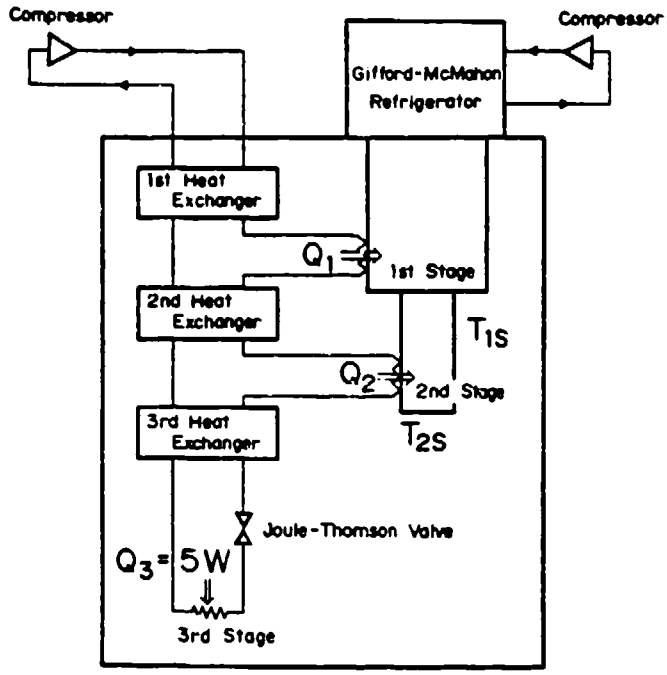

Fig. 1. GM/JT refrigerator flow diagram.

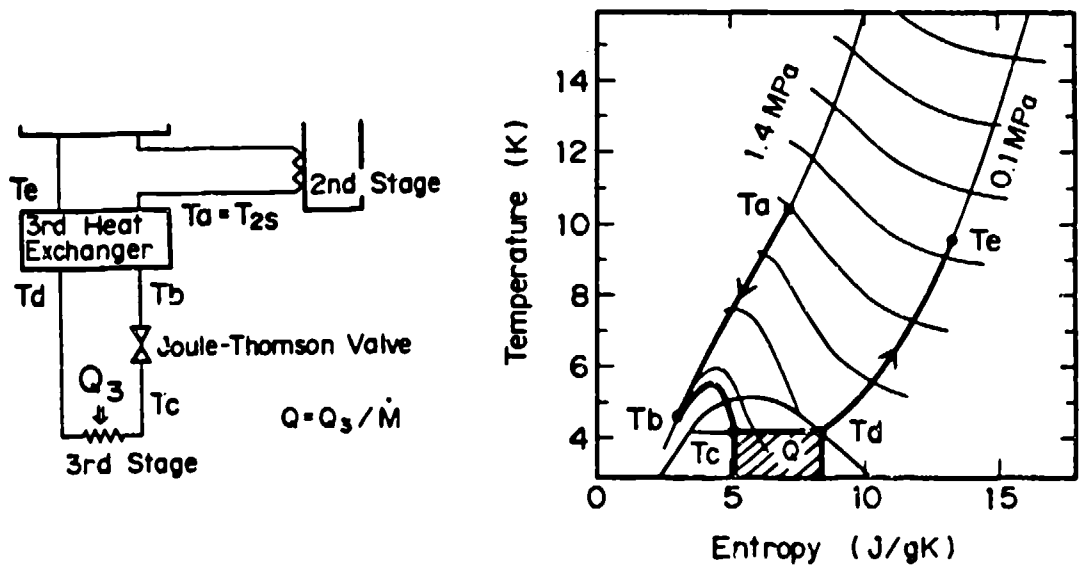

Fig. 2. Temperature-entropy (T-S) diagram for hellum.

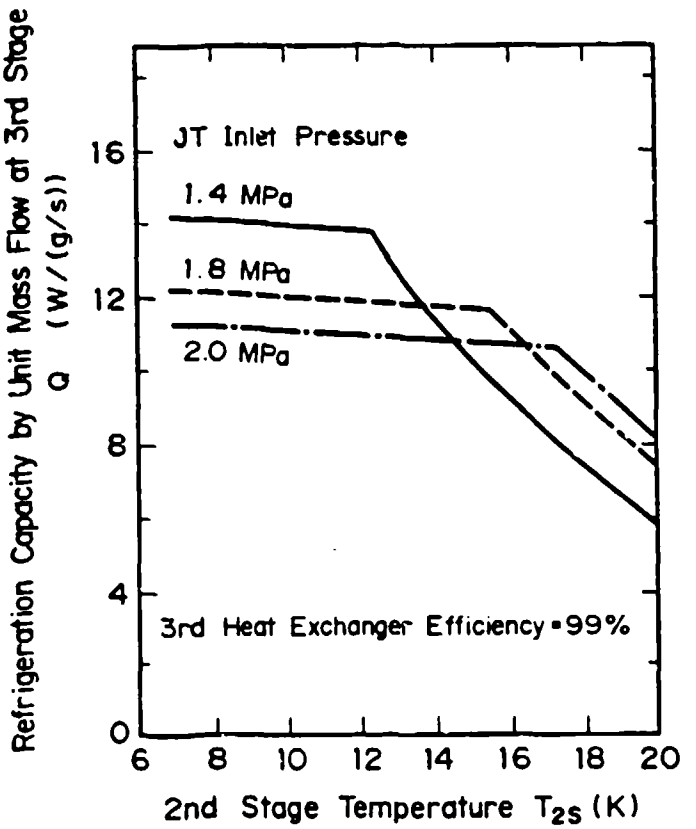

Fig. 3. Calculated refrigeration capacity by unit mass flow, as a function of 2nd stage temperature.

sure gas returns through the 3rd heat exchanger (Td-Te). When Ta and Td are given, other points on the T-S diagram are determined. So, if Td is fixed, the Ta and Q relation is calculated from the TS diagram. The results, calculated by changing the JT circuit inlet pressure, are shown in Fig. 3. In the 2nd stage temperature region, 8-13K, the refrigeration capacity (Q_3) increases when the JT inlet pressure decreases. According to these results, the authors designed the operation points for a GM/JT refrigerator, which uses Er_3Ni as a regenerator matrix.

DESIGN AND CONSTRUCTION

The experimental apparatus consists of GM refrigerator, JT circuit, GM compressor, and JT compressor.

The GM refrigerator uses Er_3Ni spheres as the 2nd regenerator matrix. The electrical power consumption for the compressor was about

3.2 kW.

The efficiency of counter flow heat exchangers for the JT circuit has been maintained at at least 98 %, up to the about 0.6 g/s mass flow rate. The large compressor unit, equipped with a bypass line and the inlet/outlet pressure regulator, is used for the JT circuit operation. The net electrical input power to the JT compressor for each experimental condition is calculated by the inlet/outlet pressure, the mass flow rate, and the assumed compressor efficiency (55 %).

GM REFRIGERATOR COOLING CAPACITY

The GM refrigerator refrigeration temperature is very important for the present GM/JT refrigerator operation. Figure 4 shows the relation between 1st and 2nd stage temperatures for a GM refrigerator, taken by

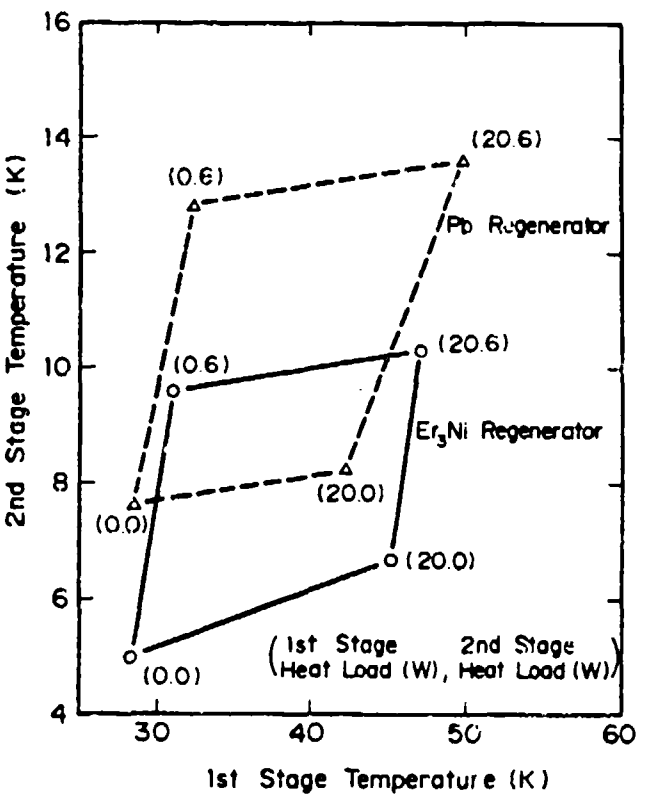

Fig. 4. Relation between 1st and 2nd stage temperature for a GM refrigerator.

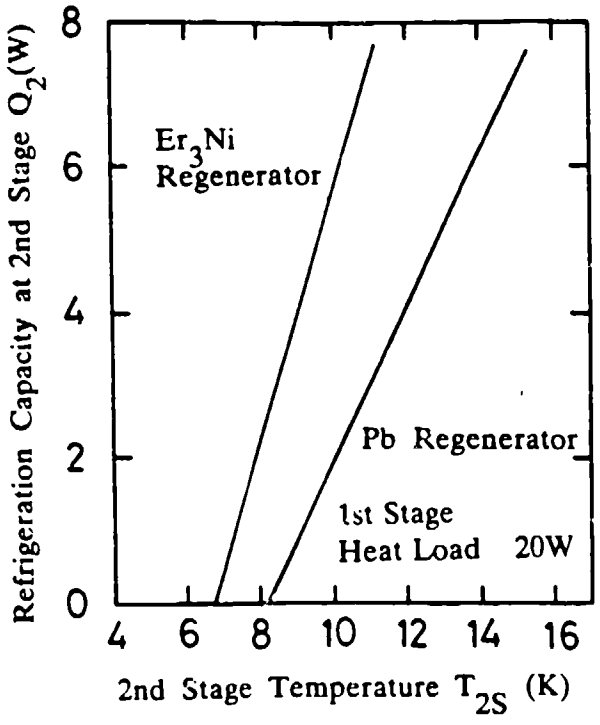

Fig. 5. Refrigeration capacity at 2nd stage of GM refrigerator for Er_3Ni regenerator and Pb regenerator.

imposing the heat load to both stages. The 2nd stage temperature for the Er_3Ni regenerator GM refrigerator drops significantly, compared with the Pb regenerator GM refrigerator. To recognize the differences between Er_3Ni and Pb regenerator more clearly, Figure 5 shows the 2nd stage refrigeration capacity values for both regenerators under the Q1=20 W condition. When the heat load to the 2nd stage is 6-8 W, the refrigeration temperature becomes 10-12 K for the Er_3Ni regenerator, and 14-16 K for the Pb regenerator.

GM/JT REFRIGERATOR REFRIGERATION CAPACITY

The refrigeration capacity for the GM/JT refrigerator, which uses the Er_3Ni regenerator, has been measured by changing the inlet pressure and the mass flow rate for the JT circuit. Figure 6 shows a typical refrigeration capacity curve when inlet pressure is 1.4 MPa and mass flow rate is 0.3 g/s.

The experimental results are compared with thermodynamic cycle

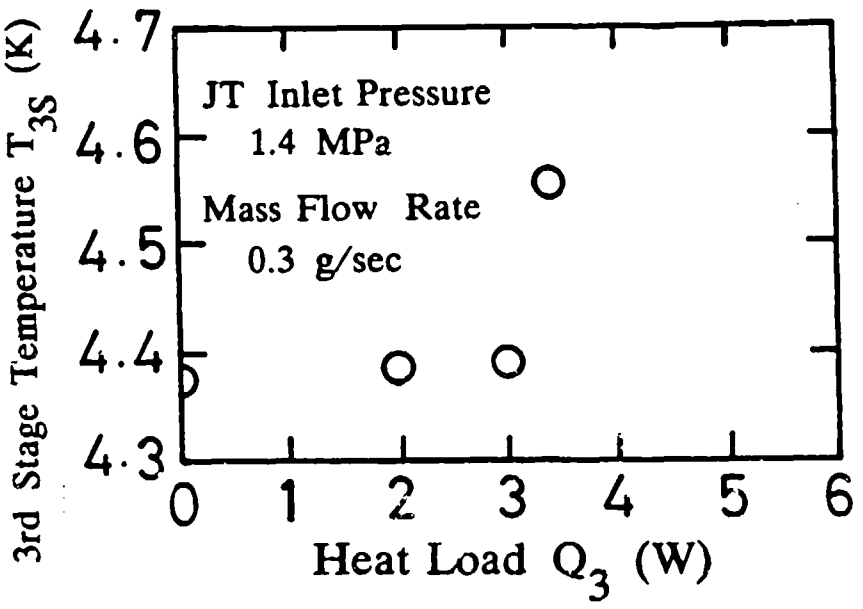

Fig. 6. Typical refrigeration capacity curve.

analysis in Fig. 7 and Fig. 8 for 1.4 MPa and 1.6 MPa inlet pressure, respectively. The difference between experimental and calculated values is explained by the discrepancy in the GM 1st stage temperature and the counter flow heat exchanger efficiencies, which are assumed as being constant values for the calculation. However the tendency for experimental data and calculated values is similar for both inlet pressures. It was confirmed that the decrease in the 2nd stage temperature and the decrease in the JT inlet pressure are effective for the increase in refrigeration capacity.

Figure 9 shows some typical experimental data. The calculated input power has been introduced from the input power of the GM compressor and the net input power for the JT compressor, which has been calculated from inlet/outlet pressure, mass flow rate, and assumed compressor efficiency (55 %). The maximum refrigeration capacity by unit mass flow was 0.63 W/(g/s)(experiment 1). The maximum refrigeration capacity of 5.64 W and the highest FOM of 1025 has been achieved (experiment 2). The Er_3Ni regenerator usefulness for the GM/JT refrigerator has been clearly demonstrated.

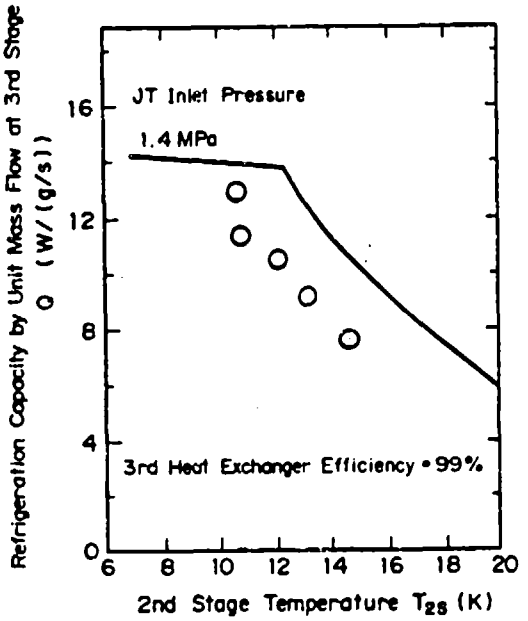

Fig. 7. Refrigeration capacity by unit mass flow rate as a function of 2nd stage temperature (JT inlet pressure 1.4 MPa).

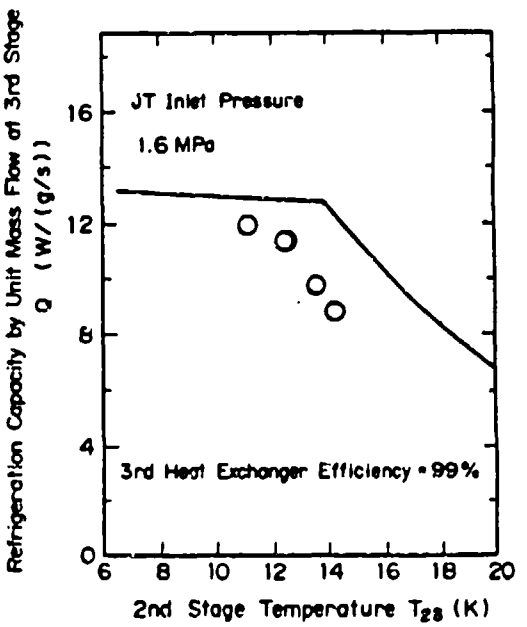

Fig. 8. Refrigeration capacity by unit mass flow rate as a function of 2nd stage temperature (JT inlet pressure 1.6 MPa).

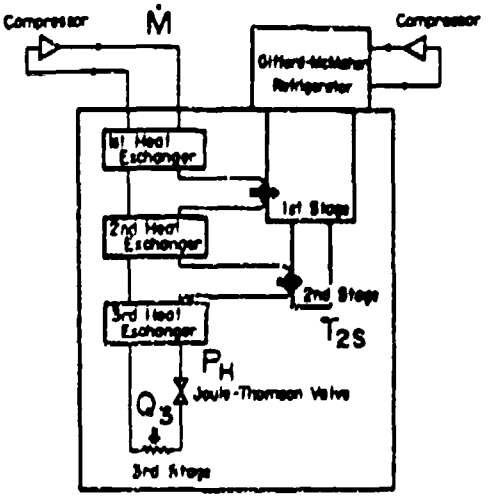

	Design Point	Experiment 1	Experiment 2
Q_3 (W)	5.0	4.61	5.64
T_{2S} (K)	12	11.0	12.4
P_H (MPa)	1.4	1.39	1.66
$\dot{M}$ (g/s)	0.36	0.355	0.50
$Q=Q_3/\dot{M}$	13.8	12.6	11.4
Calculated Input Power (kW)	5.2	4.99	5.78
Calculated FOM	1040	1106	1025

Fig. 9. Typical experimental data.

CONCLUSION

The 4 K GM/JT refrigerator, which uses an Er_3Ni regenerator for the GM cycle has been studied. The experimental results show the high refrigeration efficiency.

The thermodynamic cycle analysis for the JT circuit proved that the lower pre-cooling temperature for the GM 2nd stage temperature and the lower inlet pressure for the JT circuit give the higher 3rd stage refrigeration capacity.

The real refrigeration capacity, determined by unit mass flow, shows a similar tendency to that for the analysis results.

The maximum refrigeration capacity achieved by unit mass flow, was 0.63 W/(g/s), and the maximum refrigeration capacity, 5.64 W, and 1025 FOM have been achieved.

REFERENCES

1. T. Kuriyama et al, "Development of a 5K GM refrigerator using rare earth compounds as a regenerator matrix," Proc. Intl. Conf. on Cryogenic and Refrigeration,International Academic Publishers, Beijing, China (1989), p.91.
2. M. Sahashi et al, "Regenerative material R3T system with extremely large heat capacity between 4K to room temperature," Proc. Intl. Conf. on Cryogenic and Refrigeration, International Academic Publishers, Beijing, China (1989), p.131.
3. T. Kuriyama et al,"Development of a two-stage GM refrigerator with rare earth matrix for cooling superconducting devices," Proc. Tenth Intl. Work shop on Rare-Earth Magnets and their Application, The Society of Non-Traditional Technology, Minato-ku, Tokyo, Japan (1989), p.335.
4. M. Nagao et al, "3.3K three stage Gifford-McMahon cycle cryocooler using rare-earth regenerator, Proc. Tenth Intl. Work shop on Rare-Earth Magnets and their Application, The Society of Non-Traditional Technology, Minato-ku, Tokyo, Japan (1989), p.325.
5. T. Kuriyama et al, "High efficient two-stage GM refrigerator with magnetic material in the liquid hellum temperature region," Advances in Cryogenic Engineering, Vol.35, Plenum Press, New York (1990), p.1261.
6. T. Kuriyama et al, "Two-stage GM refrigerator with Er3Ni regenerator for hellum liquefaction," Presented at 6th International Cryocooler Conference.
7. Ralph C. Longthworth, "4 K refrigerator and interface for MRI cryostats," Advances in Cryogenic Engineering, Vol.31, Plenum Press, New York (1986), p.517.
8. F. Scott Murray et al, "Refrigerator operating experience on whole body MRI magnet systems," Advances in Cryogenic Engineering, Vol.31, Plenum Press, New York (1986), p.525.
9. Yoon-Mung Kang et al, "Development of a 4K GM/JT cryocooler," Proceedings of the 12th International Cryogenic Engineering Conference, Butterworths, (1988), p.582.
10. G.Claudet et al, "3 K closed cycle refrigerator for SIS receivers at millimeter wavelength," Proceedings of the 12th International Cryogenic Engineering Conference, Butterworths, (1988), p.592.

TWO-STAGE GIFFORD-MCMAHON CYCLE CRYOCOOLER OPERATING AT ABOUT 2 K

Takashi Inaguchi, Masashi nagao, and Hideto Yoshimura
Central Research Laboratory, Mitsubishi Electric Corporation
Tsukaguchi-Honmachi 8-chome, Amagasaki, Hyogo, 661 Japan

ABSTRACT

A two-stage Gifford-McMahon (G-M) cycle cryocooler operating at about 2 K has been developed. The main features of this G-M cryocooler are to use a rare earth compound as the regenerator material, and to operate the G-M cryocooler at the optimum cycle frequency. The no-load temperature of 2.41 K has been achieved when the cycle frequency is 20 rpm. The maximum net cooling capacity at 4.2 K was 0.8 W when the cycle frequency was 45 rpm. This paper describes the principal design features and performance of the two-stage G-M cryocooler.

INTRODUCTION

It has recently become possible to generate net cooling capacity at 4.2 K (boiling point of helium at 101.3 kPa) by G-M cryocoolers[1-5]. This is due to the discovery of regenerator materials such as $Gd_xEr_{(1-x)}Rh$[6] and Er_3Ni[7], which have enough specific heat below 10 K. However, the net cooling capacity at 4.2 K was very small and it has been needed to increase net cooling capacity at 4.2 K for practical use.

We tried to increase net cooling capacity at 4.2 K by a two-stage G-M cryocooler, using Er_3Ni as regenerator material. By optimizing cycle frequency, we could decrease no-load temperature of the G-M cryocooler to 2.41 K (mean temperature) and remarkably increase the net cooling capacity at 4.2 K.

The performance of this two-stage G-M cryocooler depends on cycle frequency. Cycle frequency has a great influence on no-load temperature, not cooling capacity, and indicated work of the cryocooler.

Therefore, we investigated the effect of cycle frequency on no-load temperature and indicated work, changing the cycle frequency from 15 rpm to 72 rpm. Also, we investigated the effect of cycle frequency on the net cooling capacity of the second stage, changing cycle frequency from 30 rpm to 60 rpm.

In this paper, we describe the main features of the two-stage G-M cryocooler and the instruments of experiments. Then we show the experimented results.

EXPERIMENTED METHOD

EXPERIMENTAL MACHINE

Figure 1 shows schematic view of the experimental machine. The experimental machine is a two-stage G-M cryocooler. The difference between our G-M cryocooler and an usual G-M cryocooler on the market is in regenerators. The first regenerator has two layer structure. In the high temperature part, we stacked phosphor bronze screens whose number of mesh is 150. In the low temperature part, we packed lead shots whose diameter is 0.3 mm~0.5 mm with a porosity factor of 0.33. The specific heat of lead is larger than that of phosphor bronze below 50 K. Therefore we selected lead in the low temperature part of the first regenerator.

The second regenerator was composed of Er_3Ni grains. The grain size was 0.2 mm~0.5 mm. The porosity factor of the second regenerator was 0.46. Figure 2 shows the specific heat of Er_3Ni[7] compared to the specific heat of GdRh[6], lead, and helium at constant pressure (2 MPa and 0.5 MPa). The specific heat of Er_3Ni is almost the same as that of GdRh at about 4 K. Also, though the specific heat of GdRh sharply decreases above 20 K, the specific heat of Er_3Ni monotonously increases above 20 K and it is almost the same as the specific heat of lead above 20 K. This is the reason that we selected Er_3Ni as the second regenerator material of the cryocooler. In Figure 2, 2 MPa is the intake pressure of the G-M cryocooler and 0.5 MPa is the exhaust pressure. We can notice the specific heat capacity of helium at constant pressure is the largest at 4.2 K.

The displacers are made of cotton reinforced phenolic resin and they reciprocate with a Scotch Yoke mechanism by a stepping motor. The stroke is 3.17 cm. In order to change cycle frequency, we changed a rotational speed of a stepping motor by changing pulse number generated at pulse generator.

The cylinder is made of stainless steel. The diameter of the first expansion space in the cylinder is 61.9 mm and that of the second expansion space is 40 mm.

The performance of seals has a great influence on performance of a G-M cryocooler. We selected a capseal for the first displacer and a piston ring for the second displacer. Both seals are made of glass loaded Teflon.

The compressor which we used in this experiment was CTI-CRYOGENICS model 1020RW.

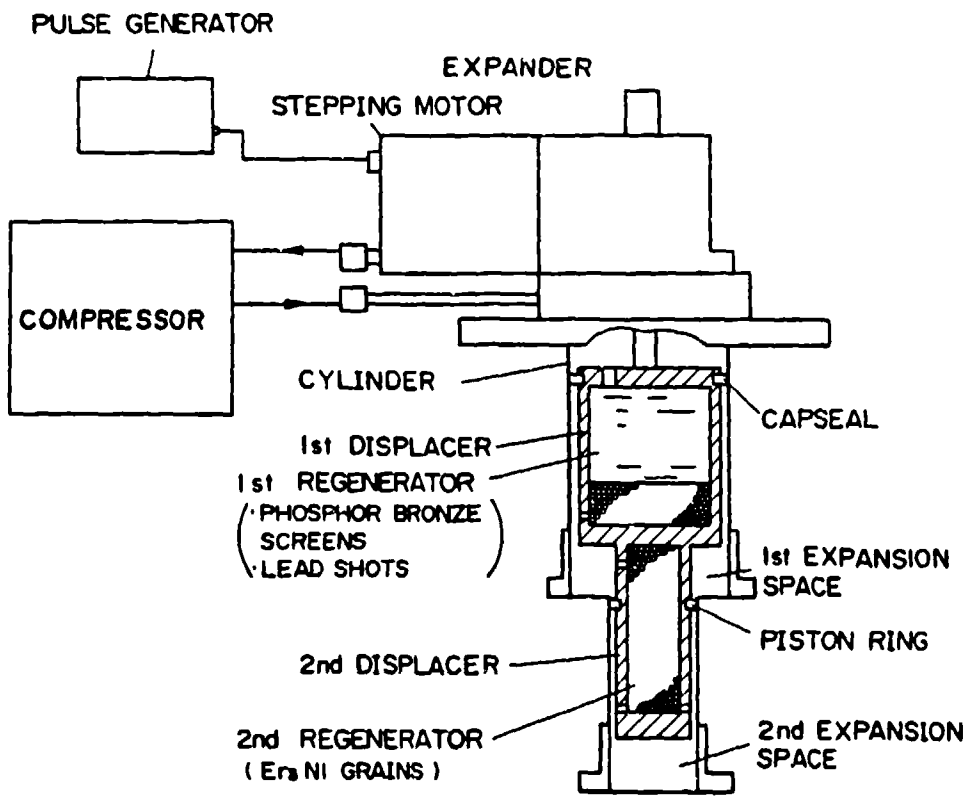

Fig.1. Schematic view of the two-stage Gifford-McMahon cycle cryocooler

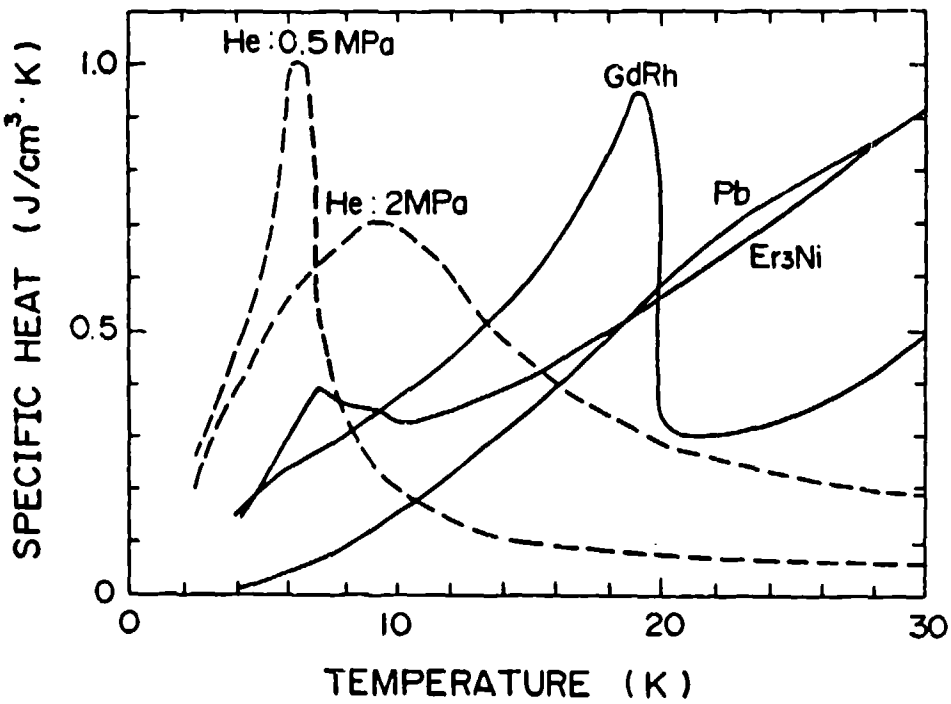

Fig. 2. Specific heat of Er_3Ni compared with specific heat of GdRh, lead, and helium at constant pressure(2MPa and 0.5MPa)

INSTRUMENTS

The experimental apparatus is shown in Figure 3. The two-stage G-M cryocooler was investigated in a vacuum chamber. A radiation shield made of copper was attached to the first stage, and it enclosed the second stage to prevent the radiant heat from room temperature to the second stage. The temperature of the first stage was measured using a Pt-Co resistance sensor. The temperature of the second stage was measured using a calibrated germanium resistance sensor below 10 K and it was measured using a Pt-Co resistance sensor above 10 K. A Pt-Co or germanium resistance sensor was inserted into the hole, which we made in the first or second stage.

We measured net cooling capacity by loading heat of a heater to the second stage. As a heater, a cartridge heater was used and it was inserted into the hole, which we made in the second stage.

We also measured P-V diagrams of the second expansion space and obtained indicated works. In order to measure pressure of the second expansion space we made a hole in the bottom of the second stage and brazed a capillary tube at the bottom. This capillary tube is made of stainless steel. The inside diameter is 0.2 mm and the wall thickness 0.1 mm. The capillary tube was connected with a pressure transducer at room temperature and pressure was measured. The movement of displacers was measured by a linear displacement converter. The pressure and the movement were simultaneously measured.

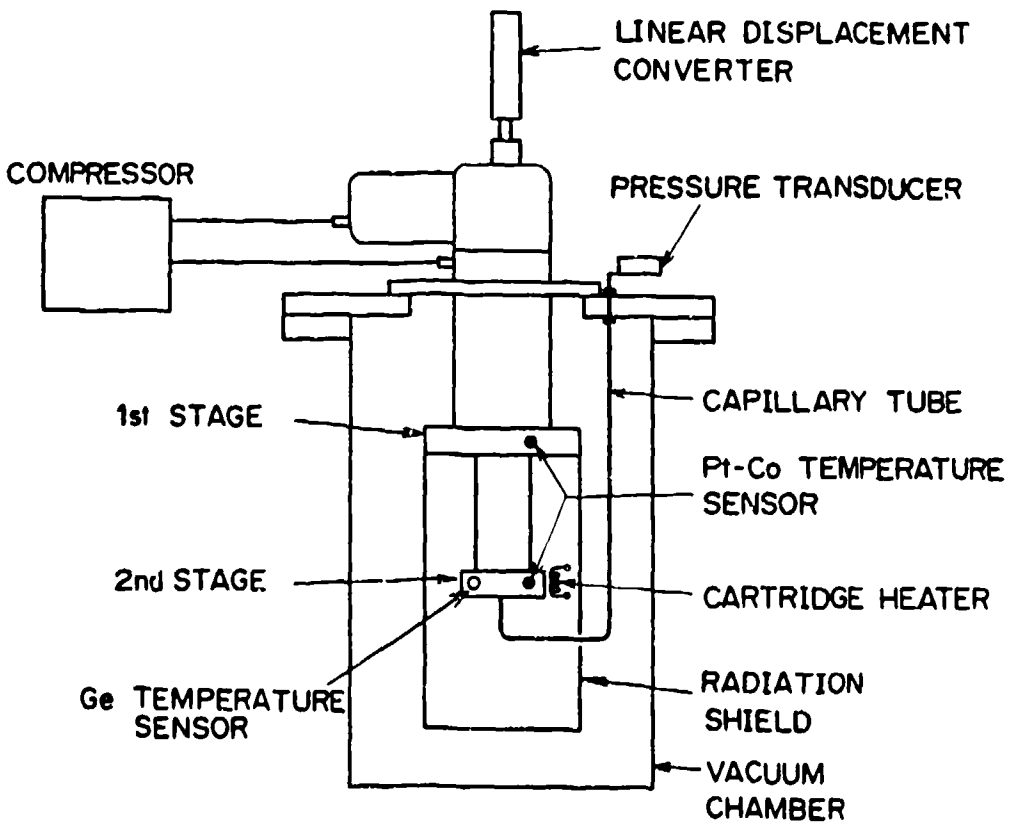

Fig.3. Experimental apparatus

EXPERIMENTED RESULTS

COOL-DOWN PROCESS

Figure 4 shows the cool-down process of each stage of the cryocooler. The operation was done at the cycle frequency of 45 rpm. The rate of temperature change at the second stage was larger than at the first stage until 50 minutes had passed from the start of the operation. After that, the rate of temperature change at the second stage decreased. The temperature of the second stage is about 10 K in 50 minutes. The specific heat capacity of helium become larger than that of Er_3Ni below about 10 K (Fig.2). The performance of the second regenerator decreases. Therefore the rate of temperature change at the second stage decreases. It took about 210 minutes for both stages to reach a steady state. When both stages reached the steady state, the temperature of the first stage was 27.8 K, and that of the second stage was 2.8 K (mean temperature).

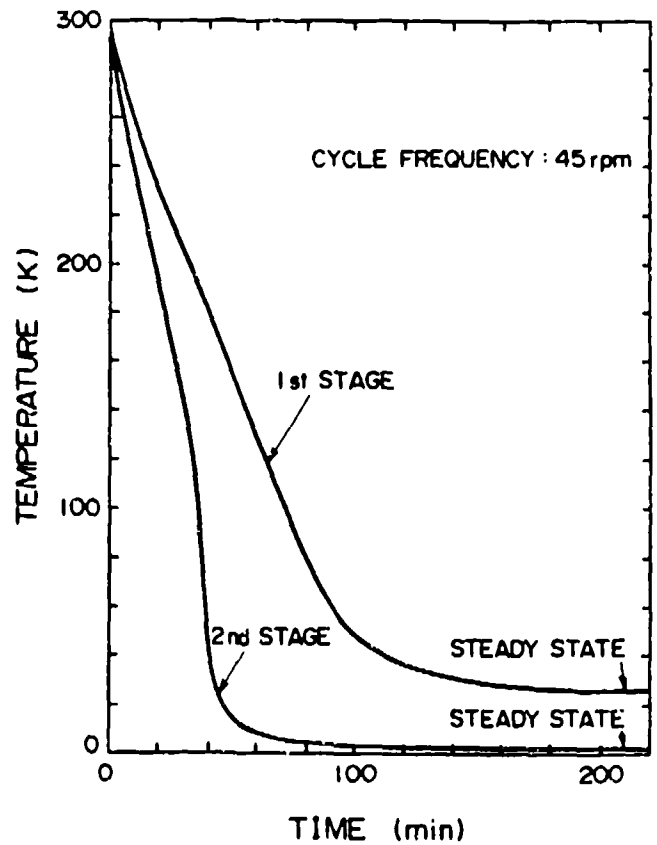

Fig.4. Cool-down process of each stage of the two-stage G-M cryocooler

NO-LOAD TEMPERATURE

Effect of Cycle Frequency on No-Load Temperature

Figure 5 shows effect of cycle frequency on no-load temperature. The no-load temperatures of the first and second stages depend on cycle frequency. The optimum cycle frequency for each stage exists. The no-load temperature of the second stage became lowest when the cycle frequency was 20 rpm, and the temperature was 2.41 K (mean temperature). The no-load temperature of the first stage became lowest when the cycle frequency was about 40 rpm, and the temperature was 27.3 K. The optimum cycle frequency for the no-load temperature of the first stage is 20 rpm higher than that for the no-load temperature of the second stage.

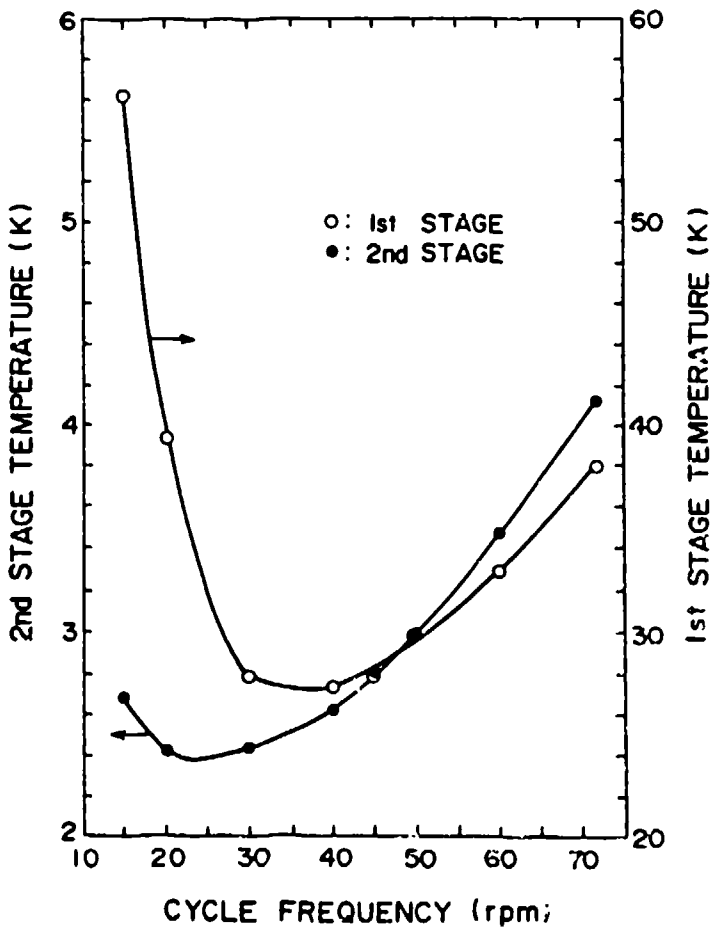

Fig.5. Effect of cycle frequency on no-load temperature

Effect of Cycle Frequency on Indicated Work

Figure 6 shows the effect of the cycle frequency on the indicated work of the second expansion space at the no-load temperature. The indicated work was 30 W at the cycle frequency of 45 rpm. As cycle frequency increased, the indicated work increased. But the increase rate was not linear. Because the capacity of the compressor become insufficient as cycle frequency increases.

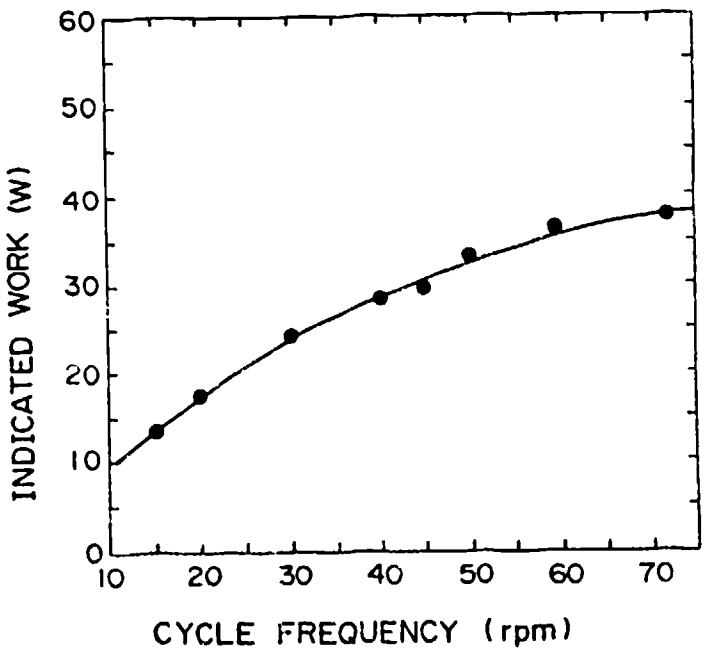

Fig.6. Effect of cycle frequency on indicated work

Temperature Swing

The temperature of the second stage periodically swings in accordance with inflow and outflow of helium to the expander. We call this swing the temperature swing. Figure 7 shows temperature swings of the second stage and the pressure change of the second expansion space. The cryocooler operated at the cycle of 20 rpm. The number inside the ○ in Figure 7 indicates opening and shutting timing of the intake and exhaust valves, and it coincides with the number in the text.

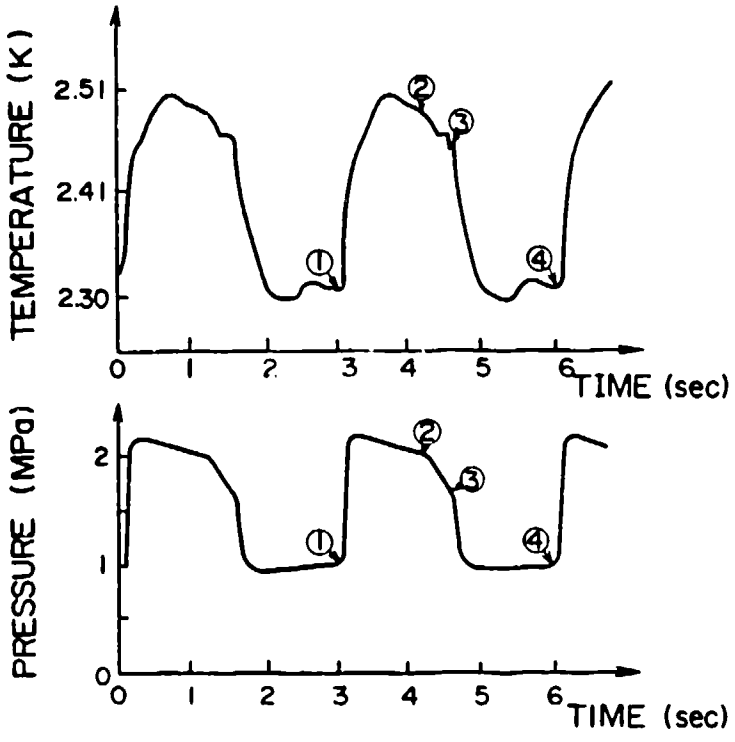

Fig.7. Temperature swing of the second stage and pressure change of the second expansion space (cycle frequency: 20rpm)

At ①, the intake valve opened and the exhaust valve shut. Helium flowed into the expander from the compressor. At②, the intake valve shut. Helium flowed neither into nor out of the expander. At③, the exhaust valve opened and helium returned to the compressor from the expander. While helium flowed into the compressor(①➡②), the temperature of the second stage increased up to 2.51 K. While helium flowed neither into nor out of the expander (②➡③), the temperature decreased a little. And when helium gas flowed into the expander (③➡④), the temperature decreased until 2.30 K.

NET COOLING CAPACITY

Net Cooling Capacity at the Cycle Frequency of 45 rpm

We measured the net cooling capacity at the cycle frequency of 45 rpm by loading heat of a heater to the second stage. To the first stage, heat was not added. Figure 8 shows the net cooling capacity of the second stage. The no-load temperature was 2.8 K (mean temperature). The net cooling capacity was 0.8 W at 4.2 K and it was 1.5 W at 5.2 K (critical temperature of helium). The electric power supplied to the compressor was approximately 5 kW. Thus the efficiency of the cryocooler was 1/6250 (0.8 W/5 kW) at 4.2 K, and it was 1/3333 (1.5 W/5 kW) at 5.2 K.

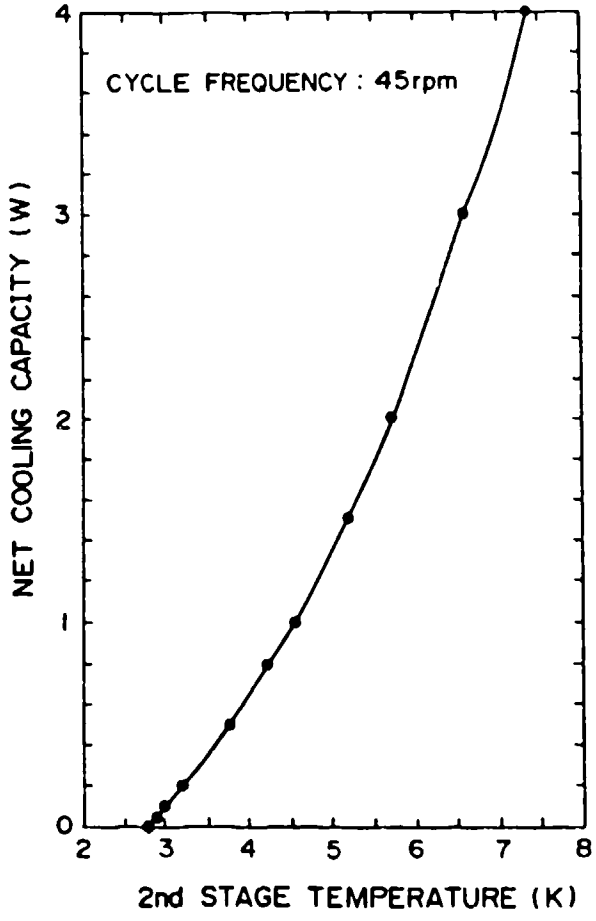

Fig.8. Net cooling capacity of the second stage

Effect of Cycle Frequency on Net Cooling Capacity

The net cooling capacity depend on cycle frequency as well as no-load temperature. Figure 9 shows effect of cycle frequency on net cooling capacity at 4.2 K. The net cooling capacity has the maximum and the optimum cycle frequency exists. The net cooling capacity at 4.2 K became the largest at the cycle frequency of 45 rpm ano it was 0.8 W as stated above.

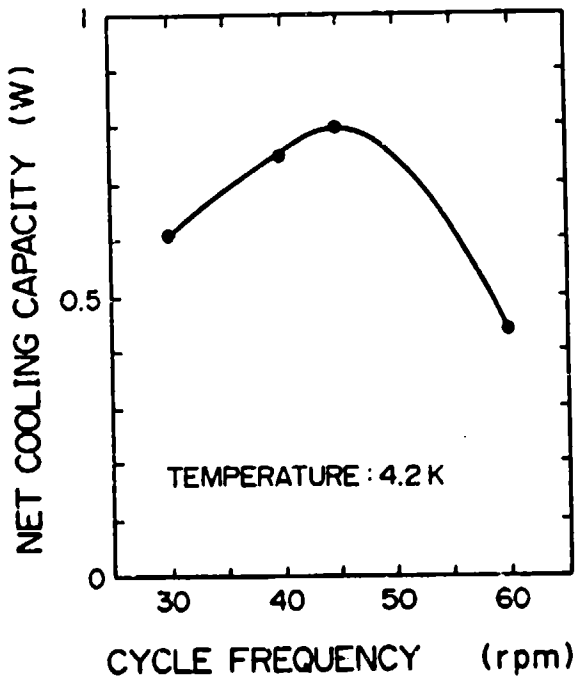

Fig.9. Effect of cycle frequency on net cooling capacity of the second stage

CONCLUSIONS

We have developed a two-stage G-M cryocooler operating at about 2 K using Er_3Ni in the second regenerator. Optimizing the cycle frequency, we achieved no-load temperature of 2.41 K and net cooling capacity of 0.8 W at 4.2 K . This net cooling capacity at 4.2 K is the world record of a G-M cryocooler.

REFERENCES

1. H. Yoshimura, M. nagao, T. Inaguchi, T. Yamada, and M. Iwamoto, "Helium liquefaction by a Gifford-McMahon cycle cryogenic refrigerator," Review of Scientific Instruments, vol. 60, No. 11(1989)p. 3533

2. M. Nagao, T. Inaguchi, H. Yoshimura, T. Yamada, and M. Iwamoto, "HELIUM LIQUEFACTION BY A GIFFORD-MCMAHON CYCLE CRYOCOOLER, "Advances in Cryogenic Engineering, vol. 35B(1990)p. 1251

3. T. Inaguchi, M. Nagao, and H. Yoshimura, "EFFECT OF REGENERATOR ON GIFFORD-MCMAHON CYCLE CRYOCOOLER OPERATING AT ABOUT 4 K, "Advances in Cryogenic Engineering, vol. 35B(1990)p. 1271

4. T. Inaguchi, M. Nagao, and H. Yoshimura, "ADVANCED HELIUM REFRIGERATOR FOR SUPERCONDUCTING MRI MAGNET, "11TH INTERNATIONAL CONFERENCE ON Magnet Technology(1989)p. 1355

5. T. Kuriyama, R. Hakamada, and H. Nakagome, "HIGH EFFICIENT TWO-STAGE GM REFRIGERATOR WITH MAGNETIC MATERIAL IN THE LIQUID HELIUM TEMPERATURE REGION, "Advances in Cryogenic Engineering, vol. 35B(1990)p. 1261

6. K. H. J. Buschow, J. F. Olijhoek, and A. R. Miedema, "Extremely large heat capacities between 4 and 10 K, "Cryogenics, vol. 15(1975)p. 261

7. M. Sahashi, Y. Tokai, T. Kuriyama, and H. Nakagome, "NEW MAGNETIC MATERIAL R_3T SYSTEM WITH EXTREMELY LARGE HEAT CAPACITIES USED AS HEAT REGENERATORS, "Advances in Cryogenic Engineering, vol. 35B(1990)p. 1175

GENERATION OF SUPERFLUID HELIUM BY A GIFFORD-McMAHON CYCLE CRYOCOOLER

Masashi Nagao, Takashi Inaguchi, Hideto Yoshimura,
Shirou Nakamura, Tadatoshi Yamada, and Masatami Iwamoto
Central Research Laboratory, Mitsubishi Electric Corp.
Amagasaki, Hyogo, 661, Japan

ABSTRACT

This paper describes the principal design features and performance test results of a three-stage Gifford-McMahon cycle cryocooler by which the authors have achieved a no-load temperature of 2.09 K and succeeded in generating superfluid helium. The cooling capacity is 3 mW at the lambda point (2.172 K). This is the first time that a regenerative-cycle cryocooler has generated superfluid helium.

Three key points contributed to this success. These key points are:
1) Selection of $Gd_xEr_{1-x}Rh$ compounds as a regenerator material
2) Optimizing the operating speed of the cryocooler (12 cycles/min)
3) Optimizing the operating pressure (2.45 MPa)

INTRODUCTION

We succeeded in liquefying helium by using a three-stage Gifford-McMahon cycle cryocooler (hereinafter called G-M cryocooler), and achieved a temperature of 3.3 K in 1989.[1] From the thermodynamic properties of helium, we found it is possible to achieve temperatures below 3.3 K with G-M cryocoolers. To demonstrate this possibility, we have been trying to improve the performance of a three-stage G-M cryocooler by varying the regenerator materials, operating speed, and operating pressure.[2] As a result, the authors have achieved a temperature of 2.09 K and succeeded in generating superfluid helium with a three-stage G-M cryocooler. It is probably the first time in the world that superfluid helium has been generated by means of regenerative-cycle cryocoolers. This paper first describes the principal design features of the three-stage G-M cryocooler and then provides performance test results.

THREE-STAGE G-M CRYOCOOLER

The fundamental structure of the three-stage G-M cryocooler is shown in

Fig. 1. The fundamental structure is almost the same as that of the G-M cryocooler that we used to successfully liquefy helium.[1] The cooler consists of the compressor for compressing the helium gas and the expander for expanding the gas to generate cryogenic temperatures. The cylinder is constructed of stainless steel and has three cooling stages through which a heat load is transferred into the cylinder. The cooling stages are fabricated of oxygen-free copper and brazed on the outside of the cylinder.

A displacer assembly in the cylinder contains three types of regenerators. Three seals are mounted on the displacer assembly. The first seal is a cap seal. The second and third seals are piston rings of the step-cut type whose surface

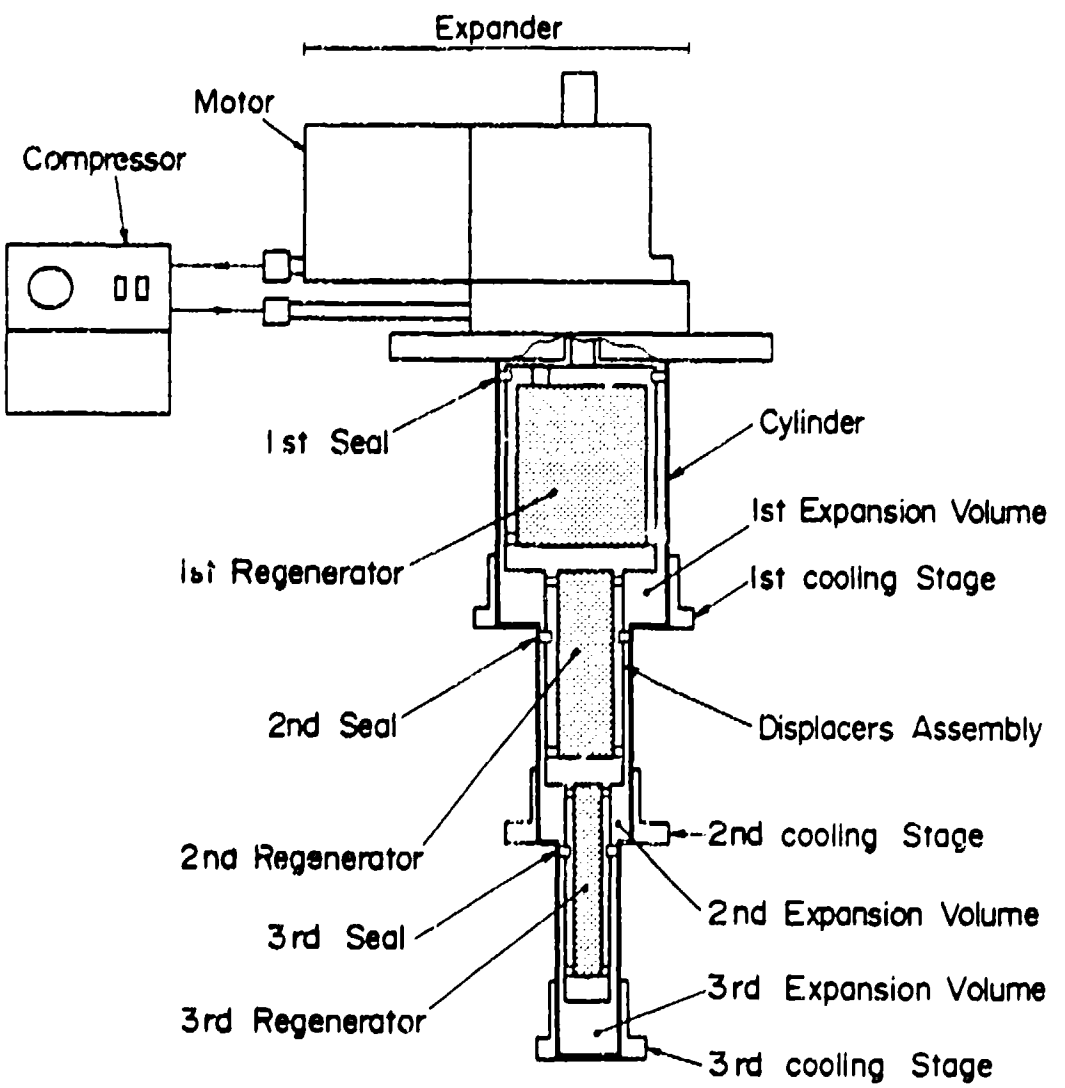

Fig. 1. Schematic of three-stage G-M cryocooler.

pressure is small and whose sealing performance is high. The piston ring material is glass-filled Teflon. The material of the first and second displacers is bakelite, which has a small thermal conductivity and a coefficient of thermal expansion similar to that of stainless steel. The material for the third displacer is stainless steel, which easily achieves high dimensional precision and is low in thermal conductivity over the cryogenic temperature region. The outside diameter is 18 mm. Each displacer is connected by a pin so as to be aligned automatically. The displacer assembly is driven reciprocally, with stroke of 3.174 cm, by a low-speed synchronous motor.

To increase efficiency, materials with a large specific heat were selected in each operating temperature range. The first regenerator has a two-layer structure. Phosphor bronze screen disks (150 mesh) are used in the high temperature part, and lead shot (0.55 mm-0.5 mm) in the low temperature part. The second regenerator has mono-layer structure filled with lead shot (0.3 mm-0.5 mm).

For the third regenerator, we considered several kinds of compounds containing rare earth elements (called rare earth compounds), which have a magnetic ordering transition over the cryogenic temperature region. Figure 2 shows the specific heat (heat capacity per unit volume) of these rare earth compounds in comparison with that of lead.[3] At first we tested the third regenerator with a mono-layer structure using GdRh. Then we tested the third regenerator with a three-layer structure using GdRh, $Gd_{0.5}Er_{0.5}Rh$, and ErRh to improve regenerator

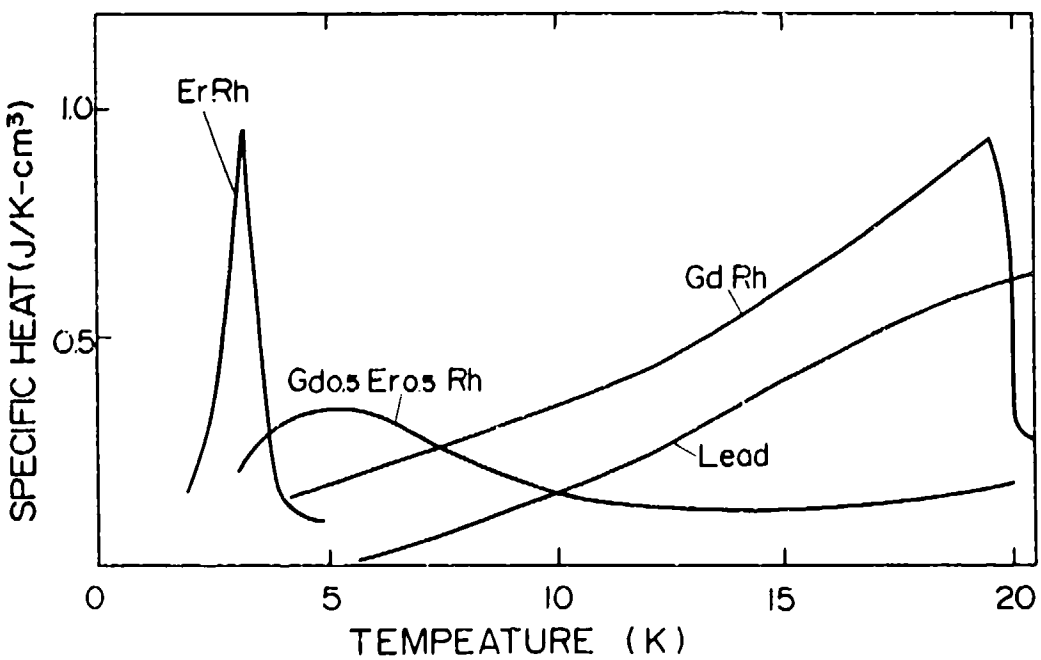

Fig. 2. Specific heat (heat capacity per unit volume) of rare earth compounds in comparison with that of lead.

Fig. 3. Photograph of GdRh grains.

efficiency, since $Gd_{0.5}Er_{0.5}Rh$ has a larger specific heat than GdRh below 7.5 K and ErRh has a larger specific heat than $Gd_{0.5}Er_{0.5}Rh$ below 3.7 K. The grain size of these materials is between 0.3 and 0.5 mm. Figure 3 shows a photograph of GdRh gains used in the regenerator. $Gd_{0.5}Er_{0.5}Rh$ and ErRh grains have the same shape as the GdRh grains.

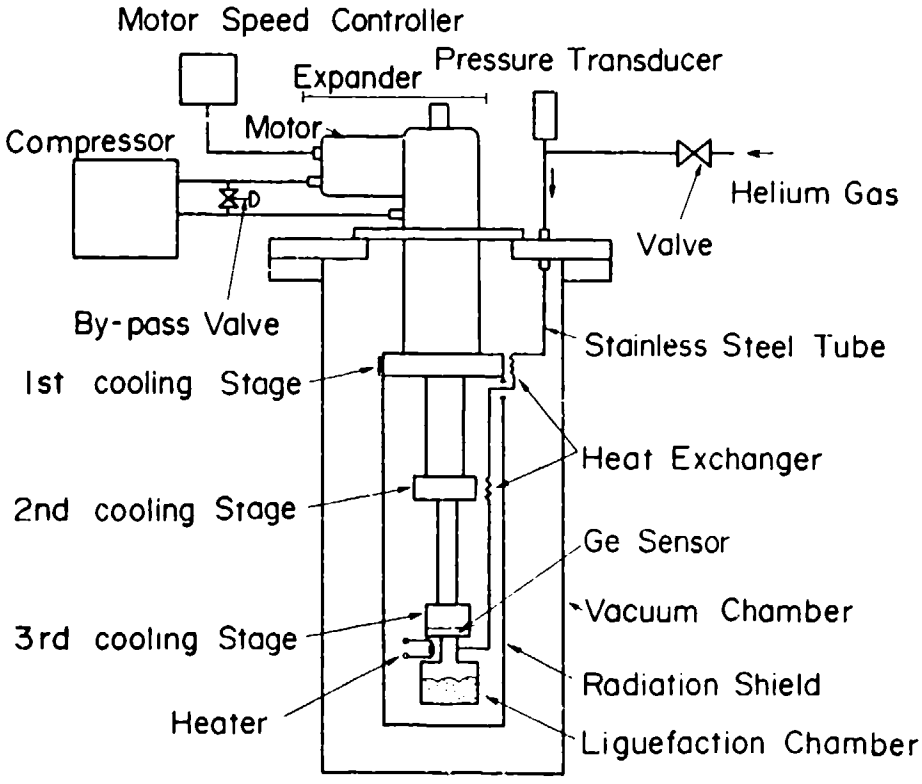

Fig. 4. Schematic of test configuration.

TEST METHOD

A schematic of the test configuration is shown in Fig. 4. The three-stage G-M cryocooler was tested in a vacuum chamber. A liquefaction chamber made of cooper is attached to the third cooling stage with indium foil. Helium gas from helium gas cylinder (not shown) is fed into the liquefaction chamber through a stainless steel tube (diameter: 1.0 mm, wall thickness: 0.5 mm and length: 2000 mm) which is thermally connected to the first and second cooling stages. The second and third cooling stages are surrounded by a radiation shield which is attached at the first cooling stage. The temperature of the radiation shield was maintained at about 40 K during the performance tests. A heater is wound around the liquefaction chamber and is used to apply a heat load to measure the cooling capacity of the third cooling stage.

A platinum-cobalt temperature sensor was used to measure temperature of the first and second cooling stages. The temperature of the third cooling stage was determined from the vapor pressure of the liquid helium in the liquefaction chamber. To measure vapor pressure, a pressure transducer mounted in an ambient temperature area was used. The indicated value was compared to the value obtained from a calibrated germanium resistance sensor. Figure 5 shows

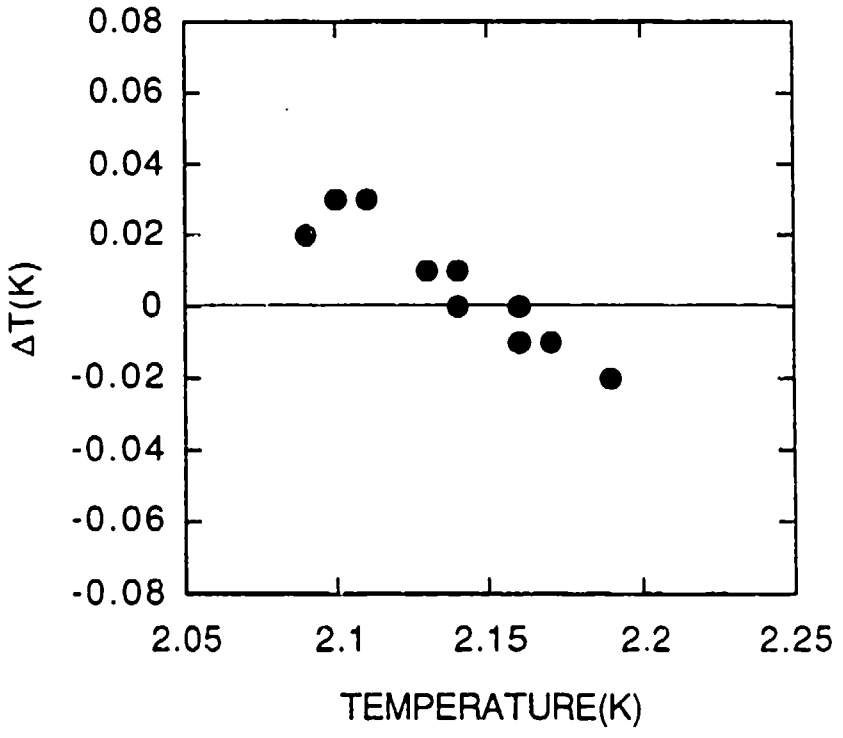

Fig. 5. Difference between the temperature from the vapor pressure and the temperature from the germanium resistance sensor.

this result. The maximum difference between the temperature from the vapor pressure and the temperature from the germanium resistance sensor was 0.03 K.

The operating pressure of the compressor can be adjusted by varying the charging pressure and adjusting the by-pass valve. The operating speed of the cryocooler can be controlled from 9 to 72 cycles/min by a motor speed controller using an inverter.

TEST RESULTS

EFFECT OF OPERATING SPEED ON THE NO-LOAD TEMPERATURE

We performed an experiment to determine the effect of operating speed on the no-load temperature. First, we tested the third regenerator, which has mono-layer structure using GdRh. The results are shown in Fig. 6. The no-load temperature was 4.32 K at 60 cycles/min, but decreased when the operating

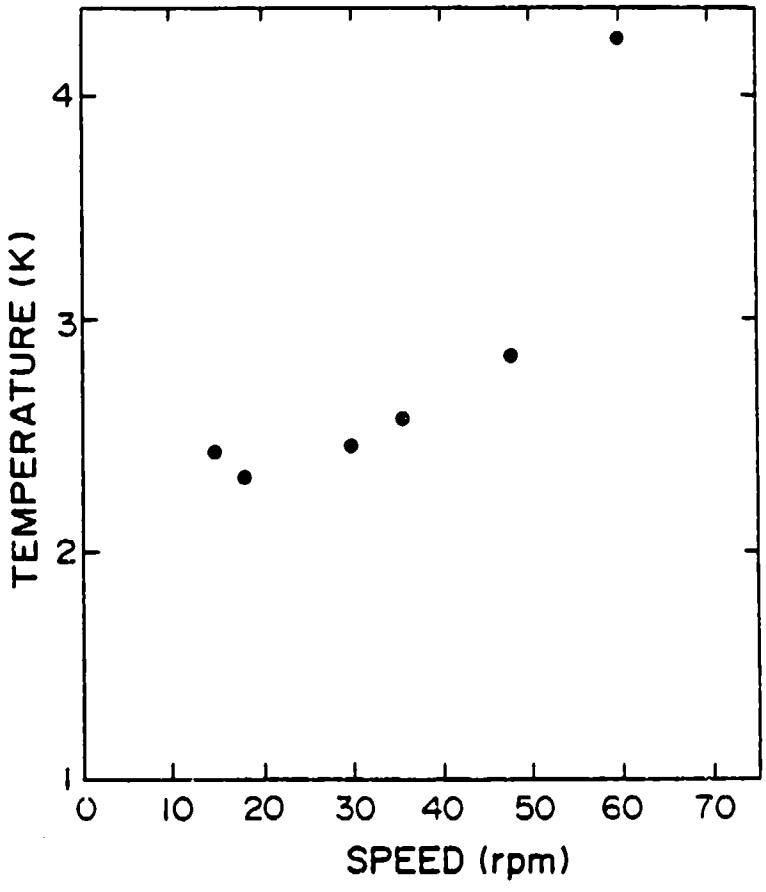

Fig. 6. Effect of operating speed on the no-load temperature (GdRh).

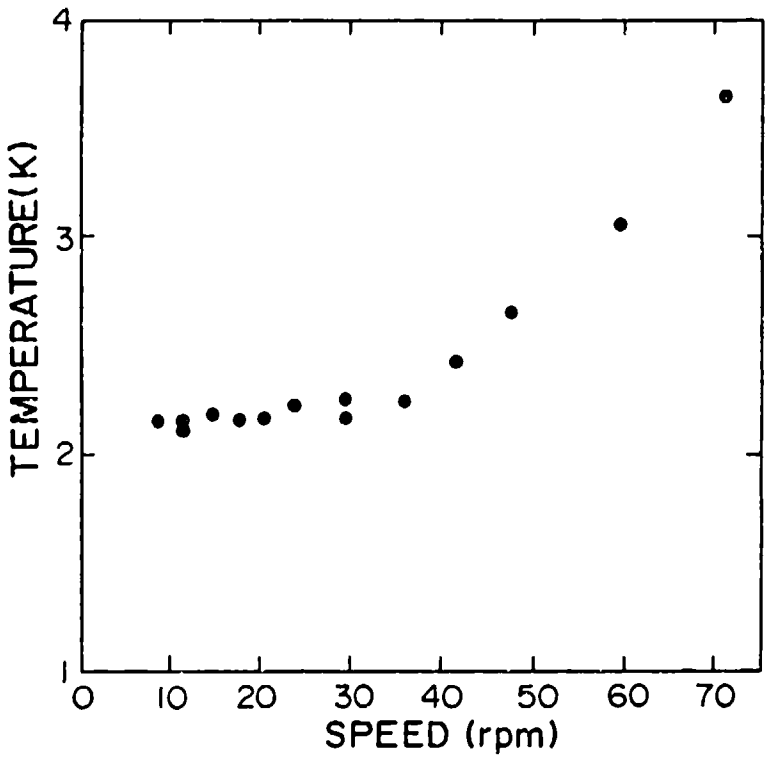

Fig. 7. Effect of operating speed on the no-load temperature (GdRh, $Gd_{0.5}Er_{0.5}Rh$, ErRh).

speed was decreased. The lowest temperature was 2.32 K at 18 cycles/min. However, the temperature again increased at 15 cycles/min.

To reach lower temperatures, we tested the third regenerator with a three-layer structure using GdRh, $Gd_{0.5}Er_{0.5}Rh$, and ErRh. The results are snown in Fig. 7. At 12 cycles/min, the no-load temperature was 2.14 K, that is, below the lambda point (2.172 K). This means that the helium in the liquefaction chamber is in a superfluid state.

EFFECT OF OPERATING PRESSURE ON THE NO-LOAD TEMPERATURE

We performed an experiment to determine the effect of operating pressure on the no-load temperature. The operating speed was fixed at 12 cycles/min in this experiment. The pressure difference between intake and exhaust pressure was controlled at about 1.5 MPa. The results are shown in Fig. 8. When the intake pressure increased, the no-load temperature decreased, and we have achieved a no-load temperature of 2.09 K at 2.45 MPa. Amplitude of temperature oscillation (peak to peak) is about 5 mK.

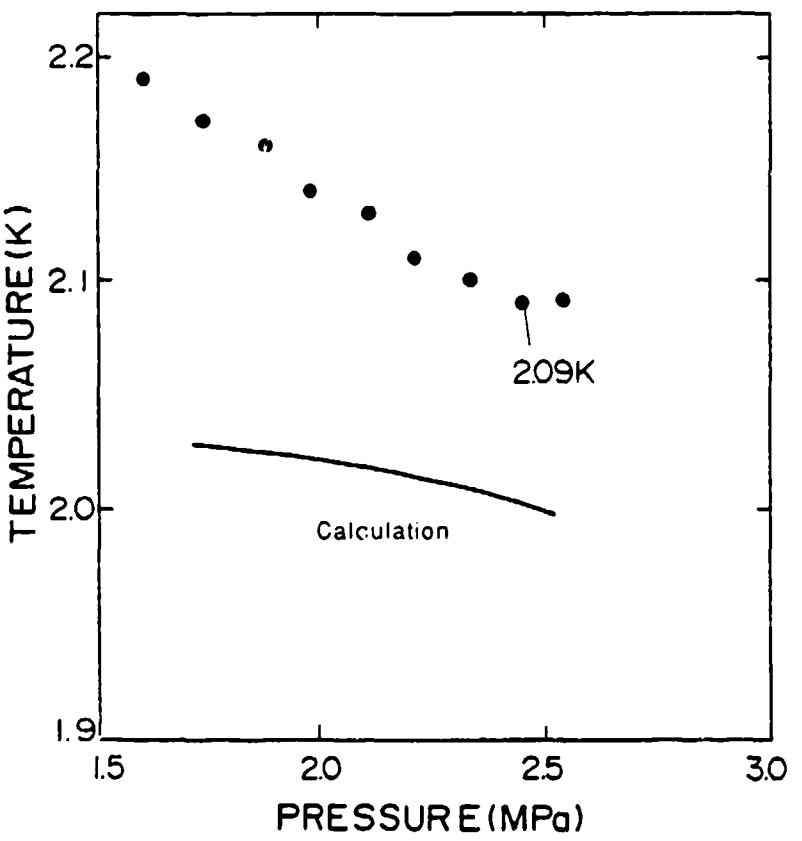

Fig. 8. Effect of operating pressure on the no-load temperature (The pressure difference between intake and exhaust pressure was controlled about 1.5 MPa.).

Figure 9 shows the experimental results for the third stage cooling capacity performance of the three-stage G-M cryocooler. The third cooling stage delivers 3 mW at the lambda point (2.172 K).

Figure 10 shows the effect of the third cooling stage temperature on the amplitude of temperature oscillation (peak to peak). When the temperature decreased, the amplitude of the temperature oscillation decreased. This phenomenon is associated with the thermodynamic properties of helium. Figure 11 shows a schematic of the T-S diagram near the lambda point.[4] When the temperature decreases, the isobaric line of the intake pressure gets closer to the isobaric line of the exhaust pressure. As a result of this approach, the amplitude of the temperature oscillation decreases. At the point where the two isobaric lines cross, cooling of the cooler is equal to zero. This crossover point is the lower limit of the no-load temperature. In Fig. 8, the lower limit of the no-load temperature calculated from the helium property program (HEPROP) by NIST is indicated by the solid line. The calculated value and the experimental value

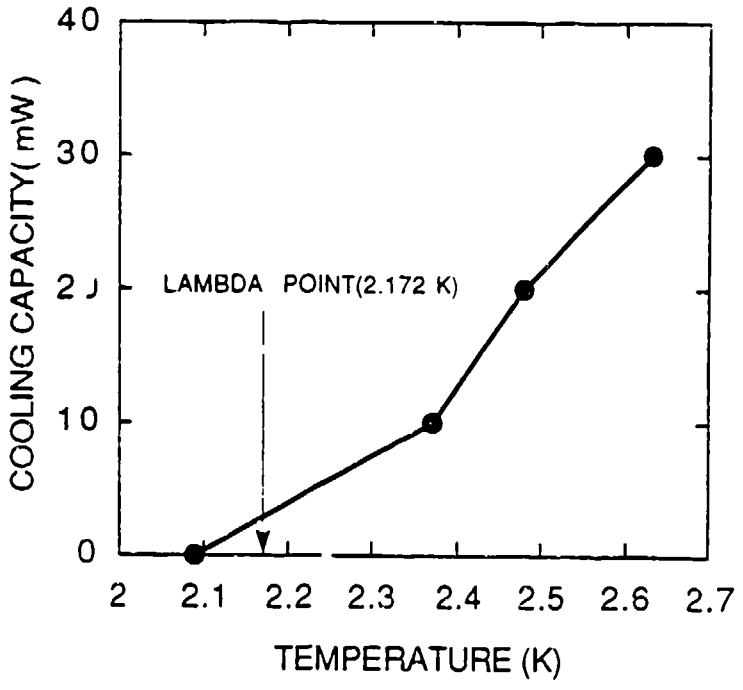

Fig. 9. Cooling capacity performance of the three-stage G-M cryocooler.

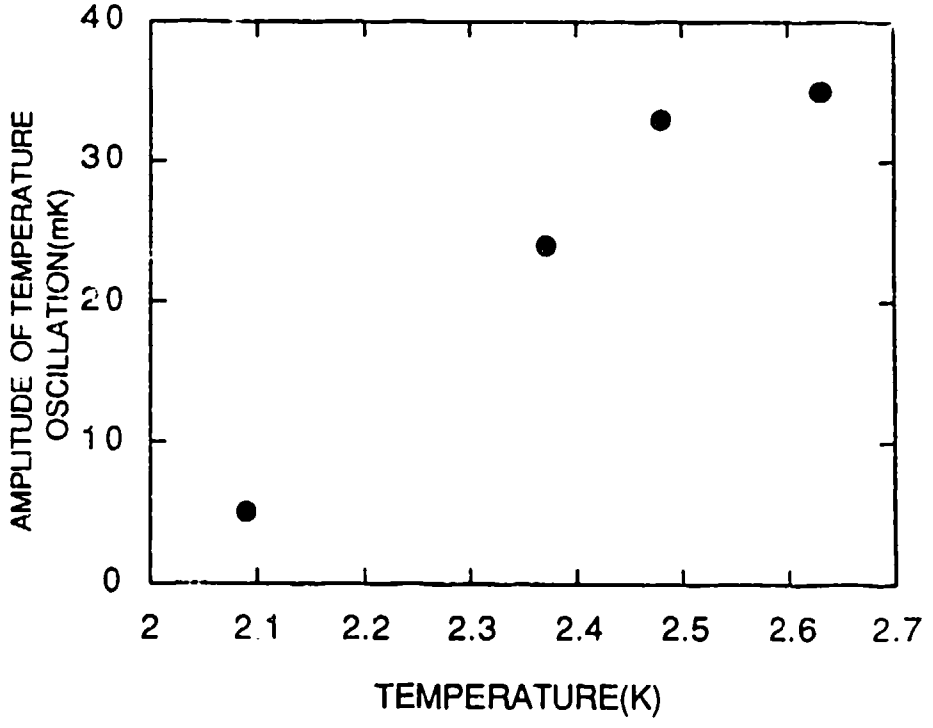

Fig. 10. Effect of a temperature of the 3rd cooling stage on amplitude of temperature oscillation.

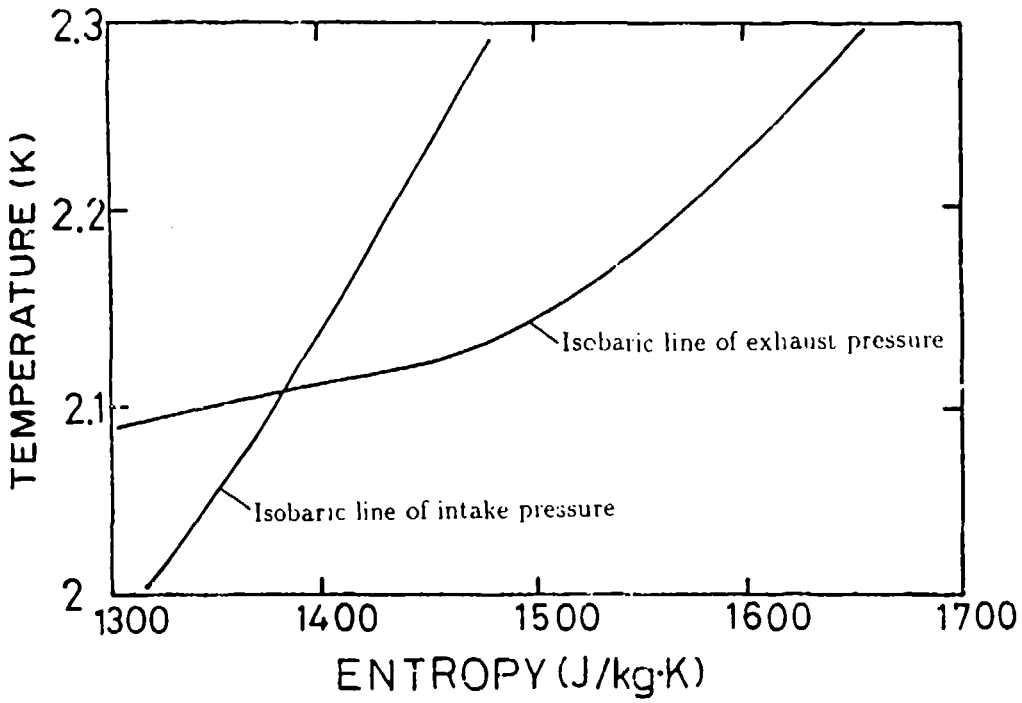

Fig. 11. Schematic of a T-S diagram near lambda point.

essentially agreed, with an error of about 0.1 K. The result of the experiment is understood to be close to the thermodynamic limit.

CONCLUSIONS

The authors have achieved no-load temperature of 2.09 K and succeeded in generating superfluid helium with a three-stage Gifford-McMahon cycle cryocooler using $Gd_xEr_{1-x}Rh$ compounds as the third regenerator material. This no-load temperature is close to the thermodynamic limit of regenerative-cycle cryocoolers. The cooling capacity of the third cooling stage is 3 mW at the lambda point (2.172 K). It is probably the first time in the world that superfluid helium has been generated by a regenerative-cycle cryocooler.

This three-stage Gifford-McMahon cycle cryocooler has a considerable potential for a reliable, low cost, compact and easily operated cryocooler below the lambda point.

REFERENCES

1. M. Nagao, T. Inaguchi, H. Yoshimura, T. Yamada, and M. Iwamoto, "Helium Liquefaction by A Gifford-McMahon Cycle Cryocooler," *Advances in Cryogenic Engineering*, Vol. 35B (1990) p. 1251.

2. T. Kuriyama, R. Hakamada, and H. Nakagome, "High Efficient Two-Stage GM Refrigerator with Magnetic Material in the Liquid Helium Temperature Region," *Advances in Cryogenic Engineering*, Vol. 35B (1990) p. 1261.

3. K.H.J. Buschow, J.F. Olijhoek, and A.R. Miedema, "Extremely Large Heat Capacities between 4 and 10 K," *Cryogenics*, Vol. 15 (1975) p. 261.

4. Steven W. Van Sciver, *"Helium Cryogenics,"* Plenum Press, New York (1986).

Session VIA — Stirling Coolers II

Chairperson: Yoichi Matsubara, Nihon University

Co-Chairperson: Michael Superczynski, DTRC

Session VIB — Joule-Thomson Coolers II

Chairperson: Steve Bard, JPL

Co-Chairperson: Fred Cogswell, Boreas, Inc.

Development of an Efficient, Bellows Driven Stirling Cycle Cryocooler

Sibley C. Burnett, John R. Purcell, and Carl J. Russo

CDC Partners

ABSTRACT

A highly efficient, Stirling Cycle based refrigerator has been developed by CDC partners, a partnership of Advanced Cryo Magnetics, Cryocooler Development Corporation and American Superconductor. The single stage, laboratory model produces 3.6 Watts of output power at 80 K and 1.7 Watts at 50 K. Efficiency, determined by torque measurements, is between 17 and 21 percent of the Carnot efficiency. The expansion and compression bellows were developed for long life, maintenance free operation. Preliminary life testing has demonstrated over 35 million cycles of operation at 5 Hz. A computer model has been developed and correlated with experimental data. Scaling up to 100 Watts of output power is predicted to require less than 1200 Watts input power. Experimental results, comparison to modeling data, and lifetime information will be presented.

INTRODUCTION

High efficiency cryocoolers are important for a number of applications like high-T_c superconductors and cooled electronic circuits. To date, little work has been done to address the needs of cryocoolers operating in the 30-60 K range. Two types of Stirling cycle machines were developed over the last two years, with the same performance goal of about 2 W at 50 K. Also, a computer code was written to understand the complicated trade-offs between all important machine parameters. Different configurations of regenerators and different gap thicknesses were tested and evaluated on the first machine. Pressure, temperature, and thermal load monitoring was built into the test stand. PV and thermal characteristics were compared to those derived by the computer program. The regenerator concepts used on the second machine were also tested on the first machine.

DESIGN

The first test stands, utilized off-the-shelf bellows for the compressor and expander to work out the concepts. The second model, machines 1A and 2A, used custom made bellows specifically designed for long life.

DESIGN GOALS

The design goals for this machine were to produce 2 W of cooling power in the 50 K range. The machine is small, lightweight and efficient, runs from 110 V ac without water cooling. The long term design goals for this Stirling cycle cryocooler will include a mean time between repairs of over 5000 hours, and a lifetime of over 50,000 hours.

HEAT BALANCE

Heat balance is calculated from four components.

1. The gross refrigeration or $\int PdV$ work.

2. Regenerator losses due to temperature difference between the gas and the regenerator.

3. Pressure losses in the regenerator

4. Heat conduction down the length of the regenerator.

It is assumed in the design that convection and radiation losses can be made very small by using vacuum insulation and radiation shields.

COMPUTER CODE

A computer code assumes isothermal compression and expansion (shown by experimental data in figure 2 to be a good approximation) and accounts for pressure drop, heat transfer losses, thermal conduction in the regenerator and support, and volume effects. By calibrating the code at one experimental point it describes the operation of the cryocooler over a wide temperature range.

MECHANICAL ISSUES

The mechanical configuration is described in Burnett et al.[1] and is shown in Figure 1

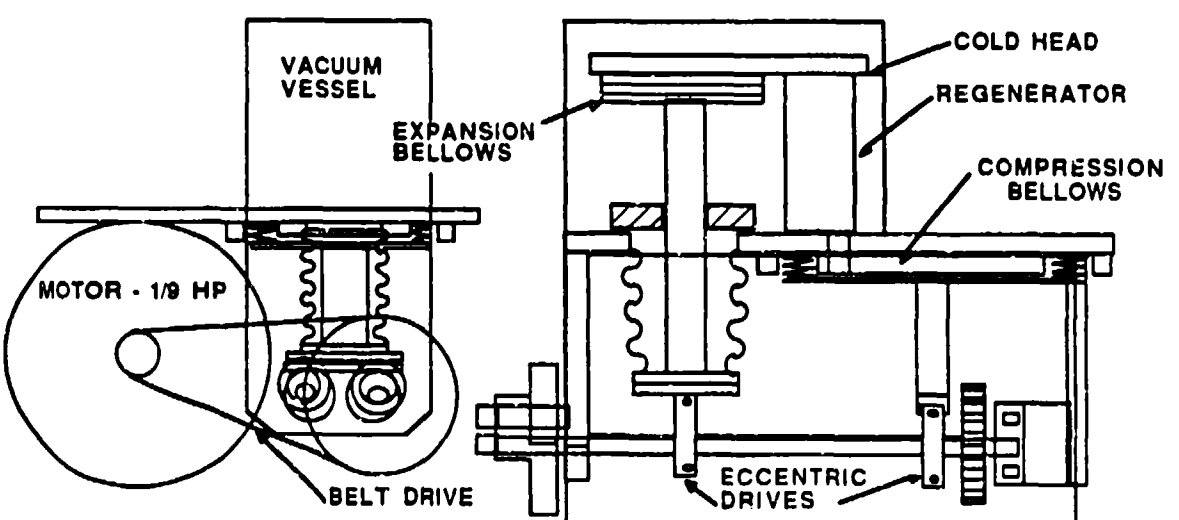

Figure 1 Two views of a 2 W Stirling Cycle Cryocooler.

The Key issue in cryocooler life is the bellows life. The key issue in bellows life is providing for minimum bellows stroke with optimized clearance ratios to give good lifetime.

The key design tradeoffs for a bellows cryocooler are clearance ratio vs. lifetime vs efficiency. Definitions for the bellows are given below

1. Compressed Volume. Volume when bellows is compressed.

2. Total Volume. Volume in bellows when open (stretched).

3. Swept Volume. Total volume minus compressed volume, i.e. the gas that is moved.

4. Clearance Ratio. Compressed Volume/Swept Volume.

We are encouraged about bellows lifetime possibilities. Our device operates at low pressure and slow speed. Companies like Metal Bellows have numerous commercial pumps that have demonstrated over 100 million cycles without failure. In bellows pumps, failure is usually related to solid contamination of the pumped stream. Our device operates with larger clearance ratios than the commercial metal bellows pumps, still with excellent efficiency. Statistics from Stirling Technology's heart pumps confirm that long bellows lifetime is feasible[2] (6.9 years at 30 Hz).

REGENERATOR

A high efficiency regenerator is the corner stone of any Stirling Cycle refrigerator. Colgate[3] showed that the task of designing a cryogenic regenerator can be reduced to the difficult design problem of relating the following conflicting variables:

1. Non-ideal heat exchange between the working fluid (e.g. helium or nitrogen, etc.) and the regenerator material.

2. Extra work and frictional heat due to viscosity which causes pressure drop in the regenerator.

3. Loss because of dead volume of gas within the regenerator that does not expand or contract during the cycle, thus limiting the cycle compression ratio.

4. Departure from isothermality, because of the mass of the regenerator material.

5. Thermal conduction in the direction of the primary heat flow, i.e., the axial or longitudinal direction of the regenerator.

Optimization of these five variables lead to a channel cryogenic regenerator with the working fluid moving with laminar flow through the channels. Variables 1,2, and 3 above deal mainly with the geometry of the regenerator, while variables 4 and 5 deal mainly with the materials of construction.

If the regenerator is to span a large temperature range, then the regenerator may be divided into sections. Each section can be independently optimized for heat capacity and longitudinal and axial thermal conductivity (material specific) and channel flow area, area of working fluid, contact and length (geometry specific). Colgate took this path for the conceptualization of a 4 K machine. Another approach is to use a regenerator with variable material properties. This was the approach taken by Purcell and Sarwinski[4].

CONSTRUCTION

The machine consists of a mechanical drive, compression and expansion bellows, a regenerator, and a cold stage. The drive shown in Figure 1 has cams which are driven in a 90° phase relationship between the expander and the compression bellows. The computer program shows that adjustable phase angle has very little effect on machine performance.

The bellows are specially designed for long service in this application. The regenerator is constructed from polymer based materials to minimize axial thermal conductivity. Lower thermal conductivity allows the length of the regenerator to be much shorter than an equivalent regenerator made from stainless steel. The expander bellows is supported by a G-10 support tube and driven by a small G-10 tube from the cold to the warm side. A small copper tube, which is the cold stage, connects the regenerator to the expander bellows.

PERFORMANCE CHARACTERISTICS

TEST PROCEDURES

When the machine is run with a new regenerator configuration the cryocooler is cooled to its lowest temperature at zero heater power. The equilibrium temperature is measured at 1 and 2 watts input. Finally the output as a function of speed is found.

MEASUREMENTS

The measurements below were performed on models 1A and its successor model 2A. Nearly all of the data presented below are from model 1 A. The data were taken at different times, so that the data in table 1 represents results from the same cryocooler taken at different times but under generally similar conditions.

TEMPERATURE

Temperature measurements were made using a calibrated silicon diode and a Scientific Instruments temperature read out.

INPUT POWER

Input power was measured by a torque method. Since the cryocooler is a belt driven machine, it was convenient to detach the motor, mount it on a

balance board, connect it to the cryocooler through a longer belt, and measure the torque. Motor torque was measured by using a weight placed at the appropriate distance from the center of the scale to give balance as a function of cryocooler operation. Torque was converted to output power by multiplying the cryocooler shaft rotation rate and the pulley ratio connecting the cryocooler to the motor by 2π.

OUTPUT POWER

Output power was measured by the heat dissipated in a wire wound resistor connected to the cold stage. No account is taken of the thermal losses inherent in the leads connecting to the wire wound resistor or the losses from the leads connecting to the temperature sensor. Lead losses are estimated to be less than 100 mW. A comparison of actual output power compared to actual data is shown in figure 2. PV curves also closely match the computed values.

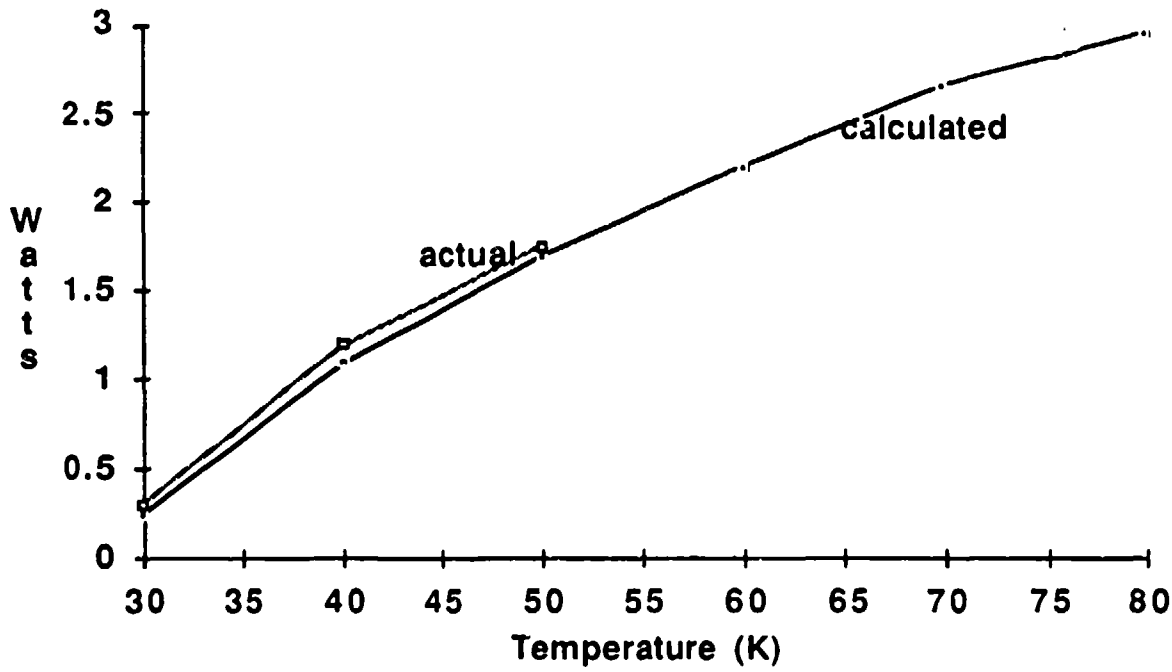

Figure 2. Comparison of output power to computer calculation.

HELIUM AND VACUUM LEAKS

Helium leaks and poor vacuum seriously degrade the performance of a cryocooler as was evident in our early testing of the first test stand. A helium leak detector and a diffusion pumped vacuum station were included in the early testing to resolve vacuum and helium leak problems early in the design cycle of the second machine.

COOL-DOWN TIME

Cool-down times were measured and recorded as a first cut characterization of the cryocooler. If the cryocooler did not make certain temperatures in a given time it was usually a sign that some part of the cryocooler was not operating properly. Since no attempt has been made to minimize thermal mass, cooldown times are usually on the order of tens of minutes.

When the speed of the cryocooler is changed then power output is optimized for a different temperature range. Fifteen Hz is more effective above 100 K, 8 Hz is most effective between 65 K and 100 K, and 5 Hz cools best below 75 K.

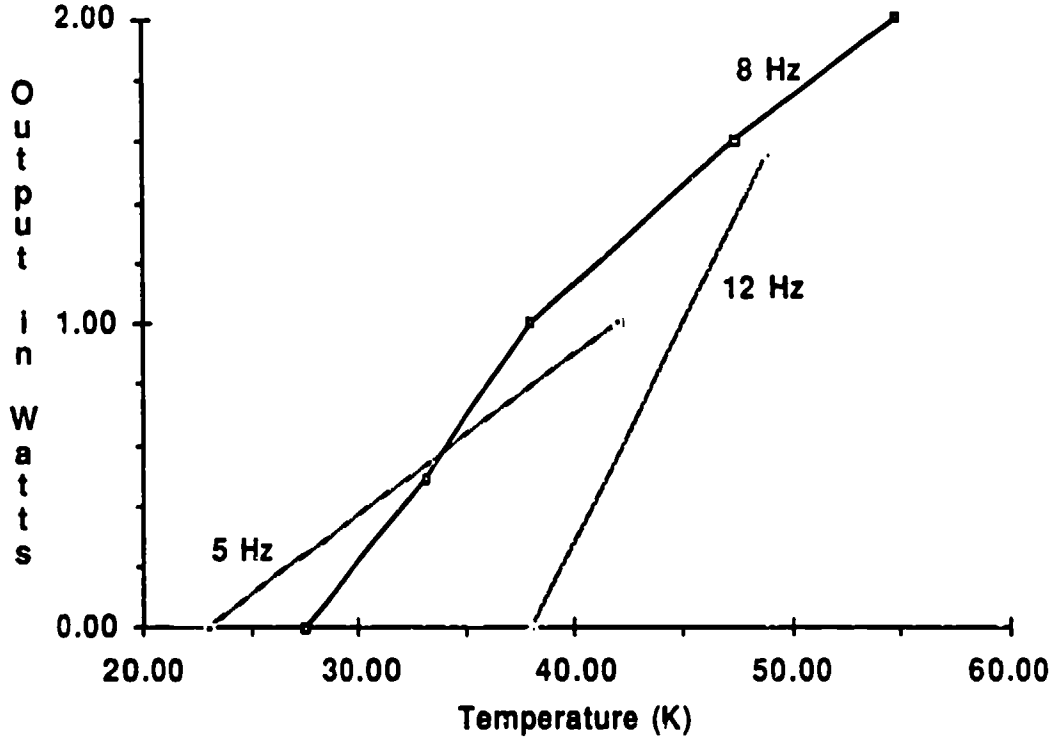

Figure 3. Output power as a function of temperature for a variety of cam speeds.

PARASITIC LEAKS

Thermal performance of the cryocooler was measured a number of ways. These included cool down and heat up curves with and without a resistive load. If large parasitic leaks are present they can be identified and corrected. Less serious leaks are compensated for in the calculations of output

power in order to get a full data run. Note that in Table 1, only the 80 K data has been so compensated

Table 1. Composite Thermal Performance of CDC Partners Cryocooler 1A Nominal Values at 8 Hz. T_{min} = 27 K. Moderate Clearance Bellows

Operating Temperature (K)	80*	80	55	50	40
Input Power (W)	50	50	58	----	----
Cooling Power (W)	3.6*	3.0	2.0	1.7	1.2
Carnot Efficiency	21*	17	16	----	----

*Corrected for 0.6 W larger than normal parasitic leak as measured by rate of rise.

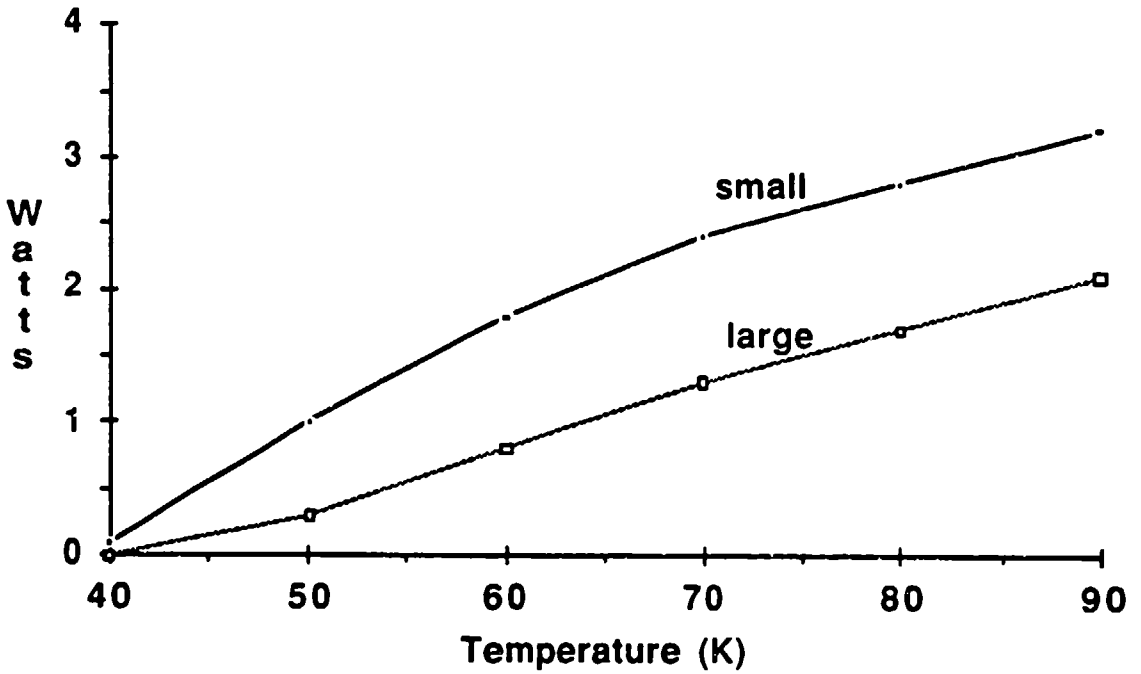

Figure 4. Measured cooling power as a function of clearance ratio.

LIFE TESTING

We have been testing a cryocooler at 44 K with small clearance ratios operating at 5 Hz. At this temperature there is no net cooling available, but cooling losses from the environment are estimated at 1-1.5 W are intercepted by the cold head. We have run for over 35 million cycles without a bellows failure. Even if one failed now the prognosis is good. By reducing the stress a small amount, the lifetime of the bellows is greatly increased. Stress and stroke are directly related. A small reduction in the stroke can greatly im-

prove bellows life. Figure 4 shows the trade-off between clearance ratio and cooling power.

FUTURE WORK

We are planning to scale up this device to a larger power, and we are also considering a two stage machine for temperatures in the 20 K range.

CJR:cjr

---

[1]Sibley C. Burnett, John R. Purcell, Wiliiam P. Creedon, Chandrashekhar Harihar Joshi, "Improved Stirling Cycle Machine", U. S. Patent.

[2]Maurice A. White, S. Grant Emigh, and Peter Riggle, "Practical Bellows Seals for Stirling Engines", Society of Automotive Engineers Technical Paper 870104, presented at the International Congress and Exposition, Detroit, Michigan, February 23-27, 1987.

[3]Stirling A. Colgate, "Stirling Cycle Machine", U. S. Patent.

[4]John R. Purcell and Raymond E. Sarwinski, "Cryogenic Regenerator", U. S. Patent .

SUPERFLUID STIRLING REFRIGERATOR: A NEW METHOD FOR COOLING BELOW 1 KELVIN

V. Kotsubo and G. W. Swift
Condensed Matter and Thermal Physics Group,
Los Alamos National Laboratory, Los Alamos, New Mexico 87545

ABSTRACT

We have invented and built a new type of cryocooler, which we call the superfluid Stirling refrigerator (SSR). The first prototype reached 0.6 K from a starting temperature of 1.2 K. The working fluid of the SSR is the ^{3}He solute in a superfluid ^{3}He-^{4}He solution. At low temperatures, the superfluid ^{4}He is in its quantum ground state, and therefore is thermodynamically inert, while the ^{3}He solute has the thermodynamic properties of a dense ideal gas. Thus, in principle, any refrigeration cycle that can use an ideal gas can also use the ^{3}He solute as working fluid. In our SSR prototype, bellows-sealed superleak pistons driven by a room-temperature camshaft work on the ^{3}He solute. Ultimately, we anticipate elimination of moving parts by analogy with pulse-tube refrigeration.

INTRODUCTION

The ^{3}He-^{4}He dilution refrigerator, invented about 30 years ago, is now routinely used[1] to reach temperatures below 1 K. The endothermic heat of mixing of liquid ^{3}He with liquid ^{4}He produces the cooling in the dilution refrigerator; steady refrigeration is achieved by adding a fractional distillation chamber to remove the ^{3}He from the solution, and room-temperature pumps to return the ^{3}He to the refrigerator. Modern dilution refrigerators routinely reach temperatures below 0.01 K, exhausting their waste heat above 1 K.

There are only two other techniques[1] for cooling below 1 K. The evaporation of pure ^{3}He can be used to reach 0.3 K; but, at lower temperatures, the vapor pressure is too low for significant cooling power. Adiabatic demagnetization of a paramagnetic salt, the oldest method for cooling below 1 K, is inconvenient because of the frequent requirement for magnetic shielding between the refrigerator and the apparatus to be cooled.

Here, we describe the first experiments with a new technique for cooling below 1 K: the superfluid Stirling refrigerator (SSR). The SSR uses the ^{3}He solute in a superfluid ^{3}He-^{4}He solution[2] as a thermodynamic working medium, compressing and expanding the solute alone to provide heating and cooling. In such a solution, the ^{4}He, forming a Bose liquid, undergoes a superfluid transition at 2.2 K, and below 1 K it is, for our purposes, in its quantum ground state. It has no entropy, and flows without dissipation; thermodynamically it is a vacuum. The ^{3}He solute in such ^{4}He behaves like an ideal gas, with an equation of state $P_{os} = n_3 k_b T$, and heat capacity per particle $\simeq (3/2)k_b$, where P_{os} is osmotic pressure, n_3 is the ^{3}He number density, k_b is Boltzman's constant, and T is the temperature. Because of this similarity, any refrigeration cycle that uses ideal gases as a working fluid should be adaptable[3] to the regime below 1 K using the ^{3}He solute working fluid. We chose to use the Stirling cycle[4], shown in detail in Fig. 1.

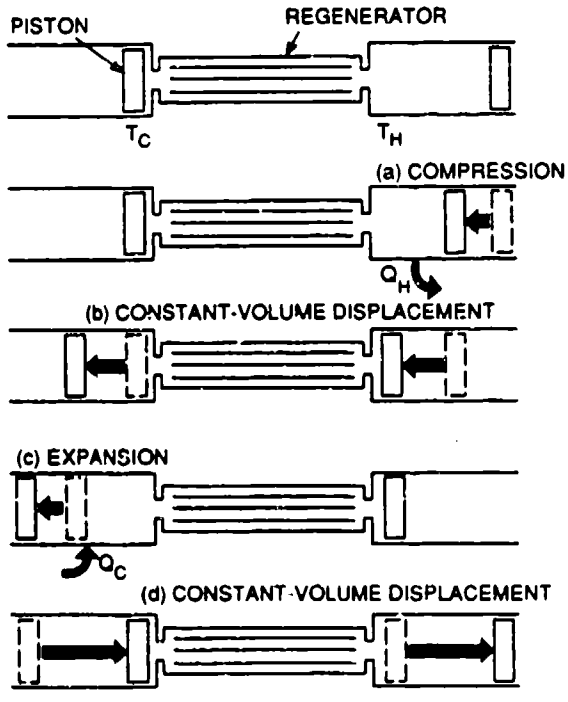

Fig. 1. Four steps of a Stirling-cycle refrigerator. (a) The first step of the cycle is isothermal compression of the fluid in the hot cylinder, rejecting the heat of compression Q_h out of the refrigerator to an external heat sink at T_h. (b) In the second step, both pistons move, displacing the fluid to the left. Because of the good lateral thermal contact in the regenerator, heat is transferred there, between fluid and high-heat-capacity solid, under locally isothermal conditions, reversibly changing the fluid temperature from T_h to T_c as it flows leftward. (c) In step three, isothermal expansion in the cold cylinder absorbs the heat of refrigeration Q_c from the load at T_c. (d) Displacement of the fluid to the right then causes regenerative heat transfer, changing the fluid temperature from T_c back to T_h.

DESIGN AND CONSTRUCTION

Building the SSR required several unique design features, shown schematically in Fig. 2. The compressor and expander had to work on only the ^{3}He solute, and not the relatively incompressible bulk liquid, so superleak pistons were used. Each of these consisted of a 4.65-mm long, 0.36-mm-diam rod of microscopically porous Vycor glass (Corning 7930) sealed with Stycast 2850 epoxy into a hole drilled through the length of a copper piston. The piston was then sealed between two bellows (Servometer FC-16 nickel bellows), forming two containment volumes for the solution connected by the glass rod. Vycor glass, which has channel diameters of about 10^{-8} m, viscously locks the ^{3}He solute, allowing only the superfluid ^{4}He component to flow through, so a displacement of the piston compresses only the ^{3}He. The copper pistons were designed to take up as much as possible of the excess volume within the bellows to maximize the compression ratio. The final total fluid volume within each bellows was about 2 cm^3.

The pistons were driven with long rods from a camshaft and dc motor/gearbox assembly at room temperature. Each drive rod consisted of a moving 1.77-mm-od stainless tube inside of a 2.4-mm-od, 1.8-mm-id stationary tube, bent slightly where necessary, much like a bicycle cable. The two cams were 5.08-cm-diam ball bearings mounted 0.32-mm off center to provide 0.64-mm displacements. The cams were mounted on separate but colinear driveshafts connected by a clamp, so the phase between the cams could be adjusted by loosening the clamp and rotating one cam with respect to the other. Because the overall drive system was not completely rigid, 0.64-mm camshaft displacements at the top of the cryostat caused only about 0.4 - 0.5-mm displacements at the pistons, and the resulting piston motions were hysteretic and non-sinusoidal. Final volume displacements were about 0.9 cm^3/stroke, but were different for each piston, and also drifted over time.

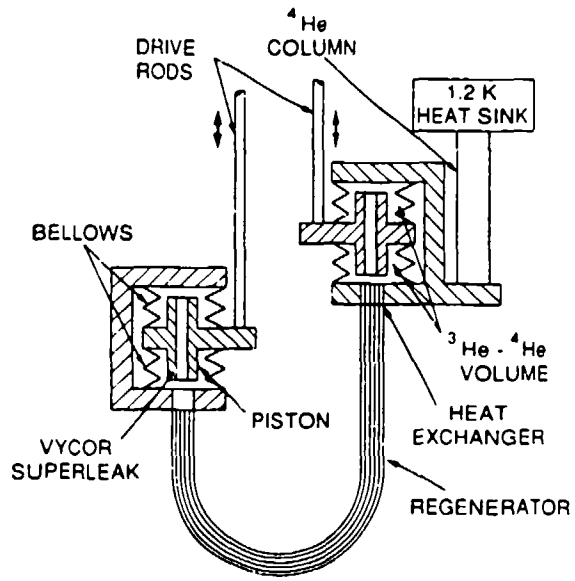

Fig. 2. Schematic of the SSR. Entire assembly is sealed in a vacuum can, which is immersed in a 4-K liquid ^{4}He bath.

One of the bellows volumes at each piston was sealed off with a flange, acting simply as a reservoir for the ^{4}He superfluid that flows through the superleak. The other volume was the actual compression/expansion space for the refrigerator, and was sealed with a ported flange connecting to the regenerator. On the compressor, the port consisted of 19 0.8-mm-diam holes drilled through the 1-cm thick copper flange to act as a heat exchanger to remove the large amount of heat rejected. The working fluid flowed through these holes, then into the regenerator. The copper flange was connected to a 1.91-cm-diam, 18-cm long copper tube filled with pure ^{4}He, which acted both as a thermal reservoir and a thermal link to a standard pumped ^{4}He coldplate[5] which provided a starting temperature of about 1.2 K. There was no heat exchanger on the expander--the heat load was simply the heat capacity of the expander. The expander was thermally isolated from the compressor by three 25-cm long, 0.64-cm-od thinwall stainless-steel support tubes.

The regenerator was an array of 30 0.20-mm-id, 0.37-mm-od, 38-cm long CuNi capillaries, stuffed into a series arrangement of a 0.47-cm-diam, 2.86-cm long CuNi tube, a 6.35-mm-od, 25-cm long stainless-steel tube, a 6.35-cm long section of 0.64-cm-od, 0.32-cm-id bellows, and a 0.32-cm-diam, 2.5-cm long CuNi tube, all sealed together with soft solder. The bellows formed a U-shaped bend to allow the regenerator to match the positioning of the ports of the expander and the compressor; the smaller diameter tubes at either end fit into the ports. The capillaries were sealed to the outer tube assembly's ends with soft solder, so that the ^{3}He-^{4}He solution could flow through the capillaries, and the outer tube assembly was filled with pure ^{3}He, thereby immersing the capillaries in a high-heat-capacity reservoir (which would be provided by solid parts in a conventional Stirling refrigerator). The total heat capacity of the regenerator was calculated to be 1.1 J/K at 0.6 K and 1.2 J/K at 1 K.

Two separate fill lines were used to fill the refrigerator. One fill line filled the refrigerator itself, and the other filled the reservoir volumes on the back of each piston. By having two separate fill lines, the concentrations on either side of the superleaks could be adjusted separately by filling each side first with the required amount of ^{3}He, and then adding ^{4}He. The fill lines were closed using low-temperature valves pneumatically operated with pressurized ^{4}He. Without the valves, liquid moved up and down the fill lines between the warm and cold parts of the refrigerator during operation, thus causing a substantial heat leak.

Resistance thermometers were mounted on the outsides of the flanges which connected the expander and compressor to the regenerator, and a resistance wire heater was mounted on the outside of the flange of the cold expander. Following the method described by Kierstead[6], the ^{3}He concentrations were determined from the dielectric constant of the solution, which was measured using compact 5-pF capacitors mounted in the end flanges in direct contact with the liquid within the expander and compressor.

EXPERIMENTAL RESULTS

The refrigerator was filled with a 12% ^{3}He solution. Although at this high concentration, the thermodynamic properties of the ^{3}He solute deviate slightly from ideal-gas behavior[2], this concentration was chosen to improve the cooling power at high temperature by increasing the oscillating osmotic pressure. Several cooldowns were performed with various drive speeds and various phases between the compressor and expander.

For one set of measurements, the speed was set to 0.25 rpm, and the phase between the maximum of the compressor cam and the minimum of the expander cam was varied between 70° and 130°. The lowest average temperature of about 0.65 K was reached during these runs with the phase set at about 100°. A set of measurements was then made with the phase set at 100°, with speeds of 0.07, 0.25, 0.31, and 0.45 rpm. For these runs, the lowest temperature reached was also 0.65 K, also at a speed of 0.25 rpm. Fig. 3 displays the average expander temperature as a function of time for this run. For these cooldowns, the compressor temperature was not regulated, and varied from 1.16 K at the slowest speeds to 1.23 K at the highest speed, so the largest temperature difference, about 0.55 K, was reached with the speed of 0.31 rpm. Other temperature differences were 0.54 K, 0.53 K, and 0.45 K at speeds of 0.25, 0.45, and 0.07 rpm respectively. In a later cooldown, where the backside of each piston was filled with only a 2% solution, and the concentration in the refrigerator was about 10%, a low temperature of 0.59 K was reached. Peak-to-peak concentration amplitudes were about 0.45 of the average concentration, and peak-to-peak temperature amplitudes in the expander at the lowest temperatures were about 50 mK.

The net cooling power of the refrigerator was determined from cooling-rate data such as Fig. 3 by using the measured heat capacity of the expander, adding the calculated heat capacity of 1/2 the regenerator, and then multiplying by the rate of change of temperature. To obtain what we call the gross cooling power, two corrections are added to the net cooling power: a correction of 33 μW/rpm due to heating from the bellows motion, determined by running the expander with no liquid in the refrigerator; and a second correction for thermal conduction down the regenerator, support structure, and fill lines of 11.5 μW/K, determined by measuring the warmup rate with the refrigerator not running. Gross cooling power as a function of T_c is shown in Fig. 4.

Figure 5 shows the average concentration in the expander and compressor as a function of expander temperature for the speeds mentioned above. For ideal-gas behavior, the relation between the temperatures and concentrations would be $X_cT_c = X_hT_h$, where X_c and X_h are the concentrations in the expander and compressor, and T_h is the average compressor temperature. In Fig. 5, $X_cT_c \cong 1.6X_hT_h$. The deviation from ideal-gas behavior is partly due to the ^{3}He solute showing slight effects of the Fermi degeneracy, and mostly due to heat

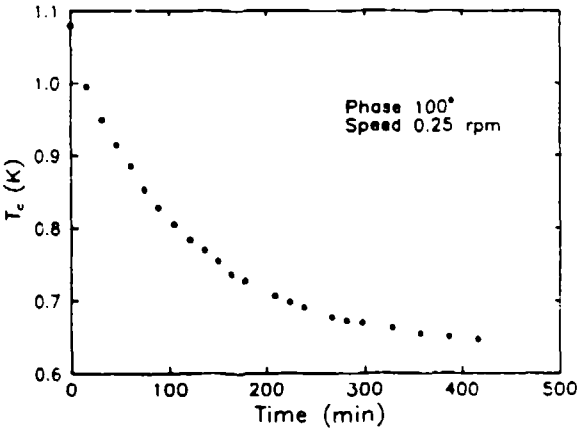

Fig. 3. Expander temperature as a function of time for a typical cooldown.

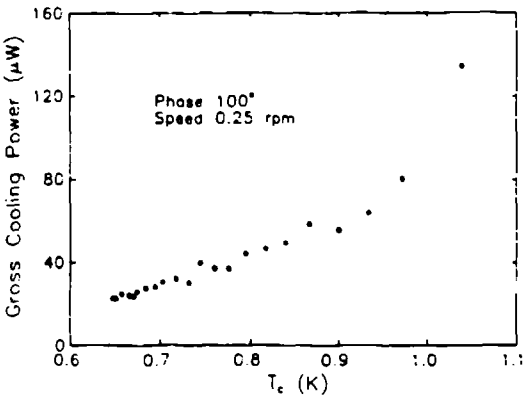

Fig. 4. Typical gross cooling power as a function of temperature.

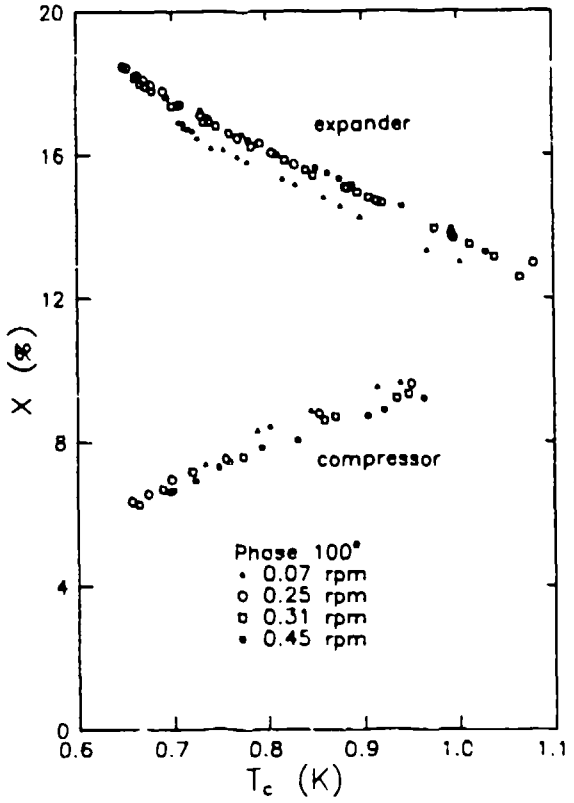

Fig. 5. Average ^{3}He concentration in the expander and compressor as a function of expander temperature, taken at four different speeds. As expected, the curves intersect at 12% when $T_c = T_h$.

flushing. In the heat-flush effect, the presence of a temperature gradient causes the ^{4}He normal-fluid excitations to flow down the temperature gradient, and the superfluid component to flow up the temperature gradient, with superfluid-normal fluid conversion taking place at the heat source and sink. The ^{4}He normal fluid drags ^{3}He atoms along with it, causing an excess buildup of ^{3}He atoms at the cold end. The factor of 1.6 agrees with rough extrapolations from data by Gestrich, Walsworth, and Meyer[7].

INITIAL INTERPRETATION OF RESULTS

Because of high local heat capacity and good thermal contact with the working fluid, a perfect regenerator allows no local temperature oscillations of the working fluid within the regenerator. For insight into the consequences of this characteristic, we write the energy flux density for hydrodynamic flow of an ordinary fluid:

$$H = \rho v(v^2/2 + w) \quad ,$$

where ρ is the fluid density, v is the fluid velocity, and w is the specific enthalpy. In an oscillating flow, ρ and w can be expanded as $\rho = \rho_0 + \rho_1$, $w = w_0 + w_1$, and $v = v_1$, where ρ_0 and w_0 are the average values and ρ_1, w_1, and v_1 are the first-order oscillating quantities. Substituting, taking the time average, and keeping only the lowest order terms:

$$H = \rho_0 \overline{v_1 w_1} \quad ,$$

where the overbar denotes time average. Using $dw = Tds + (1/\rho)dP$ and $ds = (c_p/T)dT - (\beta/\rho)dP$,

$$H = \rho_0 c_p \overline{T_1 v_1} + (1 - T_0\beta)\overline{P_1 v_1} \quad ,$$

where T_0 is the local average temperature, P is the pressure, c_p is the isobaric specific heat, and β is the isobaric expansion coefficient. For an ideal gas, $T_0\beta = 1$, so the second term vanishes. *Thus, in a perfect regenerator, where there are no temperature oscillations, the energy flow is zero.* The phasing of the pistons, however, is such that the work flow, given by the time average $\overline{P_1 \dot{V}_1}$, where $\dot{V}_1$ is the volume flow rate, is nonzero, flowing from the compressor to the expander. Since the energy flow through the regenerator is zero, the heat absorbed by the expander, $\dot{Q}_c$, must be equal to the work done on the expander, $\overline{P_1 \dot{V}_e}$, where $\dot{V}_e$ is the volume displacement rate of the expander.

Thus, we expect the cooling power of the SSR to be approximately $2\pi f P_{0s} V_1 \cos\varphi$, where P_{0s} is the osmotic pressure amplitude, V_1 is the volume displacement, f is the frequency, and φ is the phase angle

between P_1 and V_1. We infer P_{os} from measurements of n_3 using $P_{os} = n_3 k_b T$. V_1 was measured at room temperature. The phase was determined from the time between the maxima of the cam position and the concentration. In this way, we estimate the cooling power for the cooldown in Fig. 5 at the lowest temperatures to be 50 μW, close to the observed cooling power. This estimate is not expected to be better than a factor of two, since the piston motions were extremely non-sinusoidal, and the volume displacements were not accurately known.

To make further progress, we display in Fig. 6 $Q_c(1+T_h/T_c)$ vs T_h-T_c, where Q_c is heat per cycle removed by the expander, obtained by dividing the measured cooling power of Fig. 4 by the operating frequency. In the classical-gas Stirling cycle, with given volume displacements in the expander and compressor, a 90° phase shift between the two, and negligible regenerator volume, the cooling per cycle[8] is frequency independent and has a temperature dependence given by $(1+T_h/T_c)^{-1}$, so that $Q_c(1+T_h/T_c)$ is temperature independent. In contrast, in Fig. 6 $Q_c(1+T_h/T_c)$ has a slight frequency dependence and a large temperature dependence. The frequency dependence is likely due

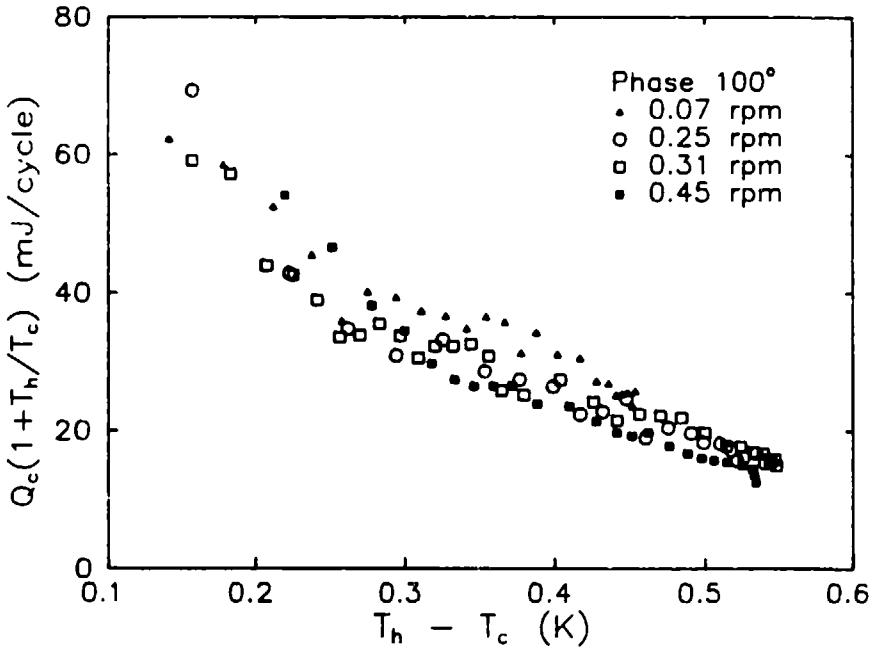

Fig. 6. $Q_c(1+T_h/T_c)$ vs the temperature difference between the compressor and expander. For a reversible, ideal-gas Stirling cycle refrigerator, this quantity is independent of temperature. The temperature dependence in this figure reflects the non-ideality of our prototype. We use T_h-T_c, rather than T_c, as abscissa because the compressor temperature was not well regulated, varying from 1.16 K at the slowest speed to 1.23 K at the highest speed.

either to viscous losses or imperfect thermal contact in the regenerator[9], as both processes are velocity dependent. But the large deviation from constancy with temperature in Fig. 6, corresponding to about 25 mJ/cycle of lost cooling power at the lowest temperatures, must be due to processes that are independent of velocity. We list several candidates here.

The most likely source of inefficiency is the dependence of the heat capacity of the ^{3}He solute on number density[10]. As the ^{3}He concentration increases, the heat capacity per ^{3}He atom deviates from the ideal gas value of $(3/2)k_bT$. This causes a parasitic flow of heat down the regenerator since the heat capacity, and therefore the amount of heat transported, are different on the high concentration and low concentration strokes of a cycle. The heat flow due to this effect[11] is $\pi/2\ \partial c/\partial X\ V_1\ \Delta X \Delta T$, where ΔX is the concentration amplitude and ΔT is the temperature difference between the hot and cold ends of the regenerator. At our lowest temperatures, we estimate this heat load to be about 20 mJ/cycle.

Another irreversible mechanism is that, in the ideal Stirling cycle, the compressions and expansions are isothermal. In our refrigerator, since the thermal penetration depths are on the order of the dimensions of the fluid volumes within the pistons, the compressions are partially adiabatic, and so there is irreversible heat transfer across finite temperature differences[12], such as when the fluid enters the regenerator. The excess entropy generated in this process is $\Delta S \simeq \rho c V \delta T^2 / T$, where ρ is the fluid density, c is the heat capacity per mass, V is the volume of fluid displaced into the regenerator, δT is the temperature amplitude in the piston, and T is the temperature of the piston. The work is $T\Delta S$, and is about 1 mJ per cycle at the lowest temperatures, not large enough to account for the losses, and without the strong temperature dependence observed in Fig. 6.

Finally, there are effects in the SSR that are unique to it, not occurring in ideal gas Stirling refrigerators. These include superfluid turbulence[13], where the turbulent state consists of a tangle of quantized vorticity; the heat-flush effect discussed above; and the ^{4}He normal-fluid excitations, which are numerous near 2 K.

Clearly, there is much about the SSR that we do not yet understand.

LIMITATIONS AND IMPROVEMENTS

The ultimate performance of the SSR will be limited by the thermodynamics of the ^{3}He solute as it approaches complete Fermi degeneracy[2] at low temperatures, at concentrations at or below the low-temperature solubility of 6.4%. For example, in a 5% solution, the Fermi temperature is 0.34 K; so that, at about 50 mK, the cooling power of a fixed-volume-displacement SSR is only half what it would be for a classical gas of the same number density, and rapidly drops to zero at

lower temperatures.

Many improvements to the SSR seem possible by analogy with ideal-gas Stirling refrigerators. A single stage may ultimately span an order of magnitude in temperature, and two-stage SSRs could reach very low temperatures. A dual-parallel SSR could eliminate the need for the pure ^{3}He heat reservoir: Two SSRs running at the same average temperatures but 180° out of phase in time could regenerate each other. An orifice-pulse-tube[14] configuration would be an exceeding important practical advance, as it would eliminate the moving parts at T_C. Elimination of the remaining moving parts could then be accomplished by use of a thermocompressor.

APPLICATIONS AND ADVANTAGES

Since satellite-borne infrared and X-ray sensors work best at low temperatures, some effort is now spent on adapting dilution refrigeration[15] and demagnetization refrigeration to the space environment. However, both of these conventional methods for cooling below 1 K have drawbacks in the space environment. Both are inefficient; the first doesn't naturally work in zero gravity; the second requires large magnetic fields. As the SSR works quite independently of gravity and magnetism, and has immediate potential for an efficiency of the order of Carnot's efficiency, further development may demonstrate its utility for sub-1-K cooling in space.

Most of the cost in the earth-bound dilution-refrigerator industry is for large room-temperature plumbing and pumps; these will not be required in the SSR, which may be much less expensive as a result. This low cost could make low-temperature research easier everywhere, and feasible for the first time at small colleges and in developing countries. The high efficiency offered by the SSR would also be a modest advantage in this arena; the $100-$200 per week electric bill for operation of a typical dilution refrigerator is a significant cost to some researchers.

ACKNOWLEDGMENT

This work is supported by the Division of Materials Sciences in DOE's Office of Basic Energy Sciences.

REFERENCES

1. O.V. Lounasmaa, *Experimental Principles and Methods Below 1 K*, Academic Press, New York (1974).

2. J. Wilks, *The Properties of Liquid and Solid Helium*, Clarendon Press, Oxford (1967).

3. H. London, discussion, Proc. Int. Conf. Low Temp. Phys., Oxford, 1951, p. 157.

4. G. Walker, *Cryocoolers*, Plenum, New York (1983).

5. L.E. DeLong, O.G. Symko, and J.C. Wheatley, "Continuously operating ^{4}He evaporation refrigerator", Rev. Sci. Instrum., vol. 42 (1971) p. 147-150.

6. H.A. Kierstead, "Dielectric constant, molar volume, and phase diagram of saturated liquid ^{3}He-^{4}He mixtures", J. Low. Temp. Phys., vol. 24 (1976) p. 497-512.

7. D. Gestrich, R. Walsworth, and H. Meyer, "Transport properties in ^{3}He-^{4}He mixtures near the superfluid transition", J. Low Temp. Phys., vol. 54 (1984) p. 37-61.

8. I. Urieli and D.M. Berchowitz, *Stirling Cycle Engine Analysis*, Adam Hilger Ltd., Bristol (1984), Fig. 2.18.

9. P.C. Allen, G.H. Fisher, W.R. Knight, D.N. Paulson, and J.C. Wheatley, "Heat regeneration in Malone-type liquid engines using a parallel-plate thermodynamic pile geometry", J. Appl. Phys., vol. 52 (1981) p. 3876-3883.

10. D.O. Edwards, D.F. Brewer, P. Seligman, M. Skertic, and M. Yaqub, "Solubility of ^{3}He in ^{4}He at 0 K", Phys. Rev. Lett., vol. 15 (1965) p. 773-775.

11. P.C. Allen, W.R. Knight, D.N.Paulson, and J.C.Wheatley, "Some heat engine cycles in which liquids can work", Proc. Natl. Acad. Sci. USA, vol. 77 (1980) p. 31-35.

12. Ref. 8, ch. 4.

13. J.T. Tough, "Superfluid turbulence", *Progress in Low Temperature Physics*, D.F. Brewer, ed., North Holland, Amsterdam (1982), vol. 8, p. 133-219.

14. R. Radebaugh, "A review of pulse tube refrigeration", *Advances in Cryogenic Engineering*, Plenum, New York (1990), vol. 35, p. 1191-1205.

15. U.E. Israilsson, D. Petrac, H.W. Jackson, and D.M.Strayer, "Use of an electric field gradient instead of gravity to obtain a suitable ^{3}He-rich/^{4}He-rich interface in the mixing chamber of a dilution refrigerator"; and P.R. Roach, "Thermal efficiency of a zero-g dilution refrigerator", Proc. Int. Cryocooler Conf. 5, Monterey CA, 1988, p. 187-204.

A LINEAR DRIVE STIRLING CYCLE CRYOCOOLER FOR EO/IR APPLICATIONS

ALAN L. WEEKS, P.E.
CTI-CRYOGENICS, A DIVISION OF HELIX TECHNOLOGY CORPORATION
266 SECOND AVENUE
WALTHAM, MA 02254

ABSTRACT

A joint development effort between CTI-CRYOGENICS and GE-AESD Utica, NY has produced a dual piston, linear driven, Stirling cycle cryocooler for airborne applications. The split cycle cryocooler consists of a linear compressor, 70 inch transfer line, and free stroking expander. The extremely long transfer line, required by this application, presented many unique design challenges. The linear compressor makes use of active position control over both moving pistons to insure trouble free operation throughout the flight environment. A moving magnet linear motor was selected for high efficiency, low weight, and isolation of the motor coils from the helium gas volume to combat contamination and facilitate heat removal. The resultant cryocooler represents a light weight, low vibration, long life alternative to current rotary cryocooler technology.

This paper describes the system tradeoffs and design, emphasizing test data accumulated to date on two engineering prototypes. Performance data for a range of applications is presented graphically. The status of life and environmental testing is also included. The prototype development was completed in only six months through the application of "Simultaneous Engineering" applied in a project team setting. This early-on collaboration between engineering and manufacturing has resulted in a producible and simple design, which has only three moving assemblies and a low part count.

INTRODUCTION

Stirling cycle cryocoolers have found widespread usage within the electro-optics community during the past ten years to provide cooling, in the liquid nitrogen region, for infrared sensors and electronics [1]. Early Stirling cryocoolers were integral cycle rotary drives using spring loaded lip seals for critical, life limiting sealing. The inherent performance limitations of the integral Stirling cycle for applications requiring low self induced vibration at the sensor interface gave way to the development of the split Stirling cycle cryocooler. As Stirling cryocooler technology began to evolve it became clear that longer, more reliable operation was required. Spring loaded lip seals were replaced by hard on hard and hard on soft clearance seals [2]. Conventional rotary motor drives with a piston and crank mechanism were identified as a reliability limitation and

major source of helium gas contamination; yet another obstacle to long life.

The elimination of the piston and crank mechanism by using a linear motor can significantly reduce the number of mechanical parts needed in a Stirling cycle compressor. Ball and needle bearings, connecting rods and wrist pins are no longer required to convert rotary motion into reciprocating motion. Any reduction in the number of contacting or moving mechanical parts will increase the overall reliability of the cryocooler.

Linear drive motors used in place of conventional rotary motors can also extend cryocooler life by eliminating many contaminants from the helium gas. Several implementations of linear motor technology have the potential to isolate motor coils and eliminate lubricants from the helium gas volume. A low side load linear motor will also decrease the seal wear in comparison to a conventional rotary crank mechanism. Early linear drive designs utilized loudspeaker type moving coil motors with flexible lead wires [3]. A major disadvantage of these systems was the inability to isolate the motor coils from the helium gas volume. As research continued, moving iron and moving magnet type motors have provided additional benefits and design flexibility. Continued development of linear drive Stirling cycle cryocoolers, supported by government funding, has produced reliable systems for long life operation in excess of 2500 hours (Mean Time To Failure, MTTF) [4].

CTI-CRYOGENICS has been a leading supplier of Stirling cycle cryocoolers for the past 18 years. Cryocoolers have been supplied for a wide variety of applications including night vision, missile guidance, fire control, space and airborne IR. Development of linear drive cryocoolers at CTI-CRYOGENICS, started in the early 1980's, has produced several common module type designs using a variety of linear drive design options [5]. Moving iron and moving magnet type motors have been applied to single and dual piston compressor designs. Single piston designs require a dynamic vibration absorber tuned to a single operating frequency. Dual opposed piston compressors are inherently balanced at any operating frequency providing additional flexibility.

The dual opposed piston concept with a moving magnet linear motor was selected to meet the needs of the GE-CTI joint development based upon experience with several different types of linear compressor designs. The joint development called for GE-AESD to design and package power electronics for the motor to maximize the special capabilities of GE-AESD and CTI-CRYOGENICS. Control electronics were developed by CTI-CRYOGENICS, but packaged by GE-AESD. The unique arrangement allowed GE engineers to trade off power conversion options and EMI concerns while making optimum use of system electronics and available space. CTI-CRYOGENICS was able to concentrate on development of the cryocooler and control circuitry, without concern for packaging of electronics within the often restrictive cryocooler envelope.

Key design parameters for the cryocooler are summarized in Table 1. The 70 inch transfer line required by this application presented many design challenges. The random vibration seen during flight operation was a major factor in the decision to use active position control over both moving pistons in the compressor. Selection of the linear drive compressor concept was based primarily upon the optimization of size, weight, efficiency and life capability.

DESIGN TRADEOFFS

The design tradeoffs performed as part of the joint development effort were focused upon all aspects of the compressor, expander and transfer line. Thermodynamic simulations of performance using CTI-CRYOGENICS' split Stirling computer program provided a baseline for component sizing and operating parameters. High frequency operation in the 50-60 HZ range was not feasible within the power limits of the specification due to the extremely long transfer line. Computer predictions suggested increased helium charge pressures to reduce compressor size and weight, without sacrificing performance. The inner diameter of the transfer line was also recognized as an important parameter for optimization of performance and power levels. Results of analytical thermodynamic tradeoffs identified the following range of variables for prototype testing:

CHARGE PRESSURE: 800 - 1200 PSIG
OPERATING FREQUENCY: 30 - 40 HZ
TRANSFER LINE ID: 0.049 - 0.057 INCHES

PARAMETER	SPECIFICATION
MAXIMUM COMPRESSOR WEIGHT:	4.54 kg
COMPRESSOR ENVELOPE:	83 mm Diameter x 211 mm Long
COLD CYLINDER ENVELOPE:	9.5 mm Diameter x 27.7 mm Long
TRANSFER LINE LENGTH & OD:	1778 mm Long x 1.75 mm Diameter
TEMPERATURE ENVIRONMENT:	-54°C TO 71°C Amb.
IMPOSED FLIGHT VIBRATION:	4.5 g Random, 2-2000 HZ
MAXIMUM POWER CONSUMPTION:	200 Watts RMS @ 71°C Amb.
REFRIGERATION CAPACITY:	0.75 Watts @ 65 K @ 71°C Amb.
COOLDOWN TIME:	< 8 minutes (800 Joule load)
LIFE REQUIREMENT:	2500 Hour MTTF, 4000 Hour Goal

TABLE 1 - KEY DESIGN PARAMETERS

An existing, proven, pneumatically driven expander design was modified to obtain additional capacity for operation with the linear compressor to shorten the cryocooler development cycle. Several options for regenerator matrix material and internal hardware were selected because of the inherent uncertainties involved in modeling a free stroking pneumatically driven expander. This provided the capability to fine tune the system for optimum performance during prototype testing.

As previously discussed, the linear compressor concept selected for this application was a dual opposed piston design with two moving magnet linear motors. The dual opposed piston design has several advantages over the single piston compressor with a vibration absorber. From a total weight standpoint, given the same operating frequency and motor type, the dual opposed piston compressor will weigh less than a single piston system. For a given swept volume, the total moving mass for each compressor type will be approximately the same. A vibration absorber is required to obtain dynamic balance for a single piston system. The entire weight of the vibration absorber represents additional weight beyond that required for a dual opposed piston compressor. Limitations also exist regarding the efficiency of a vibration absorber and the narrow resonant frequency band which restricts operating range. The primary advantage of the single piston compressor is the need for a single linear motor and accompanying electronics. The advantage may be evident in cost savings, but only at the expense of increased weight. A single piston system was not considered a viable option for this development because of the extreme importance of reduced weight for airborne applications.

The selection of a linear motor design has probably received more attention and debate over the past ten years than any other aspect of linear cryocooler design. CTI-CRYOGENICS evaluated three linear motor options during the design tradeoff phase of this development. Moving coil, moving magnet, and moving iron type designs were analyzed for size, weight and efficiency. Additional concerns were also considered such as side load, life and reliability. The moving coil design, although attractive in many ways, was rejected because of the challenges associated with delivering current to a moving assembly. The inability to isolate the motor coils from the helium environment was viewed as another significant disadvantage to the moving coil design. The moving iron design, which is actually a variable reluctance motor, is poorly suited for high power applications because of its relatively low efficiency. A moving magnet motor is extremely efficient due to energy storage in the magnet thickness which forms part of the air gap. Heat removal characteristics, the ability to isolate the motor coils from the helium gas, high efficiency and low system weight led to the selection of a moving magnet motor.

The moving magnet linear motor will possess higher side load characteristics than the alternative motor types. Side loads are dependent upon flux density in the motor air gap, geometric alignment of plunger and stator center lines and permanent magnet uniformity. Two different

motors were constructed for each prototype compressor to investigate the effects of air gap variation on side load and efficiency. The base design used an 0.050 inch air gap, while the second compressor motor was modified to obtain an 80% increase in air gap. The increase was accomplished by a reduction in permanent magnet radial thickness. This provided a test vehicle to tradeoff input power, peak current, and motor efficiency for reduced side load. The potential for wear, induced by the motor side loads, was easily managed by using large bearing areas for the plunger magnet supports.

System level tradeoffs were conducted at GE-AESD to determine the optimum voltage level for cryocooler power. Three phase, 400 HZ aircraft power is available at the 270 VAC level (line to line). It was quite probable, however, that if unconditioned aircraft power were used to drive the linear motors, unacceptable EMI levels would effect the imaging system. GE conducted a comprehensive evaluation of available motor drives. Recent innovations in the packaging and application of DC to DC converters were identified as a low noise method for motor drive. Rectified three phase 270 VAC aircraft power can be reduced to 48 VDC by using a DC to DC converter. Low level DC is then available for cryocooler power to drive the linear motors. The output of the DC to DC converter can be continuously varied to provide an alternative to traditional pulse width modulated (PWM) motor drive power. The resulting power spectrum is anticipated to significantly reduce EMI levels.

A control block diagram is shown in Figure 1 for the dual piston linear compressor. Feedback control over both moving pistons is used to minimize vibration and maintain optimum refrigeration capacity during the flight environment. The relatively large motor size, driven by the high power requirements, increases the size of the moving mass associated with the pistons. A large moving mass will require some form of feedback motion control in the presence of a given acceleration field. As shown in Figure 1, both pistons are controlled from the same sine wave master reference. This eliminates the need for any secondary phase control loops to lock one side to the other. Higher order harmonics present in free periodic motion are eliminated by controlling piston motion to a sine wave reference. The resulting self induced vibration will be lower for a system with feedback motion control which can minimize the unbalanced acceleration components on each side of the compressor.

Several combinations of position sensors were considered to form the feedback control loop between the motor current input and position output. Linear variable differential transformers (LVDT), Hall effect devices (HED) and optical methods were all evaluated for accuracy, linearity, temperature sensitivity and packaging. The favored approach, LVDT's, was unavailable in an appropriate package at the time of evaluation. CTI-CRYOGENICS had developed expertise in the application of Hall effect devices for position sensing on prior development programs. Combined with the absence of packaging

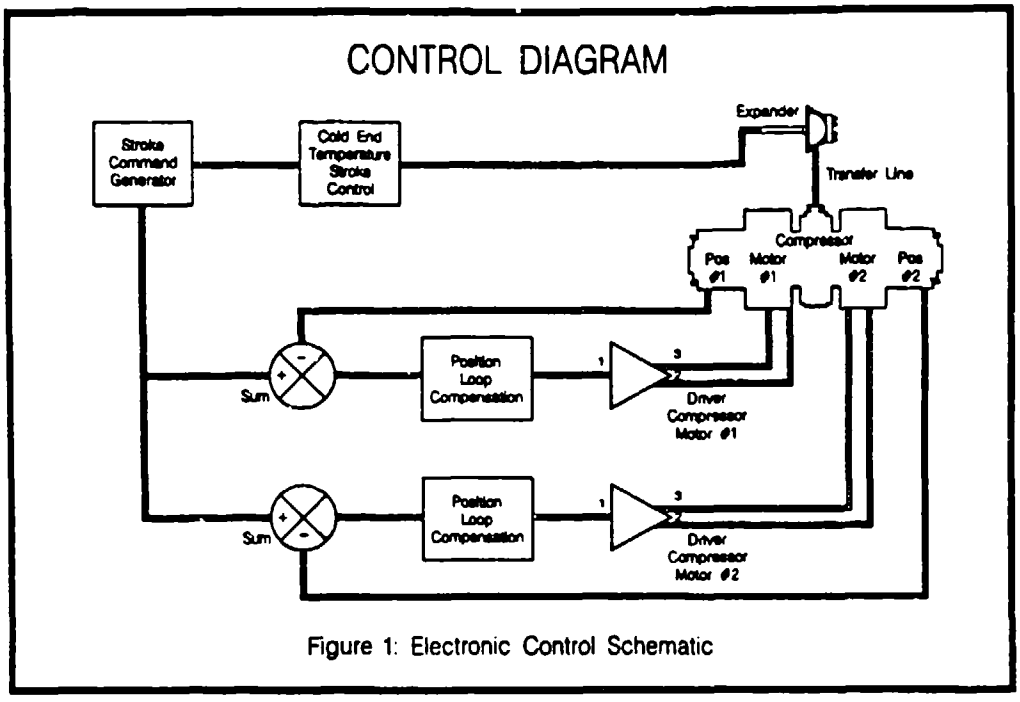

Figure 1: Electronic Control Schematic

constraints, the HED was selected for position sensing of the the compressor piston motion.

It was originally hoped that the motor magnets could function as target sensing magnets for the HED. The influence of induced flux from the motor coils prohibits location of a HED in close proximity to the motor. As shown in Figure 2, a separate target magnet, remote from the motor, had to be used. The use of two sensors is intended to provide a redundant arrangement capable of temperature compensation.

PROTOTYPE DEVELOPMENT

The prototype linear compressor, shown in Figure 2, was designed based on the tradeoff decisions presented in the previous section. Aluminum and titanium were used extensively, where possible, to meet the weight goals of the specification. Aluminum was the material of choice for ease of manufacture and heat dissipation. Titanium was used where additional structural strength was required, such as for the pressure vessel. In most instances, the materials selected had to be non-magnetic to prevent interaction with the linear motor. The configuration shown in Figure 2 is representative of the small air gap motor. Motor stators were constructed using radial laminations to reduce eddy currents. A laminated stator provides additional efficiency for high power applications. The gas clearance seals, which isolate the working and non-working helium gas volumes, also serve as

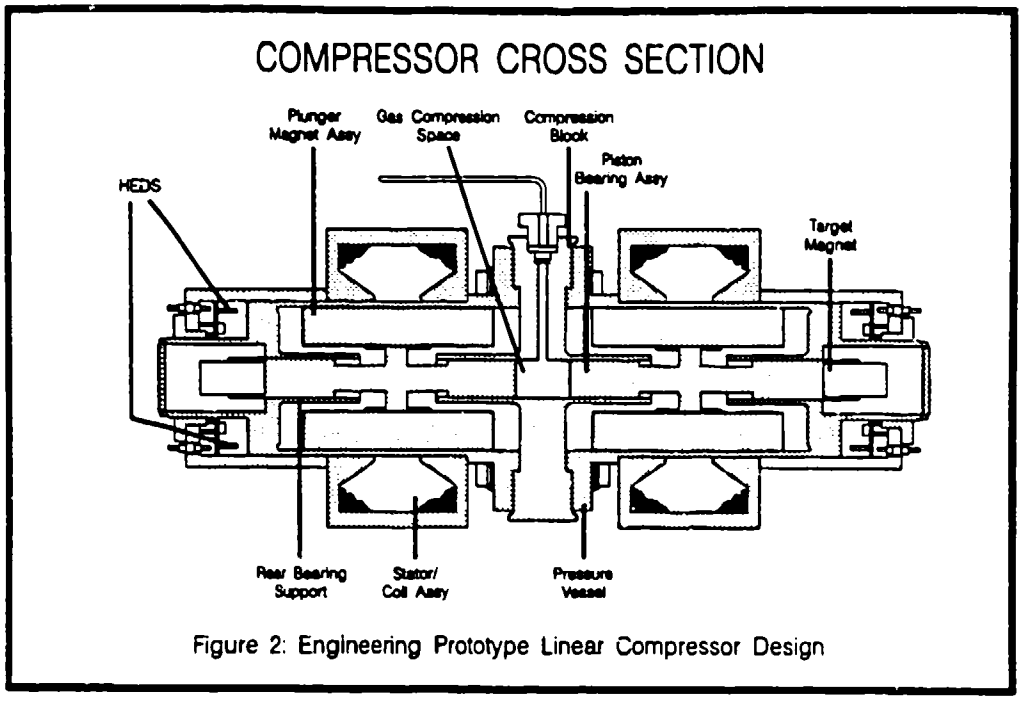

Figure 2: Engineering Prototype Linear Compressor Design

bearing surfaces.

The large bearing areas minimized seal wear for the limited life requirements of the prototype compressors. A long life version of the prototype, which eliminates bearing loads from the clearance seals, is currently undergoing initial testing at CTI-CRYOGENICS.

The moving magnet linear compressor has been designed to operate at the resonant frequency of the internal gas spring-mass system. The piston area, stroke, moving mass and compression ratio have all been selected to obtain the resonant frequency for an assumed single degree of freedom linear oscillator. The gas forces imposed upon the piston are cancelled by the inertial load of the moving mass when operating the compressor at resonance. The motor only needs to overcome the flow losses (viscous load) within the system. Theoretically the motor load will be zero at each end of stroke, while reaching a maximum at mid-stroke which coincides with maximum velocity. There are many nonlinearities present in the real system, such as friction and gas force imbalances, which lead to significant variations from the idealized linear oscillator. The theoretical model is still quite useful for initial sizing and preliminary design tradeoffs.

The linear compressor is cooled by a liquid heat exchanger which contacts the full outer circumference of the motor stators and compression block. The external coils associated with the moving

magnet linear motor provide an ideal path for motor heat removal. A radial heat conduction path from the compression chamber to the external cooling jacket effectively removes the heat generated during compression. The high input power required by this application, driven by the long transfer line, dominated the design of the compressor. The motor selection and choice of materials, in many instances, resulted from the need to dissipate high power levels over relatively small surface areas.

The use of adhesives and non-metallics within the helium volume has been kept to a minimum in an effort to reduce contamination outgassing. Any adhesives and non-metallics used have superior outgassing properties. The reduction of internal contaminants, which prolongs life, is one of the major advantages of linear drive cryocoolers.

The goal of prototype development was to establish a performance baseline that met the goals of the specification within a minimum period of time. A dedicated project team was established to accelerate the traditional development cycle. The project team combined members from engineering, quality and manufacturing. The concept of "Simultaneous Engineering", the early-on involvement of engineering and manufacturing, produced some dramatic results. Significant time savings were realized by structuring the design around readily available materials, standard gaging and nominal size stock. Prototype drawings were reduced to a producible form prior to the machining of any parts. The transition to full scale development and production will also involve much less risk by building in quality and producibility from the concept stage.

The net result of a dedicated project team operating in a simultaneous design mode was the completion of prototype testing in only nine months. Two linear compressors (each with a different motor), expanders and a variety of transfer lines were designed and fabricated in approximately five months. The majority of parts were made in-house at CTI-CRYOGENICS' development machine shop. The remaining four months were spent conducting an extensive series of tests to determine the optimum combination of hardware and operating conditions to maximize refrigeration capacity. The regenerator matrix material and expander stroking were defined during this testing period. The small air gap motor proved to have superior force/current characteristics without any wear induced problems caused by excessive side load. All power measurements presented were based on tests conducted using the small air gap motor compressor. Thermodynamic performance data was statistically equivalent for the two prototype compressors tested. The range of operating conditions and transfer line inner diameters, discussed in the previous section, were resolved as follows:

CHARGE PRESSURE: 900 PSIG
OPERATING FREQUENCY: 30 HZ
TRANSFER LINE ID: 0.052 INCHES

	ACTUAL	SPECIFICATION
COMPRESSOR WEIGHT (kg)	3.4	4.54
REFRIGERATION CAPACITY (WATTS) @ 65 K @ 71°C AMB.	1.0	0.75
INPUT POWER @ CAPACITY @ 71°C (WATTS)	165	200
REFRIGERATION CAPACITY (WATTS) @ 65 K @ 23°C AMB.	1.4	0.75
INPUT POWER (WATTS) REQUIRED FOR 0.75 WATT CAPACITY @ 65 K @ 23°C	87	200
COOLDOWN TIME (MINUTES) FROM 300 K TO 65 K	3.15	8

TABLE 2 - PROTOTYPE DESIGN VS. SPECIFICATION VALUES

The performance of the final system, tested with breadboard electronics, is shown in Table 2 with the specification values. All testing was conducted in an environmental chamber equipped with a CTI-CRYOGENICS' Cryo-Torr vacuum pump to maintain cold end Dewar vacuum levels below 10 microns. Heat was removed from the linear compressor with a liquid cooling jacket connected to an environmental control unit (ECU) located external to the test chamber. The expander warm end was convectively cooled using an air stream indicative of the actual air flow in the GE system. Cooling was sufficient to limit the surface temperature rise of the compressor and expander to approximately 20°C above ambient.

The values shown in Table 2 have completely satisfied, and in many areas, exceeded project goals. Plans are underway at CTI-CRYOGENICS to complete full scale development (FSD) and initiate limited production based upon the success of prototype development.

The 25% reduction in weight from the specification goal, shown in Table 2, was a substantial achievement. Weight was designated as a key parameter for reduction during prototype development. A current summary of weight was always maintained by tabulating all piece part weights on individual detail drawings. All layout work and detail drawings were generated using CTI-CRYOGENICS' computer aided design (CAD) system. The CAD system proved to be an invaluable tool in

evaluating the effect of design changes on piece part weights. The entire thermodynamic design of the linear cryocooler was driven by the 0.75 Watt capacity requirement at 71°C ambient. The resulting 1.0 Watt capacity demonstrated by two prototypes represents adequate margin for the inevitable variations encountered in production. Maximum capacity values were obtained with the linear compressor operating at 100% of available stroke. The compressor stroke can be reduced to maintain a temperature set point at 65 K for the lower heat load used by the GE application of 0.75 Watts. The input power is reduced substantially relative to the 200 Watt limit specified under closed loop temperature control. The 87 Watt value measured at the temperature control point shown in Table 2 required the compressor to stroke at approximately 75% of the maximum stroke. Life and power consumption will be considerably enhanced during normal operating modes with reduced stroke.

Cooldown time is the final measurement of cryocooler performance and is shown in Table 2. Not to be overlooked, cooldown time is extremely fast resulting from the combination of inherent high capacity and relatively high operating pressures.

TEST DATA

The linear cryocooler has been tested using two configurations of transfer lines to provide a comprehensive series of test data for IR system designers and potential users. Data is presented in Figures 3 and 4 for the 70 inch transfer line, required by the GE application, and also for a shorter 9 inch line. Testing with the short line was conducted for the same combination of operating parameters and hardware presented in the previous section.

Significant power reductions were not realized with the short line due to the dramatic increase in capacity and higher mass flow through the regenerator. If needed, the system could be re-optimized for the shorter line at a different charge pressure and operating frequency. Given the abundant capacity shown in Figure 3, re-optimization would be done primarily to reduce power at the expense of capacity. Input power for the performance presented in Figure 3 at 65 K was 165 and 150 Watts for the long and short lines respectively. Power will fall slightly as refrigeration level and cold end temperature increase. Power consumption at 90 K was approximately 5% less than the power consumed at 65K.

The linear cryocooler was designed to be fully functional over the traditional military temperature range. Refrigeration capacity versus ambient temperature for both the long and short line configuration is presented in Figure 4. Data is presented at 65 K and 80 K for comparison of different IR sensor types. Long term operation at temperatures above 89°C ambient should generally be avoided due to the practical limitations involved in maintaining internal temperatures below the limit of structural adhesives. Improvements in performance at low ambients became diminished by the decreased internal pressure that

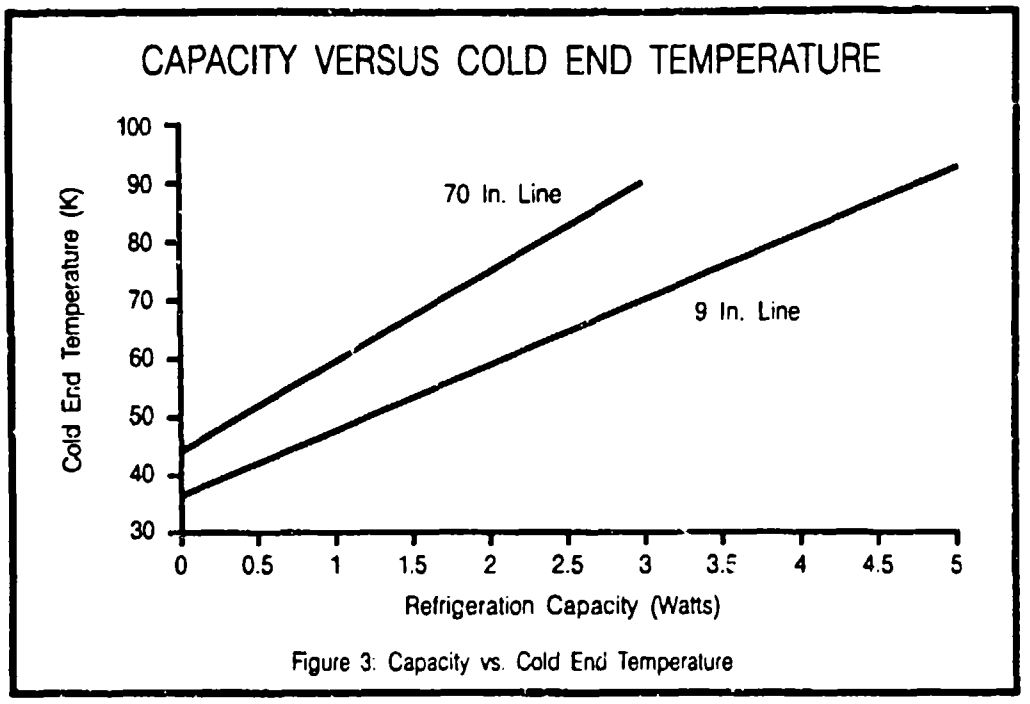

Figure 3: Capacity vs. Cold End Temperature

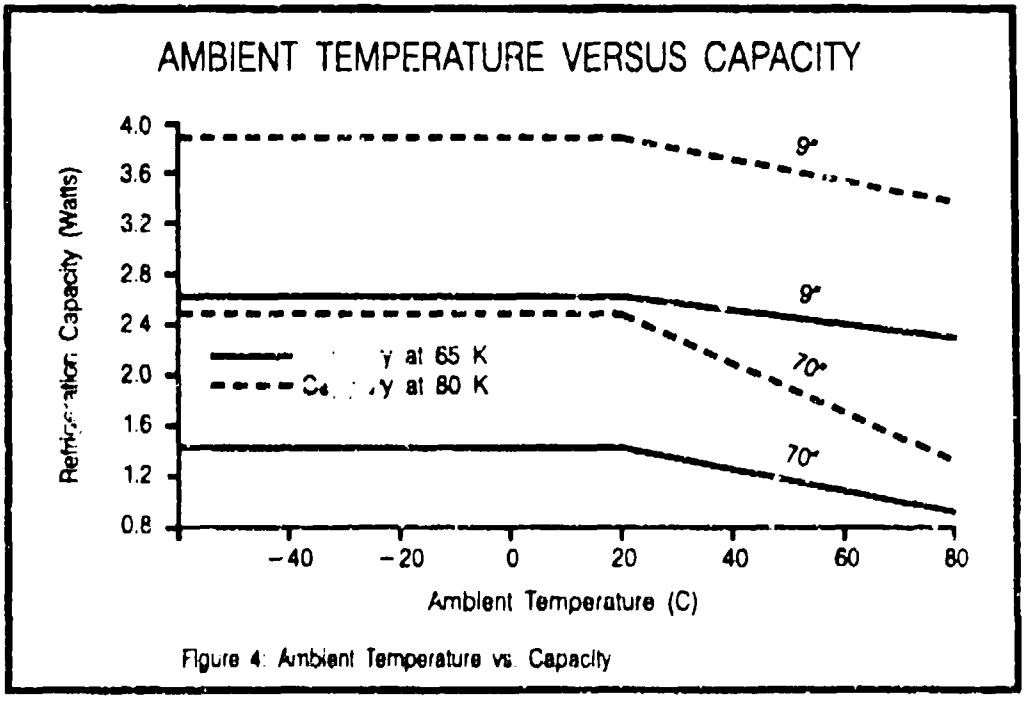

Figure 4: Ambient Temperature vs. Capacity

occurs within a closed cycle cryocooler as temperature decreases. The effects of liquid cooling also tend to show greater performance improvements at high temperature and less change at temperatures below 0°C ambient.

Compressor stroke can be reduced to maintain a desired temperature set point and level of refrigeration. Stroke variation is a new dimension of flexibility which can result in significant power savings during normal operation. Test data for both long and short transfer lines at 65 K and 80 K is presented in Table 3 for selected levels of refrigeration. The data clearly shows the dramatic power savings available during temperature control operation. For this application, and in many instances, a cryocooler must be sized for an "off-normal" operating condition such as high ambient temperature. Additional capacity must be added to the cryocooler in cases where a constant heat load must be maintained at high ambient. The sizing point may also represent only a small percentage of the actual operating profile of the cryocooler. Life can be prolonged in addition to reducing power by using temperature control to reduce unnecessary capacity. Temperature control via compressor stroke reduction provides an alternative to conventional frequency variations which would upset the resonant balance of a linear system.

One of the engineering prototype compressors was subjected to rigorous vibration testing to assess the efficiency of the control system and insure mechanical integrity. The compressor must have the ability to

INPUT POWER (WATTS) / COMPRESSOR STROKE (% OF MAXIMUM)		
COLD END TEMPERATURE LEVEL	65 K	80 K
0.75 WATTS REFRIGERATION MAINTAINED USING A 70 IN. TRANSFER LINE	87 W / 74 %	50 W / 54 %
2.0 WATTS REFRIGERATION MAINTAINED USING A 9 IN. TRANSFER LINE	100 W / 81 %	64 W / 62 %

TABLE 3 - TEMPERATURE CONTROL PERFORMANCE

control stroke and maintain a cyclic pressure to drive the expander during flight. The acceleration forces imposed during the flight environment act upon the moving masses within the compressor to the extent allowed by the stiffness of the control system. The use of position feedback to control stroking was driven in part by the 4.5 g random flight vibration environment specified. The compressor was mounted along the center line axis of motion in a vertical vibration tester. All excitation was along the axis of motion. Several types of testing were conducted, both operating and non-operating. Sinusoidal frequency sweeps at 1 and 3 g's, between 2 and 2000 HZ, were completed prior to random vibration at 4.5 g. A more severe 9.5 g test was also performed to fully explore the limits of the compressor design. Random vibration was conducted at the same frequency interval used for the sine sweeps. Non-operating sine sweep data proved useful in determining the mechanical resonance and damping characteristics of the linear compressor. Operational testing under 4.5 g random vibration verified the ability of the control system to maintain stroke during flight. The control system was sufficiently stiff to prevent impact at the compressor end stops while operating at 80% stroke. Disassembly after vibration testing showed no signs of damage or degradation induced by any of the testing. Subsequent performance testing demonstrated pre-vibration capacity within the limits of test repeatability.

SUMMARY

The preliminary design concepts for the linear compressor were completed near the beginning of April, 1989. Detail drawings were finished by late spring and machining was well underway by mid-summer. Initial testing was started in early fall at the conclusion of fabrication and assembly. By year end electronic controls had been debugged and testing was completed to establish the required performance. The long life design was also completed and procurements were initiated to support FSD during the testing period. The entire process which spanned approximately 9 months, was completed on schedule and within the established cost boundaries.

The project team, operating on a cross functional basis, was essential to the success of this development. By creating an autonomous unit, fueled with company resources, the project team gained the ability to accelerate the pace of development. The power to make decisions, analyze failures, and chart a new course was handled within the project team. Many technical issues were resolved within a limited amount of time by taking a variety of parallel path approaches to hedge risk in key areas. Conventional methods must be abandoned for improved efficiency to accelerate the pace of development in today's business environment. The resulting cryocooler, as previously stated, met or exceeded the specification goals in all areas.

The reliability of any mechanical assembly containing a variety of parts will always be proportional to the total number of parts. A similar generalization could also be made concerning the number of

parts that are in motion or in contact. There has been a major focus on minimizing the number of parts, particularly moving assemblies from the beginning of prototype development. During the design layout activity, given some extra effort, it is quite feasible to use parts for multiple functions. In many instances parts are used to retain, guide and/or support. The total number of parts required can be reduced when a part can be used in a multi-functional manner. The resulting linear cryocooler contains only three moving assemblies and five stationary structural parts. A low part count cuts all aspects of cost including drawing maintenance, procurement, inspection, inventory and assembly time.

The combination of inherent reliability and ease of manufacture enhances the value of the CTI-GE linear cryocooler. This joint development was made possible by the expertise of GE-AESD in providing high reliability military electronics packaging and power drive for the cryocooler. The proven high capacity and ability to operate in temperature and vibration environments, minimizes risks commonly encountered in the later stages of development. The long life design, currently undergoing initial testing at CTI-CRYOGENICS, provides a vehicle to obtain the specified MTTF of 2500 hours.

REFERENCES

1. F. Eberth, F. Chellis, "Comparing Closed Cycle Cryocoolers", Electro-Optical Systems Design, November 1979.

2. F. W. Pirtle, P. K. Bertsch, P. J. Kerney, "Cryogenic Cooler Seals Investigation", AFWAL-TR-87-3046, Air Force Wright Aeronautical Laboratories, September 1987.

3. F. Stolfi, A. K. de Jonge, "Stirling Cryogenerators with Linear Drive", Phillips Technical Review, Volume 42, No. 1, April 1985.

4. L. Knox, P. Patt, R. Maresca, "Design of a Flight Qualified Long Life Cryocooler", Proceedings of the Third Cryocooler Conference, NBS Special Publication 698, pg. 99, 1984.

5. P. J. Kerney, G. J. Higham, J. Vigilante, "Linear Resonance Split Cryocooler Design and Component Development Program", CTI-CRYOGENICS Final Report, Contract # DAAK 70-82-C-0222, February 1985.

VIBRATION CHARACTERISTICS OF SMALL ROTARY AND LINEAR CRYOGENIC COOLERS FOR IR SYSTEMS

W. J. Gully and M. W. Hanes
Electron Dynamics Division
G.M. Hughes Electronics, Torrance, California

ABSTRACT

We have been developing miniature linear resonant split-Stirling cryogenic coolers for use in infrared imaging systems. Since cooler output vibration is of critical importance in these applications, we have investigated the vibration spectra of rotary and linear coolers of comparable size. The spectra are discussed, and methods of estimating the vibration in related applications are presented.

INTRODUCTION

Hughes Thermal Products manufactures small electromechanical coolers specifically designed for electro-optic equipment such as night vision sensors. We have found electrically driven cryocoolers operating on the Stirling cycle to be the most practical in our applications. These single stage coolers typically provide between 0.35 watts and 3 watts of refrigeration and operate near 80K.

Because of the end use of the cooler, environmental aspects such as EMI and output vibration are especially important in the cryocooler design. Most of our cryocoolers are of the split-Stirling type in order to decouple the compressor from the sensor being cooled. We have been developing linear coolers to replace rotary coolers primarily because of their increased operating life. We discuss in this article typical output vibration spectra for a number of our current rotary and linear split-Stirling coolers to illustrate the environmental impact of the design change. All of the coolers have free piston displacers that are driven by pneumatic forces derived from the pressure wave rather than by a crank or motor. They incorporate clearance seals throughout, and have motor driver circuits that operate from DC power.

ROTARY COOLER VIBRATION

We first present the spectra of a rotary compressor as an example of what is currently used in many systems. When operated nominally this particular cooler

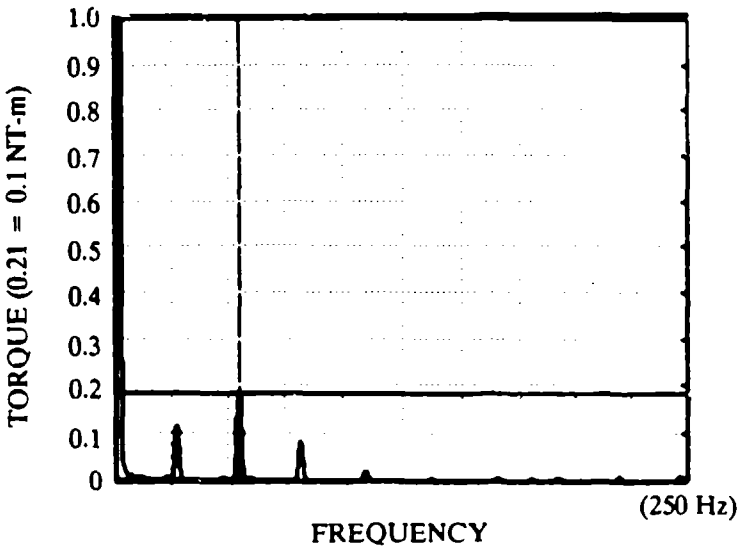

a) LOW FREQUENCY VIBRATION

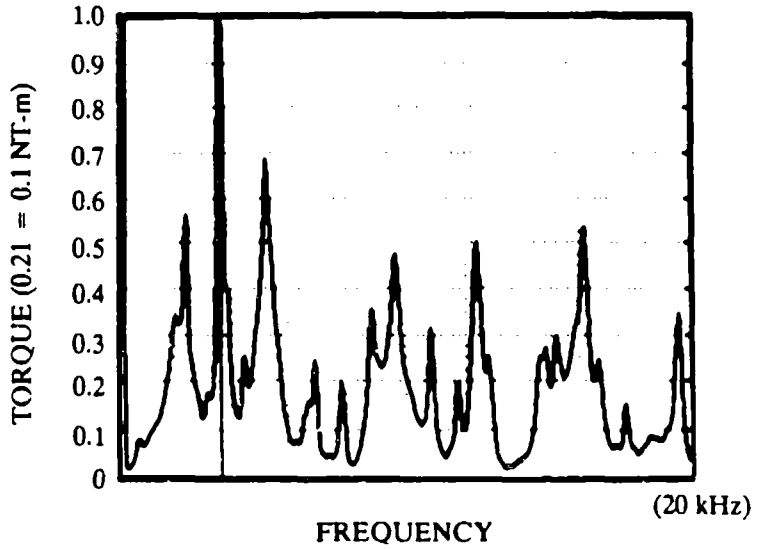

b) HIGH FREQUENCY VIBRATION

Figure 1 Rotary compressor vibration at low and high frequency.

provides a minimum of 1 watt of refrigeration at 80K, for 50 watts of input power. We show in Figure 1 the output torque deduced from the acceleration of a freely suspended heavy block of known inertia.

In Figure 1-a we show the low frequency vibration spectra for the cooler. We can understand the principal features of the spectra by analyzing the dynamics of the rotor, since the torque to the case is the reaction to the torque accelerating the rotor.

From the spectra we see that the principal torque delivered to the case is at 55 Hz, twice the operating speed of the cooler. This occurs because the connecting rod between the piston and the rotor crosses over the motor axis at top and bottom dead center when the oscillatory force due to the fluctuating gas pressure is a maximum. Since the moment arm changes sign the torque oscillation is at twice the fundamental frequency. The magnitude of the torque can be estimated from the input power to the cooler. The work done per cycle is given by the average torque times 2*pi radians. In a typical unit the average torque providing this work is approximately equal to the rms value of the fluctuating components, so we can estimate the magnitude of the fluctuating components to be

$$\text{Torque} = \text{Power}/(2*\text{pi}*\text{operating frequency})$$

For the data illustrated, the "PV" input power at the charge pressure chosen for this test was approximately 20 watts, which corresponds to 0.75 joule/cycle and 0.1 Nt.-meter of torque. Note that the output torque will scale with charge pressure and compressor displacement, but will not depend strongly upon the operating frequency or rotor inertia.

In Figure 1-b we show the high frequency torque spectra of the cooler. These high frequency signals clearly dominate the vibration spectrum, even though they typically involve smaller motions and lower energies than the vibrations at the low frequencies. These vibrations arise from the motion of a number of internal components that have to be left limber in order to allow unconstrained operation of the rotating mechanism which insures low wear and longer life. Because these vibrations contain little energy, it is practical to dampen them in the system by including an energy absorbing soft mount for the compressor in this split-Stirling design approach.

ROTARY EXPANDERS

The expander vibration is more difficult to filter out because it is directly coupled to the sensor. The axial motion of the displacer along the coldfinger axis at the cooler operating frequency causes the fundamental vibration. We show a typical output force spectrum in Figure 2. As the numerous harmonics of the

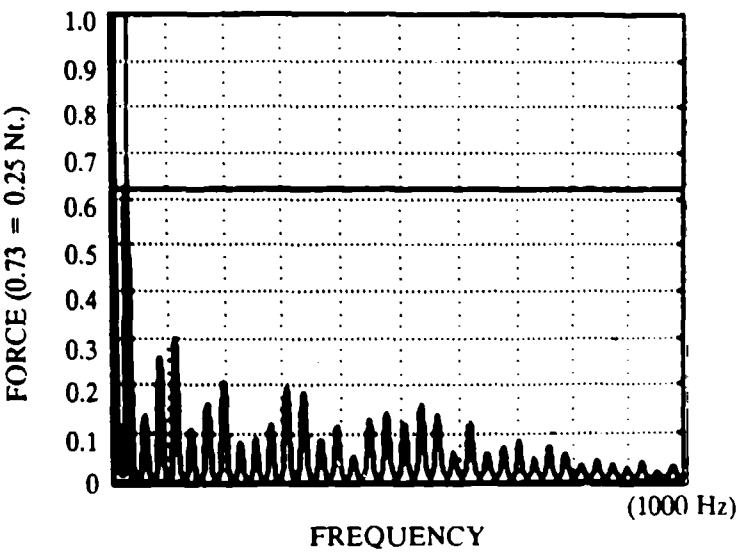

Figure 2 Rotary cooler expander axial vibration.

fundamental operating frequency indicate, the displacer motion is nearly a square wave. This is characteristic of thermally optimized free piston expanders, whose stroke is restrained by bumpers.

We can again estimate the magnitude of the output force by analyzing the dynamics of the displacer assembly. We could calculate it precisely by deducing the acceleration from the displacer stroke trace and multiplying it by the displacer mass. We can get an approximate value by equating the allowed stroke with the peak to peak amplitude of simple harmonic motion.

$$F_{pk} = M * R_{pk} * W \wedge 2$$

$$F_{pk} = (0.0086 \text{ Kg}) * (0.002 \text{ M}) * (2 * pi * 28 \text{ Hz}) \wedge 2 = 0.5 \text{ Nt.}$$

Note that the output force apparently depends upon the displacer mass. This is true as long as the kinematics of the free displacer are not seriously affected by mass, as they are for the free displacer.

The frequency dependence of this output force is an important consideration in demand temperature control of the rotary cooler. We control the expander temperature by reducing the rotational frequency of the cooler as we approach the desired temperature. Since the compressor displacement is unchanged, the free piston displacer continues to full stroke. This suggests that the output forces will decrease as the square of the frequency, which is verified in Figure 3. The output forces therefore rapidiy drop as the unit goes into demand.

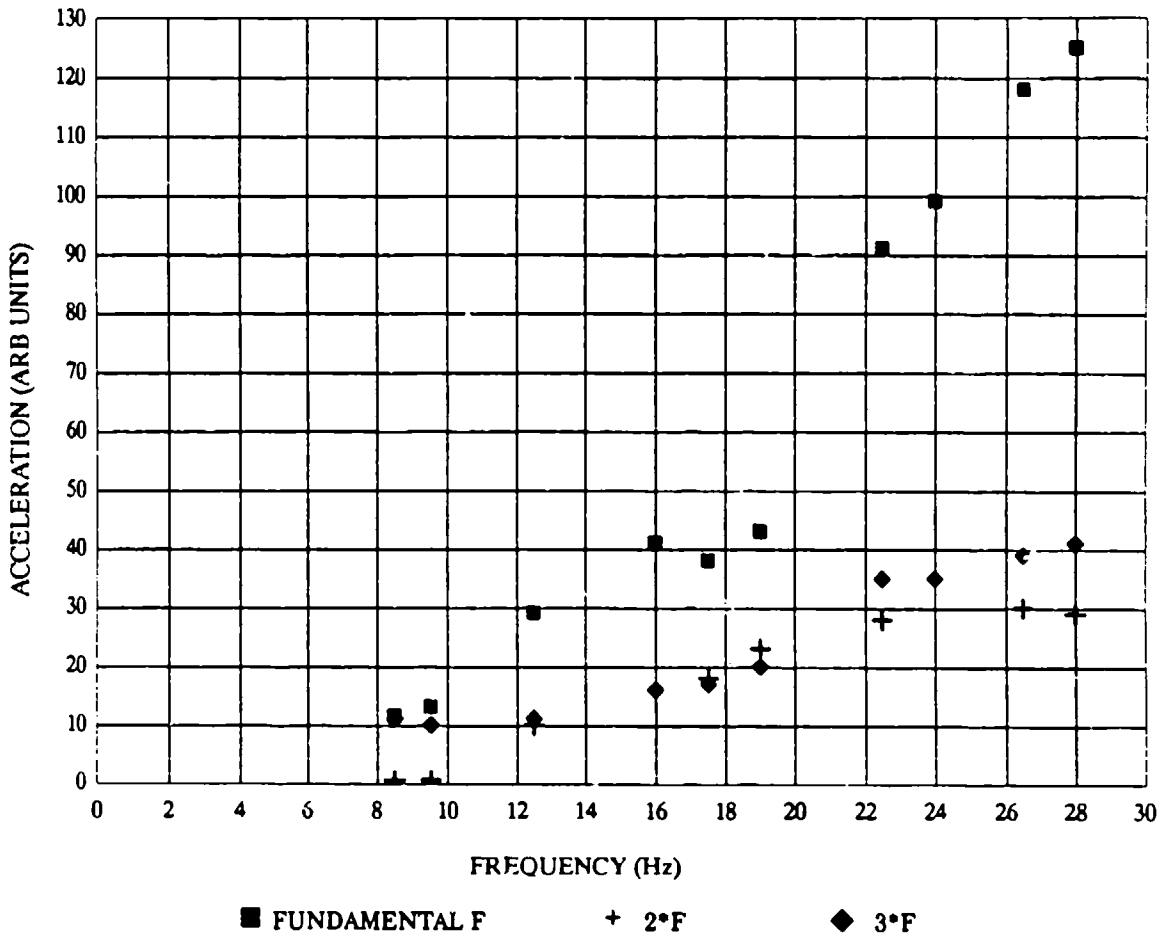

Figure 3 Expander vibration spectrum as a function of cryocooler operating frequency.

LINEAR COOLERS

Linear coolers differ from rotary coolers in that they have resonant linearly oscillating compressors. In these compressors the motor and piston are coaxial, which eliminates side forces. This reduces wear and increases the life of the cooler.

One of a number of problems with these compressors is the unbalanced axial force associated with a simple linear motor. A variety of mechanisms have evolved to deal with this force. For example, one can accept the force in a particular cooler, and operate pairs of coolers in opposition synchronously. This is an elaborate procedure requiring sophisticated electronic control. It would clearly be advantageous to develop a passively balanced linear compressor for applications where cost is important and a less complex mechanism would be adequate. An example

of this would be the use of a resonant counterweight to cancel the vibration due to the reciprocation of a simple motor (1). The effectiveness of this approach is limited, though, because the counterweight is a negative feedback device, and because it is limited to the fundamental unbalance force. We have investigated a number of other designs, and the results for two of them are presented below.

The essential design of a single motor approach is shown in Figure 4. Both the armature and stator of the motor are mounted on springs and free to move. The components counteract to mutual forces in a way that results in perfect balance at all frequencies. In essence, the stator acts as the counterweight, which is a more effective use of space. A disadvantage of this design is the need for a flexible internal transfer line between the cylinder and the stationary housing.

The output vibration spectrum of a one watt capacity cooler using this principle is shown in Figure 5. In 5-a we show that there is only about 0.5 Nt. of unbalanced force when the cooler is operated vertically. In Figure 5-b, however, we show that the output vibration increases to approximately 3 Nt. when the unit is

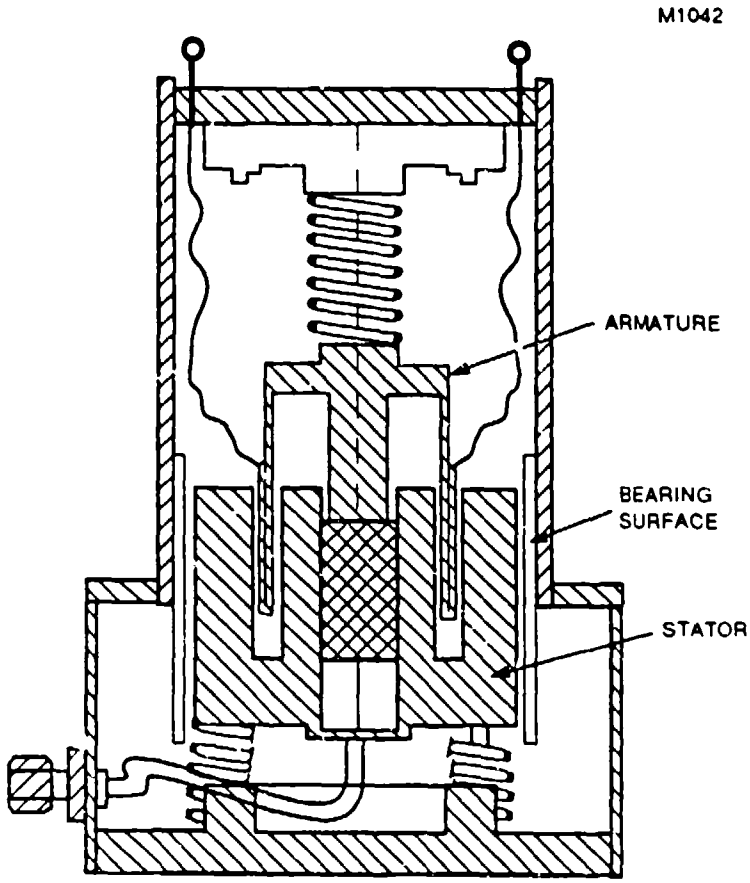

Figure 4 Schematic of a single motor linar compressor.

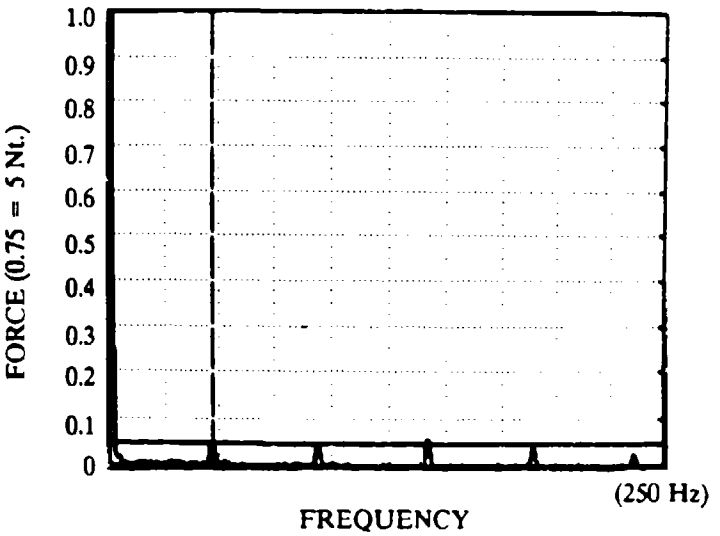

a) VERTICAL

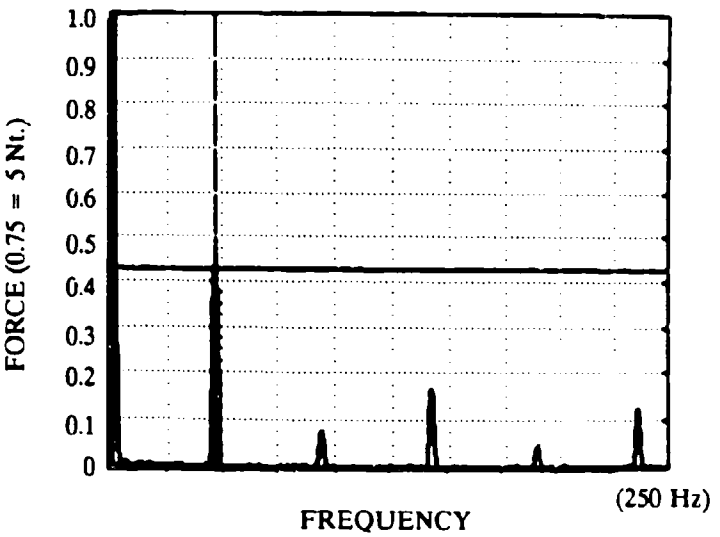

b) HORIZONTAL

Figure 5 Low frequency vibration spectra of a single motor linear compressor.

operated in the horizontal orientation. This is due to the drag of the stator when it is gravitationally held against its bearing surface. There is no counteracting force from the armature to the case because it operates in the bore of the stator. The presence of harmonics in the spectra in Figure 5-b indicates that the trace is nearly a square wave, indicative of Newtonian friction. And in addition, the output vibration is independent of compressor stroke.

The high frequency spectra of this linear cooler are shown in Figure 6. The spectra is due to the oscillations of the mechanical springs used to locate parts, and is not orientation sensitive. We can compare the magnitudes of these forces with those of the rotary cooler by multiplying these forces by the radius of the cooler, which is about 0.025 m. We can see that these "effective torques" are much smaller than the corresponding values for the rotary compressor. An immediately perceptible consequence is that the linear compressors are relatively quiet.

We have also experimented with the more standard twin opposed cooler, illustrated in Figure 7. This is actually a symmetric pair of compressors operated head to head with strong coupling between the armatures due to the gas. All of the forces should cancel since the two moving parts are identical. We show the results for a twin opposed piston compressor for a three watt capacity cooler in Figure 8. The unbalance in the horizontal orientation is approximately 1.0 Nt. at the fundamental frequency. This unbalance arises because of the difference in motor strengths and spring forces between the two sides. However, in Figure 8-b, we show that forces increase dramatically when the cooler is oriented with its axis

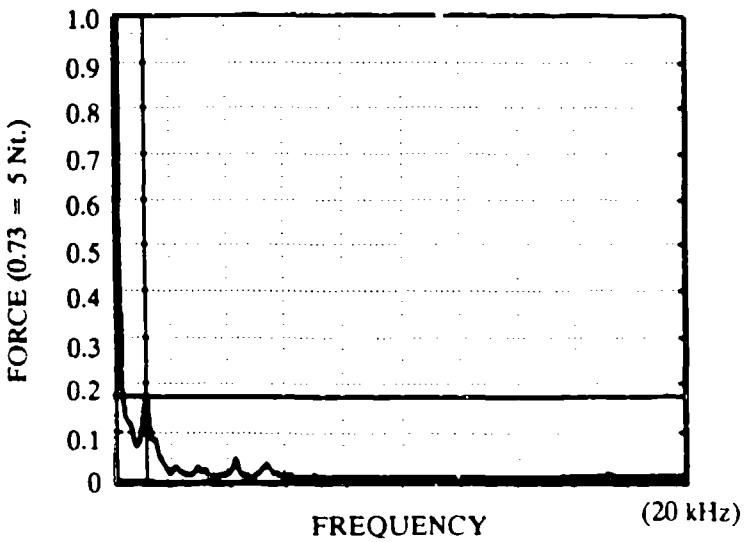

Figure 6 High frequency vibration spectrum of a single motor linear compressor.

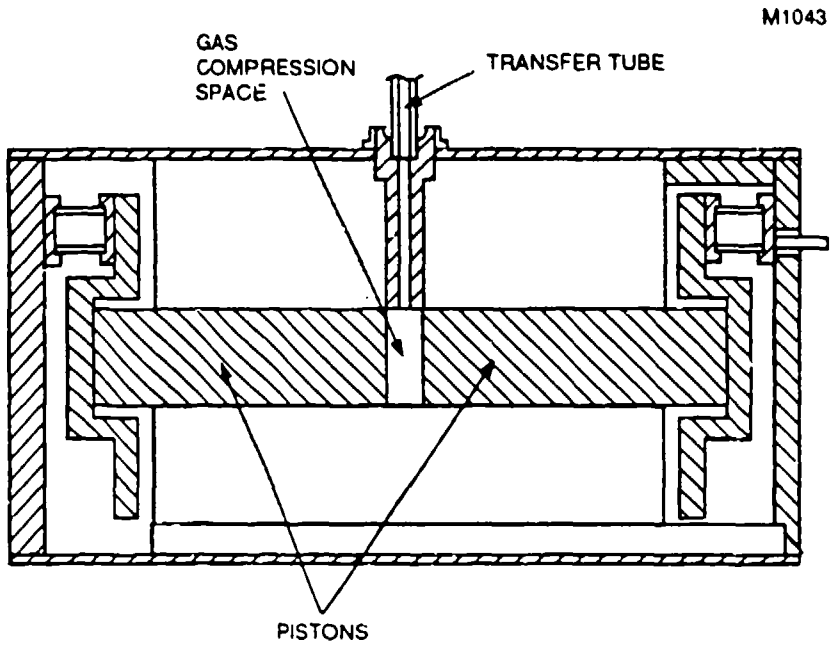

Figure 7 Twin opposed compressor schematic.

vertically. There is a force at twice the operating frequency of about 4 Nt. This unbalance is a result of the motors losing their similarity as one coil falls into the motor, while the other falls out of it. This effect can be eliminated by making the coil much longer than the magnetic circuit, but this reduces the overall electrical efficiency of the cooler.

LINEAR EXPANDERS

We show in Figure 9a the output spectra of an expander for a one watt linear cooler. The forces are nearly double those of the rotary cooler expander partly because of a higher operating frequency, and partly because of an increase in the size and weight of the displacer. In Figure 9-b we show the high frequency forces due to the impact of the displacer at each end of its stroke. These forces are proportional to the momentum of the displacer and depend upon the looseness and elasticity of the components. Although the compressor vibration has improved, in this case the expander vibration has gotten worse.

Since a linear compressor has to operate at constant frequency to maintain its resonance, we introduce demand temperature control by decreasing the length of the compressor stroke to reduce the pressure ratio and expander drive force. We illustrate the effect with the output vibration of a three watt capacity cooler

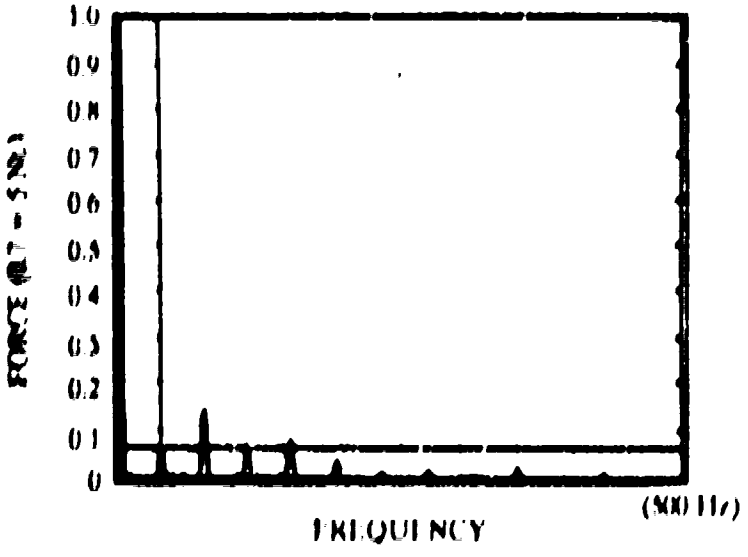

a) HORIZONTAL ORIENTATION

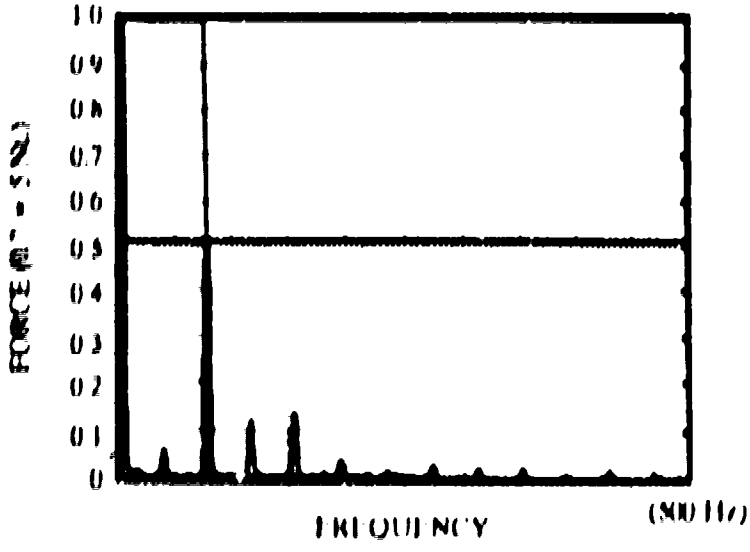

b) VERTICAL ORIENTATION

Figure 8 Low vibration spectra of a twin opposed compressor.

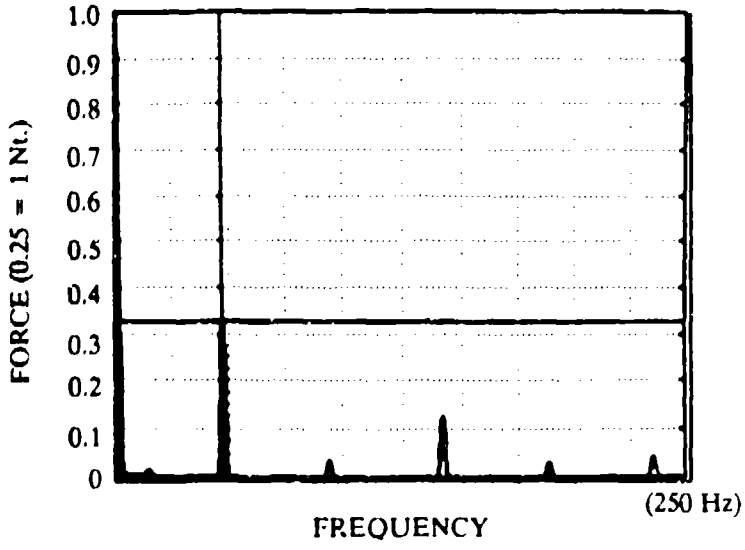

a) LOW FREQUENCY

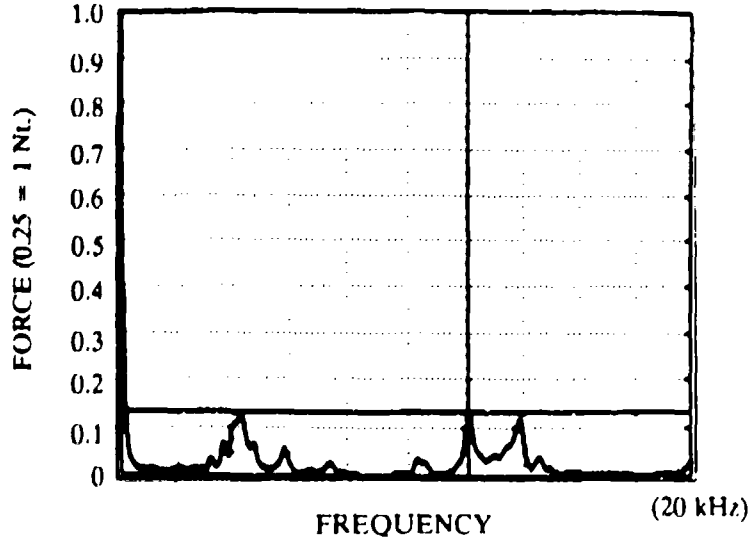

b) HIGH FREQUENCY

Figure 9 Vibration spectra for the expander of a one watt linear cooler.

expander in Figure 10. The magnitudes of the vibration are somewhat lower than those of the one watt cooler expander in Figure 9 because we have reduced the weight and lowered its operating frequency. The higher harmonics are a significant fraction of the vibration at full power, but significantly reduced at low power. This happens because the displacer shortens its stroke and no longer strikes its limits. In this region the expander is acoustically quiet.

SUMMARY

We have found that the output vibration characteristics of rotary and linear coolers are quite different. There have been significant improvements in the output vibrations of the linear compressors, especially at high frequencies. But the expander vibrations have gotten worse, primarily because of the high operating speeds involved. Continued effort is needed to remove the orientation effects afflicting linear coolers, and to decrease the vibrations in the expander.

1. D. Lehrfeld, "Split Stirling, Linear Resonant, Cryogenic Refrigerators", in Proceedings of the Second Biennial Conference on Refrigeration for Cryogenic Sensors, Dec. 1982 (NASA Pub.2287)

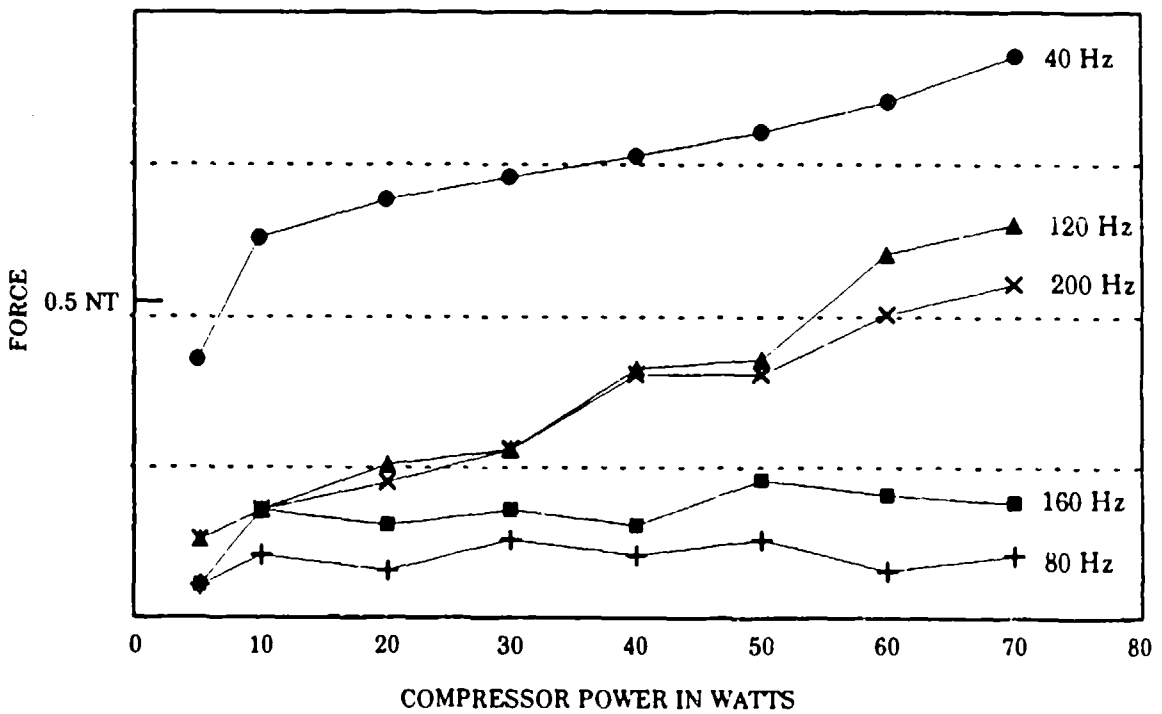

Figure 10 Vibration spectra for a 3 watt linear expander as a function of cooler input power.

A GAS-FIRED DUPLEX-STIRLING CRYOREFRIGERATOR TO LIQUEFY NATURAL GAS FOR AUTOMOTIVE FUEL

Woody Ellison, Ernest E. Atkins
Dr. Graham Walker, Steven G. Zylstra

General Pneumatics Western Research Center
Scottsdale, AZ 85260

ABSTRACT

The subject Department of Energy Small Business Innovation Research project is for a prototype of a practical, general use system for liquefying natural gas to fuel private and commercial vehicles. The system is a duplex arrangement of a Stirling cryorefrigerator driven by a natural-gas-powered Stirling engine. The system employs the Ross drive linkage to minimize side forces and wear, composite regenerators for high thermo-fluid efficiency, and compressed helium and air or nitrogen working fluids for practicality and economy. The prototype design is for a refrigeration capacity of 1 kW at 110 K to produce 8 liters of liquid natural gas per hour. Larger capacities are anticipated for commercial versions.

INTRODUCTION

Natural gas (or methane) offers many advantages as a vehicle fuel over gasoline, diesel, and alcohol fuels. A major attraction is lower vehicle operating and maintenance costs. Other benefits of natural gas include smoother, quieter operation, cleaner combustion with much less pollution, increased safety, and an ample domestic supply for reduced dependence on imported oil.

Liquid natural gas (LNG) is preferable to compressed natural gas (CNG) as a vehicle fuel because of the savings possible in the size, weight and cost of the vehicle fuel tank. The cost of a properly insulated LNG storage tank is significantly less than an equivalent CNG high pressure storage bottle with concomitant savings in weight and volume.

Also, the refrigeration available in the LNG (the normal boiling point for methane is 112 K) could be used to air condition the vehicle for significant savings in the cost of air conditioning equipment, maintenance, and better mileage.

LNG is presently not widely used because there is no suitable, low capacity, cryocooler available. The liquefier described herein is to fill this need.

PROJECT OBJECTIVES

The system under development is a natural-gas-powered Stirling-Stirling cryocooler with a refrigeration capacity of 1 kW to produce approximately 8 liters of liquid natural gas per hour. The sizing and performance analyses, design configuration studies, cross-sectional layout drawings, and preliminary fabrication and test plans were completed in Phase I of the development. Phase II, now in progress, is to carry out the detail piece parts design, fabrication, assembly, and testing of a prototype natural gas liquefier, and demonstrate the system potential practicality for producing automotive fuel from pipeline gas. Emphasis is placed on achieving simple fail-safe operation, low-maintenance reliability, energy efficiency, and cost effectiveness for private as well as commercial use.

PHASE I DESIGN RESULTS

The Stirling-Stirling Arrangement

Figure 1 shows the cross-sectional design layout of the prototype Stirling-Stirling natural gas liquefier derived in Phase I of the development.

The basic objective of a Stirling-Stirling design is to efficiently match the work output of the Stirling power system to that required by the Stirling refrigerator. For mechanical simplicity it is best for both units to operate at the same speed with the same working fluid and mean pressure. Depending on the design of the drive linkage, the pistons may or may not have the same strokes or diameters. Given commonalities of speed, pressure and stroke, it is likely that the pistons of the power system must be significantly larger than those of the refrigerator. Variation of the piston diameters is the principal design parameter to ensure that the work output of the power system is sufficient to drive the refrigerator.

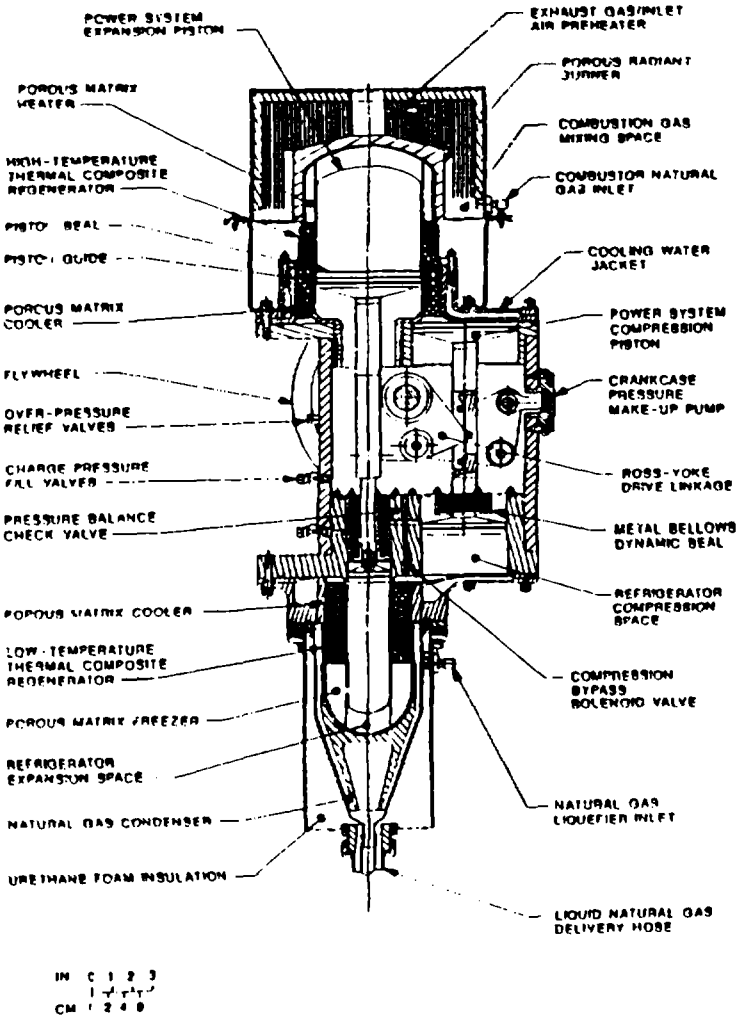

FIGURE 1. NATURAL-GAS-FIRED STIRLING-STIRLING NATURAL GAS LIQUEFIER

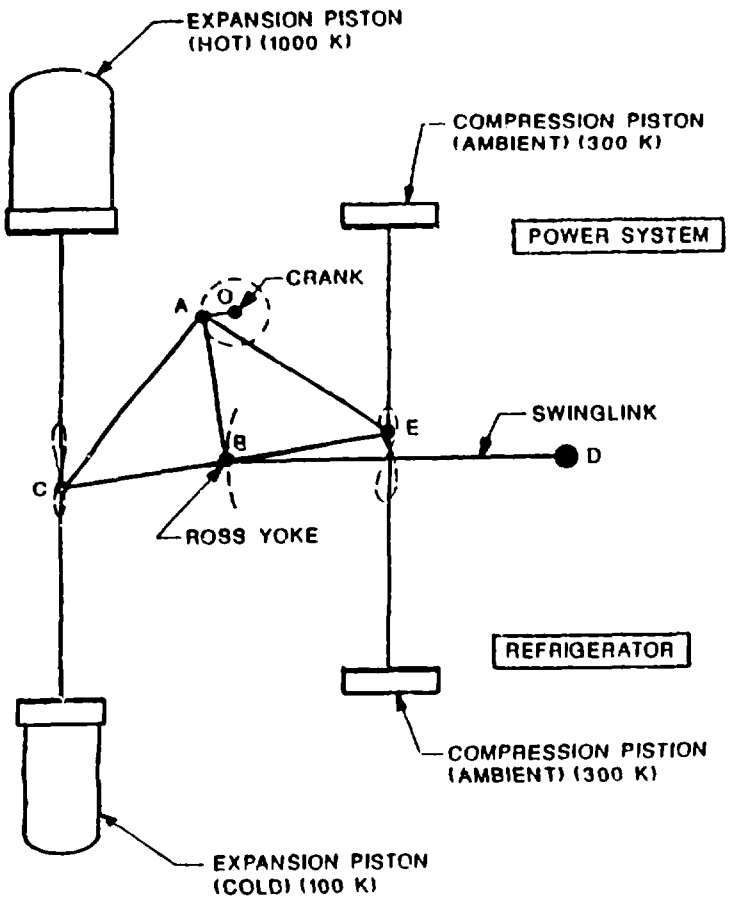

FIGURE 2. THE ROSS STIRLING-STIRLING ARRANGEMENT

Drive Linkage, Bearings, and Seals

In a Stirling-Stirling system, it is advantageous to use directly linked pistons, as shown in Figure 1, to couple the power system and the refrigerator. This facilitates direct transfer of work with minimum bearing loads. In principle, no kinematic mechanism need be involved. In practice, a drive mechanism serves to couple the pistons to a crankshaft and flywheel to facilitate starting, control, and accessory drive.

Drive mechanisms such as a crank and connecting rods create significant side forces on the pistons, which promotes wear. The subject prototype design employs the Ross drive linkage[1], as diagrammed in Figure 2, which minimizes side forces and associated wear. The crank 'OA' rotates about the crankshaft axis 'O'. A rigid yoke 'ACE' is attached to the crankpin at 'A' and to the swinglink at 'B', which has a fulcrum at 'D'. As the crankpin 'A' rotates, the swinglink bearing 'B' describes a circular arc while the extremities 'C' and 'E' describe very narrow 'figure eights'. Thus points 'C' and 'E' depart only slightly from a straight line motion along the axes of the cylinders. The resulting piston motion is very closely sinusoidal with a 90° phase difference necessary for Stirling performance.

Due to the sinusoidal motion of the Ross linkage, the dynamic forces at multiples of the running speed are minimized. A computer model has been developed for the simulation of the dynamic loading and balancing in a Stirling system having a Ross linkage as the drive mechanism[2]. The masses and moments of inertia of all moving components and reactions at all pin connections and mounting locations have been included in the model. The computer program will be used for evaluating trade-offs in geometry, velocities, accelerations, dynamic loading and vibration in Phase II of the development.

The crankshaft employs four, sealed, angular contact ball bearings; the shaft support bearings (one at each end), and the yoke bearings (a duplex pair at the crank lobe). These bearings were chosen for their low drag and friction characteristics along with the ability for long life. The shaft support bearings, at 'O' on Figure 2, are spring preloaded to compensate for expansion and contraction and tolerance stack up which would otherwise result in axial play. The yoke bearings, at 'A', are a preloaded duplex pair to provide high radial and axial rigidity for locating the yoke.

The swinglink bearings, at 'B' and 'D', are roller bearings because of the need for compact load carrying capacity with non-continuous rotation. These bearings are also sealed and lubricated.

The lubrication preliminarily chosen for these bearings is Chevron's SRI #2, a lithium based grease particularly well suited for high temperature bearing applications. The bearing grease seals are commercially available lip seals designed specifically for these purposes. The incorporation of additional seals to prevent lubricant vapors or other contaminants in the crankcase from migrating into and condensing in the refrigerator cold working space will be part of the Phase II detail design. A prospective means is to include metal bellows behind the refrigerator pistons, as shown in Figure 1, to close off the cylinders from the crankcase. This scheme has been successfully tested at General Pneumatics in the development of contamination free, high-pressure (20 MPa) compressors.

The use of very low vapor pressure silicone or fluorocarbon bearing greases to avoid the need for the bellows seals will also be investigated. The refrigerator piston seals would not be vulnerable to frozen contaminants because they are positioned to operate in the near-ambient-temperature regions of the cylinders. Prototype testing will be required to investigate to what degree trace condensibles in the cold regions might be life limiting or necessitate frequent maintenance.

Flexures are used for the piston rod connections at 'C' and 'E', since the lateral and angular movements at these points are very small.

The piston guides and seals are made of polymeric reinforced TFE from Dixon Industries called Rulon® J. This material has a proven track record as a dry rubbing seal with excellent wear and friction characteristics.

Heat Exchangers

The Stirling power system and refrigerator each include three heat exchangers; a cooler, a regenerator, a heater (for the power system) or condenser (for the refrigerator).

For the coolers, coils of metal tubing are embedded in porous sintered metal matrices through which the Stirling working gas flows. Cooling water circulates through the tubing and through an air-cooled, finned-tube 'radiator'. By proper selection of the particulate material, size, and geometry, the porosity, fluid friction and heat transfer characteristics of the sintered matrix can be precisely

tailored to the configuration for minimum dead volume and high thermal effectiveness.

The regenerators utilize new technology recently developed by Energy Science Laboratories (ESL) of San Diego, California. ESL has pioneered the development of a class of novel composite materials for use in aerospace thermal energy storage applications. These thermal composite materials consist of layers of high conductivity materials (metal or crystalline graphite fibers) which conduct heat into high heat capacity ceramic matrix materials. The layered structure allows a very large anisotropy in thermal conductivity, which suppresses axial conduction loses. Thermal composite regenerators offer thermal flux, penetration, and specific heat capacity far surpassing conventional materials. In addition, the high radial conductance of thermal composites permits using solid regenerators, having little or no void volume, which can be located outside the flow to minimize dead volume, fluid friction, and susceptibility to contamination. The resulting potential benefits for the Stirling compression ratio, efficiency, and reliability are very significant.

A promising development in gas-burner technology, a porous radiant burner (PRB), is incorporated in the natural gas combustor of the Stirling power system. PRB devices operate by stabilizing a premixed flame inside, or near, a non-combustible porous medium. The enthalpy of combustion released in the gas phase heats the porous matrix which then emits thermal radiation to a heat load. In small-scale applications PRB's have already shown performance gains over conventional open-flame burners in the form of higher efficiencies, lower NO_x emissions, and more uniform heating.

Research and development studies of PRB devices are in progress in the College of Engineering and Applied Sciences at Arizona State University under the direction of Dr. Robert Peck[3], who is a consultant for Phase II of this program.

Working Fluid

For system size and power efficiency, the internal Stirling working fluid should be pressurized to as high a charge pressure as is structurally practical and safe. The most thermodynamically efficient Stirling working fluid is hydrogen, but safety and containment problems make it unsuitable for the subject application. Helium offers the next best performance, in terms of system power density and efficiency, but still is much more difficult and expensive to contain than nitrogen or air.

The simplest, easiest to maintain working fluid would be atmospheric air pressurized on site. This might work well in the engine, but the 112 K liquefaction temperature for methane necessitates that the working fluid in the refrigerator contain no condensible contaminants such as moisture, carbon dioxide, or compressor lubricants. Atmospheric air could be purified through a somewhat costly desiccant/filter system, or by using some of the refrigeration generated to condense and trap contaminants from the pressurized air before it is injected into the refrigerator. The latter would require having a pressure reservoir for clean air to charge the system for start-up in the event charge pressure is low.

A more fundamental problem with using air, or nitrogen, as the refrigerator working fluid is that to reach below the 112 K methane liquefaction temperature, the maximum cycle pressure would have to be limited to approximately 0.7 MPa to avoid condensing the working fluid in the expansion chamber. The engine operating pressure must be correspondingly limited to minimize the pressure differential imposed on the bellows which seal the refrigerator from the crankcase. This would result in an excessively large system with poor power efficiency.

It was determined that a charge pressure of 2 MPa with a peak cycle pressure of 4 MPa is needed for overall system efficiency and practicality. This dictates the use of helium in the refrigerator. Although the refrigerator section is well sealed against helium loss, if the crankcase losses pressure the refrigerator must also to limit the pressure differential across the bellows. The crankcase pressure must be maintained against leakage through shaft seals. To avoid need for a large, high-pressure, hermetic enclosure around the flywheel and starter motor, or frequent replenishment of helium, the crankcase and engine can be charged with air or nitrogen from a regulated pressure reservoir. Air or nitrogen are easier to seal in than helium, and the leak rate can be limited to require replacement of the supply bottle with routine maintenance such as twice a year. This approach is further favored by noting that only the refrigerator section requires especially clean working fluid (helium). Leakage from the crankcase and engine could be compensated for by a small compressor using filtered atmospheric air.

The refrigerator and engine would both be charged to 2 MPa from regulated pressure reservoirs of helium and air, respectively. Check valves between the refrigerator and crankcase would limit the pressure differential across the bellows while preventing backflow into the refrigerator from

the crankcase. Redundant pressure relief valves would prevent excessive crankcase pressure or unbalance with the refrigerator charge pressure.

Analysis and Computer Simulation

Two versions of Stirling simulation programs were used for the Phase I analysis and optimization studies of the gas-fired Stirling-Stirling natural gas liquefier; MARWEISS for the power system, and CRYOWEISS for the refrigerator. These programs were developed at the University of Calgary by M. Weiss, Dr. G. Walker, and R. Fauvel[4,5]. They are based on the Martini second order, isothermal, decoupled corrections simulation technique[6]. A total of over 200 iterative cases were simulated and examined. Focus was placed on machine operation in the lower speed range of 500 to 1500 revolutions per minute to limit flow losses and rubbing wear.

Starting with the refrigerator at cold and ambient temperatures of 100 K and 300 K, respectively, the studies predicted a refrigeration capacity of 1 kW at liquid methane temperature (110 K) with a coefficient of performance of 0.2 corresponding to a power input requirement of 5 kW.

Following selection of the refrigerator dimensions and operating parameters, attention was directed to the power system. The same mean pressure, speed, piston stroke, and Ross-Stirling drive mechanism dimensions used for the refrigerator were carried into the power system. The cylinder dimensions and heat exchanger details were then manipulated to obtain a brake power output in excess of 5 kW. This is to provide sufficient power to drive the refrigerator with enough margin to operate a cooling water pump and cooling air fan.

The basic physical parameters for the combined system design are summarized as follows:

Working fluid	helium
Charge pressure	2 MPa (300 psi)
Speed	16.7 Hz (1000 rpm)
Expansion pistons stroke	2.8 cm (1.1 in)
refrigerator diameter	7.6 cm (3.0 in)
power system diameter	14.0 cm (5.51 in)
Compression pistons stroke	2.8 cm (1.1 in)
refrigerator diameter	12.0 cm (4.72 in)
power system diameter	14.0 cm (5.51 in)

Auxiliary Equipment

Auxiliary equipment for starting, cooling and control of the prototype natural gas liquefier system will consist of commercially available components.

An automotive starter motor, sprocket engagement mechanism, flywheel, and 12 vdc storage battery will be used for starting the system. The battery will also power the control system, thereby providing protection against public electric utility surges, sags, noise, or short term outage. The battery's charge will be maintained by a standard 110 vac trickle charger.

To limit the torque required to start the system, solenoid actuated compression bypass valves are included in the refrigerator and power system. During starting, the valves will open to relieve the normal compression/expansion cycling. When starting speed is reached, the power system compression bypass valve will close allowing power to develop. When operating speed and power are reached, the refrigerator compression bypass valve will close. Inclusion of these bypass valves in the prototype system will also facilitate testing of various starting and operating characteristics.

Heat of compression must be dissipated at near ambient temperature by the coolers of the power system and refrigerator. The computer analyses show this to be approximately 6 kW from the power system and 6 kW from the refrigerator. It is important for the thermal efficiency of the system that the coolers be as compact (minimum dead volume) and as cool as practical. For this, an automotive type closed cycle liquid cooling system will be more effective than simple air cooling. The total of 12 kW heat dissipation is well within the capacity of a typical automotive 'radiator'. The radiator fan and a water pump will be driven by a V-belt from the flywheel shaft.

Gas flow to the combustor will be controlled by a solenoid actuated on-off valve and a thermostatically regulated valve like for a gas furnace. Similarly, a solenoid valve will control gas flow to the liquefier condensing chamber. The normally-closed solenoid valves will shut off gas flow in the event of a fault condition, control system power loss or turn off. Pressure buildup in the condensing chamber will be vented by a spring-loaded relief valve to the combustor. The exhaust stack will contain a catalytic combustion element to ensure no unburned methane is vented to the atmosphere.

Exhaust gas heat will be used to preheat inlet combustion air for high thermal efficiency of the power system. The exhaust gas/inlet air preheater, shown in Figure 1 enclosing the porous radiant burner on the power system heater head, will be a multiple-start counter-flow concertina fabricated from aluminum sheet. To facilitate flow through the preheater, combustor, and exhaust stack, inlet air will be inducted from behind the system cooling radiator fan through a wire reinforced nylon duct like used on gas-fired clothes dryers.

Liquefied natural gas will drain from the bottom of the condensing chamber through a flexible delivery hose such as commercially available for liquid nitrogen service. A suitable, commercially available hose consists of a double-wall, vacuum-insulated, stainless steel flexible bellows inner conduit sheathed in braided stainless steel. A six-foot length of such hose with a six millimeter inner diameter would have a heat loss of approximately 0.5 watt (less than 0.05 percent of system refrigeration capacity).

The delivery hose will connect to the vehicle's fuel tank through a quick-connect ball coupling like that which is manufactured by General Pneumatics. Each half of the coupling contains a spring loaded ball valve. The coupling engages with a quarter turn of a collar which locks to prevent accidental uncoupling. The action of engagement rotates both balls to align bores through them and allow flow. The seals and seal positions are such as to prevent any leakage or spillage during and after coupling or uncoupling.

For the natural gas liquefier application, it is planned to add the following to the coupling:

- a circuit closure which will allow the system gas admission solenoid valves to open only when the coupling is properly engaged;

- a tank-full sensor, or a circuit connection in series with a switch activated by the vehicle's fuel level sensor, which will shut off the system when the vehicle tank is full;

- a coupling release spring mechanism which will be cocked by the action of engagement and will be released by a solenoid, in response to the system shutting off, to automatically disengage the coupling and allow the hose to retract from the vehicle should the driver fail to do so. The vehicle could have a safety switch at the tank coupling which prevents starting the vehicle when the hose is engaged.

System Operation, Control, and Safety

Operation will be automated, requiring only that the operator connect the delivery hose to the vehicle, set a timer or select 'FILL', and press a 'START' button. The liquefier will then automatically execute a start sequence and operate until the vehicle fuel tank is full, the set time elapses, a fault condition occurs, or the operator presses a 'STOP' button.

The start signal will open the compression bypass solenoid valves in the refrigerator and power system, and the solenoid valve to admit gas to the combustor. The gas will be ignited in the combustor by an electronic spark ignitor like in a standard gas appliance. A time-delayed temperature sensor will monitor for combustion. If combustion fails, the gas admission valve will close and a panel light will indicate the fault. A bimetal actuated flapper valve will initially facilitate combustion by allowing combustion air and exhaust gasses to bypass the exhaust gas/inlet air preheater.

A heater head temperature sensor will monitor for proper operating temperature. A shaft speed sensor will monitor rpm. When operating temperature is reached the starter motor will be engaged until a time or upper rpm limit is reached. When a lower, starting rpm is reached the compression bypass valve in the power section will close to initiate power generation. The starter motor, aided by the flywheel, will continue engagement until, as power develops, an upper, starter disengagement rpm is reached confirming power system start. Subsequently, if the heater head temperature or shaft speed are not within minimum or maximum limits the system will shut off and a panel light will indicate the fault.

When full operating speed is reached the compression bypass valve in the refrigerator will close to initiate refrigeration. A sensor will monitor for the condensing chamber temperature to reach 100 K which will signal for the solenoid valve to admit natural gas to the condensing chamber.

A one way check valve downstream of the condensing chamber gas admission solenoid valve will prevent any backflow from the condensing chamber to the gas main in the event of a sudden pressure surge or blockage of the delivery hose. A one way venting valve will connect the condensing chamber to the gas combustion space. Any over-pressure of LNG evaporating, such as may occur after normal shutdown and disengagement of the hose coupling, will be vented for

disposal to the gas combustion space and catalytic combustor in the exhaust stack.

The crankcase pressure and cooling water temperature will also be monitored. Thus, if the delivery hose connection or combustion are interrupted, if the heater head temperature, shaft speed, condensing chamber temperature, crankcase pressure, or cooling water temperature do not remain within proper limits, or if the selected time elapses or the vehicle tank fills, the natural gas admission valves will close to shut off the system, the delivery hose will disengage and retract from the vehicle, and a corresponding panel light will indicate the condition. Over-pressurization of the system will also be prevented by check valves which vent the refrigerator working space into the crankcase, and pressure relief valves which will limit crankcase pressure. Over-heating of the combustor will also be prevented by a thermostatically controlled gas shut-off valve.

CONCLUSION

Development of the subject natural gas liquefier will facilitate the increased utilization of natural gas to fuel private, commercial, and government vehicles.

Natural gas offers many advantages as a vehicle fuel, including lower vehicle operating and maintenance costs, cleaner combustion with less pollution, and reduced dependence on imported oil. LNG is preferable to CNG as a vehicle fuel because of increased safety and because of the savings possible in the size, weight and cost of the vehicle fuel tank. Also, the refrigeration available in the LNG could be used to air condition the vehicle for savings in the cost of air conditioning equipment, maintenance, and better milage with reduced air pollution.

Preliminary analyses indicate that about 30 percent of the total natural gas input will be required for combustion to power the liquefier system. Studies are in progress to compare this to the real energy, as well as environmental and equipment, costs of other vehicle fuels such as compressed natural gas, methanol, gasoline, and diesel.

The liquefier under development is sized for a refrigeration capacity of 1 kW at 110 K. This is adequate in an eight hour period to fuel an average private automobile, rated with gasoline at 8 km/liter (20 miles/gallon), for a round trip of 300 km (186 miles). The prototype liquefier will serve to verify the computer

modeling, design approaches, and operational features, thereby providing a basis for the design of larger, higher capacity versions for commercial and government fleet use.

REFERENCES

1. Ross, Andy of Ross Experimental, Columbus, Ohio, "Compact Crank Drive Mechanism", U.S. Patent No. 4,532,819, August 1985.

2. Doige, A. G. and Walker, G., "Dynamics of the Ross-Stirling Engine", Proc. Third Intl. Stirling Engine Conf., Rome, Italy, June 1986.

3. Sathe, S. B., Kulkarni, M. R., Peck, R. E., Tong, T. W., "An Experimental Study of Combustion and Heat Transfer in Porous Radiant Burners", Paper No. WSCI 89-89 Fall Meeting of the Western States Section of the Combustion Institute, October 1989.

4. Weiss, M., Walker, G., Fauvel, O. R., "Microprocessor Based Stirling Engine Design Aid", Proc. 23rd Intersociety Energy Conversion Engineering Conf., Denver, CO, July 1989.

5. Walker, G., Weiss, M., Fauvel, O. R., "Microcomputer Simulation of Stirling Cryocoolers", 12th Intl. Cryogenic Engineering Conf., Southhampton, UK, July 1988.

6. Martini, W., Stirling Engine Design Manual, Second Edition, NASA-LeRC, 1982.

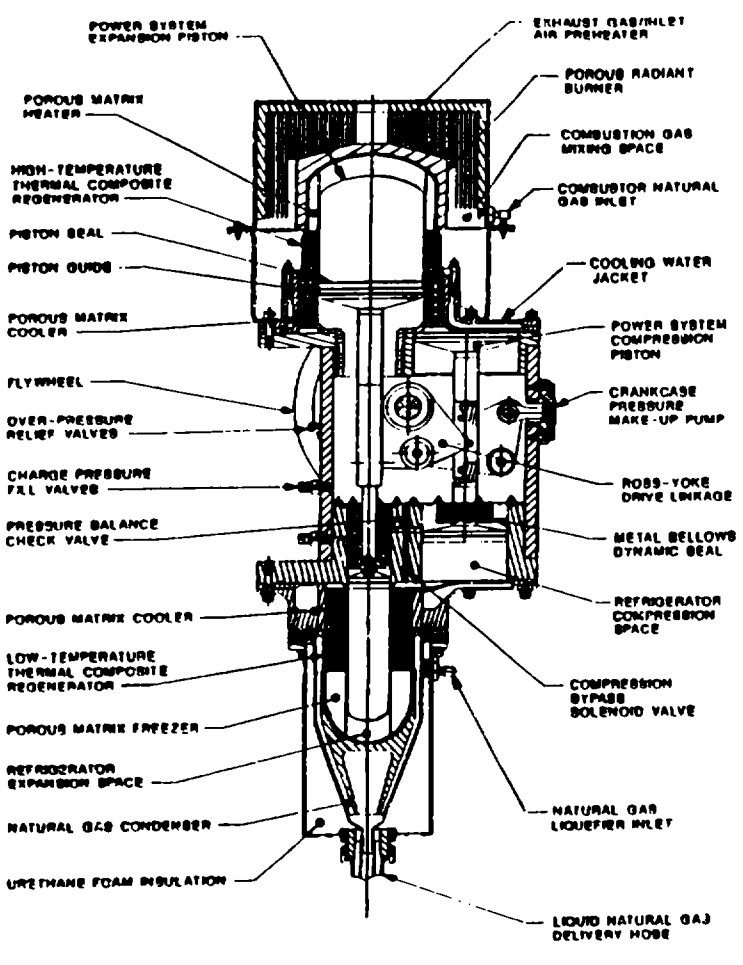

FIGURE 1. NATURAL-GAS-FIRED STIRLING-STIRLING NATURAL GAS LIQUEFIER

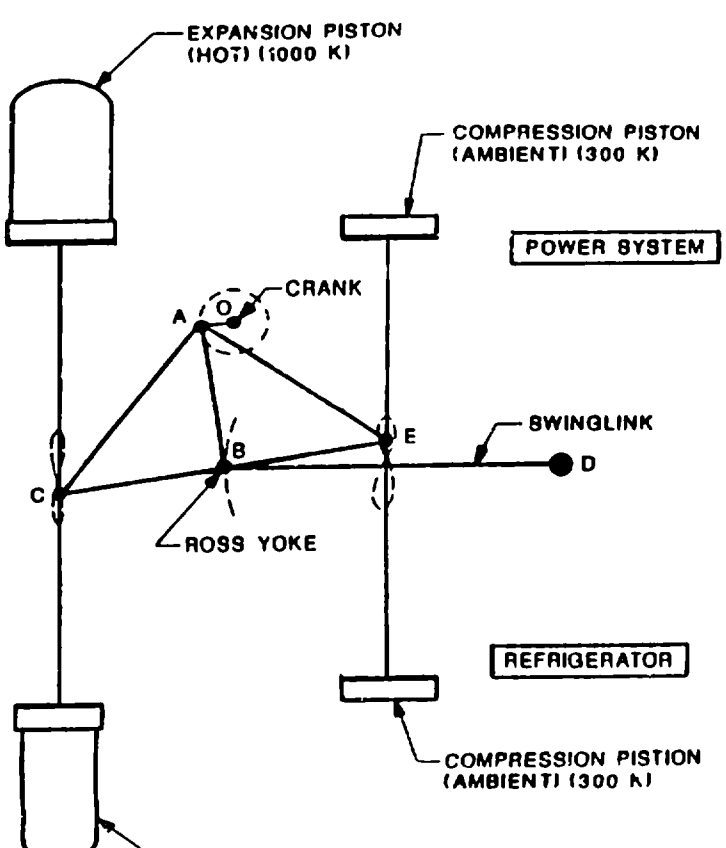

FIGURE 2. THE ROSS STIRLING-STIRLING ARRANGEMENT

THERMODYNAMIC ANALYSIS OF MIXED FLUID JOULE-THOMSON CRYOCOOLERS

B. Maytal[1] and S. W. Van Sciver
Applied Superconductivity Center, University of Wisconsin

P. D. McMahon
Department of Chemical Engineering, University of Wisconsin
Madison, Wisconsin 53706, USA

ABSTRACT

The potential of mixtures as the working fluids in Joule-Thomson cryocoolers is examined. The Peng-Robinson equation of state is used to model the properties of pure cryogenic fluids and their mixtures. Results are presented for a number of mixtures to illustrate the relationships between the cryocooler operating temperature, the isenthalpic JT effect, $(\Delta T)_H$, the isothermal JT effect, $(\Delta H)_T$, and the mixture composition.

It is shown that while some mixture properties—such as $(\Delta H)_T$—are almost linear mole fraction averages of the pure fluid properties, others—such as the lowest achievable temperature—can be sufficiently non-linear to confer a comparative advantage on mixture cryocoolers.

The importance of the flow excess operation and of the heat exchanger in determining the lowest achievable temperature is discussed. Finally, the selection of mixtures for use in cryocoolers is discussed with particular reference to the limiting role of solid-fluid equilibria.

INTRODUCTION

In this paper we consider whether one can improve the performance of an open cycle Joule-Thompson (JT) cryocooler by using a cryogenic mixture as the working substance. Of course, the optimum cryogenic fluid will vary with the application of interest. For example, to minimize the flowrate through an open cycle cryocooler, we would choose the cryogen and inlet conditions to provide the most refrigeration at a given evaporator temperature, whereas to minimize the compression costs we

[1]On leave from RAFAEL and TECHNION, Israel Institute of Technology, Haifa, Israel.

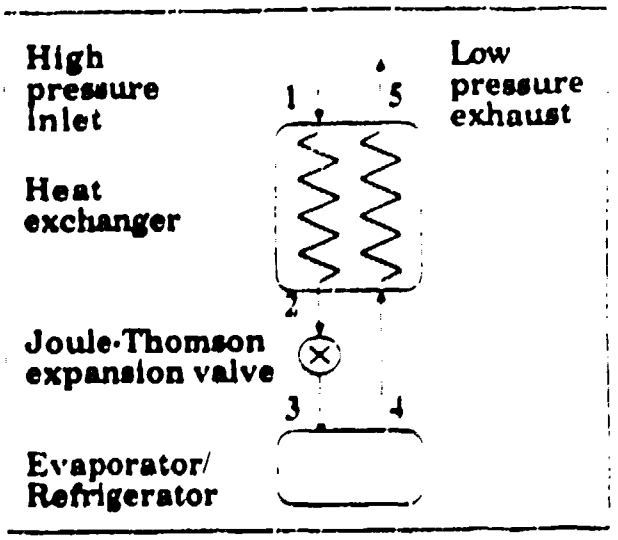

Figure 1: Schematic of a Joule-Thomson cryocooler.

would choose the cryogen to minimize the required inlet pressure for a given refrigeration. In this paper we will mainly focus on maximizing the refrigeration while operating at liquid nitrogen temperatures (77 K) and an inlet pressure of 30 MPa—typical operating conditions for nitrogen cryocoolers.

Consider the pure-fluid JT cryocooler shown schematically in figure 1. During steady state operation an amount of heat Q is absorbed in the evaporator for every mole of cryogen expanded. Q is equal to the enthalpy increase in going from the two-phase fluid that enters the evaporator through the JT valve, to the saturated vapor that leaves the evaporator: $Q = H_4 - H_3$. If parasitic heat gains in the heat exchanger are small and can be ignored, the refrigeration effect will also equal the enthalpy increase in going from the high pressure inlet stream to the low pressure exit stream: $Q = H_5 - H_1$. Since the low-pressure fluid cools the high-pressure fluid in the heat exchanger, T_5 cannot exceed T_1. Thus the isothermal JT effect, $(\Delta H)_T \equiv H(T_1, P_5) - H(T_1, P_1)$, is the upper limit for the steady state refrigeration: $Q_{max} = (\Delta H)_T$. Thus pure cryogens can be compared by evaluating $(\Delta H)_T$ either experimentally or from an equation of state. In table 1 we show $(\Delta H)_T$ as calculated from the Peng-Robinson equation of state for several important cryogens and refrigerants. For purposes of comparison we assumed in these calculations an inlet temperature of 300 K, an inlet pressure of 30 MPa, and an exhaust pressure of 0.1 MPa. $(\Delta H)_T$ increases with the normal boiling point, suggesting that the optimum cryogen will have a high boiling point. Unfortunately, we must use a low-boiling cryogen to achieve a low operating temperature in an open-cycle cryocooler that exhausts at atmospheric pressure because the evaporator operates at the normal boiling point of the cryogen. It is this dilemna that has motivated research into mixed-fluid cryocoolers. One hopes to find a mixture of low- and

Table 1: Properties of some cryogenic gases and refrigerants. T_b: normal boiling point; T_m: melting point; T_c: critical temperature; P_c: critical pressure; ΔH_m: enthalpy of fusion; ω: acentric factor; $(\Delta H)_T$: Peng-Robinson prediction for the JT-effect at 300 K and 30 MPa.

Cryogen/Refrigerant	T_b (K)	T_m (K)	T_c (K)	P_c (MPa)	ΔH_m (J/mol)	ω	$(\Delta H)_T$ (kJ/mol)
Helium	4.2	—	5.3	0.23	—	-.265	< 0
Hydrogen	20.4	13.8	33.0	1.29	117	.000	< 0
Neon	27.1	24.5	44.4	3.40	337	.000	< 0
Nitrogen	77.4	63.2	126.2	3.40	714	.045	1.2
Argon	87.3	83.8	150.9	4.90	1,119	.000	1.8
Oxygen	90.2	54.4	154.6	5.08	442	.019	1.9
Methane	111.6	90.7	190.6	4.64	941	.010	3.6
Tetrafluoromethane	145.2	89.3	227.7	3.74	699	.191	6.1
Ethylene	169.4	104.0	282.7	5.11	3,348	.087	9.1
Ethane	184.5	89.9	305.5	4.89	2,859	.099	10.7
Nitrous oxide	184.7	171.0	309.7	7.22	6,540	.328	13.2
Trifluoromethane	191.0	118.2	299.0	4.83	4,058	.271	11.8
Chlorotrifluoromethane	192.0	91.6	302.0	3.87	?	.171	11.1
Carbon dioxide	194.6[a]	215.7	304.2	7.37	7,920	.231	11.8
Methyl fluoride	195.0	131.4	318.0	5.60	?	.187	12.5
Hexafluoroethane	195.0	172.0	292.0	3.06	2,686	.275	11.2
Bromotrifluoromethane	215.4	105.2	340.2	3.96	?	.171	13.7
Propylene	225.5	87.9	364.9	4.62	3,002	.140	15.0
Propane	231.1	85.5	369.8	4.25	3,524	.152	15.5
Chlorodifluoromethane	232.4	113.2	369.2	4.97	4,121	.218	16.7
Isobutane	261.4	113.6	408.2	3.65	4,540	.185	18.4
1-butene	266.9	87.8	419.6	4.02	3,848	.191	19.5
n-butane	272.7	134.8	425.2	3.80	4,661	.201	20.0

[a] sublimation temperature

high-boiling cryogens that will simultaneously give a low operating temperature and a high Q_{max}. Of course, these are not the only properties that must be considered in choosing a cryogenic mixture. One might also, for example, want to maximize the isenthalpic JT effect, $(\Delta T)_H$, because it provides a measure of the driving force for heat transfer in the exchanger; the greater $(\Delta T)_H$, the smaller the exchanger and the less time needed to attain steady state operation.

Although several experimental reports[1,2] have appeared in the literature, we have not found a theoretical investigation of the selection of mixtures for JT cryocoolers. This paper reports on our first steps in that direction. In the next section we briefly discuss the equation of state we used to model cryogenic mixtures. We then present the results of our calculations for the isothermal JT effect and for the isenthalpic JT effect. We also discuss the operating temperature for mixtures, and, in particular, the role of liquid-liquid and solid-liquid phase equilibria is selecting mixtures. We focus on nitrogen mixtures because for many applications the desired operating temperatures are in the liquid nitrogen range.[3]

EQUATION OF STATE

The thermodynamic properties of a pure fluid or a fluid mixture can be determined from a knowledge of the ideal gas heat capacities and a PVT equation of state for the fluid.[4] Many different equations of state have been used for cryogenic fluids and their mixtures.[5-8] Although the Benedict-Webb-Rubin-Starling (BWRS) equation is highly accurate for cryogenic systems and is often the first choice in industry,[9] we have used the Peng-Robinson (PR) cubic equation of state[10] for convenience. Of the two, the PR equation is much simpler to use, and the parameters needed for applying it to mixtures are more readily available. In addition, it gives reasonably accurate descriptions of cryogenic systems. We believe that the qualitative conclusions we reach about the relative merits of different mixtures will not change much if the calculations are repeated using a more refined equation of state.

The PR equation takes the form

$$P = \frac{RT}{V-b} - \frac{a(T)}{V^2+2bV-b^2} \tag{1}$$

$$a = \sum_{i=1}^{n}\sum_{j=1}^{n} y_i y_j (1-k_{ij})\sqrt{a_i a_j} \tag{2}$$

$$b = \sum_{i=1}^{n} y_i b_i \tag{3}$$

where P is the pressure, T the temperature, V the molar volume, R the gas constant, and y_i the mole fraction of component i in the mixture. The pure

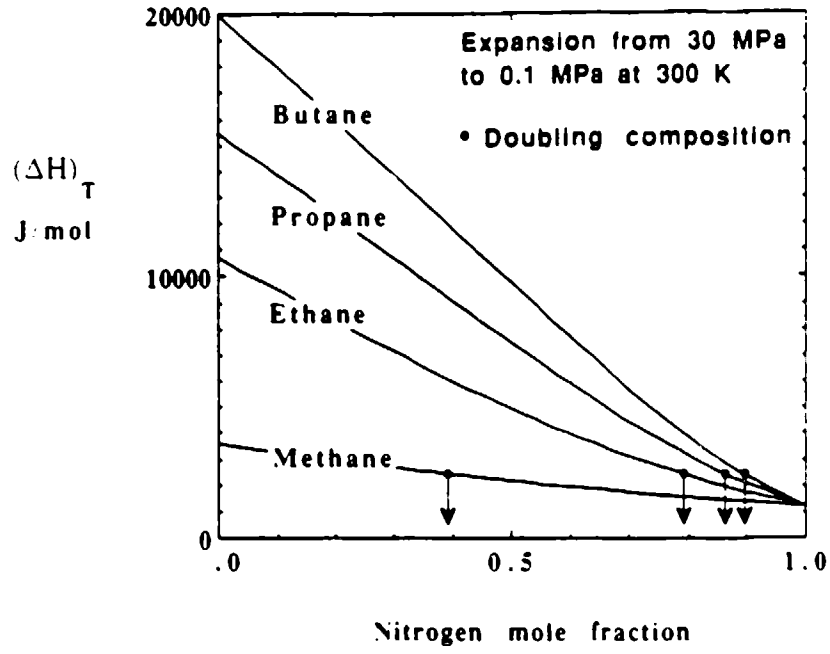

Figure 2: The effect of composition on $(\Delta H)_T$.

component parameters $a_i(T)$ and b_i can be determined from the critical properties and acentric factors of the pure materials.[4] Note that equation 2 contains a binary interaction parameter, $k_{i,j}$. This parameter is included to obtain better agreement in mixture calculations: its value is determined by fitting experimental mixture data. We took interaction parameters from the DECHEMA data collection,[11] except for a few mixtures for which data was not available; for these we estimated the interaction parameters from mixtures of homologous compounds. Expressions for the enthalpy of a fluid mixture modeled by the PR equation are given by Walas.[4] We used the ideal gas heat capacity correlations given by Sandler.[12] The isothermal and isenthalpic JT effects for any pure or mixed cryogen were calculated numerically. We also used the PR equation to determine the fugacities of pure fluids and mixtures. This allowed us to model fluid-fluid and solid-fluid phase equilibria and to determine cryocooler operating temperatures for different cryogens.

ISOTHERMAL AND ISENTHALPIC JOULE-THOMSON EFFECTS

We have used the PR equation to calculate $(\Delta H)_T$ as a function of composition for several binary mixtures in which nitrogen is the low-boiling component. The results for an expansion from 30 MPa to 0.1 MPa at 300 K are shown in figure 2. Notice that $(\Delta H)_T$ is a near-linear function of the nitrogen mole fraction. Even a small amount of a second, high-boiling component greatly increases the maximum possible refrigeration. The solute mole fractions needed to double Q_{max} are indicated in the figure: the higher the boiling point of the solute, the less needed.

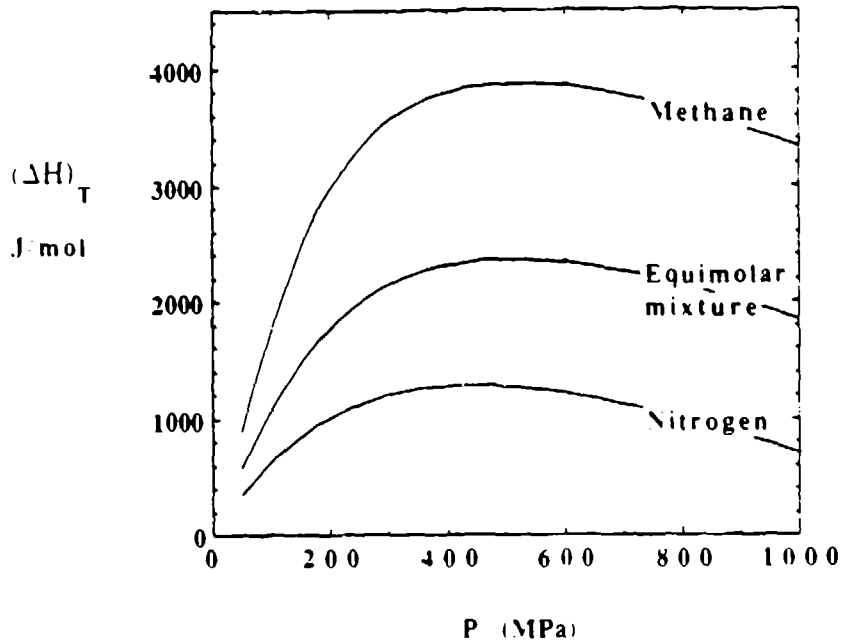

Figure 3: Effect of inlet pressure on $(\Delta H)_T$ at 300 K.

We have also calculated the effect of the inlet pressure on $(\Delta H)_T$; in figure 3 we compare an equimolar mixture of nitrogen and methane to pure nitrogen and pure methane. As in the pure fluid $(\Delta H)_T$ reaches a broad maximum at pressures of about ten to thirteen times the critical pressure ($P_r = P/P_c \approx 10$–13).[13] Pure fluid cryocoolers are often operated in this pressure range to maximize $(\Delta H)_T$.

The time needed to cool a cryocooler down to its steady state operating conditions is an important design consideration. Normally at startup the heat exchanger, the evaporator, and the entering gas are at the ambient temperature. When the gas is allowed to expand across the throttling valve the initial temperature drop will be given by the isenthalpic JT effect evaluated at the inlet conditions: $(\Delta T)_H = T(P_5, H_1) - T(P_1, H_1)$. Assuming that there is a negligible applied heat load during the cool-down process, the temperature of the gas entering the low pressure side of the heat exchanger will initially be $(\Delta T)_H$ below the ambient temperature. Thus, $(\Delta T)_H$ provides an measure of the initial driving force for heat transfer at the cold end of the heat exchanger; the greater this temperature difference, the more rapidly the heat exchanger should reach equilibrium. We have calculated the initial temperature drop as a function of composition for a number of binary nitrogen mixtures; the results are shown in figure 4. These calculations are again based on an inlet condition of 300 K and 30 MPa and an exit pressure of 0.1 MPa. Small amounts of a second high-boiling component improve the initial thermal driving force. The high-boiling components again lead to the greatest improvements. (The maxima in the predictions for the ethane, propane, and butane mixtures correspond to the onset of partial liquefaction; that is, a nitrogen–ethane

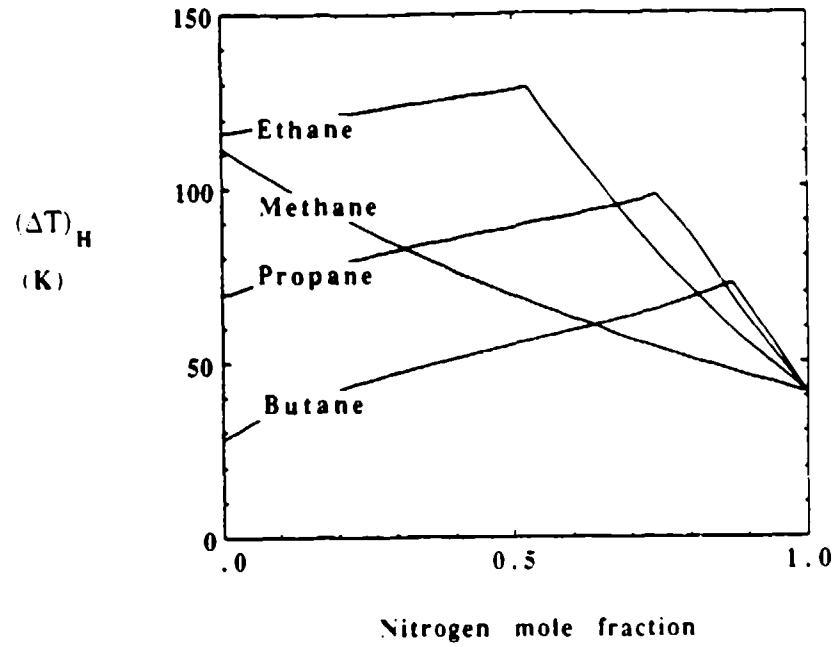

Figure 4: Effect of composition on $(\Delta T)_H$.

mixture with less than 48 mole% nitrogen will partially condense when expanded from 30 MPa to 0.1 MPa even without precooling in the heat exchanger.)

ENTHALPY-TEMPERATURE DIAGRAMS

In analyzing the behavior of cryocoolers we have found it useful to plot the process on an enthalpy-temperature diagram. (This type of diagram is not widely used in applied thermodynamics partly because lines of constant pressure can intersect one another; that is, specifying the temperature and enthalpy need not uniquely fix the thermodynamic state.) Figure 5 shows an enthalpy-temperature plot for a typical open-cycle Joule-Thompson process. We show the enthalpies along the 30 MPa and 0.1 MPa isobars as determined from the PR equation. The values of enthalpy were calculated relative to a reference state of 298 K and 0.1 MPa. This plot is convenient for cryocooler applications because at any given temperature the vertical separation between the two isobars shows the isothermal JT effect at that temperature, while the horizontal separation shows the isenthalpic JT effect. Point 1 is fixed by the inlet conditions, here assumed to be 300 K and 30 MPa. As start-up points 1 and 2 coincide: there is no temperature drop along the heat exchanger, and the initial driving force for heat transfer is just $(\Delta T)_H$ evaluated at T_1. As the device cools down, point 2 drops to lower temperatures. As the same time the temperature drop across the throttling valve changes. This is reflected in the changing horizontal separation between the two isobars. Initially, the temperature drop increases because the high-pressure fluid has the larger heat capacity, $C_P = (\partial H/\partial T)_P$. Ultimately point 4 is fixed by the condition that only

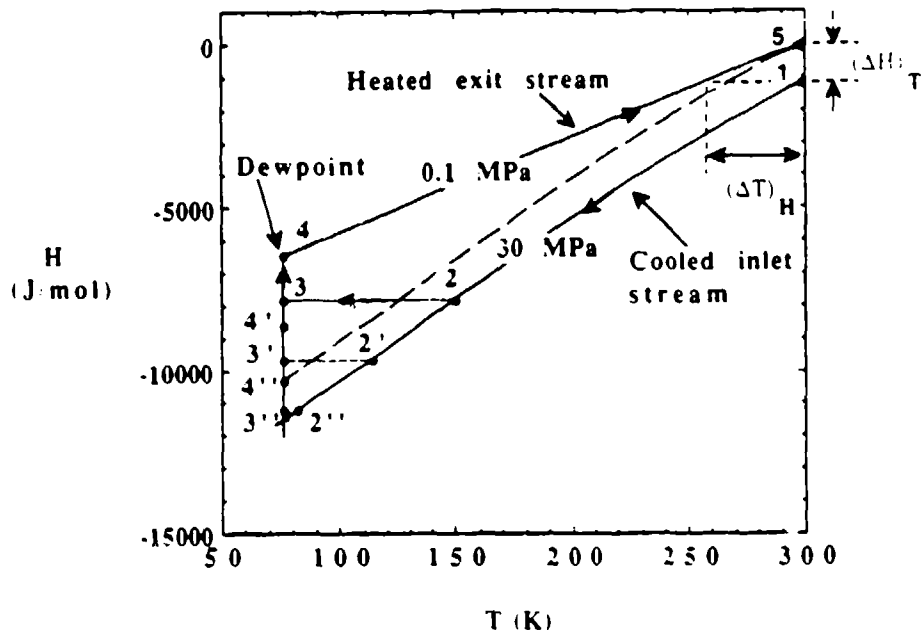

Figure 5: Enthalpy-temperature diagram for pure nitrogen.

saturated vapor is returned from the evaporator. During steady state operation when the heat load in the evaporator equals Q_{max}, point 5 is fixed by the condition that $T_5 = T_1$. Also point 3 is fixed by the fact that $(H_4 - H_3) = (H_5 - H_1)$ when there is no parasitic heat load, and point 2 is fixed by the condition that $H_3 = H_2$. This allows us to plot the entire steady-state cycle on the diagram. Finally, notice that the isobars intersect at low temperatures (77.35 K) and that the low pressure isobar has a vertical section at this temperature. This corresponds to the vapor-liquid transition at the normal boiling point. The cycles 1-2′-3′-4′-5 and 1-2″-3″-4″-5 in figure 5 will be discussed in the next section.

The broken line in figure 5 represents the "operating line" at $Q = Q_{max}$. This line is just the high pressure isobar shifted upwards by the amount of refrigeration provided. It is a useful construction because if a vertical line is drawn upwards from state 2 and a horizontal line is then drawn from the intersection with the operating line, the horizontal line intersects the low pressure isobar at state 4. Furthermore, one can show from an enthalpy balance that the horizontal separation between the operating line and the low-pressure isobar gives the temperature difference (the thermal driving force) for heat transfer at the corresponding point (or temperature) in the heat exchanger. Thus, the intersection of the operating line with the low pressure isobar (at point 4″) determines the minimum operating temperature. That is, the intersection represents the appearance of a temperature pinch at the cold end of the heat exchanger. Since the operating line in figure 5 was drawn for $Q = Q_{max}$, it also intersects the low-pressure line at point 5 because a temperature pinch must occur at the hot end of the exchanger at the maximum heat load.

EVAPORATOR TEMPERATURE AND OPERATION WITH PARTIAL EVAPORATION

In certain circumstances it may be desirable to operate a JT cryocooler so that the low pressure fluid returned to the heat exchanger from the evaporator is a two-phase vapor–liquid mixture rather than a saturated vapor. If the liquid is subsequently evaporated in the heat exchanger through heat transfer from the high pressure fluid, then one can show from an overall enthalpy balance that there is no net effect on the amount of heat absorbed in the evaporator—the lost enthalpy of vaporization of the liquid returned to the heat exchanger is exactly balanced by a decrease in quality and enthalpy of the two-phase mixture entering from the valve. We refer to this as operating with partial evaporation. In this mode of operation one would obtain a cycle like 1–2′–3′–4′–5, figure 5. Note that the temperature at point 2′ can never be lower than the temperature at point 4″ because the low-pressure stream cools the high-pressure stream; that is, $T_{2'}$ is limited by the appearance of a temperature pinch at the cold end of the heat exchanger. However, since $(\Delta H)_T$ at 300 K is much less than the enthalpy of vaporization, the pinch temperature (point 4″) in figure 5 is just the normal boiling point of nitrogen. Obviously, once we abandon the requirement that the returning fluid at point 4′ be a saturated vapor, there are many acceptable sets of operating conditions at the cold end that are consistent with operating at maximum molar heat load (points 2′–3′–4′, 2″–3″–4″, etc.). Which conditions occur depends on the heat exchanger. Physically, in a miniature Joule-Thompson cryocooler with a coiled-tube Giaque-Hampson heat exchanger operating with partial evaporation in the refrigerator would amount to keeping some of the lower coils submerged in a column of liquified cryogen. This can be achieved by using a long heat exchanger. If it is sufficiently long, point 2′ will closely approach the pinch point. In practice, however, before this occurs the assumption of negligible parasitic heat load in the heat exchanger may fail: the longer the heat exchanger, the more low temperature surface exposed to raditative heat gain across the dewar vacuum.

Figure 5 shows that there is no profit in operating a pure fluid JT cryocooler with partial evaporation because it simply requires a longer heat exchanger without changing the evaporator operating temperature or Q_{max}. The situation is different for a mixture, however, because a non-azeotropic liquid mixture boils over a range of temperatures. As a mixture is vaporized at constant pressure, the liquid is enriched in the high-boiling components, and the boiling temperature continuously increases. Thus the operating temperature in a mixture cryocooler will depend on the composition of the mixture. For non-azeotropic mixtures it will lie between the normal boiling points of the pure components. Furthermore, since the mixture entering the evaporator will boil over a range of temperatures, the operating temperature will actually be given by the upper limit of that range because heat must be absorbed in the evaporator. Thus, if a mixed fluid cryocooler is operated

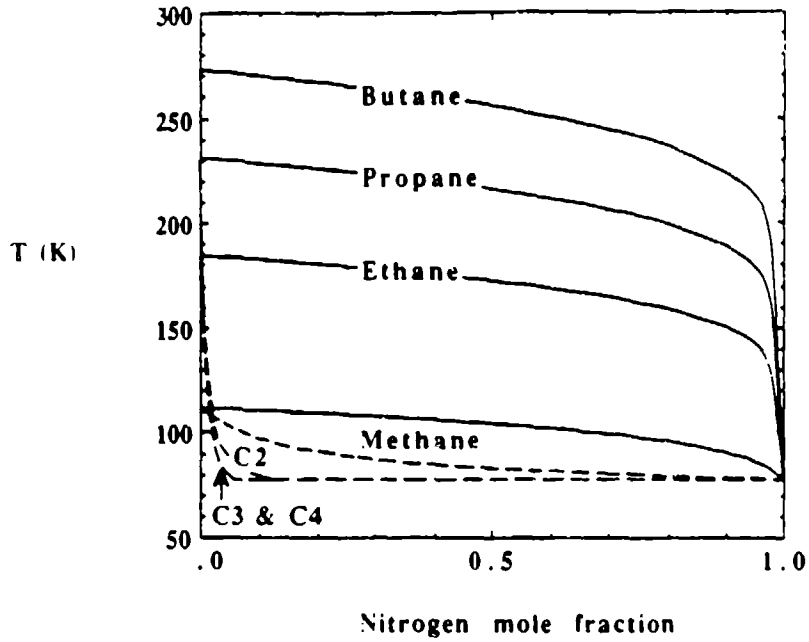

Figure 6: Dewpoint (——) and bubblepoint (- - -) curves for nitrogen mixtures at 0.1 MPa.

with complete evaporation, the operating temperature will simply be the mixture dewpoint temperature at the evaporator pressure. Figure 6 shows the dewpoint curves for some nitrogen mixtures at 0.1 MPa as calculated from the PR equation. Clearly, adding a high-boiling component to nitrogen drastically increases the operating temperature, and the higher the boiling point of the second component, the worse the effect on the operating temperature. Furthermore, because of the non-linearity of the dewpoint curve, the solute's deleterious effect on the operating temperature outweighs the improvement in Q_{max} seen in figure 2. Unfortunately, this type of dewpoint curve is typical of non-azeotropic mixtures in which there are large differences in the normal boiling points of the components.

The problem can be avoided if the cryocooler is operated with partial evaporation. Suppose that only a small part of the liquid entering through the JT valve is vaporized in the evaporator and that the remainder is returned for evaporation in the heat exchanger. As with a pure fluid cryocooler, an enthalpy balance shows that partial evaporation has no net effect on the amount of heat absorbed in the evaporator: the lost enthalpy of vaporization of the liquid returned to the heat exchanger is balanced by a decrease in quality and enthalpy of the two-phase mixture entering from the valve. Now, however, decreasing the quality of the entering two-phase mixture lowers its temperature towards the bubblepoint. In addition, since the fluid leaving the evaporator is also a two-phase mixture, its temperature is lower than the dewpoint temperature for that overall composition. Finally, since the heat added in the evaporator is normally a small fraction of the

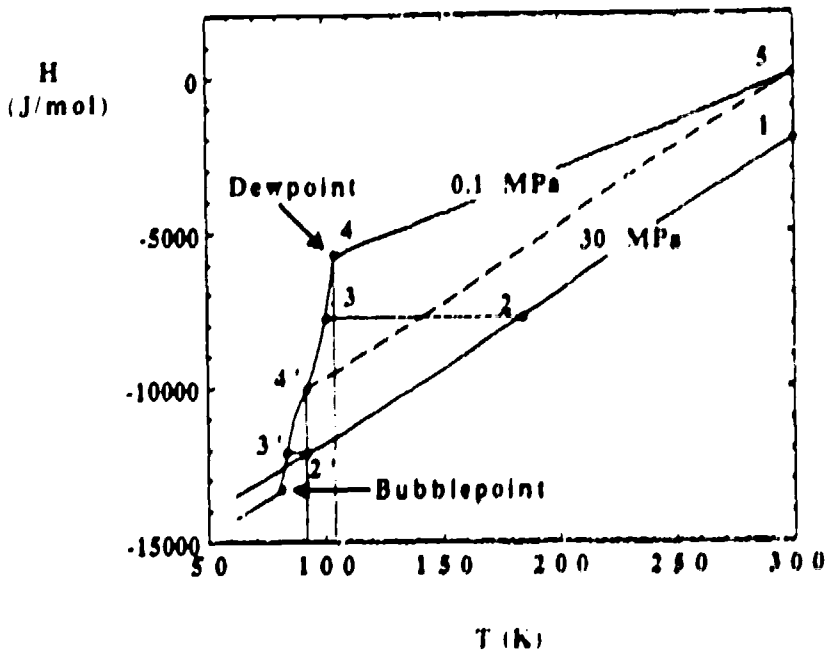

Figure 7: H-T diagram for an equimolar mixture of nitrogen and methane.

enthalpy of vaporization of the mixture—$Q_{max} \ll \Delta H_{vap}$—it is possible to operate at temperatures only slightly above the mixture bubblepoint, provided a heat exchanger of sufficient length is used. Bubblepoint curves for nitrogen mixtures are also shown in figure 6; they are highly non-linear too but, unlike the dewpoint curves, they have favorable curvatures: small amounts of solute do not much affect the bubblepoint temperature. Thus, when operating with partial evaporation, the presence of a second component in low concentrations only slightly increases the operating temperature, while still giving a large increase in capacity. The bubblepoint curves in figure 6 are typical of non-azeotropic mixtures in which there are large differences in the normal boiling points. Note that for the high-boiling solutes the bubblepoint curve often has a horizontal section over a large composition range near liquid nitrogen temperatures; this behavior, which is due to liquid-liquid equilibrium, will be discussed in the next section. Finally, we note that in the above calculations we have ignored the possibility of solid-liquid-vapor equilibria. This too will be discussed later.

The advantages of partial evaporation can also be seen from the enthalpy-temperature diagrams for mixtures. Figure 7 shows two isobars calculated from the PR equation for an equimolar nitrogen-methane mixture. Note that the vertical region associated with vapor-liquid equilibrium at 0.1 MPa in figure 6 has been replaced in figure 7 by a region of finite slope because the boiling temperature increases with fraction vaporized. We have marked two possible cycles on the diagram for a mixture that enters at 30 MPa and 300 K and exhausts at 0.1 MPa and 300 K. One cycle, 1-2-3-4-5, corresponds to operating at maximum

Table 2: Liquid-liquid-vapor triple points in binary nitrogen mixtures at 0.1 MPa.

Solute	Temperature (K)	Solute mole percent: Solute-rich liquid	Nitrogen-rich liquid	Vapor
Ethane	77.62	87.61	1.86	3.275×10^{-7}
Propane	77.49	94.31	0.09	1.349×10^{-10}
1-Butene	77.48	95.74	4.26	1.677×10^{-13}
Butane	77.48	93.57	0.02	5.570×10^{-14}

refrigeration with complete evaporation in the evaporator. The other, 1-2′-3′-4′-5, corresponds to operating at maximum refrigeration with the lowest possible quality mixture leaving the evaporator. The latter condition is determined by the appearance of a temperature pinch at the cold end of the heat exchanger (that is, $T_{3'} = T_{4'}$). The partial evaporation cycle has a lower operating temperature (92 K versus 105 K), even though the inlet and exhaust conditions and Q_{max} are the same for both cycles. A cryocooler using this equimolar mixture as the working fluid would operate somewhere between these two forms of limiting behavior, depending on the length of the exchanger. A significant improvement in $(\Delta H)_T$ for the mixture and the accompanying improvement in $(\Delta T)_H$ becomes apparent on comparing figures 6 and 7.

LIQUID-LIQUID EQUILIBRIA IN CRYOGENIC MIXTURES

As mentioned earlier, the results presented in figure 7 are incomplete because we have ignored the complicating effects of liquid-liquid and solid-liquid equilibria. For example, some of the bubblepoint curves in figure 6 have horizontal sections at low temperature. This is not an artifact; instead it reflects the fact that many cryogenic mixtures are only partially miscible in the liquid phase.[11] This has been seen experimentally for liquid mixtures of nitrogen and ethane[15,16] and for mixtures of nitrogen and propane.[17,18] When a region of liquid-liquid equilibrium intersects a region of vapor-liquid equilibrium, a liquid-liquid-vapor triple point results. This gives rise to a horizontal section in the bubble-point curve. Mixture triple points can be located by standard numerical techniques that look for solutions to the phase equilibrium fugacity conditions.[4] For example, in figure 8 we show the temperature-composition phase diagram for a mixture of nitrogen and ethane at 0.1 MPa by using the PR equation to calculate the liquid and vapor mixture fugacities. There is a region of vapor-liquid equilibrium at high nitrogen concentrations and between the triple point and the pure nitrogen boiling point, but it is not visible on the scale of figure 8. The conditions at the LLV triple point are given in Table 2, together with the corresponding values for some other binary nitrogen mixtures. These calculations show that a LLV triple point can be

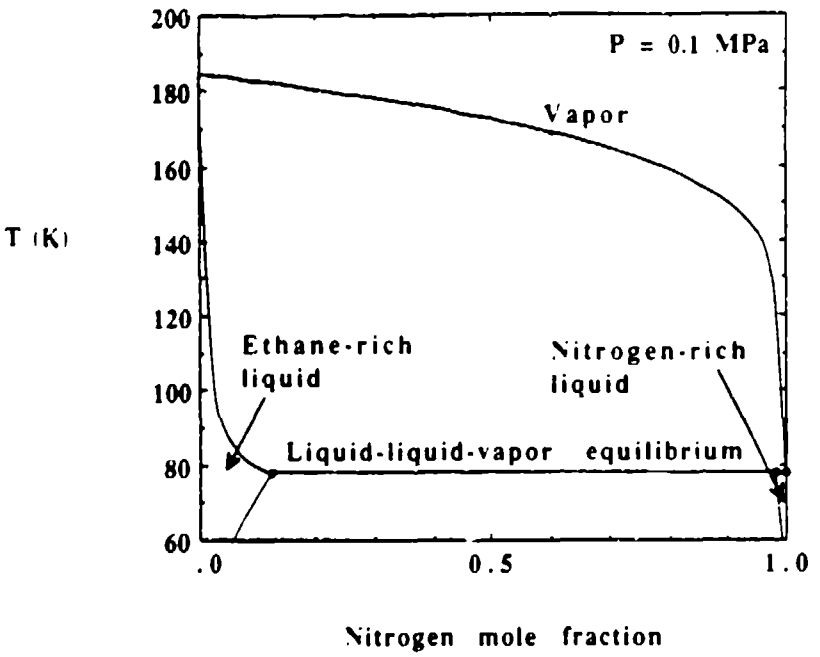

Figure 8: Liquid-liquid-vapor equilibrium in a mixture of nitrogen and ethane at 0.1 MPa.

advantageous because it often occurs at a temperature close to the boiling point of the low-boiling component. Thus, a LLV triple point in a nitrogen mixture usually means that the bubblepoint temperature is close to 77.35 K over a large composition range. For example, any nitrogen–ethane mixture with an overall nitrogen composition greater than 12.5 mole% has a bubblepoint at 77.62 K.

Another desirable feature of LLV triple points is that they lead to constant temperature boiling in the mixture. For example, consider an equimolar mixture of nitrogen and ethane, figure 8. At 0.1 MPa and low temperatures, say 70 K, the mixture will separate into two coexisting liquid phases: a nitrogen-rich phase and an ethane-rich phase. If the mixture is heated, the temperature and the enthalpy of the two-phase mixture will increase slowly until the triple point is reached. At that point the temperature will remain constant while heat is added until the nitrogen-rich liquid phase has boiled off. That is, heat will be absorbed at constant temperature just as in boiling a pure liquid. With the further addition of heat the temperature will gradually rise to the dewpoint as the solute-rich liquid (the only remaining liquid phase) gradually evaporates. Thus, if a nitrogen-ethane mixture is employed in a cryocooler and if it is cooled sufficiently in the heat exchanger that it expands to give a liquid-liquid-vapor mixture, the initial heat added in the evaporator will not raise the temperature. We will see later that with some mixtures two liquid phases remain throughout the evaporation process even at the maximum refrigeration. Such mixtures operate at a constant evaporator temperature: the triple point temperature.

SOLID-LIQUID EQUILIBRIA IN CRYOGENIC MIXTURES

In table all the cryogens that have boiling points higher than nitrogen also have melting points higher than the normal boiling point of nitrogen, with the sole exception of oxygen. (Flourine and carbon monoxide, which are not listed in the table, also have relatively low melting points but these are not widely used because of their toxicity.) The pure solute melting points are also above the liquid-liquid-vapor triple points for the mixtures in table 2, and as a result these mixtures may actually freeze above the (metastable) liquid-liquid-vapor triple points. This would drastically limit the minimum cryocooler operating temperatures because to avoid clogging the device one must operate at temperatures high enough to avoid precipitation of the solute. Thus, we face a dilemma: on the one hand we would like to use a mixture of two components with widely different boiling points in order to achieve a low operating temperature (near the normal boiling point of the low-boiling component) and a high capacity (characteristic of high-boiling component), while on the other hand, all species in the mixture should have low melting temperatures to avoid freezing and precipitation.

In solid-liquid phase equilibria in organic mixtures the solutes usually precipate out as pure solids. Assuming that a negligible amount of nitrogen dissolves in the solid phase, the solute precipates when its fugacity in the liquid mixture, $\hat{f}_i^l(T, P, x_i)$, equals or exceeds its fugacity as a pure solid, $f_i^s(T, P)$. The liquid phase fugacity can be calculated from the PR equation. The pure solid fugacity can be related to the fugacity of a (metastable) pure liquid solute[4]

$$f_i^s(T,P) = f_i^l(T,P)\exp\left[\frac{\Delta H_m}{R}\left(\frac{1}{T_m}-\frac{1}{T}\right)\right] \tag{4}$$

Here ΔH_m is the normal latent heat of fusion of the pure solid and T_m is its melting temperature. This expression is approximate but quite reliable at low pressures and for temperatures not too far below T_m. Finally, the fugacity of the subcooled pure liquid can be approximately determined from the PR equation, which, like other cubic equations of state, does not exhibit a solid-liquid transition and so can be used to model metastable liquid phases.

We have located solid-liquid-vapor (SLV) triple points for several mixtures. The results are given in table 3. We found that indeed, except for the nitrogen–methane system, all the binaries considered earlier have SLV triple points and in each case the triple point temperature is only slightly below the melting point of the high-boiling solute. Thus, for these binary mixtures the minimum cryocooler operating temperature will essentially be limited by the melting point of the high boiling component. This will result in operating temperatures significantly higher than the (metastable) mixture LLV triple point. However, we will show in the next section that one can avoid solid-fluid equilibria by using slightly more complex mixtures.

Table 3: Solid-liquid-vapor triple points in binary nitrogen mixtures.

Solute i	Temperature (K)	Solute mole percent	
		Liquid	Vapor
Ethane	88.6	94.4	9.69×10^{-4}
Propylene	86.2	92.2	1.23×10^{-6}
Propane	84.4	93.4	2.58×10^{-7}
1-Butene	86.0	89.5	1.29×10^{-9}
Butane	134.3	98.5	8.50×10^{-4}

TERNARY MIXTURE CRYOCOOLERS

Consider a mixture of two high-boiling cryogens, ethane and propane, for example. Even if these form an ideal liquid solution, there is a composition range in which the freezing point of their mixture will be depressed relative to the two pure solids. If we assume ideal liquid mixtures and immiscible pure solid phases, we can use the Schroeder equation to estimate the eutectic composition and temperature for a given binary.[4] The Schroeder equation gives an expression for the liquidus curve

$$x_i = \exp\left[\frac{\Delta H_{mi}}{R}\left(\frac{1}{T_{mi}} - \frac{1}{T}\right)\right] \tag{5}$$

where ΔH_{mi} is the latent heat of fusion of pure component i, T_{mi} is its melting temperature, and x_i is its mole fraction in the liquid at equilibrium at a temperature T. This equation can be applied to both components in a binary mixture. At the eutectic point the two liquidus curves intersect, and the composition and freezing temperature of the eutectic mixture can be determined from the solution to the two equations. For ethane and propane we calculate $T_e \approx 75.5$ K and $x_{1e} \approx 0.48$. Thus, a near-equimolar mixture of ethane and propane will have a normal freezing point below the boiling point of pure nitrogen—assuming ideal solution behavior in the liquid. This suggests that we can find a nitrogen–ethane-propane mixture which will completely condense to a liquid mixture occurs before it begins to solidify. Since both ethane and propane form partially miscible liquid mixtures with nitrogen at low temperatures, figure 6, we expect that the system will actually condense to two coexisting liquid phases: a nitrogen-rich phase, and a hydrocarbon-rich phase. The minimum operating temperature will then be limited by the appearance of a ternary mixture liquid-liquid-vapor triple point close to the boiling point of pure nitrogen, rather than by the precipitation of ethane or propane.

Using the PR equation for the liquid phase and the method given earlier for the pure solid fugacities, we have determined the concentration region in which the nitrogen-ethane-propane mixture will completely liquify before solidification. On a triangular composition diagram this is a region of three phase liquid-liquid-vapor (LLV) triple points, bounded by four-phase solid-liquid-liquid-vapor coexistence,

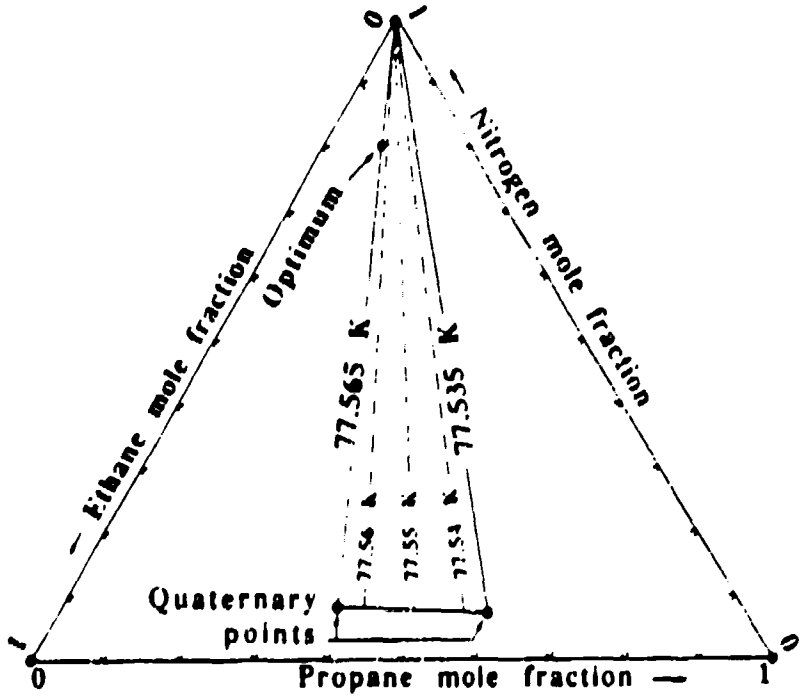

Figure 9: LLV region at 0.1 MPa in the nitrogen–ethane–propane mixture.

figure 9. Several tielines connecting the two liquid phases in equilibrium are shown in the figure, together with the corresponding triple point temperatures. Tielines connecting the liquid and vapor phases are not shown because neither the vapor phase nor the nitrogen-rich liquid phase can be distinguished from pure nitrogen on the scale of this diagram. We list the properties at the four-phase coexistence points in table 4. Notice that for the nitrogen–ethane–propane mixture there are two quaternary points since either ethane or propane can precipate as a pure solid.

Other substances besides ethane and propane can be mixed to form a pseudo-solute having a melting temperature below the boiling point of pure nitrogen. The most promising should be those with relatively low melting points as pure substances. Table 5 shows the Schroeder equation predictions for the eutectic temperature and composition for some further mixtures. Generally, we expect the mixtures with eutectics below 77.4 K to behave similarly to the nitrogen–ethane–propane ternary. For example, figure 10 shows the LLV composition region and triple point temperatures for a ternary mixture of nitrogen, propane, and 1-butene. There is an obvious qualitative similarity to the nitrogen–ethane–propane region. In contrast, mixtures that include nitrogen and methane will behave slightly differently because, unlike most alkanes, methane is totally miscible in liquid nitrogen at 0.1 MPa. We show the results for the LLV triple point region for a ternary mixture of nitrogen, methane, and ethane in figure 11. This mixture has only one quaternary point—corresponding to the

Table 4: Solid-liquid-liquid-vapor coexistence points in ternary nitrogen mixtures.

Temperature			Species mole fraction		
			Nitrogen-rich	Nitrogen-poor	
(K)	Species i	Solid	liquid	liquid	Vapor
77.565	N_2	0.0	0.98943	0.08398	1.0
	C_2H_6	1.0	0.01010	0.54179	1.9×10^{-7}
	C_3H_8	0.0	0.00047	0.37422	5.9×10^{-11}
77.535	N_2	0.0	0.99319	0.07134	1.0
	C_2H_6	0.0	0.00615	0.34513	1.2×10^{-7}
	C_3H_8	1.0	0.00066	0.58354	8.7×10^{-11}
77.483	N_2	0.0	0.99938	0.05054	1.0
	C_3H_8	1.0	0.00058	0.59699	8.5×10^{-11}
	1-C_4H_8	0.0	0.00004	0.35247	6.3×10^{-14}
77.482	N_2	0.0	0.99949	0.04850	1.0
	C_3H_8	0.0	0.00045	0.46477	6.6×10^{-11}
	1-C_4H_8	1.0	0.00006	0.48673	8.7×10^{-14}
79.128	N_2	0.0	0.74437	0.22457	0.99278
	CH_4	0.0	0.20728	0.31941	7.2×10^{-3}
	C_2H_6	1.0	0.04835	0.45602	3.6×10^{-7}

Table 5: Eutectic compositions and temperatures of some binary mixtures.

Species 1	Species 2	Temperature (K)	Mole fraction of species 1
Methane	Ethane	69.3	0.68
Methane	Propane	69.4	0.68
Methane	1-Butene	71.1	0.71
Methane	i-Butane	80.8	0.86
Methane	n-Butane	84.7	0.92
Ethane	Propane	75.5	0.41
Ethane	1-Butene	76.9	0.53
Ethane	i-Butane	85.0	0.80
Ethane	n-Butane	87.4	0.90
Propane	1-Butene	76.3	0.55
Propane	i-Butane	82.5	0.84
Propane	n-Butane	84.0	0.92

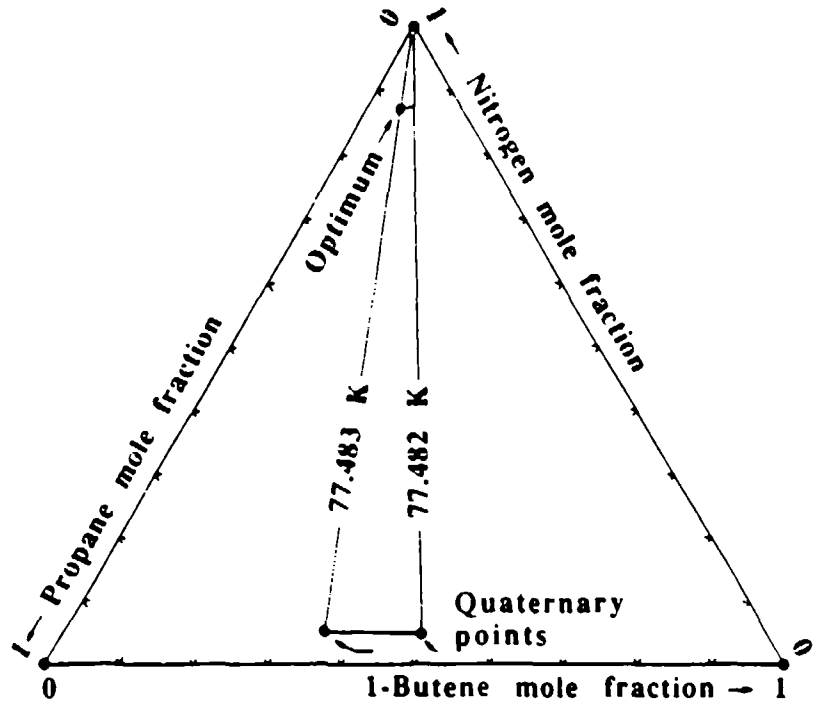

Figure 10: LLV region at 0.1 MPa in the nitrogen–propane–1-butene mixture.

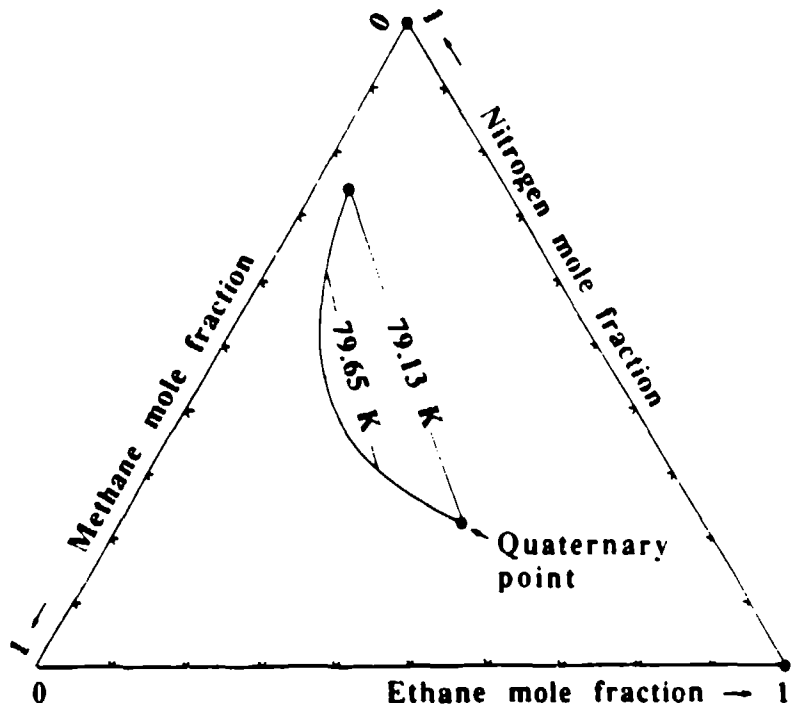

Figure 11: LLV region at 0.1 MPa in the nitrogen–methane–ethane mixture.

precipation of pure ethane—because the region of liquid-liquid immiscibility does not extend all the way over to the nitrogen-methane binary.

A minor complication that appears first in ternary systems is that for a mixture of a fixed overall composition the triple point temperature changes slightly as one moves from the bubble triple point, where there are finite amounts of two liquid phases and an infinitesimal amount of the vapor phase, to the dew triple point, where there are finite amounts of one liquid phase and of the vapor phase and an infinitesimal amount of the second liquid phase. However, we find that for these systems the change in temperature is small (< 1 K) and not noticable on the scale of figures 12 and 13. The triple point temperatures shown on the tielines in figures 9-11 are for the bubble triple points. Notice also that they vary only slightly in the LLV region. This might lead one to believe that the cryocooler operating temperature would be relatively insensitive to the composition in these regions. However, we will see in the next section that this is not necessarily the case and that furthermore Q_{max} is highly sensitive to the composition.

OPTIMUM MIXTURE COMPOSITION

Consider a ternary mixture of nitrogen, ethane, and propane. By analogy with binary mixtures, figure 2, we expect that $(\Delta H)_T$ will increase as the mole fractions of the high-boiling components increase. In figure 12 we show the enthalpy-temperature diagram for a mixture containing 75 mole percent methane, 12.5 mole percent ethane, and 12.5 mole percent propane, a composition within the triple point region, figure 9. Clearly Q_{max}(3.3 kJ/mol) has improved from its value for pure nitrogen expanded from the same conditions (1.2 kJ/mol). However, the H-T plot also shows that the cryocooler will not operate at the triple point temperature of 77 K when providing the maximum refrigeration. This becomes clear when operating lines are drawn on the diagram; lines for 25%, 50%, 75%, and 100% of Q_{max} are shown in figure 12. At 100% of Q_{max} the pinch appears at 165 K, an unacceptably high operating temperature. (A second pinch also appears at the hot end of the heat exchanger because the inlet and exit temperatures are the same at maximum refrigeration.) Thus, even though the mixture can be completely condensed to a liquid-liquid mixture at 77 K, it will not reach that temperature in a JT cryocooler operating at maximum refrigeration. To avoid this problem, one could operate at less than 100% of Q_{max}; as can be seen from the other operating lines, the pinch temperature drops with the required heat load. This amounts to operating in an excess flow mode, that is, with a flow rate of cryogen greater than required to supply a given refrigeration rate. Alternatively, one can adjust the composition of the mixture. If the nitrogen composition is increased slightly, one finds that the pinch point occurs at the triple point temperature even at maximum refrigeration, figure 13. The transition in operating temperature that occurs as the nitrogen mole fraction is increased is a sharp transition for this mixture because of

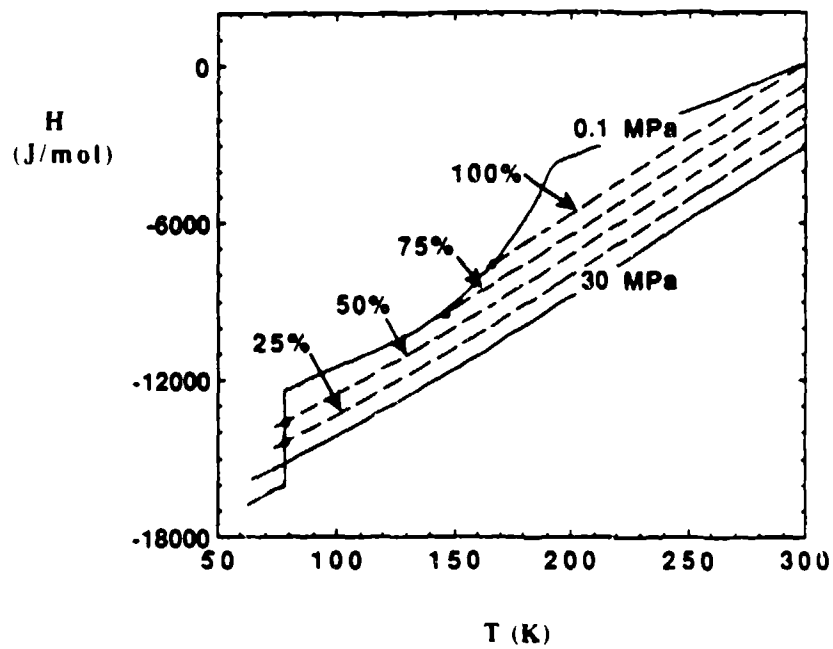

Figure 12: *H-T* diagram for a 75% nitrogen, 12.5% ethane, 12.5% propane mixture.

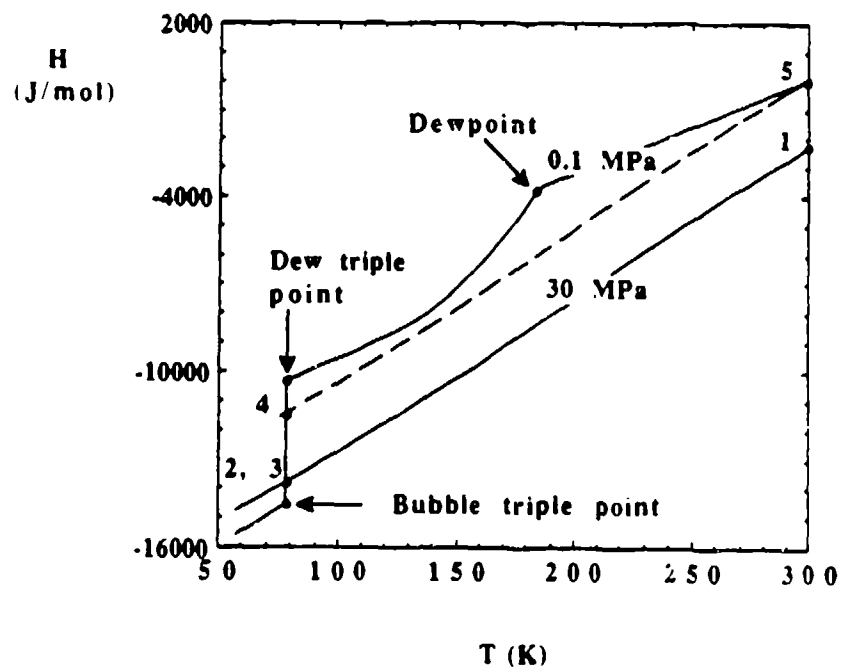

Figure 13: *H-T* diagram for a 83% nitrogen, 10% ethane, 7% propane mixture.

Table 6: Optimum compositions in ternary nitrogen mixtures.

Species i	Mole fraction of species i	$(\Delta H)_T$ (kJ/mol)
N_2	0.80	2.65
C_2H_6	0.12	
C_3H_8	0.08	
N_2	0.87	2.42
C_3H_8	0.08	
$1\text{-}C_4H_8$	0.05	

the convex-downwards shape of the low-pressure isobar between the dewpoint and triple points. One can determine the compositions at which the operating curve just touches the low-pressure isobar tangentially. Thes compositions, which are shown as a dotted line in figure 9, mark the transition to an acceptable low operating temperature on the nitrogen-rich side of the lines. We have determined which of the transition compositions gives rise to the largest value for Q_{max}; the results are given in table 6. This is the optimum nitrogen—ethane—propane mixture composition for expansion from the given inlet conditions.

In practice, however, the nitrogen composition must be increased a little further to ensure a finite temperature difference between the two streams in the heat exchanger at the intermediate temperatures. Figure 14 shows ΔT, the temperature difference between the high- and low-pressure sides along the exchanger, as a function of the temperature on the high-pressure side. Results are shown for pure nitrogen and for a mixture with 83% nitrogen, 10% ethane, and 7% propane—slightly more nitrogen than the optimum. Both fluids were expanded from 30 MPa and 300 K to 0.1 MPa. The mixture has the larger heat transfer driving force at the hot end of the heat exchanger, but pure nitrogen does better at intermediate temperatures. Except at the pinch points at either end, there is always at least a 10 K temperature difference. Of course, Q_{max} is now slightly less than at the transition composition, but it is still twice that of pure nitrogen (2,364 J/mol versus 1195 J/mol). This appears to be a typical improvement. For example, the nitrogen–ethane–1-butene mixture also gives a near two-fold improvement in $(\Delta H)_T$ ove- that of pure nitrogen when expanding from 30 MPa and 300 K to 0.1 MPa, Table 6. Finally, we note that again that there is a slight increase in temperature as one moves from the dew triple point to the bubble triple point but that for these systems the change is small (< 1 K) and not noticable on the scale of figures 12 and 13.

As mentioned earlier the time required for cooldown is an important design consideration. Figure 14 showed the initial temperature drop across the nozzle for various nitrogen mixtures. It indicated that the initial rate of cooldown would be

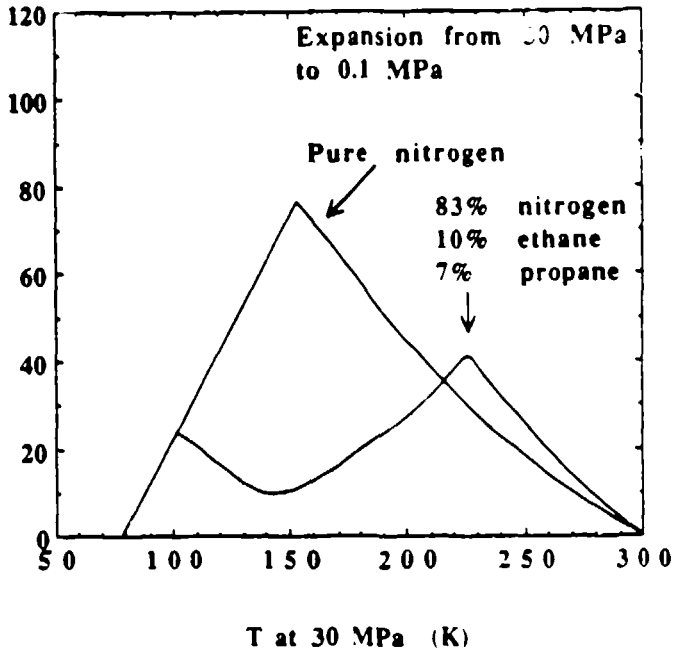

Figure 14: Heat exchanger ΔT for pure nitrogen and for a nitrogen–ethane–propane mixture.

greater for the mixtures than for pure nitrogen. Figure 15 amplifies on this point. It shows the temperature drop across the nozzle as a function of the temperature at the inlet to the nozzle. This will equal the temperature difference at the cold end of the heat exchanger if there is no heat load in the evaporator, as might occur during startup. Results are shown for a nitrogen—ethane—propane mixture and for pure nitrogen, with both fluids being expanded from 30 MPa and 300 K down to 0.1 MPa. The results show that the mixture has the initial advantage, but that the advantage shifts to the pure fluid later in the startup process. Overall, the average temperature difference during the startup is comparable for the two fluids. Thus, for equal molar flowrates and comparable heat transfer coefficients the relative cooldown rates should be determined by Q_{max}, which gives the capacity of the working fluid to remove the sensible heat of the cryocooler during the cooldown when no load is being applied in the evaporator. This gives an advantage to the mixture cryocooler, although it will be partly offset by the greater sensible heat of the mixture cryocooler due to the increased heat exchanger length. A detailed unsteady-state model for the heat exchanger would be required to make any more definite conclusion.

DISCUSSION

We can now interpret the experimental results that have appeared in the literature. For example, Little reports that a quaternary mixture of 50% nitrogen, 28.4% methane, 14.2% ethane, and 7.1% propane provides refrigeration at 81.3 K

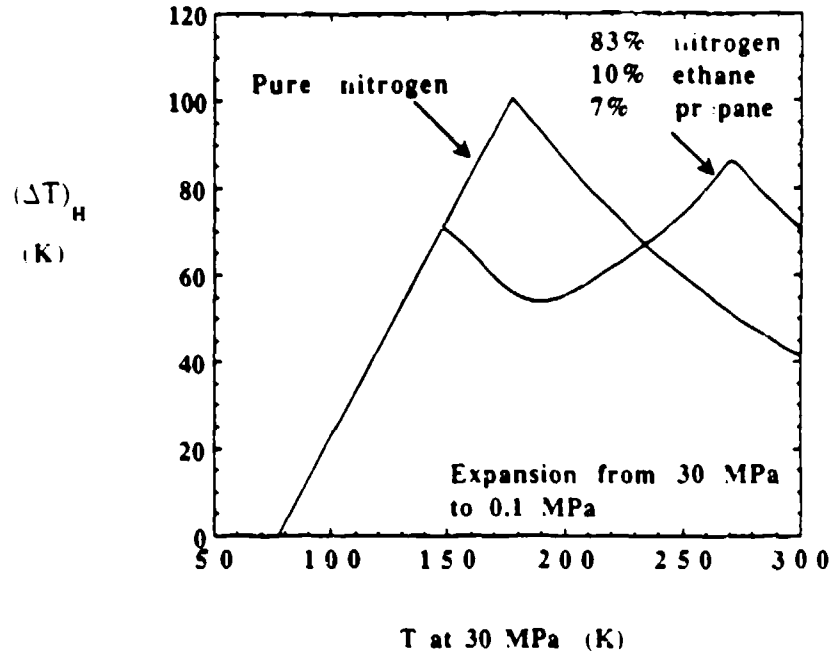

Figure 15: ΔT across the nozzle for a pure nitrogen and for a ternary mixture.

when expanded from 5.6 MPa.[2] We have calculated the enthalpy-temperature diagram for this mixture, figure 16. The PR predictions are in good agreement with Little's experimental results. The operating temperature is fixed at 80 K by the LLV triple point. Q_{max} is small (1,100 J/mol) but considerably larger than that for pure nitrogen expanded from the same conditions (350 J/mol). The advantage of this mixture is that it provides a Q_{max} at 5.6 MPa that could be obtained from pure nitrogen only by expanding from 30 MPa, figure 3. The non-linear shape of the 5.6 MPa isobar is also interesting. Note that there is always a large temperature difference for heat transfer. The 30 MPa isobar is also shown in figure 16 for comparison. Q_{max} is much larger (3.5 kJ/mol) for the higher pressure, but so is the operating temperature (140 K) at maximum refrigeration.

From these results it is clear that mixture cryocoolers may offer significant advantages over pure fluid cryocoolers. By a suitable choice of mixture one should be able to increase the maximum refrigeration provided for given inlet conditions. However, the problem of solute precipitation requires that ternary or greater mixtures be used, and it limits one to relatively low concentrations of high-boiling components in the working fluid. This appears to limit the gains to perhaps doubling Q_{max} when expanding from high pressures. although larger relative gains are possible at lower pressures.

REFERENCES

1. V.M. Brodyansky, A.K. Gresin E.M. Gromov, V.M. Yagodin, V.A. Nicolsky, and V.N. Alpheev, "The use of mixtures as the working gas in throttle

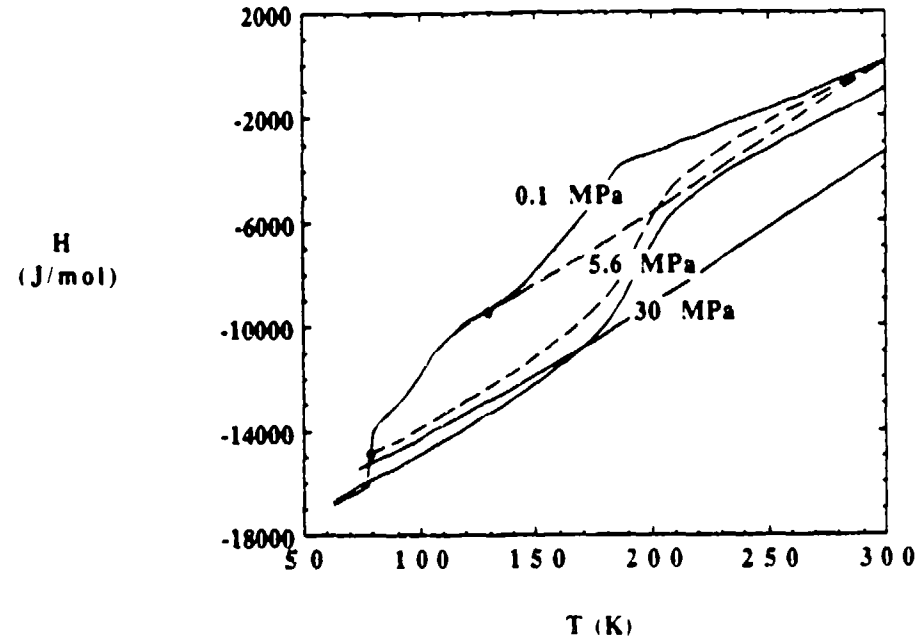

Figure 16: *H-T* diagram for a 50% nitrogen, 28.4% methane, 14.2% ethane, and 7.1% propane mixture.

Joule-Thompson cryogen refrigerators," *Proc. 19th Int. Cong. Refrig.*, Washington DC, USA (1971), *Prog. Refrig. Sci. Tech.*, vol. 1, p. 43 (1973)

2. W.A. Little, "Recent developments in Joule-Thompson cooling: gases, coolers, and compressors." *Proc. 5th Int. Cryocooler Conf.*, Monterey, CA, USA (August 18-19, 1988), p. 3.

3. G. Walker, *Miniature refrigerators for Cryogenic Sensors and Cold Electronics*, Clarendon Press, Oxford, (1989).

4. S.M. Walas, *Phase Equilibrium in Chemical Engineering*, Butterworth, Boston, (1985).

5. W.M. Haynes, A.J. Kidnay, N.A. Olien, and M.J. Hize, "Status of thermophysical properties data for pure fluids and mixtures of cryogenic interest," *Adv. Cryogenic Engineering*, vol. 29, p. 919 (1984).

6. S.I. Jenkins, A.K. Majumdar, and R.C. Hendricks, "Investigation of two and three parameter equations of state for cryogenic fluids," *Adv. Cryogenic Fluids*, vol. 35, p. 1487 (1990).

7. C.J. Lin and S.W. Hopke, "Application of the BWRS equation to methane, ethane, propane, and nitrogen systems," *A.I.Ch.E. Symp. Ser.*, vol. 70, no. 140, p. 37 (1974).

8. C. Tsonopoulos and J.M. Prausnitz, "Equations of state," *Cryogenics*, Oct., p. 315 (1969).

9. S.B. Adler, C.F. Spencer, H. Ozkardesh, and C.M. Kuo, "Industrial use of equations of state: a state-of-the-art review," in: *Phase Equilibria and Fluid Properties in the Chemical Industry*, T.S. Storvick and S.I. Sandler, eds., A.C.S. Symp. Series, no. 60, A.C.S., Washington, p. 150 (1977).

10. D.Y. Peng and D.B . Robinson, "A new two-component equation of state," *Ind. Eng. Chem. Fundamen.*, vol. 15, p. 59 (1976).

11. H. Knapp, R. Doring, L. Oellrich, U. Plocker, and J.M. Prausnitz, *Vapor-Liquid Equilibria for Mixtures of Low Boiling Substances*, DECHEMA Chemistry Data Series, vol. VI, Frankfurt/Main (1982).

12. S.I. Sandler, *Chemical and Engineering Thermodynamics*, 2 ed. Wiley, New York, 1989, p. 582.

13. B. Maytal and S.W. Van Sciver, "Characterization of coolants for Joule-Thompson cryocoolers," Paper presented at 6th Int. Cryocooler Conference, Plymouth, MA (1990).

14. M.J. Hiza, A.J. Kidnay, and R.C. Miller. *Equilibrium Properties of Fluid Mixtures*, IFI/Plenum, New York (1975).

15. R.T. Ellington, B.E. Eakin, J.D. Parent, D.L. Gami, and O.T. Bloomer, "Vapor-liquid equilibria in the binary systems of methane, ethane and nitrogen," *Thermodynamic and Transport Properties of Gases, Liquids, and Solids*, A.S.M.E., New York (1959) p. 180.

16. P. Yu, I.M. Elshayal, and B.C.Y. Lu, "Liquid-liquid-vapor equilibium in the nitrogen-methane-ethane system," *Can. J. Chem. Eng.*, vol. 47, p. 495 (1969).

17. D.L. Schindler, G.W. Swift, and F. Kurata, "Phase equilibrium studies of the nitrogen-propane, helium-propane, and helium-nitrogen-propane systems," *Proc. Ann. Conv. Nat. Gas Processors Assn.* Tech. Paper vol. no. 45, p. 40 (1966).

18. D.P.L. Poon and B.C.Y. Lu, "Phase equilibrium for systems containing nitrogen, methane, and propane," *Adv. Cryogenic Engineering*, vol. 19, p. 292 (1973).

A LONG LIFE OIL LUBRICATED J-T CRYOCOOLER FOR SPACE APPLICATIONS

James Lester, Robert Levenduski, and Roger Scarlotti
Ball Aerospace
Electro-Optics/Cryogenics Division
Boulder, Colorado 80302

ABSTRACT

Development of J-T cryocooler technology incorporating an oil lubricated compressor is nearing completion. Performance testing of the compressor, cold head, and gas purification train has been completed. Endurance testing is underway in all critical areas. The next-generation cryocooler has been designed and is currently being built.

This paper presents the results to date of on-going development efforts. Test data are presented and compared to performance predictions. Features of the next-generation design are provided.

INTRODUCTION

Cryocoolers based on the Joule-Thomson (J-T) cycle are currently under development for future space applications. The cycle was chosen because of the inherent feature of providing a benign environment at the load interface. The lack of moving parts in this area eliminates vibration, minimizes electromagnetic interference, and promotes high reliability. The closed-loop circulating fluid of this cycle allows active contamination control. As a consequence, the more conventional approach of oil lubrication can be used to achieve compressor reliability.

The current project is broken into two phases; breadboard and prototype. The objective of the breadboard phase has been to verify performance characteristics and identify any remaining reliability issues. Performance testing has been completed and critical subsystems have begun reliability testing. The prototype is the next-generation design. The design effort is complete and fabrication has begun.

SYSTEM OVERVIEW

SYSTEM DESCRIPTION

The Ball J-T cryocooler is a long-life closed-cycle cryocooler that uses the Joule-Thomson effect to produce up to 4 watts of constant temperature cooling at temperatures in the range of 64 to 70 K.

The cryocooler consists of four subsystems; the compressor, cold head, gas purification train, and control electronics. The subsystems are illustrated in Fig. 1 and are shown schematically in Fig. 2.

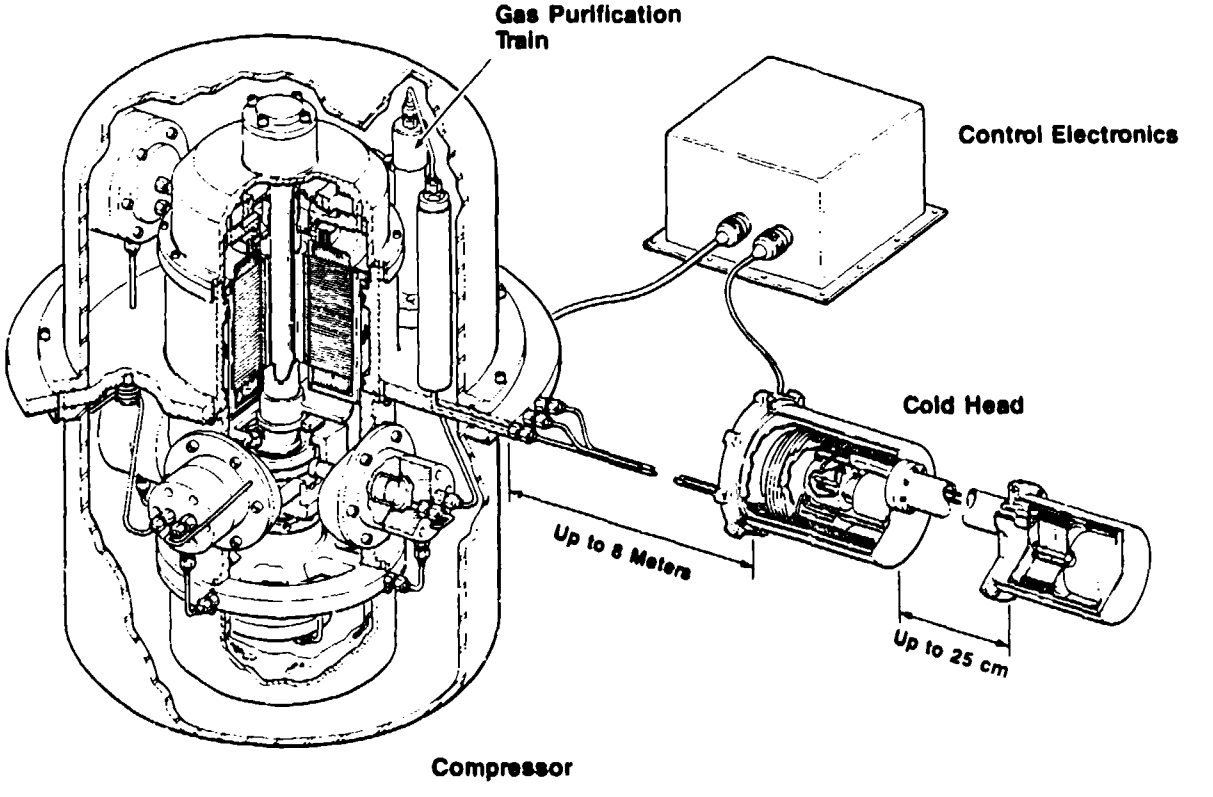

Fig. 1. Ball J-T cryocooler.

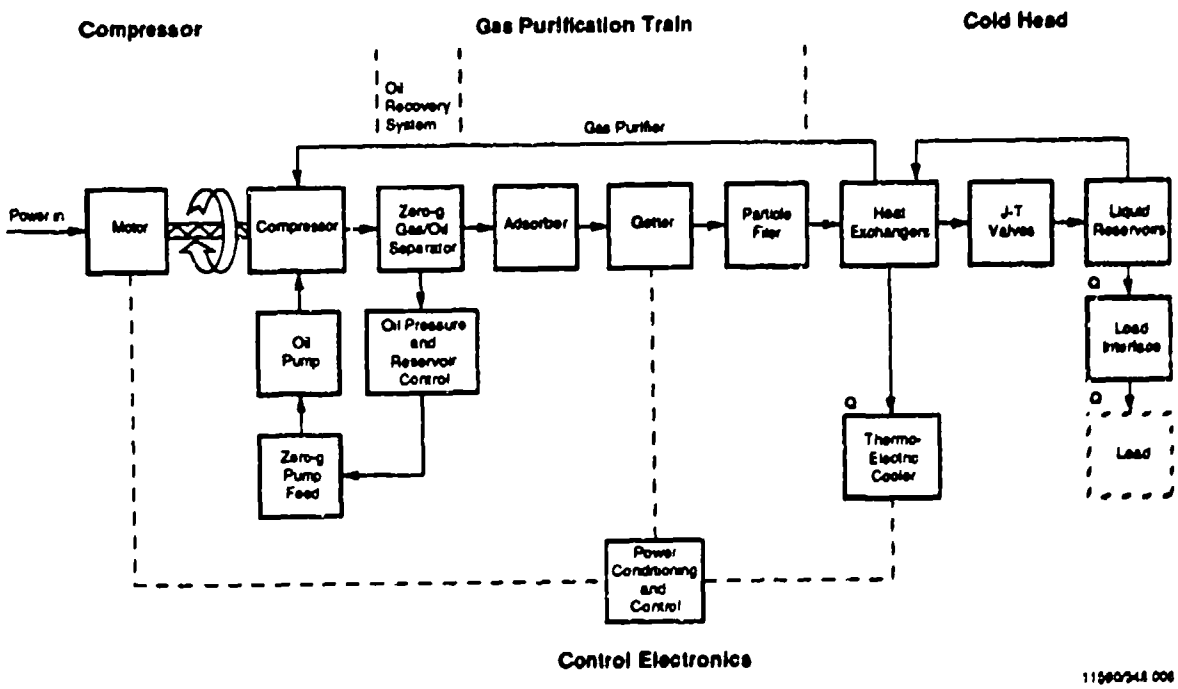

Fig. 2. Components of the Ball J-T cryocooler.

SYSTEM OPERATION

A four-stage oil lubricated radial compressor produces high pressure gas (69 bar, 1000 psia) and flows the gas into the gas purification train. The first component of the gas purification train, the oil recovery system, removes 99.998 percent of the oil from the gas stream and returns it to the compressor by way of a p ssure reducer. The remaining oil and gaseous contaminants enter the second component of the gas purification train, the gas purifier. Within the gas purifier, the remaining oil and gaseous contaminants are removed by the adsorber and reactive getter, and particulates are captured by the particle filter.

Clean gas enters the cold head and is initially precooled in a hybrid heat exchanger that couples the recuperative cooling from the returning gas with cooling from a thermo-electric cooler. After exiting the hybrid heat exchanger, the flow splits into two streams.

Ninety percent of the flow is directed into a precooling loop and expands through a J-T valve to produce cooling at 100 K. This loop precools the remaining flow and can be designed to provide cooling for a secondary heat load. The remaining 10 percent of the

flow passes through a second recuperative heat exchanger and J-T valve and produces useful cooling for the primary load.

The system provides constant temperature cooling and variable cooling capacity. Constant temperature cooling is accomplished by adjusting the compressor speed when the heat load changes to maintain the desired pressure on the liquid bath, thereby controlling the liquid's temperature. The change in cooling capacity is a consequence of the change in heat load in the closed system. If the heat load increases, liquid evaporates and the system responds by increasing the compressor speed and mass flowrate. The higher mass flowrate exiting the compressor increases the supply pressure to the J-T valves, which in turn increases the mass flowrate through them. The higher pressure and mass flowrates provide greater cooling capacity. The cycle continues until the cooling capacity again equals the heat load. The cycle reverses itself when the heat load decreases, i.e., liquid accumulates while the supply pressure decays until the system again reaches equilibrium.

SUBSYSTEM DESCRIPTIONS

COLD HEAD

The cold head (Fig. 3) receives high pressure nitrogen gas and produces useful cooling by the J-T process. Two stages of J-T cooling are used to increase overall power efficiency and to provide cooling at both 64 to 70 K and 100 to 110 K. Thermoelectric coolers (TEC) are attached to the counter flow heat exchanger to remove heat at 250 and 220 K and also for the purpose of increasing cycle efficiency. This hybrid arrangement therefore, is a four-stage cooler requiring only one compressor. The cold head is currently configured in two sections; the larger section is a precooler and contains the hybrid heat exchanger, TECs, and the 100 to 110 K cooling station. The smaller section contains a final counter flow heat exchanger and the 64 to 70 K cooling station. The cold head was configured in two sections to demonstrate the separation of these cooling stations and the adaptability of the geometry to different cooling applications. Multi-layer insulation inside the vacuum housing minimizes parasitic heat leak.

The 69 bar (1000 psia) supply gas is precooled in the hybrid heat exchanger and then splits into two streams for the two cooling stages. The 100 to 110 K stage precools the 64 to 70 K stage. This arrangement allows the flow in the colder stage to be a small fraction of the total flow in order to obtain the required low temperature cooling. An advantage of low flow in the cold stage is that the low pressure cylinder of the compressor can be made

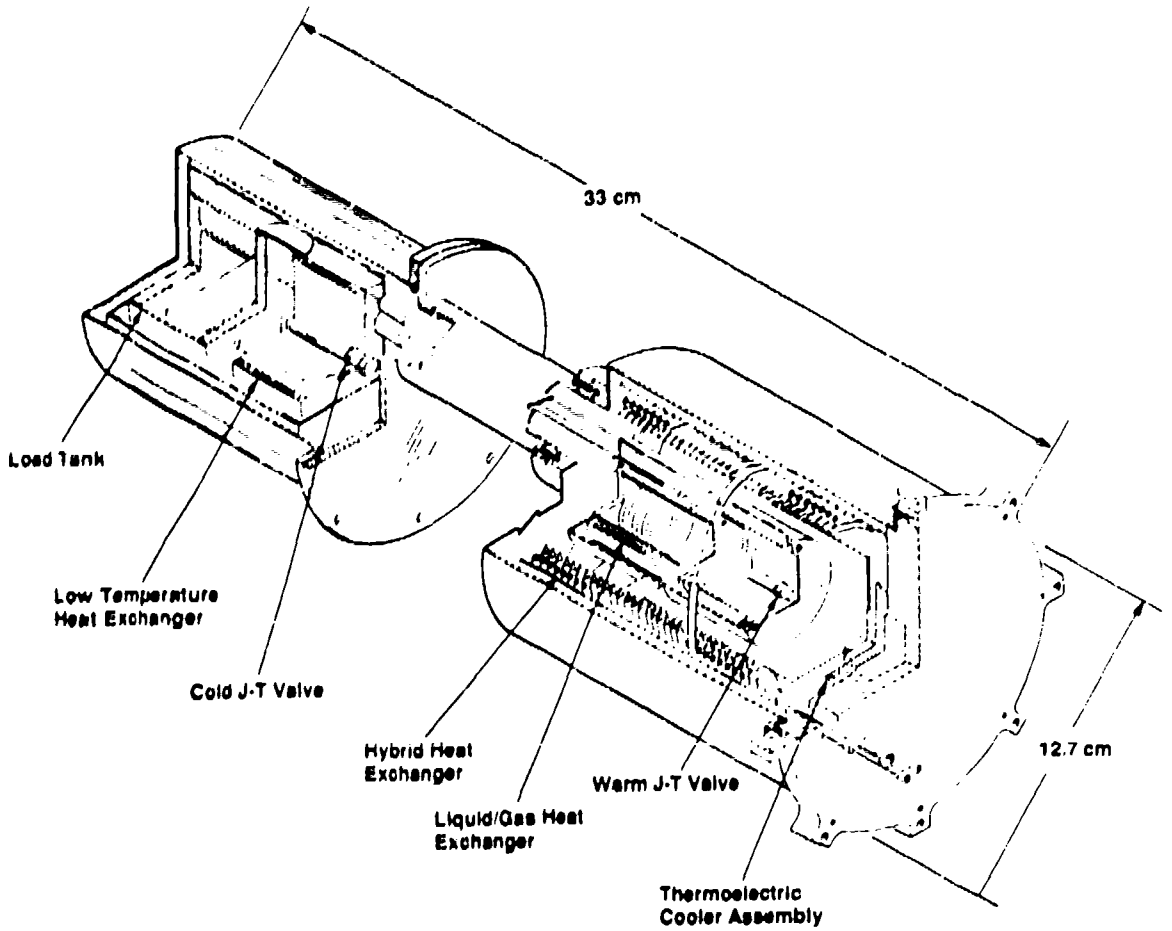

Fig. 3. Prototype cold head.

reasonably small. Another advantage is that the pressure drop through the low flow heat exchangers is minimal since recuperating all of the available precooling is not critical. The heat exchangers consist of simple tubing coils attached to each other by soldering.

Much attention has been paid concerning blockage due to contamination freezing. To minimize contaminants in the working gas that might freeze in the J-T valves, all components are clean metals that are thoroughly vacuum baked. The J-T valves are configured as capillaries that have much larger cross-sectional areas than the small orifices they replace, and are therefore much less likely to become plugged by frozen contaminants or solid particles. Defrost heaters on the J-T valves can be used in the unlikely event of a freeze-up. Testing has shown these measures to be effective in eliminating contamination problems.

Since the cooler is intended for space application, zero-gravity liquid retention is required. This function is accomplished by a copper foam insert in the liquid retention tanks at both cooling stations.

COMPRESSOR

The compressor is a four-stage oil lubricated radial compressor that incorporates a scotch yoke drive. The compressor is illustrated in Fig. 4. The radial arrangement was chosen because of its compact size and low vibration. Oil lubrication was selected because of its proven ability to attain long life in positive displacement machines. The scotch yoke incorporates cam bearings in order to eliminate sliding between the cam and the pistons and is effective in uniformly distributing the loads between the pistons and cylinders.

The oil lubrication system provides pressurized oil to the pistons and cylinders, scotch yoke assembly, and bearings. The pressurized oil is used to lubricate the moving parts and to provide the piston sealing during compression. The system is designed to operate in any orientation in 1-g and in 0-g. Screened cavities are located within the compressor so that in any orientation in 1-g, enough oil is available to continuously feed the pump. Any screen area that is not directly covered by the oil is sealed against gas breakthrough by surface tension principles. In 0-g, the rotating parts force the oil to the case walls thereby ensuring that oil is constantly available to the screens.

The motor, synchro, and tachometer are custom designed to reduce vibration. The motor and drive electronics are designed to produce very little cogging and ripple torque and the tachometer is designed to provide a virtually noise-free signal to the control electronics. To eliminate contamination, the motor, synchro, and tachometer windings are sealed from the working gas.

The compressor operating speed range is from 2 to 8 Hz (120 to 480 rpm). The low operating speed minimizes the number of cycles on the moving parts and any vibration associated with dynamic imbalance.

The compressor produces high pressure gas at 69 bar (1,000 psia) and accepts return gas at approximately 7.5 bar (110 psia) and at a low pressure ranging from 0.145 to 0.384 bar (2.1 to 5.6 psia). The pressure of the low pressure stream is increased in the first two stages to approximately 7.5 bar where it joins the other stream and is pressurized in the last two stages to 69 bar. This two-stream, four-stage approach is required for the dual pressure operation of the cold head.

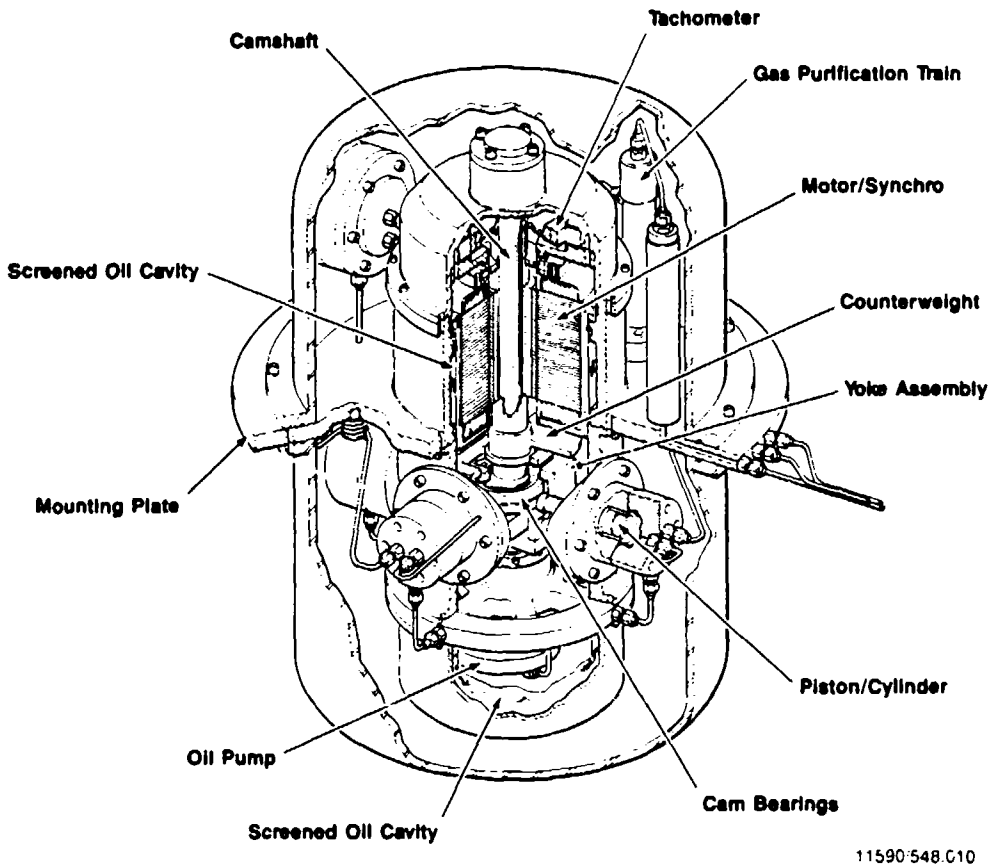

Fig. 4. Prototype compressor.

GAS PURIFICATION TRAIN

A built-in gas purification train continuously cleans the working gas. Fig. 5 shows the basic components of this system and the levels of purity obtained by each component. The high pressure gas leaving the compressor contains minute quantities of oil vapor, a much larger amount of liquid oil, and trace gases from the initial charge of working gas. Trace gases also evolve from the materials of construction and from the oil. The first task of the gas purification train is to remove and recirculate most of the liquid oil. This must be done both in zero gravity and on Earth. These functions are accomplished using passive surface tension principles that have been demonstrated to work in all gravity orientations, thus proving zero-g operation. Next, the small residual amount of liquid oil is removed by a series of coalescing filters. At the exit of these coalescers, the quantity of liquid oil is negligible or far less than would be needed to plug a J-T valve. An adsorber containing

- **Required purity for no freeze ups in 5 years = $1.2(10^{-13})$ g/s**

Contaminant Flow (g/s)

	LIQUID OIL	OIL VAPOR	WATER, CO_2, AND OTHER
Compressor	0.04 *	7.2×10^{-15}	4.4×10^{-10}
Oil Recovery Device	1.4×10^{-6} *	7.2×10^{-15}	4.4×10^{-10}
Coalescer	$<1 \times 10^{-16}$	7.2×10^{-15}	4.4×10^{-10}
Adsorber	$<1 \times 10^{-16}$	$<1 \times 10^{-16}$	4.4×10^{-10}
Hot Getter	$<1 \times 10^{-16}$	$<1 \times 10^{-16}$	2.8×10^{-16} *
To Cold Head			

* Measured values

11590/548.002

Fig. 5. Gas purification train performance.

activated charcoal and molecular sieve materials performs a coarse removal of trace gases. The activated charcoal removes residual hydrocarbons and other heavy gases while the molecular sieve primarily removes water. Finally, a hot reactive getter thoroughly cleans the gas prior to its passing to the cold head. Purity levels have been shown to be in the sub parts per trillion level.

Implementation of these purification devices eliminates concern about the use of an oil lubricated compressor in a closed cycle Joule-Thomson cryocooler. Long-term testing is currently under way.

CONTROL ELECTRONICS

The control electronics contains the power conditioning electronics, the motor driver, the vibration control electronics, and the temperature control electronics.

The power conditioning electronics performs typical conditioning of the raw power and provid_s the required power to the various boards and chips.

The motor driver contains the logic to commutate the 3-phase brushless dc motor, provides current limiting for hardware safety, and provides the shaft position and motor current for testing purposes.

The vibration control electronics controls the speed of the compressor within each revolution to minimize the torsional vibration. Changes in compressor speed impart a torque to the compressor mounting structure that is identified as torsional vibration. Minimizing the speed changes of the compressor minimizes the torsional vibration transmitted to the mounting structure. A control servo analysis was done and a design has been completed. The results of the analysis are shown in Fig. 6. The graph shows that no component of the vibration exceeds 0.035 N-m (0.3 in-lb).

The temperature control electronics controls the load interface temperature to within 0.25 K of a selected temperature with a varying heat load by adjusting the compressor speed. A temperature sensor on the load interface detects a temperature change that is associated with a load change. When the temperature departs from the selected set point, the control electronics changes the compressor speed appropriately to adjust the pressure on the liquid bath thereby changing the liquid temperature. The new liquid temperature provides a heat sink temperature that allows the load interface to return to the set point. When the set point is reached, the system is in equilibrium at the new load.

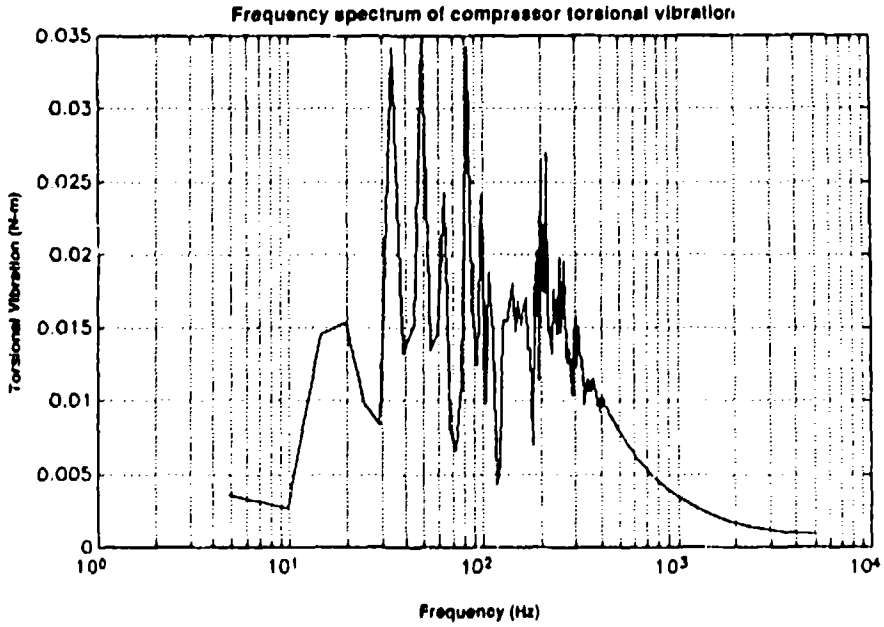

Fig. 6. Control servo analysis results.

BREADBOARD TEST RESULTS

BREADBOARD COLD HEAD TESTING

The breadboard cold head was tested for the purposes of demonstrating the thermodynamic performance of the closed-loop dual pressure cycle, obtaining data to correlate the system model, and demonstrating closed loop, constant temperature cooling with varying heat load. All of the objectives were achieved. A schematic of the cold head is shown in Fig. 7.

The thermodynamic performance of the dual pressure cycle was demonstrated by the correlation between the test data and expected values of pressures, mass flowrates, temperatures, cooling capacity and heat exchanger effectiveness.

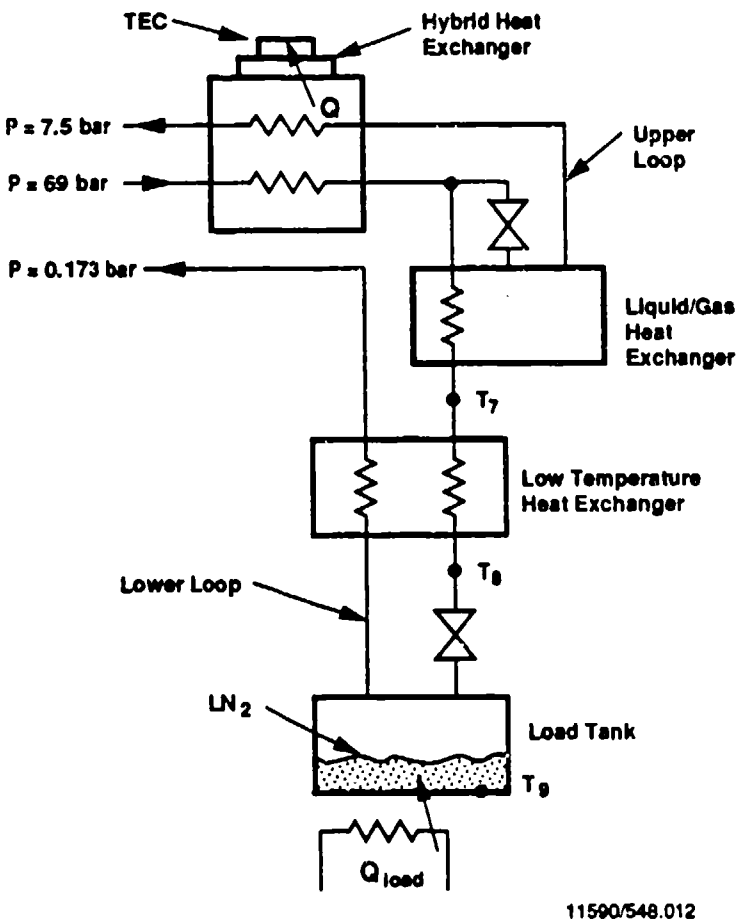

Fig. 7. Breadboard cold head schematic.

The system model was highly effective in predicting the steady state and transient operation of the cold head. The breadboard system model is the same model that was used to design the prototype cooler with changes made to reflect the actual breadboard hardware. A comparison between the test data and model predictions for the cooldown process is shown in Fig. 8. The total mass of the cold head was approximately 1.5 kg and was distributed as 0.6 kg at the hybrid heat exchanger, 0.4 kg at the liquid/gas heat exchanger, and 0.5 kg at the load tank. The exaggerated temperature fluctuations of Temp 8 in the modeling results occur because the entire thermal mass of the lower loop is incorporated at the load tank.

Constant temperature cooling with varying load was demonstrated by applying a step change in the heat load and manually adjusting the compressor speed as required to maintain the desired temperature. The manual control of the compressor speed emulates the function of the temperature control electronics that is incorporated in the prototype cooler. Test results are shown in Fig. 9.

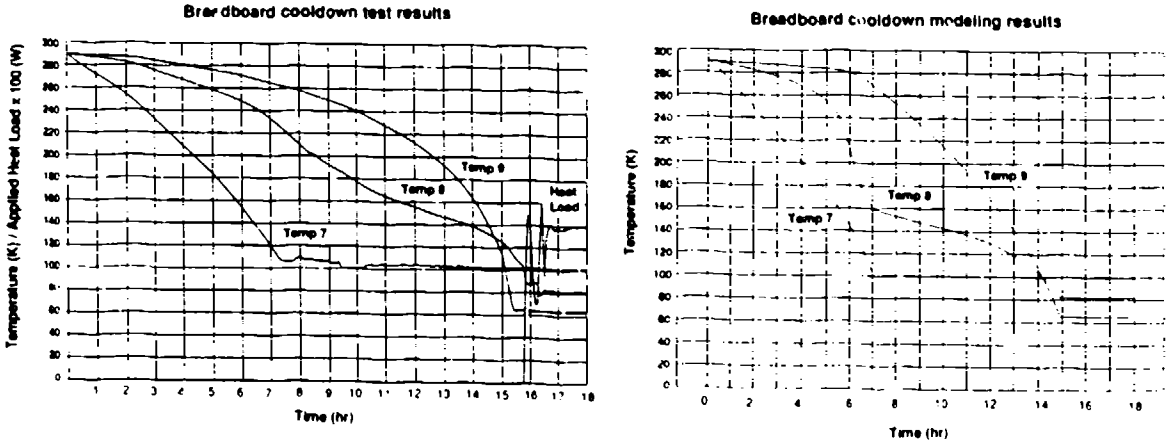

Fig. 8. Breadboard cold head test data versus model predictions.

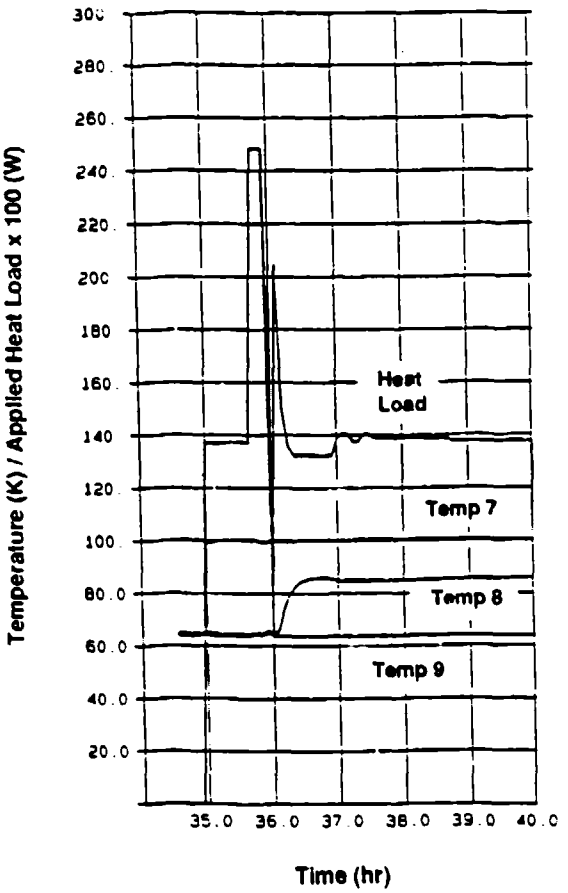

Fig. 9. Breadboard peak load test results.

BREADBOARD COMPRESSOR TESTING

A four-stage radial compressor employing all of the features previously discussed was fabricated for test. The objectives of the test series were to verify the flow and pressure design analysis, evaluate the lubrication system, and evaluate wear, lifetime, and reliability characteristics. The compressor was operated for over 600 hours prior to a planned disassembly. The operation included runs at various speeds and pressures with numerous sensors recorded on an automatic data acquisition system. The mass flowrate of the first stage piston was greater than expected, see Fig. 10. This was primarily due to more efficient operation of the first stage inlet port than was originally estimated. The mechanical efficiency of the compressor was measured to be 70 percent.

	DESIGN	MEASURED
Low pressure gas flow (g/s)	0.0088	0.0131 ± 0.0005
Intermediate pressure gas flow (g/s)	0.1075	0.116 ± 0.001
Inlet stage 1 (psia)	2.2	2.2 ± 0.04
Outlet stage 1 (psia)	15.1	16.5 ± 0.37
Outlet stage 2 (psia)	111.5	111.0 ± 1.6
Outlet stage 3 (psia)	331.9	356.0 ± 1.5
Outlet stage 4 (psia)	1000.0	1000 ± 6.0
Oil carryover (cc/s)	0.01	0.0055

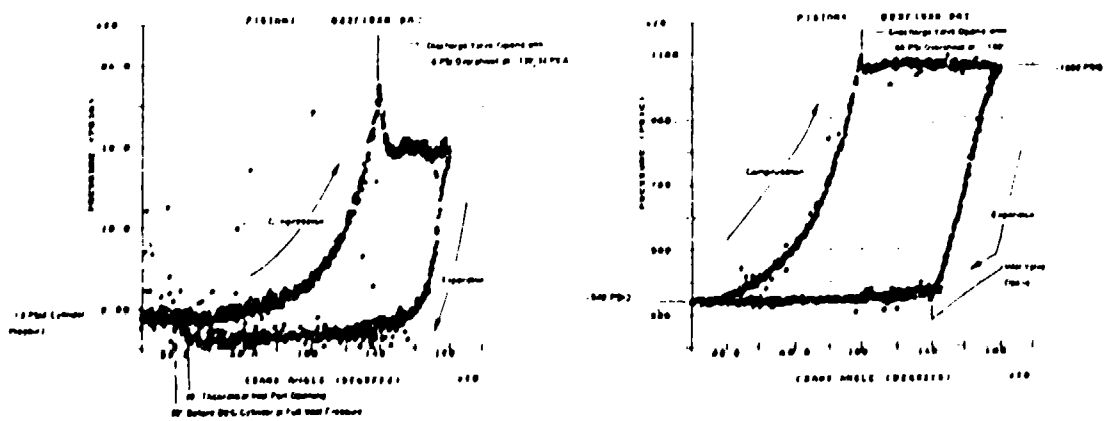

Fig. 10 Breadboard compressor performance at 3 Hz.

When the compressor was disassembled, all critical parts were measured and inspected for wear. Little wear was found on the piston/cam interface and no detectable wear was found on the piston/cylinder interface, see Fig. 11. The oil was analyzed for particulates and chemical changes. The results indicate that this design, with the change to the all rolling scotch yoke drive, should be capable of exceeding the 5-year lifetime requirement.

GAS PURIFIER TESTING

A gas purification train was fabricated for long-term testing. The objective of this testing is to show that the oily gas supplied by the compressor can be adequately purified to pass through the J-T cold head without causing freeze-up problems for many years. Since such a test requires dedicated hardware, namely a compressor and a cold head, we configured the test, as shown in Fig. 12. We use a commercial metal diaphragm compressor, which is readily available and achieves compression without oil. This is done to avoid tieing up our development oil lubricated compressor. We installed an oil injection system downstream of the diaphragm compressor to simulate the conditions produced by our

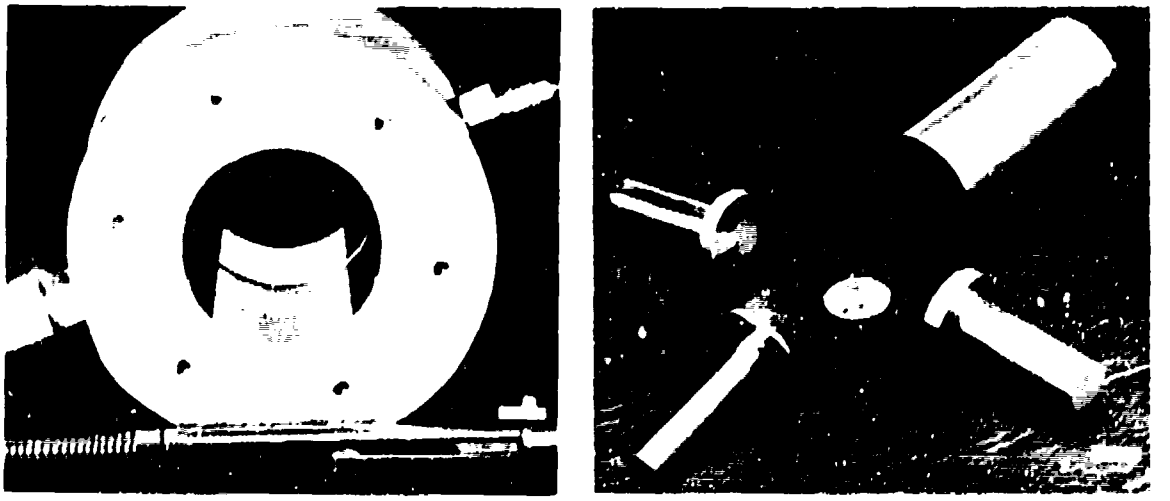

Fig. 11. Compressor hardware after 620 hours of operation.

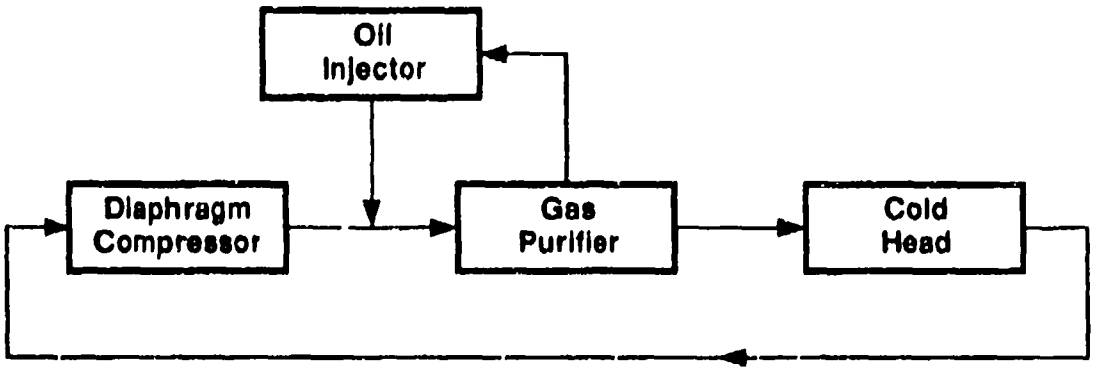

Fig. 12. Gas purification system test.

development compressor. The gas purification train is designed to handle the gas and oil flow rates at the pressures expected in the cryocooler. The purified gas passes through a cold head containing counterflow heat exchangers and two small orifice type J-T valves. These valves are considerably more sensitive to plugging by contamination than the ones used in the cryocooler by virtue of their smaller size and configuration.

The first series of tests consisted of reverifying the performance of the oil scavenger section. This device was developed on an earlier program. Next, closed-loop, long-term operation was started. To date several hundred hours of operation have been logged without difficulty.

CONCLUSION

Testing of the breadboard hardware has demonstrated the J-T cryocooler's thermodynamic capability. An analytical model has been developed and correlates well with the test data. The next-generation design is complete and is expected to meet all of its program requirements.

DEVELOPMENT OF A FAST COOLDOWN J-T COOLING SYSTEM

G. Pähler, H. Maier, R. Maier and M. Bareiss
AEG Aktiengesellschaft
Infrared and Night Vision Devices
D-7100 Heilbronn
Federal Republic of Germany

ABSTRACT

A fast cooldown, highly shockresistant cooling system for IR-detectors has been developed. The system consists of a detector housing with integrated J-T cooler and a single-element or multi-element $Hg_{1-x}Cd_xTe$ detector.

Prototypes with a gas supply volume of 20 cm^3/800 bar Argon could be operated for more than 15 s with typical cooldown times of less than 0.4 s. The units have been shock tested up to 40,000 g without damage or degradation.

The paper will focus on heat exchanger and housing design criteria as well as operation with various gases or gas mixtures. Ongoing and future activities will be discussed.

INTRODUCTION

In several present and future applications IR detector systems are requested to reach their operating temperature of below 100 K in less than a few seconds after system initiation. In addition to the fast cooldown requirement some applications demand the withstanding of extremely high g loads up to 40.000 g. One way to realize such an IR detector system is the combination of a fast Joule Thomson cooling system with a detector housing of very low thermal mass and high mechanical stability.

The subject paper describes the development of a fast cooldown highly shock-resistant IR detector/cooler system.

SYSTEM DESIGN

Specified requirements of the IR detector/cooler system where as follows:

1) Cooldown time shorter than 1 second
2) Operation time greater 10 seconds with 20 cm^3 gas storage volume
3) Operating temperature below 100 K
4) High shock resistance up to 40,000 g

As shown in Fig. 1 the latest prototype of the detector/cooler system mainly consists of 4 subassemblies. The bottom part is the gas bottle (1) wich supplies the Joule Thomson cooler with pressurized gas. As indicated by the drawing, the J/T heat exchanger is designed as a plane spiral (3) with the exhaust nozzle being in the center of it. The detector is attached onto a small metallic plate (4) mounted close to the exhaust nozzle to form the cold tip of the cooling system in the center of the medium part (5). The assembly is completed by the IR transparent window (6), which hermetically seals the detector against the environment. A photograph of a prototype is shown in Fig. 2.

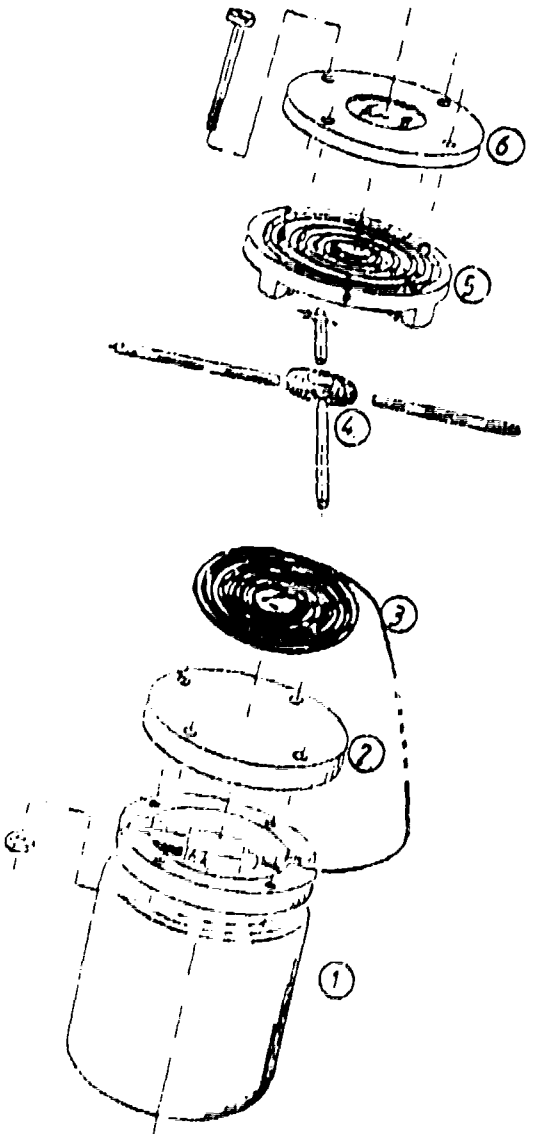

Fig. 1. Exploded view of the fast cool down detector cooler system.

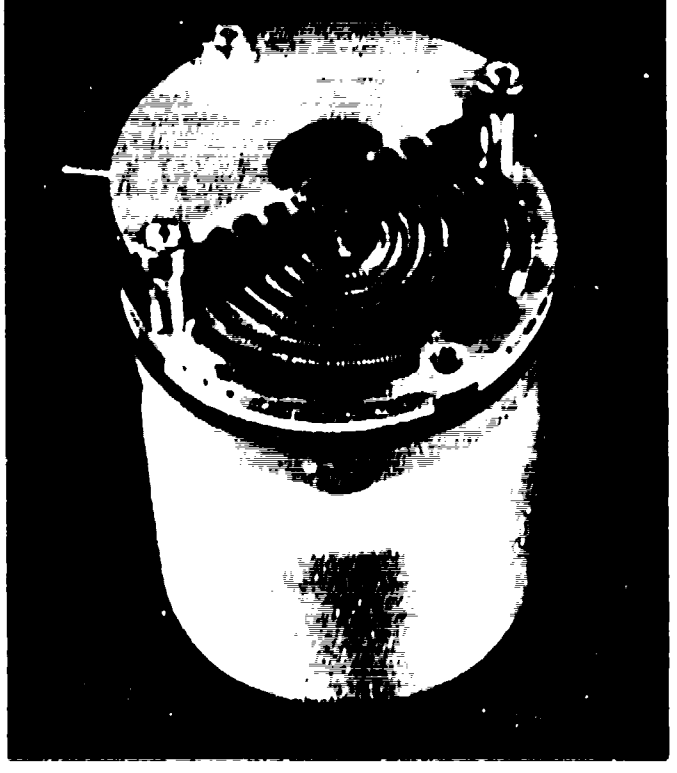

Fig. 2 Photograph of detector/cooler system

HEAT EXCHANGER DESIGN

Counterflow finned tube type heat exchangers out of various materials were fabricated and tested:

1) Steel tube with copper fins

2) Copper tube with copper fins

3) Copper tube with silver fins

Type (3) can be considered as the design with the best results with respect to the cooldown time. Various different spacings of the fins have been tested to find an optimum compromise between cooldown time and boiling temperature of the liquified gas.

TEST STATION

For aiding the development program a test station according to Fig. 3 was designed and built. This test station allows operation and test of J/T coolers with supply pressures up to 1350 bar and supply gases of Nitrogen, Argon, Synth. Air, CH_4 and defined mixtures or sequences thereof.

High Pressure Test Equipment for Joule Thomson Cooler Systems
Schematic Diagram

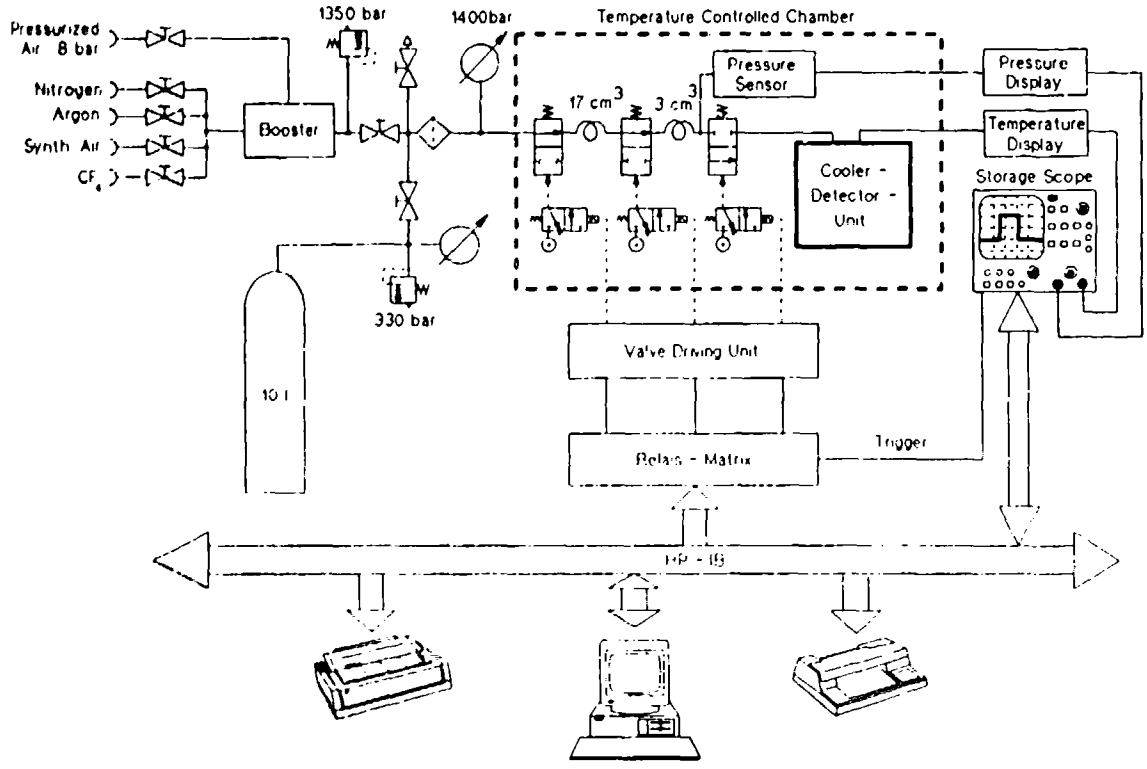

Fig. 3 Schematic diagram of the high pressure test station

Additionally, the test station is capable of simulating supply volumes in the range of 3 cm^3 to 100 cm^3 and temperature environments within 20°C to 100°C. On line recording of cold tip temperature and supply pressure is provided fo each test run.

EXPERIMENTAL RESULTS

For the sake of brevity, only the most interesting results, achieved with 20 cm^3/800 bar Argon and 3 cm^3 CF_4 followed by nitrogen 280 bar dual gas operation will be presented.

Fig. 4 shows the results of a test run at ambient temp. with mentioned 20 cm^3/800 bar Argon. This data plot indicates, that a temperature of 100 K is reached within a cooldown time of less than 0.2 s. In this case the heat exchanger was optimized with respect to cooldown time, regarding the boiling temperature of the liquid.

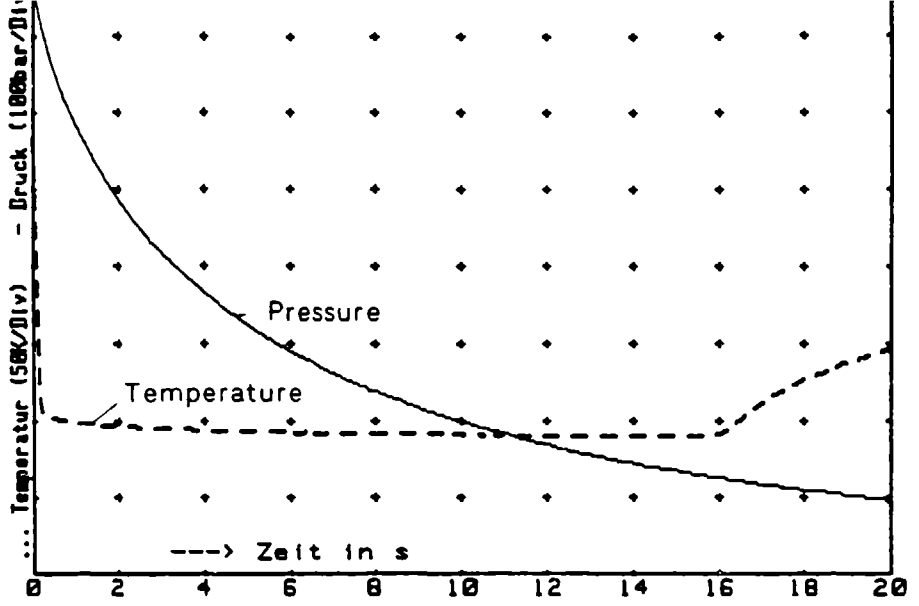

Fig. 4 a

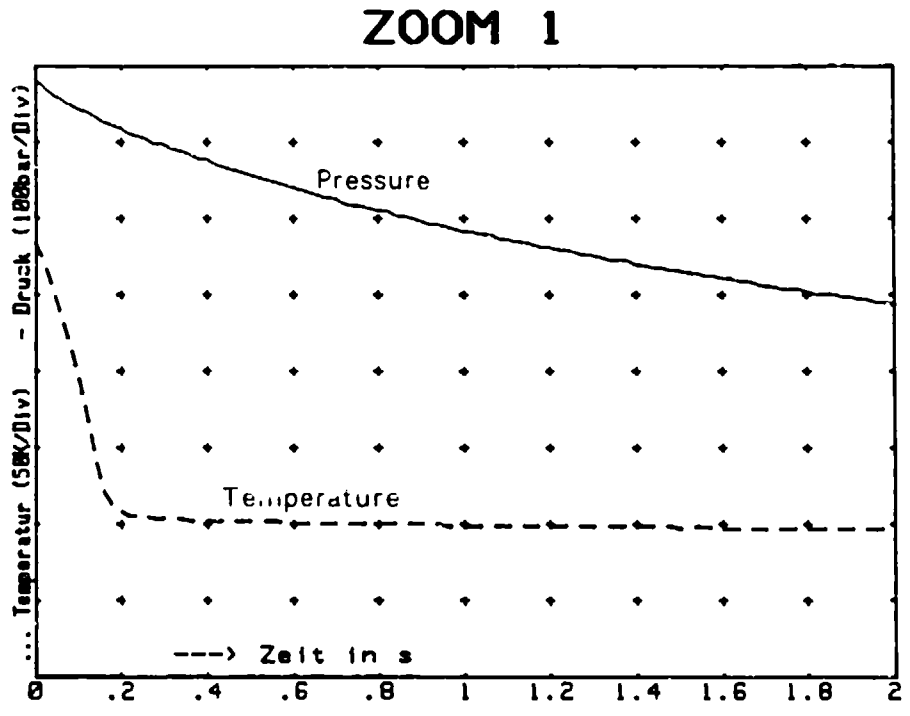

Fig. 4 b Cooldown phase only

Fig. 4 Temperature and gas supply pressure versus time with gas supply 20 cm^3 Argon 800 bar

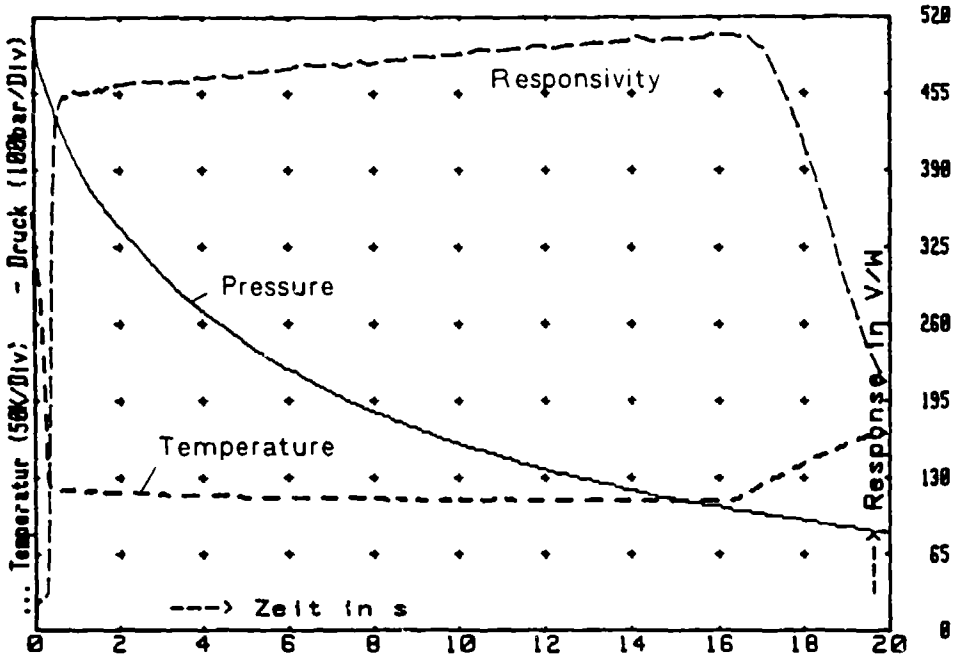

Fig. 5 a

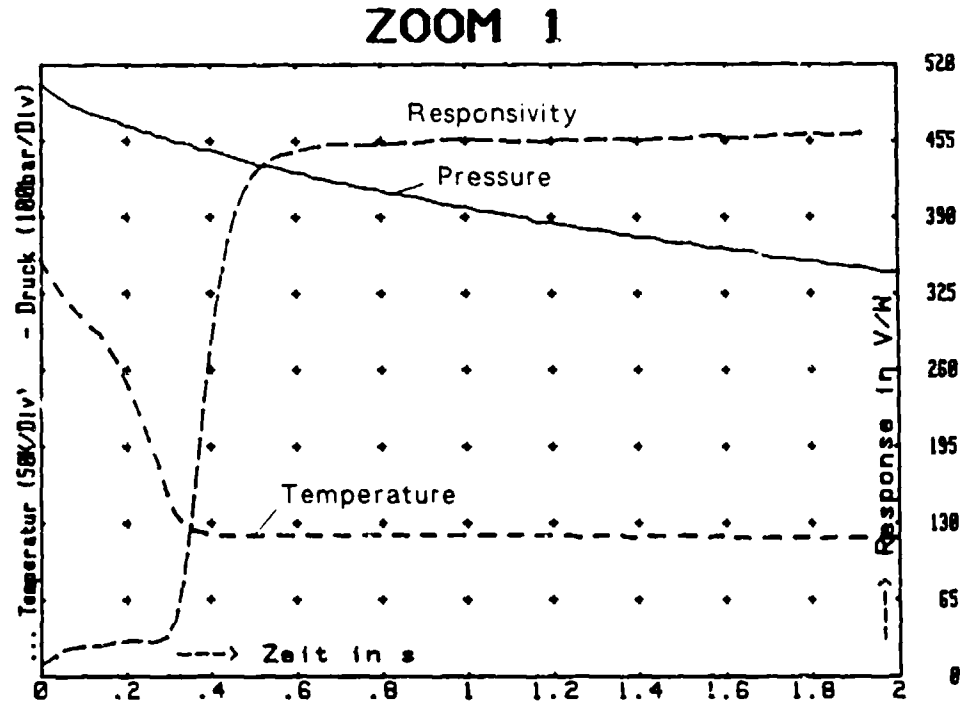

Fig. 5 b Cooldown phase only

Fig. 5 Responsivity, temperature and gas supply pressure versus time.

Fig. 5 shows the test results of a prototype equipped with a IR-detector sensitive in the 8-12 µm wavelength band. The slightly longer cooldown time of this prototype is the result of the earlier mentioned compromise between cooldown time and cold tip temperature.

For applications with photovoltaic CMT detectors, where cooling temperature of less than 90 K are required, dual gas operation can help. In this case, the fast cooldown feature can be combined with the potential of lower operating temperature.

Fig. 6 shows for example the results of such a dual gas test run. Here 3 cm^3 CF_4 were followed by an unlimited volume nitrogen at 280 bar. As indicated by the temperature plot, operating temperatures of less than 80 K were achieved within cooldown times of less than one secound.

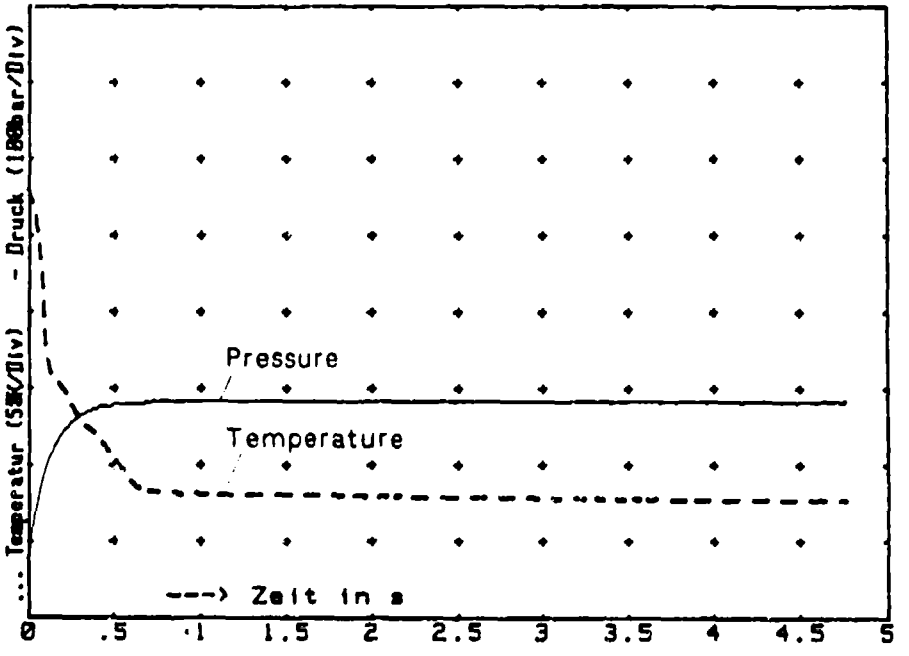

Fig. 6 Example for a two gas system using 3 cm^3 CF_4 followed by nitrogen 280 bar.

CONCLUSION

Prototypes of a fast cooldown J/T cooler system for IR detector application have been developed, fabricated and successfully tested with 20 cm^3/ 800 bar Argon gas supply. Typical cooldown times of less than 0.4 s and operation times of more than 15 s could be demonstrated.

For applications, requiring lower cooling temperatures, the system can easily be adapted by suitable dual gas operation. Within the scope of the subject development program the basis technologies could be established. Ongoing and future effort will focus on specific appications.

The development program was supported by the German Ministery of Defence.

DEVELOPMENT OF A FAST COOLDOWN, JOULE-THOMSON MICROMINIATURE REFRIGERATOR AND VACUUM PACKAGE, FOR OPERATION OF INFRARED, FOCAL PLANE ARRAYS AT 70K.

W. A. Little and R. L. Paugh
MMR Technologies, Inc
1400 North Shoreline Blvd, #A5
Mountain View, California, 94043

ABSTRACT

A need exists for coolers for large focal plane arrays for use in thermal imaging. We report on the development of a rugged, extremely compact, microminiature, two stage, laminated glass, Joule Thomson refrigerator for such a purpose, using a nitrogen-hydrocarbon gas mixture in the first stage and pure nitrogen in the second. The exhaust of the first stage drives a miniature venturi pump which reduces the pressure at the boiler of the second to allow operation at 70K. Cooldown from ambient to 70K in under fourteen seconds has been achieved. The vacuum package is designed to provide a ten year shelf life. Details of the cryogenics, the performance of the refrigerator, and the design of the vacuum package will be presented.

INTRODUCTION

Joule-Thomson (JT) refrigerators have been available for many years for the cooling of infrared seekers. Some of these are capable of cooling to operational temperatures near 90K in a few seconds. However, with the development of larger infrared imaging arrays a need has arisen for the rapid cooldown of these larger devices and the provision of an operating temperature for them below 80K. In an effort to address this issue we have developed a fast cooldown JT refrigerator and vacuum package suitable for cooling such arrays that incorporates a number of novel features and new capabilities not found in earlier cryostats. The system to be described is based on the use of a specially developed, planar, microminiature refrigerator for cooling the focal plane array which is housed in a small, extremely rugged vacuum package. The two developments have required the creation of new technology and the adaptation of old technology from other fields for use in this. We report here briefly on several of these developments to give a glimpse of the new capabilities and potential of these cryogenic devices.

DESIGN PHILOSOPHY

During the past decade we have developed, so called, *microminiature* JT refrigerators which are fabricated by a photolithographic process from thin glass laminates[1]. These can be made in a wide variety of sizes and capacities and, unlike conventional finned tube refrigerators, have a planar, low profile configuration. To make maximum use of this configuration we have developed a package for the cooler which is commensurate with this profile. In the design of the refrigerator, itself, we have aimed at achieving a moderately rapid cooldown to operating temperatures of ten seconds, while keeping the gas consumption during this cooldown to an acceptable value. We have aimed at maintaining an operating temperature of 70K or below, and a refrigeration capacity which is not significantly impaired under conditions of high ambient temperature. For the package, our goal is a shelf life of ten to twenty year. This we expect to achieve by the use of well established, ceramic-to-metal vacuum system fabrication processes and the exclusion of all organic materials from the vacuum enclosure. These constraints have created a number of materials problems and the need for developing some new technology. Not all of these have been solved at this time but good progress has been made in a number of areas. We describe below the various considerations which have gone into the development of the two major components of the system, the refrigerator and the vacuum package and the results which have been obtained with them.

CRYOGENIC DESIGN

The cryogenic design is based on a number of considerations which involve the choice of the working gas. Some twenty years ago, Alfeev et al.[2] gave the composition of certain nitrogen-hydrocarbon gas mixtures which when used as refrigerants in JT refrigerators gave refrigeration capacities at temperatures close to 80K which were as much as 10- to 12-fold greater than those of nitrogen alone. In previous studies we had confirmed the essence of their claims and have shown, further, how these mixtures can be rendered non- flammable without impairing their refrigeration abilities at these temperatures, by the addition of the fire retardant, Halon to the mixture [3]. However, as pointed out earlier [4], these mixtures are not without their disadvantages and, in particular, they exhibit a marked drop off in refrigeration capacity at temperatures below 100K, where only the nitrogen component of the mixture contributes to the heat absorption. On the other hand, the refrigeration capacity attainable at the higher temperatures is large and is only weakly dependent upon the ambient temperature for tempertures near 300K. The reason for this is, that the inversion temperature of these mixtures is much higher than that of nitrogen.

CHOICE OF GASES

In order to obtain the best of both worlds we have designed the refrigerator to use one of the Alfeev, nitrogen-hydrocarbon gas mixtures in the first of two stages of the refrig-

erator, to provide the large refrigeration capacity necessary to obtain a rapid cooldown of the bulk of the refrigerator to a temperature of 130 - 140 K, to provide a thermal sink and guard at this temperature, and to precool the second stage, which uses pure nitrogen. The gas mixture is chosen to attain a temperature of 130 -140 K after expansion in the first boiler, and to cool the incoming nitrogen stream to a similar temperature. With this amount of precooling the nitrogen can be liquified at pressures of 7 MPa or less, and temperatures down to the triple point of nitrogen (63.1K) can be achieved, in principle, with only a small drop off in capacity at the lowest temperatures. In addition, it is possible to obtain a range of different performance characteristics with the same refrigerator simply by varying the composition of the mixed gas. The high capacity of the mixed gas stage also allows one to use a relatively inefficient, final stage heat exchanger for the nitrogen circuit. This choice guarantees a small pressure drop across this exchanger and, when the pressure at the exhaust is reduced below ambient, permits the nitrogen boiler to operate at a pressure well below ambient.

REFRIGERATOR DESIGN

For the cooling of focal plane arrays it is important not only to maintain the average temperature of the array constant, but also to keep the temperature variation across the array as small as possible. This becomes more important as the size of the arrays are increased. In conventional refrigerators, the refrigerator is normally mounted to the ambient temperature support at one end. This tends to introduce a temperature gradient across the cold stage. The effect of this is greater, the smaller the size of the refrigerator. To offset this effect in this refrigerator, we have designed it to be supported at both ends, with the cold stage in the middle. This gives greater strength to the unit and a much more symmetric temperature distribution across the cold stage. On the otherhand, it requires double the number of heat exchangers and the novel requirement that the two sides of the refrigerator must be balanced in capacity and flow. Fortunately, the fabrication process permits the use of arbitrarily complicated flow patterns, with little additional cost, and, in practice, excellent matching of the two sides has been achieved, with good yield.

The layout of the heat exchangers is shown in Fig 1. The refrigerator consists of five glass substrates each of 0.025 cm thickness which are fused together in the final assembly. It is composed of the four heat exchangers shown in the figure, plus a cover slide in which a rectangular aperture is cut overwhich the detector substrate is mounted, allowing the underside of the detector to be bathed in liquid nitrogen. In our tests, a rectangular alumina piece of the same thermal mass as the detector, is substituted for the detector. The channel dimensions for the high pressure circuits are typically 86 μ wide by 40 μ deep and are designed to operate safely at 30 MPa. The low pressure return channels have deeper and wider channels handling as they do, the lower pressure gas.

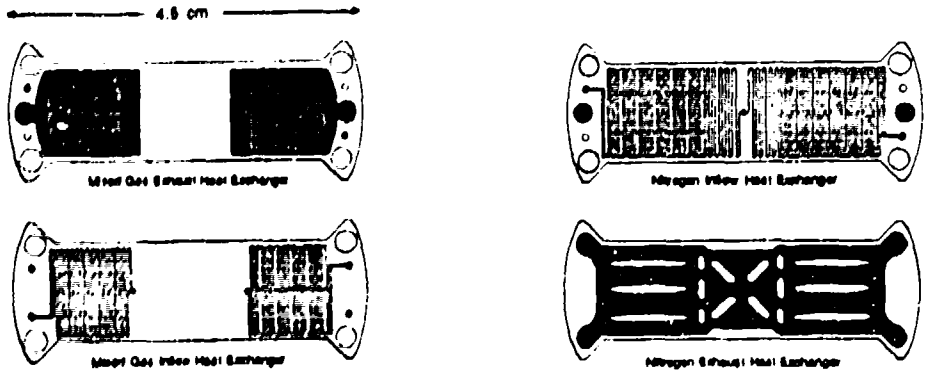

Figure 1. Layout of the four heat exchangers. These are stacked on top of one another with a cover slide over the nitrogen exhaust heat exchanger, and fused together to form the final refrigerator.

The cold stage is of alumina, is 1.1 cm x 0.88 cm in size, and 0.05 cm thick. To minimise the thermal mass of the rest of the refrigerator, but at the same time to provide adequate area for the mounting of the refrigerator and provide space for the large exhaust lines needed for low temperature operation, the refrigerator is ground after fabric n, to the shape shown.

The refrigerator is designed to cool to 70 K in ten seconds using for the first stage, a nitrogen- hy · arbon gas mixture (28.8% N_2, 39.5% CH_4, 27.7% C_2H_6 and 4% C_3H_8) at a pressure of 30 MPa and a flow of 4.3 L/m, and pure nitrogen at a pressure of 12.4 MPa and a flow of 0.8 L/m for the second.

To obtain a final temperature below the normal boiling point of nitrogen, it is necessary for the nitrogen stage boiler to be operated at a pressure below ambient. In our design this is achieved by using the relatively large flow of the mixed gas to drive a miniature venturi pump, which is used to reduce the pressure in the nitrogen boiler. We have fabricated such a venturi using the same photolithographic procedures used to build the refrigerator. It is shown in Fig 2. A microminiature Laval nozzle with a throat 0.028 cm wide by 0.025 cm deep is driven by the mixed gas exhaust and accelerates the mixed gas to Mach 3.18, where its pressure falls to 10 kPa. Here it is mixed with the nitrogen from the vacuum intake nozzles, decelerated through the deceleration nozzle and finally passed through a normal shock to bring it back to ambient pressure before exhausting to the outside. The small flow from the nitrogen stage is designed not to overload the pump and thus allows the final stage to operate at or about 30 kPa permitting operation below 70 K.

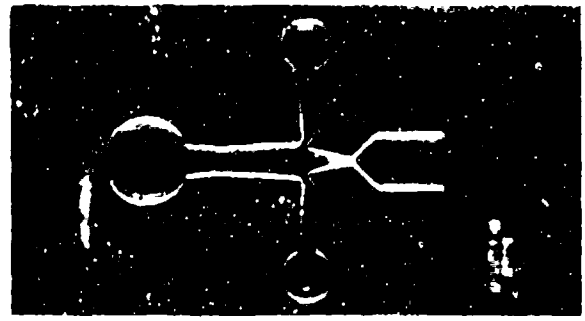

Figure 2. Microminiature Venturi Pump fabricated in glass. Gas is injected from the left, expands through the Laval nozzle entrains gas from the two side arms and then decelerates to the exhaust port to the right.

A unique feature of this venturi pump is its planar design. This allows it to be fabricated in the same manner as the refrigerator. However, this planar configuration does introduce some loss of efficiency due to the additional frictional losses from the close proximity of the walls. However, we have achieved the capacity and operating pressure which we need with the pump at an input pressure of 750 kPa. This pressure is 40% higher than our initial design goal but we believe it can be reduced further by recognizing the limitations imposed by the planar design and compensating for it by increasing the throat angle and shortening the expansion nozzle.

PERFORMANCE

The detailed design has gone through several iterations. The major uncertainty has been the determination of the proper dimensions for the mixed gas outflow heat exchanger. In this region the flow is two phase, and the ratio of the two phases is a rapidly changing function of position in the exchanger. Because of this, the effective viscosity of the mixture is difficult to estimate. Restriction of this flow causes an increase in the pressure at the first boiler, and thus of the temperature of the first stage boiler which, in turn affects the nitrogen stage. The effect of this back pressure is large because the bubble point temperature for these gas mixtures is a much more rapidly rising function of pressure than for a single, pure component. A small increase in back pressure through the exchanger can raise the boiler temperature significantly and the uncertainty in this back pressure gives us the uncertainty in the design.

The present state of the design is illustrated by the cooldown curve shown in Fig 3. In this test a cooldown from 300 K to 70.1 K was achieved in a little under 14 seconds. Vacuum for the nitrogen stage was provided in this test by an external vacuum pump, not the venturi.

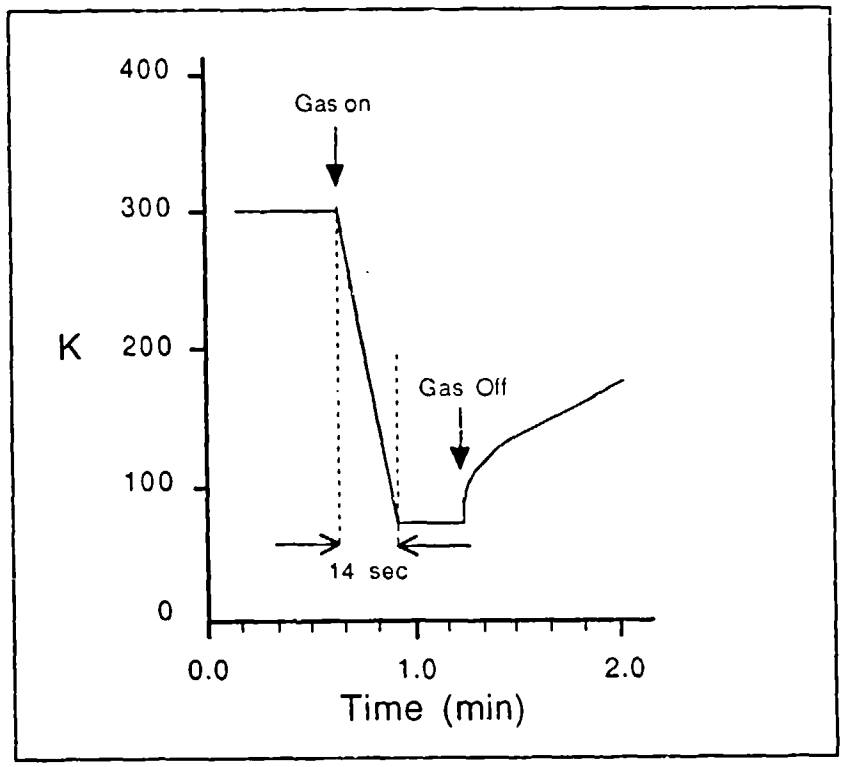

Figure 3. Cooldown curve of prototype refrigerator using the nitrogen-hydrocarbon gas mixture described in the text in the first stage, at 30.4 MPa inlet pressure, and nitrogen at 12.4 MPa for the second stage. Cooldown time to 70 K is just under 14 seconds.

VACUUM PACKAGE

The vacuum package was designed to provide a compact, rugged enclosure for the refrigerator. In order to achieve the goal of a 10 to 20 year shelf life, it is planned to exclude in the final package all organic materials and to use only Kovar, stainless steel, alumina and glass which are compatible with high vacuum practice, in the construction. However, this goal has not yet been achieved. Some problem areas remain. We have yet to replace an epoxy pre-form used for the mounting of the refrigerator and a silicone adhesive used for the mounting of the cold stage. While we have demonstrated in a separate study, the possibility of replacing these with brazed joints, we have not yet adapted this procedure to the specific conditions of assembly of this package. More work in this area is needed.

The focal plane array under consideration requires thirty seven feedthrough leads and, in addition, other leads are needed for firing or refiring of the getters and for providing diagnostic information on the temperature and vacuum. These leads are provided for by a thin Kovar lead frame fused between two thin alumina spacers which are themselves brazed to the body of the chamber, which is machined out of Kovar. The package is

evacuated through a copper tube which is brazed into the bottom of the chamber and after pump out, is pinched off with a cold weld.

After the alumina pieces are brazed to the vacuum chamber and the feedthrough lead frame is sealed to them , the refrigerator is mounted to the underside of the upper portion of the chamber, and the base with copper pump-out line attached, is laser welded to it. The detector can now be mounted and the leads wires gold bonded to it. Finally the window assembly is laser welded in place.

In order to reduce the heat leak to the detector, the Kovar leads are bonded to an alumina heat sink which is mounted on the mixed gas boiler. This heat sink is maintained at 140 K by the first stage refrigerator and acts as a thermal guard ring round the detector stage and provides cooling for the cold shield. Wire bonds are made between it and the contact pads on the detector substrate, which is in close proximity to it.

The gas lines to the refrigerator are taken out of the front of the package, rather than the back as in conventional refrigerators. This permits the package to be mounted on a gimbal system with very little clearance behind it. It is planned to mount the venturi on the outside of the package on the two sets of exhaust lines.

In Fig 4. is shown the individual components which go into the making of the package. Starting from the left is shown the copper pump-out tube, the base, alumina cold pad, alumina heat sink, refrigerator and refrigerator mount with gas lines, alumina spacer, Kovar lead-frame, alumina spacer, upper chamber, window mount and finally the sapphire window.

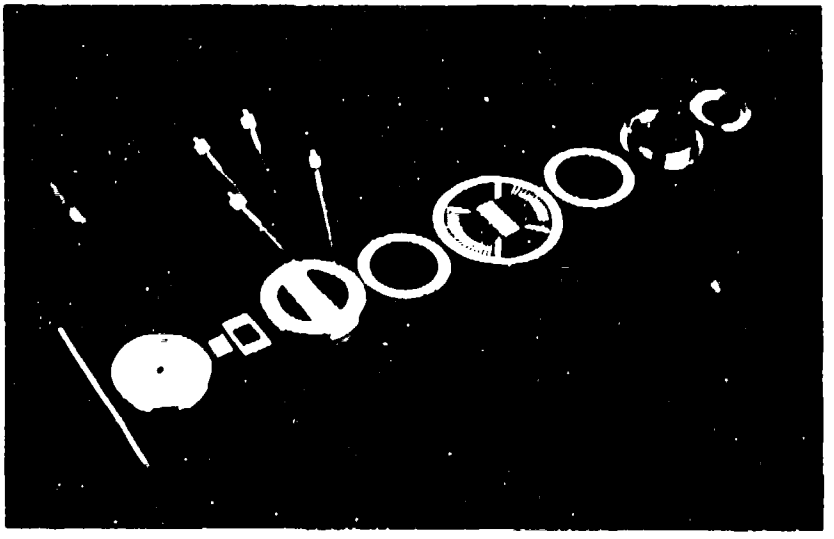

Figure 4. Individual components of the refrigerator and vacuum package. (See text.)

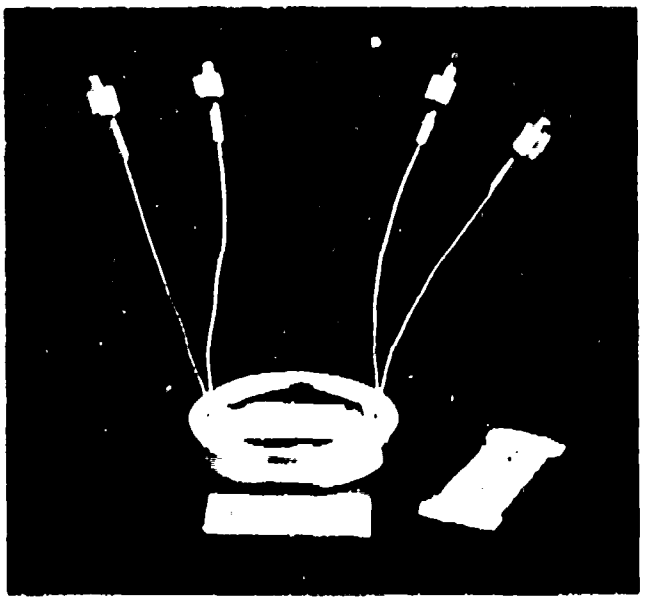

Figure 5. Refrigerator Mount with gas lines to the two halves of the refrigerator. Next to it is another, untrimmed and unmounted refrigerator.

In Fig 5. is shown a close-up of the refrigerator mount with gas lines, and an additional, untrimmed refrigerator next to it. The final package is shown in Fig 6. The outer

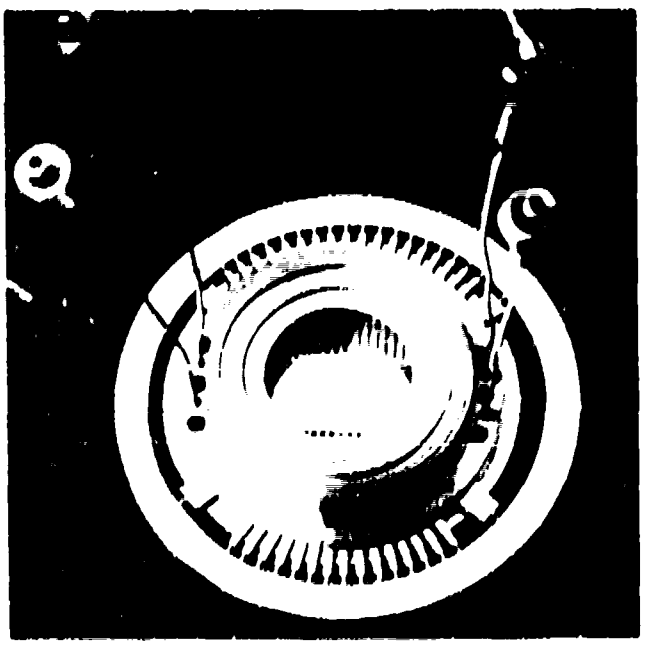

Figure 6. Top view of final package, 5.0 cm O.D. and 1.6 cm high. Kovar lead frame is still attached to the feedthroughs

ring of the Kovar lead-frame is still attached to the feedthrough leads. This will subsequently be sheared off at the thin support sections at the end of each feedthough, prior to attachment of the external wire harness. The final package is 5.0 cm in diameter and 1.6 cm high.

CONCLUSION

We have successfully demonstrated a new type of fast cooldown Joule Thomson refrigerator suitable for cooling large infrared imaging arrays to temperatures well below those normally available with JT coolers. The vacuum package which has been designed to go with it, is extremely compact and rugged. Through the exclusive use of ultra-high vacuum compatible materials and, in particular, the exclusion of organic materials from its construction, the system has the potential of providing a 10 to 20 year shelf life.

ACKNOWLEGEMENTS

We are indebted to the engineering and manufacturing staff at MMR Technologies, Inc. for the fabrication and testing of the refrigerators and for much of the detailed design, in particular, Dave Connell, Mark Dubois, Wing Lok Chiu, Herb Edman, Frank Tochez, Carlos Fuentes, and Elizabeth Bailey. We wish to acknowledge partial support through Contract N60530-88-C-0537 from the Naval Weapons Center, China Lake, CA. for the development of the system, and ONR Contract N00014-86-C-0301, and N00014-88-K-0334 for support of work on the gas mixtures, which made this development possible.

REFERENCES

1. W.A.Little, Microminiature Refrigeration, *Rev. Sci. Instrum.* 55, 661 (1984)

2. V.N.Alfeev, et al., Great Britain Patent No. 1336,892 (1973)

3. W.A. Little, U. S. Patent application, Serial No. 919,699 (1985) Patent Pending.

4. W.A. Little, "Recent Developments in Joule-Thomson Cooling: Gases, Coolers and Compressors", *Proceedings of the Fifth Cryocooler Conference*, Monterey (19880 in press; W.A. Little, "Advances in Joule-Thomson Cooling"*Advances in Cryogenic Engineering*, Vol.35,1305 - 1314, ed. R.W. Fast, Plenum Press, New York, 1990.

RECENT PRACTICAL APPLICATIONS OF OPEN CYCLE, COMPRESSOR BASED JOULE-THOMSON COOLING

Paul Benson
Dowty Weapon Systems
Gloucester, England

ABSTRACT

The Dowty company has for several years had under development and in manufacture a range of small compressors and gas cleaning equipment. Designated High Pressure Pure Air Generators (HiPPAG), these systems were originally designed to support the cryogenic cooling of thermal imaging equipment in ground and helicopter-borne applications. The capability of the equipment has been extended to cover the altitude range of modern fighter aircraft for the support of infra-red guided missiles.

The progress of these developments is reviewed, together with the philosophy adopted in the equipment design and recent practical applications of the equipment in the USA and Europe.

BACKGROUND

Dowty became involved in Pure Air for thermal imaging equipment when it was selected by the UK Ministry of Defence to manufacture Pure Air bottle charging equipment. During this period Dowty engineers were fortunately able to witness exercises in Germany. It became obvious that the use of bottles to supply the cooling gas requirements introduced many problems. These were chiefly:

1. Disruption of operation due to limited bottle capacity.
2. High Logistic support burden associated with recharging equipment, spare bottles, transportation and manpower requirements.

3. Contamination introduced through bottle handling prejudices system reliability.

It was concluded that a small electrically driven compressor and gas purification system could help to overcome many of these problems. Such a system would give greatly extended operating periods and free the operators of the necessity to ensure an uninterrupted supply of charged bottles. The Dowty engineers christened the subsequent equipment design "HiPPAG" - High Pressure Pure Air Generator.

HiPPAG DESIGN CONSIDERATIONS

CHOICE OF OPERATING CONDITIONS

It was necessary to determine the optimum operating pressure for the system. To this end a study was made of cryostat operating characteristics and compressor performance. Figures 1 and 2 show the cooldown and steady state mass flow requirements of representative Joule Thomson cryostats. These curves suggest that a minimum operating pressure of 200 Bar (20 MPa) should be maintained to ensure efficient performance over the operating temperature range.

Figure 3 shows the isothermal work of compression to raise the pressure of air from 1 Bar (0.1 MPa) to the indicated pressure, neglecting seal friction. Figure 4 shows the work input per gramme of gas when compressor efficiency is taken into account and due allowance made for seal friction etc.

In Figure 5 the compressor performance and cryostat flow characteristics are combined to give the overall system performance in terms of mechanical input power per watt of cooling. The net result of this analysis is the clear indication that the optimum operating pressure is in the range 200 to 300 Bar (20 to 30 MPa).

HARDWARE CONFIGURATION

Compressor Design

Several design options were considered, but the configuration chosen was judged to give the most compact design and to be most capable of adaptation to varying installation requirements. The compressor is a wobble plate design, with axially disposed pistons driven by double ball-jointed piston rods. This arrangement minimises piston side loads. The cylinder head assembly contains all inlet and outlet valves, interstage passages and volumes. There is no necessity for external piping to connect the various compression stages. For the HiPPAG 100 three stages of compression were chosen, with equal work per stage.

MASS OF AIR TO START TO MAKE LIQUID TYPICAL CRYOSTAT IN TEST DEWAR

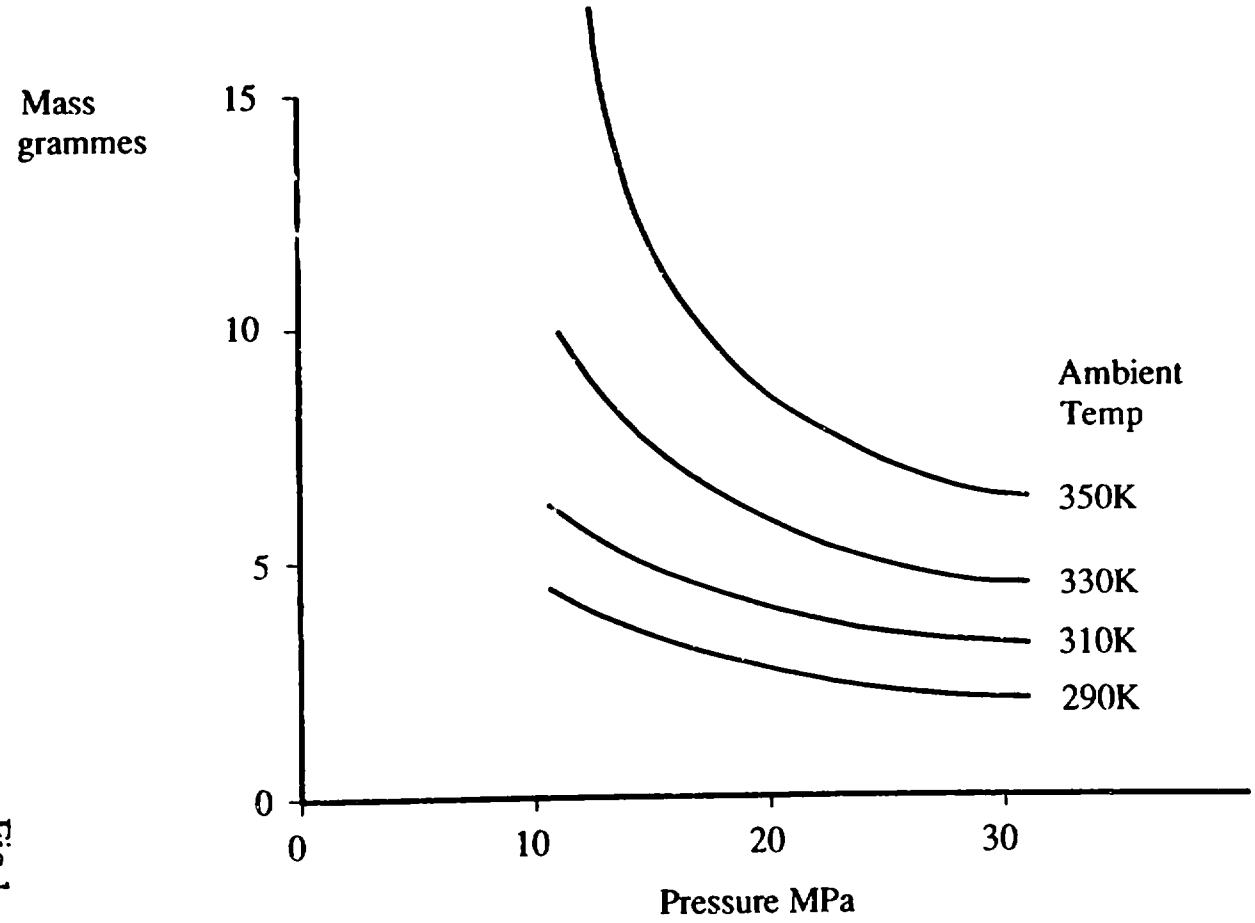

Fig 1

TYPICAL CRYOSTAT FLOW vs PRESSURE

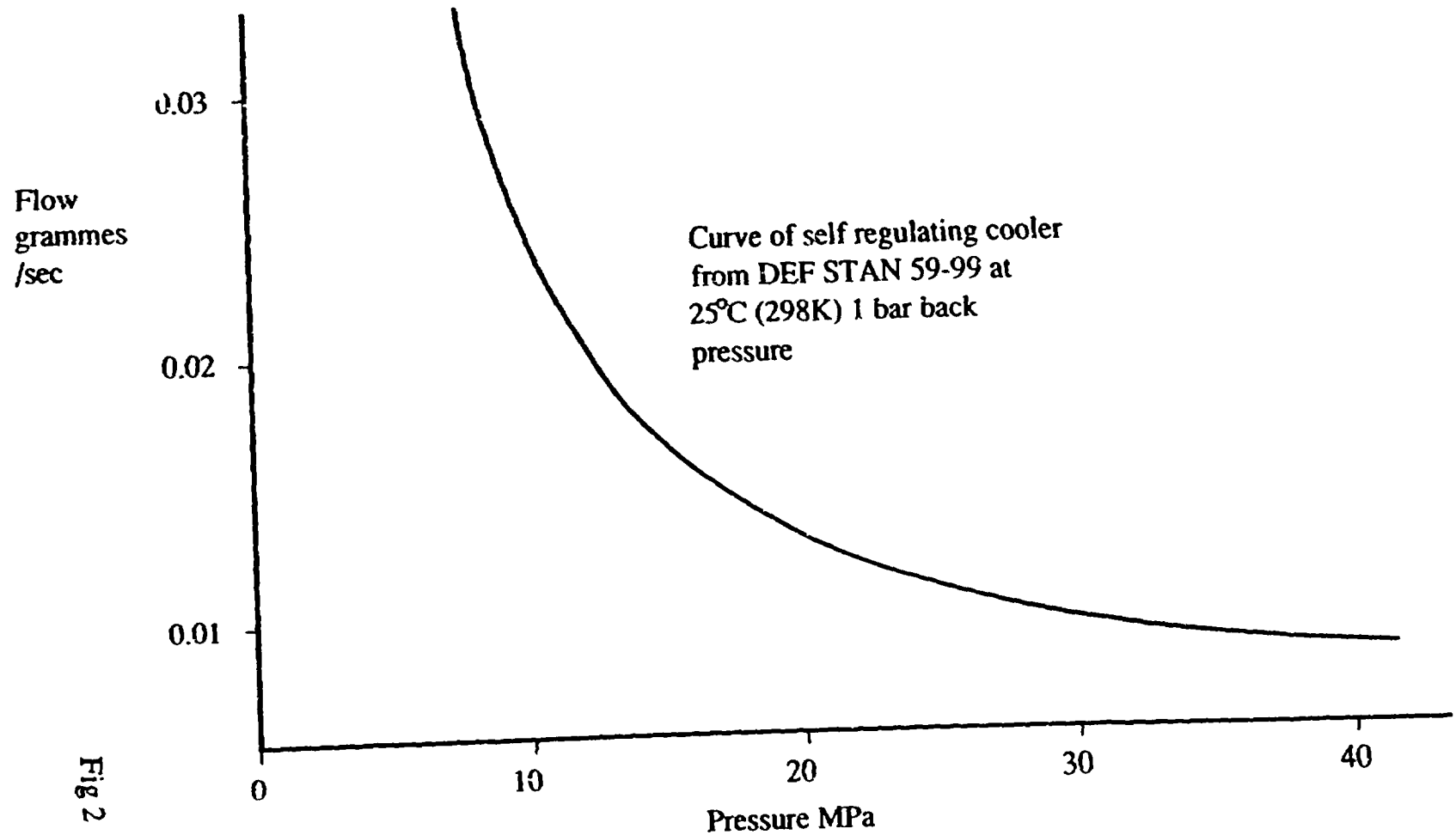

Fig 2

DOWTY

WORK OF ISOTHERMAL COMPRESSION FROM 1 bar

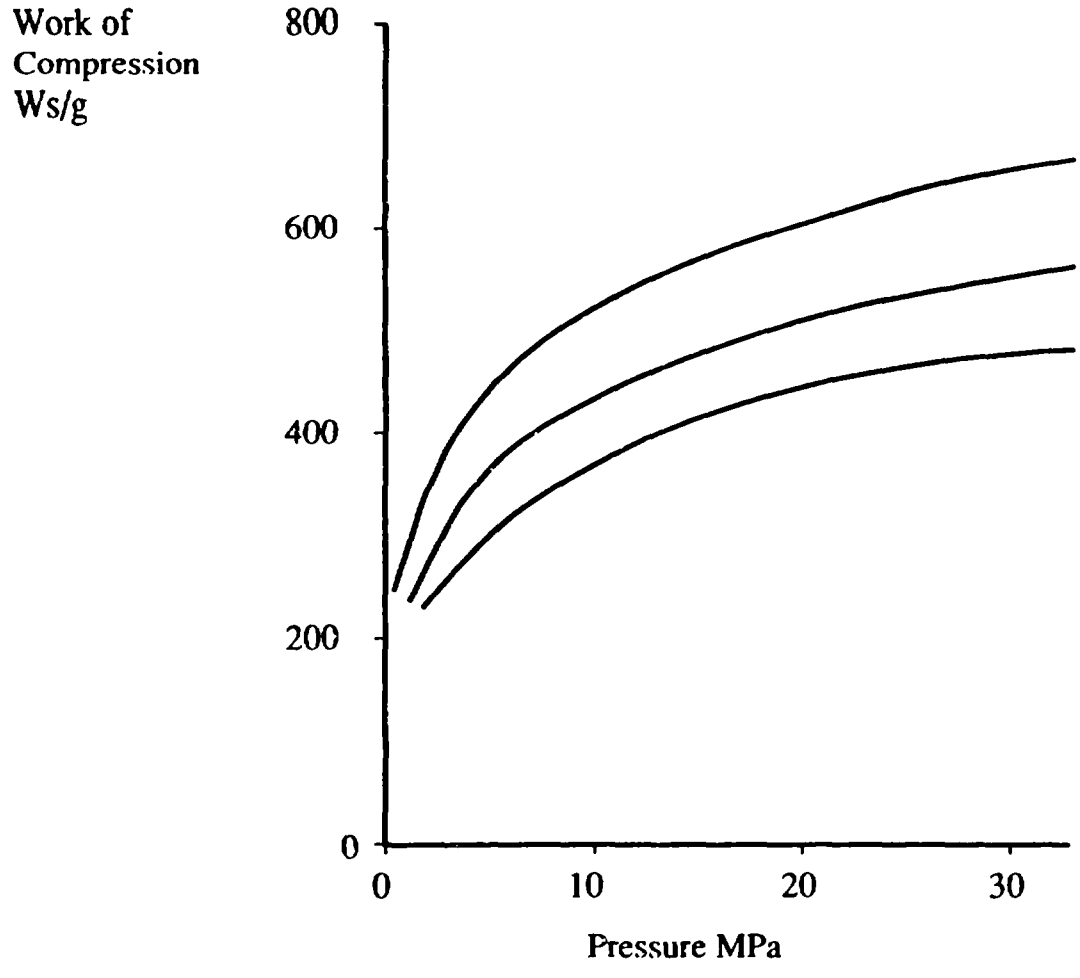

Fig 3

DOWTY

PREDICTED COMPRESSOR PERFORMANCE - WORK INPUT PER GRAMME OF GAS

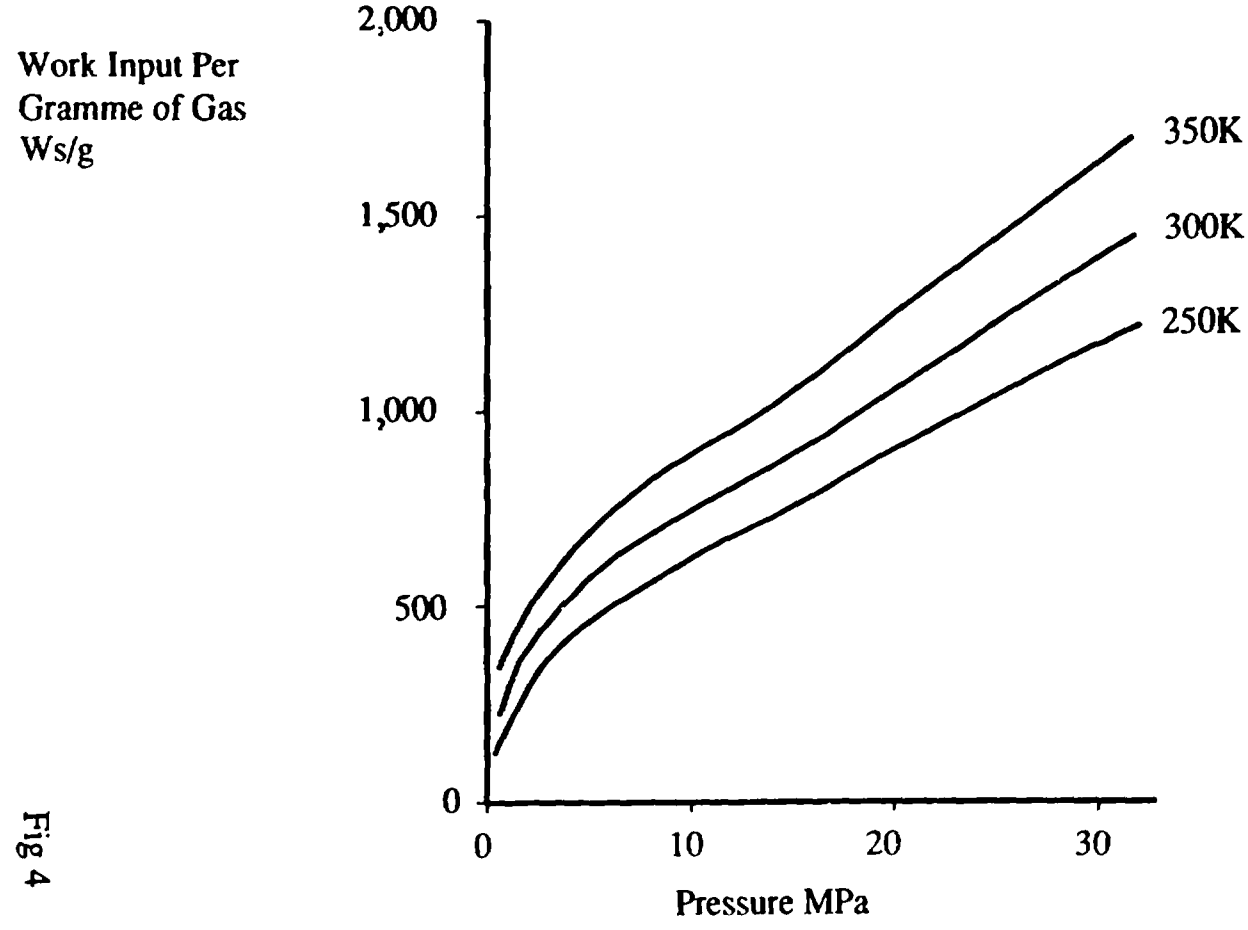

Fig 4

DOWTY

SYSTEM PERFORMANCE MECHANICAL INPUT POWER PER WATT COOLING

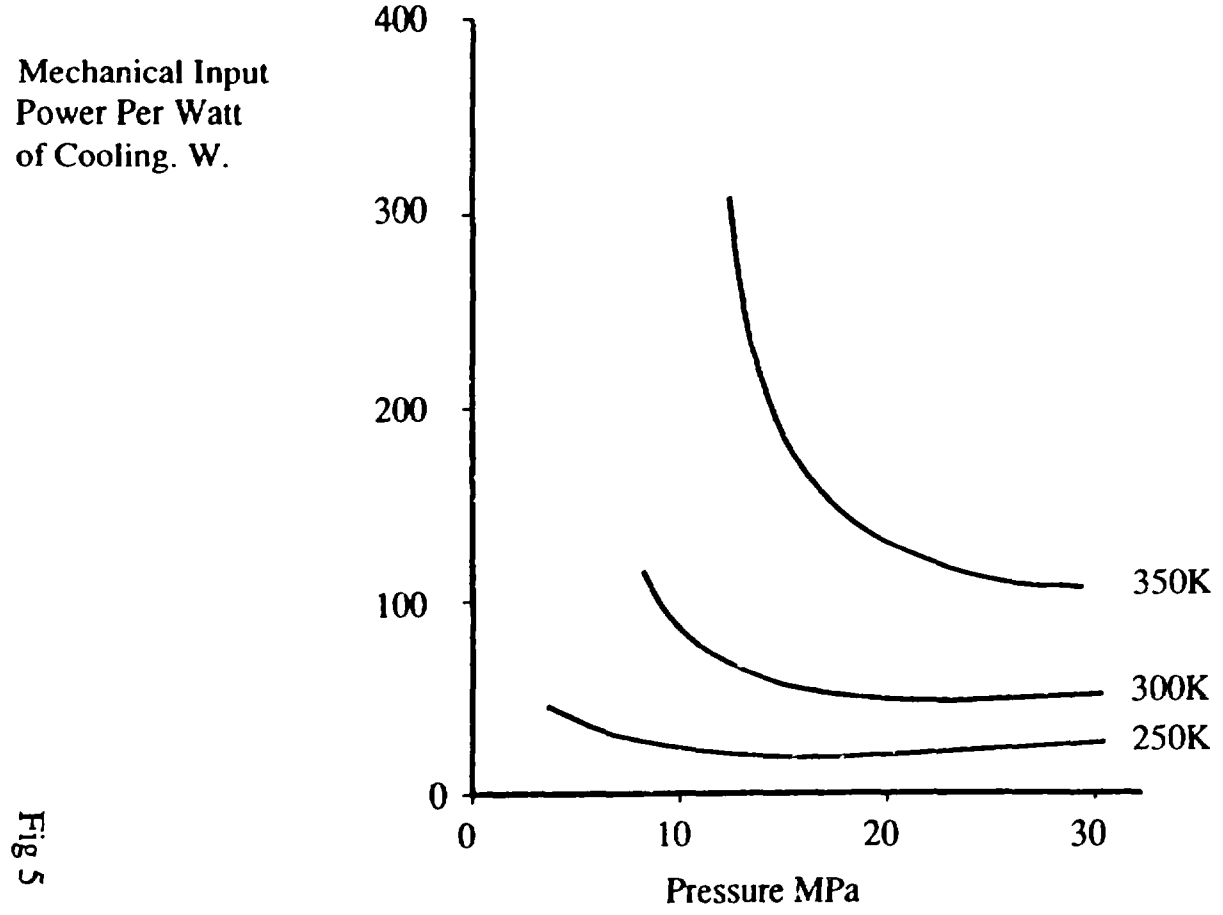

Fig 5

Motor Design

For helicopter and fighting vehicle applications a 28 V dc power supply was chosen. The compressor was designed to rotate comparatively slowly necessitating the use of a reduction gearbox between motor and compressor. The brushless motor is speed controlled to match compressor output to cryostat mass flow requirements, with a pressure transducer continuously monitoring system pressure.

Air Purification

Air purity requirements are met by two stages of gas cleaning. Firstly a water separator removes water generated during compression. A solenoid valve controlled by the system electronics vents the collected water to atmosphere at preset intervals. Secondly zeolite molecular sieves are used to remove water vapour, carbon dioxide and other contaminants to achieve the purity levels required by Joule Thomson cryostats. Additionally HiPPAG systems are fitted with intake filters to remove airborne particulate contamination and to give NBC protection.

Overall System Layout

Figure 6 shows the final design adopted for the HiPPAG 100 range of equipment. The equipment was designed to be as compact and lightweight as possible within the design constraints. The motor and electronic package is achieved only by the use of custom hybrid circuits. Additionally the motor contains an integral cooling fan to ensure that the system is completely self contained.

Varying interface requirements for the many applications have necessitated additional electrical boxes and mechanical interface adaptors, but the basic design remains unchanged for this series of equipment.

Modularity

From the outset the design aim was to make the HiPPAG system a modular construction. This approach was to make servicing as simple as possible. In the HiPPAG 100 design the major modules are motor/elecronics, compressor, filter assembly and wiring harness. The design is such that any module may be readily changed without the need for special tools or for any setting or adjustment.

This modular design approach has had additonal benefits in adaptation of the equipment for specific applications as discussed below.

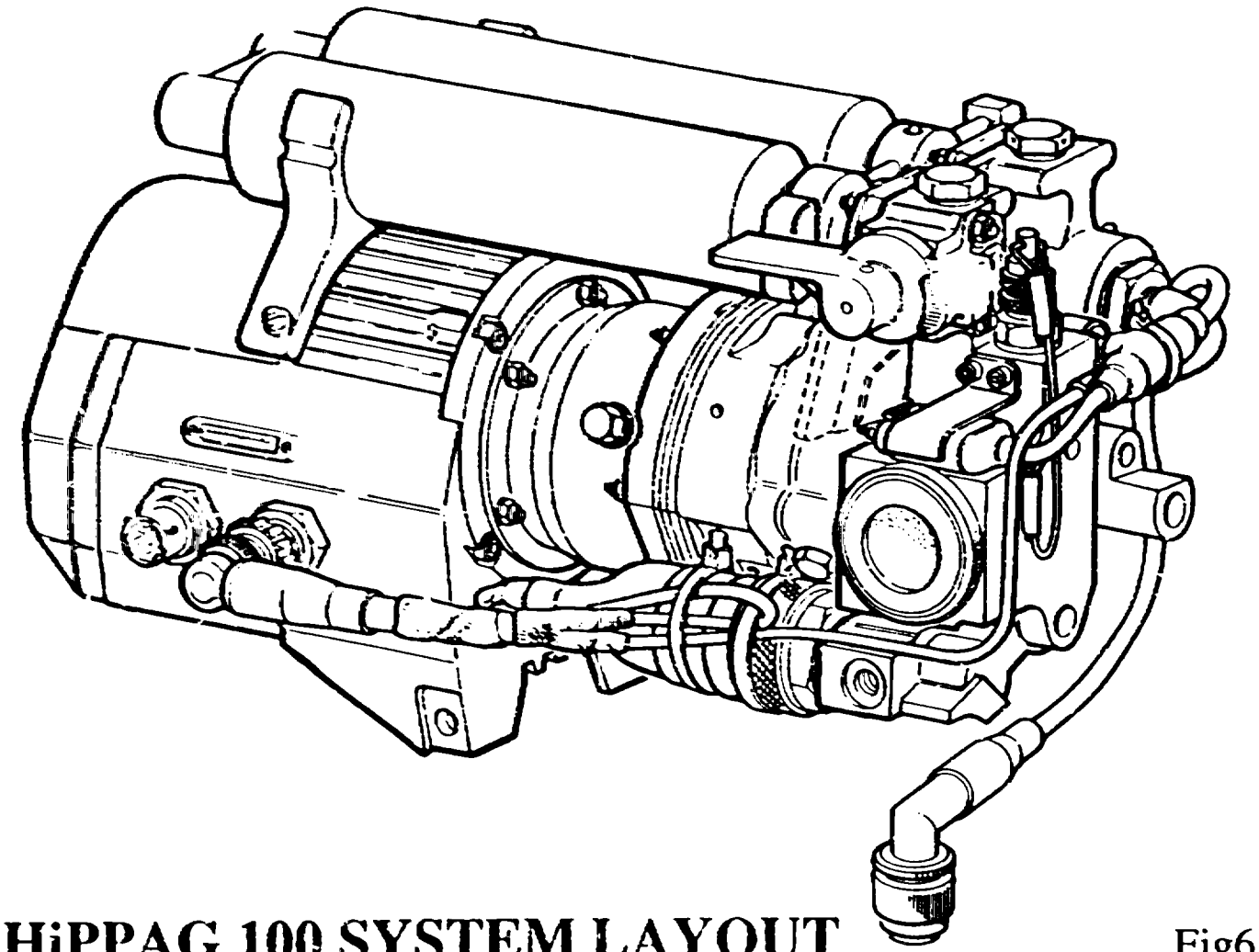

HiPPAG 100 SYSTEM LAYOUT

Fig6

HiPPAG 100 APPLICATIONS

GROUND, NAVAL AND HELICOPTER APPLICATIONS

HiPPAG 100 has been selected for a variety of ground, naval and helicopter-borne applications. Some of these are as follows:

Sea Owl Passive Identification Device for the Royal Navy Lynx Helicopter.

British Army Lynx TI TOW Missile

SAAB/Ericsson HELIOS TOW sight

Ground Surveillance at UK Air bases

Samsung Aerospace Naval Fire Control System

FIGHTING VEHICLE APPLICATIONS

Certain fighting vehicles have a unique operation requirement. This is the so-called "silent watch" mode, when power useage is limited to avoid either running down batteries or using the vehicle auxiliary engine. Dowty engineers were able to propose a unique solution to this problem.

Although originally designed to support the TICM II imager up to an altitude of 3000 metres, at typical ground operating conditions the equipment has a significant excess flow capacity. Thus a secondary bottle charging role could be proposed in which a charged bottle would supply coolant gas for the silent watch mode, and the HiPPAG system would automatically recharge the bottle during normal operation. The installation is effected so that an emergency charging facility is available to charge bottles for man-portable equipment, such as MILAN rocket launchers.

The bottle charging circuit is isolated from the main imager circuit by means of a preset back-pressure maintaining valve. The purpose of this valve is to ensure that the fighting vehicle thermal imager always has priority. Only when steady state operating conditions are achieved and the system pressure rises above the preset minimum will the excess flow capacity of the HiPPAG be diverted to the bottle charging circuit.

This variation on the HiPPAG 100 theme has been supplied for the British Army Warrior Observation Post Vehicle. A similar installation is now being designed for the Swingfire mid-life update programme.

HiPPAG 200 - FOR RPV TURRET APPLICATIONS

The HiPPAG 200 is based on the 100 series motor and compressor but specially adapted for the sensor turret on the PHOENIX Remotely Piloted Vehicle for the British Army. The prime contractor for this project is GEC Avionics, with GEC Sensors designing the infra-red sensor turret. Having selected J-T cooling, the choice was between an external gas supply, requiring rotating couplings, or a self contained turret containing its own cooling gas source. The required mission duration ruled out the use of bottles.

Dowty engineers were able to propose the configuration shown in Figure 7. The design was optimised to fit the available space, with close cooperation necessary between the two companies to ensure a layout which could accommodate the HiPPAG system was achieved. An additional benefit of the design approach adopted by GEC is that they can offer a stand alone turret for many other sensing applications.

MISSILE SUPPORT APPLICATIONS FOR FIXED WING AIRCRAFT

HiPPAG 320 DESIGN CONSIDERATIONS

Following award of the project definition contract for design of a cooling system for the ASRAAM missile, Dowty saw the opportunity for replacing the coolant gas bottle on LAU-7 launchers for Sidewinder missiles. The impetus to carry out this design work came from an analysis of life cycle cost comparisons for bottle operated and HiPPAG supported equipment. This analysis suggested large savings could be made in switching to HiPPAG, and the number of launchers in service worldwide presented a significant business opportunity.

In order to meet the gas flow requirements of the Sidewinder detector at the service altitudes of modern aircraft a new compressor design was required. A four stage design was chosen, this giving similar stage pressure ratios and piston loadings at these altitudes to those of the HiPPAG 100 series. The large diameter first stage piston is sized to meet the cryostat demand flow for continuous operation up to 15 km. Due to the stored air capacity within the high pressure gas cleaning unit, the equipment can continue to supply cooling gas to the detector for extended periods at altitudes in excess of 15 km.

In addition to overall performance considerations several other design constraints had to be addressed. As well as packaging the equipment to meet the available space envelope, the launcher mass properties had to be maintained. Access to the gas purification filter had to be provided via the launcher aft clamshell doors and a combined electrical and pneumatic connector had to be designed. This connector allows a straightforward push-to-connect

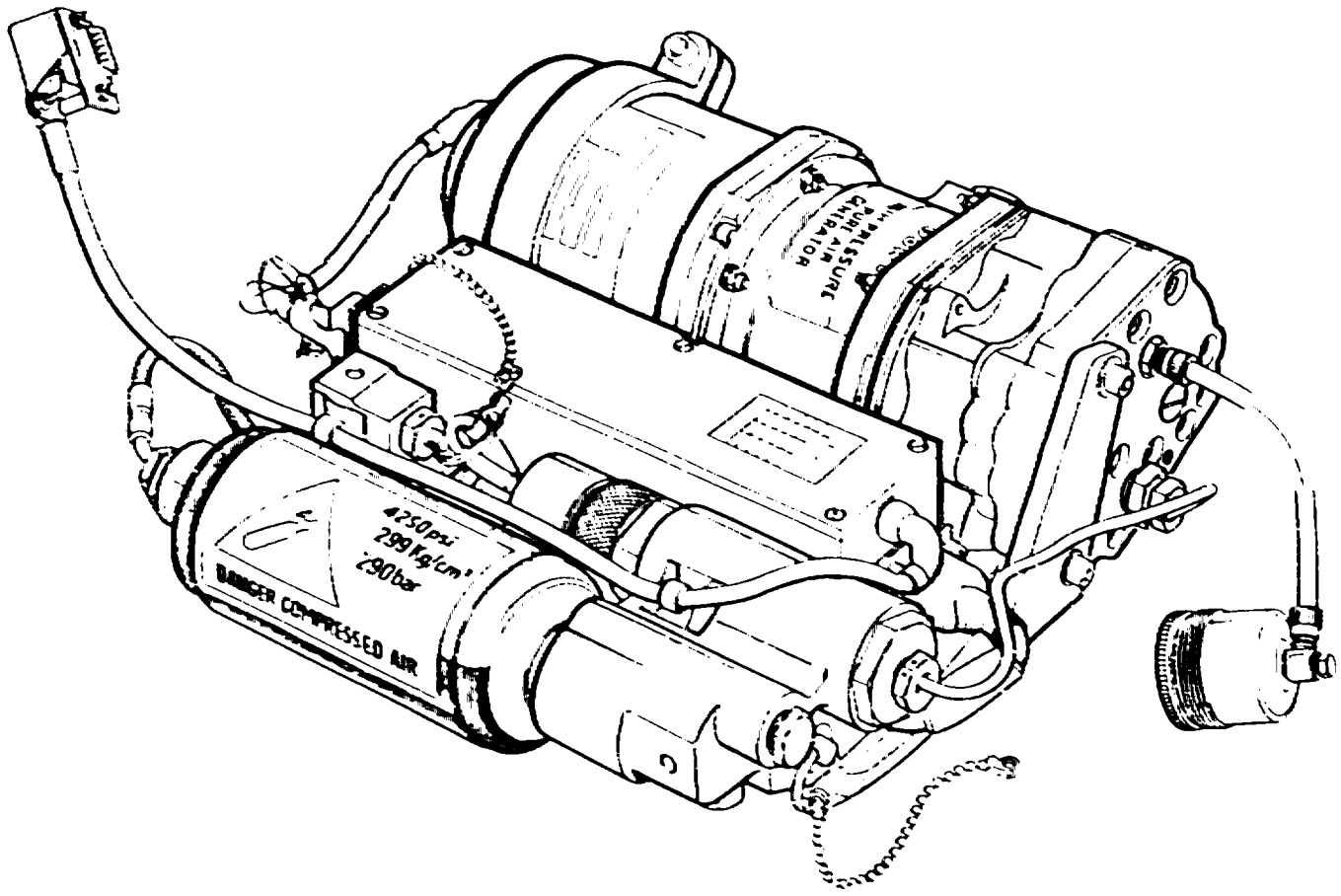

HiPPAG 200 SYSTEM LAYOUT

Fig7

action for all power, signal and pure air connections when installing the equipment in the launch rail.

Figure 8 shows the layout of the HiPPAG 320 equipment for the LAU-7 launcher installation.

PROOF OF CONCEPT TESTING

The ability of the HiPPAG 320 system to support the Sidewinder missile was adequately demonstrated in Proof of Concept testing carried out by NAVAIR. This testing consisted of both ground and flight tests. The ground tests were carried out in the UK and USA to test the system performance over the full military environmental range. Vibration and shock testing was carried out to certify the equipment for flight trials in the demanding FA-18 wingtip carriage environment.

The Proof of Concept testing culminated in April 1989 in flight tests on a Canadian CF-18 aircraft. During the flight tests the performance of the HiPPAG system in supporting a captive Sidewinder missile was compared with that of a standard Nitrogen bottle. The tests were carried out over the full flight regime and covered a variety of target acquisition modes. The conclusion of the tests was that the HiPPAG system was indistinguishable from the Nitrogen bottle in the quality of cooling gas supplied to the missile seeker.

Following these tests NAVAIR placed a contract on Dowty Weapon Systems for the supply of HiPPAG 320 units for qualification testing. These units are now being shipped and the qualification programme will shortly commence.

APPLICATIONS TO OTHER LAUNCHERS

As with other HiPPAG variants, the HiPPAG 320 was designed as a set of discrete modules. This allows several installations to be proposed using the same basic modules as are undergoing qualification testing for the LAU-7 application.

Certain aircraft have the need for additional capability to dispense chaff as a counter-measure against enemy missiles. The space occupied by the nitrogen bottle in the LAU-7 launcher can be used for this purpose, and the Swedish company Bofors has developed a LAU-7 variant containing chaff dispensing equipment. Dowty is able to propose a repackaging of the HiPPAG 320 modules to mount on the front of the launcher for this application.

Other launcher applications on which design studies are being carried out include:

EFA Tip Stub Pylon Launcher
Frazer-Nash CRL
LAU-127 MRL
ACMA Multi Purpose Rail Launcher
MHI XAAM4 Launcher

HiPPAG - THE FUTURE

Developments are now under way on future applications for HiPPAG equipment and technology applications. Novel design solutions are being applied to meet the changing requirements of thermal imaging detectors. It is hoped that some of these developments may be presented to a future Cryocoolers conference.

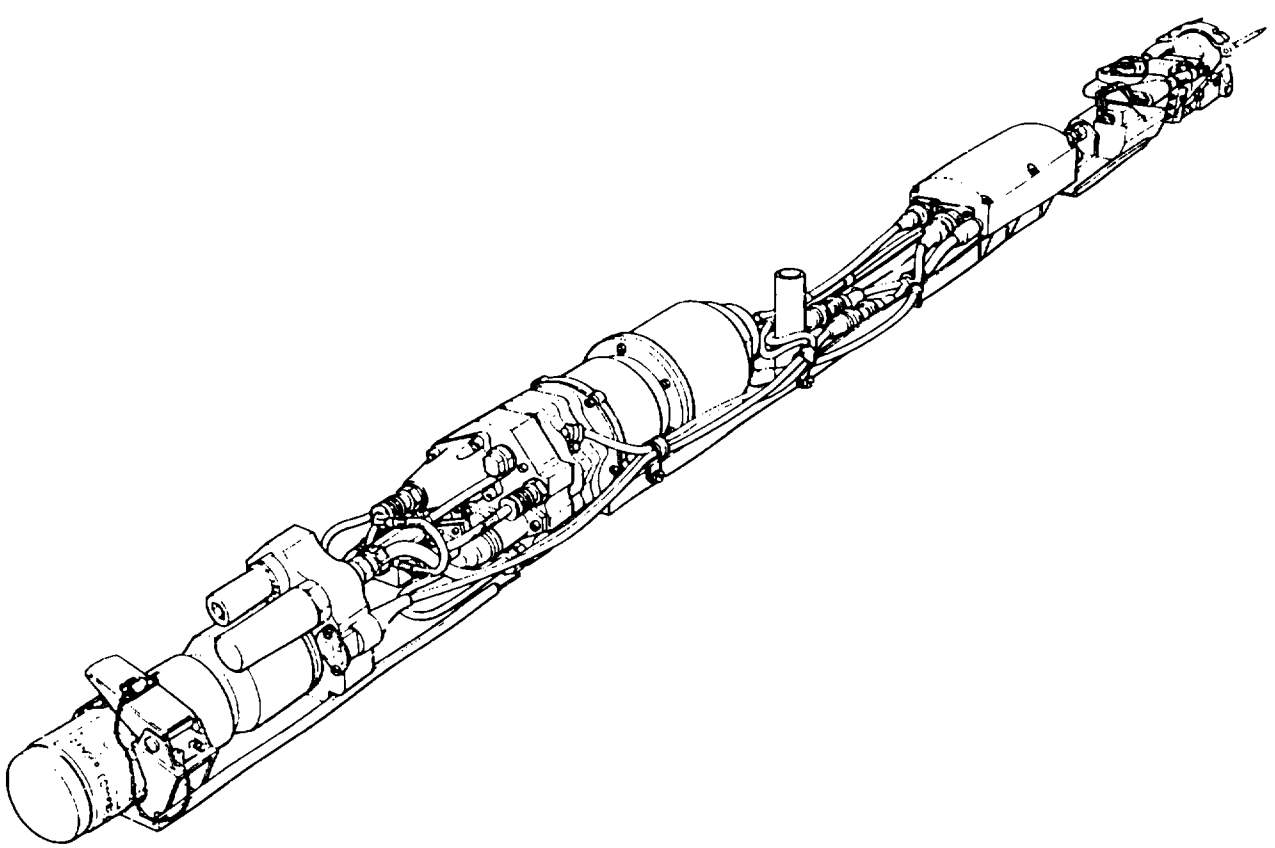

HiPPAG 320 SYSTEM LAYOUT Fig8

Session VIIA — Magnetic Coolers

Chairperson: Marvin Gunn, DOE

Co-Chairperson: Alan Crunkleton, Boreas, Inc.

Session VIIB — Space Coolers II

Chairperson: Jim Lester, Ball Aerospace

Co-Chairperson: Bill Wyche AFSTC/SWS

DESIGN OF THE REGENERATIVE MAGNETIC REFRIGERATOR OPERATING BETWEEN 4.2 K AND 1.8 K

Sangkwon Jeong and Joseph L. Smith, Jr.
Cryogenic Engineering Laboratory
Department of Mechanical Engineering
Massachusetts Institute of Technology
Cambridge, MA 02139

Takenori Numazawa* and Yukikazu Iwasa
Francis Bitter National Magnet Laboratory
Massachusetts Institute of Technology
Cambridge, MA 02139

ABSTRACT

The active regenerative magnetic refrigerator has been designed for the temperature range between 4.2 K and 1.8 K. The magnetic core is composed of many small GGG spheres whose diameters are 0.8 mm. For the heat transfer medium, the low pressure helium 3 has been selected to reduce the adverse effect of entrainment and to avoid the undesirable superfluidity in the core. It is important to get rid of the dead volume between the active magnetic core and the heat exchangers. In order to make the energy transfer of the magnet easy, the twin superconducting magnets should be symmetrical and each magnet will be made by two different coils; one for the persistent mode and the other for the variational mode.

The expected design value of the refrigeration capacity is 100 mW at 1.8 K. After the design study, the prototype of this magnetic refrigerator is now under construction.

INTRODUCTION

Magnetic refrigeration has been usually used as a technique to obtain temperatures below 1K for a long time. However, in the last ten years, the technology has been

---

* a visiting scientist from National Research Institute for Metals in Japan

developed for refrigeration applications above 1K or even up to room temperature. An efficient continuous magnetic refrigerator has been necessary for many applications. The magnetic refrigeration system operating between 1.8 K and 4.2 K is important in that its application is to be able to produce superfluid liquid helium. One of the important applications is superfluid helium-cooled superconducting magnets of NbTi wire which carry about 25 % higher current density at 1.8 K than at 4.2 K.

A regenerative magnetic refrigerator was investigated in the MIT Cryogenic Engineering Laboratory for the last 5 years. In the previous papers[1,2] of this project, they have clarified the importance of field-flow mismatching problem, entrainment effects, and the minimization of dead volume. Based on our past experiences, the new tandem magnetic refrigerator was designed. Figure 1 shows the schematic diagram of the tandem magnetic refrigerator. The two magnetic systems, each consisting of a core, superconducting magnet, and warm and cold end heat exchangers are connected by a displacer.

The advantages of tandem system are as follows.

* Higher frequency of refrigeration power for its load
* Small displacer volume and easy control
* Potential simplification in magnet energization

Each component design will be discussed briefly in this paper.

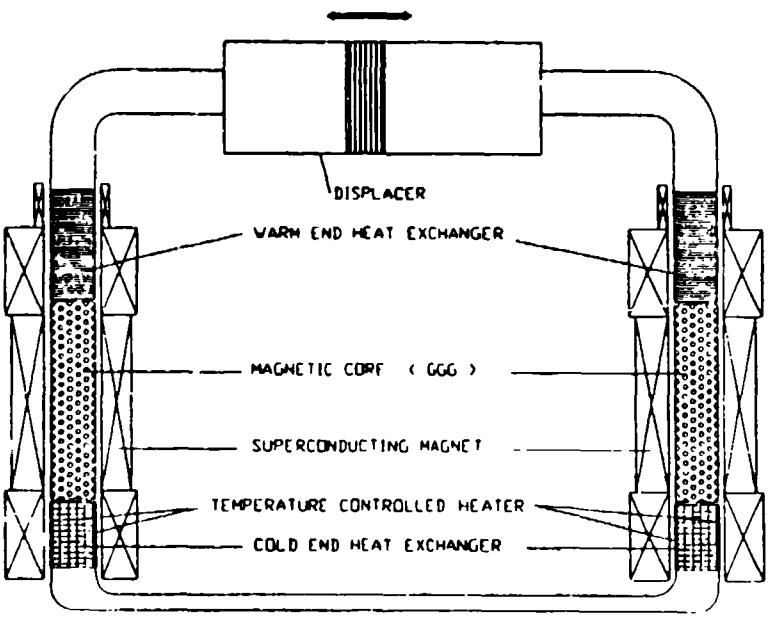

Fig.1. Schematic diagram of the tandem magnetic refrigerator

DESIGN FEATURES

MAGNETIC CORE

The packed bed type regenerator core was chosen for our system , which consists of tiny spheres of GGG($Gd_3Ga_5O_{12}$). In this configuration, axial conduction which was one of the major deteriorating factors in the MIT system, is small because of the thermal contact resistance at each granule contact.[1] The packed bed type had been considered for the previous MIT system but it was discarded for its relatively high porosity. A typical porosity for packed beds of random spheres is about 38%. However, if we use a low-pressure helium as the working fluid, the helium mass entrained in the core is relatively small compared to the total shuttle mass. This fact makes it possible for the packed bed configuration to be adopted in our system.

The favorable magneto-thermodynamic property of GGG in the lower temperature regions demonstrates that GGG is a logical choice as our magnetic refrigerant. The amount of GGG required was determined as 270 g for the refrigeration capacity of 100 mW at 1.8 K.

In this regenerative magnetic refrigerator, there should be a heat transfer medium which passes through the magnetic core carrying entropy between heat exchangers. The subatmospheric He^3 isotope will be used as the heat transfer medium in order to avoid any superfluidity inside core. Also, the low operating pressure will reduce the amount of entrained helium in the core which was one of the sources of entropy generation.

SUPERCONDUCTING MAGNET

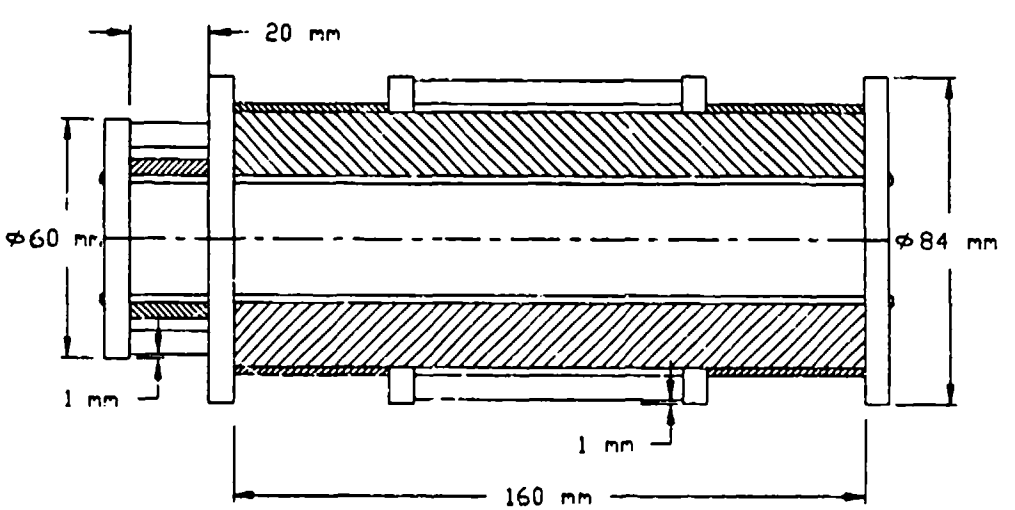

Fig.2. Dimensions of the superconducting magnet

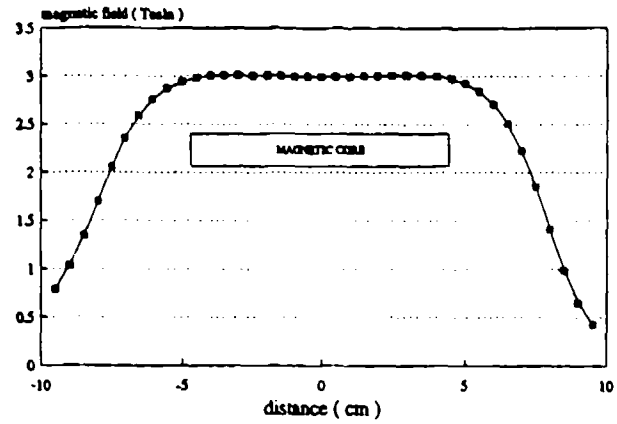

Fig.3. Magnetic field distribution of the designed magnet

A superconducting magnet is necessary to produce a high magnetic field for the core. Figure 2 shows the actual dimensions of the designed magnet. The secondary notch coils have been added to get uniform magnetic field. The purpose of the inverse coil in the top of the magnet is to reduce A.C. loss in the warm end heat exchanger by cancelling some of the magnetic field of primary and secondary coil near the heat exchanger. The magnet is to be energized by a maximum of 15 A to provide 3 Tesla at the core region. The resultant magnetic field in the axial direction is shown in Figure 3.

In order to make the energy transfer of the magnet easy, the actual magnet is made by two different coils; one for the persistent mode coil and the other for the variational mode coil. The self inductance of each coil is 1.8 H while the total inductance is 7.2 H. With the small inductance value, the amount of energy to be transferred at one time from the magnet can be reduced by a factor of 1/4.

WARM END HEAT EXCHANGER

Both warm and cold end heat exchangers will be located as close as possible to the GGG core to reduce the bad effect of dead volume. The important factor to consider in the heat exchanger design is A.C. loss. Since the eddy currents are induced by a fluctuating magnetic field, the resultant heat generation will add some additional load to the heat exchangers. The plate fin type heat exchanger was selected since the fin configuration in axial direction can minimize the A.C.loss. The outside diameter of the heat exchanger is set to be the same as that of the magnetic core so that we can use a single stainless steel tube for both the core and heat exchangers. Figure 4 is the schematic diagram of the warm end heat exchanger, which also includes a liquid helium port to cool it at 4.2 K. The inside diameter of the heat exchanger, or port diameter, was optimized to achieve the maximum overall heat transfer coefficient.

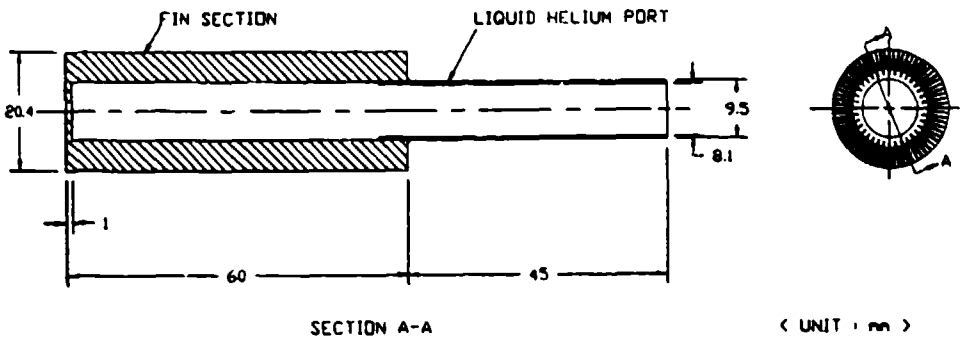

Fig.4. Schematic diagram of the warm end heat exchanger

COLD END HEAT EXCHANGER

The cold end heat exchanger is principally designed to measure the refrigeration power at 1.3 K. During the flow demagnetization process, the cold helium which comes out of the core is heated to 1.8 K by the temperature controlled heater. In order to minimize the A.C. loss, single crystal (quartz , SiO_2) will be tried as the heat exchanger material. Figure 5 shows the schematic diagram of the cold end heat exchanger. The structure of this heat exchanger is quite simple. It consists of 10 disks of single crystals with 91 holes. Because of the manufacturing difficulty , the height of each block was limited to 3 mm. The thermofoil heater is used to heat these blocks so that the exit temperature of helium is being kept at 1.8 K.

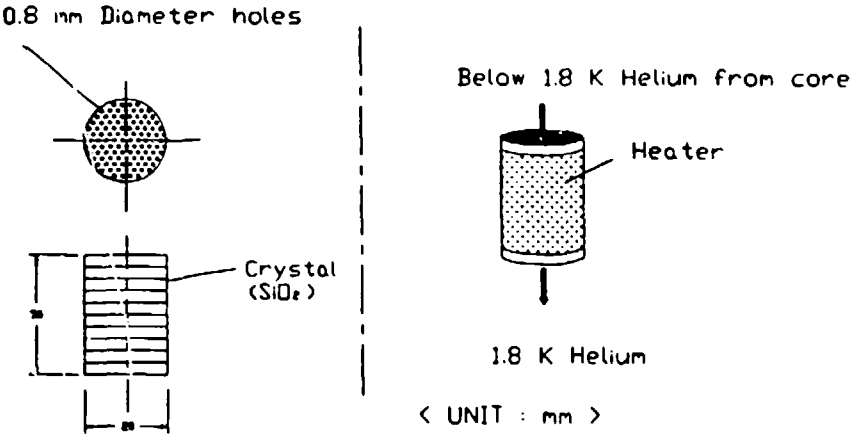

Fig.5. Schematic diagram of the cold end heat exchanger

DISPLACER

The last major component to be discussed here is the displacer. As shown in Figure 6, the large volume of He^3 will be pushed and pulled by the piston, which is accurately fitted to the cylinder. Clearance between the piston and cylinder will be maintained at about 0.025 mm by adjusting the plastic sleeve. Such restricted tolerances will not pose a problem in construction, but some friction may be caused by warping of the cylinder from the improper fitting of the cylinder heads. This displacer is submerged in liquid helium and an indium O-ring will be used for sealing at 4.2 K.

SIMULATION RESULT

In the designed tandem magnetic refrigerator, every GGG sphere in a core follows a different magnetic refrigeration cycle according to its location in temperature coordinates. The computer program was developed to simulate the actual thermal behavior in the magnetic core. It was shown that after a few transient periods, a stable, steady temperature profile in the magnetic core could be obtained.

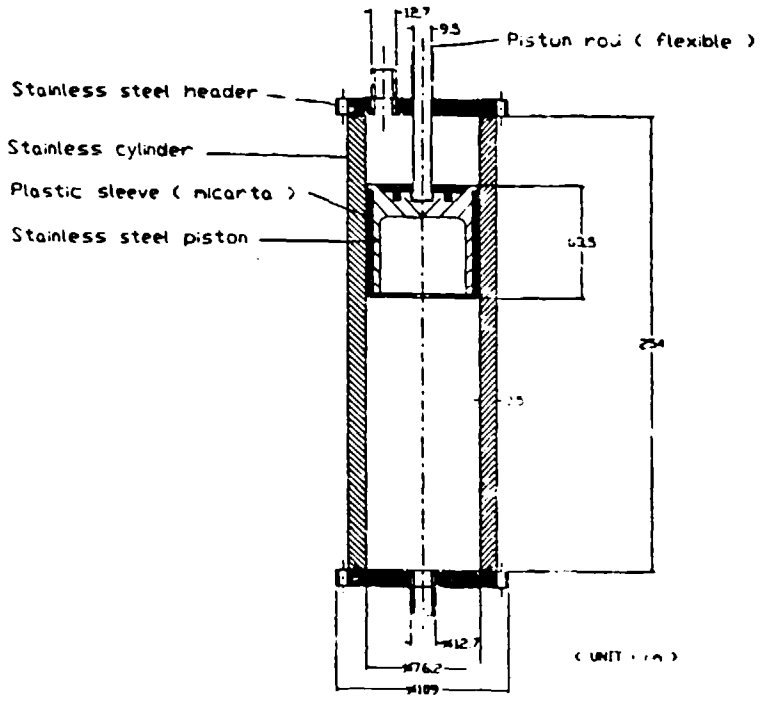

Fig.6. Schematic diagram of the displacer

In this computer simulation, the main considerations are listed below.

(1) Thermodynamic properties[3,4] of GGG and He^3
(2) Estimation of the actual heat transfer coefficient[5] in core
(3) Unsteady temperature profile development
(4) Breathing effect of porous core

The major calculation parameters are:

(1) Warm reservoir temperature ---------- 4.2 K,
(2) Cold reservoir temperature ---------- 1.8 K,
(3) Amount of GGG ---------- 135 g * 2,
(4) Core volume ---------- 30.5 cc * 2,
(5) Core diameter ---------- 2.0 cm,
(6) Diameter of GGG spheres ---------- 0.8 mm,
(7) Core porosity ---------- 0.38,
(8) Operating pressure of He^3 ---------- 0.053 atm,
(9) # of segments in axial core direction ------- 31 segments,
(10) Total shuttle mass of helium ---------- 0.27 g,
(11) Initial magnetic field ---------- 0.0T,
(12) Final magnetic field ---------- 3.0 T,
(13) Adiabatic magnetic field swing ---------- 0.5 T.

Figures 7 through 10 are the temperature trajectories as the magnetic field varies in one cycle. The different temperature profiles during the flow processes in figure 8 and figure 10 show that the processes are not exactly isothermal. In other words, the field-flow mismatch problem still exists. Figure 11 is also obtained, which shows some typical magnetic cycles of the GGG core in different locations. The intrinsic entropy generation problem can be alleviated by adjusting the magnetic field along the core axis or by changing the core diameter non-uniformly. This is the next task we will try.

The expected refrigeration capacity calculated by the simulation program was 73 mW.

SUMMARY

Thus far, the design of the magnetic refrigeration system for 1.8 K has been discussed. Each component of the system has been designed to optimize its performance.

The main design features are listed below.

(1) GGG ($Gd_3Ga_5O_{12}$) is the proper magnetic material for the temperature range between 1.8 K and 4.2 K.

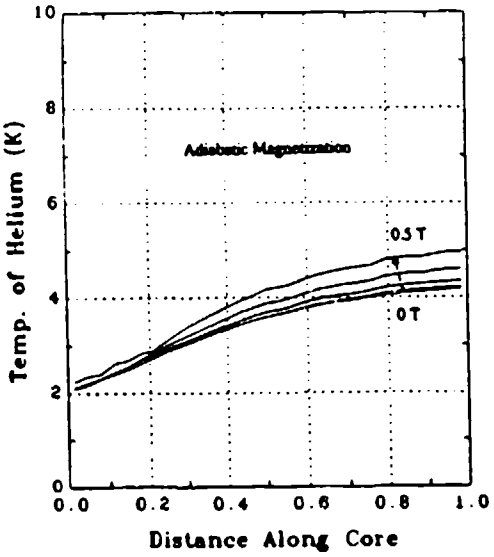

Fig.7. Temperature profiles during adiabatic magnetization

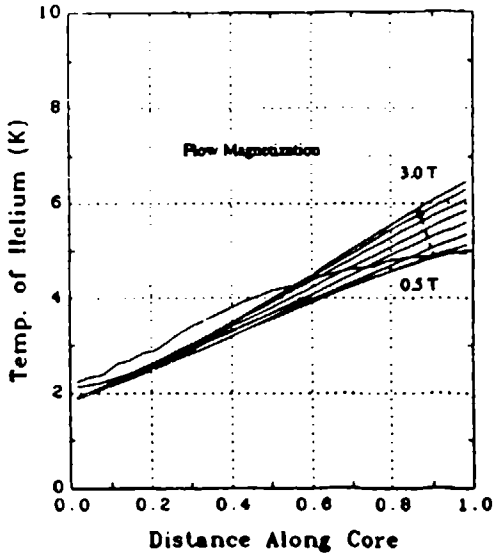

Fig.8. Temperature profiles during flow magnetization

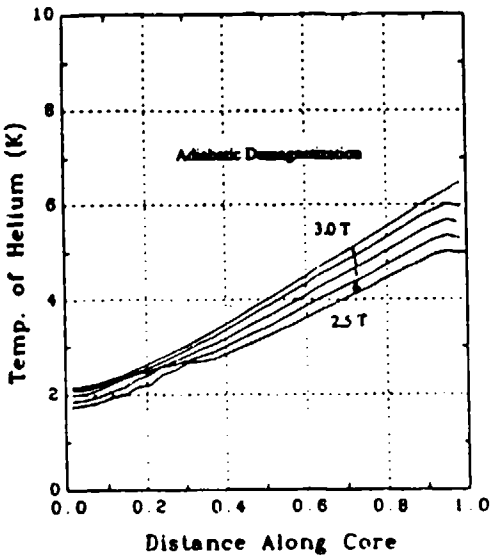

Fig.9. Temperature profiles during adiabatic demagnetization

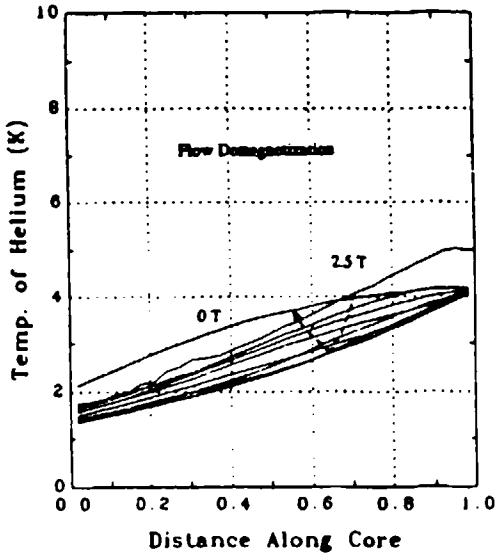

Fig.10 Temperature profiles during flow demagnetization

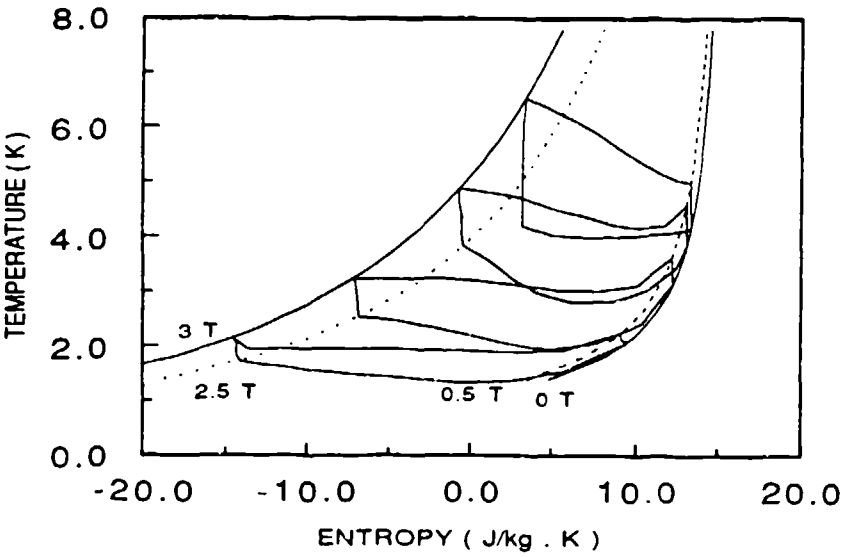

Fig.11. Simulated magnetic cycles in GGG T-S diagram

(2) Low pressure He^3 is the heat transfer medium used for the purpose of reducing the entrainment effect and avoiding superfluidity.
(3) The heat exchangers are located close enough to reduce dead volume.
(4) The heat exchangers have been designed to minimize the eddy current loss.
(5) A tandem system is implemented to make it possible to transfer magnetic energy from one magnet to the other.
(6) The superconducting magnet consists of a persistent coil and a variational coil which are symmetric exactly.

The prototype of this magnetic refrigeration system is now under construction.

ACKNOWLEDGMENTS

This work has been sponsored by Sumitomo Heavy Industries, Inc., with additional support from National Research Institute for Metals in Japan.

REFERENCES

(1) C.P. Taussig, G.R. Gallagher, J.L. Smith, Jr., and Y. Iwasa, "Magnetic refrigeration based on magnetically active regeneration," *Proc. of the Fourth International Cryo-coolers Conference* (1986) p.79-88.
(2) J.L. Smith, Jr., Y. Iwasa and F.J. Cogswell, "Material and cycle considerations for regenerative magnetic refrigeration," *Advances in Cryogenic Engineering*, vol. 35, Plenum Press, New York (1990), p.1157-1164.
(3) G.R. Gallagher, "Analysis of a magnetically active regenerator," *MIT M.S. Thesis* (

1986).
(4) S.G. Sydoriak et al., "The 1962 He^3 scale of temperatures, II. Derivation," *Journal of Res. NBS-A*, vol. 68A, no. 6 (1964) p.559-565
(5) W. Kays and A.L. London, *Compact heat exchangers*, McGraw-Hill (1964),p.131

ANALYSIS OF A MAGNETIC REFRIGERATOR OPERATING TEMPERATURE BETWEEN 10 K AND 1.4 K

Takenori Numazawa, Hideo Kimura, Mitsunori Sato and Hiroshi Maeda
National Research Institute of Metals
1-2-1, Sengen, Tsukuba, Ibaraki 305, Japan

Masahiko Takahashi and Hideki Nakagome
Energy Science and Technology Laboratory, Toshiba Co.
4-1, Ukishima-cho, Kawasaki, Kanagawa 210, Japan

ABSTRACT

A magnetic refrigerator which operates on the Carnot cycle between 10 K and 1.4 K has been developed. A pulsed magnet and heat pipe were used to produce various refrigeration temperatures below 4.5 K without moving the magnetic material. A Gifford-McMahon (GM) refrigerator was used as the auxiliary refrigerator. The heat from the magnetic material was transferred to the GM refrigerator through a rejection heat thermal switch. This system could provide temperatures below 2 K directly from 8 K. For the magnetic refrigerants, pure single garnet crystals, $Gd_3Ga_5O_{12}$ (GGG) and $Dy_3Al_5O_{12}$ (DAG) with a diameter of 45 mm and a height of 50 mm, were used. Typical refrigeration capacities were 550 mW at 4.5 K for the DAG magnetic material and 100 mW at 1.8 K for the GGG. The refrigeration temperature could reach 1.35 K in the case of the GGG. The cycle simulation for the GGG which took account of the heat capacity losses was consistent with the experimental data. The Carnot efficiency at 2 K was 17% and the maximum refrigeration power was obtained at the 0.035 Hz cycle. The dominant factors to improve the refrigeration capacity over 400 mW below 2 K are discussed.

INTRODUCTION

Magnetic refrigeration makes use of a magneto-caloric effect by which certain magnetic materials absorb or reject the heat by applying a magnetic field. This effect is due to the entropy changes of the magnetic spin system in the material. Especially below the 20 K region, a few tesla of magnetic field can provide enough entropy change to operate on the Carnot cycle. Some advantages of the magnetic Carnot

cycle have been reported, such as high efficiency, simple operation, compactness and ease in which low temperatures below 4 K are obtained.[1-3]

Liquid helium temperatures below 4 K are important for current cryogenic applications. In these regions, two kinds of magnetic refrigerators have been studied. One is for helium liquefaction at 42 K,[2] and the second for production of superfluid helium II below 2 K.[3] The latter study reported that the magnetic Carnot refrigeration had considerably more advantages with high efficiency and easy operation, as compared with gas-cycle refrigeration. However, these refrigerators used liquid helium as the rejection heat source, with their Carnot cycles operating between only 1.8 K and 4.2 K. In order to extend the operating temperature, it will be necessary to use a cascade cycle. For example, two Carnot cycles, with ranges of 1.8 K to 4.2 K and 4.2 K to 10 K, have to be cascaded. However, with this approach, the system becomes more complex and less efficient.

We have investigated a new 'static' magnetic Carnot refrigerator operating temperature range between 1.4 K and 10 K. A Gifford-McMahon (GM) gas-cycle refrigerator was used to extend the rejection heat temperature of the magnetic refrigerator. A mechanical thermal switch for the rejection heat portion of the cycle was also developed.

First, this paper will describe the structure of the refrigerator and summarize the experimental results. Second, the analysis of the experimental cycles will be investigated by the simulations. Here, the analysis will be focused on the Carnot cycle of the GGG, especially below the 2 K region. The improvement factors for the refrigeration capacity will also be discussed.

STRUCTURE AND EXPERIMENTAL RESULTS

The static magnetic refrigeration system consists mainly of the magnetic material, the heat pipe thermal switch for the absorbing heat, the mechanical contact thermal switch for the rejection heat portion of the cycle, the pulsed magnet and the auxiliary GM refrigerator. For the magnetic refrigerants, pure single garnet crystals, GGG ($Gd_3Ga_5O_{12}$) and DAG ($Dy_3Al_5O_{12}$) with a diameter of 45 mm and a height of 50 mm, were used. Since the description of the structure and the experimental results have been presented elsewhere,[4,5] both the recent reconstruction and some additional data are shown here.

Figure 1 shows the overall view of the refrigeration system. To provide temperatures below 4 K, a closed heat pipe was used. The heat from the magnetic material generated during the magnetization process was transferred through the mechanical thermal switch of the quartz single crystal rod, and then was absorbed by the auxiliary GM refrigerator. The heat transfer rate depended largely on the contact

gap width between the quartz rod and the magnetic material; thus, both surfaces were polished within 0.5 μm of roughness. This mechanical switch attained a heat transfer coefficient over 2 W/K. However, the overall coefficient of the heat rejection part was 3 times less than that of the mechanical switch, because the heat flow path from the magnetic material to the GM refrigerator was considerably longer, as shown in Fig. 2. This length was necessary to decrease the alternating current losses produced by the periodic magnetic field changes during the cycle operation. In order to improve the overall heat transfer rate, the Cu-wire nets were soldered between the GM refrigerator and the Cu rod which was connected to the quartz thermal switch.

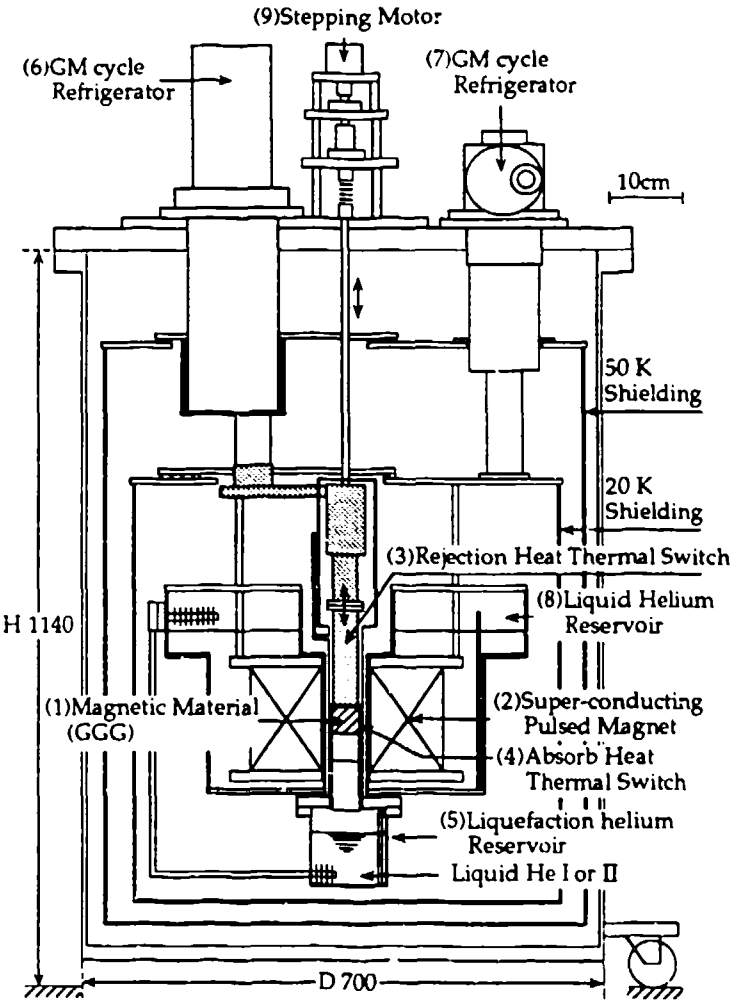

Fig. 1. Overall view of the static magnetic refrigerator.

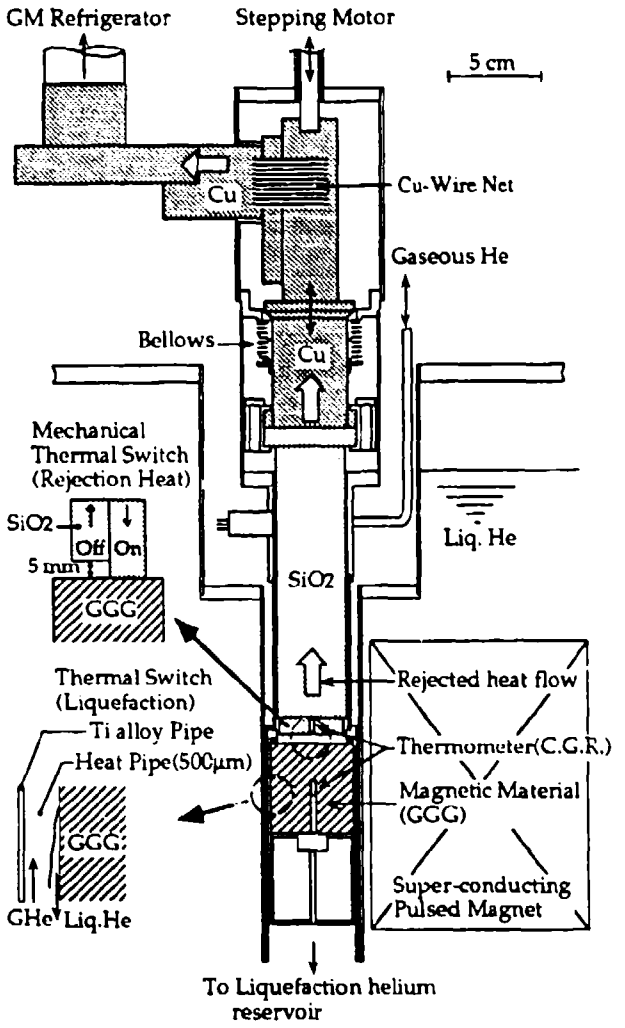

Fig. 2. Details for the thermal switches.

The experiment started at an initial condition of 4.2 K, 1.013 MPa (1 atm). During the cycle operation, the temperature of the liquefaction helium reservoir went down along with the saturation vapor pressure. The refrigeration power was measured by putting the heater power into the reservoir. The temperature variations in the steady cycle, i.e., the input heater power balanced to the refrigeration power at a certain temperature, were within ± 30 mK below the 2 K region. The Carnot cycle, operating between 2 K and 10 K, was stable over 3 hours.

The experimental data for the refrigeration power as a function of the temperature are shown in Fig. 3. It includes the data for the GGG and the DAG

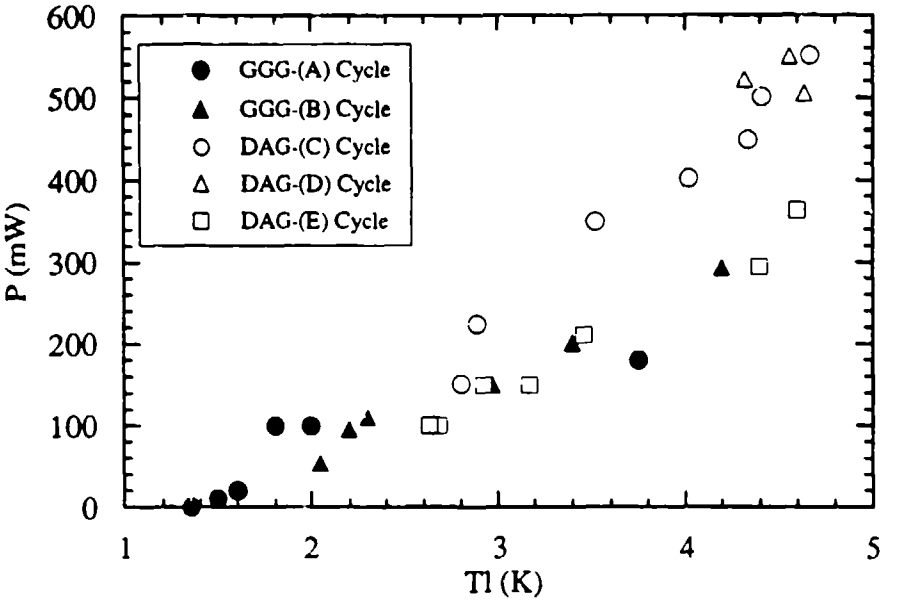

Fig. 3. The experimental results of the refrigeration capacity. The cycle parameters for the GGG are given in Table II.

Table I. Summary of the experimental results.

Refrigeration capacity	100 mW at 1.8 K, 300 mW at 4.4 K for GGG 100 mW at 2.6 K, 550 mW at 4.5 K for DAG
Cooling load temperature	1.35 K to 4.4 K for GGG 2.4 K to 4.5 K for DAG
Cooling load	Helium I or II with electrical heater
Heat rejection temperature	8 K ~ 12 K, depends on the cooling load temperature
Rejection heat source	GM refrigerator, 8 W at 11 K
Heat rejection thermal switch	Mechanical (contact and conduction of helium) 0.7 W/K (average)
Heat absorb thermal switch	Heat pipe (condensation of helium) 2.5 W/K (average)
Heat leaks into the GGG	20 ~ 40 mW/K
Magnetic field operation	Trapezoidal, maximum 5 T
Cycle	Carnot, 30 ~ 60 second period

magnetic materials. The refrigeration power of DAG was larger in the 4 K region, although it could not reach below 2 K. On the other hand, it is clear that the GGG is suitable below 2 K. Since we already fixed the helium leaking problem reported previously, this refrigerator could provide as low as 1.35 K with the GGG material. A summary of the experimental results are shown in Table I.

CYCLE ANALYSIS BY SIMULATION

A trace of temperature variations of the real cycle on the entropy-temperature (S-T) diagram can give information which can be used to analyze the Carnot efficiency and the heat switch performance. Unfortunately, the data obtained were not accurate enough for such a trace on the S-T diagram. The temperature change during the adiabatic magnetization or demagnetization process was too fast to allow the temperature and the magnetic field to be measured accurately at the same time. As a result, the estimated refrigeration power from the trace on the S-T diagram was not consistent with the experimental data.

SIMULATION SCHEME

Figure 4 shows the schematic cycle operation with the parameters of the magnet and the thermal switch. The cycle is determined by the magnetic field operation during T_{f1} to T_{f4} and the heat rejection switch during T_{s1} and T_{s1}. Note that the absorption heat thermal switch (heat pipe) goes on by itself while the temperature of magnetic material (T_m) is below the cooling load temperature.

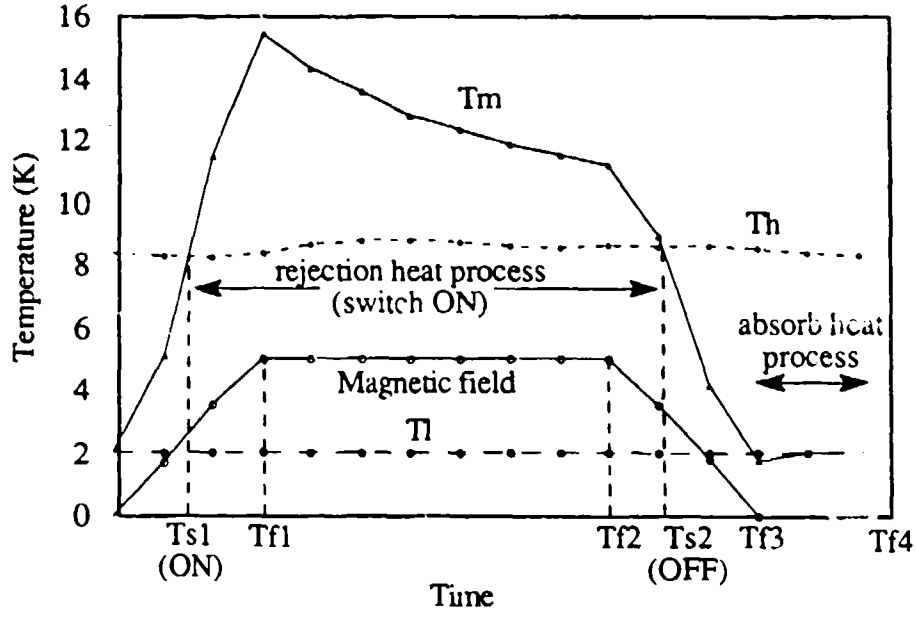

Fig. 4. The schematic cycle of the static magnetic refrigerator.
The control parameters are T_{f1},T_{f2},T_{f3},T_{f4} for the magnet operation and T_{s1},T_{s2} for the rejection heat thermal switch operation.

The energy balance equations for each period of the cycle can be written as follows:

1) Magnetization:

$$q_m = q_{lk} + q_{hc} \qquad (t < t_{s1}) \qquad (1\text{-}1)$$

$$q_m = q_{lk} + q_{hc} + q_{re} \qquad (t_{s1} \le t < t_{f1}) \qquad (1\text{-}2)$$

2) Constant field:

$$q_m = q_{lk} + q_{re} \qquad (t_{f1} \le t < t_{f2}) \qquad (2)$$

3) Demagnetization:

$$q_m = q_{lk} + q_{re} \qquad (t_{f2} \le t < t_{s2}) \qquad (3\text{-}1)$$

$$q_m = q_{lk} + q_{hc} \qquad (t_{s2} \le t \le t_{f3},\ T_m > T_h) \qquad (3\text{-}2)$$

$$q_m = q_{lk} + q_{hc} + q_{ab} \qquad (t_{s2} \le t \le t_{f3},\ T_m \le T_h) \qquad (3\text{-}3)$$

4) Zero field:

$$q_m = q_{lk} + q_{hc} + q_{ab} \qquad (t_{f3} \le t < t_{f4}) \qquad (4)$$

Where q_m = heat change in the GGG material, q_{lk} = heat leaks from the rejection heat switch into the GGG material, q_{hc} = heat capacities around the GGG material, q_{re} = rejected heat from the GGG material into the GM refrigerator and q_{ab} = heat absorbed from the cooling load by the GGG material. These terms are given by the following expressions:

$$q_m = T_m \left[\left(\frac{\partial S}{\partial T_m} \right)_B \frac{dT_m}{dt} + \left(\frac{\partial S}{\partial T_m} \right)_T \frac{dB}{dt} \right] \qquad (5)$$

$$q_{lk} = h_l (T_h - T_m) \qquad (6)$$

$$q_{hc} = h_c (T_c - T_m) \qquad (7)$$

$$q_{ex} = h_e (T_h - T_m) \qquad (8)$$

$$q_{ab} = h_a (T_l - T_m) \qquad (9)$$

Where T_m, T_h, T_c, and T_l are the temperatures of the GGG material and the rejected heat reservoir, the heat capacity, and the cooling load, respectively. S is the entropy of the GGG material and B is the magnetic field.

The heat transfer coefficients, h_l, h_c, h_e were obtained from the experimental results. The coefficient of the condensation heat transfer, h_a, is given by Nusselt and Rohsenow's equation above the λ-point (2.18 K) of helium.[6] Below the λ-point, the following equation has been obtained by Lacaze et al:[7]

$$q_{ab} = 0.008A(T_l^4 - T_m^4) \quad (10)$$

where A is the heat transfer area.

From these equations, we can derive the differential equation about the T_m. Note that T_h and T_l are constant values given by the experimental results. Some heat capacities exist around the GGG material such as gaseous helium in the heat pipe or the housing materials. These capacities behave as an additional heat load for the GGG material. Thus, the equation about T_c is given as follow:

$$q_{hc} = C(T_c)\frac{dT_c}{dt} \quad (11)$$

where $C(T_c)$ is the heat capacity which consists of gaseous helium and titanium alloy used as the housing material. The parameters for the cycle simulation are shown in Table II.

Table II. Parameters used for the cycle simulation.

Size of the GGG	45 mm in diameter, 50 mm in height
Heat transfer area	70.7 cm^2 (absorb heat), 15.9 cm^2 (reject heat)
Heat capacity losses	12.6 cm^3 of gaseous helium 11.7 cm^3 of titanium alloy
Heat transfer coefficients	h_e = 0.7 W/K h_c = 0.1 W/K h_l = 0.02 ~ 0.04 W/K
Experimental cycle (A)	$(T_{f1},T_{f2},T_{f3},T_{f4})$ = (5,15,5,3) unit in second (T_{s1},T_{s2}) = (3,17)
cycle (B)	$(T_{f1},T_{f2},T_{f3},T_{f4})$ = (16.5,15,13.5,4) (T_{s1},T_{s2}) = (3.5,29)
Carnot operating temperature obtained by the cycle (A)	T_l = 1.5 K, T_h = 8.2 K T_l = 2.0 K, T_h = 8.5 K T_l = 2.9 K, T_h = 9.3 K T_l = 4.4 K, T_h = 11.0 K

RESULTS OF THE SIMULATION

Comparison with Experimental Results

The calculated results for the refrigeration power (W) as a function of the cooling load temperature are shown in Fig. 5. Here, two kinds of cycles, (A) and (B), are used for the calculation. These curves almost agreed with the experimental results. The (B) cycle gives the smaller power than (A). This difference depends on the cycle period. At 2.0 K, the (A) cycle provides 100 mW, and it seems that the lowest temperature without the cooling load will reach to 1.4 K, where the refrigeration power will balance the heat leaks and the heat capacity losses. Figure 6 shows the Carnot efficiency, which is defined by the ratio of the calculated (C.O.P.) to the (C.O.P.) of the ideal cycle.

The efficiency of the (B) cycle was larger than that of the (A) cycle above 1.8 K. It is clear that the longer period in (B) provides a higher heat transfer efficiency. On the contrary, in the lower temperature range, the (A) cycle was larger, because the refrigeration power in the cycle (B) became almost zero. The calculation results indicated that the Carnot efficiency might be 17% at 2 K with 100 mW and 7% at 1.5 K without the cooling load.

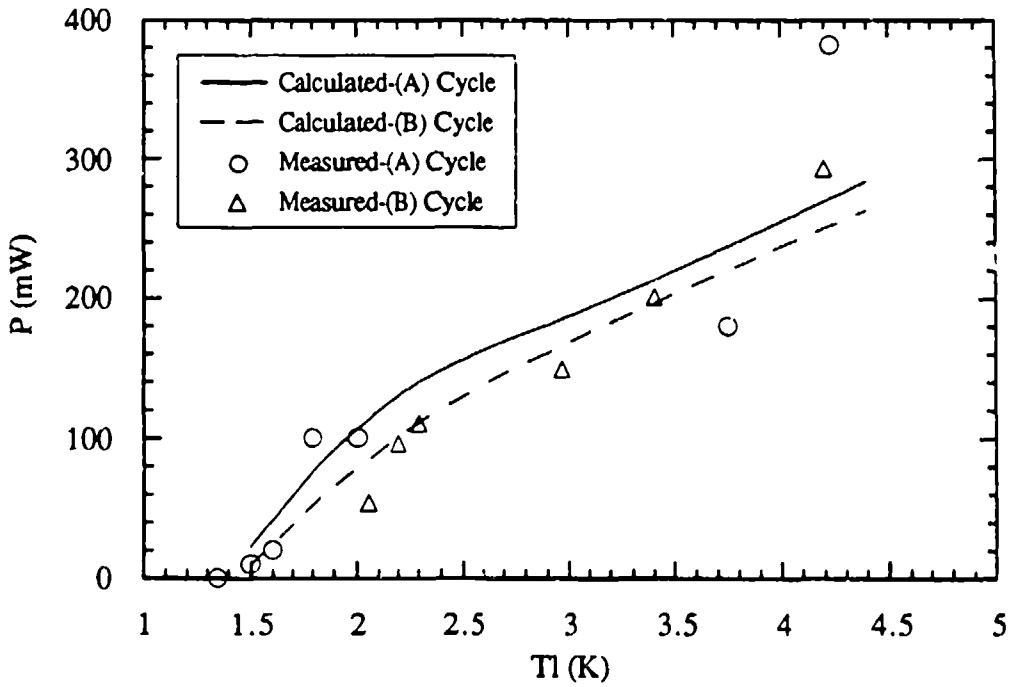

Fig. 5. Calculation results for the Tl dependence of the refrigeration power.

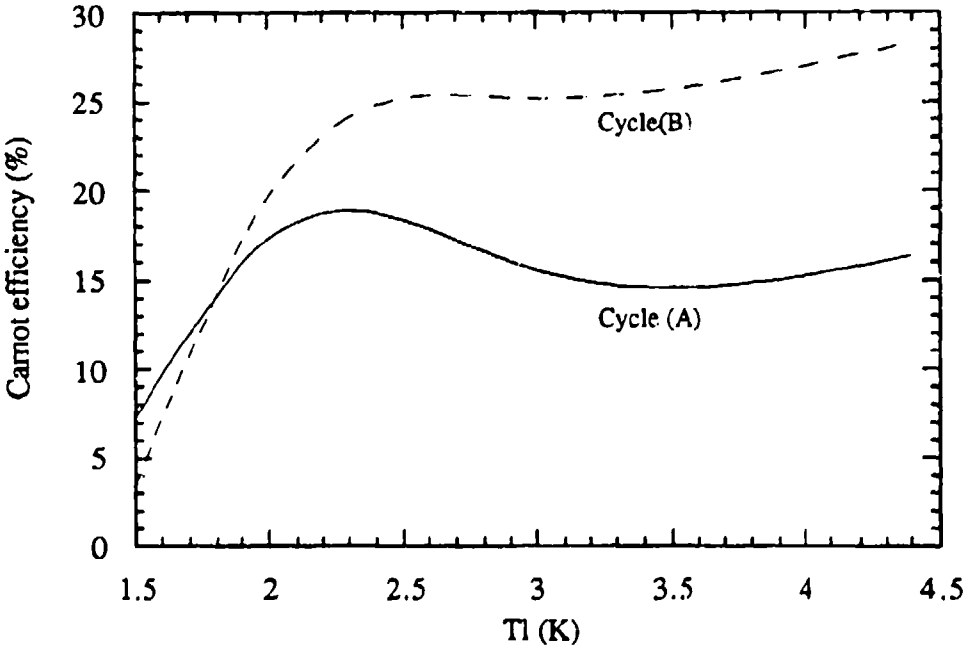

Fig. 6. Calculated results for the Carnot efficiency.

Cycle Frequency

It is important to know what frequency of the cycle gives the maximum refrigeration power. In Fig. 7, the calculation results for the frequency dependence and the Carnot efficiency at T1 = 2 K are shown. The (A) cycle pattern was used here. The power indicated the maximum around 0.035 Hz, i.e., 28.6 second cycle period. The experimental results for this cycle pattern have shown that a 30 second period produced the largest power in the 2 K region. Therefore, it seems that the experimental results gave one of the optimum conditions for the power.

Heat Capacity Losses

In magnetic refrigeration, the heat capacity around the magnetic material behaves as an additional loss. The adiabatic processes of the Carnot cycle can't be realized if this capacity is considerable. Actually, this loss has been seen in previous refrigerators as the unknown factor which decreased the refrigeration power and the efficiency. Although the current system was designed so that this loss was as small as possible, it could not be negligible. Figure 8 shows the refrigeration power as a function

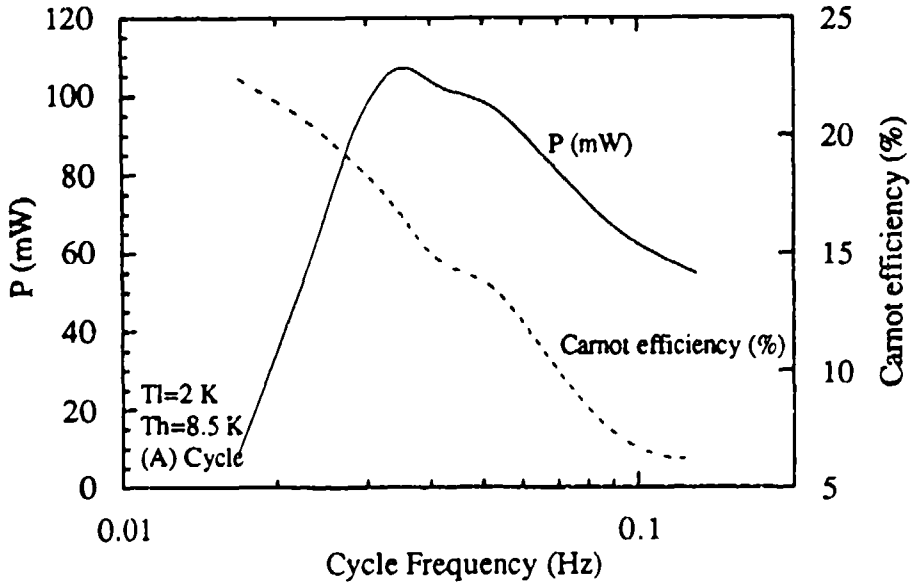

Fig. 7. Calculated results for the frequency dependence of the refrigeration power.

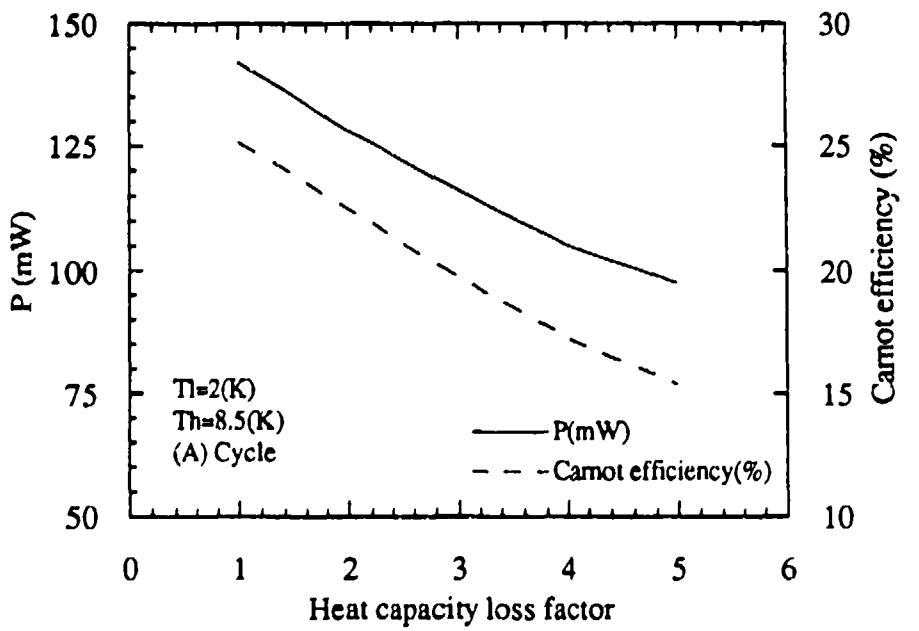

Fig. 8. Calculated results for the heat capacity loss factor dependence.

of the heat capacity loss factor. The factor is normalized by the calculated loss based on the design. The experimental data for 2 K should be 142 mW if the loss is the same as the design value. The experimental result was 100 mW, and indicated that the losses were over 4 times larger than that of the design. It is difficult to specify an exact reason for this difference at this time. However, it may be explained by expanded gaseous helium heated by the GGG producing the forced heat flow, and then the heat flow reaching to the liquefaction helium reservoir. Since only the conduction heat flow is assumed in this calculation, the forced convection heat flow will contribute to a high level of the heat loss. In the present simulation, the value obtained from the experimental result has been used.

FURTHER IMPROVEMENT

In order to improve the refrigeration capacity, some parameter dependencies have been investigated. One of the most interesting simulations is the dependency of the rejection heat temperature. Because of the great amount of current progress in the GM refrigerator, it will be possible to use the lower temperature in the rejection heat source. Figure 9 shows the rejection heat temperature (Th) dependence of the refrigeration power and the Carnot efficiency. It also includes the rejection heat transfer rate dependence. It is clear that the lower Th gives the larger refrigeration power, and its dependence is almost linear. If we use a GM refrigerator with the capacity of 2.7 W at 5 K, the refrigeration power of the magnetic refrigerator at 2 K will be 236 mW and 381 mW in the case of h_e = 1.4 W/K.

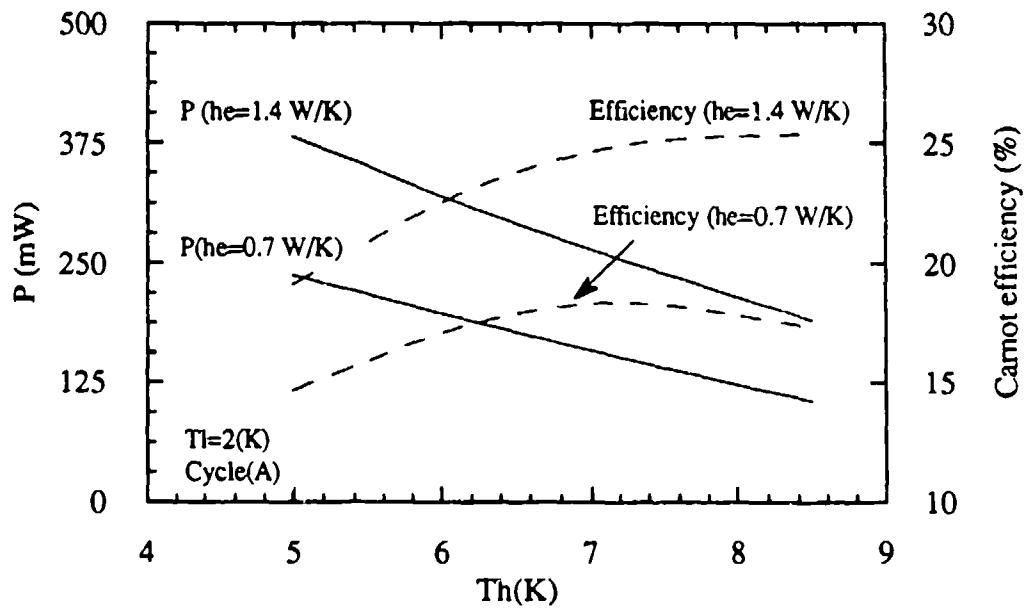

Fig. 9. Calculated results for the Th and he dependence.

The Th dependence of the Carnot efficiency seem to be complex. The Carnot efficiency becomes smaller in the lower Th, and in the case of $h_e = 0.7$ W/K, the broad peak appears around Th = 7 K. This can be explained by the trace on the S-T diagram shown in Fig. 10. The lower Th cycle rejects the larger amount of heat at each temperature level, because the entropy change in the lower temperature becomes larger. Since the heat transfer rate h_e is constant, the inefficiency of the rejection heat process will be larger for the lower Th cycle. It is also confirmed by the calculation for the inefficiency of the rejection heat portion of the cycle. This inefficiency is defined by the ratio of the amount of rejection heat while the rejection thermal switch is on to the rejection heat in the ideal Carnot cycle. The results for $h_e = 0.7$ W/K were 133% at $T_h = 5$ K and 111% at $T_h = 8.5$ K.

We have also taken into consideration how much refrigeration capacity the current system can produce if the dominant parameters are improved. The dominant factors are the overall heat transfer rate in the rejection heat path, the condensation area and the rejection heat temperature. Figure 11 shows the calculated results for several refrigeration temperatures (T_l). It seems that these parameters are not so far from being realized by the current system. The refrigeration capacity will be expected to be 431 mW at 2 K and 216 mW at 1.5 K.

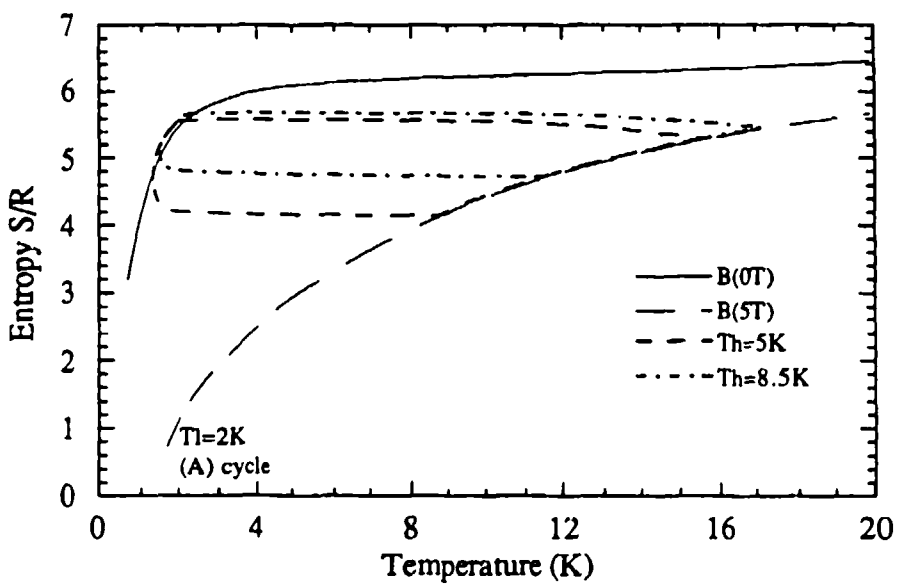

Fig. 10. Traces of the calculation results for the Th dependence on the S-T diagram.

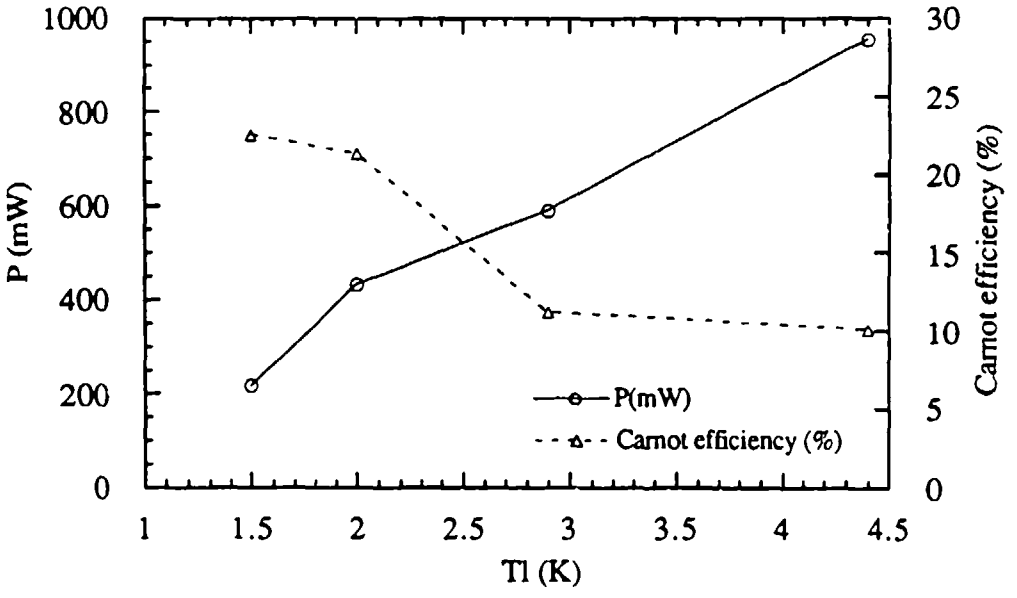

Fig. 11. Calculated results by using the improved parameters; T_h=5 K, h_e=1.4 W/K, condensation area=141 cm^2.

SUMMARY AND CONCLUSION

This paper has described and analyzed the experimental results for the static magnetic refrigerator in the 2 K region. The experimental results were the capacity of 100 mW with the Carnot efficiency of 17% at 2 K and the lowest temperature of 1.35 K without the cooling load. By using the cycle simulation, these results were one of the optimum values. The improvement factors have also been discussed. The capacities of 431 mW at 2 K and 216 mW at 1.5 K will be obtainable given the improved design of the current system. For the next stage, this study will concentrate on the lowest temperature range and should be considered the overall system which will be used in space and in other special applications.

REFERENCES

1. J.A. Barcley, "Magnetic Refrigeration: A Review of a Developing Technology", Advances in Cryogenic Engineering, *33*, 719 (1988).

2. H. Nakagome, N. Tanji, O. Horigami, T. Numazawa, Y. Watanabe and T. Hashimoto, "The helium magnetic refrigerator I: Development and Experimental Results", Advances in Cryogenic Engineering, *29*, 581 (1984).

3. C. Delpuech, R. Beranger, G. Bon Mardoin, G. Claudet and A.A. Lacaze, "Double Acting Reciprocating Magnetic Refrigerator: First Experiments", Cryogenics, *21*, 579 (1981).

4. T. Numazawa, H. Kimura, M. Sato, H. Maeda, M. Takahashi, R. Hakamada, H. Nakagome and M. Sakamoto, "Static Magnetic Refrigerator I-Cycle Operation-", Proceedings of Third Japanese-Sino Joint Seminar, 95 (1989).

5. T. Numazawa, H. Kimura, M. Sato, H. Maeda, M. Takahashi and H. Nakagome, "A Study of Static Magnetic Refrigerator", Cryogenics, to be published.

6. W.M. Rosenow, Film Condensation, chap. 12 in *"Handbook of Heat Transfer"*, McGraw–Hill Book Company, New York, 1973.

7. A.F. Lacaze, R. Beranger, G. Bon Mardion, G. Claudet and A.A. Lacaze, "Double Acting Magnetic Refrigerator: Recent Improvements", Advances in Cryogenic Engineering, *29*, 573 (1984).

A PRELIMINARY NUMERICAL STUDY OF MAGNETIC REFRIGERATION

C. Carpetis
Institute for Technical Thermodynamics
German Aerospace Research Establishment (DLR)
7000 Stuttgart 80, F.R. Germany

ABSTRACT

The basic computational model is a thermodynamic cycle simulation starting with given temperature distribution in the magnetic substance (refrigerant). Temperature changes and magnetic forces are calculated for discrete material segments at a number of time intervals over a complete operation cycle. The computation of the change in magnetic entropy is based on the molecular field theory and the calculation of the flow and heat transfer irreversibilities is based on the heat transfer properties of packed beds.

In the case of an active magnetic refrigerator the temperature distribution in the refrigerant is determined through numerical solution of the differential equations which describe the heat transfer between the refrigerant and the heat transfer fluid. The simulation illustrates the cool-down procedure and the time-dependent temperature profiles in the active magnetic refrigerator until a steady cyclic state is established.

Computational results are given for both magnetic refrigerator stages with external regenerator and the active magnetic regenerative refrigerators. The quality factor and the power density are calculated as a function of the temperature span and the operational frequency. Two sample refrigerants (Gd and GdNi) have been considered.

1. INTRODUCTION

The primary motivation for recent research efforts in magnetocaloric refrigeration[1] has been the expectation that magnetic refrigerators will be more efficient than gas compression-expansion systems. However, it still remains to be seen how close (and at what cost) the perfomance of the magnetic refrigerator can approach to the "Carnot-machine" ideal.

As a better understanding of the loss mechanisms in the magnetic refrigerator is needed, more detailed analytical modeling and investigation become important. The analytical approach described in this paper illustrates the influence of several design parameters on the

major loss mechanisms and on the resulting quality factor and power density. Results for two ferromagnetic materials, Gd and GdNi alloy, serving as refrigerants in the range 300 to 250 K and 67 to about 40 K respectively, are presented here. After a short description of the computational approach, the results for the magnetic Brayton process with external regeneration are presented. After the determination of the quasi-stationary temperature profiles in the refrigerant, similar results are presented for the corresponding case with active magnetic regeneration.

2. ANALYSIS APPROACH

2.1 COMPUTATIONAL MODELS

The initially developed model is essentially a simulation of a thermodynamic cycle starting with a given temperature state of the refrigerant. The magnetization and demagnetization processes are simulated for several time intervals. For each time interval the magnetic entropy is calculated for several discrete refrigerant segments by means of the molecular field theory. The temperature change and the magnetic forces are then calculated for each segment. Thus, the work expenditure for one thermodynamic cycle can be calculated. Heat transfer from the refrigerant occurs under a constant magnetic field and is calculated for constant mass flow of the heat transfer fluid. For the results presented in this paper the heat transfer properties of packed beds are used for the calculation of the entropy production due to non-zero temperature differences (between the magnetic substance and fluid) and to flow friction.

The second model has been developed to account for the particular attributes of the active magnetic regenerative refrigerator (AMRR). In this model it is essential that a temperature gradient is established along the flow direction of the heat transfer fluid. Thus, each refrigerant segment acts like an "elementary" refrigerator operating between two temperatures dependent on the position of the segment along the flow axis. The fluid flow alternates here. After demagnetization the flow is directed from the hot to the cold end of the refrigerant, cooling the load. This "stroke" is called the cold blow (CB). After magnetization, the fluid flows in the opposite direction, transferring the magnetization heat to the high temperature reservoir. This stroke is called the warm blow (WB).

The problem of unsteady heat transfer must be solved for both heat transfer periods (strokes) of the thermodynamic cycle. The differential energy equations for the refrigerant and the fluid are evaluated for each refrigerant segment and several time intervals, where the

inlet temperature represents the boundary condition. Thus, the temperature distributions in the refrigerant at the end of the cold blow (CB) and warm blow (WB) can be determined and used as the starting conditions for the calculation of the temperature distribution after magnetization and demagnetization respectively. A complete thermodynamic cycle can then be simulated. Starting from the initial state the calculation can be repeated for several cycles until a steady cyclic state is attained, effectively simulating the cool-down procedure. A similar analysis for an AMRR stage with no refrigeration load (thus determining the maximum temperature span) has been published by Matsumoto and Hashimoto.[2] Following the simulation of the cool-down, the work expenditure, losses, and efficiency, etc. are calculated in essentially the same manner as described above for the first model.

2.2 SIMULATION OF THE MAGNETIC BRAYTON PROCESS WITH EXTERNAL REGENERATOR

The simulation is based on the first model described above. In addition, the external regenerator is modeled by a minimum of ten isothermal stages[3] with essentially the same flow control as described by Jaeger et. al.[3]. Only steady state operation has been simulated. The simulation is initiated by defining the four temperature values at the beginning and the end of the low-field and high-field regeneration phases. This also defines the temperature change of the refrigerant during heat transfer to the low-temperature heat exchanger and hence to the refrigeration load.

2.3 SIMULATION OF THE MAGNETIC BRAYTON CYCLE WITH ACTIVE MAGNETIC REGENERATOR

A numerical simulation based on the second model outlined in section 2.1 starts with a given temperature state (e.g. uniform temperature) in the refrigerant. A variable thermal load can be simulated at the cold end. For a constant load condition a steady cyclic state can usually be established after 30 to 40 periods.

The refrigeration load is simulated in the following manner. During warm blow (WB) the intake fluid temperature at the cold end (Tfcin) is defined to be higher than the average of the fluid temperature (Tfcav) at the cold end during cold blow (CB):

$$Tfcin = Tfcav + DT.$$

The temperature increase DT (typically a few degrees) is a measure of the refrigeration load.

The entropy production, power density, and quality factor, etc. are evaluated for the steady cyclic state. Plots of the temperature distribution in the refrigerant at various instants in the cycle (e.g. after magnetization, warm blow, demagnetization, cold blow) are particularly useful, especially in the identification of mismatched cases: e.g. unfavorable operating temperature levels for a specific refrigerant, too high fluid mass flow, etc.

2.4 THE DEFINITION OF THE IDEAL CARNOT-CYCLE USED AS A REFERENCE

The coefficient of performance (COP) of a real refrigerator is defined as:

$$COP_{real} = Q/W$$

where Q is the useful refrigeration and W is the work expenditure for one cycle. The quality factor (QF), that is the percent Carnot efficiency, is then related to the COPideal of the corresponding ideal Carnot cycle:

$$QF = \%\text{Carnot efficiency} = COP_{real}/COP_{ideal}$$

However, what is the "corresponding" Carnot cycle? The real Brayton cycle as well as all cycles that can be achieved with active magnetic regenerators have a non-isothermal load, whereas they have to be compared with an isothermal-load ideal, the Carnot cycle. An earlier paper questioning the justification of using the Carnot ideal for comparing real cycles was given by Jacobs.[4]

In fact, defining the ideal Carnot cycle by using the lower and upper temperatures of the hot and cold heat exchangers is not realistic, because it arbitrarily penalizes the real processes. The usage of the entropic average (Tm) for the equivalent isothermal heat transfer as discussed for example by G. Alefeld[5] avoids this discrepancy. The definition $Tm = Q/DS$ more realistically portrays the non-isothermal heat exchange (transfer of the heat quantity Q by changing entropy by DS), without the arbitrary assumptions mentioned previously. In this study the ideal Carnot cycle is therefore defined by using the entropic average temperature of the high and low-temperature heat exchangers.

2.5 EFFICIENCY LOSSES

In the discussion of the results given in the next sections three mechanisms of efficiency loss related to the Carnot ideal are identified. The losses are denoted L1, L2, and L3, so that

Real cycle efficiency = ideal Carnot efficiency -L1 -L2 -L3

The losses L2 and L3 are due to the entropy production during heat transfer between fluid and refrigerant:

L2 = loss due to heat transfer across non zero temperature difference
L3 = fluid frictional loss

The remaining loss L1 corresponds to the entropy production (inherent to the entropy function of the refrigerant) which would be present even if the heat transfer would be reversible (that is if L2 = L3 = 0):

L1 = refrigerant cycle inefficiency

The efficiency loss L1 occurs because the real entropy function of the refrigerant does not fulfill the conditions necessary for reversible magnetic cycle operation.

In the case of a magnetic Brayton cycle with external regenerator, where the refrigerant mass[6] is changing temperature as a whole, the cause is easily identified. Perfect regeneration requires parallel entropy-temperature isofield curves, which is not satisfied by the entropy function of the ferromagnet.

In the case of the active magnetic regenerator the "regeneration effect" is attained by cascading "elementary" refrigerators, each operating (within a "differential" refrigerant segment) between two local temperature levels (Tc at B = 0 and Th at B » 0). As initially pointed out by Taussig et. al.[7], if every elementary refrigerator is to operate reversibly, then the ratio Th/Tc should be a constant along the flow axis. The real entropy functions of the ferromagnets do not allow this condition to be fulfilled. The resulting (non-ideal) temperature distribution causes the elementary refrigerators to work inefficiently. Thus,the loss L1 is the combined effect of all the local enthalpy flux -temperature mismatchings.

3. RESULTS

3.1 GENERAL REMARKS

The most significant variable to be considered in the following presentation is the total heat transfer duration per cycle (htd) which accounts for

a) the heat transfer to the hot and cold heat reservoir and for the regenerative heat transfer in the case of external regeneration

b) the warm and cold blow duration in the case of active magnetic regeneration.

The time (htd) is the significant part of the cycle duration (tc):
tc = htd + time for the adiabatic parts of the cycle
The cycle duration (tc) or the operational frequency (1/tc) is normally considered the critical variable. However, depending on the design of the particular device, the adiabatic part of the cycle is usually much shorter than htd and does not significantly contribute to the main loss mechanisms (in contrast, htd strongly affects L2 and L3). Thus, for generality we prefer to consider htd as the significant variable.

The other critical variable is the temperature span of the refrigerator stage, which is defined by using average entropic temperatures (see section 2.4). It strongly affects the losses L1. In some diagrams, the upper temperature average, denoted Thot, is held constant, whereas the lower entropic average is the independent variable.

In all cases discussed here gaseous heat transfer fluid has been considered. Its mass flow is denoted by mf. The maximum magnetic field (Bmax), the gas pressure level, and the particle size in the refrigerant bed have been varied, but the results cannot be appropriately covered in this paper. The particle size is an especially important variable, because it defines the optimum trade off between losses L2 and L3 (the frictional and heat transfer losses). It has been varied between 0.3 and 3 mm. The optimal size for each particular case (minimizing L2 + L3) has been used for the results provided in the following sections.

3.2 REFRIGERATOR STAGES WITH EXTERNAL REGENERATION

In figure 1 the real cycle efficiency (QF) and the inefficiencies L1, L2, L3 are compared for different temperature spans (40 and 58 K) and heat transfer durations (18 sec and 38 sec). The refrigerant used here is Gadolinium (Thot = 295 K).

The corresponding results for GdNi alloy (Thot=73 K) are given in figure 2.

In both cases it can be seen that the "magnetic cycle inefficiency" (L1) (increasing with the temperature span) is at least as significant as the heat transfer losses L2 and L3 (which increase for shorter htd).

In figure 3 (Gadolinium) and figure 4 (GdNi alloy) the quality factor is plotted as a function of the lower (cold end) temperature

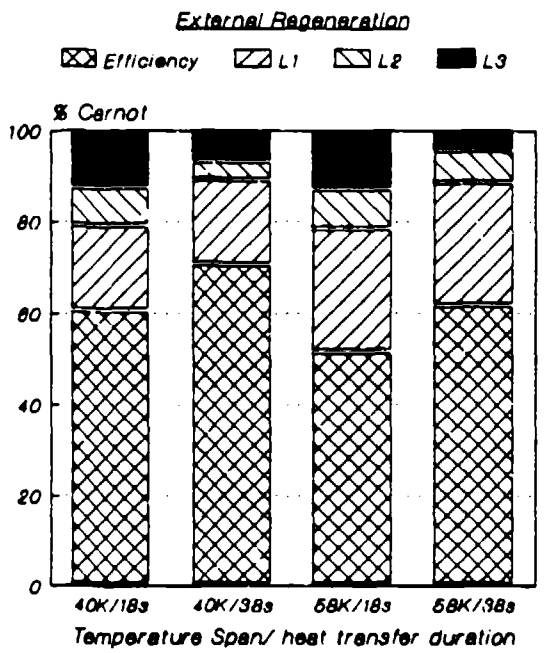

Fig.1 Real cycle efficiency and losses L1,L2,L3 for Gd ; Bmax=6 Tesla ; Thot=295 K

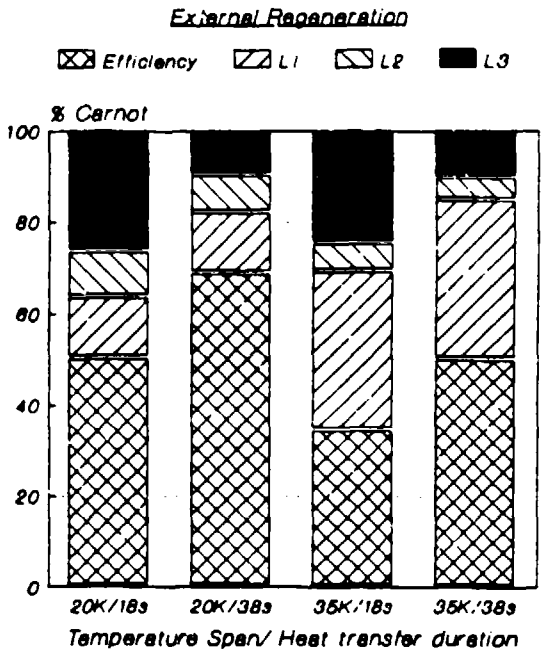

Fig.2 Real cycle efficiency and losses L1,L2,L3 for GdNi ; Bmax=6 Tesla ; Thot=74 K

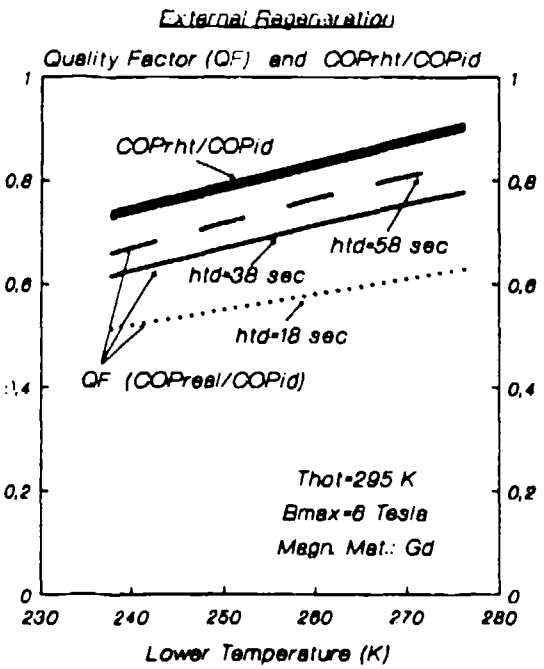

Fig.3 Quality Factor (COPreal/COPid) and ratio COPrht/COPid, for Gd

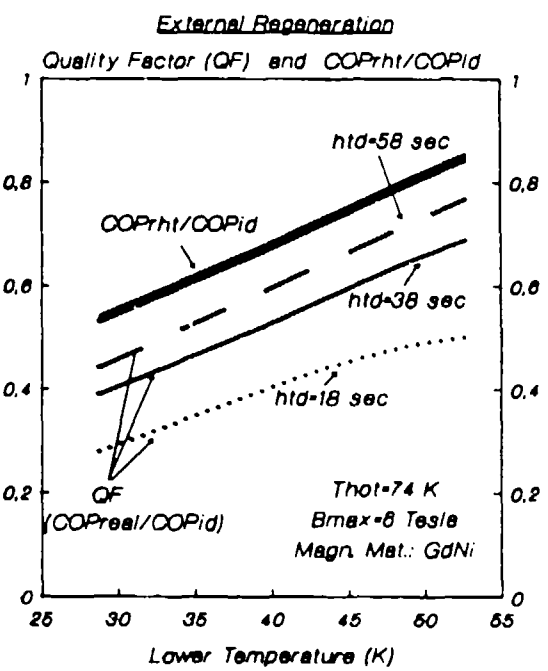

Fig.4 Quality Factor (COPreal/COPid) and ratio COPrht/COPid, for GdNi

for several values of the heat transfer duration htd. In order to differentiate the influence of the loss (L1) from that of the other losses (L2 + L3), the ratio COPrht/COPideal is also plotted. COPrht represents the coefficient of performance for the case of reversible heat transfer between refrigerant and fluid. The loss of efficiency in this case, which increases with the temperature span, is due to the non-ideal entropy function of the refrigerant (discussed in section 2.5). The additional heat transfer losses (L2 + L3) result in the lower efficiency of the real cycle. They are higher for shorter htd values, as shown in the figures. Heat transfer durations of at least 20 sec appear to be necessary in order to achieve favorable quality factors. However, the gain in efficiency is not proportional to the increase in htd, so that very long cycle durations are of minor advantage in this respect.

3.3 ACTIVE MAGNETIC REGENERATIVE REFRIGERATION (AMRR)

Prior to presenting similar results for the AMRR, some results concerning cool-down behavior and temperature profiles in the active magnetic regenerator will be discussed. For these results the heat transfer duration (time for warm and cold blow) is assumed to be htd = 8 sec. The temperature profiles in the refrigerant are shown for the steady cyclic state.

Figure 5 shows the cool-down of an AMRR stage with Gadolinium as refrigerant. The intake fluid temperature during warm blow is assumed to be 8 K higher than the average outlet temperature during cold blow (Tfcin = Tfcav + 8). This corresponds to a refrigeration load of about 18 W/kgMM (Watts per kg of Magnetic Material).

Figure 6 shows the temperature distribution in the refrigerant at the end of the four strokes (magnetization, warm blow, demagnetization, cold blow) as a function of the axial position given in percent of the total refrigerant bed length.

For lower refrigeration loads the temperature at the cold end becomes much lower after the same number of periods:

In figure 7 the cool-down of the Gadolinium AMRR stage initially takes place without load. After 15 periods a load of about 9 W/kgMM is applied according to the condition Tfcin = Tfcav + 4 K. The corresponding temperature distribution in the refrigerant is shown in figure 8. When applied to an AMRR stage with GdNi alloy the identical load condition (Tfcin = Tfcav + 4 after the 15th cycle) will produce much different cool-down conditions:

Figure 9 illustrates the cool-down in this case and figure 10 shows the corresponding temperature distribution. Although the refrigeration is now only about 3.5 W/kgMM, this stage is already "heavily

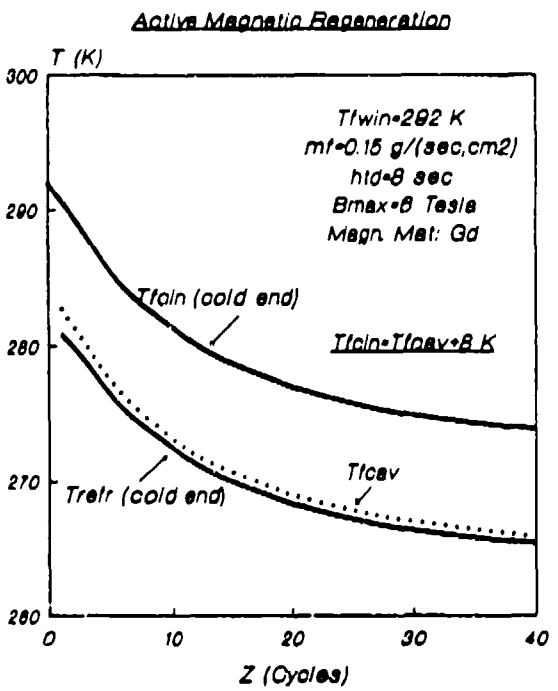

Fig.5 Cool-down of the AMR, Gd stage with constant load (DT=8 K)

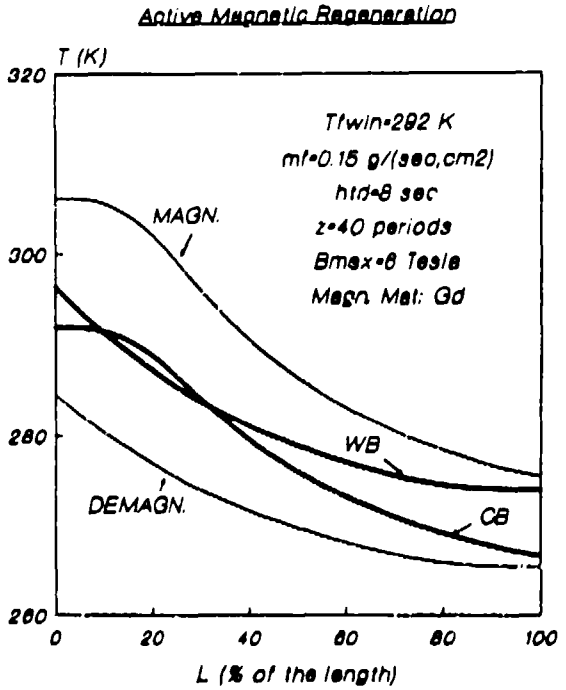

Fig.6 Temperature distribution in the AMR of Fig. 5, after 40 cycles.

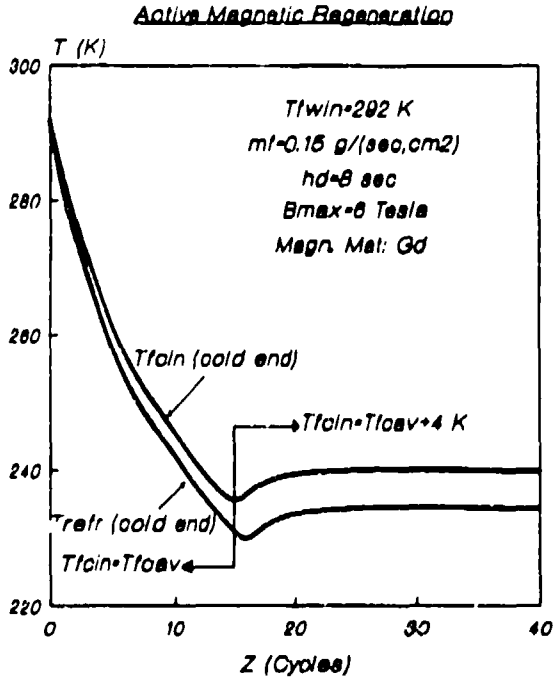

Fig.7 Cool-down of the AMR, Gd stage, with load (DT=4 K) applied after 15 cycles

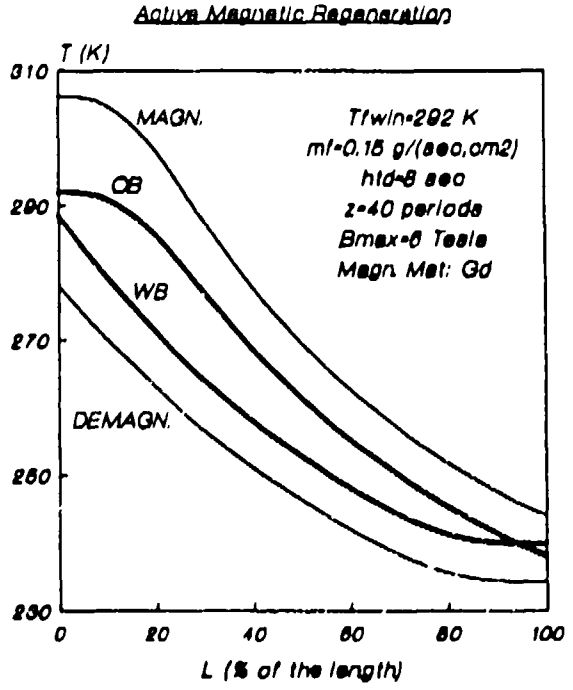

Fig.8 Temperature distribution in the AMR of Fig. 7, after 40 cycles.

loaded", as is the Gadolinium stage of figure 6. This results in a relatively small temperature span at steady cyclic state (Fig. 9). Note that the shape of the temperature distributions after warm blow (WB) and cold blow (CB) in figure 10 are very similar to those of figure 6 for Gadolinium (not to those of figure 8 with the same Tfcin - Tfcav value). In general, the shape of the temperature distribution is an indicator of the extent to which the refrigerant capacity is used.

The refrigeration power of an AMRR stage can be varied by changing the mass flow mf. Increasing mf may result in higher power density, but the penalty in efficiency must be taken into account. The mass flow values used for the results shown in figures 5 to 10 are a trade off between quality factor and power density. The following case (with increased mass flow) is less than optimal in this respect:

The figures 11 and 12 illustrate the operational conditions of the GdNi stage discussed previously, when the fluid mass flow is increased up to 0.14 g/sec/cm2 . As shown in figure 11, the temperature span is now somewhat smaller. In addition, the temperature distributions at cyclic equilibrium (Fig. 12) show the typical attributes of the enthalpy flux-temperature mismatching, which result in lower efficiency. In fact, the quality factor in this case is by about 20% lower compared to the case of figures 9 and 10.

Ultimately, the trade-off between quality factor and refrigeration power density is a matter of economic optimization, which is beyond the scope of the present study.

Further study shows that the magnetic cycle inefficiency (L1) is rather severe in the case of AMRR due to local entropy imbalance losses. In figure 13 for example, the quality factor and the inefficiencies L1, L2, and L3 for an AMRR stage with Gadolinium as refrigerant are compared for various temperature spans and heat transfer durations. The results for an AMRR stage with GdNi as refrigerant are given in figure 14. Because of the high L1 losses, temperature spans as high as those attainable with external regeneration are rather prohibited in the AMRR case.

For constant fluid mass flow the refrigeration power of the AMRR is practically a linear function of the temperature span. Figure 15 shows the dependance of the refrigeration power density on the lower (refrigeration) temperature for the Gadolinium stage. Figure 16 shows the same thing with GdNi as a refrigerant.

In figure 17 (Gadolinium) and figure 18 (GdNi alloy) the quality factor is plotted as a function of the lower (refrigeration) temperature for several values of the heat transfer duration htd. As in figures 3 and 4, the ratio COPrht/COPideal is also plotted as a reference. Heat transfer durations of at least 4 sec per cycle appear to be

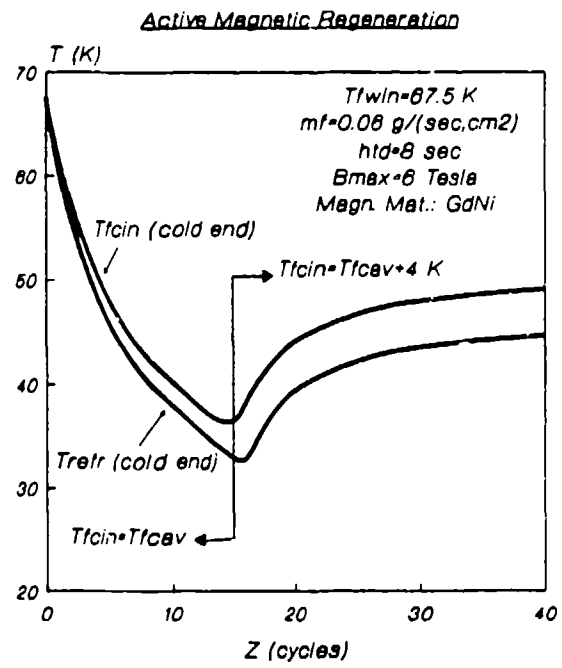

Fig.9 Cool-down of the AMR, GdNi stage, with load (DT=4 K) applied after 15 cycles.

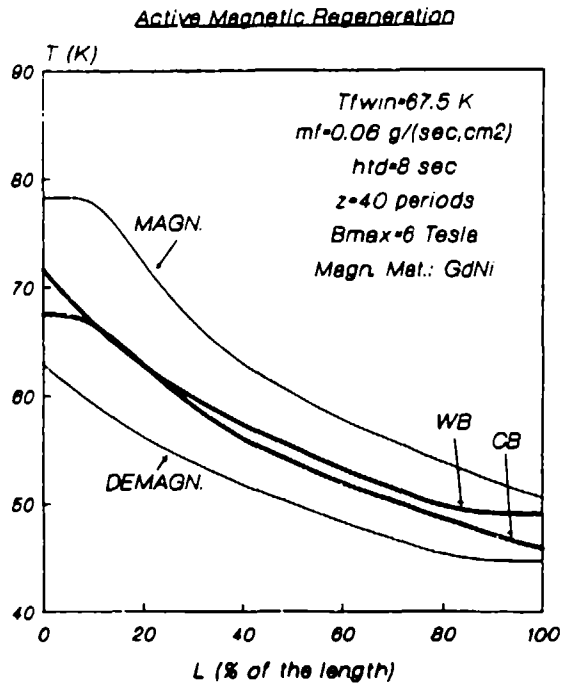

Fig.10 Temperature distribution in the AMR of Fig. 9, after 40 cycles.

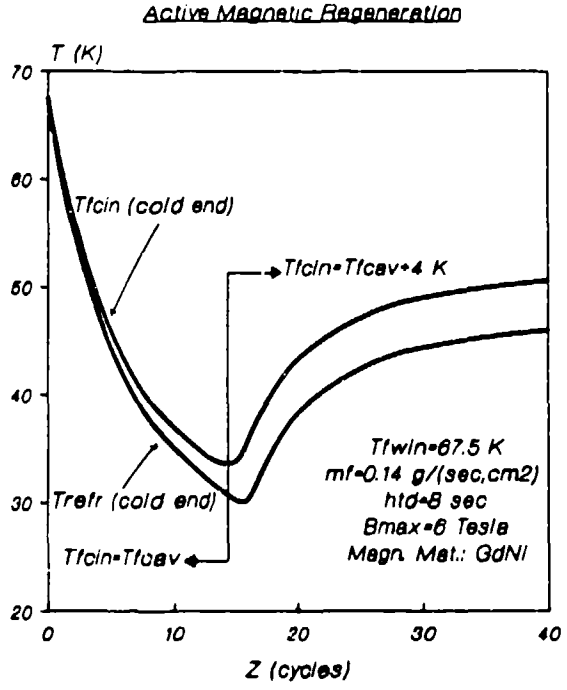

Fig.11 Cool-down of the GdNi stage as in Fig.9, however, with increased mass flow

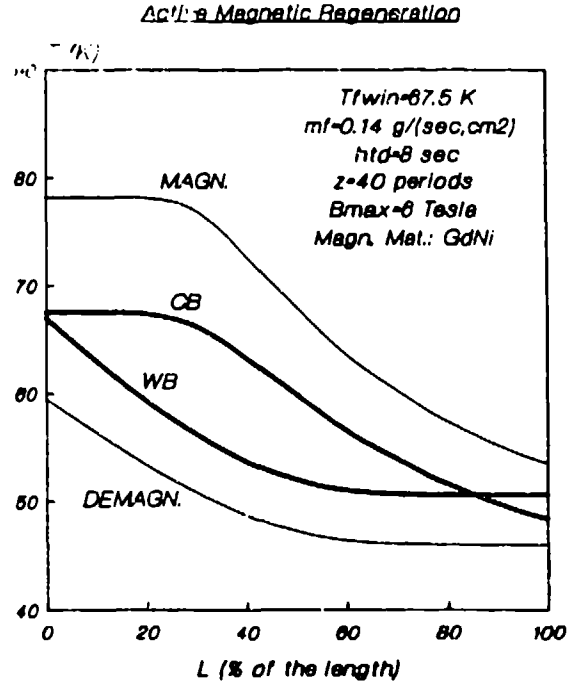

Fig.12 Temperature distribution in the AMR of Fig. 11, after 40 cycles.

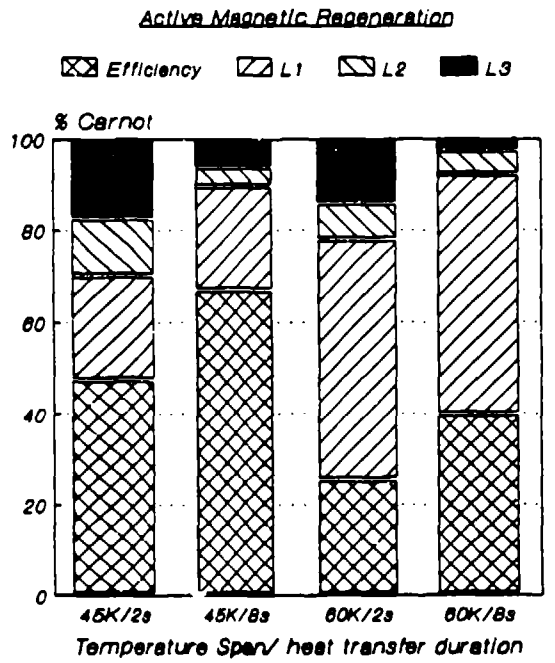

Fig.13 Real cycle efficiency and losses L1,L2,L3 for Gd (Active Magnetic Regenerator) Bmax=6 Tesla; Thot=295 K.

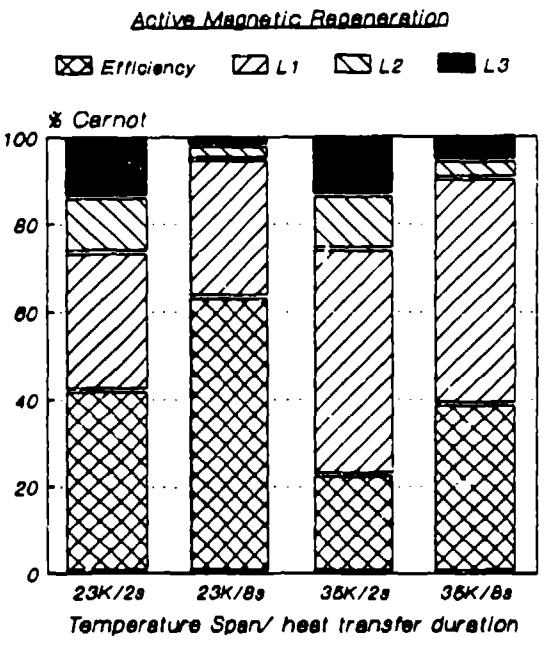

Fig.14 Real cycle efficiency and losses L1,L2,L3 for GdNi (Active Magn. Regenerator) Bmax=6 Tesla; Thot=73 K

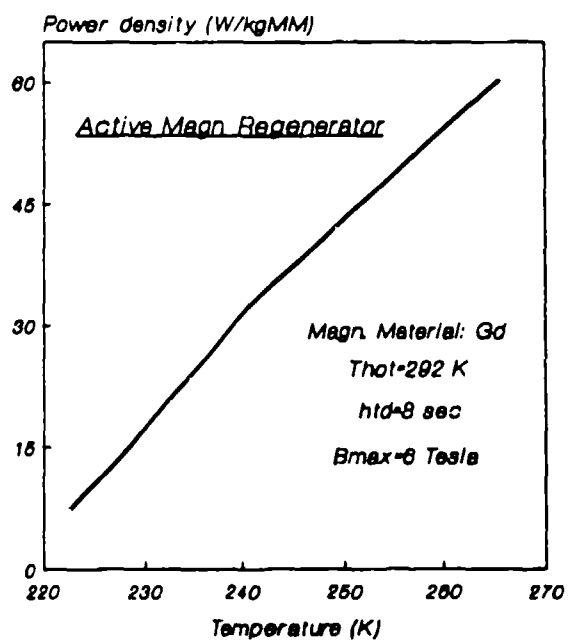

Fig.15 Refrigeration power per Kg of the refrigerant vs. cold end temperature.

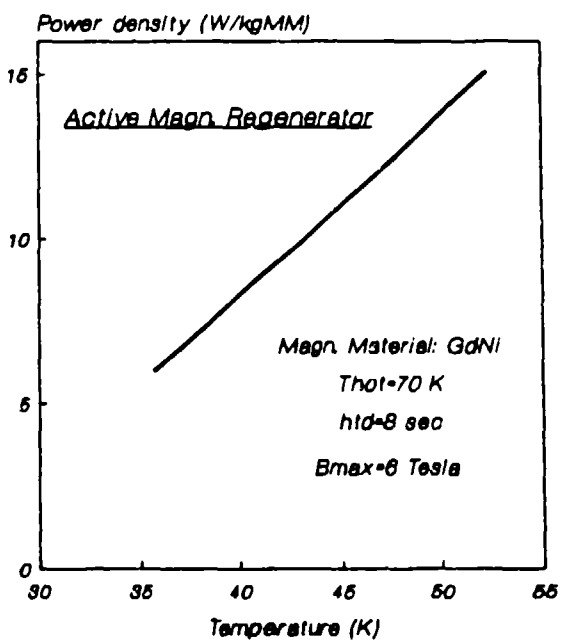

Fig.16 Refrigeration power per kg of the refrigerant vs. cold end temperature.

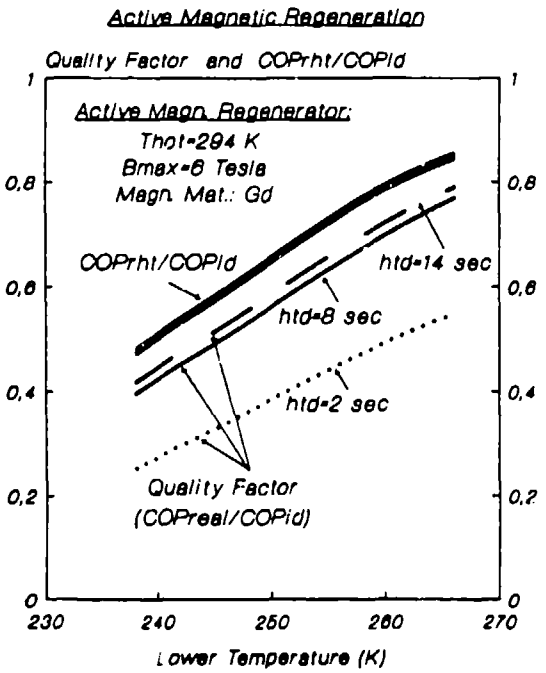

Fig.17 Quality factor (COPreal/COPid) and ratio COPrht/COPid, for Gd

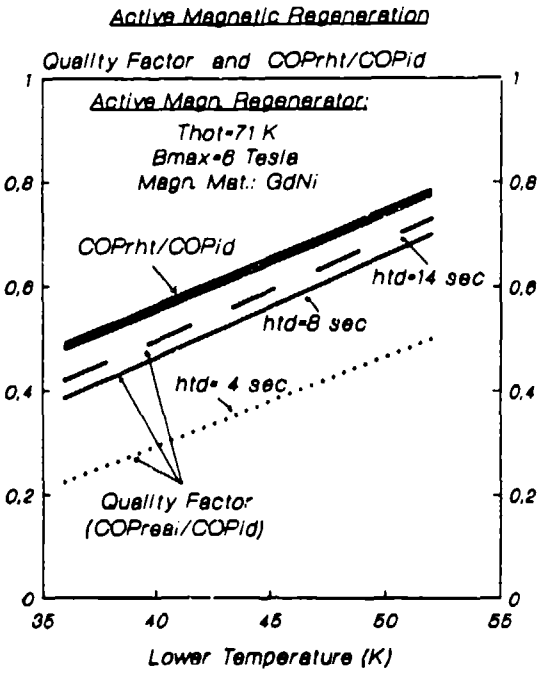

Fig.18 Quality factor (COPreal/COPid) and ratio COPrht/COPid, for GdNi

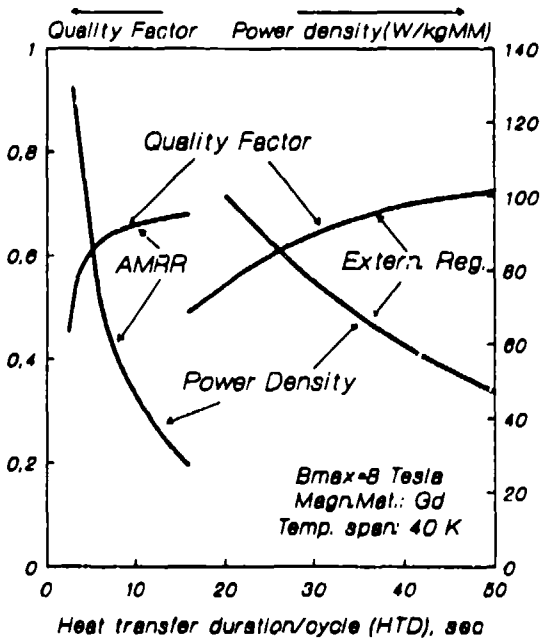

Fig.19 Quality factor and refrigeration power per kg of the magnetic material (Refrigerant: Gd)
(Period= HTD+Time for the adiabatic steps of the cycle)

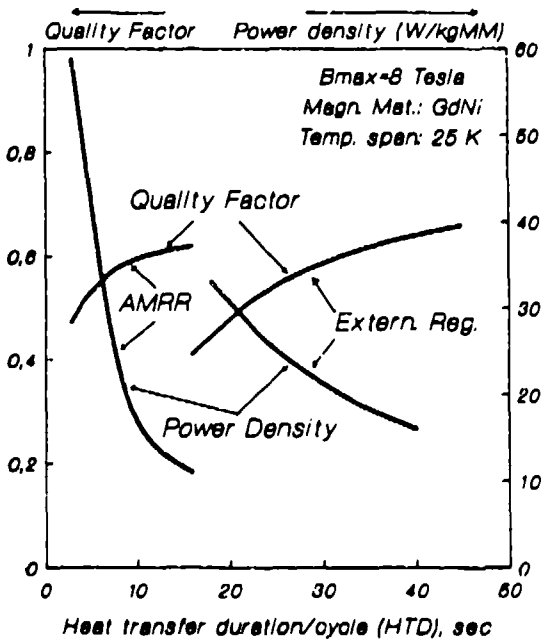

Fig.20 Quality factor and refrigeration power per kg of the magnetic material (Refrigerant: GdNi)
(Period= HTD+Time for the adiabatic steps of the cycle)

necessary in order to achieve favorable quality factors. However, htd values higher than about 10 sec are of minor advantage with respect to efficiency gain.

The cyclic heat transfer durations needed for AMRR operation are therefore, in general, substantially shorter in comparison to those needed with external heat regeneration. However, as will be seen in the next section, this does not result in accordingly higher refrigeration power density. This is because much more refrigerant mass per Joule of refrigeration is needed here. In the absence of an external regenerator the regeneration effect is achieved by cascading the "elementary" refrigerators (see section 2.5). Each of which operates over a correspondingly smaller temperature span, thus making a smaller contribution to the total amount of refrigeration.

4. SUMMARY OF THE RESULTS

The results are summarized in figure 19 and figure 20 for the two refrigerants discussed here. Both the quality factor and the power density (refrigeration per kg of refrigerant) are plotted as functions of the heat transfer duration per cycle. The temperature spans here are a constant 40 K for the Gadolinium stage and 25 K for the GdNi stage. According to the results shown here, these temperature spans can be considered to be realistic for actual applications. Other variables, like particle size in the refrigerant bed for example, have been optimized where possible.

As the figures illustrate, comparable quality factors are achievable with both approaches (external regeneration and active magnetic regeneration). Although the cyclic heat transfer duration with an active magnetic regenerative refrigerator can be substantially shorter, the power density appears to be lower for comparable quality factors. However, it should be kept in mind that the AMRR is more easily controlled. Further, active magnetic regeneration is necessary for non-linear (rotating) magnetic refrigerators.

5. CONCLUSIONS AND PERSPECTIVES

The objective of this paper has been to investigate the major losses, the resulting quality factor and the power density of magnetic refrigerator stages with a unique working material. The real magnetocaloric properties of the refrigerant have been considered. Heat exchange to the transfer fluid occurs under a constant magnetic field. Under these conditions the results show that the operation of magnetic refrigeration systems with efficiencies considerably higher than conventional refrigeration systems is attainable.

A continuation of this work will utilize more detailed analytical models demanding the evaluation of the complete set of differential heat transfer and fluid dynamic equations including all diffusion, convection and source terms for the system consisting of refrigerant, transfer fluid and container. In addition to identifying additional losses not considered in this study, potential options for loss reduction should be revealed.

Additional losses (not covered in this study) are due to heat conduction, convection (especially during adiabatic processes) and to "parasitic" thermal addendum and heat sources. Conduction sources can be minimized to a large degree by proper design, whereas convection losses and thermal addendum can be critical in certain refrigerant-transfer fluid combinations.

On the other hand, there is real potential for reducing the loss (L1) due to the non-ideal isofield entropy function of individual ferromagnets. The literature identifies two ways of doing this:

a) Field-flow phasing and/or field modulation. This idea appeared[8] in early papers, for example in the case of internal regeneration, which is beyond the scope of this study. Applications are discussed for example by Gogswell et. al.[9].

b) The second method is simply not to use a single material for the entire refrigerant bed. Instead, a number of different magnetic materials with different ordering temperatures is blended or "stuffed" together, thus approximating the ideal entropy function at different locations in the bed.[2,7] This type of complex refrigerant has already been demonstrated by Hashimoto et. al.[10]. Note that complex refrigerants are not applicable when every element of the bed is active over the entire temperature range of the stage, as in the case of external regeneration.

The use of complex (blended) refrigerants appears very promising as a means of reducing the loss (L1) in the AMRR case. The computational model described above will be used for the full analysis of the cycle in this case. The final goals of the investigation will be to judge the two basic methods of regeneration (external and active), as well as determine the (economical) trade-off between quality factor and power density.

REFERENCES

1. J.A. Barclay, "Magnetic Refrigeration: A Review of a developing Technology", Advances in Cryogenic Engineering, vol. 33 (1988) p. 719-731

2. K. Matsumoto and T. Hashimoto, "Thermodynamic Analysis of Magnetically Active Regenerator", Proc. Int. Conference on Cryogenics and Refrigeration, Hangzhou, P.R. of China (May 1989)

3. S.R. Jaeger, J.A. Barclay and W.C. Overton, Jr., " Analysis of Magnetic Refrigeration with external Regeneration", Advances in Cryogenic Engineering, vol. 33 (1988) p.751-755.

4. R.B. Jacobs, "The Efficiency of an Ideal Refrigerator", Advances in Cryogenic Engineering, vol. 7 (1962) p.567-571.

5. G. Alefeld, "Efficiency of Compressors Heat Pumps and Refrigerators derived from the Second Law of Thermodynamics" Intern. Journal of Refrigeration, vol. 10, no. 6 (1987) p. 331-341.

6.C.R. Cross, J.A. Barclay e.a., "Optimal Temperature-Entropy Curves for Magnetic Refrigeration", Advances in Cryogenic Engineering", vol. 33 (1988) p.767-775.

7. C.P. Taussig, G.R. Gallager, J.L. Smith and Y. Iwasa, "Magnetic Refrigeration based on Magnetically Active Regeneration", Proccedings 4th Int. Cryocooler Conference, Easton, MD, USA, (September 1986) p. 79-88.

8. G.V. Brown, "Magnetic Heat Pumping near Room Temperature", Journal of Applied Physics, vol. 47,no. 8 (1976) p. 3673-3680.

9. F.J. Gogswell, J.L. Smith,Jr, and Y. Iwasa, "Regenerative Magnetic Refrigeration over the Temperature Range of 4.2 to 15 K", Proceedings 5th Int. Cryocooler Conference, Monterey, Cal., USA, (August 1988) p. 81-90.

10. T. Hashimoto,T. Kuzuhara, A. Tomokiyo and H. Yayama, "New Application of Complex Materials to the Magnetic Refrigerant in an Ericson Magnetic Refrigerator", Journal of Applied Physics, vol. 62 no.9 (1987) p. 3873-3878.

THE MAGNETOCALORIC EFFECT IN NANOCOMPOSITES

Robert D. Shull, Lydon J. Swartzendruber, and Lawrence H. Bennett
Magnetic Materials Group
Materials Science and Engineering Laboratory
National Institute of Standards and Technology
Gaithersburg, Maryland 20899

ABSTRACT

The magnetic properties of nanocomposites containing extremely small magnetic particulates dispersed in a nonmagnetic matrix can be very different than those of the bulk magnetic material. Here we consider the consequences of such a microstructure on the magnetocaloric effect[1]. Upon the application of an external magnetic field, the magnetic spins in a material tend to align with the field, thereby reducing the magnetic entropy of the spin system. If this process is performed adiabatically, the specimen's temperature will rise. The incremental temperature rise, dT, is related to the degree of spin alignment and the magnitude of the magnetic spin moment. Creation of a nanocomposite with many very small ferromagnetic regions provides an effective enhanced magnetic moment which can result in certain temperature and field ranges in an increased dT over that provided by either paramagnetic or ferromagnetic materials, with potential application to magnetic refrigeration. Efficient magnetic refrigerators may then be operated at higher temperatures ($T > 20$ K) or lower fields ($H < 5$ T). The details of how the altered magnetocaloric effect is governed by composition and processing are discussed.

INTRODUCTION

Magnetic refrigeration cycles depend on the reduction in magnetic entropy of the refrigerant as a magnetic field is applied. This reduction in magnetic entropy is a consequence of the partial alignment of the magnetic moments (thereby creating a more "ordered" state) of the atoms comprising the refrigerant. If the field application is performed adiabatically then the lattice entropy is increased by an amount equal to the decrease in magnetic entropy, and the temperature of the refrigerant will increase. The temperature increase, ΔT (also referred to as the magnetocaloric effect), varies with the material. Materials presently used as refrigerants for magnetic refrigeration cycles fall into two categories: (1) paramagnetic substances[2] (e.g. $Gd_3Ga_5O_{12}$, gadolinium gallium garnet, GGG) for use at temperatures up to ~20 K and (2) substances which possess an

ordered magnetic state (e.g. ferromagnetism or antiferromagnetism) at low temperatures[3]. The latter class of refrigerants (e.g. Gd or $DyAl_2$) possess a maximum in ΔT near their magnetic ordering temperatures, and are consequently useful in refrigeration cycles operating at temperatures greater than 20 K. For use at room temperature, however, no materials from either of these two refrigerant types have been found which yet possess a large enough magnetocaloric effect for efficient operation of a magnetic refrigerator. For other applications[4] materials have been atomically engineered to possess the particular properties required. A particularly attractive class of materials which provides a unique laboratory for such atomic engineering of materials with specific magnetic properties is that of nanocomposites (sometimes also referred to as granular metals). These materials[5] are comprised of an intimate mixture of at least two constituent phases (at least one being magnetic) wherein the size scale of one or all species is on the order of a few nanometers. Their magnetic properties are highly composition dependent and can be varied from that related to the constituent phases to that completely different from them by proper processing and composition control. As will be shown in the following sections this class of materials opens up a completely new area for materials development in connection with magnetic refrigeration applications, especially in terms of use at $T > 20$ K. Initially from the basic differential equation expressing the magnetocaloric effect in terms of the important material properties derivations will be presented for the magnetocaloric effect possessed by paramagnetic materials, ferromagnetic materials, and nanocomposite materials exhibiting superparamagnetic behavior. The paper will conclude with recent preliminary experimental results on an iron+silica gel magnetic nanocomposite which exhibits an enhanced magnetocaloric effect in this latter class of materials.

MAGNETOCALORIC EFFECT

According to classical thermodynamics, the change in total internal energy, dU, of a system (defined here as the lattice and magnetic spins of the atoms on the lattice) due to work, dW, performed by the system on its surroundings is expressed as $dU = dQ - dW$, where dQ is the incremental change in heat of the system. This expression can be expanded in terms of the relations $dQ = TdS$ and $dW = PdV - \sum \mu_i dN_i - \mu_o VHdM$, where T, P, μ_i, and H are the temperature, pressure, molar chemical potential of species "i", and magnetic field respectively. dS, dV, dN_i, and dM are the changes in entropy, volume, number of moles of species "i", and volume magnetization respectively of the system. The three terms in the dW expression are from left to right the mechanical, chemical, and magnetic work performed by the system. The terms μ_o and V are respectively the magnetic permeability of free space and the sample volume. If there is no volume change or material exchanged with the surroundings (i.e. a "closed" system), then the first two terms in the dW expression are zero and the total energy differential is as follows:

$$dU = TdS + \mu_o VHdM \quad . \qquad (1)$$

Following the derivation by Barclay[6], if the differential entropy is expressed as a function of H and T then $dS=(\delta S/\delta T)_H dT+(\delta S/\delta H)_T dH$. Since equation (1) is an exact differential, then $[\delta S/\delta(\mu_o VH)]_T=[\delta M/\delta T]_H$. Consequently, since $\mu_o V$ is a constant, $\mu_o V[\delta M/\delta T]_H=[\delta S/\delta H]_T$. Substituting this expression and the equality (for a reversible change in T) $[\delta S/\delta T]_H=C_H/T$ into the expression for dS, one obtains $dS=(C_H/T)dT+\mu_o V[\delta M/\delta T]_H dH$. By setting this expression for dS equal to zero (for an adiabatic process) and rearranging, one obtains the basic equation for the incremental change in temperature accompanying an incremental reversible adiabatic application of the magnetic field:

$$dT=-(T/C_H)\mu_o V(\delta M/\delta T)_H dH \qquad (2)$$

where C_H is the heat capacity of the material at constant field H. The total magnetocaloric effect upon the application of a field H is the integral of (2):

$$\Delta T=\int dT=\int -(T/C_H)\mu_o V(\delta M/\delta T)_H dH \quad . \qquad (3)$$

In general $(\delta M/\delta T)_H$ is a function of both H and T. Note from either (2) or (3) that the magnetocaloric effect is proportional to H, T, and the temperature dependence of the magnetization at constant field and is inversely proportional to the heat capacity at constant H. In order to search for materials with larger effects, these are the material properties which must be adjusted.

Magnetocaloric Effect in a Paramagnet

In a paramagnetic material, the elemental magnetic moments, μ, act independently against the randomizing effect of temperature and the aligning effect of an external magnetic field. In the absence of a magnetic field the magnetic spins are oriented at random as shown in figure 1a. The magnetization of such an assembly of magnetic spins, M, is the vectorial sum of all the elemental spins: $\underline{M}=\Sigma_i \underline{\mu}_i$ (here, the underlining denotes a vector quantity). For a paramagnet with no applied field $\underline{M}=0$. Upon the application of a magnetic field, the magnetization becomes non-zero as some of the moments align along the direction of the field. In this case (considering the common situation where $|\underline{M}|$ is in the same direction as $|\underline{H}|$ so that the vector designations are dropped) $M=\chi H$, where χ is the magnetic susceptibility. The temperature dependence of the magnetization of such a material may be expressed as follows[7]:

$$M=N\mu[\coth(a)-(1/a)] \qquad (4)$$

where N is the number of elemental magnetic moments in the material and $a=\mu H/k_B T$ (with k_B being the Boltzmann constant). For small values of "a" ($a \leq 1.2$) the expression enclosed in square brackets, called the Langevin Function, in equation (4) can be

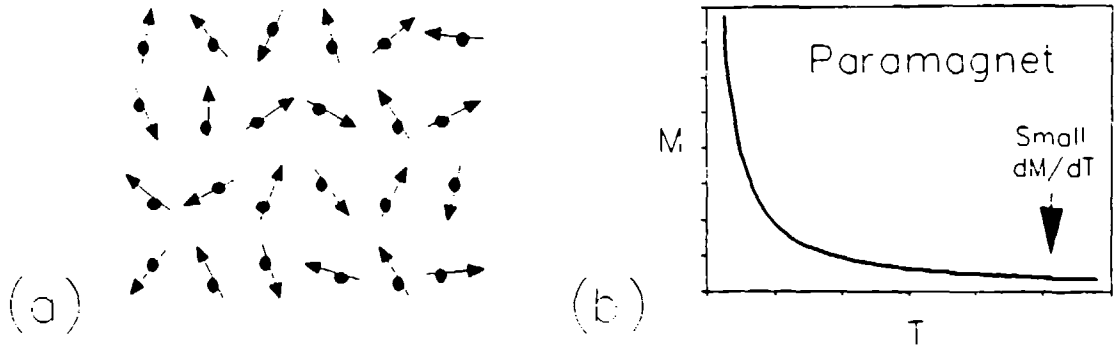

Fig. 1. Schematic of the (a) magnetic spins in a paramagnetic material and (b) the temperature dependence of its magnetization at constant applied field.

approximated[8] by a/3. Consequently,

$$M = N\mu^2 H/3k_B T \qquad (5)$$

which is shown in figure 1b. The fact that the term μ appears as a square in this expression (also called the "Curie Law") is important to the analysis which follows. One factor of μ in equation (5) comes from the $N\mu$ term for the maximum magnetic moment of the system and the second factor of μ comes from the $\mu H/k_B T$ spin alignment term. Taking the derivative $[\delta M/\delta T]_H$ of this expression and substituting into equation (2), the incremental magnetocaloric effect for a paramagnet (with small "a") is as follows:

$$dT_{para} = (1/C_H)\mu_o V[N(\mu^2)/(3k_B)]\{H/T\}dH \; . \qquad (6)$$

Note that this is small at high temperatures and diverges toward infinity as $T \to 0$ K. If the elemental magnetic moments are not all from magnetic spin (S), but also possess some orbital (L) contribution, then $\mu^2 = g^2 J(J+1)\mu_B^2$. g is the gyromagnetic splitting factor (normally ≈ 2), $J = L+S$, and μ_B is the Bohr magneton constant. In terms of the total magnetic moment quantum number, J, equation (6) becomes

$$dT_{para} = (\mu_o V/C_H)[N\{g^2 J(J+1)\mu_B^2\}/(3k_B)](H/T)dH \; . \qquad (7)$$

Magnetocaloric Effect in a Ferromagnet

In a ferromagnet the elemental magnetic moments strongly interact with each other to the extent that below the Curie Point, T_C, they line up in the same direction within large regions called domains, even in the absence of an external magnetic field (see figure 2a). Application of H causes domains whose moments are oriented in the direction of H to grow at the expense of those not oriented along H. In this ferromagnetic state the

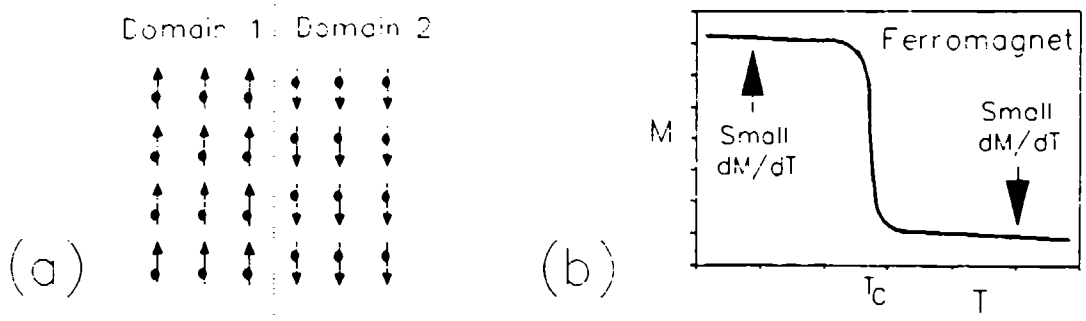

Fig. 2. Schematic for a ferromagnetic material of the (a) magnetic spins showing a boundary (dashed) between domains and (b) the temperature dependence of its magnetization at constant H.

magnetization is not a linear function of H and shows a hysteresis when H is cycled. In this low temperature region, M in a constant applied field is relatively constant as shown in figure 2b. Consequently, for $T << T_C$, $dT_{ferro} \approx 0$. At temperatures above T_C the magnetic moments weakly interact; in this temperature region, M is linear to H and can be described by the well known Curie-Weiss relation:

$$M = (N\mu^2 H)/[3k_B(T-T_C)] \quad . \tag{8}$$

The value of T_C depends upon the strength of the interaction between magnetic moments and is consequently also useful as an indicator of this interaction. Note that this approximation breaks down at T_C because $1/(T-T_C)$ diverges at $T=T_C$. Differentiating equation (8) with respect to temperature and substituting into equation (2) one obtains the following for the incremental magnetocaloric effect for a ferromagnet above T_C:

$$dT_{ferro} = (1/C_H)\mu_o V[N(\mu^2)/(3k_B)]\{HT/(T-T_C)^2\}dH \quad . \tag{9}$$

Consequently, the magnetocaloric effect peaks around the Curie point. Note by comparing equations (6) and (9) that at high temperatures ($T > T_C$) the only difference between the magnetocaloric effects for a paramagnet and a ferromagnet are the terms in curly brackets. Since $\{T/(T-T_C)^2\}$ is much larger than $\{1/T\}$, at high temperatures the magnetocaloric effect for a ferromagnet is much larger than that for a paramagnet.

Magnetocaloric Effect in a Superparamagnetic Nanocomposite

In a nanocomposite possessing superparamagnetic behavior the magnetic species are in the form of nanometer-sized clusters of atoms finely dispersed in either a non-magnetic or weakly magnetic matrix. Each magnetic cluster is a single ferromagnetic domain wherein all the magnetic moments of the atoms of the magnetic species are aligned. However, the magnetic interaction between clusters is weak so that each cluster acts

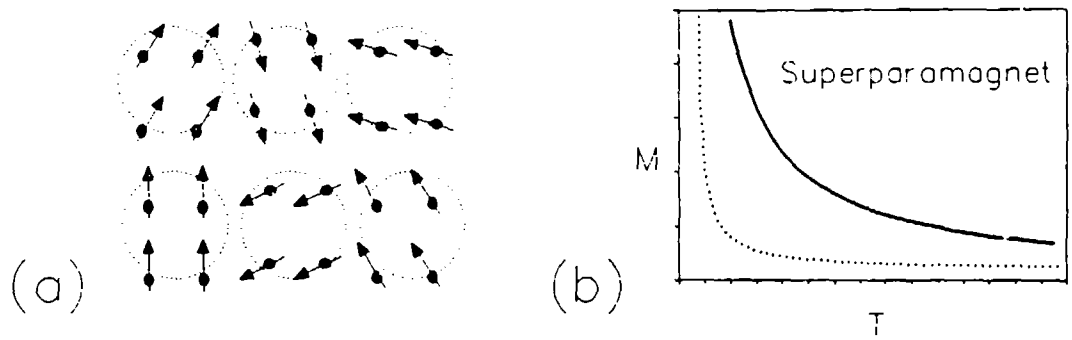

Fig. 3. Schematic of the (a) magnetic spins in a superparamagnet with the magnetic clusters indicated by dashed circles and (b) the temperature dependence of M for a superparamagnetic nanocomposite (solid line). Also shown for reference in (b) is the M vs T curve (dashed) for a paramagnet possessing only 1/3 the magnetic moment of the superparamagnet.

independently. Figure 3a shows a schematic of the magnetic spins in such a system. The magnetization of a system of independently acting cluster moments is analogous to that already described in equation (5) for a paramagnet. The only difference is that instead of the number of elemental moments, N, the number of cluster moments, n, must be used. Also, instead of the elemental moment, μ, an effective moment for the cluster, $\mu_{cluster}=(N/n)\mu$, must be used in equation (5). Accordingly, the following expression for the magnetization of a superparamagnetic nanocomposite is obtained:

$$M=n[(N/n)\mu]^2H/[3k_B(T)] \quad . \qquad (10)$$

This temperature dependence at constant H is shown on figure 3b, along with that for a paramagnet. Differentiating equation (10) with respect to temperature and substituting it into equation (2) as before, one obtains the following expression for the incremental magnetocaloric effect in a superparamagnetic nanocomposite:

$$dT_{nano}=(1/C_H)\mu_o V[(n(N/n)^2)(\mu^2)/(3k_B)][H/(T)]dH \quad . \qquad (11)$$

The only difference between this expression and that for a paramagnet in equation (6) is the term enclosed in square brackets. However, since "n" is much smaller than N, the term $n(N/n)^2=N^2/n$ in equation (11) is much larger than the term N which appears in equation (6). Consequently, for $\mu H/k_BT$ small enough such that the low field approximation of equation (5) holds,

$$dT_{nano} >> dT_{para} \quad . \qquad (12)$$

Thus, considering the case for higher temperatures and reasonable fields the nanocomposite can give an enhanced temperature change. Note that this effect means that

a superparamagnetic nanocomposite can potentially provide the same magnetocaloric effect for a given field application as presently provided by conventional paramagnets, but at higher temperatures. Alternatively, these new materials may provide the same effect at lower temperatures, but with much smaller magnetic field applications.

As in the case of a paramagnetic material, dT_{nano} increases as T→0 K and decreases at high temperatures. Consequently, it would appear that for the superparamagnetic nanocomposites there is an upper temperature limit for use in magnetic refrigeration cycles. Nanocomposites, however, may also be prepared in such a way as to provide for interactions between the cluster moments. In such a case the magnetization may be described as in the case for a ferromagnet above T_C. Using equation (8) and making the same substitutions for N and μ as performed above in the case of non-interacting clusters, one obtains the following expression:

$$M = n[(N/n)\mu]^2 H/[3k_B(T-T_I)] \qquad (13)$$

where analogous to T_C for isolated interacting moments, T_I is an interaction temperature which depends on (and therefore is indicative of) the strength of the interaction between cluster moments. Below T_I long range interaction will exist between the clusters and M would be relatively constant with temperature (for constant H). Differentiating equation (13) with respect to T and substituting into equation (2) would result in an incremental magnetocaloric effect as follows:

$$dT_{nano^*} = (1/C_H)\mu_o V[(n(N/n)^2)(\mu^2)/(3k_B)]\{HT/(T-T_I)^2\}dH \quad . \qquad (14)$$

Comparison of equations (9) and (14) shows that for equivalent interaction temperatures, $T_C = T_I$, the only differences are the expressions enclosed in square brackets. Since "n" is smaller than N, the magnitude of equation (14) can be much larger than equation (9). Consequently, at temperatures and fields such that the approximation of equation (8) holds, the following hierarchy of magnetocaloric effects can be concluded:

$$dT_{nano^*} >> dT_{nano} >> dT_{ferro} >> dT_{para} \quad . \qquad (15)$$

Thus, in this region of operation, enhanced magnetocaloric effects are potentially obtainable in the case of superparamagnetic nanocomposites. For high temperature use, nanocomposites prepared to possess interactions between clusters would potentially possess the largest magnetocaloric effects. The interaction temperature, T_I, varies with the size and separation of the ferromagnetically-aligned clusters, and these parameters may be chosen by the composition and processing of the nanocomposite[9-11].

As an example of the magnitudes of enhancement possible Table I has been provided showing the values of the terms in the above equations which are important for

Table I. Magnetocaloric enhancements in superparamagnetic nanocomposites

f	N'	(N'/n) =atoms/cluster	$n(N'/n)^2 = f(N'/n)N$ =N*enhancement	H/T Limit (Tesla/K)
0.8	0.8N	10	8N	0.2
		100	80N	0.02
		1000	800N	0.002
0.5	0.5N	10	5N	0.2
		100	50N	0.02
		1000	500N	0.002
0.1	0.1N	10	N	0.2
		100	10N	0.02
		1000	100N	0.002

comparison. In this table allowance has also been made for a dilution in the magnetocaloric effect due to a dilution in the amount of magnetic species in the material caused by the presence of a mediating non-magnetic species. Dilution effects are accounted for by defining a new value for the number of magnetic spins in the system, N'=fN, where f is a fraction expressing the dilution. The enhancement in the expected magnetocaloric effect by creating a superparamagnetic nanocomposite from the bulk material is determined by comparing the values in the third column to N. The limiting value of H/T for which the full enhancement applies is shown in the last column.

The enhancements shown in Table I have been determined for superparamagnetic nanocomposites under the low field assumption ($\mu H/k_B T \leq 1.2$). Consequently, the predicted enhancements will be limited by the point at which this assumption breaks down. For large cluster sizes, very low fields may be used to obtain the maximum dT effect. As an example, an assembly of 10 nm diameter Fe-atom clusters (e.g. each containing ~1000 atoms) will still be in the low-field regime at 30 K with the application of only 200 Gauss. In this case a 500-fold enhancement in the magnetocaloric effect is predicted from Table 1, assuming a 50% dilution in magnetic species when forming the nanocomposite.

EXPERIMENTAL PROCEDURE

In order to examine the above predictions for the enhanced magnetocaloric effect in superparamagnetic nanocomposites, an adiabatic calorimeter for making such measurements was constructed and a schematic is shown in figure 4. The sample was supported at the end of a teflon rod attached to the bottom flange of a 1.2 m long thin-walled stainless steel tube. Surrounding the sample was a 3.2 mm thick walled stainless

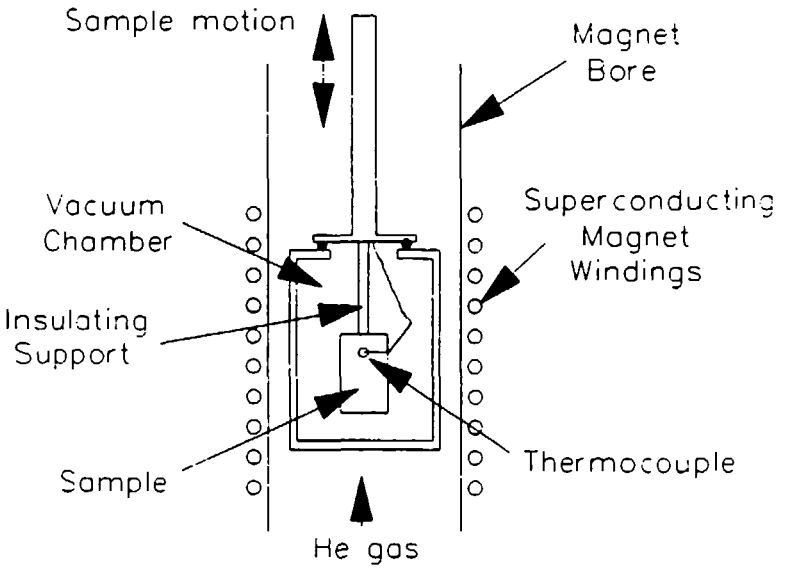

Fig. 4. Schematic of the adiabatic calorimeter used to measure the magnetocaloric effect in this study.

steel can joined to the bottom flange of the tube using a replaceable indium o-ring vacuum seal. The can and bottom flange served as the temperature reservoir to which the sample was thermally connected via the thin thermocouple wires. These wires (each ~100 μm diameter) were thermally equilibrated at the bottom flange of the tube and stretched for ~30 cm before attaching to the center of the specimen in order to minimize the thermal link between the heat reservoir and sample. In order to fit inside a 5 Tesla superconducting magnet in our laboratory the diameter of the stainless steel can was ~3.2 cm. The sample, ~6.5 mm diameter by 20 mm long and weighing ~1 g, consisted of a powder compact (held together with a couple drops of very thinned down and dried low temperature adhesive and thermal conductor G.E. #7013 varnish[12]) surrounding a Type T (Cu-constantan) thermocouple. The inside of the can was evacuated to a pressure of 10^{-7} Torr before cooling and the sample surroundings were cooled by passing cooled He gas past the stainless steel can. By adjusting the flow rate of the helium gas and also its temperature (by means of a small heater around its supply tube) the temperature of the specimen chamber could be adjusted between 10 K and room temperature. The measurement of the magnetocaloric effect was accomplished by monitoring the temperature of the sample as a function of time before and after withdrawing the sample from the center of the superconducting magnet coils and also after reinserting the sample back into the magnetic field. The data were automatically measured and saved on a computer disk. Elimination of eddy current heating effects was performed by averaging the temperature discontinuities measured on extraction and reinsertion into the field. Since the samples were non-conducting, however, eddy current heating effects were found to be insignificant. The largest sources of error were the induced voltage transients in the thermocouple during sample motion and the temperature calibration change of the

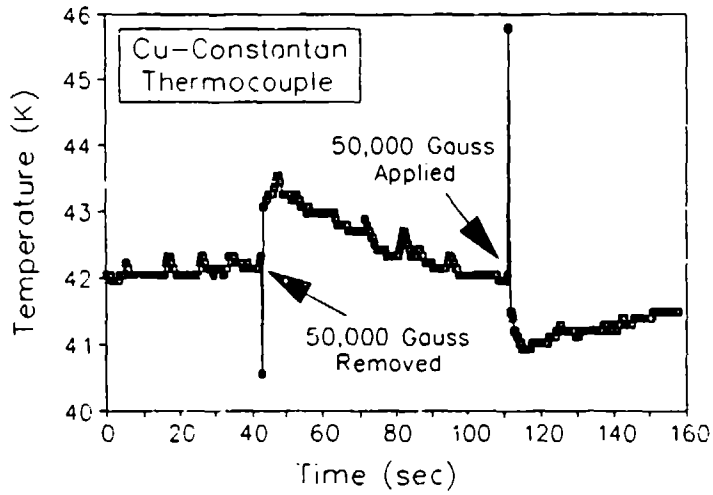

Fig. 5. Temperature vs. time data for a Cu-constantan thermocouple (TC) as a 5 Tesla (i.e. 50,000 Gauss) magnetic field was first removed and then applied to the TC.

thermocouple due to the magnetic field. The latter error results in too low a temperature measurement when in the presence of the magnetic field. Figure 5 clearly shows this calibration error effect at ~42 K. The data shown in this figure are for the measuring thermocouple located in the sample holder, but without any sample around it. Note that as the sample holder-thermocouple assembly was withdrawn from the 5 Tesla field there was a steady state temperature rise and vice versa by about the same amount when the assembly was reinserted into the magnetic field. The magnitude of this effect (which is temperature dependent) varies with the thermocouple and with the sample-thermocouple configuration, and consequently it has not yet been calibrated nor added to the data shown herein measured for the sample. Note that since this temperature error is in a direction opposite that of the magnetocaloric effect, it effectively reduces the actual temperature change of the sample upon removal from the field. Consequently, temperature changes reported in this paper are only lower limits for the true magnetocaloric effects. Efforts are presently underway to correct this error by a combination of changing thermometers and calibration in the presence of high magnetic fields.

RESULTS AND DISCUSSION

As a test of the calorimeter figure 6 shows magnetocaloric measurements performed using a 5 g (0.005 moles) sample of gadolinium gallium garnet ($Gd_3Ga_5O_{12}$ or GGG) at ~30 K. The large initial temperature deviations accompanying the field changes are artifacts due to induced voltages (V) in the wire loop comprising the thermocouple as

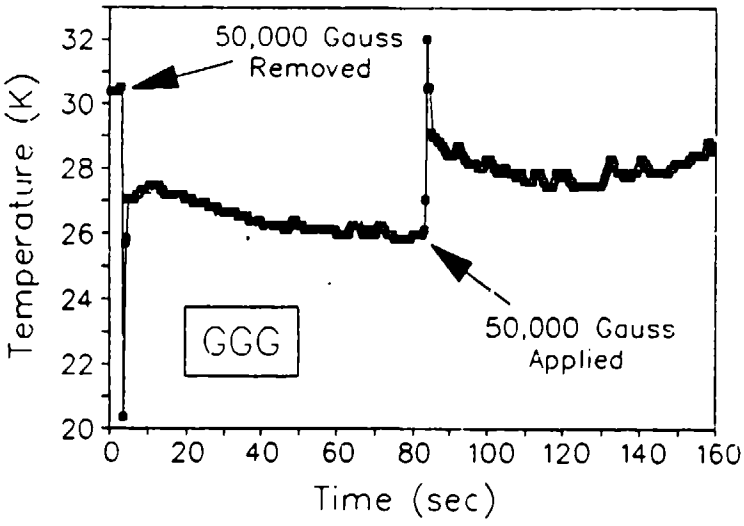

Fig. 6. Temperature vs. time data for gadolinium gallium garnet as a 5 Tesla magnetic field was first removed and then applied to the sample.

magnetic flux (Φ) through the loop changed quickly according to Faraday's Law $V=-d\Phi/dt$. These are transient voltages and decay with a time constant $\tau \approx 2$ sec. The measured effect (-2.5 degrees at 30 K) upon the application of a 5 Tesla magnetic field is consistent with that previously measured for this material[13], showing both the sensitivity of the calorimeter for the measurement of small samples and that the calorimeter was operating properly.

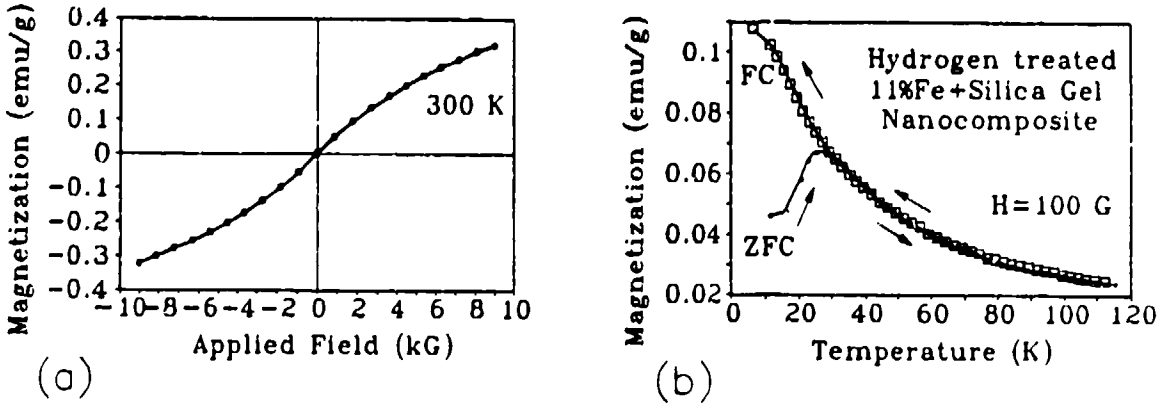

Fig. 7. Magnetization for a H_2-treated 11%Fe+silica gel nanocomposite vs. (a) field at 300K and (b) temperature at an applied field of 100 G, measured (1) during cooling (FC) and (2) while warming (ZFC) after first cooling to 10 K in zero field.

The nanocomposite chosen for testing our predicted magnetocaloric effect enhancement was one prepared earlier in our laboratory for a completely different purpose: magnetic information storage. It is a bulk sample (prepareable in kilogram quantities, if required) prepared by adding the appropriate amount of an aqueous solution of ferric nitrate to a 50% solution (by volume) of tetraethoxysilane and ethanol, with a few drops of aqueous HF added as a catalyst. During gelling (~12 hours) and subsequent air drying into a hard brittle solid the iron formed in nanometer-sized regions homogeneously dispersed in the silica gel matrix[9]. Subsequent heat treatment (378°C for 20 hrs) in an atmosphere of hydrogen gas converted the material to a superparamagnet at room temperature (shown by the non-linear field dependence of the magnetization in figure 7a for this material). At temperatures less than 30 K, the H_2-treated material becomes a magnetic spin glass[9-10] which can be seen from the temperature at which the two magnetization curves for this sample shown in figure 7b converge. This is not a ferromagnetic transition; however, it is around this temperature that the maximum magnetocaloric effect might be expected to occur in this material. Magnetic nanocomposite materials prepared by this method are particularly attractive in refrigeration cycles wherein a gas is used as a heat transfer medium since the gel structure contains an interconnected network of micron- and submicron-sized pores through which the gas may pass and make intimate contact with the nanometer-sized refrigerant. The pore size may also be adjusted by the processing.

Magnetocaloric measurements near 70 K for the H_2-treated 11%Fe + Silica Gel nanocomposite are shown in figure 8. The data in figure 8 show that a significant effect is obtainable in a superparamagnetic nanocomposite. This effect is much larger than that

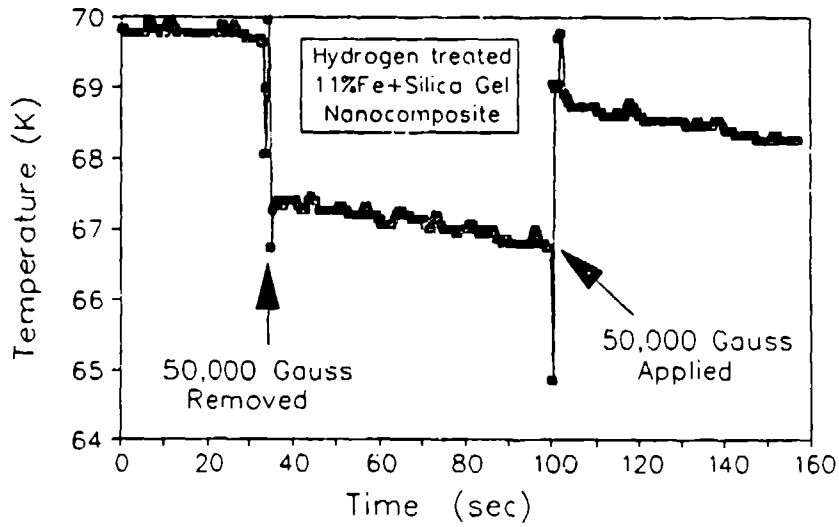

Fig. 8. Temperature vs. time data for a superparamagnetic H_2-treated 11%Fe+silica gel nanocomposite as a 5 Tesla magnetic field was first removed and then applied to the sample.

expected for a similar paramagnetic material at the same temperature and field. Its magnitude is slightly greater than that expected for a superparamagnetic material of the same composition under optimized conditions, indicating that there must be some interaction between the clusters in this material. This interaction is also suggested by the magnetization data in figure 7b. Since the magnetocaloric effect is roughly proportional to the relative amount of magnetic species in the material, loading the nanocomposite to 40 % Fe might be expected to give some increase in the magnetocaloric effect. Further measurements are in progress to determine the temperature dependence of ΔT for this material and to examine the effects of increased loadings.

CONCLUSION

In conclusion we have presented a basis for expecting enhanced magnetocaloric effects in superparamagnetic nanocomposites under certain conditions of operation. Secondly, we have experimentally tested one such material. This nanocomposite material may be prepared in the large quantities required once optimal materials have been developed. By adjustment of the processing of such materials, the temperature at which their magnetocaloric effect is maximum may also be chosen over wide ranges, even approaching room temperature. The question of over what range of temperatures and fields these materials might have usefulness is still being explored. Their greatest potential appears to lie in the high temperature, low field area where operation over a broad temperature range is needed.

ACKNOWLEDGEMENT

The authors would like to thank Dr. J.J. Ritter for preparing the Fe+silica gel nanocomposite measured in this study, Dr. A.J. Shapiro for helping characterize this material by electron microscopy observations, and Dr. R.J. McMichael for critical discussions. This work was supported by the NIST Materials Science and Engineering Laboratory with additional support from a NIST Director's Innovation Award.

REFERENCES

1. Patent Pending

2. J.A. Barclay and W.A. Steyert, "Materials for magnetic refrigeration between 2 K and 20 K," Cryogenics, vol. 22, 73 (1982).

3. G.V. Brown, "Magnetic heat pumping near room temperature," J. Appl. Phys., vol. 8, 3674 (1976); T. Hashimoto, T. Numasawa, M. Shino, and T. Okada, "Magnetic refrigeration in the temperature range from 10 K to room temperature: the

ferromagnetic refrigerants," Cryogenics, vol. 21, 647 (1981); T. Hashimoto, "Recent Investigations on Refrigerants for Magnetic Refrigerators," Advances in Cryogenic Engineering Materials, vol. 32, 261 (1986); G. Green, W. Patton, and J. Stevens, "The Magnetocaloric Effect of some Rare Earth Metals," Advances in Cryogenic Engineering Materials, vol. 33, 777 (1988).

4. B. Abeles, "Granular Metal Films," Appl. Solid State Sci., vol. 6, 1 (1976); F.D'Orazio, J.L. Dormann, D. Fiorani, and F. Lucari, "Optical and Magnetooptical Study of Fe-Al_2O_3 Granular Thin Films," J. Magn. Magn. Mater., vol. 54-57, 1309 (1986); M.S. Multani, "Nanophysics: A Kaleidoscopic View of Highlights," Phase Transitions, vol. 24-26, 3 (1990).

5. Gang Xiao, S.H. Liou, A. Levy, J.N. Taylor, and C.L. Chien, "Magnetic relaxation in Fe-(SiO_2) granular films," Phys. Rev. B, vol. 34, 7573 (1986); R.D. Shull, U. Atzmony, A.J. Shapiro, L.J. Swartzendruber, L.H. Bennett, W.J. Green, and K. Moorjani, "Magnetic properties of thin-film Ag+iron oxide granular metals," J. Appl. Phys., vol. 63, 4261 (1988); R.D. Shull and L.H. Bennett, "Nanocomposite Magnetic Materials," to appear in Acta Metallurgica (1990).

6. J. Barclay, "Magnetic Refrigeration: A Review of a Developing Technology," Advances in Cryogenic Engineering Materials, vol. 33, 719 (1988).

7. B.D. Cullity, Introduction to Magnetic Materials, Addison-Wesley Publ. Co., Reading, MA (1972) p. 94.

8. As an example consider Fe (μ=2.65 μ_B = 2.46 erg/Oe): at room temperature and 5 Tesla field, $a=\mu H/k_BT=[(2.46\times10^{-20}$ erg/Oe)$(5\times10^4$ Oe)$/(1.38\times10^{-16}$ erg/deg)(300 deg)]=0.032. At 100 K and 30 K, a=0.09 and 0.3 respectively.

9. R.D. Shull, J.J. Ritter, A.J. Shapiro, L.J. Swartzendruber, and L.H. Bennett, "Iron Magnetic Moments in Iron/Silica Gel Nanocomposites," J. Appl. Phys., vol. 67, 4490 (1990).

10. R.D. Shull, J.J. Ritter, A.J. Shapiro, L.J. Swartzendruber, and L.H. Bennett, "Magnetic Properties of Iron/Silica Gel Nanocomposites", in: Multicomponent Ultrafine Microstructures, L.E. McCandlish, B.H. Kear, D.E. Polk, and R.W. Siegel, eds., Mat. Res. Soc. Publ., Pittsburgh (1989) p. 179.

11. R.D. Shull and J.J. Ritter, "Spin Glass Magnetic Behavior of Iron/Silica Gel Nanocomposites", to be published in Physical Phenomena in Granular Materials, G. Cody, P. Sheng, and T. Geballe, eds., Materials Research Society, Pittsburgh (1990).

12. The use of trade names is for informational purposes only and does not imply an endorsement by NIST or the U.S. Government.

13. Unpublished data measured by Thermo Magnetic Devices (Astronautics Corporation) for G. Green, David Taylor Research Center, Annapolis, MD.

RARE-EARTH INTERMETALLIC COMPOUNDS FOR MAGNETIC REFRIGERANTS

Alexander Tishin
Physics Department, Moscow State University,
Moscow 119899, USSR

ABSTRACT

Research on the use of a number of gadolinium-based ferro- and ferrimagnetic intermetallic compounds for magnetic refrigeration has been carried out. To calculate the magnetic entropy change ΔS_M, the molecular field theory for single and double sublattice magnetics is used.

The applicability of this approach is verified by experiment. It is shown that ferrimagnetic compounds may have a considerable value for ΔS_M over wide temperature ranges.

INTRODUCTION

Investigations of physical properties of rare-earth intermetallic compounds have revealed the ability of this class of materials to be used for magnetic refrigeration over a wide temperature range. Until recently the attention of researchers has been principally centered on two compounds such as RAl_2 and RNi_2. An investigation of RAl_2 as well as of compounds based upon it has been made.[1,2] The structure and magnetic properties of these compounds have been studied.[3] The present paper discusses possible applications of a number of ferro- and ferrimagnetic compounds on the basis of some rare-earth elements for the purposes of magnetic refrigeration. The compounds of Gd with Ni attract attention, from the point of view of refrigeration, as first having a large magnetic moment per formula unit. The increase of the Curie point θ for Gd-rich compounds is due to the Gd ions being close to one another. The structural stability can be affected by the localization of the Fermi level with respect to the upper part of 3d band. The ferromagnetic compound GdNi has an orthorhombic structure of CrB. The value of the effective magnetic moment μ_{eff} is close to the value for the Gd^{+3} ion. The Curie point θ is in the range of 71 to 73 K.[4] Nickel has been reliably established to be nonmagnetic.

In the compound $GdNi_2$ where there seems to be no momentum suppression by the crystalline field the value of μ_0 is also close to g_JJ. It has a cubic structure like that of $MgCu_2$. The ordering is of ferromagnetic character and Ni is nonmagnetic. The Curie point θ ranges from 75 to 90 K.[4] A literature survey of the properties of the $GdNi_5$ indicates that Ni is nonmagnetic in this compound since its 3d band is filled with Gd conduction electrons. The low temperature value of θ = 28 K is accounted for by Gd-Gd interactions. The value of the μ_{eff} for $GdNi_5$ is in agreement with the theoretical value for the moments of free Gd ions. The magnetic moment of Ni in the compounds $GdNi_3$, Gd_2Ni_7 and Gd_2Ni_{17} is extremely small and its existence does not seem to have been precisely proven so far.[4] If Ni has a moment in these compounds, the ordering must be of ferrimagnetic character. It is possible that the compounds of RNi_3 have noncollinear spin structure.

THEORETICAL MODEL AND EXPERIMENT

To calculate the magnetic entropy change the present investigation made use of the molecular field theory approximattion. To calculate the magnetization, the following expression is normally used.

$$I(T) = I(O)B_J(x),$$

where $B_J(x)$ is Brillouin function. If the compound has two sublattices the magnetization can be written as:

$$I(T) = I_R(T) - I_{3d}(T),$$

where I_R and I_{3d} are magnetizations of rare-earth and 3d sublattices, respectively. The magnetization of compounds GdNi, $GdNi_2$, $GdNi_3$ and $GdNi_5$ was investigated by experiment.

A comparison of the results of magnetization measurements both for ferro- and ferrimagnetic compounds of Gd has shown that these compounds are fairly well described within the framework of the molecular field approximation. This fact enables us to use this theory for calculating magnetic entropy change ΔS_M in these compounds. The calculated values of ΔS_M as a function of field at the Curie point θ of a number of ferromagnets are shown in Fig. 1. It is evident that the most promising compound is GdNi (experimental Curie point θ = 73 K). The calculations of refrigerant capacity $\Delta S_M \Delta T_{cyc}$ were carried out assuming that a Brayton type magnetic cycle at B = 6 T was realized in the device. As is evident from our results, the refrigerant capacity of these compounds can reach large values (44.5 J/mol for GdNi). These intermetallic compounds are suitable for magnetic refrigeration. More thorough studies are necessary, however, similar to those made for GdNi by Zimm et al.[5]

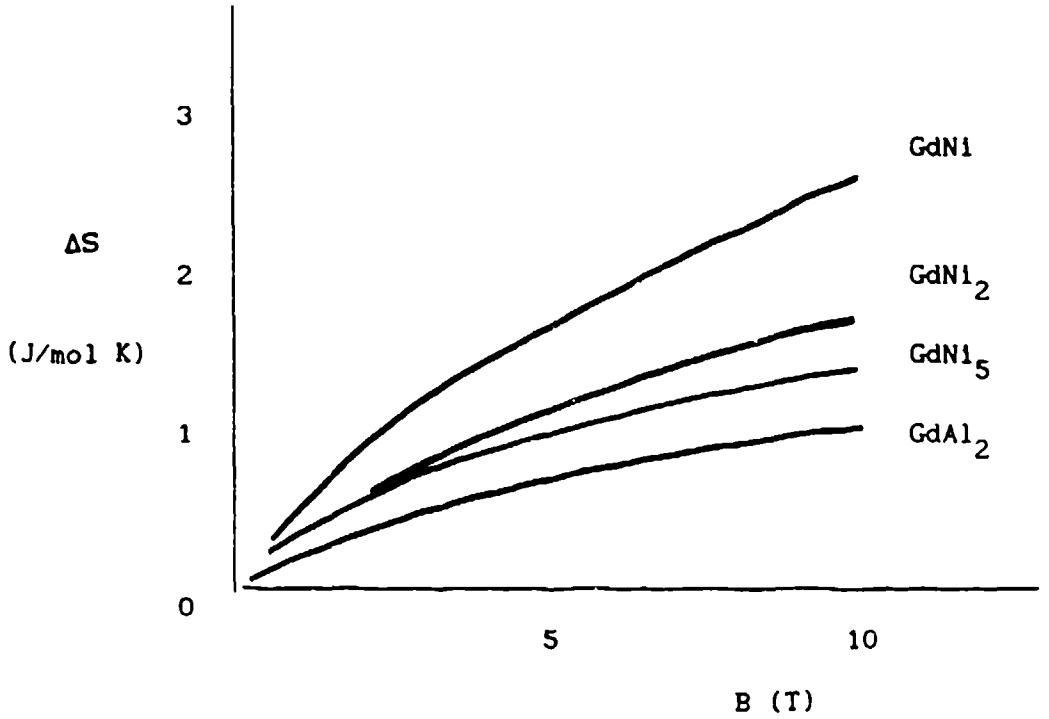

Fig.1 Magnetic entropy change in intermetallic compounds in the vicinity of Curie point Θ.

The ferrimagnetic compounds of heavy rare-earth metals with 3d metals are also extremely promising. The rare-earth atom in them conserves its moment, and ordering temperatures vary over extremely wide ranges. We have also investigated the possibility of using other compounds of Gd. Estimates for the ferromagnetic compound GdGa, for instance, which has a Curie temperature $\theta \sim 200$ K, indicate that at the field B = 6 T in the vicinity of θ the entropy change may reach $\sim$ 1.6 J/mol K.

Also of considerable interest are amorphous alloys of Gd, which have compositions near $GdNi_2$ and Gd_xNi_{1-x} since they possess a large magnetic moment per formula unit.

ACKNOWLEDGEMENTS

The author wishes to thank S.A. Nikitin and Z.C. Umhaeva for their interest and support of the work. This work was supported by the D.W. Taylor Naval Ship R&D Center.

REFERENCES

1. C.B. Zimm, C.K. Campenni, and J.A. Barclay, "Magnetothermal conductivity of $ErAl_2$ for cryogenic applications," *Journal Appl. Phys.*, vol. 63 (1988) p. p. 4294-4296.

2. K. Matsumoto, T. Ito, and T. Hashimoto, "An Ericsson magnetic refrigerator for low temperature," *Advances in Cryogenic Engineering*, vol. 33, Plenum Press, NY (1988) p. 743-750.

3. M. Rossignol, Thesis, Unviersity of Grenoble (1980).

4. K.A. Gschneidner, Le Roy Eyring, *Handbook on the physics and chemistry of rare-earths*, North-Holland Publishing Company, Amsterdam (1978).

5. C.B. Zimm, W.F. Stewart, J.A. Barclay, W. Overton, C. Olsen, D. Harding, R. Chesebrough, and W. Johanson, "Measured properties of GdNi for magnetic refrigeration applications," *Advances in Cryogenic Engineering*, vol. 33, Plenum Press, NY (1988) p. 791-798.

SUPERCRITICAL HELIUM DEWAR SPACE FLIGHT RESULTS

Paul Forney
Lockheed Palo Alto Research Laboratory
3251 Hanover Street
Palo Alto, California 94304

ABSTRACT

The Delta 180 mission was flown for SDIO (Space Defense Initiative Office) on September 5, 1986. The Delta 181 mission was flown for SDIO on February 8, 1988. Both of these missions included in their payloads infrared radiometers built at Lockheed Palo Alto Research Laboratory. The cryogenic system chosen for use was a supercritical helium dewar that included a solid nitrogen guard tank. The purpose of this dewar was to cool the optics of the radiometer below 60 K and the focal planes to approximately 15 K.

This paper describes the design philosophy and trade-off studies that lead to the final design. The construction details that are considered necessary to understanding the system, and also novel details, are discussed. The test program for the dewar as a subsystem is described, as well as the system level radiometer testing. Final acceptance and environmental testing is also described. Unique handling requirements associated with the launch facilities created interesting problems whose solutions are shown.

INTRODUCTION

The missions that were flown required operation as soon as possible after launch and continuous operation throughout the mission. In the case of Delta 180, the mission was three hours long; the Delta 181 mission required a lifetime of twelve hours. Because of these relatively short lifetimes, a cryogenic system was chosen that would not interfere with launch operations, would operate as soon as orbit was achieved, and would not disrupt spacecraft attitude characteristics.

Our choice was to use helium and nitrogen, which could be filled as liquids while the vehicle was on its launch pad. To prevent sloshing or movement of the liquids, we decided to allow the helium tank to pressurize so that a supercritical state

was achieved with the helium and to subcool the nitrogen, keeping it frozen throughout the mission. During the Delta 180 mission, cryogen venting was allowed to occur at the instrument. However, the Delta 181 mission was to have a vent management system which collected both cryogen vents and exhausted them through the center of mass of the spacecraft. The size of the cryogen tanks was designed to provide a margin equal to the mission lifetime.

The dewar designs of the Delta 180 and Delta 181 instruments were identical except for size. Therefore all below discussions will refer only to the Delta 181 design.

DESIGN

DESIGN FEATURES

The cryogen system which had both a supercritical helium dewar and a solid nitrogen dewar provides cooling for both the infrared focal planes and the optical system. Figure 1 shows the sensor layout. The focal planes run at about 16 K. The optics run at the temperature of the solid nitrogen, which varied during the mission.

Surrounding the helium dewar is a guard tank of nitrogen. The helium dewar exhaust line is coiled around and welded to this guard tank. The initial fill with liquid nitrogen cools the guard tank to 80 K and starts precool of the helium dewar. When the helium dewar is being filled with helium, the exhaust helium gas further subcools the nitrogen to 30 K, thus solidifying it. When the helium dewar is full, it is allowed to pressurize by closing the atmospheric exhaust and valving in a 48 psia absolute pressure relief valve. It normally takes 6 to 9 hours to reach this pressure. This is designed to match the built-in launch hold time. The design cryogen lifetime is 24 hours after launch.

When the fill procedure is complete, the helium dewar is at about 5 K and the nitrogen tank is about 30 K. When launched, the helium dewar is at about 8 K and the nitrogen dewar at about 50 K. The heat capacity of the helium boiloff vapor is used to cool the nitrogen tank and hence the optics, which are hard mounted to it. The solid nitrogen tank together with multilayer insulation wrapped around it minimize the heat leak into the helium dewar.

As the mission starts and the instrument is turned on, a focal plane heater is controlled to hold the focal plane temperature at its optimum operating temperature, 16 K. As the mission progresses, the helium dewar gradually warms to 12 K while the nitrogen tank warms to the triple point of nitrogen which is 63.2 K.

The following data are presented for reference:

A) Dewar Capacity:
   Helium: 9 L @ 48 psia in a 9.5 L tank
   Nitrogen: 6 L @ 1 psia in a 6.05 L tank
B) Total Weight of cryogens: 12.7 lbs.
C) Lifetime:
   Hold Time = 9 hours
   Operation = 24 hours
D) Flow Rates:
   Helium:
      ≈ 2 to 2.7 sL/m with no power
      ≈ 4.7 sL/m with full power
      (sL/m=standard liter/minute)
   Nitrogen remains solid throughout mission.

VALVING ARRANGEMENT

As can be seen in Fig. 2, there are four ports into the dewar. Each is protected by a relief valve. The operation of the valves is as follows: during nitrogen fill, shut the absolute relief vent out by closing the fill valve. Then, fill with nitrogen, cap and open this fill valve. It should be noted that if the helium dewar is not precooled, its initial flow of helium will cause its warm gases to heat the nitrogen system.

The helium fill is started at low pressures with the two 70 and 80 psia relief valves protecting against plugged lines. If a launch delay necessitates a refill, the helium vent valve is used to relieve the pressure that has built up.

HEAT DISSIPATION

The completed design allowed for parasitic heat loads of 5.89 watts on the nitrogen system due to the fiberglass supports, multilayer insulation, electronics and radiation. These effects also contributed 0.06 watts to the helium system.

The dissipative factors were due to the filter wheel which contributed 1.0 watts to the nitrogen system and the focal plane heater contributed 0.1 watts to the helium system. Also the helium system had an additional heating of 0.1 watts due to the focal plane itself.

In summary, the nitrogen system had a total of 6.89 watts of heat load while the helium system had 0.26 watts.

TEST RESULTS

HEAT RATE

Several laboratory tests established the parameters of the system. These tests were conducted with the flight system operating as it would in actual flight. A flow

meter was attached to each cryogen exhaust. Flow rates, dewar temperatures, and times were recorded as the test progressed. The dewar was weighed before and after each test, but the mass flow rates were used to calculate the mass history.

Figure 3 shows in one graph the history of mass flow rate, mass, heat rate and temperature. This figure shows that after venting (10 hours after fill, or about 1 hour after intended launch), the temperature remains lower than 8 K for 29 hours, thus exceeding the 24 hour design lifetime.

Nitrogen temperatures climb to the 63.2 K triple point in 15 hours after fill. However at launch (nine hours after fill), the temperature has reached 55 K.

LIFE TIME IN TEST

The mass history and event timeline are given in the table below.

Mass History (In LBS)

Time	Event	Helium	Nitrogen	Total
L-9(0)	Final Fill	2.5	10.21	12.71
L (9)	Launch	2.5	10.21	12.71
L+1(10)	Helium Vent Starts	2.5	10.21	12.71
L+4(13)	Nitrogen Vent Starts	2.35	10.21	12.56
L+12(21)	End of Mission	1.89	7.97	9.86
L+21(33)	Design Life	1.15	4.61	5.76
L+38(47)	Nitrogen Depletion	0.40	0.00	0.40
L+46(55)	Helium Depletion	0.00	0.00	0.00

SPACE QUALIFICATIONS

The dewar, along with the entire instrument, was subjected to qualifying tests in order to insure proper operation in space. These tests consisted of vibration and thermal/vacuum testing at the instrument level and acoustic testing at the spacecraft level.

The vibration test consisted of a sine sweep in the thrust axis only, followed by a random vibration test in all axes. The levels were:

Sine Vibration: Frequency from 15 to 21 Hz, Level 3.5 g,
Sweep Rate 3 seconds per Hz

Random Vibration:

Radial Axis		Thrust and Tangential Axes	
Frequency (Hz)	Level	Frequency (Hz)	Level
10-40	0.001 g^2/Hz	10-40	0.001 g^2/Hz
40-100	+12 dB/octave	40-100	+10 dB/octave
100-160	0.04 g^2/Hz	90	0.016 g^2/Hz
160-200	+16 dB/octave	90-400	+3 dB/octave
200-550	0.13 g^2/Hz	400-700	0.07 g^2/Hz
550-2000	−5 dB/octave	700-2000	−7 dB/octave
2000	0.015 g^2/Hz	2000	0.006 g^2/Hz
Overall g rms = 10.6 60 sec duration		Overall g rms = 7.9 60 sec duration/axis	

The thermal vacuum test consisted of running the mission timeline (12 hours duration) three times: at 60, 20 and 0 C.

The acoustic test levels were:

Octave Band, Center Frequency (Hz)	Maximum Flight Level (dB)
31.5	128
63	131
125	137
250	140
500	144
1000	137
2000	134
4000	130
8000	127

Overall SPL = 147 dB Duration 60 seconds

MISSION RESULTS

To allow performance of a safe, reliable fill procedure to be used on the launch pad, the system described in Figs. 4 and 5 was constructed and operated.

For operations on the pad with the vehicle's shroud in place, a special manifold was built. This manifold is shown in Fig. 6. The shroud had an access port cover installed that upon removal allowed the manifold to be installed. Therefore, valving and fill operations could be accomplished with all activities being handled outside the shroud envelope.

The instrument was filled (top off) 9 hours prior to launch. The last housekeeping reading obtained some 11 hours after launch showed that the focal plane temperatures had not changed during the mission and that the nitrogen temperature started at 56.5 K and rose to 60.8 K during the mission. Note that this last temperature indicates that the nitrogen is still subcooled below its triple point of 63.2 K.

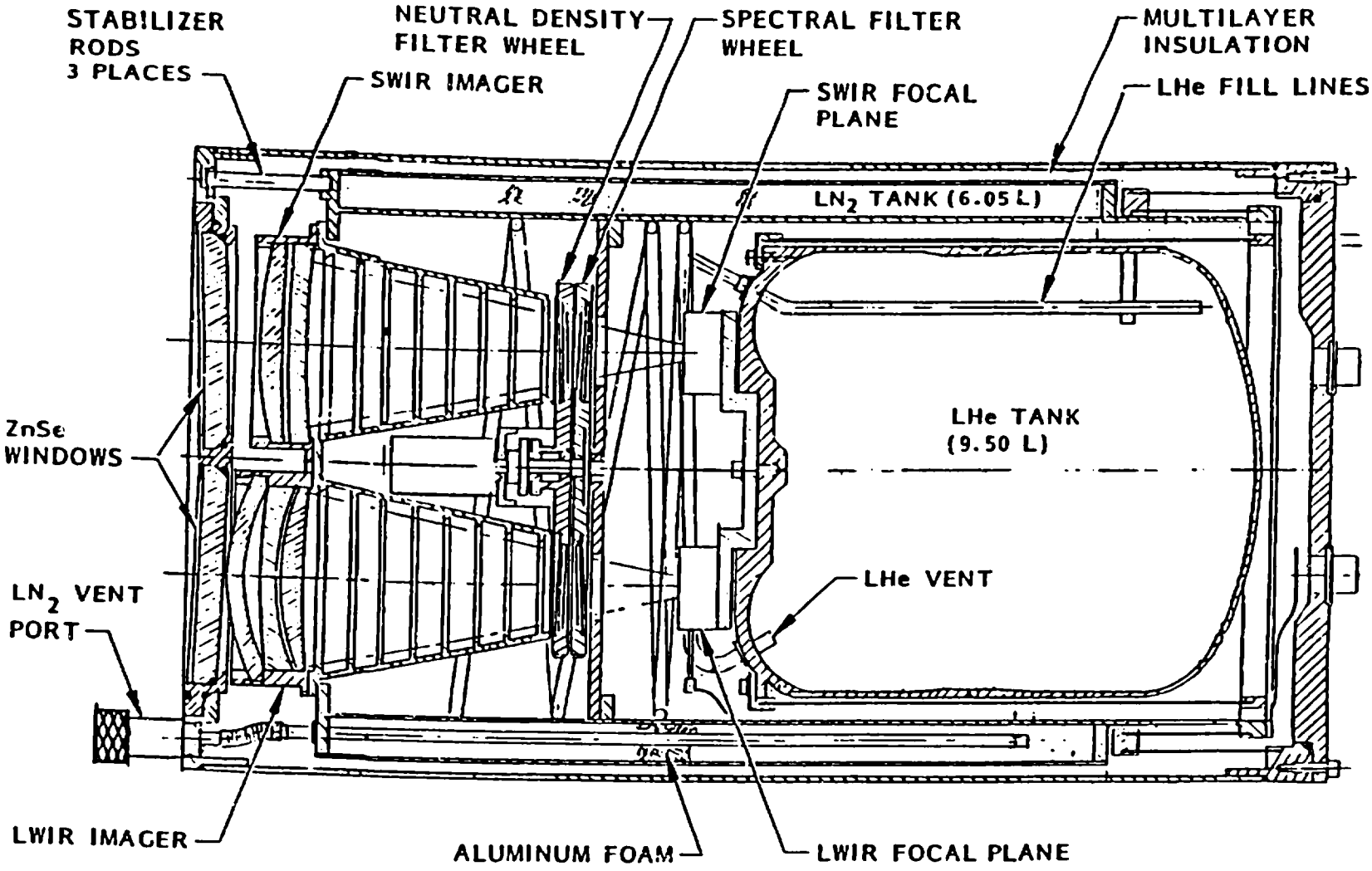

Figure 1 Sensor Layout

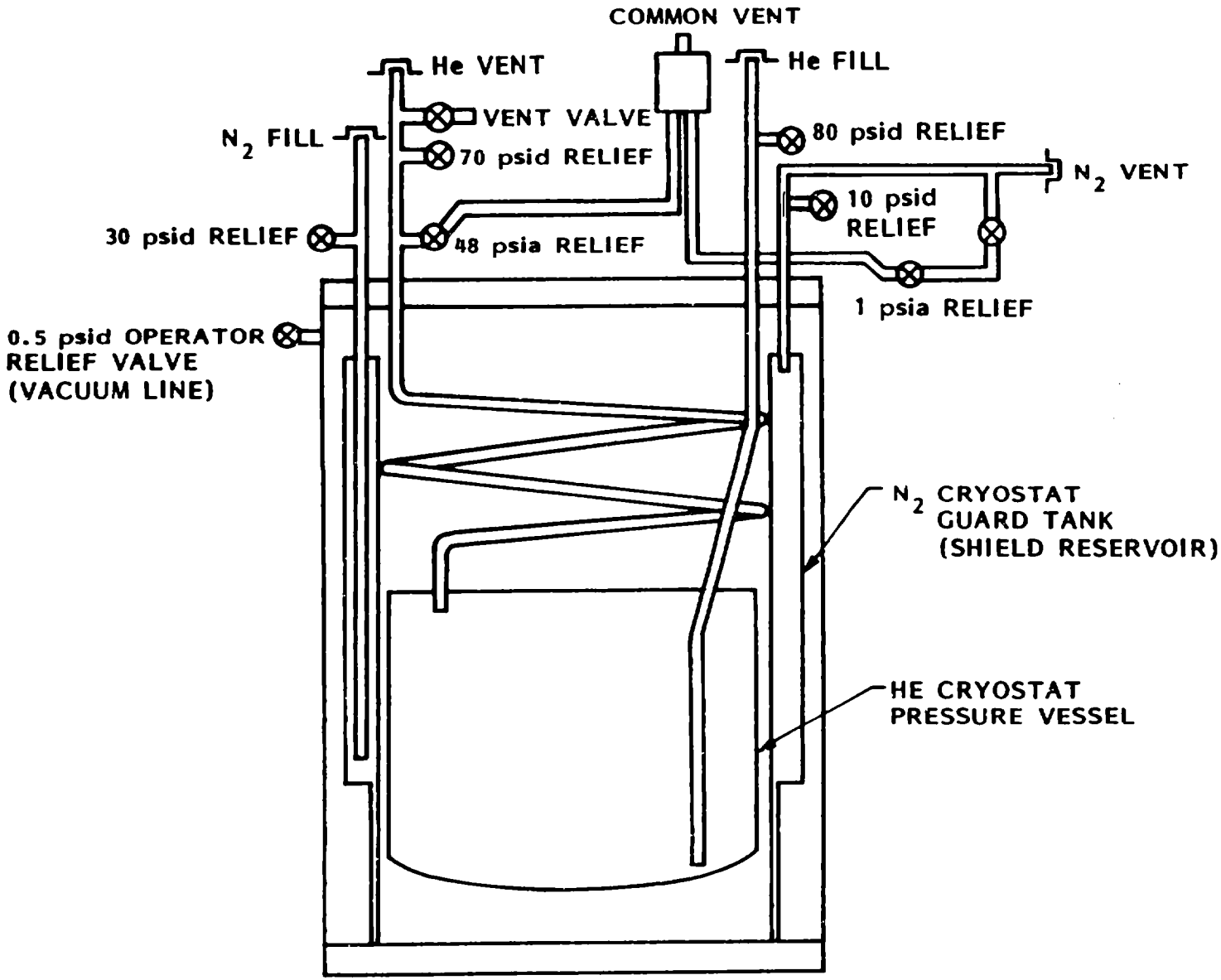

Figure 2 Dewar Valving

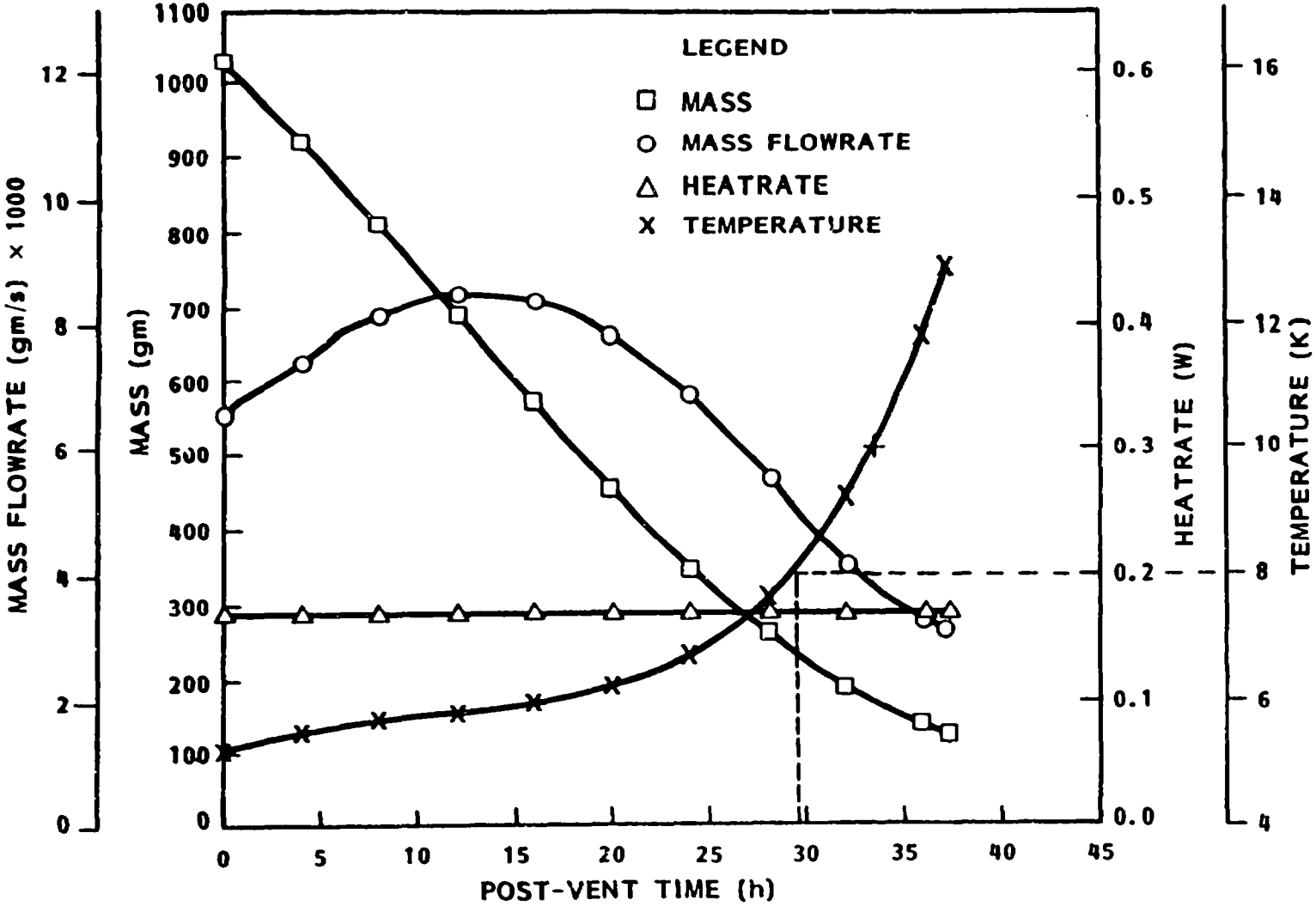

Figure 3 Helium Test Results

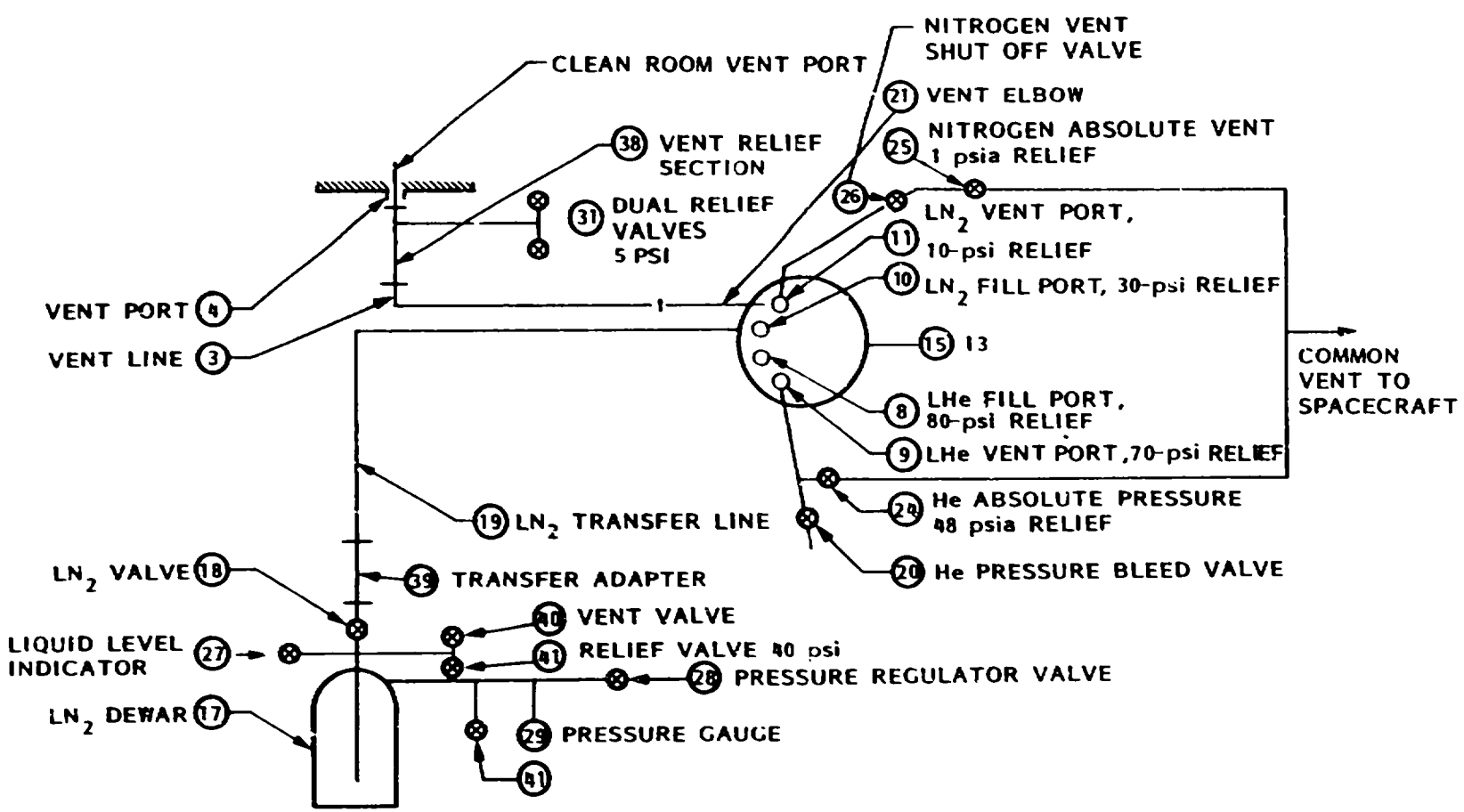

Figure 4 Liquid Nitrogen Transfer System Schematic

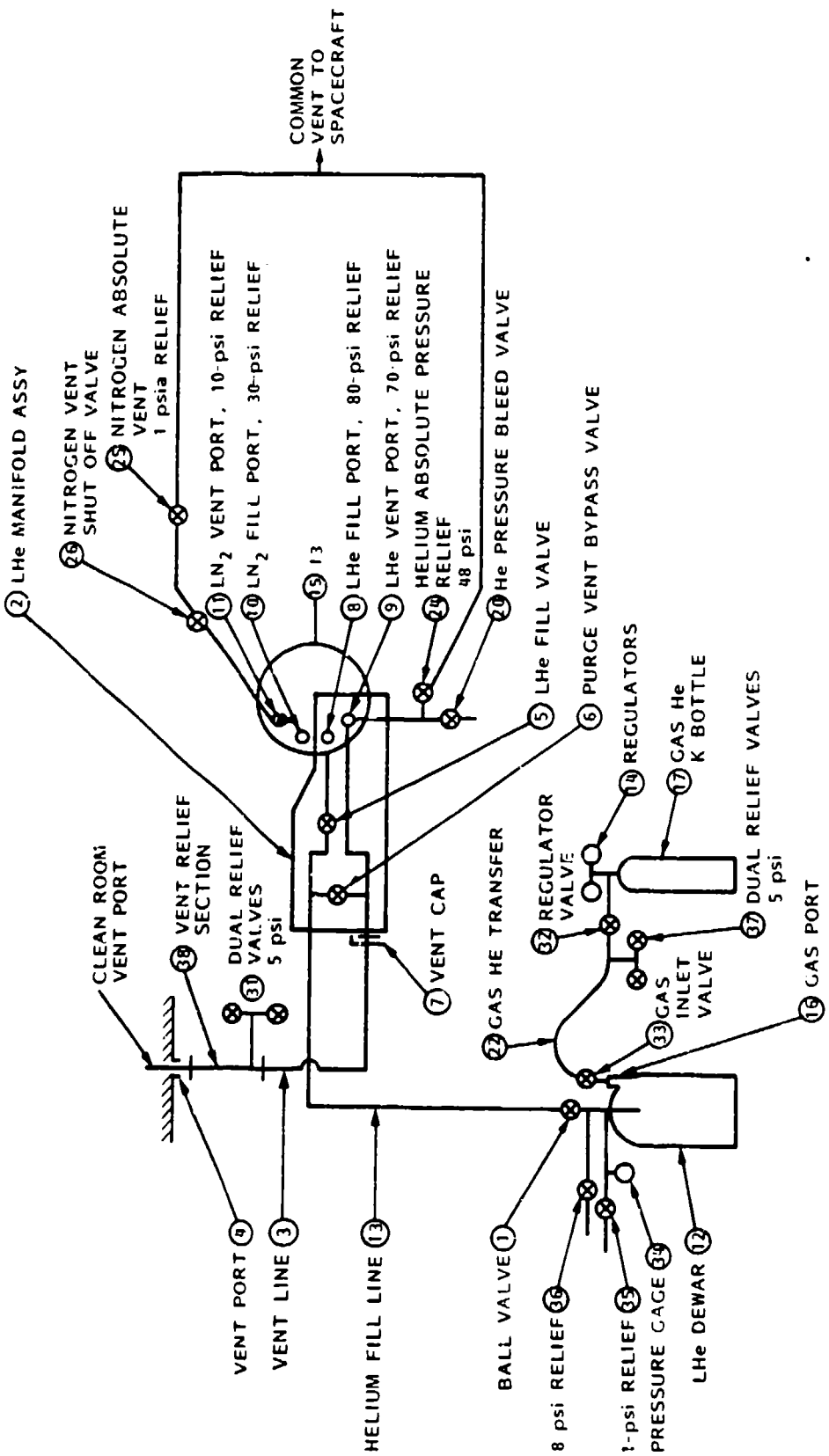

Figure 5 Liquid Helium Transfer System Schematic

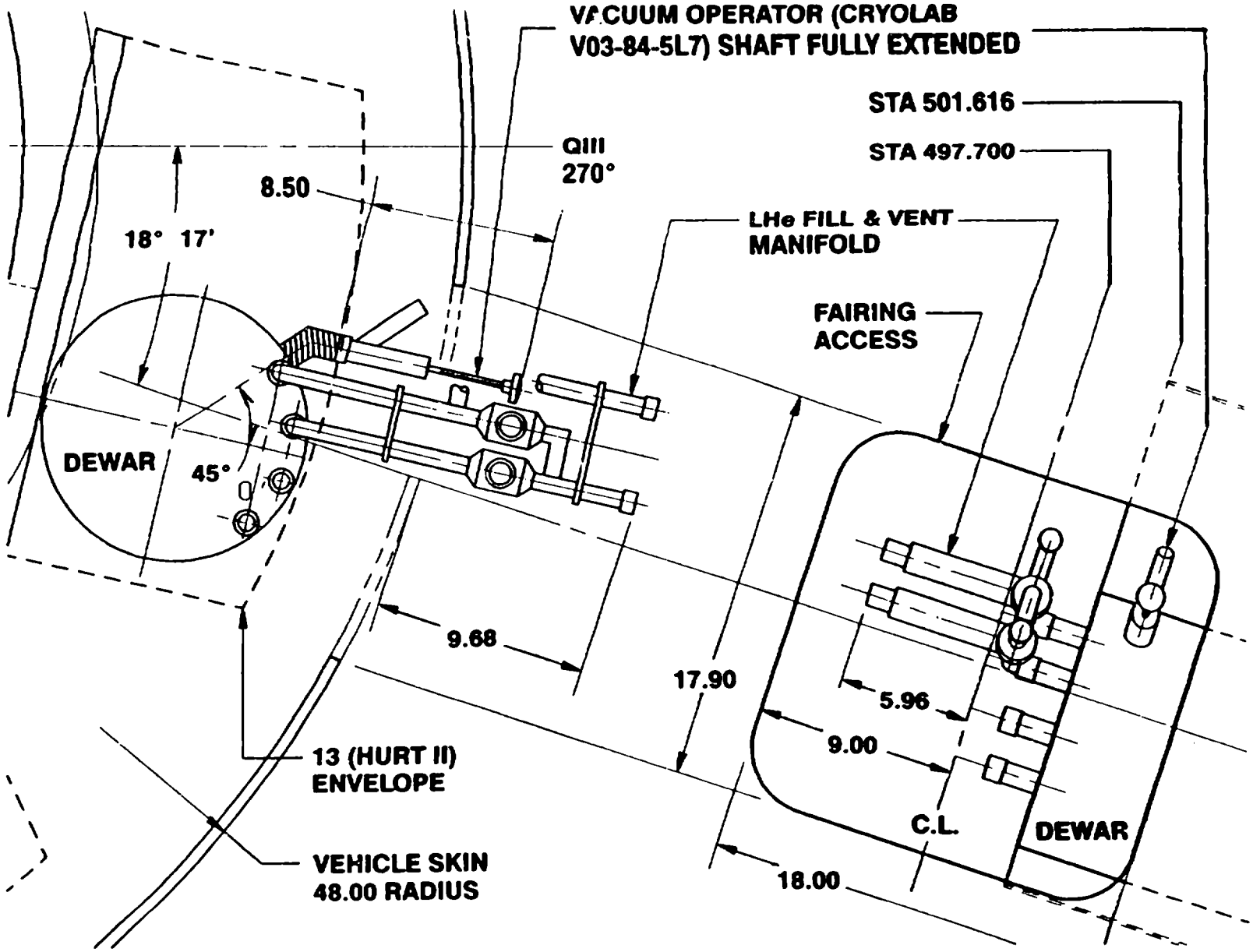

Figure 6 Cryogen Port Access

A CONTINUOUSLY-OPERATING DILUTION REFRIGERATOR FOR SPACE APPLICATIONS

Pat R. Roach
Technology Development Branch
Space Projects Division
NASA Ames Research Center
Moffett Field, California 94035

Ben Helvensteijn
Sterling Federal Systems
Palo Alto, California 94303

ABSTRACT

A preliminary design has been developed for a continuously-operating dilution refrigerator suitable for use in zero gravity. The design uses a condenser at 0.4 K to liquefy the He-3 gas distilled from the He-3-He-4 mixture at 0.7 K. The condensed He-3 returns to the mixing chamber where it again mixes with He-4, producing cooling at 0.1 K. The important development is the method of cooling the condenser at 0.4 K. In order to eliminate moving parts, the condenser will be cooled by two He-3 pots operating alternately. While one He-3 pot is pumped to 0.4 K by a charcoal pump at 2.0 K, the other He-3 pot is being refilled at 2.0 K from gas being desorbed from its charcoal pump heated to 30 K. Heat switches are used to couple the condenser to whichever He-3 pot is cold.

Confinement of the liquids to their chambers will be accomplished in all cases by surface tension forces arising in sintered sponges of metal or ceramic. Confirmation of the gravity-independence of this method of confinement is currently being tested on a single-cycle dilution refrigerator.

INTRODUCTION

Infrared and X-ray detectors for deep-space astronomy can benefit greatly from having detectors cooled to 0.1 K or below. At lower temperatures the heat capacity of bolometers is smaller and the thermal conduction to their

surroundings is less so that they have a greater sensitivity to incident radiation. Also, thermal Johnson noise is less at lower temperatures. In the laboratory the most commonly used technique for reaching temperatures of 0.1 K or less is the He-3–He-4 dilution refrigerator.

DILUTION REFRIGERATOR TECHNIQUE

Basically, a dilution refrigerator is a system that passes the rare isotope He-3 into and through a stationary portion of liquid He-4, producing cooling at the phase boundary where the two isotopes mix. This is shown in fig. 1. The cooling process can be thought of as 'evaporative' cooling: the He-3 'evaporates' into the background of He-4. The popularity of the technique comes from the fact that it can be operated in a continuous mode. By returning the He-3 that has been pumped off back to the mixing chamber, a continuously-operating refrigerator can be created that is invaluable for very-long-term experiments or experiments where very large amounts of heat must be removed.

COMPACT DILUTION REFRIGERATOR

We have been working on a new form[1,2] of dilution refrigerator which is very attractive for space applications. Its design uses gas-adsorption onto charcoal at low temperatures to provide He pumping. This leads to a self-contained refrigerator with no external gas handling system, shown in fig. 2.

This particular version is a single-cycle refrigerator; the system must be recycled when the mixing chamber runs out of He-3. In order to start up a

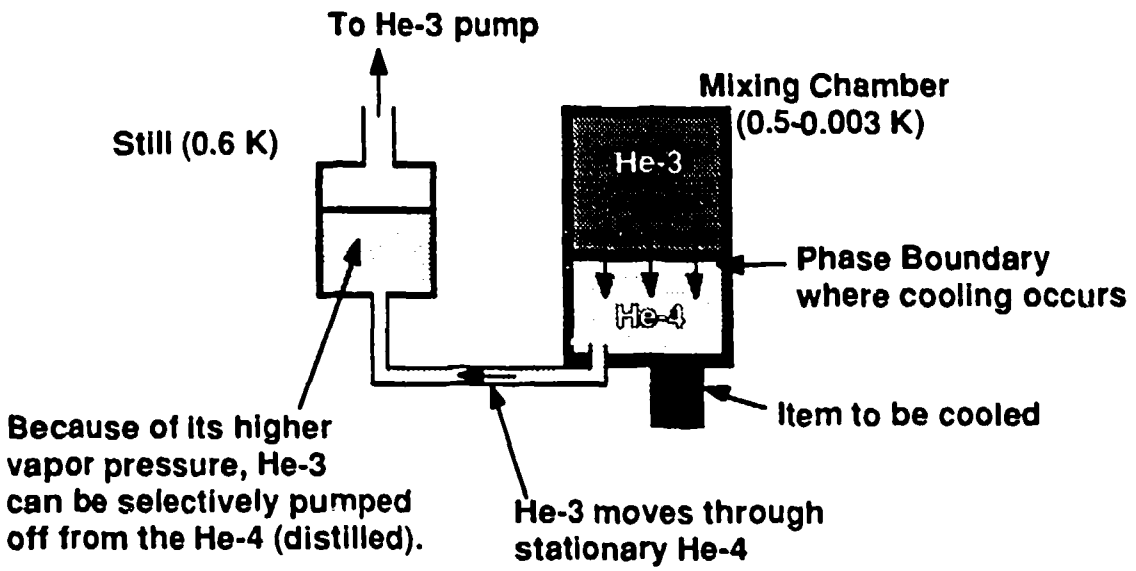

Fig. 1. Basic elements of a dilution refrigerator.

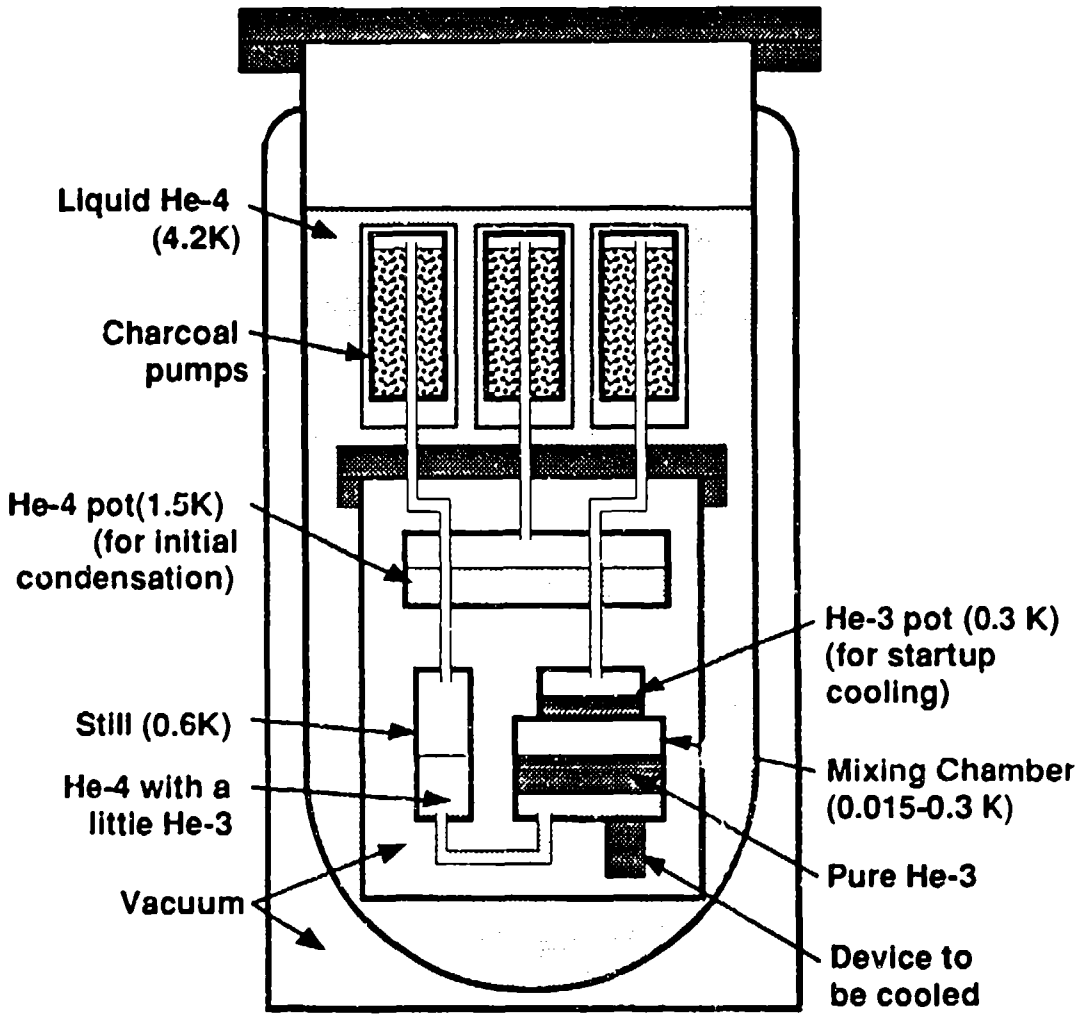

Fig. 2. Compact single-cycle dilution refrigerator.

single-cycle refrigerator it is necessary to provide a He-4 pot for condensing the operating mixture of He-3 and He-4. In addition, it is necessary to have a separate He-3 pot attached to the mixing chamber to provide precooling to 0.3 K so that the dilution process can be efficiently started. Once the mixture in the mixing chamber is at 0.3 K, the He-4 pot and the He-3 pot have done their jobs and will not be needed again until the system has finished the cooling cycle and it is time to start another complete cycle. At 0.3 K the dilution process can be started by allowing the mixture pump to pump on the dilute He-3 in the still. This will draw He-3 out of the mixing chamber, across the phase boundary, cooling the mixing chamber and any device attached to it. Temperatures as low

as 0.015 K have been achieved with such a system. Depending on the heat load and the operating temperature, this cooling can last 10-20 hours for the system under consideration.

All pumping and recycling operations are controlled by heaters; there are no moving parts in the refrigerator. During operation none of the helium leaves the low-temperature region. These factors lead to very reliable performance and make possible the complete automation of all aspects of its operation so that no operator attention is required.

CONTINUOUS REFRIGERATOR

We have developed a design for a continuously-operating refrigerator that maintains the advantages[3,4] of the single-cycle design above. Figure 3 shows the layout of the refrigerator as it might be implemented to operate in zero gravity for a satellite application. It takes advantage of the likely availability of a 2.0 K

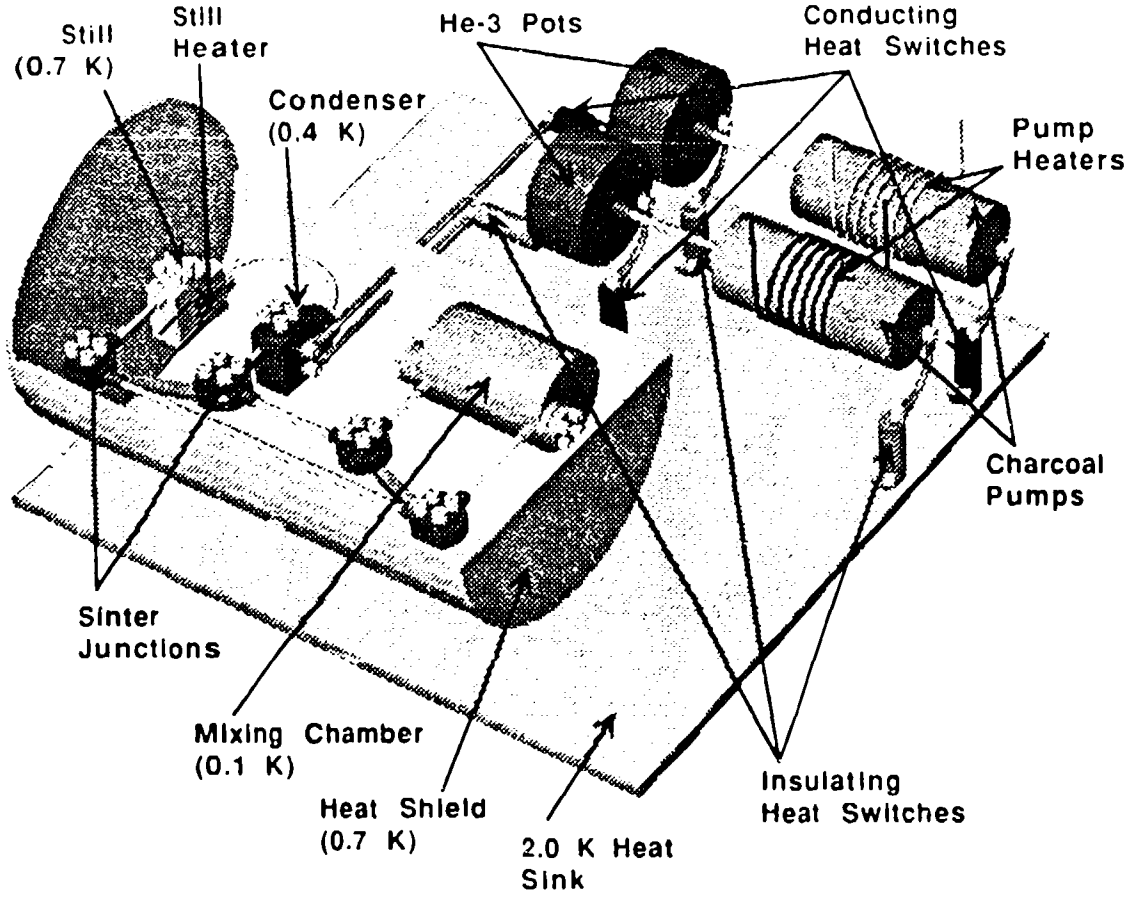

Fig. 3. Layout of continuous dilution refrigerator.

heat sink to which all heat from the refrigerator is rejected. This allows the elimination of the 1.5 K He-4 pot for condensing He-3; 2.0 K is low enough for this. The main difference in this design is the presence of the 0.4 K condenser. Here the gaseous He-3 which is boiled out of the still is liquified and returned to the mixing chamber, making the operation of the refrigerator continuous.

PUSH-PULL HE-3 POTS

The most difficult part of this design is the need to keep the condenser at 0.4 K by means of charcoal pumps without introducing mechanical valves or other moving parts which would compromise the reliability of the system. Here this is accomplished by the use of two charcoal-pumped He-3 pots and numerous heat switches. At any given time one of the He-3 pots is at 0.4 K. Its associated charcoal pump is cooled to 2.0 K by a heat switch so that the liquid in the pot is pumped by the charcoal. This cold pot is connected to the condenser by a heat switch in its conducting state.

The other He-3 pot is isolated from the condenser while it is being recycled. This warm He-3 pot is coupled by a heat switch to the 2.0 K heat sink while He-3 is condensed into it from its associated charcoal pump. This pump is isolated from the 2.0 K heat sink and heated to 30 K to desorb its load of He-3 and condense it into the warm pot. When the warm pot is full of He-3 it will be decoupled from the 2.0 K heat sink and pumped to 0.4 K in anticipation of taking over from the cold He-3 pot when it runs out of He-3. In this way the two pots alternate between cooling and refilling without interrupting the steady cooling of the condenser.

HEAT SWITCHES

The heat switches used to couple the He-3 pots to the condenser are of a design intended to have a very large on/off ratio. The "on" conduction needs to be large in order to minimize the temperature drop between the cold He-3 pot and the condenser, and the "off" conduction needs to be small in order to minimize the heat leak from the warm He-3 pot. Figure 4 shows details of the switch. The two ends of the heat switch will be thermally isolated from each other by a tube of thin-wall stainless steel. Inside this housing will be six closely-spaced concentric cylinders. Three of these cylinders will be attached to each end cap in such a way that they interleave with (but don't touch) the set of cylinders from the other cap. In this way a relatively large surface area for heat transfer can be obtained in a compact volume. The narrow gaps between cylinders will be filled with He or pumped empty by a tiny charcoal pump located remotely from the switch.

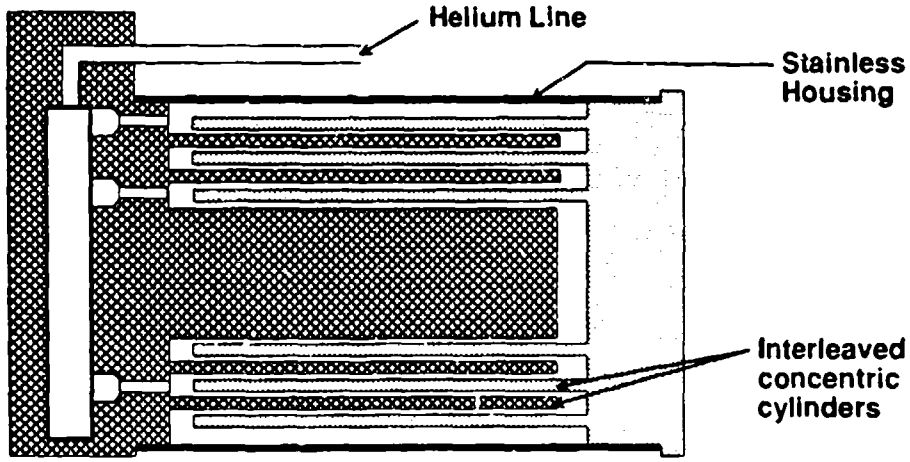

Fig. 4. Cross section of heat switch.

LOW-TEMPERATURE STAGE

Figure 5 shows some details of the way the He-3 in the He-3/He-4 mixture is continuously circulated through the low-temperature chambers. In order to keep the liquid phases in their proper chambers in the absence of gravity, all

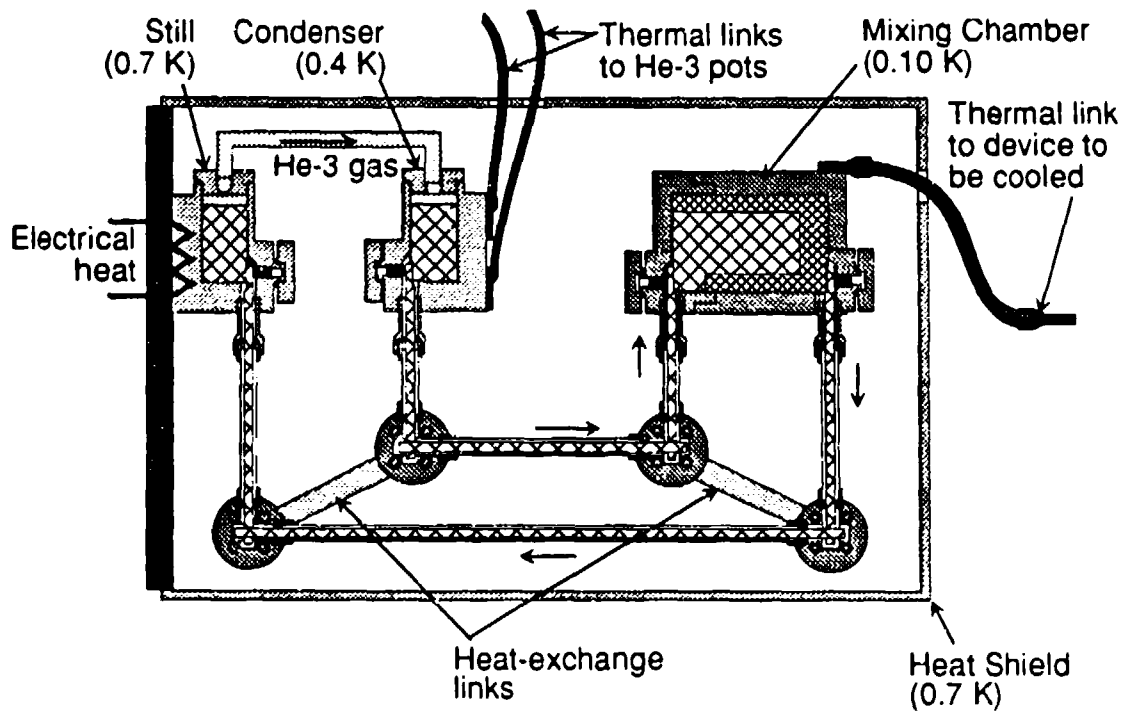

Fig. 5. Details of He-3 circulation in continuous refrigerator.

parts of the system that contain liquid, including the He-3 pots, have a matrix of sintered metal or ceramic with fine pores to contain the liquid[4]. Capillary forces in the pores will keep the liquid phases from moving outside of the regions where they are needed.

Heat Shield

The low-temperature stage is surrounded by a thermal shield attached to the still so that its temperature is ~0.7 K. This shield intercepts thermal radiation from the environment at 2.0 K and higher in order to minimize the heat load on the mixing chamber. An extra heat load on the still is of little consequence since it will simply replace a little of the electrical heat normally applied to the still in order to drive the circulation of He-3.

Connecting Lines

The lines connecting the still and condenser to the mixing chamber must be filled with porous matrix in order to provide a continuous path of capillary forces. If the connecting lines had no porous matrix, the unbalanced capillary forces in the chambers would draw the liquid out of the connecting lines and leave them empty. In order that there not be an excessive heat leak into the mixing chamber from the warmer chambers, it is necessary that the porous matrix in the connecting lines be a low-conductivity material such as stainless steel or ceramic.

In order to facilitate construction, these lines consist of straight sections of sintered material clamped together at their intersections in order to form an uninterrupted path of pores for the He flow. This sinter must also be clamped to the sinter in the various chambers for the same reason. The clamping will be done by set screws applied from the outside of the chambers; the set screws will then be sealed by an indium-gasketed cover plate. The points where sinter is clamped will have flat surfaces machined into the sinter to give adequate surface area of contact. This will probably have to be done by electric discharge machining in the case of soft metallic materials in order not to smear the surface of the sinter and close up the pores.

Another feature that is required for a continuous refrigerator is a heat exchanger so that cold liquid leaving the mixing chamber can be used to precool the warm liquid returning to the mixing chamber. In the present design this takes the form of thermal links between pairs of sinter junction blocks in the connecting lines. At these points the sinter is clamped against the block, providing good thermal contact between the liquid in the pores and the block.

Mixing Chamber

The phase boundary between the concentrated and dilute He-3 phases is

difficult to control with capillary forces because the interfacial tension between phases is very low[5-8]. For this reason, the mixing chamber must have a shell of very fine sinter in it to prevent the concentrated He-3 from passing directly into the still. In addition, the rest of the mixing chamber volume must be filled with coarse sinter to receive the concentrated He-3 returning from the condenser.

OPERATION

A continuous dilution refrigerator doesn't need the extra He-3 pot on the mixing chamber that the single cycle type does. This is because the system can be slowly precooled by circulating the mixture through the 0.4 K condenser until all the chambers are cold enough for the dilution cycle to start. The liquid that condenses at 0.4 K will be drawn by capillary forces toward the warmer parts of the system where it will evaporate and pass through the rest of the system and the still until it condenses again at 0.4 K.

Once all the helium is condensed into the refrigerator from its gas reservoir (not shown) and all the chambers have been cooled to 0.4 K, the dilution cycle can be started by applying heat to the still to raise its temperature to 0.7 K. The flow of gas from the still to the condenser is controlled by their relative temperatures. If the dilute mixture in the still is 1% He-3 at 0.7 K then the vapor above it will be nearly pure He-3 at a pressure of ~2 Pa. This will be in equilibrium with the liquid in the condenser since the vapor pressure of pure He-3 at 0.4 K is also ~2 Pa. By increasing or decreasing the still temperature the equilibrium can be unbalanced by the amount necessary to cause the flow desired.

EXPERIMENTAL TESTS

Tests have been carried out on the single-cycle form of the refrigerator to establish the influence of sinter on the performance of the refrigerator. Porous sintered copper powder has been added to the He-3 pot, the still and the mixing chamber. The test results show that the fine porous sinter has little effect on the operation of the refrigerator. Performance was essentially the same before and after the sinter was added. The results show that the refrigerator can cool to 0.1 K and remain at this temperature for more than 5 hours with a heat load on the mixing chamber of 3 μW. This is well within the range of expectations for the system.

A further test currently being set up is the addition of porous sinter to the connecting line between the still and the mixing chamber. Calculations[3] show that this connecting line is the part of the system that is most sensitive to the restrictive effects of the fine pores. The installation of this sinter requires major modifications to the refrigerator. A design of the still and mixing chamber and the connecting line between them very much like that shown in fig. 5 has been

completed and tested to 0.1 K and we are about to add sinter to the connecting line to study its effect there.

Once we have confirmed that sinter in the connecting line does not seriously affect the performance of the refrigerator, we will fill the other chambers with sinter and begin to study the extent to which the refrigerator can operate with adverse gravitational heads. This will involve operating with the still above and then below the mixing chamber and then with both chambers upside down. If a substantial degree of gravitational independence is established by these tests, then considerable confidence is gained that the system will operate in zero gravity.

REFERENCES

1. P. R. Roach and K. E. Gray, "Low-Cost, Compact Dilution Refrigerator: Operation from 200 to 20 mK", *Advances in Cryogenic Engineering*, vol. 33, Plenum Press, New York (1988), pp. 707-712.

2. Available as model 302000, RMC Cryosystems, 1802 W. Grant Rd., Suite 122, Tucson, AZ 85745.

3. Pat R. Roach, "Thermal Efficiency of a Zero-G Dilution Refrigerator", *Proc. Fifth Intern. Cryocoolers Conf.*, Monterey, CA (August 1988) pp.195-204.

4. Pat R. Roach and Ben Helvensteijn, "Development of a Compact Dilution Refrigerator for Zero Gravity Operation", *Advances in Cryogenic Engineering*, vol. 35, Plenum Press, New York (1990) pp. 1045-1053.

5. L. S. Balfour, J. Landau, S. G. Lipson and J. Pipman, "Interfacial Tension of He-3-He-4 Liquid Mixtures under Pressure", *Journal de Physique*, vol. 39, no. 8 suppl., C6 (1978) pp. 203-204.

6. P. Leiderer, H. Poisel and M. Wanner, "Interfacial Tension Near the Tricritical Point in He-3-He-4 Mixtures", *J. Low Temp. Phys.*, vol. 28, no. 1/2 (1977) pp. 167-173.

7. S. T. Boldarev and V. P. Peshkov, "Measurements of the Surface Tension in Helium by Means of Surface Waves", *Physica*, vol. 69(1973) pp. 141-147.

8. H. M. Guo, D. O. Edwards, R. E. Sarwinski and J. T. Tough, "Fermi-Liquid Behavior of He-3 Adsorbed on Liquid Helium", *Phys. Rev. Lett.*, vol. 27, no. 19(1971) pp. 1259-1263.

HEAT DRIVEN CRYOCOOLER FOR SATELLITE BUS USE*

Robert M Lerner
Lincoln Laboratory, Massachusetts Institute of Technology
Lexington, Massachusetts 02173

INTRODUCTION

We all know the problems of providing cryocoolers for satellite packages: mechanical and vibrational uncertainties, low coefficient of performance (COP), lack of inexpensive commercial laboratory prototypes, and substantial weight. It might seem presumptuous, then, to suppose a satellite bus cooling system to provide tens of watts of cooling at 75 to 90 K via the circulation of a suitable chilled brine. Yet that is precisely what we shall be considering here.

A satellite "bus" is that part of the satellite which supplies mechanical support, prime power, orbital orientation and station keeping, thermal environment, and command and status telemetry. *Bus* design differs from individual *package* design in two crucial ways. First, it is literally done first, often long before the configuration of individual packages has been determined. It is the bus architect who allocates weight and power budgets to individual users and resolves the conflicts arising from individual user demands. Secondly, only the bus designer has access to the system utilities, in particular the prime power source and its associated waste heat. Here, we propose to make use of that waste heat to run a non-mechanical cryocooler at the level of roughly 50 W of 75 K refrigeration for every 200 W of electrical prime power deliverable to package users, for a weight penalty of roughly 1 lb/W.

Figure 1 is a cartoon of a communication satellite with a bus and communications package. What we are adding is a circulating chilled "brine" cooling system with refrigerator in the bus and heat loads in the package. In order to use the heat that would otherwise be directly radiated by the solar paddles, these will be eliminated and replaced by a solar concentrator. This sort of change is possible only at the bus design level. It cannot be accomplished in individual packages.

In what follows, we consider the working fluids available for circulating cold brine; mention some heat-driven refrigeration cycles and their possible performance; and select the sorption refrigerator as an example of one that might be used. Finally, we indicate how a sorption cooler system might be incorporated into an actual satellite layout with back-of-the-envelope weight and power budgets.

*This work was supported by the US Navy and, under the auspices of the Consortium for Superconducting Electronics with partial support by the Defense Advanced Research Projects Agency (Contract MDA 972-90-C-0021).

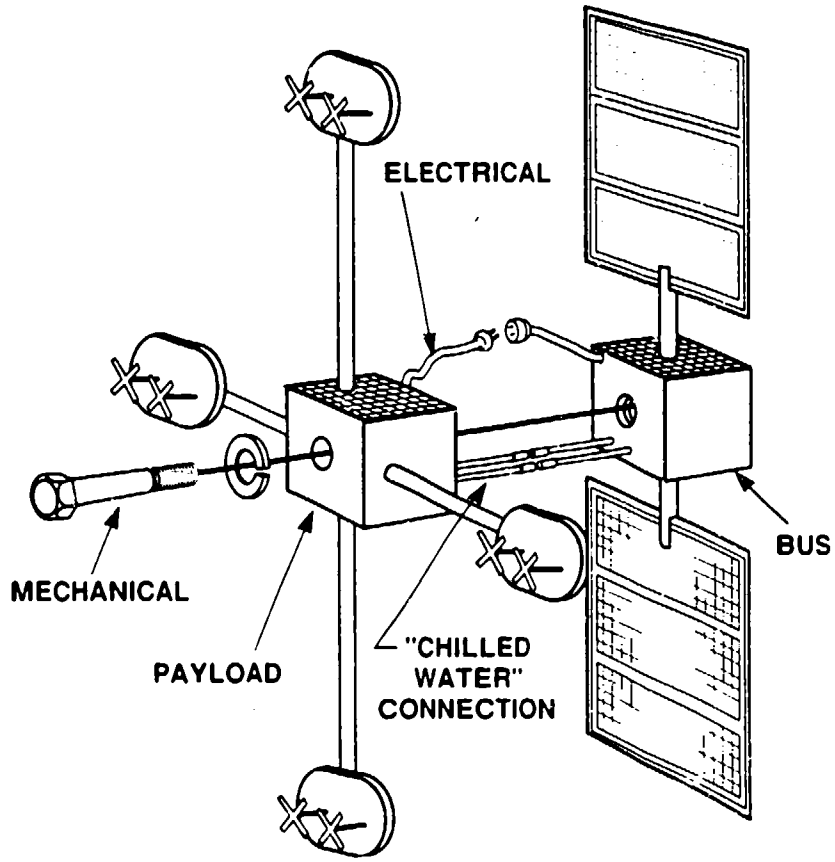

Fig. 1. Bus-payload interface with bus cooling.

BRINES

The first requirement of a chilled brine system is to have a chillable brine. As a last resort, one could use a gas such as hydrogen or neon as a circulating coolant. One would then have to face the problem of a pump to circulate it. The problem of building long-lived devices to pump gases has been the bane of the cryo-cooler art. They all tend to have the life of automobile engines, not the ten years of continuous duty required for general satellite use.

For ease of containment, high volumetric heat capacity, and ease of ground testing, liquid brine is preferable. Ideally, this fluid should remain a modest-viscosity liquid from room temperature to below the operating temperature of the cryo-cooler. Any moving circulation pump parts can be designed to float at neutral buoyancy in such a liquid, and so reproduce 0-g operation in ground life tests.

Figure 2 gives the liquid ranges of a number of pure substances. Critical points are also shown, as asterisks. None have a range from low to room temperature. Ordinary gases such as those found in the atmosphere (A, N_2, O_2, CO, CO_2), hydrogen, and neon have very short liquid ranges, and their critical temperatures are nearby on a log scale. The long ranges belong to hydrocarbons like propane and α-butylene, and to exotic materials like NF_3 and F_2O, fluorine analogs of ammonia and water, respectively.

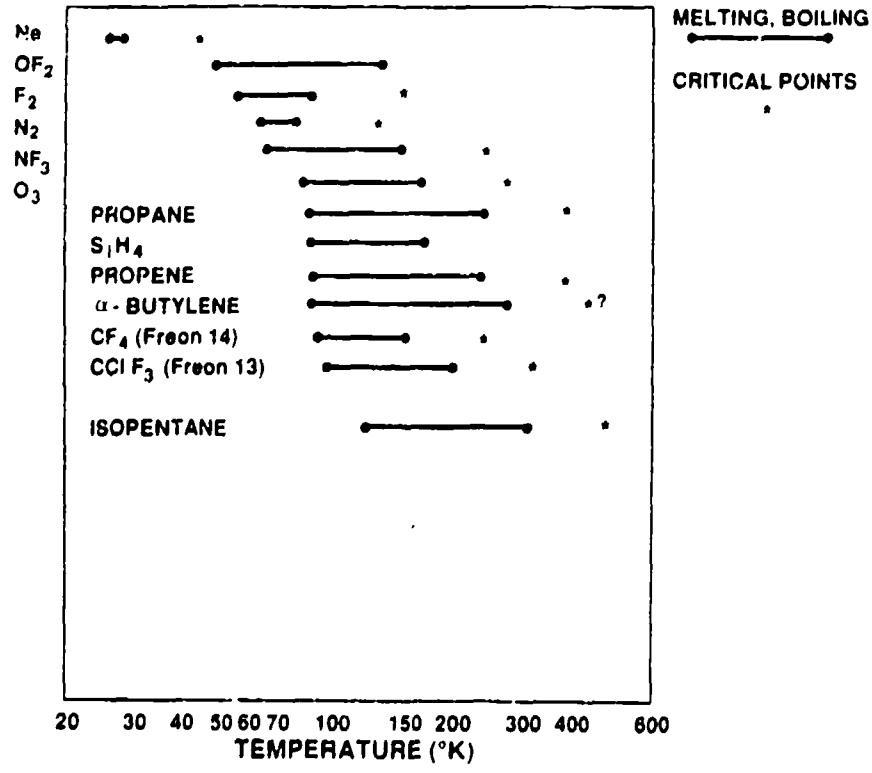

Fig. 2. Melting, boiling, and critical points of various compounds.

None of the materials shown spans the range from 75° to 300 K. One does run from under 90° to 270°. However, when substances are miscible in the liquid state but not in the solid state, they will often exhibit a eutectic freezing point well below that of either component. Is this possible with the fluorine exotics or with hydrocarbons? The evidence in the case of hydrocarbons is both tantalizing and scanty.

Would you believe distilled gasoline? In 1917 Professor Jaroslav Formánek took some Galician[1] gasoline and ran it through a fractionation column.[2] The fraction which condensed at 24° to 40 °C remained liquid down to 70 K. The fraction which came off the still at 40° to 60 °C remained liquid to 75 K. Professor Formánek complains in his text that he experimented because there was little published data. While he gives the specific gravity of the distillates (0.6324 and 0.6593, respectively), he does not provide a chemical analysis of these fractions.

I have tried, without success, to uncover more complete and modern information. Here is a homework problem for someone. What was Formanek's Galician gasoline, and how can we reproduce the remarkable liquid range that he reported?

THERMODYNAMIC LIMITATIONS

A typical cryocooler available today might produce up to a watt of 75 K cooling for 30 W of electrical input. Obviously, such performance cannot be scaled up to tens of watts of cryo-cooling without consuming more than the entire available electrical power of a typical 200 to 300 W satellite. This level of electrical power is the result of converting 15%

to 20% of the energy in 1 to 1 1/2 square meters of sunlight into solar-cell electricity, discarding the waste heat directly to space. It can also result from converting 5% to 7% of the 1000 °C hot shoe heat of a 4.8 kW radio-isotope thermal source with a thermopile,[3] discarding the waste heat to space at about 600 K.

The question arises, is there enough waste heat from such sources to drive a ten to fifty W 75 K refrigerator?

In refrigeration, the engineering measure of performance is the COP, the ratio of Q, the heat removed at the refrigerator temperature, to E, the total energy supplied. See Fig. 3a. Conservation of energy gives the total heat out as Q + E. The associated entropies are zero for a mechanical or electrical E, $(Q + E)/T_B$ for the output heat, and Q/T_A for the input heat. Since total entropy can only increase, there is a 2nd Law performance limitation, call it the "Carnot COP":

$$COP \leq [T_B / T_A - 1]^{-1} \qquad (1)$$

If the ratio of warm to cold temperatures is not much greater than unity (as in air conditioning practice), this number can be large. If the temperature ratio is substantial, then the Carnot COP is less than unity. For a cooler operating between 75 K and 300 K, the Carnot COP is one-third. A real refrigerator won't be that good. The best one sees in practice is about 30% of Carnot; typical cryocoolers are 15% of Carnot, or worse.

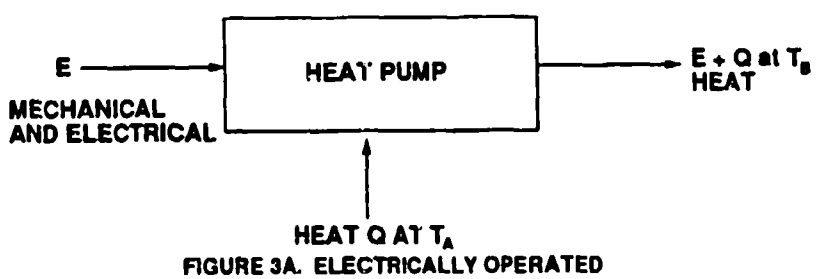

FIGURE 3A. ELECTRICALLY OPERATED

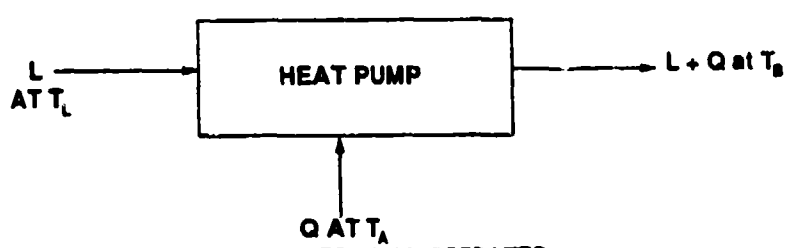

FIGURE 3B. THERMALLY OPERATED

Fig. 3. Carnot heat pumps.

In Figure 3a, the input energy was assumed to be mechanical or electrical. The associated entropy was zero. Now, suppose that the energy is supplied as heat L at temperature T_L. The output energy is still L + Q, but the input entropy is increased by L/T_L. This lowers the maximum COP by the Carnot efficiency of a heat engine working between T_L and T_B.

$$COP \leq [1 - T_B / T_L] * [T_B / T_A - 1]^{-1} \qquad (2)$$

It is reasonable to suppose a satellite design in which waste heat can be collected from the satellite prime power source at about 600 K, for discard to space at 300 K. For such a case, the thermally driven COP ceiling would be half that available from a zero-entropy energy source.

Of course, there will be a practical efficiency penalty over and above the constraint of Eq. (2). However, one ought to take the penalty of practical inefficiency only once, especially with a refrigeration cycle that has no compressors. The overall practical efficiency of a thermally operated sorption refrigerator can be as high as 60% of theoretical; nevertheless, we shall use 30% of theoretical in the estimates below.

HEAT DRIVEN REFRIGERATION

Heat-driven refrigeration is a significant component of real-world practice. Here are three examples.

- The Servel Cycle is used in gas-flame operated refrigerators and freezers. It is also used in the apartment-size mini-refrigerator even though the heater in this case is electric.

- The Steam-Driven Jet Pump can replace any mechanical compressor or vacuum pump and thus eliminate the need for short-lived packings, bearings, and cylinders.

- The Sorption Cooler can function over as wide a temperature range as there are suitable sorbants for the working vapor.

The Servel Cycle uses ammonia as the refrigerant and relies on gravity for circulation of gases (hot gases rise). It is not appropriate for use in space.

An example of the industrial use of steam jet pumps in an evaporative cooler for chilled water is shown in Fig. 4, much simplified from the 1960 ASHRAE[4] Handbook. The steam jets are at the top of the figure, where they compress water vapor into a water-cooled condenser. Note that there are in addition some feed water and circulation pumps. The power consumed by these is incidental. You would not build a satellite system this way; but if you did, moving parts can be designed to float at neutral buoyancy in the liquid being pumped. This would allow life test of moving parts at 0G on the ground.

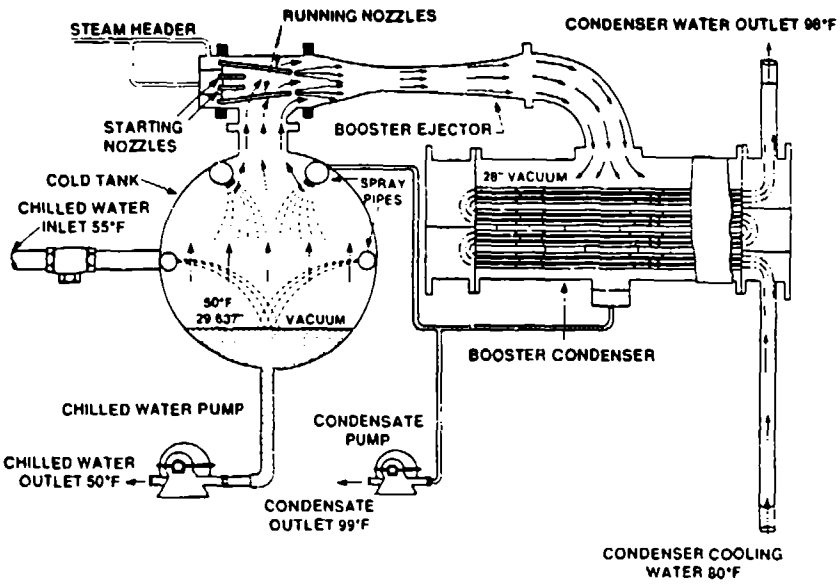

Fig. 4. Steam jet-pumped evaporation refrigerator.

Another feature of this diagram is use of droplets for a return stream. This is a simple but elegant form of counterflow heat exchange between the vapor phase of a substance moving in one direction and the liquid phase moving in the other. A similar droplet-to-gas scheme is used in the Servel Cycle.

Figure 5 shows the principles of a sorption cooler system. There is a cold zone in which the chilled brine is cooled, a warm zone (from which heat is discarded), and a hot zone in which the working fluid G is separated (by conventional boil-off) from the warm-temperature sorbant B.

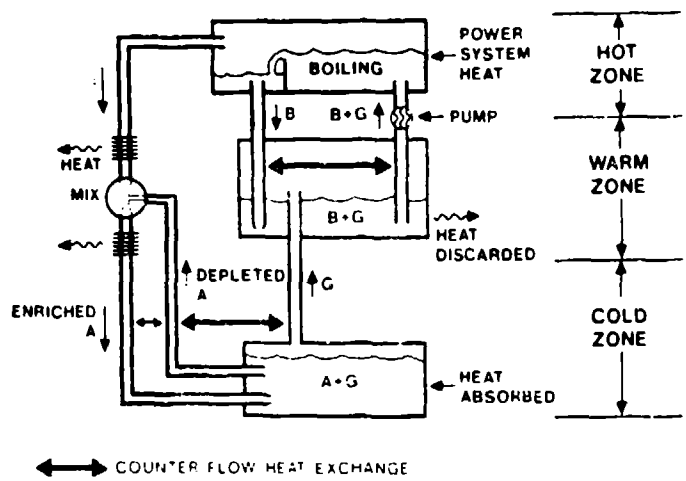

Fig. 5. Sorption cooler system.

Here's how it works. Heat which is absorbed at the low temperature boils off working fluid G. The vapor passes (at constant pressure) into the warm zone where it is re-absorbed with the release of heat.

The working fluid G is once again boiled off in the hot chamber. This chamber has a much higher partial pressure of G than do the other two. The figure shows a feedwater pump between them, and metering nozzles where higher pressure liquid reenters lower pressure zones. The pump is convenient, not necessary. As in the Servel Cycle, the pressure can be equalized by use of an inert fill gas in the warm and cold chambers.

Finally the working fluid must be recombined with the original host A, at a temperature in which the heat of re-combination can be discarded. In the figure, this is done by bringing some of the depleted cold fluid up to the warm zone, through a liquid-to-liquid heat exchanger.

The same process is shown (not to scale) as a thermodynamic cycle on the T-S plane in Fig. 6. This diagram emphasizes the fact that to maintain the same pressure of G over both low and warm temperature sorbants, the sorption *entropy* change must be roughly the same in each case. Since heat of transition at constant temperature is $T\Delta S$, this automatically produces a ratio of heat discarded (along path 3 in the figure) to heat refrigerated (along path 1) in the ratio of T_B to T_A.

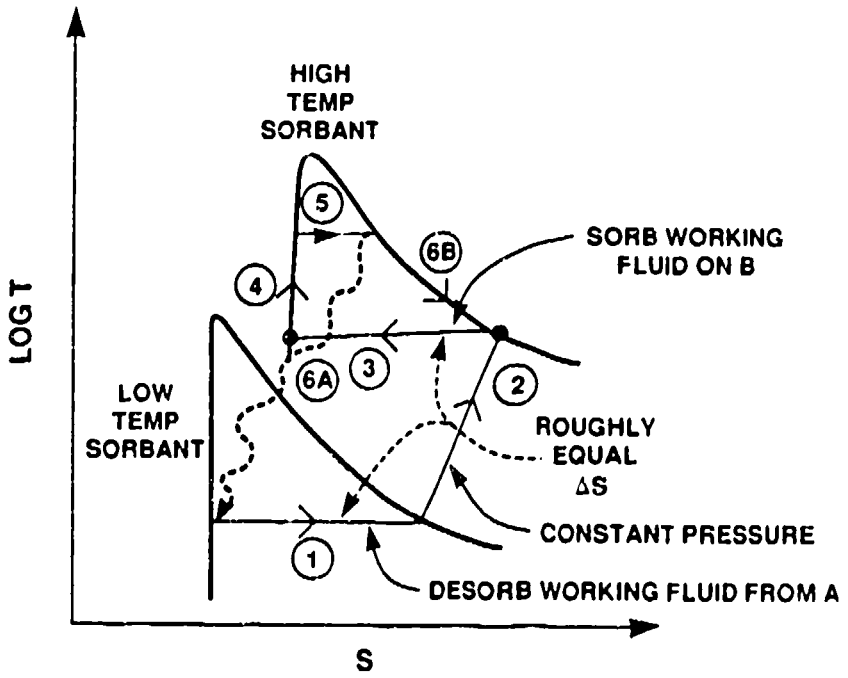

Fig. 6. Sorption cycle.

While we speak of the heat source "driving" the cooling, and an efficiency equivalent to that of running a thermo-mechanical engine, such terminology implies the wrong order of events. In sorption cooling cycles, heat is discarded (along path 3) *before* the driving energy is supplied (at path 5)! This fact nevertheless provides a means by which the refrigerator can continue to operate while a sun-powered satellite is in earth shadow. One needs only to supply sufficient refrigerant (and sorbant) to last for the time the earth blocks the sun.[5] The refrigerant can be re-processed (over paths 4-5-6A in the figure) after the sun returns.

SATELLITE DESIGN AND PERFORMANCE

The question now arises, could we put all of this into a satellite? Figure 7 is an artist's concept of a satellite mechanically laid out to incorporate heat driven refrigeration. The actual refrigeration unit is not shown.

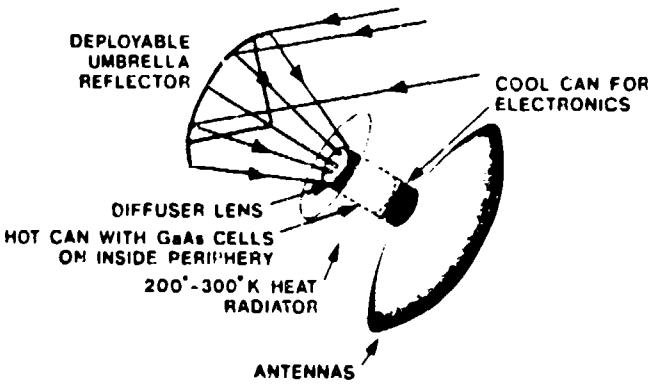

Fig. 7. Combined prime power and cooler satellite envelope.

The usual solar cell paddles have been replaced by GaAs cells arranged around the inside of a hot can, running at roughly 600 K. Sunlight is collected by an unfurlable umbrella mirror structure , a 15:1 concentration ratio. In another context, the writer has run weight per electrical watt numbers for such structures. The weight comes out about the same as, perhaps a little lighter than, conventional solar paddles.

Surrounding the hot can is the cylindric heat emitting surface. For getting rid of the heat from 1 sq.m. of sunlight, one needs at 300 K about 3 sq.m. in this radiator, so as to make it roughly 1 meter diameter by 1 meter high. If the satellite is in low earth orbit, then for the same *average* electrical power and heat discard capacity the umbrella and the heat discard surface will be twice as large as for a high altitude orbit, on account of earth shadow half the time.

At the bus design level, all facets of satellite system engineering interact. I should remark that this drawing is naive about relative geometry of sun and earth. It would have been better if the antenna dish had been turned through 90°.

Figure 8 shows the bare bones of the placement of sorption refrigerator components between the cans and the shield. The hot, warm, and cold zone fluid containers are shown as toroidal tanks of the kind once used to hold ammonia or hydrazine for cold-gas-jet station keeping. Such tankage need not resist extreme pressure; it can be light weight. The figure omits the station-keeping tank, which is now usually spherical.

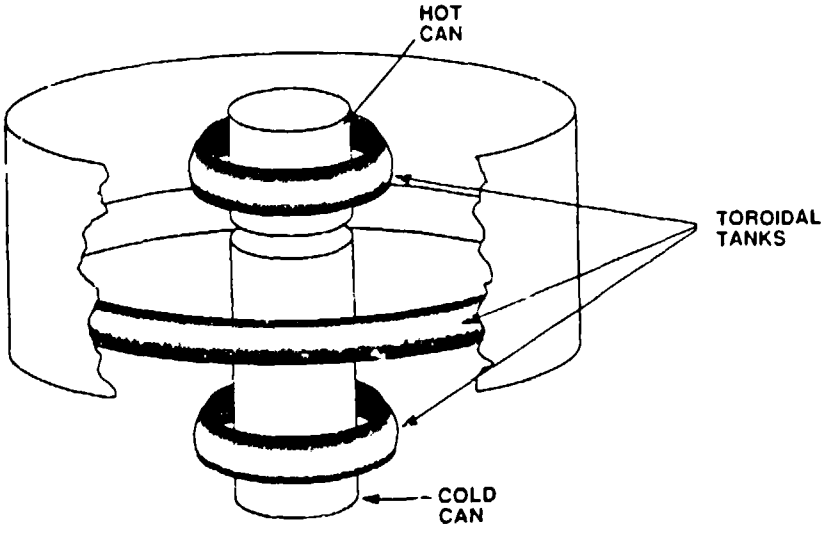

Fig. 8. Tankage layout.

One cannot produce precise weight and power budgets for these roughly drawn configurations. Nevertheless, they rely on combinations of fairly standard components, so that one can make some acceptable "back-of-the-envelope" estimates.

One can assume, for example, roughly 1 square meter of solar collector producing 1350 W of solar input to the can of GaAs cells. Modern GaAs cells, optimized for use in concentrators, can produce 20% conversion efficiency even while operating at 300 °C or 600 K. Thus the bus has available to it 270 W of electrical prime power and 1080 W of 600 K waste heat. Carnot efficiency, with heat discard at 300 K, according to Eq. (2) a heat-driven refrigerator could produce 180 watts of cooling at 75 K!

$$Q = [300 / 600 - 1] / [300 / 75 - 1] (1080) = 180 \qquad (3)$$

The practical efficiency will be less; let us assume 30% of theoretical. The result is 54 W of refrigeration to go along with 270 W of electrical power. Not all of this can be delivered to the customers. In particular, the raw electrical power must be conditioned in various ways, and some power is used by the bus itself. Similarly, some of the refrigeration will be lost to bus piping. Nevertheless, the prospect is that roughly 50 W of 75° circulating brine refrigeration and roughly 200 W of electrical power will be available to package users.

For a satellite with radio-isotope thermal generation, the amount of refrigeration available per electrical watt is substantially greater, on account of the substantially lower efficiency of thermoelectric conversion. Here, the prospect is for 150 W of refrigeration accompanying 200 W of electrical power. Almost the entire package complement of such a satellite could operate at 75 K, including logic and communications transmitters.

Back-of-the-envelope weights estimated from concentrator studies and from known mechanical components are given in Table 1.

TABLE 1. Weight estimates for 75 K cooler.

SOLAR CELL POWER SYSTEM:	Slight Decrease from Conventional Paddle Arrangement.
TANKS, VALVES, HEAT PIPES:	10 lbs apiece for each of 3 subsystems.
HEAT RADIATOR:HEAT:	3 sqm of 10 mil 2nd surface quartz glass mirror (4 lbs) plus structural support. Total about 10 lbs.
REFRIGERANT:	Assuming desorption heat at 200 J/gr, 2 lbs/hr circulation required for 55 W of cooling.
THERMAL STORAGE:	Not considered here.
OVERALL WEIGHT PENALTY:	Roughly 1 lb/W.

There are any number of engineering details that have been glossed over in preparing this table. For example, the weight of the chilled brine distribution piping has not been considered; it would be assessed against the package users, not against the bus. (Such are the privileges of bus architecture!) Nevertheless, it seems clear that the weight penalty is 1 lb/W class, not 3 lb/W or 1/3 lb/W.

CLOSURE

What is being proposed is comparable to heating and cooling a building by central air conditioning, rather than to cool it with open windows or individual air conditioners. The result is a revolutionary change in architecture, not an evolutionary one. While components of a much scaled-down version of the postulated heat driven refrigeration might be tested in space as packages, there is little prospect of testing a full-scale system in space except as part of a satellite designed to use it.

In the past, this writer has pooh-poohed the possibility of using cryogenics for generation of r.f. and laser power on board satellites. Too much power, he argued, was required to pump the left-over heat uphill to where it can be conveniently discarded from reasonable radiators. He was wrong. He had not considered using waste heat from the prime power source to drive the cooler.

The cryogenic satellite is an idea whose time may have come.

FOOTNOTES

1. Galicia is part of present-day Poland.

2. J. Formánek, J. Knop, and J. Korber, "Beiträge zur Untersuchung von Benzinen und Benzolen," *Chemiker Zeitung*, vol. 41, nr 11 (1917) p. 731-733.

3. The Voyager satellites were powered by such sources, as well as Lincoln Experimental Satellites LES-8 and LES-9.

4. American Society of Heating, Refrigerating, and Air Conditioning Engineers.

5. The maximum eclipse time interval is forty to forty-five minutes. It is nearly independent of the orbital altitude for circular orbits. In the higher orbits, the earth shadow merely occurs less often.

KEY ATTRIBUTES AND GENERIC REQUIREMENTS FOR CRYOCOOLER APPLICATION ON MICROSATS

John Lester Miller
Martin Marietta Space Systems
P.O. Box 179
Denver, Colorado 80201

ABSTRACT

Large interest is developing within the Department of Defense, NASA and the commercial sector for use of extremely small satellites. Several of these "Microsats" require cryogenic cooling for infrared sensors. A Microsat poses unique considerations and requirements on a cryocooler not normally considered for tactical applications. Key attributes of closed cycle cryocoolers are discussed from a user's perspective. Emphasis is on concerns and goals for space use and microsat basing such as: surviving launch, power consumption, power conditioning vacuum operation and cryocooler vibration. Historical lightsat data is used to develop an estimate of the added satellite mass as a function of cryocooler power and mass.

INTRODUCTION

Large worldwide interest is developing for employing a constellation of small satellites to accomplish the system requirements of large satellites or to replace a large satellite with a small one with reduced requirements. This is because small satellites are less expensive, provide for quick launches and increase overall operational flexibility.

As the name "Microsat" implies, they are small satellites or light lightsats. ESA applied the term to any spacecraft of less than 50 Kg.[1] The advantage to such a small satellite is that they can be launched inexpensively and quickly on Pegasus, Taurus, Scout or grouped with other payloads on STS, Titan or Ariane. The basic characteristics of a microsat include:

- Low mass (< 100 Kg)
- Low orbital average power (<200 W)
- Rapidly designed and built (usually < 1 year)
- Rapid Launch processing (usually less than a month)
- Low cost (usually less than a million dollars)

Typical examples include: Brem-sat, Amsat-Na, Iridium, Eyesat, Brilliant Pebbles, HAIR, LAOSS, TechStar.

Microsats have a variety of missions, a recent survey by Wirin & Solomonov [2] indicate that 43% of future non - military Microsat programs will be dedicated to physics and astronomy and 8% to earth observation. If one assumes half of these will contain electo-optical payloads, and half of these E-O payloads will call for cryocoolers, then ~ 13% of new microsat programs will require cryocoolers. Aside from sensor uses, cryocoolers may be required to cool high T_c superconducting materials or electronics.

GENERIC PERFORMANCE REQUIREMENTS

Cryocooler performance is obviously mission sensitive, and unique to the sensor being cooled. However, by definition microsats cannot support large sensors, large cryocoolers or extremely low temperatures. Some upper bounds on performance can be estimated, given the current state of the art.

Table 1 lists some expected requirements. Static heat load probably will be one watt or less because of small sensor size and the necessity of limiting cryocooler size. Temperature control is likely to be tighter than typical FLIR applications because margins on a microsat are less, and sensor calibration and testing is likely to be over a smaller FPA temperature range. The MTTF of the cryocooler will be the lifetime driver of the Microsat. Microsat applications will vary with the maximum time the cryocooler continuously operates from a few hours to its total life.

Table 1 Generic Performance Requirements

Cooling:	1 Watt or Less @ 60 - 80 K for PT:Si 60 - 200 K for HgCdTe 100 - 200 K for PbS 60 - 120 K for InSb 60 - 150 K for Quantum Wells
Temperature Control:	+/- 1 K
MTTF:	1000 Hours Min, 10,0000 Desirable

LAUNCH ENVIRONMENT

The first requirement a microsat based cryocooler must satisfy is to survive launch. The launch environment depends on the launch vehicle, microsat structure, and launch profile.

However, some generalizations can be made and are summarized in Table 2. For microsat applications, the cryocooler will service a payload that is inactive during launch. Thus, The cryocooler will need to survive these environments, but not function in them.

Table 2 Representative Launch Environment

Acceleration	10 - 20 g
Shock	500 g for <=1 millisecond during booster staging
Thermal	-50° to +50°C
Vibration	0.5 g^2/hz from 50 to 1000 Hz
Pressure Drop	Sea Level to Vacuum

DESIRABLE ATTRIBUTES AND CHARACTERISTICS

A spacecraft is an island, it must generate all its power, then radiate all heat away, the power bus must be regulated and all vibration damped to sufficient levels. Many of the following characteristics are largely determined by space operation, but their importance is determined by the small nature of the satellite bus.

EFFICIENCY

Electrical power must be wisely used and disposed of on a small satellite platform, so efficiency is more important on a microsat because it can't afford a large Electrical Power System (EPS) and thermal control systems. Current cryocoolers of 40 W/W at 80 K are about the lowest efficiency that can be reasonably accommodated. Moreover, it is highly desirable for the efficiency not to degrade throughout the life of the cryocooler.

Figure #1 shows the satellite systems affected by supplying electrical power to a Cryocooler. For every watt that must be supplied the batteries and electrical conditioning circuits and solar panels must grow. This larger EPS causes increased Microsat Mass. Also, the Larger Solar panels cause increase in the orbital drag for Low Earth Orbiting satellites. This increase in drag means that more fuel is required (an increase in mass).

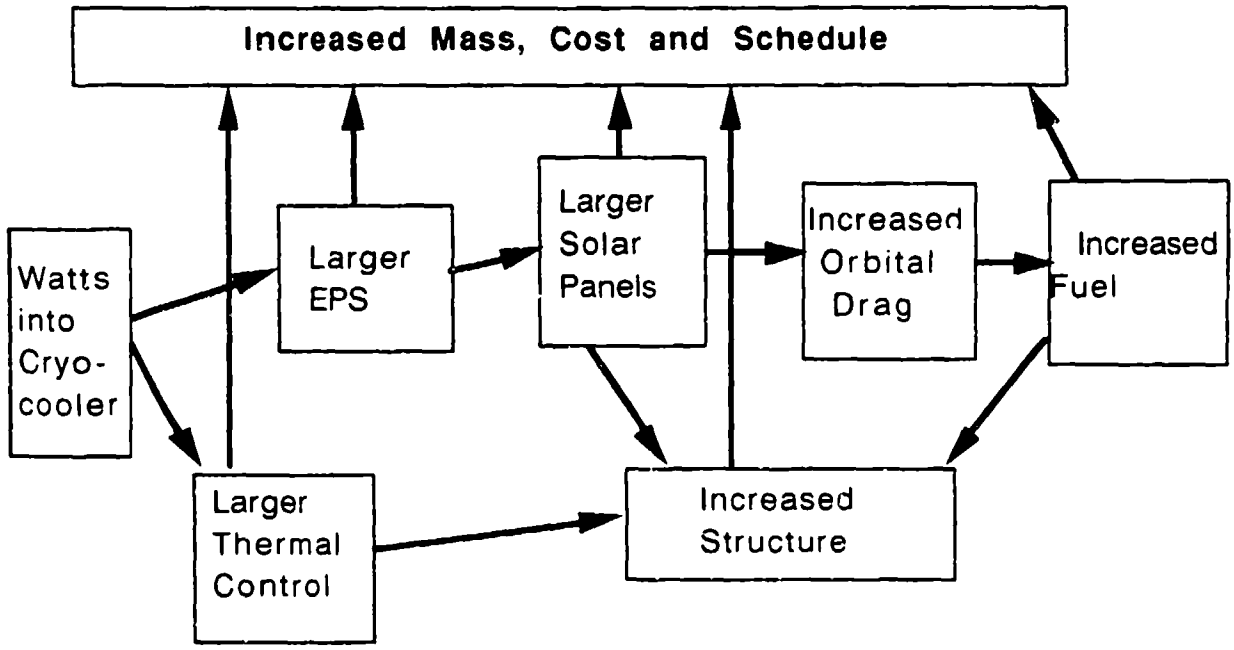

Figure # 1 Cryocooler's Impact On other Microsat Systems

Carrying more fuel to compensate for the added drag, causes the structural mass to increase. Every watt supplied to the compressor must be rejected to a radiator and radiated away. This larger Thermal Control system also adds mass to the microsat. The mass impact on a microsat EPS for an additional watt is nearly 100 grams; however, the entire spacecraft may increase twice that. The result is that if efficiency degrades, the satellite may no longer be a microsat.

ELECTRICAL POWER CONDITIONING

Because the microsat is self-contained, it is desirable for the cryocooler to have clean power characteristics. Generally, all emissions (including magnetic) must be shielded. DC motors and operation is preferred to reduce ripple and EPS size.

Reflected ripple back onto the bus must be kept low, even at the expense of adding filters to the cryocooler. The EPS of the Microsat is likely to supplying delicate instruments with power. Therefore, reflected ripple of more than a few tens of millivolts cannot be tolerated without adding massive chokes and filters to the EPS bus. The ripple includes on/off transients.

Ground loops in a small spacecraft cannot be tolerated. The cryocooler should be compatible with a single point ground concept. All grounded items must be tied together to form a single ground plane. This becomes subtle with wiring terminations. All power wires should be braided and separate positive and negative wires brought out to the input power connector. A minimum dc resistance of a mega-ohm is desirable between primary power return, signal return, command return and case.

Fuses, for protection, will be required if the Microsat mission is not entirely dependant on the cryocooler or if there is a redundant cryocooler.

VACUUM OPERATION

Operation in a vacuum poses special considerations on a cryocooler that are nonexistent in aircraft basing.

First, is heat rejection. The only technique available to reject heat is through conduction to the microsat outer surface (or radiator). The compressor and electronics must be able to function without convection. The larger the temperature range that the compressor case can accommodate, the simpler and lighter the microsat thermal design will be. It would be desirable for the compressor to function from ~-20°C, when turned on, to +60°C after some long period of operation. Narrow case temperature ranges of +20 to +40°C can be met with an increase in microsat thermal control system complexity.

Outgassing is another concern. All surfaces must be clean. No volatile materials can be used in construction or be completely sealed within the unit. The exterior must be free from oils, human oils, solvents, dust and all outgassing agents. Special consideration must be given to all lubricants, rubbers and plastics. This includes the insulation on wires. Standard wire insulation traps air inside which may burst through ripping a hole in the insulation or contaminate some surface. Additionally, the inks and materials for wire insulation tend to outgas in vacuum conditions.

VIBRATION

Because the cryocooler is likely to be the dominant noise source, low vibration is critical for microsat application. Moreover, microsats do not have massive active dampening systems and the compressor can be a large fraction of the entire satellite mass. Although the Microsat may be equipped with reaction wheels, these are rarely large enough to actively dampen out the compressor. One can assume that the only dampening will be passive mounting washers such as silicon. This implies that heat conduction will be through a flexible heat strap tied to the compressor.

Since microsats are usually small and stiff, so the higher frequency components are the most troublesome. There should be no strong vibrational modes above 50 hz.

Gas purity must be such that long term operation (hundreds of hours) does not cause the deposition of impurities on a cold surface that would increase vibration intensity more than ~10%.

Since microsats are often built on short schedules, it is critical for the integrator to have detailed knowledge of the vibration power spectral density early in the design phase. Cryocooler manufacturers should be equipped with detail vibration specifications during the proposal phase. This will allow the manufacturer to complete dynamic modeling.

PHYSICAL ENVELOPE

A microsat being a small lightweight spacecraft packaging constraints are usually great on a microsat dictating that the cryocooler must also be of small size and low mass.

The satellite integrator must know the cryocooler's center of gravity, axis orientation, moment of inertia and unbalanced angular moments. There may also be a requirement to measure axis orientation after the unit is placed into the microsat to assure that the vibration is generated in the proper orientation.

It is unlikely that a microsat could accommodate a volume of more than 1/10 of a cubic meter a mass more than three kilograms. One kilogram or less would be desirable. The cryocooler manufacturer should explore with the satellite manufacturer the options of using composites, beryllium or titanium to decrease the cryocooler mass. The mass savings could be well worth the cost.

ESTIMATING MICROSAT IMPACTS

A cryocooler will probably be the dominant source of failures, heat, power consumption and vibration on the microsat. Therefore, the impact of incorporating one on a microsat is great from the satellite integrator perspective.

The mass impact of a cryocooler on a microsat can be estimated by considering the marginal additions needed as detailed by equation 1.

(1) Additional Spacecraft Mass= Structural Mass Fraction X [(Addition to Power System Mass) + (Impact to Thermal Control Mass) + (Cryocooler Support and Vibration Isolation) + (Cryocooler Mass)]

This can be estimated by using historical lightsat data to be:

(2) $SM\Delta \approx 1.2[0.1(P_r) + 0.035(P_r) + 0.2(M_C) + (M_{CC})]$

Where:
$SM\Delta$ = Additional Mass to Spacecraft in Kilograms
P_r = Electrical Power required by Cryocooler in watts
M_C = Mass of the Compressor in kilograms
M_{CC} = Mass of the Cryocooler in kilograms

Typical spacecraft structure to mass ratios are from 1.15 to 1.3. Microsats tend to use composites and high stiffness to weight materials; indicating ~1.2 is the more reasonable figure.

The marginal increase in the power system is ~ 100 grams per watt. The thermal control system is ~ 35 grams per Watt. Brackets and supports tend to have a mass of 10 - 25% of what they are supporting. The compressor will require a high degree of isolation so the larger term was chosen. By combining terms and assuming the compressor contains most of the mass, equation 2 can be simplified to equation #3.

(3) $SM\Delta \approx 0.16(P_r) + 1.4(M_{CC})$

Figure 2 plots the additional satellite dry weight (including the cryocooler mass) required for cryocoolers of various mass and orbital average power requirements. To understand the impact, recall that the total satellite mass is considered less than 100 kilograms. Clearly a large portion of a microsat mass can be considered supporting its cryocooler.

Microsat basing requires that the cryocooler be of a small, efficient variety. Assuming one with a mass on the order of 1 Kg and needing 20 w orbital average (ie: provide 0.5 w continuous cooling at 40 w/w), one can estimate the impact on a microsat to support this cryocooler. The 20 watts will require ~3.2 Kg of extra satellite systems and the 1 Kg mass will add ~1.4 Kg. Thus, a figure of merit can be derived for small efficient state of the art cryocoolers on microsats of:

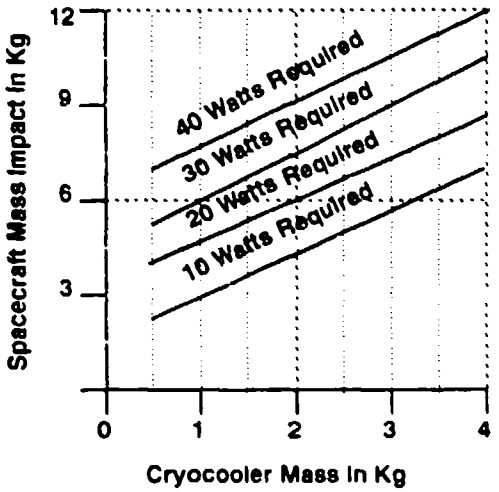

FIGURE # 2: Microsat Mass Gain as a function of Cryocooler Mass and power

(4) $$FOM = 3.2(P_r) + 1.4(M_{cc})$$

Where: FOM = A Figure of Merit to Minimize (units meaningless)
Pr = Power required

This shows that for current SOA Cryocoolers with a 1 Kg mass and 40 W/W that efficiency is approximately twice as important as mass for microsat applications.

Equations 1,2,3 and 4 do not consider the effects of atmospheric drag. Atmospheric drag in low earth orbit is related to the solar panel size which is determined by the orbital average power of which the cryocooler is a major component. The effects of drag is not easily put into analytic form. The amount of fuel needed to compensate for increased drag is a function of the aerodynamic coefficient, orbit lifetime, fuel ISP, microsat mass, altitude and solar array configuration.

Clearly adding a cryocooler increases the fuel requirement due to increased mass and increased drag resulting from larger solar panels. Thus, the added mass to support a cryocooler is greater than the equations indicate. Exception being if a cryocooler can be accommodated with body-mounted solar cells only or if lifetime is allowed to decrease.

CONCLUSION

Cryocoolers will play a significant role in the design and use of microsats. However, improvements are needed over standard tactical coolers in the characteristics of Power Conditioning, Cleanliness, Vibration, Vacuum Operation and Efficiency. Additionally, for specific microsat use, improvements in Mass, Size and Efficiency are needed over current space Cryocooler developments.

REFERENCES

1) King, McGweir,Price and White, "The In-Orbit Performance of Four Microsat Spacecraft," Proceedings of The 4th Annual AIAA/USU Conference on Small Satellites, Vol 1 (1990)

2). Wirin and Solomonov, "Small Payload Opportunities Aboard Soviet Launch Vehicles," Proceedings of The 4th Annual AIAA/USU Conference on Small Satellites, Vol 1 (1990)

DEVELOPMENT OF SMALL VUILLEUMIER CRYOCOOLERS FOR SPACE USE

Masakuni Kawada, Shunsuke Hosokawa and Isao Kudo
Electrotechnical Laboratory
Tsukuba-shi,Ibaraki 305,Japan

Hideto Yoshimura, Kiyotoshi Furuya and Masaki Kamifuji
Mitsubishi Electric Co.,
Amagasaki-shi,Hyogo 661,Japan

ABSTRACT

The Vuilleumier cryocooler has the potential advantages of long-life operation and low mechanical vibration. We have designed, fabricated and tested two Vuilleumier cryocoolers.The first machine was manufactured to study the possibility of cold generation, which is influenced by many operating parameters. The machine had a cooling capacity of 1.6 watts at 80 K under the input power of 150 watts, charge pressure of 3 MPa and cycle speed of 4 s^{-1}. It has been operated in an atmospheric environment for over 4,800 hours and has maintained good cooling performance from the beginning to 3,900 hours.The second one was designed for demonstrating the practical use in a vacuum environment. The machine had the same structure as the first one except for the diameter of the cold displacer. The heat generated by the machine was trasferred from the crankcase and the base plate to a passive radiator by a single-phase flow loop. It was found that the machine had a cooling performance of 40 K at no heat load and a cooling capacity of 1.4 watts at 80 K in the vacuum environment.

INTRODUCTION

There are drawbacks in the use of passive radiators for the cooling of IR sensors used for earth observation satellites. Although passive radiators which cool sensors by radiating heat to deep space, have been used for small-size sensors, the heat generation from sensors and heat leakage from Dewars have recently become greater than the cooling capacity of passive radiators. The JERS (Japanese earth resources satellite)-1 project was started in 1984 and is presently on-going.[1] JERS-1 is the largest satellite in Japan and weighs 1,400 kg. The launch of the satellite using the H-1 launch vehicle is scheduled for 1992. The Stirling cryocooler was adopted for SWIR (short-wave infrared radiometer) sensor cooling, and its specifications were a cooling capacity of 1 watt at 80 K and a lifetime of 2,000 hours at the beginning the JERS-1 project. The Stirling cryocooler was selected because as a space cryocooler, is the most efficient of all cryocoolers, although limitations on the useful operating lifetime of this machine arose due to wear of seals.

For realizing the long lifetime operation of an active cooler over 3,000 hours, we started the development of a small-size Vuilleumier cryocooler, and have designed, fabricated and tested two such cryocoolers.The first machine was manufactured for tests to study the feature of cold generation, which is influenced by many operating parameters :

temperature, charge pressure and cycle speed. Cryocooler performance is usually dependent on size. In general, small-size cryocoolers like this machine have total losses due to low mass flow and low thermal conduction and only give a small amount of cold generation. These losses exert influence on the cooling performance, which is usually estimated by a series of performance mapping tests in terms of the net cooling capacity, due to the difficulty of modelling losses accurately. Calculation of the thermodynamic cycle on the machine design is based on the Schmidt theory.[2),3)]

The second machine was designed for demonstrating the operation in the vacuum environment. As maintaining a cold head temperature lower than 50 K is, however, a difficult problem, this machine was slightly modified from the design of the cold displacer of the first one. The heat which the machine generated could be significantly transferred from both a crankcase and a base plate to the passive radiator by using a single-phase flow loop. This new approach which we adopted has been successful.

DESCRIPTION OF VUILLEUMIER CRYOCOOLER

The first machine has a cooling capacity of 1.5 watts at 80 K under the input power of 150 W, charge pressure of 2.5 MPa and cycle speed of 4 s^{-1}. This cycle speed is somewhat lower than that of conventional coolers. Although this machine is designed to operate at as high a temperature as possible, the metallurgical limit of a hot cylinder made of SUS 316 determines the temperature. Helium gas is selected as the working gas. Figure 1 shows the external view and cutaway sketch of the machine. The nominal dimensions of this machine are 280 mm high, 300 mm wide and 150 mm deep. The weight of the complete machine is 6 kg. In figure 1(b), aluminum alloy is used for the crankcase, which is the heaviest component, to realize a lighter system and to obtain stable thermal characteristics at the intermediate stage. A heat exchanger for cooling the helium gas is built into the crankcase with a flowing water coolant. A heater coil is wrapped around the hot cylinder head. A cooling water tube is brazed around the bottom of the hot cylinder for heat rejection from the cylinder wall. The thermal insulator material of the hot cylinder is calcium silicate. The cold cylinder effectively prevents thermal conduction from the intermediate temperature portion. A hot displacer is fabricated from machinable ceramics in a hot regenerator. A cold displacer is fabricated from phenolic resin in a cold regenerator. As the

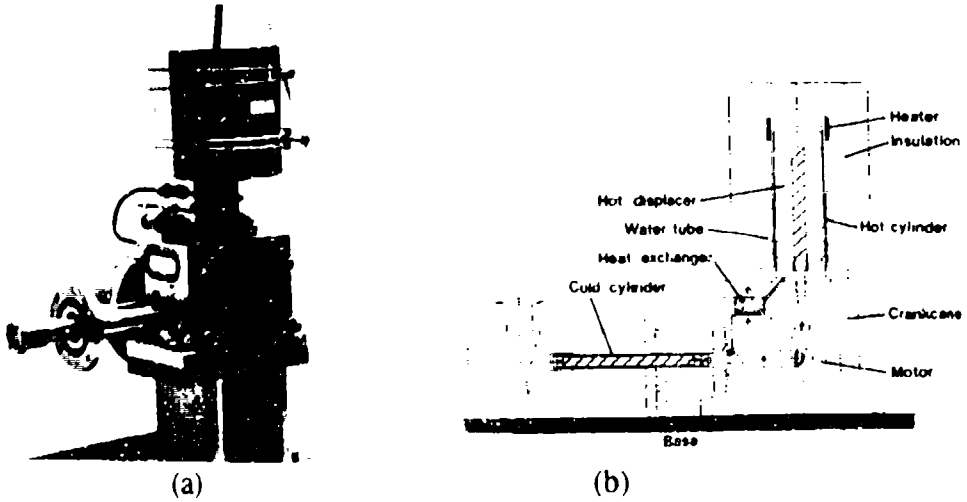

(a) (b)

Fig.1 External view and cutaway sketch of Vuilleumier cryocooler.

material of the hot and cold regenerators, a matrix made of stainless steel screen is used. A crank-mechanism is used to shuttle the hot displacer and the cold displacer, while a 90° phase angle is maintained between the relative positions of the displacers. The great feature of the Vuilleumier cryocooler is that little work is required to operate the displacers and to overcome the pressure drop of the working fluid and the mechanical friction problem of seals and bearings. The displacers are driven by a small, clean stepping motor, which can be used in a vacuum environment. Composite materials are used for seals and riders. Kap-seals of 15 % glass-loaded PTFE ensure that helium gas flows through the hot and cold regenerators, and rod seals prevent leakage between the working volume and crankcase volume. The driving forces on both the hot and cold displacers act in the direction of movement, and the side load and friction load are extremely low. A rider ring is mounted on the lower part of the hot displacer to prevent the displacer from touching the hot cyclinder. A high-vacuum grease is used as a lubricant of ball bearings located in the crankcase to eliminate helium gas contamination.

COOLING PERFORMANCE AND LIFE TEST PERFORMANCE

EXPERIMENTAL CONDITION AND TEST INSTALLATION

The schematic diagram of the test installation for the first machine is shown in figure 2. It is composed of the Vuilleumier cryocooler, the heater controller, the motor controller, the circulator, and the measuring instrument. The coolant is supplied separately to the heat exchanger and the hot cylinder. The high temperature (hot wall temperature) is measured by a thermocouple (nickel-chromium vs nickel-aluminum) brazed on the hot cylinder head. The cold temperature is measured using a calibrated thermocouple (Au-.07 % Fe vs nickel-chromium) fixed on the cold head. The alternating pressure in the working volume is measured using a pressure transducer at the heat exchanger.

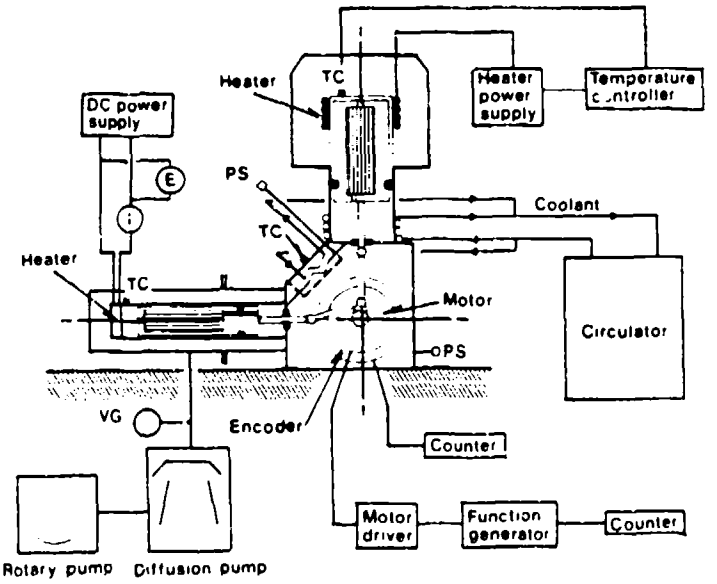

Fig.2 Schematic diagram of Vuilleumier cryocooler with its control and power system.

The cooling performance is determined not only at the design point, but also at the off-design points. The charge pressure, hot wall temperature and cycle speed are major operating parameters. The cooler is operated and tested 8 hours/day. At first, the hot cylinder head is heated to 923 K for 15 minutes and kept at that temperature for 2 hours for data acquisition. The temperature is next dropped to 903 K, where it is maintained for 1.5 hours. It is then reduced to 873 K. After the test, the temperature of the hot cylinder is controlled to decrease to room temperature in 1 hour. As for the cooling performance test, the heat load is applied by a thin film electric heater, which is placed on the cold head. After that, the cold head temperature is monitored with no heat load at a hot wall temperature of 923 K. The cold production is measured on the cold head. After the performance mapping test, the durability test of the machine was carried out to investigate both mechanical breakdowns and degradation of the cooling performance with time.

PERFORMANCE MAPPING TEST

The performance of the Vuilleumier cryocooler is obtained by varying the hot wall temperature and intermediate temperature. The former temperature easy controls the stability of the small-size cryocooler. Figure 3 shows the effect of the cold head temperature on the heat load with change of the hot wall temperature. The results show that the cooling capacity was 1.6 watts at 80 K, and the cold head temperature was 57 K with no heat load under the condition of a hot wall temperature of 923 K. A typical cooldown time was 42 minutes down to the temperature of 80 K and 70 minutes to 57 K. The test results obtained are in good agreement with the calculations. The cooling capacity at 80 K increased with the cycle speed and the charge pressure. Maximum cooling capacity at 80 K was 2.2 watts with the cycle speed of 5.33 s^{-1} and charge pressure of 3 MPa.

Performance mapping at 80 K is shown in figure 4. The cooling capacity increases with the hot wall temperature and cycle speed. A maximum cooling capacity of 2 W is obtained with the hot wall temperature of 923 K and the cycle speed of 5.33 s^{-1}.

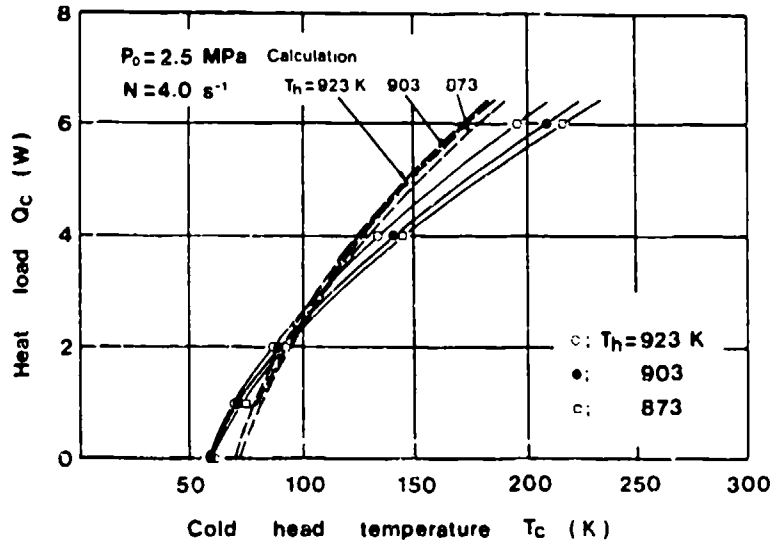

Fig.3 Comparison of experimental results with calculated results.

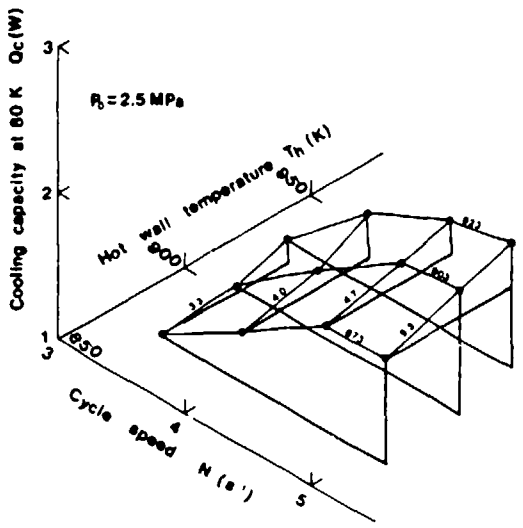

Fig.4 Three-dimensional representaion of cooling capacity at 80 K as functions of cycle speed and hot wall temperature for charge pressure of 2.5 MPa.

CRYOCOOLER PERFORMANCE

The effect of cycle speed (N) and charge pressure (P_0) is investigated for the cooling performance under the condition of the hot wall temperature of T_h=923 K. Figure 5 shows the heater input power versus cold head temperature with the fixed values of $P_0 \cdot N$. The cooling capacity at 80 K was from 1 watt at $P_0 \cdot N$=8 MPa·s^{-1} to 2 watts at $P_0 \cdot N$=13 MPa·s^{-1}, while the heater input power at the hot cylinder head was varied from 135 W to 160 W. It is found that two parameter sets of charge pressure P_0=2.5 MPa and cycle speed N=3.33 s^{-1}, and P_0=2 MPa and N=4 s^{-1} are selectable in order to obtain 1 W cooling at 80 K.

Figure 6 shows the figure of merit (FOM) as a function of cooling capacity at 80 K. The results of FOM evaluation showed that this machine had demonstrated a better cooler performance than that of another similar machine which operates on the same principle.

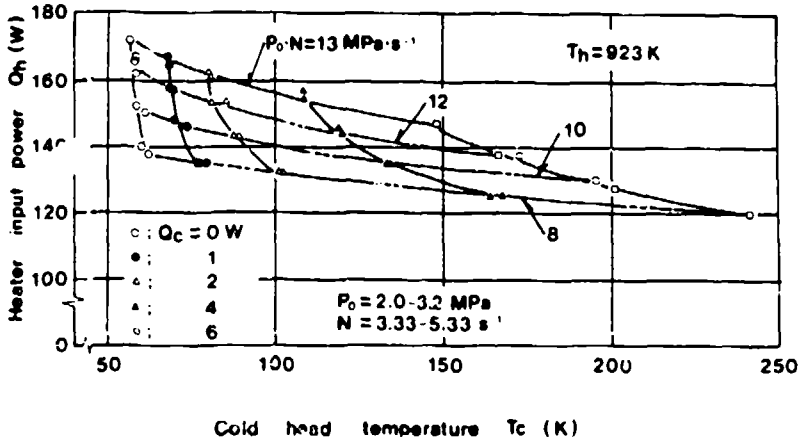

Fig.5 Cooler performance at various products of charge pressure and cycle speed.

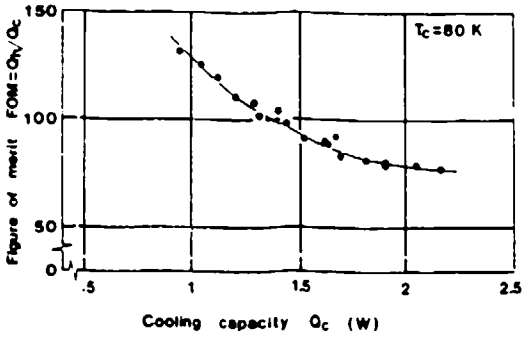

Fig.6 Figure of merit of Vuilleumier cryocooler as a function of cooling capacity at 80 K.

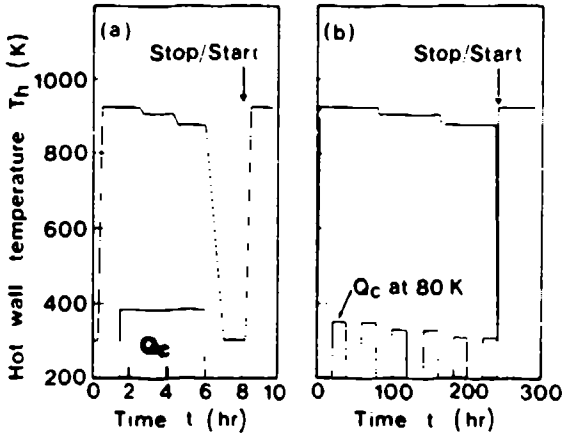

(a) Phase 1 (b) Phase 2

Fig.7 Operating mode of life test.

LIFE TEST

To evaluate the performance of the machine, the life test of over 4,800 hours was planned. Figure 7 shows the operating mode of the life test. During the first 2,500-hour test period, the machine was operated under much the same operating conditions as those of the performance mapping test (phase 1). After that time, the machine was subject to a cyclic test, whose test period was 243 hours (phase 2). The critical parameters of the machine, heater input power, cooling performance at no heat load, and cooling capacity at 80 K, were measured two times per day in order to detect the performance changes with the operating time.

The curves in figure 8 are plotted from measurements of the cooling capacity at 80 K under the operating conditions of a charge pressure of P_0=2.5 MPa and 3 MPa, hot wall temperature of T_h=923, 903 and 873 K, and cycle speed of N=4 s^{-1}. During the 2,500 hours of operation, data indicated that the cooling capacity at 80 K decreased over a long period of time. The decrease rate during 2,500-hour operation was 50 mW/2,500 hours under the charge pressure of 3 MPa and 130 mW/2,500 hours under the charge pressure of

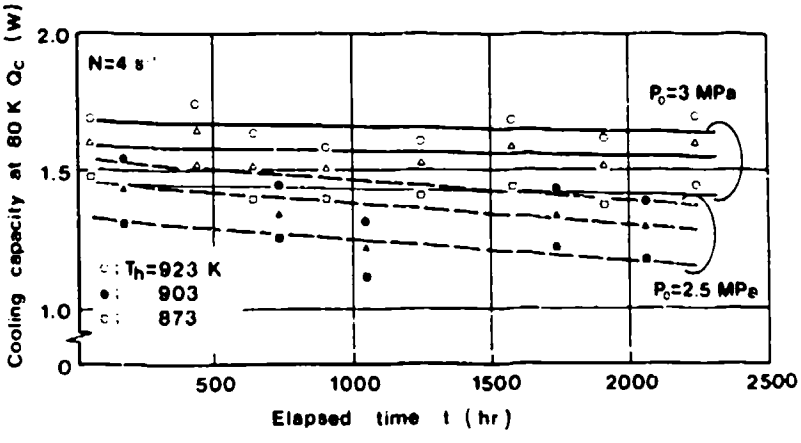

Fig.8 Degradation trend of cooling capacity at 80 K.

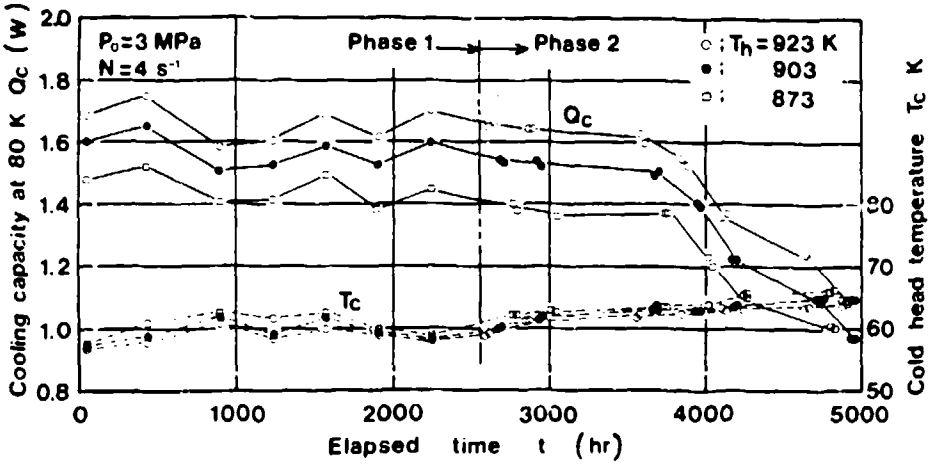

Fig.9 Cooling performance change with elapsed time.

2.5 MPa. The effect of the fixed value of $P_0 \cdot N$ was investigated for the cooling performance before 2,500 hours. It is found that the degradation of the cooling performance at high charge pressure is slight for the accumulated operation time of 2,500 hours.

After 2,500 operating hours, a 243-hour continuous operation test was resumed. Before each test period, the machine was taken off the calibration of the monitoring instrumentation and the charge pressure was checked. The experimental results which were obtained in the way described are shown in figure 9. The cooling capacity at 80 K was degraded slightly with time through 3,900 operating hours. At that point, the machine had the cooling capacity of 1.6 watts at 80 K under the condition of a hot wall temperature of T_h=923 K, and the cold head temperature with no heat load rose to 50 K, compared with the initial test results. Comparing the cooling capacity at 80 K (Q_C) and the cold head temperature with no heat load (T_C) curves in figure 9, Q_C became degraded as T_C rose with the operating time. The cooling performance of the machine markedly changed when T_C was above 64 K.

CRYOCOOLER PERFORMANCE TEST IN VACUUM ENVIRONMENT

EXPERIMENTAL CONDITION AND TEST INSTALLATION

The schematic diagram of the vacuum test using the second machine is shown in figure 10. The nominal dimensions of the vacuum chamber are an inner diameter of 1,500 mm and a length of 2,500 mm. A liquid nitrogen thermal shield is installed on the right side of the vacuum chamber shown in this figure. The liquid nitrogen flows from a storage tank through a transfer line to the thermal shield. When the liquid nitrogen has been supplied, the pressure in the vacuum chamber can be maintained at the range of a high vacuum of 10^{-5} Pa.

The second machine was fabricated and had the same design features against the first one except that the heat rejection device was added. The device was a single-phase flow loop and small passive radiator set installed inside the vacuum chamber. The water, which was selected as the coolant, was pumped to the machine, and the flow rate was controlled by a bypass valve. A heater attached to the passive radiator permits control of the temperature for heat radiation.

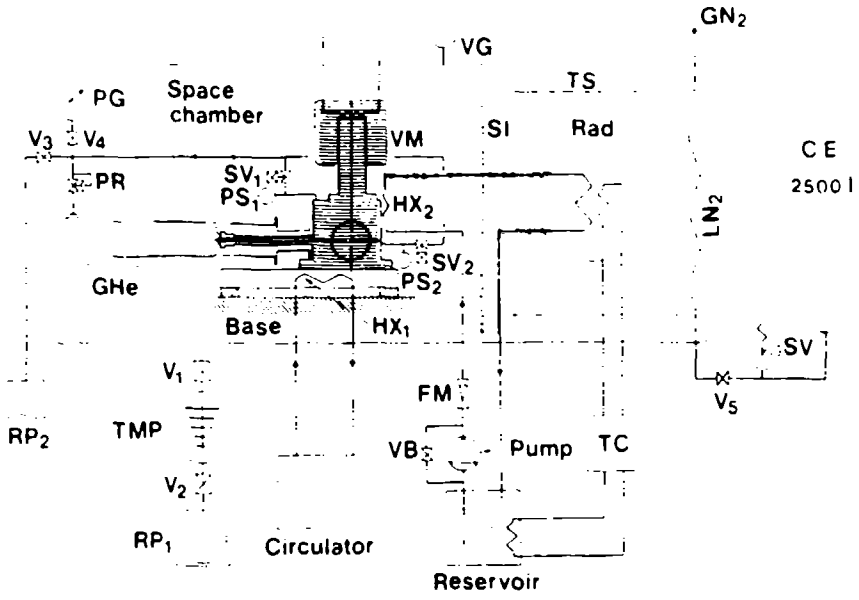

Fig.10 Vacuum test facility for Vuilleumier cryocooler.

The requirements of the heat rejection loop are a radiating capability higher than 150 watts with the coolant temperature between 273 K and 303 K and a nominal flow rate of 1.2 l/min. We calculated a heat path of the heat rejection loop by a simple thermal model. The radiator of 900 mm in diameter has a heat rejection capability of more than 150 watts at a radiation temperature of 273 K based on the calculated results.

The heat leaks from the fluid pipeline between the machine and the passive radiator are negligible because the difference of the water temperature from the surrounding temperature (inner wall temperature of t e vacuum chamber) is small and the fluid pipeline is covered with a multilayer insulator.

COOLING PERFORMANCE TEST

The test results in an atmospheric environment are shown in figure 11. In this figure, ① indicates the data obtained by the second machine and ② indicates the data obtained by the first one. The second machine has the capability of cold generation of 35 K without the heat load at the cycle speed of above 9 s^{-1}.

Figure 12 shows the time history of the vacuum system and the cooldown characteristics of the machine. The time spent was about 1 hour for the thermal shield (cold panel for radiation) cooling to 115 K. When the thermal shield temperature becomes 115 K, an electric heater power is supplied to heat the hot cylinder head. The hot cylinder head temperature (hot wall temperature) was maintained constant at 923 K all the time. The cold head temperature reached 41 K after 2 hours from the start. The typical cooldown time was estimated to be 30 minutes down to the temperature of 80 K and 50 minutes to 40 K.

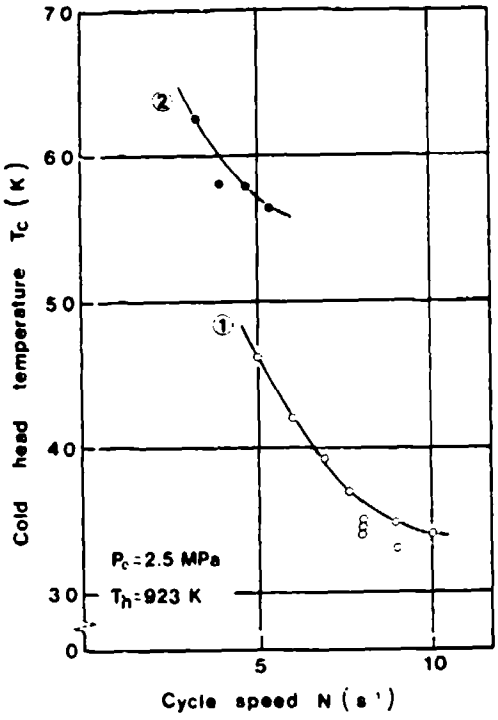

Fig.11 Comparison of cooling performance of 1st. machine with those of 2nd. one.

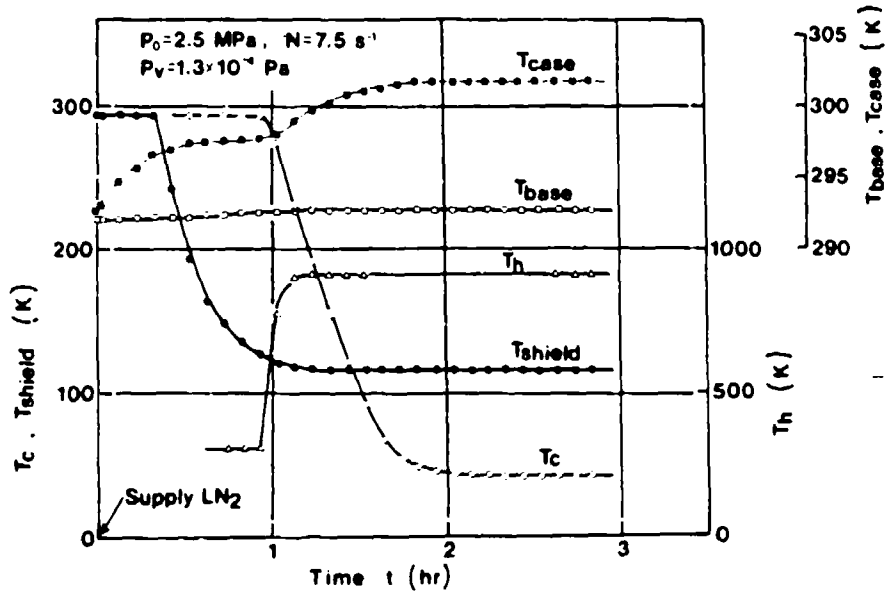

Fig.12 History of vacuum system and cooldown characteristics of machine.

Figure 13 shows the effect of the cold head temperature on the heat load when the cycle speed is changed. The results show that cooling capacity was 1.4 watts at 80 K, and the cold head temperature was 40 K at no heat load under the condition of cycle speed at 10 s^{-1}. Also, it has the cooling capacity of more than 600 mW at 60 K. The curves in this figure are plotted from measurements of the cooling capacity at 80 K and the cold head temperature at no heat load on the cycle speed. When the machine was operated at the cycle speed of above 9 s^{-1}, the cold head temperature was saturated at 40 K. The second machine was operated for over 120 hours in the vacuum environment.

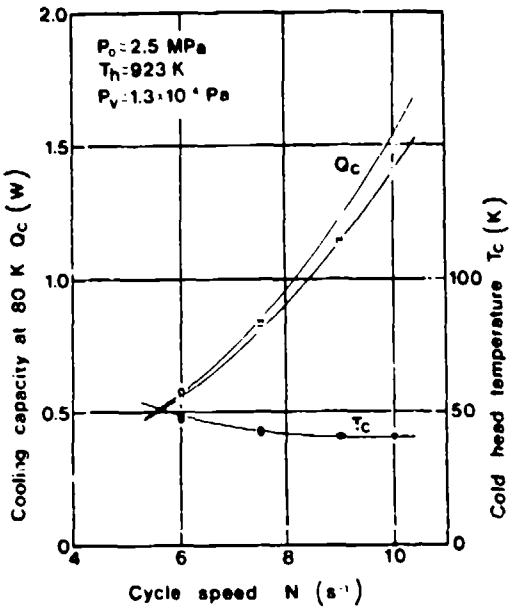

Fig.13 Effect of cycle speed on cooling performance with no heat load and cooling capacity at 80 K.

CONCLUSIONS

Two small-size Vuilleumier cryocoolers were designed, fabricated and successfully tested. The first machine could obtain 2.2 watts of maximum cold production at 80 K. Performance mapping at 80 K was carried out as functions of the hot wall temperature and cycle speed with the charge pressure of 2.5 MPa and 3 MPa. It had the cooling capacity of 1.6 watts for over 3,700 hours total under the conditions of the charge pressure of 3 MPa and cycle speed of 4 s^{-1}. It is found that the machine had better cooler performance from the evaluations of the figure of merit and specific weight. When the second machine was operated in a vacuum environment, it had the capability of cold generation of 40 K and the cooling capacity of 600 mW at 60 K.

REFERENCES

1. M.Kawada, I.Kudo," Japanese development of cryocoolers for applications in space," Proc. 3rd Japanese-Sino Joint Seminar, Okayama, Japan (October 1989) P.36-41.
2. G.Walker," Cryocoolers, I," Plenum Press, New York (1983).
3. W.R.Martini," Stirling engine design manual," NASA CR-135382 (1978).

DEVELOPMENT OF SMALL VUILLEUMIER CRYOCOOLERS FOR SPACE USE

Masakuni Kawada, Shunsuke Hosokawa and Isao Kudo
Electrotechnical Laboratory
Tsukuba-shi,Ibaraki 305,Japan

Hideto Yoshimura, Kiyotoshi Fukuye and Masaki Kamifuji
Mitsubishi Electric Co.,
Amagasaki-shi,Hyogo 661,Japan

ABSTRACT

The Vuilleumier cryocooler has the potential advantages of long-life operation and low mechanical vibration. We have designed, fabricated and tested two Vuilleumier cryocoolers.The first machine was manufactured to study the possibility of cold generation, which is influenced by many operating parameters. The machine had a cooling capacity of 1.6 watts at 80 K under the input power of 150 watts, charge pressure of 3 MPa and cycle speed of 4 s^{-1}. It has been operated in an atmospheric environment for over 4,800 hours and has maintained good cooling performance from the beginning to 3,900 hours.The second one was designed for demonstrating the practical use in a vacuum environment. The machine had the same structure as the first one except for the diameter of the cold displacer. The heat generated by the machine was trasferred from the crankcase and the base plate to a passive radiator by a single-phase flow loop. It was found that the machine had a cooling performance of 40 K at no heat load and a cooling capacity of 1.4 watts at 80 K in the vacuum environment.

INTRODUCTION

There are drawbacks in the use of passive radiators for the cooling of IR sensor used for earth observation satellites. Although passive radiators which cool sensors by radiating heat to deep space, have been used for small-size sensors, the heat generation from sensors and heat leakage from Dewars have recently become greater than the cooling capacity of passive radiators. The JERS (Japanese earth resources satellite)-1 project was started in 1984 and is presently on-going.[1] JERS-1 is the largest satellite in Japan and weighs 1,400 kg. The launch of the satellite using the H-1 launch vehicle is scheduled for 1992. The Stirling cryocooler was adopted for SWIR (short-wave infrared radiometer) sensor cooling, and its specifications were a cooling capacity of 1 watt at 80 K and a lifetime of 2,000 hours at the beginning the JERS-1 project. The Stirling cryocooler was selected because as a space cryocooler, is the most efficient of all cryocoolers, although limitations on the useful operating lifetime of this machine arose due to wear of seals.

For realizing the long lifetime operation of an active cooler over 3,000 hours, we started the development of a small-size Vuilleumier cryocooler, and have designed, fabricated and tested two such cryocoolers.The first machine was manufactured for tests to study the feature of cold generation, which is influenced by many operating parameters :

temperature, charge pressure and cycle speed. Cryocooler performance is usually dependent on size. In general, small-size cryocoolers like this machine have total losses due to low mass flow and low thermal conduction and only give a small amount of cold generation. These losses exert influence on the cooling performance, which is usually estimated by a series of performance mapping tests in terms of the net cooling capacity, due to the difficulty of modelling losses accurately. Calculation of the thermodynamic cycle on the machine design is based on the Schmidt theory.[2),3)]

The second machine was designed for demonstrating the operation in the vacuum environment. As maintaining a cold head temperature lower than 50 K is, however, a difficult problem, this machine was slightly modified from the design of the cold displacer of the first one. The heat which the machine generated could be significantly transferred from both a crankcase and a base plate to the passive radiator by using a single-phase flow loop. This new approach which we adopt has been successful.

DESCRIPTION OF VUILLEUMIER CRYOCOOLER

The first machine has a cooling capacity of 1.5 watts at 80 K under the input power of 150 W, charge pressure of 2.5 MPa and cycle speed of 4 s^{-1}. This cycle speed is somewhat lower than that of conventional coolers. Although this machine is designed to operate at as high a temperature as possible, the metallurgical limit of a hot cylinder made of SUS 316 determines the temperature. Helium gas is selected as the working gas. Figure 1 shows the external view and cutaway sketch of the machine. The nominal dimensions of this machine are 280 mm high, 300 mm wide and 150 mm deep. The weight of the complete machine is 6 kg. In figure 1(b), aluminum alloy is used for the crankcase, which is the heaviest component, to realize a lighter system and to obtain stable thermal characteristics at the intermediate stage. A heat exchanger for cooling the helium gas is built into the crankcase with a flowing water coolant. A heater coil is wrapped around the hot cylinder head. A cooling water tube is brazed around the bottom of the hot cylinder for heat rejection from the cylinder wall. The thermal insulator material of the hot cylinder is calcium silicate. The cold cylinder effectively prevents thermal conduction from the intermediate temperature portion. A hot displacer is fabricated from machinable ceramics in a hot regenerator. A cold displacer is fabricated from phenolic resin in a cold regenerator. As the

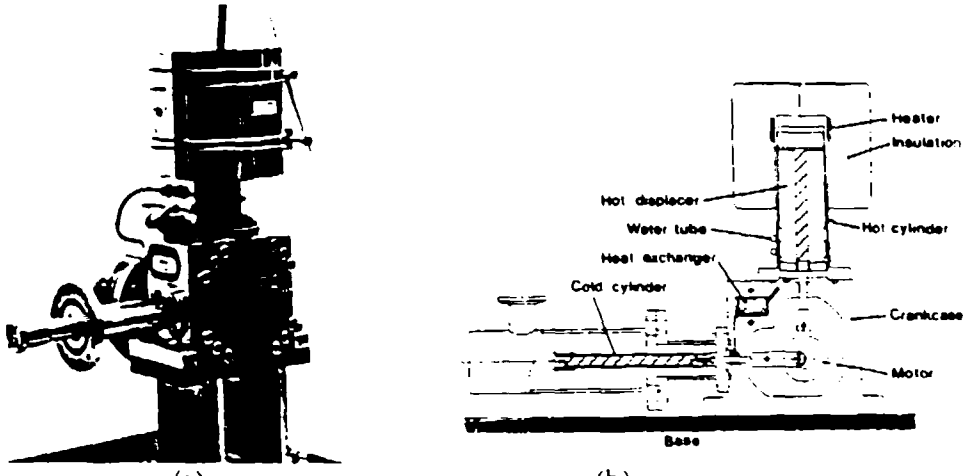

(a) (b)

Fig.1 External view and cutaway sketch of Vuilleumier cryocooler.

material of the hot and cold regenerators, a matrix made of stainless steel screen is used. A crank-mechanism is used to shuttle the hot displacer and the cold displacer, while a 90° phase angle is maintained between the relative positions of the displacers. The great feature of the Vuilleumier cryocooler is that little work is required to operate the displacers and to overcome the pressure drop of the working fluid and the mechanical friction problem of seals and bearings. The displacers are driven by a small, clean stepping motor, which can be used in a vacuum environment. Composite materials are used for seals and riders. Kap-seals of 15 % glass-loaded PTFE ensure that helium gas flows through the hot and cold regenerators, and rod seals prevent leakage between the working volume and crankcase volume. The driving forces on both the hot and cold displacers act in the direction of movement, and the side load and friction load are extremely low. A rider ring is mounted on the lower part of the hot displacer to prevent the hot cylinder from touching each other. A high-vacuum grease is used as a lubricant of ball bearings located in the crankcase to eliminate helium gas contamination.

COOLING PERFORMANCE AND LIFE TEST PERFORMANCE

EXPERIMENTAL CONDITION AND TEST INSTALLATION

The schematic diagram of the test installation for the first machine is shown in figure 2. It is composed of the Vuilleumier cryocooler, the heater controller, the motor controller, the circulator, and the measuring instrument. The coolant is supplied separately to the heat exchanger and the hot cylinder. The high temperature (hot wall temperature) is measured by a thermocouple (nickel-chromium vs nickel-aluminum) brazed on the hot cylinder head. The cold temperature is measured using a calibrated thermocouple (Au-.07 % Fe vs nickel-chromium) fixed on the cold head. The alternating pressure in the working volume is measured using a pressure transducer at the heat exchanger.

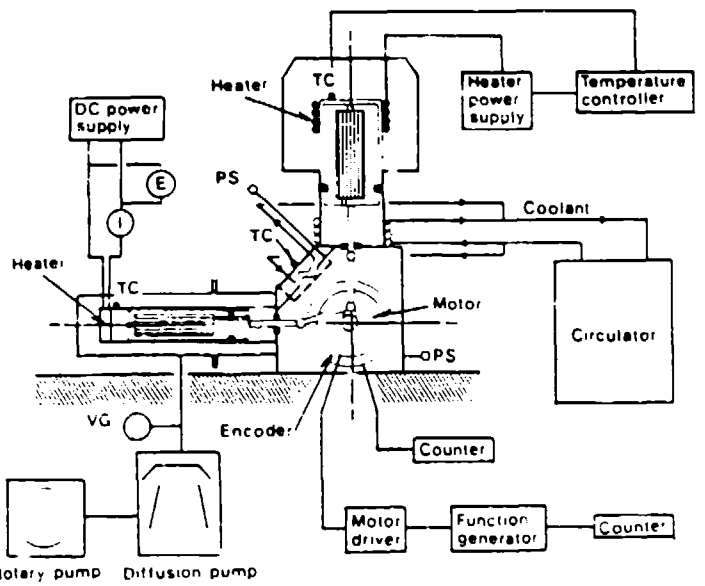

Fig.2 Schematic diagram of Vuilleumier cryocooler with its control and power system.

The cooling performance is determined not only at the design point. but also at the off-design points. The charge pressure, hot wall temperature and cycle speed are major operating parameters. The cooler is operated and tested 8 hours/day. At first, the hot cylinder head is heated to 923 K for 15 minutes and kept at that temperature for 2 hours for data acquisition. The temperature is next dropped to 903 K, where it is maintained for 1.5 hours. It is then reduced to 873 K. After the test, the temperature of the hot cylinder is controlled to decrease to room temperature in 1 hour. As for the cooling performance test, the heat load is applied by a thin film electric heater, which is placed on the cold head; and that, the cold head temperature is monitored with no heat load at a hot wall temperature of 923 K. The cold production is measured on the cold head. After the performance mapping test, the durability test of the machine was carried out to investigate both mechanical breakdowns and degradation of the cooling performance with time.

PERFORMANCE MAPPING TEST

The performance of the Vuilleumier cryocooler is obtained by varying the hot wall temperature and intermediate temperature. The former temperature easy controls the stability of the small-size cryocooler. Figure 3 shows the effect of the cold head temperature on the heat load with change of the hot wall temperature. The results show that the cooling capacity was 1.6 watts at 80 K, and the cold head temperature was 57 K with no heat load under the condition of a hot wall temperature of 923 K. A typical cooldown time was 42 minutes down to the temperature of 80 K and 70 minutes to 57 K. The test results obtained are in good agreement with the calculations. The cooling capacity at 80 K increased with the cycle speed and the charge pressure. Maximum cooling capacity at 80 K was 2.2 watts with the cycle speed of 5.33 s^{-1} and charge pressure of 3 MPa.

Performance mapping at 80 K is shown in figure 4. The cooling capacity increases with the hot wall temperature and cycle speed. A maximum cooling capacity of 2 W is obtained with the hot wall temperature of 923 K and the cycle speed of 5.33 s^{-1}.

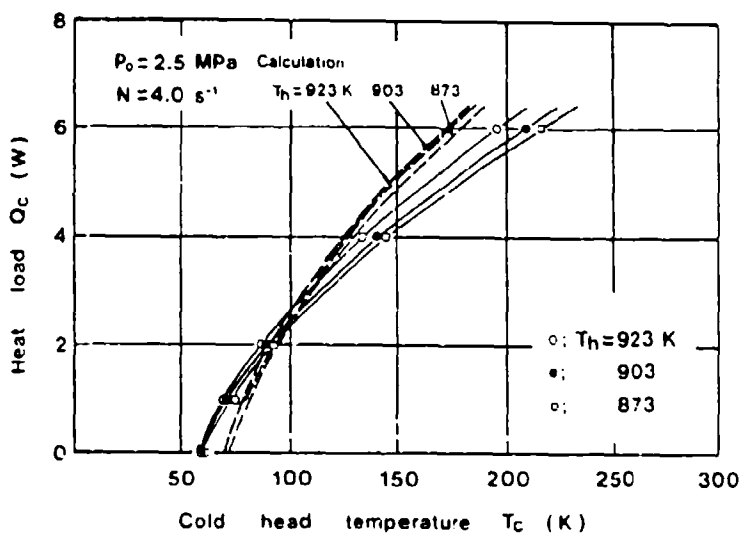

Fig.3 Comparison of experimental results with calculated results.

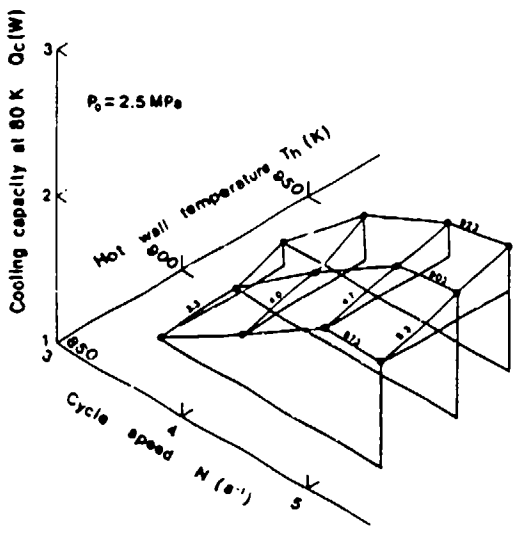

Fig.4 Three-dimensional representaion of cooling capacity at 80 K as functions of cycle speed and hot wall temperature for charge pressure of 2.5 MPa.

CRYOCOOLER PERFORMANCE

The effect of cycle speed (N) and charge pressure (P_0) is investigated for the cooling performance under the condition of the hot wall temperature of T_h=923 K. Figure 5 shows the heater input power versus cold head temperature with the fixed values of $P_0 \cdot N$. The cooling capacity at 80 K was from 1 watt at $P_0 \cdot N$=8 MPa·s^{-1} to 2 watts at $P_0 \cdot N$=13 MPa·s^{-1}, while the heater input power at the hot cylinder head was varied from 135 W to 160 W. It is found that two parameter sets of charge pressure P_0=2.5 MPa and cycle speed N=3.33 s^{-1}, and P_0=2 MPa and N=4 s^{-1} are selectable in order to obtain 1 W cooling at 80 K.

Figure 6 shows the figure of merit (FOM) as a function of cooling capacity at 80 K. The results of FOM evaluation showed that this machine had demonstrated a better cooler performance than that of another similar machine which operates on the same principle.

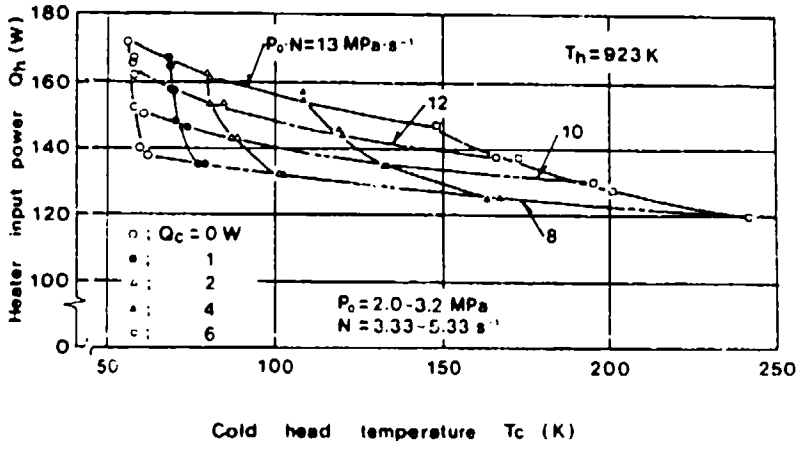

Fig.5 Cooler performance at various products of charge pressure and cycle speed.

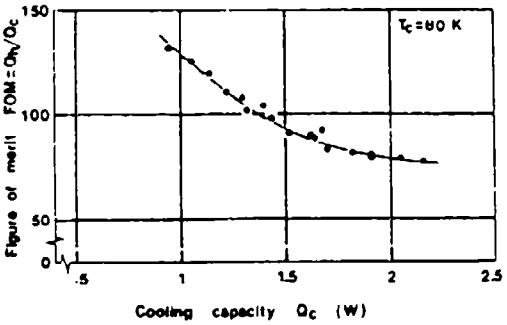

Fig.6 Figure of merit of Vuilleumier cryocooler as a function of cooling capacity at 80 K.

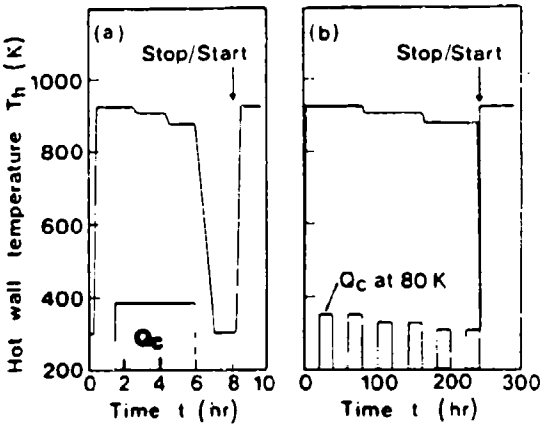

(a) Phase 1 (b) Phase 2

Fig.7 Operating mode of life test.

LIFE TEST

To evaluate the performance of the machine, the life test of over 4,800 hours was planned. Figure 7 shows the operating mode of the life test. During the first 2,500-hour test period, the machine was operated under much the same operating conditions as those of the performance mapping test (phase 1). After that time, the machine was subject to a cyclic test, whose test period was 243 hours (phase 2). The critical parameters of the machine, heater input power, cooling performance at no heat load and cooling capacity at 80 K, were measured two times per day in order to detect the performance changes with the operating time.

The curves in figure 8 are plotted from measurements of the cooling capacity at 80 K under the operating conditions of a charge pressure of P_0=2.5 MPa and 3 MPa, hot wall temperature of T_h=923, 903 and 873 K, and cycle speed of N=4 s^{-1}. During the 2,500 hours of operation, data indicated that the cooling capacity at 80 K decreased over a long period of time. The decrease rate during 2,500-hour operation was 50 mW/2,500 hours under the charge pressure of 3 MPa and 130 mW/2,500 hours under the charge pressure of

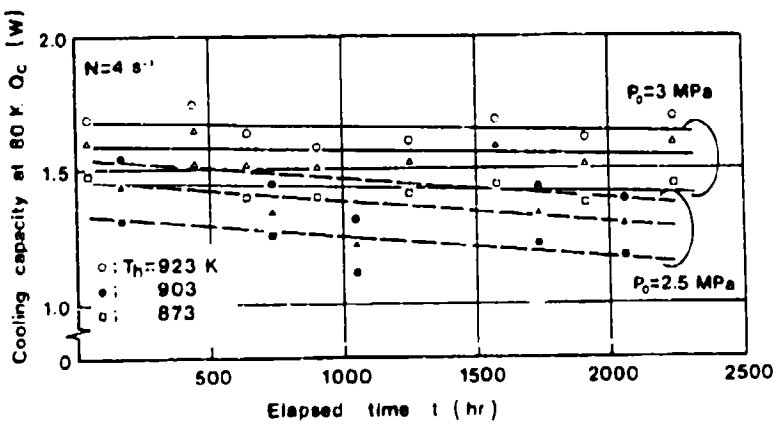

Fig.8 Degradation trend of cooling capacity at 80 K.

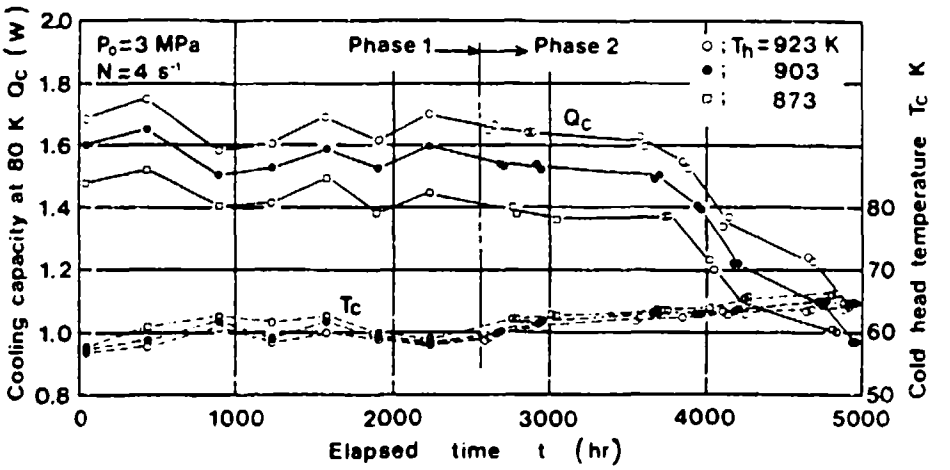

Fig.9 Cooling performance change with elapsed time.

2.5 MPa. The effect of the fixed value of $P_0 \cdot N$ was investigated for the cooling performance before 2,500 hours. It is found that the degradation of the cooling performance at high charge pressure is slight for the accumulated operation time of 2,500 hours.

After 2,500 operating hours, a 243-hour continuous operation test was resumed. Before each test period, the machine was taken off the calibration of the monitoring instrumentation and the charge pressure was checked. The experimental results which were obtained in the way described are shown in figure 9. The cooling capacity at 80 K was degraded slightly with time through 3,900 operating hours. At that point, the machine had the cooling capacity of 1.6 watts at 80 K under the condition of a hot wall temperature of T_h=923 K, and the cold head temperature with no heat load rose to 5 K, compared with the initial test results. Comparing the cooling capacity at 80 K (Q_C) and the cold head temperature with no heat load (T_C) curves in figure 9, Q_C became degraded as T_C rose with the operating time. The cooling performance of the machine markedly changed when T_C was above 64 K.

CRYOCOOLER PERFORMANCE TEST IN VACUUM ENVIRONMENT

EXPERIMENTAL CONDITION AND TEST INSTALLATION

The schematic diagram of the vacuum test using the second machine is shown in figure 10. The nominal dimensions of the vacuum chamber are an inner diameter of 1,500 mm and a length of 2,500 mm. A liquid nitrogen thermal shield is installed on the right side of the vacuum chamber shown in this figure. The liquid nitrogen flows from a storage tank through a transfer line to the thermal shield. When the liquid nitrogen has been supplied, the pressure in the vacuum chamber can be maintained at the range of a high vacuum of 10^{-5} Pa.

The second machine was fabricated and had the same design features against the first one except that the heat rejection device was added. The device was a single-phase flow loop and small passive radiator set installed inside the vacuum chamber. The water, which was selected as the coolant, was pumped to the machine, and the flow rate was controlled by a bypass valve. A heater attached to the passive radiator permits control of the temperature for heat radiation.

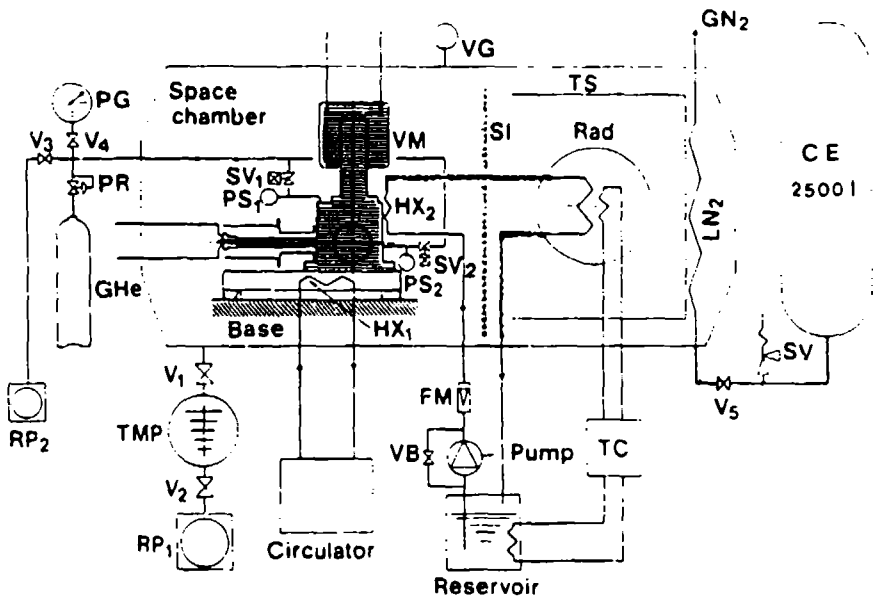

Fig.10 Vacuum test fasility for Vuilleumier cryocooler.

The requirements of the heat rejection loop are a radiating capability higher than 150 watts with the coolant temperature between 273 K and 303 K and a nominal flow rate of 1.2 l/min. We calculated a heat path of the heat rejection loop by a simple thermal model. The radiator of 900 mm in diameter has a heat rejection capability of more than 150 watts at a radiation temperature of 273 K based on the calculated results.

The heat leaks from the fluid pipeline between the machine and the passive radiator are negligible because the difference of the water temperature from the surrounding temperature (inner wall temperature of the vacuum chamber) is small and the fluid pipeline is covered with a multilayer insulator.

COOLING PERFORMANCE TEST

The test results in an atmospheric environment are shown in figure 11. In this figure, ① indicates the data obtained by the second machine and ② indicates the data obtained by the first one. The second machine has the capability of cold generation of 35 K without the heat load at the cycle speed of above 9 s^{-1}.

Figure 12 shows the time history of the vacuum system and the cooldown characteristics of the machine. The time spent was about 1 hour for the thermal shield (cold panel for radiation) cooling to 115 K. When the thermal shield temperature becomes 115 K, an electric heater power is supplied to heat the hot cylinder head. The hot cylinder head temperature (hot wall temperature) was maintained constant at 923 K all the time. The cold head temperature reached 41 K after 2 hours from the start. The typical cooldown time was estimated to be 30 minutes down to the temperature of 80 K and 50 minutes to 40 K.

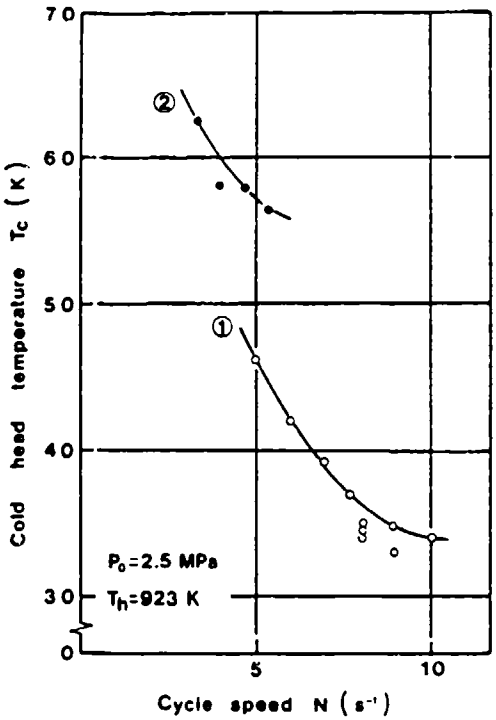

Fig.11 Comparison of cooling performance of 1st. machine with those of 2nd. one.

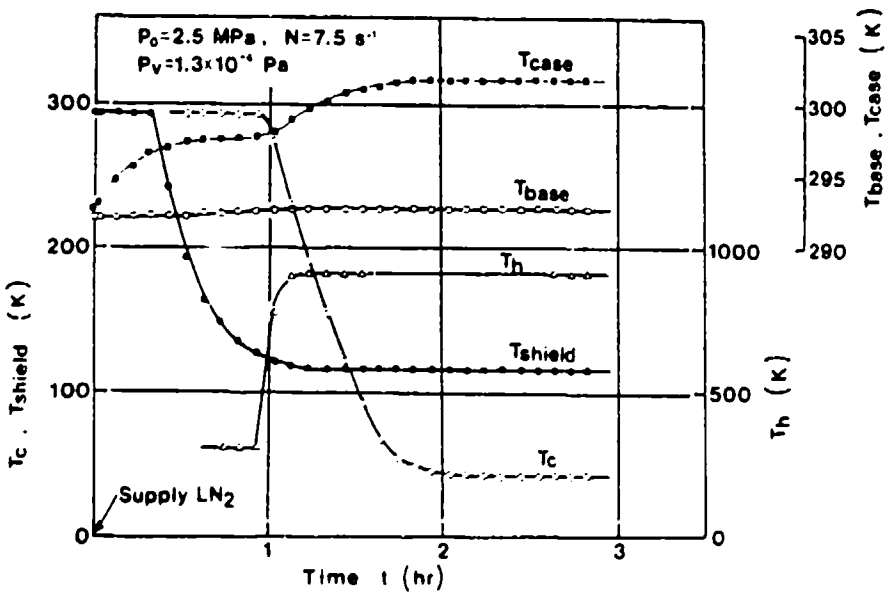

Fig.12 History of vacuum system and cooldown characteristics of machine.

Figure 13 shows the effect of the cold head temperature on the heat load when the cycle speed is changed. The results show that cooling capacity was 1.4 watts at 80 K, and the cold head temperature was 40 K at no heat load under the condition of cycle speed at 10 s^{-1}. Also, it has the cooling capacity of more than 600 mW at 60 K. The curves in this figure are plotted from measurements of the cooling capacity at 80 K and the cold head temperature at no heat load on the cycle speed. When the machine was operated at the cycle speed of above 9 s^{-1}, the cold head temperature was saturated at 40 K. The second machine was operated for over 120 hours in the vacuum environment.

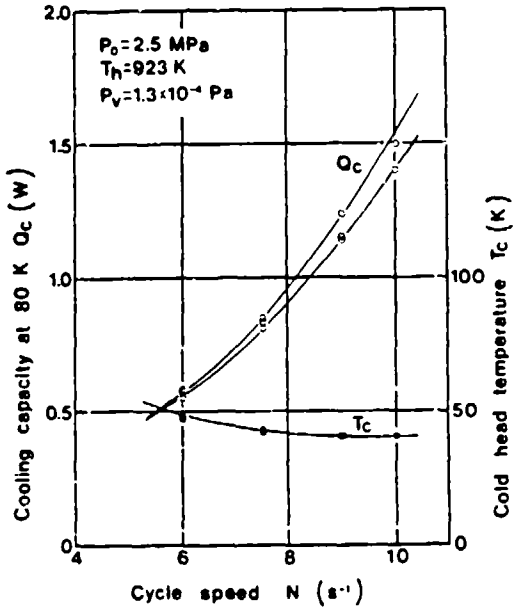

Fig.13 Effect of cycle speed on cooling performance with no heat load and cooling capacity at 80 K.

CONCLUSIONS

Two small-size Vuilleumier cryocoolers were designed, fabricated and successfully tested. The first machine could obtain 2.2 watts of maximum cold production at 80 K. Performance mapping at 80 K was carried out as functions of the hot wall temperature and cycle speed with the charge pressure of 2.5 MPa and 3 MPa. It had the cooling capacity of 1.6 watts for over 3,700 hours total under the conditions of the charge pressure of 3 MPa and cycle speed of 4 s^{-1}. It is found that the machine had better cooler performance from the evaluations of the figure of merit and specific weight. When the second machine was operated in a vacuum environment, it had the capability of cold generation of 40 K and the cooling capacity of 600 mW at 60 K.

REFERENCES

1. M.Kawada, I.Kudo," Japanese development of cryocoolers for applications in space," Proc. 3rd Japanese-Sino Joint Seminar, Okayama, Japan (October 1989) P.36-41.
2. G.Walker," Cryocoolers, I," Plenum Press, New York (1983).
3. W.R.Martini," Stirling engine design manual," NASA CR-135382 (1978).

Session VIII — Component Technologies

Chairperson: Jim Chafe, DTRC

Co-Chairperson: Jeff Bruning, Nichols Research Corporation

IMMERSION VS CONDUCTION COOLING OF A NIOBIUM JOSEPHSON JUNCTION INTEGRATED CIRCUIT: CHARACTERIZATION AND PERFORMANCE CORRELATIONS AT LOW FREQUENCIES

Edward Hershberg, Kimberly Godshalk, Vallath Nandakumar,
Soo Young Lee and Bruce Murdock
Superconductive Systems Group
Solid State Research Laboratory
Tektronix, Inc
P.O. Box 500, M/S 50-324
Beaverton, Oregon 97077

ABSTRACT

A simple Josephson sampler circuit, designed by Tektronix, has been fabricated using a Niobium IC process, and the performance has been characterized in liquid helium. We have begun testing of the same circuit in a conductively cooled environment. Differences in the measured sampling gate performance at low frequency between the two testing methods were characterized and addressed, so that performance in liquid helium, the traditional testing environment, can be reliably reproduced in the conductive cooling environment.

In this paper we present the testing methods employed, the hardware configuration, the performance variables examined and the results obtained to date. Further work will involve extending the testing to higher frequencies and the use of different refrigeration equipment.

INTRODUCTION

Superconductive microelectronic devices have the capability to operate at the terahertz (10^{12} Hz) level with nanowatt power dissipation per device, and although LSI level circuits have been demonstrated, relatively little effort has been devoted to the system issues associated with this high performance technology. In this case system issues means cryosystems, signal I/O, supporting semiconductor electronics and design of the superconductive IC for conductive cooling. At present the technology base does not exist to enable application of the proven performance of superconductive microelectronics in any practical way. Towards this end we have begun to evaluate the system issues that

must be addressed before niobium based superconducting microelectronic devices can be operated in a conductively cooled environment while in the presence of a closed cycle cryocooler operating at approximately 4.5 K.

Tektronix' superconducting systems effort is focused on the integration of superconducting circuits with cryogenic systems. One of the circuits we have fabricated with the niobium based, all refractory, integrated circuit process developed as part of our continuing joint project with the University of California at Berkeley[1] is a Josephson sampler circuit. This circuit uses a single Josephson junction for the sampling gate[2,3]. Other elements in this circuit include single Josephson junction triggers, variable delay lines, resistors, inductors and pulse generators. The design combines on one chip a test circuit and a sampler, which allows high frequency testing without having to bring high frequency, low noise signals into the cryostat. The sampler circuit has been tested at frequencies up to 70 GHz with a high frequency probe in liquid helium[4].

For this study we compared the low frequency performance and the noise signal of an isolated sampler junction cooled by immersion in liquid helium and by conductive cooling on a cold finger attached to the end of a helium transfer line. For the conductive cooling characterization, the chip was placed in close proximity to an operating Gifford-McMahon cryocooler.

TEST EQUIPMENT AND TESTING SETUP

The test apparatus consists of three main elements: a sixteen channel liquid helium probe, a vacuum test chamber for performing conductive cooling characterization studies, and a set of test electronics that includes a signal generator, oscilloscope, amplifiers and a signal converter. Figures 1 and 2 show block diagrams of the equipment arrangements.

The liquid helium probe used in this work is capable of testing superconducting integrated circuits at frequencies up to 35 MHz. The chip is varnished onto a sixteen pin chip carrier with GE 7031 varnish and the leads are spot welded in place. This chip carrier is plugged into the end of the probe, with its back pressed against a ceramic thick film heater element. A copper cap is screwed onto theMwnd of the probe over the chip carrier to protect the chip.

The test chamber for conductive cooling measurements is a 30 cm by 30 cm by 60 cm aluminum vacuum chamber designed along the lines of a chamber described by Woody[5]. Two sides and one end consist of O-ring sealed plates that can be removed to gain access to the interior of the chamber. A CTI Model 350 cryocooler is mounted in the bottom end of the chamber, with the cold head located in the middle of the work space. An Air Products Model LT-3-110 Heli-Tran helium transfer line is mounted through the top, and an extension to the Heli-Tran cold finger places the test circuit to within 3 cm of the cryocooler cold finger. Other penetrations to the chamber include a pumpout port, vacuum gauge ports, a sixteen channel coax feedthrough, and a 26 pin hermetic

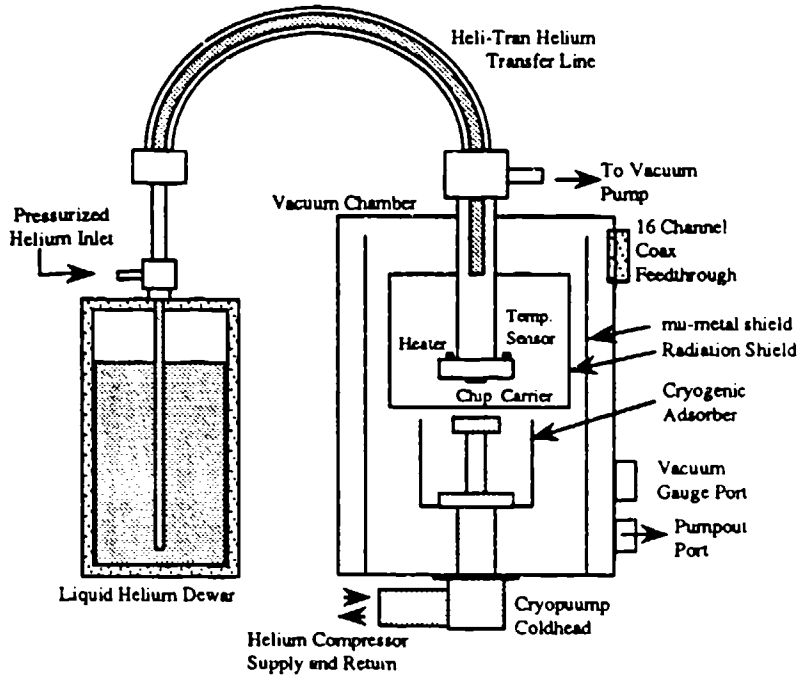

Figure 1. Schematic of the test apparatus used for conduction cooling.

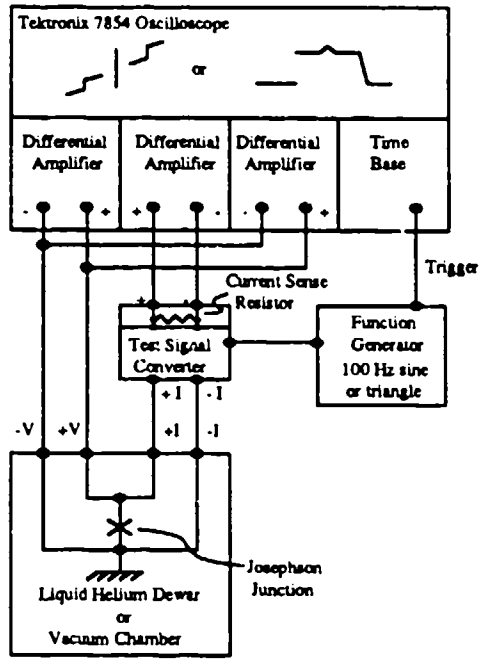

Figure 2. Block diagram of the electronic test setup.

feedthrough for sensor leads. There are also heater and sensor feedthroughs in the Heli-Tran. Additional hardware includes a copper radiation shield mounted on the Heli-Tran that encloses the cold finger, a copper foil radiation shield mounted on the first stage of the cryocooler that also acts as a cryogenic adsorber surface, and a cylindrical mu-metal shield that extends the full height of the chamber and encloses both the cold finger and cryocooler coldhead. The entire chamber is mounted on a cart, with the compressor unit underneath the chamber. The vacuum gauge controller, Heli-Tran control unit, temperature controller, and thermometer display unit are also mounted on the cart.

The temperature sensors used in this study are all silicon diode sensors from Lakeshore Cryotronics. A Lakeshore Model DRC 91C temperature controller, along with a Lakeshore Model 208 thermometer, were used for the sensor readouts. The primary sensor used in the work reported here read 4.16 K in liquid helium at atmospheric pressure. The cold finger can attain a stable temperature of 3.4 K with a vacuum pump attached to the transfer line tip flow outlet. Stable, continuous operation at 4.2 K has been maintained for over seven hours. The chamber maintains a vacuum of 5×10^{-6} Torr during operation at 4.2 K.

Testing of a Josephson junction sampling gate for comparison of immersion and conduction cooling of the gate junction involved measuring, for two different chips, the gap voltage V_g, the critical current I_c, the subgap current I_{sub}, the normal resistance R_N, and the voltage and current noise. The two chips have identical circuits but are from different wafers. For testing with immersion cooling, the chip carrier is placed on the liquid helium probe and immersed in liquid helium at 2 psi, corresponding to a temperature of 4.35 K. The center conductors of the 16 coaxial lines of the probe are connected to the pins on the chip carrier; the coax shields are terminated and float at the chip carrier. The coaxial lines run through a long tube to a set of coaxial feedthroughs at room temperature, where the coax shields are grounded.

In the conductively cooled arrangement the chip carrier is pressed against the copper cold finger attached to the cold stage of the Heli-Tran helium transfer system described earlier. The temperature of the cold finger is adjusted by controlling the flow of liquid helium against the copper cold stage and by adjusting the pumping rate on the exhaust flow. The temperature was measured with a silicon diode as shown in Figure 1, and was set to 4.17 K $\pm$ .05 K for these experiments. We chose T = 4.17 K, rather than 4.35 K, the temperature for immersion cooling, to obtain more stable operation of the Heli-Tran. This temperature difference produces at most a 2% difference in V_g. Electrical connections to the chip carrier pins, the temperature sensor and the heater are made of phosphor-bronze wire; this wire is wound around the cold finger and cold stage of the Heli-Tran up to the room temperature portion of the Heli-Tran. At this point the circuit signal lines are connected to the center conductors of coaxial cables; the coax shields are terminated and joined together here, but are not grounded. The other end of the coax cables connects to electrically isolated coax feedthroughs in the vacuum chamber. The shield and center conductor for the coax are silver plated copper.

Electrical measurements of the Josephson junction sampling gate were made using the setup shown in Figure 2. A 100 Hz sine or triangle wave is split into a differential signal to excite the junction. The junction I-V curve and/or the voltage vs time trace is viewed on the oscilloscope. The current axis for the I-V curve is provided by sending the bias current through a 1 kΩ ± 0.1% resistor and measuring the voltage across it. Flux trapped in the circuit is removed by quickly heating the chip, in the absence of bias current, to the normal state. In the liquid helium probe the heater is directly behind the chip carrier, while for the conductively cooled setup the heater is clamped to the copper cold finger ~1.5 cm from the chip carrier, as shown in Figure 1.

In measuring the circuit parameters for the comparisons, the critical current I_c is the maximum current at zero voltage. The subgap current I_{sub} is the current at 2 mV, and the normal resistance is the resistance at 3 mV. The voltage gap V_g is measured at the midpoint in the gap. In addition to measuring V_g from the I-V curve, V_g is also measured from the V vs t trace by averaging 100 traces and using cursors to measure the distance between points on the displayed waveform. We see no difference in the measured parameters for a sine or triangle wave drive signal. Noise measurements are made by expanding the voltage or current scales to the maximum possible and viewing the noise seen in I_c or V_g. Long time exposure photos of these traces are helpful in evaluating the noise in the time domain. We also observed the noise caused by operating the cryopump attached to the vacuum chamber.

RESULTS

Figures 3a and 3b show the junction I-V curve of chip #1 with immersion and conductive cooling, respectively. In the junction I-V curves, the current at zero voltage shows the supercurrent of the Josephson junction. As the current is increased above the critical current I_c, the voltage switches to the gap voltage V_g, and the current continues to increase at essentially constant voltage until the junction enters the normal state. Hysteresis is seen as the current is decreased. The I-V curve of chip #2 is shown in Figures 4a and 4b for immersion and conductive cooling, respectively. The differences in I_c and the shape of the I-V curves for chip #1 and chip #2 are due to different materials processing of the two different wafers the chips were taken from. Figures 5a and 5b show voltage vs time for chip #1, and illustrate the switching from zero voltage to V_g of the sampling gate as the current is increased above the critical current. Also shown in Figures 5a and 5b is the triangle wave bias current.

The results of the immersion vs conduction cooling of a Josephson sampling gate are summarized in Table 1. The repeatability of the measurements in the liquid helium dewar from day to day was ± 0.02 mA for I_c, and ± 0.006 mV for V_g. The repeatability of measurements with conductive cooling was ± 0.03 mA for I_c, and ± 0.01 mV for V_g. Some of the additional uncertainty in the conduction results is due to small temperature fluctuations and the precision of the temperature sensor. We can see that the results for immersion and conduction cooling are close but do not agree within our ability to make

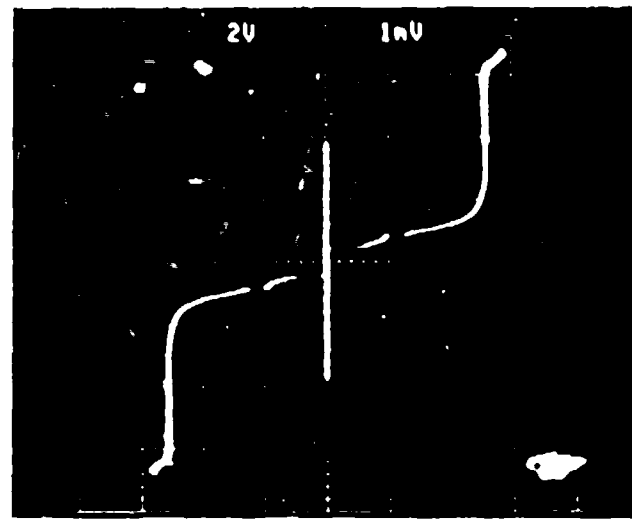

2 mA/div

1 mV/div

Figure 3 (a). I-V curve of chip #1 cooled by immersion in liquid helium.

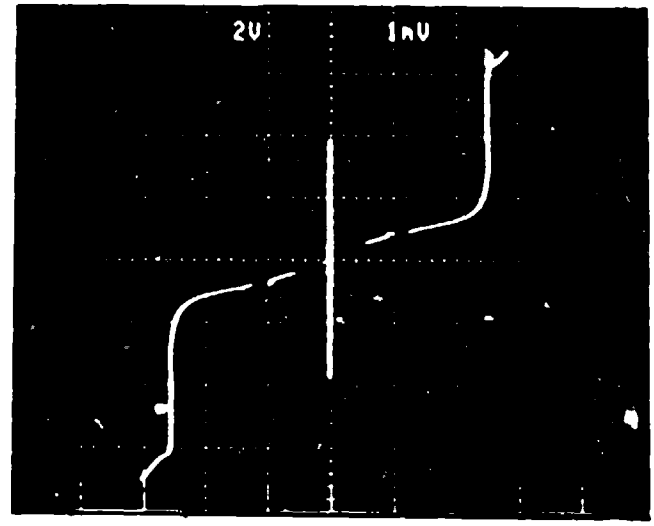

2 mA/div

1 mV/div

Figure 3 (b). I-V curve of chip #1 cooled by conduction on a helium transfer line cold finger at 4.2 K.

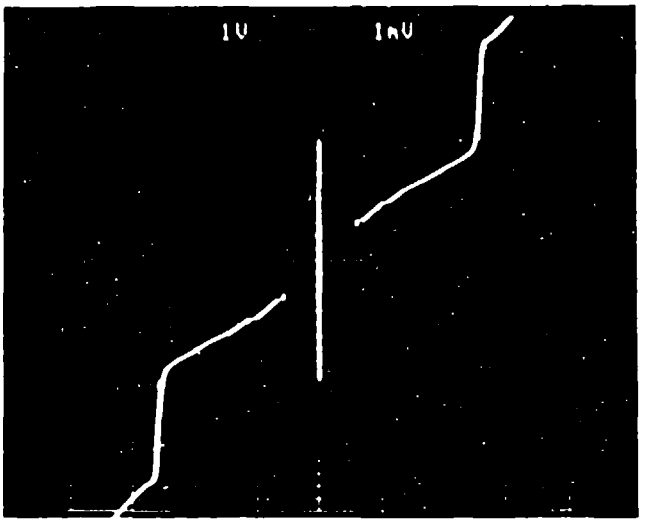

1 mA/div

1 mV/div

Figure 4 (a). I-V curve of chip #2 cooled by immersion in liquid helium.

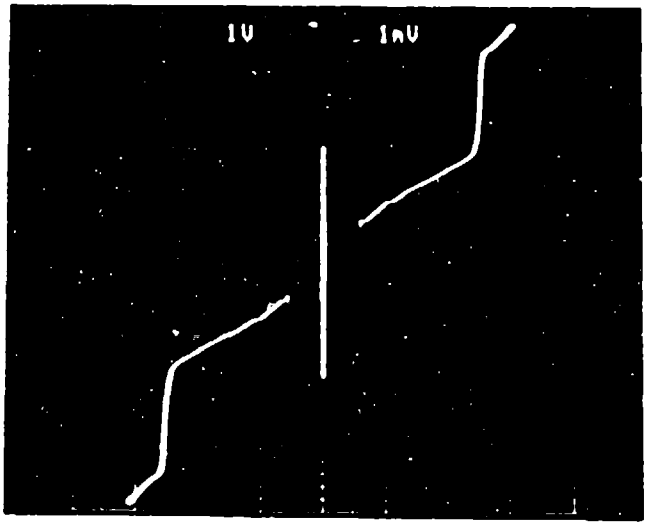

1 mA/div

1 mV/div

Figure 4 (b). I-V curve of chip #2 cooled by conduction on a helium transfer line cold finger at 4.2 K.

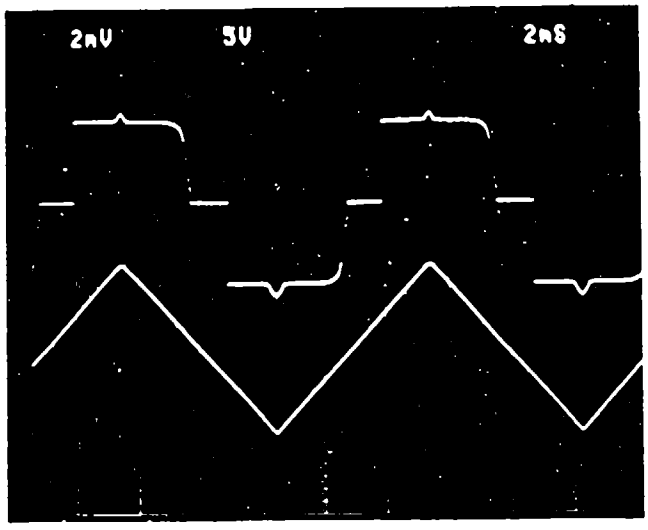

Figure 5 (a). Voltage vs time for chip #1 cooled by immersion in liquid helium. The voltage switches from zero to V_g, then enters the normal state as the current increases. The voltage decreases hysteretically as the current decreases.

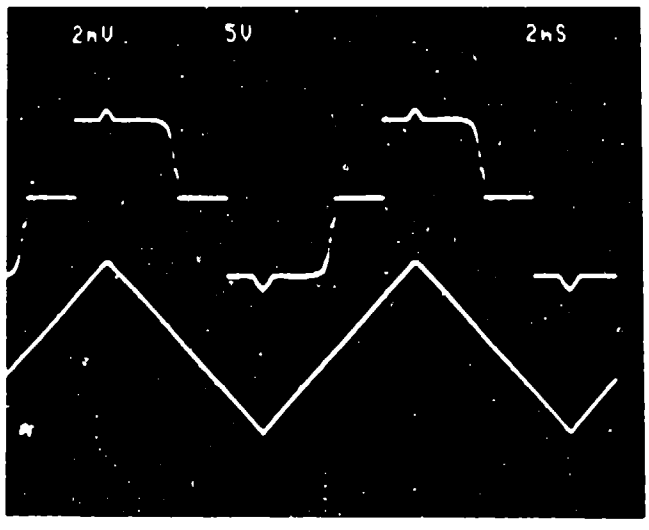

Figure 5 (b). Voltage vs time for chip #1 cooled by conduction on a helium transfer line cold finger at 4.2 K.

Table 1. Measurements of sampling gate parameters for immersion and conduction cooling. The errors listed for I_c and V_g are the reproducibility of the measurement. I_cR_N is a quantity often used to characterize junctions. $\Delta I_c/I_c$ is the fractional noise observed in the critical current.

COMPARISON				
	CHIP #1		CHIP #2	
	immersion	conduction	immersion	conduction
V_g (mV)	2.575 ±.006	2.55 ±.01	2.575 ±.006	2.54 ±.01
I_c (mA)	3.86 ±.02	3.85 ±.03	1.95 ±.02	1.84 ±.03
I_{sub} (mA)	1.20	1.24	1.46	1.46
R_N (Ω)	0.428	0.429	0.800	0.806
I_cR_N (mV)	1.659	1.650	1.56	1.483
$\Delta I_c/I_c$	0.01	0.01	0.005	0.05

the measurements. I_c and V_g are consistently lower in the conductively cooled environment, although we expected them to be slightly higher due to the lower temperature used in the conductive cooling experiment. Since our temperature sensor is not in direct contact with the chip carrier in the conductively cooled environment, we investigated the possibility that the temperature there might actually be higher than in the immersion cooling setup. We made a set of I_c vs T measurements, and found that the temperature difference required to produce the difference in I_c observed for chip #2 is 0.2 K, which implies that the temperature sensor, located approximately 1.5 cm from the circuit, would have to be reading low by 0.2 K, an unlikely circumstance. It is also possible that residual static magnetic fields could produce the observed differences. A magnetic field of 1×10^{-5} T, or 0.2 flux quantum, could produce the observed difference in I_c; this field is smaller than the earth's field by a factor of five, and stray magnetic fields are therefore a likely cause for the differences in I_c.

The noise $\Delta I_c/I_c$ reported in the table represents the noise seen in a typical, single measurement. In the conductively cooled environment the noise in the current is typically greater than that seen with the chip immersed in liquid helium. This may be due to electromagnetic shielding provided by the dewar since we found it necessary to include a mu-metal shield in the vacuum chamber of the conduction cooling setup. Until the mu-metal shield was installed, trapped flux prevented us from making meaningful measurements. Also, whereas the probe used in the helium dewar has coaxial cables from the sample to the head, this is not the case in the vacuum chamber. In the chamber, the coaxial lines are terminated just short of the Heli-Tran, with low thermal

conductivity phosphor-bronze wire wrapped around the cold finger and connected to the chip carrier via miniature metal sockets. Although this setup is not ideal, it was chosen for this first generation equipment to provide an easy solution to the heat sinking problem. However, the exposed sections of unshielded cable certainly contribute to some of the differences in electrical noise we see between the two environments. We also measured the voltage noise seen in both environments. The noise in V_g with immersion cooling was 100 μV, yet with conduction cooling the noise in V_g was less than 10 μV. The larger noise value was due to unexplained low frequency oscillations in the voltage gap. It is not yet known why this was seen in immersion cooling but not in conductive cooling. To examine the noise caused by operating the Gifford-McMahon cyrocooler we measured the noise in I_c with the cryocooler on and off. We observed no changes in the circuit parameters or noise signature when the cryocooler was operating.

To properly operate the Tektronix sampling circuit, it is clear to us that we need to reduce the noise observed in both environments. For example, with a sampling rate of 500 MHz and a resolution of 5 psec, a 100 μA change in I_c results in a 5 psec timing error for our sampling circuit; this timing error is too large for proper operation. However, it is only necessary to reduce the low frequency noise, since noise in the critical current that occurs at frequencies above 10 MHz will be averaged out of the result.

CONCLUSIONS

We have successfully operated a Josephson sampling gate in a conductively cooled environment with results nearly identical to those obtained with immersion cooling. The small but consistent difference in critical current observed between the two testing methods is most likely due to stray magnetic fields. The source of the observed differences in V_g has not yet been determined. We have also observed differences in the electrical noise in the measurements, which is most likely due to differences in the degree of signal line shielding between the two probes. Finally, we found that the proximity of an operating Gifford-McMahon refrigerator and associated helium compressor had no measurable effect on the electrical noise or circuit performance in our apparatus. These results may be dependent on the low drive frequency used in this investigation and higher frequency operation, our next step in testing, will delineate sensitivities not seen in this work.

REFERENCES

1. S.Y. Lee, V. Nandakumar, B. Murdock and D. Hebert, "PECVD SiO_2 dielectric for niobium Josephson IC process", 1990 *Applied Superconductivity Conference, Snowmass Village*, Colorado, (September 1990), Proceedings in preparation.

2. S.M. Faris, "Generation and measurement of ultrashort current pulses with Josephson devices", *Appl. Phys. Lett.*, vol. 36, (1980), p. 1005-1007.

3. S.M. Faris, "Ultra High Resolution Sampling Technique", U.S. Patent 4,401,900, (Aug. 30, 1983).

4. Murdock, et. al., in preparation.

5. D.P. Woody, C.J. Giovanine and R.E. Miler, "Dual channel 115 and 230 GHz SIS receivers in operation at the Owens Valley Radio Observatory", *IEEE Transactions On Magnetics*, vol. 25, no. 2 (March 1989) p. 1366-1370.

EFFECT OF TUBE TEMPERATURE PROFILE ON THERMAL ACOUSTIC OSCILLATIONS IN LIQUID HYDROGEN SYSTEMS

Y. F. Gu and K. D. Timmerhaus
Department of Chemical Engineering
University of Colorado
Boulder, CO 80309

ABSTRACT

Thermal acoustic oscillations have often been an annoying problem in cryogenic systems since large amounts of heat can be transferred into these systems due to such oscillations, particularly in liquid helium and liquid hydrogen systems. Recent interest in the use of slush hydrogen for the NASP (National Aerospace Plane) has again rekindled interest in these oscillations, particularly for hydrogen systems. Unfortunately, most past investigations have not included liquid hydrogen systems.

In earlier studies by the authors, a step temperature profile has been assumed to simplify the oscillation stability calculations made for liquid hydrogen systems. However, as noted in those studies, the temperature profile along the oscillating tube does have an effect on the oscillation stability. It has been found that the unstable region for thermal acoustic oscillations in a tube can be reduced considerably if the temperature profile in such a tube approaches a linear temperature distribution. With the development of a suitable computational method, these stability curves have now been defined and the results are disclosed in this presentation.

INTRODUCTION

Thermal acoustic oscillations (TAOs) have often been observed in tubes penetrating cryogenic systems. Such tubes are generally used for vent or fill lines, relief lines, pressure taps, *etc.* and are always open at the cold end and closed at the warm end[1-3]. Considerable heat can be pumped into cryogenic systems due to such oscillations. This oscillatory heat leak has been estimated to be as much as ten to a thousand times greater than the normal conductive heat leak into the system[3,4]. Further, these pressure oscillations in a tube make accurate measurement of system pressure essentially impossible.

During the process of thermal acoustic oscillations, heat is added at the high temperature sink and rejected at the low temperature sink. This process is similar to a thermodynamic cycle heat engine which produces work by the proper utilization of the pressure oscillations and is designated as a thermal acoustic engine. However, this process has received more attention in the refrigeration area since an inverse thermal acoustic oscillation cycle can be constructed to serve as a refrigeration cycle. This type of thermal acoustic refrigerator has been investigated by Hofler *et al*[5].

A step temperature profile along the oscillating tube has been assumed by previous investigators to simplify the calculations[6-10]. However, the temperature profile along the tube does not follow such a mathematically idealized step function, although Bannister[4] noted that the actual temperature profile in a helium system was very steep along the length of the tube. Several different temperature profiles along the tube have been investigated in this study by analyzing the effect of these temperature gradients on the stability of thermal acoustic oscillations in liquid hydrogen systems.

THEORY

Thermal acoustic oscillations in a gas filled tube can generally be described by the hydrodynamic equations governing the motion of a fluid in tube, namely, the equations of continuity, motion, energy and state. For the thermally induced acoustic oscillations in a gas filled tube, the amplitude of the oscillation pressure is usually much smaller than the mean pressure and the nonlinear characteristics of oscillation can be neglected. Therefore, the stability characteristics of the oscillation system can be obtained by perturbing these general equations. To obtain a theoretical solution for the thermal acoustic oscillations in a tube filled with helium gas subjected to a large temperature gradient, Rott[6,7] made the following assumptions: (1) negligible radial pressure variation in the oscillating tube, *i.e.*, $\partial p_1/\partial r = 0$; (2) negligible radial variation in the mean temperature T_m, and thus, constant viscosity of the gas; (3) minor axial heat conduction; (4) time variation of the acoustic variable expressed as $e^{i\omega t}$; (5) negligible body force; (6) newtonian fluid; and (7) tube radius r_0 much smaller than the tube length L. The resulting equation which relates to the acoustic pressure p_1 is then

$$[1 + (\gamma - 1)f^*]p_1 + \frac{d}{dx}\left(\frac{a^2}{\omega^2}(1 - f)\frac{dp_1}{dx}\right) + \frac{a^2}{\omega^2}\frac{(f - f^*)}{(1 - Pr)}\theta\frac{dp_1}{dx} = 0 \qquad (1)$$

where

$$f = \frac{2J_1(i\eta_0)}{i\eta_0 J_0(i\eta_0)}; \quad f^* = f(\eta_0\sqrt{Pr}) \qquad (2)$$

$$\eta_0 = r_0\sqrt{\frac{i\omega}{\nu}}; \quad \theta = \frac{1}{T_m}\frac{dT_m}{dx} \tag{3}$$

Here, J_0 and J_1 are the Bessel functions of the first kind with order of zero and one, respectively. For convenience, a new parameter Y is defined as

$$Y = r_0\sqrt{\frac{\omega}{\nu}} \tag{4}$$

As noted above, the time variable of the acoustic variable can be expressed as $e^{i\omega t}$, where the oscillation frequency ω generally is a complex variable. The real part represents the harmonic motion of the gas, while the imaginary part represents the exponential amplification of the oscillation. Therefore, the thermal acoustic oscillations will be damped if the imaginary part of the frequency ω is greater than zero, and be unstable if it is negative. The boundary separating the stable from the unstable region is located where the imaginary part of the frequency is zero.

If we define

$$G = [1 + (\gamma - 1)f]exp\left(\int_0^x \frac{f - f^*}{(1 - Pr)(1 - f)}\theta dx\right) \tag{5}$$

and

$$k = \frac{\omega}{a}\sqrt{\frac{1 + (\gamma - 1)f^*}{1 - f}} \tag{6}$$

Eq.(1) can be reformulated into the following first order differential equations:

$$\begin{cases} dp_1/dx = (k^2/G)\Psi \\ d\Psi/dx = -Gp_1 \end{cases} \tag{7}$$

The boundary conditions for a half-open tube are given by

$$p_1(0) = 0 \text{ (at the open end);}$$
$$dp_1(L)/dx = 0 \text{ (at the closed end)}$$

TEMPERATURE PROFILE

The temperature profile along the tube is assumed as

$$T(x) = \frac{T_1 e^y + T_2 e^{-y}}{e^y + e^{-y}} \tag{8}$$

where

$$y = \frac{4}{x_h - x_c}\left(x - \frac{x_h + x_c}{2}\right) \tag{9}$$

With the conditions of

$$T_c = T(x_c); \quad T_h = T(x_h) \tag{10}$$

we have

$$T_1 = \frac{T_c(1 + E_c^2) - T_h(1 - E_h^2)}{E_c^2 - E_h^2} \tag{11}$$

$$T_2 = \frac{T_h(1 + E_h^2)E_c^2 - T_c(1 + E_c^2)E_h^2}{E_c^2 - E_h^2} \tag{12}$$

where

$$E_c = e^{\psi(x_c)}; \quad E_h = e^{\psi(x_h)} \tag{13}$$

Different temperature profiles along the tube can be obtained by changing the value of x_c and x_h. A number of these temperature profiles are shown in Fig. 1, where curve A represents the assumed step temperature profile, curves B, C, D and E are obtained by choosing values of (x_c, x_h) equal to (-0.5, 1.5), (0, 1), (0.2, 0.8) and (0.4,0.6), respectively, and curve F represents the linear temperature profile along the tube.

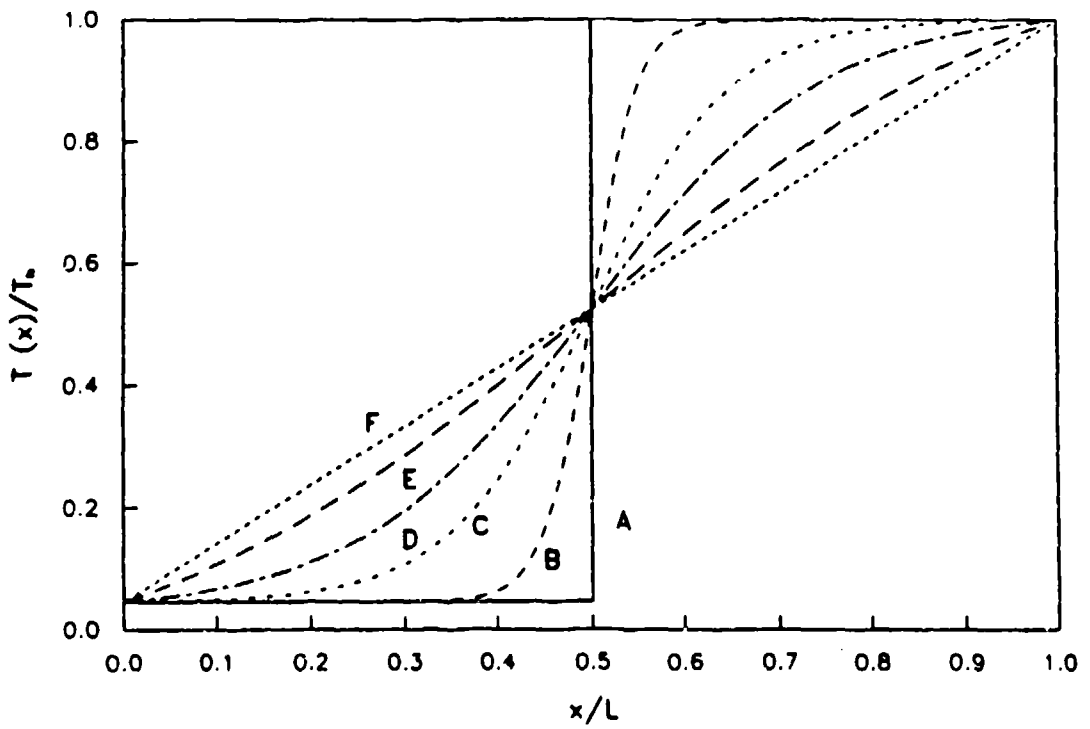

Figure 1. Different temperature profiles along the oscillating tube investigated in this study.

NUMERICAL METHOD

A shooting method has been used to solve Eq.(1) for a two-point boundary condition[11]. The boundary conditions for thermal acoustic oscillations in the half-open tube with a continuous temperature profile are established at both ends of the tube. The method used requires that $dp_1(0)/dx$ be equal to any nonzero real value in order to obtain a non-trivial solution of Eq.(1) due to the characteristics of standing wave oscillations in the tube. However, the associated oscillation amplitude in the tube is unobtainable by this numerical solution. With the shooting method and by selecting the value of $dp_1(0)/dx$ being equal to unity at $x = 0$, the two-point boundary problem can be converted into the following initial condition problem:

$$\begin{cases} p_1(0) = 0 \\ dp_1(0)/dx = 1 \end{cases} \tag{14}$$

$$\begin{cases} \Psi(0) = G/k^2 \\ d\Psi(0)/dx = 0 \end{cases} \tag{15}$$

These linear differential equations can be integrated step by step once the values of G and k are known. For a given temperature ratio α (defined as $T(L)/T(0)$), a trial and error method was employed to determine the values of the oscillation frequency and the tube radius. Generally, values of Y along with the oscillation frequency are assumed and then adjusted until the difference between the calculated value of $dp_1(L)/dx$ and the given boundary condition (equal to zero) is less than some designated error limit.

Asymptotic expressions for f and f^* have to be used in this evaluation when the values of Y are large since the Bessel functions involved increase much more rapidly than values of Y and may cause an overflow in the calculation. The value of f for large values of Y can then be calculated from

$$f = \frac{2}{\eta_0} - \frac{1}{\eta_0^2} - \frac{1}{4\eta_0^2} \tag{16}$$

The value of f^* can be determined in a manner similar to that used in evaluating f by replacing the η_0 in Eq.(16) with $\eta_0\sqrt{Pr}$. The function G can be obtained by integrating Eq.(5). However, this integration can be simplified if a power relationship ($\nu \sim T^{1+\beta}$) relating the viscosity of the fluid and its temperature is assumed. That is,

$$G = [1 + (\gamma - 1)f^*]exp\left(\frac{-2}{1+\beta}\int_0^{\eta_0(x)} \frac{f - f^*}{(1 - Pr)(1 - f)}\frac{d\eta_0}{\eta_0}\right) \tag{17}$$

The Runge-Kutta method can be used to integrate this equation.

It is apparent that the values of f and G are different for each step in the numerical calculations. Thus, numerically integrating Eq.(17) to obtain the entire curve will require a large amount of computing time. However, if we recognize that f and G are functions of η_0 only, these values can be precalculated for a series of η_0. It should also be emphasized that if an integration parameter of $1/\eta_0$ instead of η_0 is used, the numerical calculation of function G becomes more stable. Thus, values of f and G can be obtained by interpolation over a small interval of $1/\eta_0$. This numerical approach has proven to be very useful in reducing the computational time required for obtaining the desired stability curves.

STABILTIY RESULTS

Numerical calculations have recently been completed for the triple-point parahydrogen system, (*i.e.*, the temperature at the cold end of the oscillating tube is assumed to be 13.8 K). The oscillating tube was assumed to be one meter in length while ξ, the ratio of the tube length in the warm section of the tube to the tube length in the cold section of the tube, was assumed to be unity. With the aid of NBS published hydrogen properties, the constant β for parahydrogen was determined to be 0.75114.

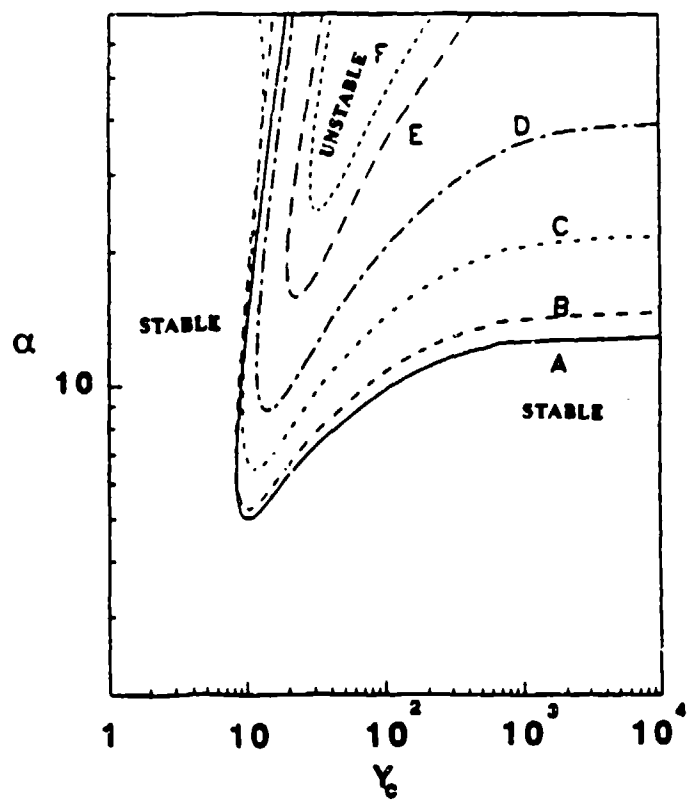

Figure 2. Stability curves for the triple-point parahydrogen systems with $\xi = 1$ and $L = 1$m. (Temperature profiles correspond to those shown in Fig. 1.)

STABILITY CURVES

Stability curves for thermal acoustic oscillations are best described by plotting α, the ratio of the temperature at the warm end of the tube to the temperature at the cold end of the tube, *vs.* the parameter Y_c as evaluated from Eq.(4) at a temperature of T_c. These results are shown in Fig. 2. The curves indicate that each stability curve exhibits a unique point where the required temperature ratio for initiating thermal acoustic oscillations in the half-open tube attains a minimum. This minimum point is bounded by both a left branch and a right branch. The region contained within these curves is designated as the unstable region where thermal acoustic oscillations are predicted to occur. The lowest temperature ratio for initiating such oscillations in the triple-point parahydrogen system appears to be about 5 (*i.e.*, the warm end temperature of the tube must exceed 70 K if oscillations are to occur) when a step temperature profile along the tube is assumed.

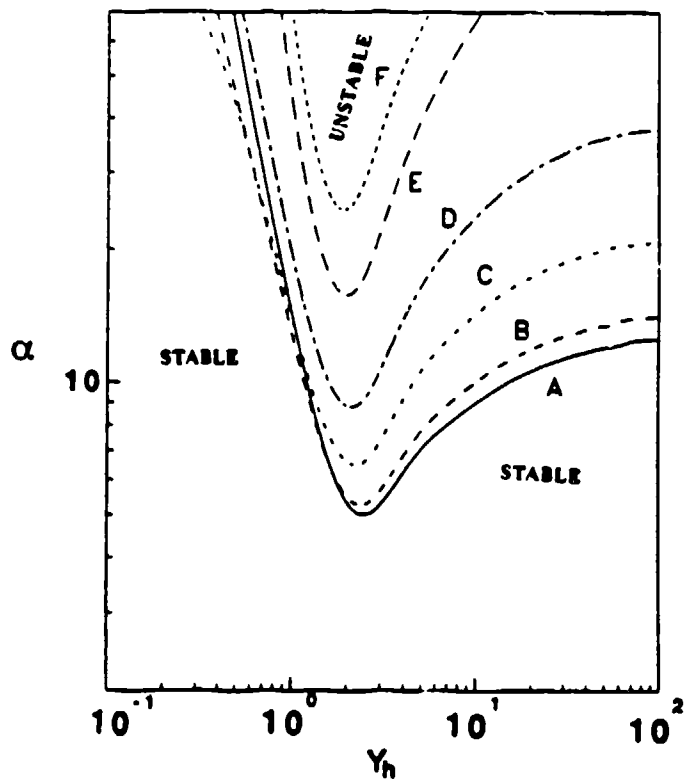

Figure 3. Stability curves as a function of Y_h for the triple-point parahydrogen systems with $\xi = 1$ and $L = 1$m. (Temperature profiles correspond to those shown in Fig. 1.)

The stability characteristics can also be expressed in terms of parameter Y at the warm end of the tube as shown in Fig. 3. Similar conclusions can be obtained

from these curves. However, note that the value of Y_h is much smaller than the corresponding value of Y_c. One plausible explanation for this significant difference could be that the thickness of the boundary layer in the warm section of the tube is much greater than that in the cold section of the tube due to the large change in the viscosity of the oscillating boundary layer. Parameter Y, from its definition, represents the ratio of the tube radius to the thickness of the boundary layer since the quantity $\sqrt{\nu/\omega}$ is proportional to the thickness of the oscillating boundary layer. Therefore, when the value of Y is small, the viscous resistance is predominant. When the viscous resistance becomes large enough, such oscillations may be damped. This is in agreement with the left branch of the stability curves. However, for large values of Y, the inertial forces required to move the fluid in the tube will be increased since the tube radius is much larger than the thickness of the boundary layer. This reasoning provides evidence for the existence of the right-hand branches of these stability curves.

It is evident that the effect of the temperature profile along the length of the oscillating tube on the oscillation stability characteristics is significant and complicated. First, the minimum temperature required for initiating thermal acoustic oscillations increases with a decrease in the slope of the temperature profile, particularly, when the temperature profile approaches a linear distribution (curve F). Second, a steeper temperature gradient for the right-hand branch of these stability curves results in a lower temperature ratio requirement for initiating such oscillations. This occurs because a less steep temperature profile results in a greater reduction in the driving force. However, the effect of temperature gradient on the inertial force is insignificant since the mass of the oscillating fluid is still related to the mean temperature along the tube and the latter is essentially unaffected by the temperature gradient. Finally, the effect of the temperature profile on the left branch of these stability curves is complicated because the viscosity is related to the temperature by a power law. This causes the left branches of curves B, C and D to cross curve A, the curve representing a step temperature profile.

FREQUENCY CHARACTERISTICS

The oscillation frequency characteristics for thermal acoustic oscillations in triple-point liquid parahydrogen are shown in Fig. 4. These results indicate that a less steep temperature profile along the tube results in a higher oscillation frequency. This is attributed to the mean velocity of sound which, in turn, is affected by changes in the temperature profile. Further, it can be observed that the oscillation frequency corresponding to the left branch of the stability curve is less than the frequency corresponding to that of the right branch, and this frequency difference for the same temperature ratio decreases with a decrease in the slope of the temperature gradi-

ent. This indicates that the propagation of the acoustic wave in the boundary layer decreases due to the viscous attenuation.

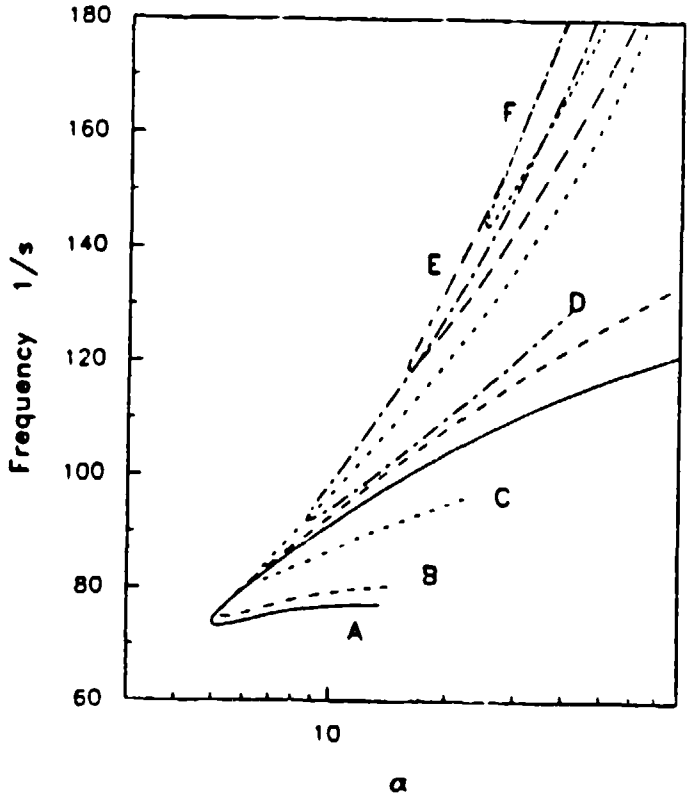

Figure 4. Oscillation frequency characteristics for thermal acoustic oscillations in triple-point parahydrogen systems with $\xi = 1$ and $L = 1$m. (Temperature profiles correspond to those shown in Fig. 1.)

CRITICAL RADIUS

The critical radii of tubes for initiating or damping thermal acoustic oscillations are shown in Fig. 5. These curves show the existence of two branches similar to those noted for previous stability curves. This indicates that thermal acoustic oscillations in a tube can be damped if the tube radius selected is located in the stable region as shown in Fig. 5. However, if the temperature at the warm end of the tube is maintained at 300 K, as in most storage situations, resulting in a temperature ratio of about 22, damping of the thermal acoustic oscillations by increasing the tube radius may only be accomplished if the tube is well insulated when the length ratio ξ is equal to unity. Particular attention needs to be given to the left-hand branches of the curves shown in Fig. 5 since a temperature profile like curve B or C may result in a smaller critical tube radius requirement for damping thermal acoustic oscillations. It should be noted that thermal acoustic oscillations can also be damped by changing the tube

length ratio or utilizing other proven damping techniques[12-13].

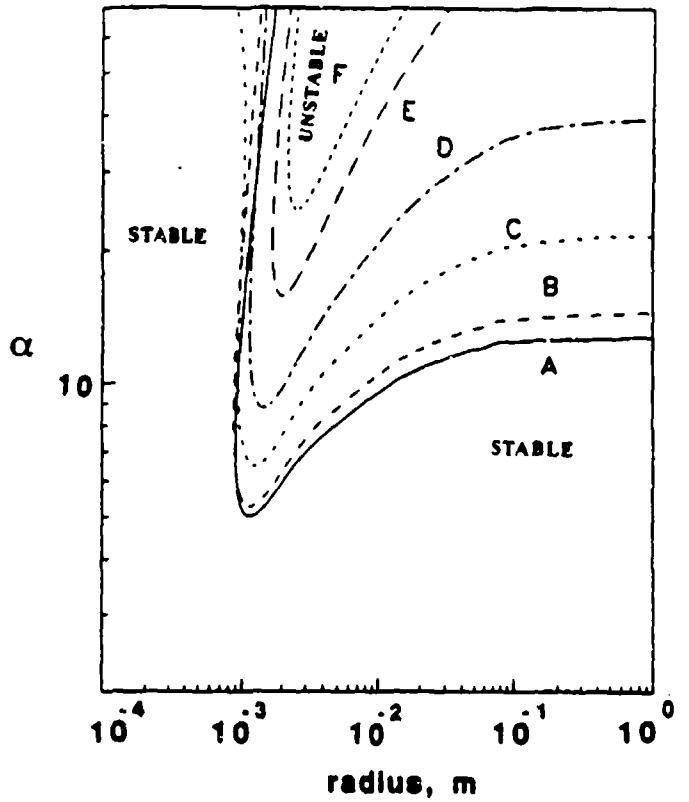

Figure 5. Critical radii associated with the thermal acoustic oscillations in triple-point parahydrogen systems with $\xi = 1$ and $L = 1$m. (Temperature profiles correspond to those shown in Fig. 1.)

CONCLUSIONS

The effect of temperature profiles on both thermal acoustic oscillations and stability characteristics have been evaluated for triple-point parahydrogen systems. Conclusions drawn from these studies are:

1. The effect of different temperature profiles on the right-hand branch of the stability curve and on the minimum temperature ratio required for initiating thermal acoustic oscillations is the same, *i.e.*, a decrease in the slope of the temperature profile along the oscillating tube makes it easier to damp these oscillations.

2. The effect of different temperature profiles in the tube on the left-hand branch of the stability curve is quite complicated. However, the unstable region for such oscillations is greatly reduced if the temperature profile approaches a linear distribution.

3. For the same temperature ratio, a less steep temperature profile along the tube results in higher oscillation frequencies.

4. A range of tube radii has been established in which thermal acoustic oscillations are predicted to occur in triple-point liquid parahydrogen systems.

ACKNOWLEDGEMENTS

The authors express their deep appreciation for the financial support by the NASA Lewis Research Center and the assistance of R. DeWitt, technical officer for this study. Appreciation is also due P. Ludtke of NIST for his helpful advice.

REFERENCES

[1] Ludtke, P. R., Slush Hydrogen Flow Facility, *NBS Report No. 9752*, 1969.

[2] Daney, D. E., Ludtke, P. R., Sindt, C. F., and Chelton, D. B., Slush Hydrogen Fluid Characterization and Instrumentation Analysis, *NBS Report No. 9701, NASA Project 91505-9150452*, 1967.

[3] Gu, Y. F., and Timmerhaus, K. D., Survey of Thermal Acoustic Oscillation, *NASP Contractor Report 1079*, 1989.

[4] Bannister, J. D., Spontaneous Pressure Oscillations in Tubes Connecting Liquid Helium Reservoirs to 300 K Environments, *Bull. Int. Inst. Refrigeration*, 127–135, 1966.

[5] Hofler, T. J., Concept for Thermoacoustic Refrigeration and a Practical Device, *Proc. of the 5th International Cryocooler Conf.*, 93–101, 1988.

[6] Rott, N., Damped and Thermally Driven Acoustic Oscillations in Wide and Narrow Tubes, *ZAMP*, **20**:230–243, 1969.

[7] Rott, N., Thermally Driven Acoustic Oscillations, Part 2: Stability Limit for Helium, *ZAMP*, **24**:54–72, 1973.

[8] Gu, Y. F., and Timmerhaus, K. D., Thermal Acoustic Oscillation in Normal Boiling Point Liquid Hydrogen Systems, *NASP Contractor Report*, 1990.

[9] Gu, Y. F., and Timmerhaus, K. D., Thermal Acoustic Oscillation in Triple Point Liquid Hydrogen Systems, *NASP Contractor Report*, 1990.

[10] Gu, Y. F., and Timmerhaus, K. D., Stability Aspects of Thermal Acoustic Oscillation in Triple Point Liquid Hydrogen System(U), *Eighth National Aerospace Plane Technology Symposium, Paper No. 77* , March, 1990.

[11] Gary, J. M., A Numerical Method for Acoustic Oscillations in Tubes, *International Journal for Numerical Methods in Fluids*, 8:81–90, 1988.

[12] Gu, Y. F., and Timmerhaus, K. D., Damping of Thermal Acoustic Oscillation in Hydrogen Systems, *NASP Contractor Report*, 1990.

[13] Haycock, R. H., Techniques for Eliminating Thermal Acoustic Oscillations in Cryogenic Instrumentation, *SPIE, Cryogenically Cooled Sensor Technology*, 245.143–148, 1980.

SIMULATION OF A NEAR-ISOTHERMAL EXPANDER

M.G. Norris, J.L. Smith, Jr., and J.A. Crunkleton

Cryogenic Engineering Laboratory
Department of Mechanical Engineering
Institute of Technology
Cambridge, Massachusetts 02139

ABSTRACT

A simulation method has been developed to predict the performance and loss distribution in reciprocating cryocooler expanders. The simulation includes heat transfer to internal surfaces, inflow pressure drop losses, inflow mixing losses, outflow pressure drop losses, outflow mixing losses, crevice flow losses, parasitic heat conduction and shuttle losses. The differential equations for mass and energy are formulated and integrated numerically. Performance is obtained from appropriate integrals over a piston motion cycle. Loss distribution is evaluated by the integration of the rate of entropy generation for each loss mechanism over the cycle. The simulation was applied to optimize the design of a near-isothermal expander providing approximately 650 watts of cooling at 77 K.

INTRODUCTION

A computer simulation model of reciprocating expanders was developed to optimize the design of a near-isothermal expander and better understand its expansion process. The simulation models both the expansion process of the gas and the heat transfer interaction with the expander surfaces. The heat transfer modeling is based on work by Lee and Kornhauser on heat transfer in reciprocating volumes.[1,2] Since heat interactions between the gas and the cylinder are important in all reciprocating devices, this simulation is generally useful.

This paper will present the equations and assumptions that form the basis of the simulation and the results of applying it to the design optimization of a near-isothermal expander. The governing equations of the simulation come from the mass and energy conservation equations applied to a control volume around the expander's working volume, along with momentum conservation equations applied to the valves and the ideal gas law. Entropy generation equations result from applying the second law to various control volumes in the expander control volume. The major assumption is perfect mixing in the expansion space. Other assumptions will be described in the body of the paper along with the inputs and solution algorithm.

The design of a liquid-nitrogen-temperature expander was optimized through parametric analysis using this simulation. The resulting design of the expander will be presented.

GOVERNING EQUATIONS

The set of differential equations that form the core of the simulation model were derived from applying the equations of energy conservation, mass conservation, mass flow rate through a valve, and heat transfer rate to the control volume shown in Figure 1. The expander control volume is the swept volume plus the dead volume not including the piston/cylinder crevice volume.

ASSUMPTIONS

The assumptions are critical to any modeling of a physical process. The validity of these assumptions varies with the process and equipment being modeled. The piston/cylinder crevice volume is included as an adiabatic fixed volume that is in pressure equilibrium with the working volume. This results in a zero enthalpy flow between the expander and the crevice over one cycle. The mass-averaged density is used to calculate the mass in the crevice volume. Two important assumptions are that the gas in the working volume is perfectly mixed and the expander surface temperatures are constant over one cycle. Except for very low temperatures the thermal capacitance of the cylinder and piston are sufficient to have negligible temperature swings during a cycle. The flow through the valves is assumed to be incompressible. This assumption for valve flow is good over the majority of the cycle. Only during the intake and exhaust valve opening, which last less than 0.02 seconds, does the gas behave as a compressible fluid. Ignoring this loss has a small effect on the results of the simulation.

ENERGY AND MASS BALANCE EQUATIONS

The energy equation applied to the control volume in Figure 1 is

$$E' = (M\, c_v\, T)' = Q' - P\, V'(t) + M'_I\ {}_{\rho} T_I - M'_O\, c_p\, T - M'_C\, c_p\, T^*, \qquad (1)$$

where T^* is T for flow into the crevice and is T_{CO} for flow out of the crevice. A list of symbols appears at the end of this paper.

The mass conservation equation applied to the control volume is

$$M' = M'_I - M'_O - M'_C. \qquad (2)$$

Assuming the pressure equilibrium between the crevice and the working volume, an ideal gas and that V_C is constant, then

$$M'_C = M' \frac{(T\, V_C)}{(T_{CR}\, V(t))} + \frac{M\, V_C}{T_{CR}\, V^2(t)} (V(t)\, T' - T\, V'(t)). \qquad (3)$$

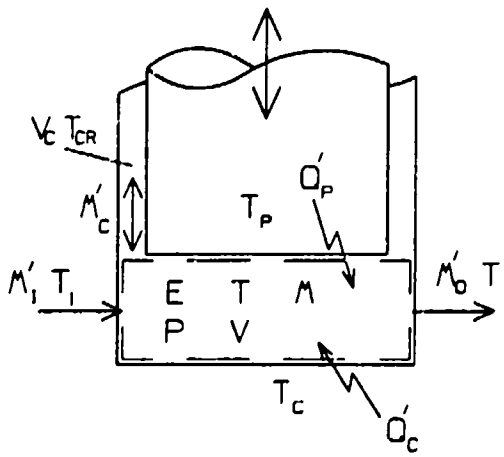

Fig. 1. Expander control volumes

The mass flow rates for an incompressible fluid across the inlet and exhaust valves are

$$M'_I = A_I(t)\left[\frac{2\rho(P_I - P)}{Cd}\right]^{1/2} \text{ and } M'_O = A_O(t)\left[\frac{2\rho(P - P_O)}{Cd}\right]^{1/2}. \quad (4)$$

The valve flow area is a defined function of time that effectively opens and closes the valve in the set of differential equation.

The rate of heat transfer into the gas (Q') is defined as

$$Q' = \frac{Nu\ k_g}{D_h}\left(A_C(T_C - T) + A_P(T_P - T)\right) \quad (5)$$

where the subscripts, C and P refer to the cylinder and the piston. The Nusselt number during expansion and recompression is calculated from Lee's equation.[1] The Nusselt number is approximately 12 for near-isothermal expanders which are characterized by an average Peclet number of order 10 or less. The Peclet number is defined as

$$Pe_\omega = \frac{\omega(D_h)^2}{4\ \alpha}.$$

During intake and exhaust an appropriate Nusselt number needs to be chosen based on the geometry of the expander surfaces.

The inlet temperature, (T_I), is the mass-averaged exhaust temperature (T_X) plus the heat exchanger temperature difference (ΔT_{HE}). The temperature of the piston crown (T_P) is determined by an energy balance on the piston crown.

ENTROPY GENERATION EQUATIONS

Specific loss mechanisms can be quantified in the expansion process by sub-dividing the expander control volume into several pieces as shown in Figure 2. These loss mechanisms can be grouped into mixing losses and heat transfer losses. The mixing losses are associated with the intake process (Control Volume C), the exhaust process (Control Volume D) and gas flow into and out of the crevice volumes (Control Volumes A and B). The heat transfer losses are associated with the heat transfer to the helium in the working volume (Control Volumes E and F) and the conduction and shuttle heat leaks (Control Volumes G and H). The control volumes A,B,C,D,E,and F are infinitesimally thin to evaluate the change in the entropy due

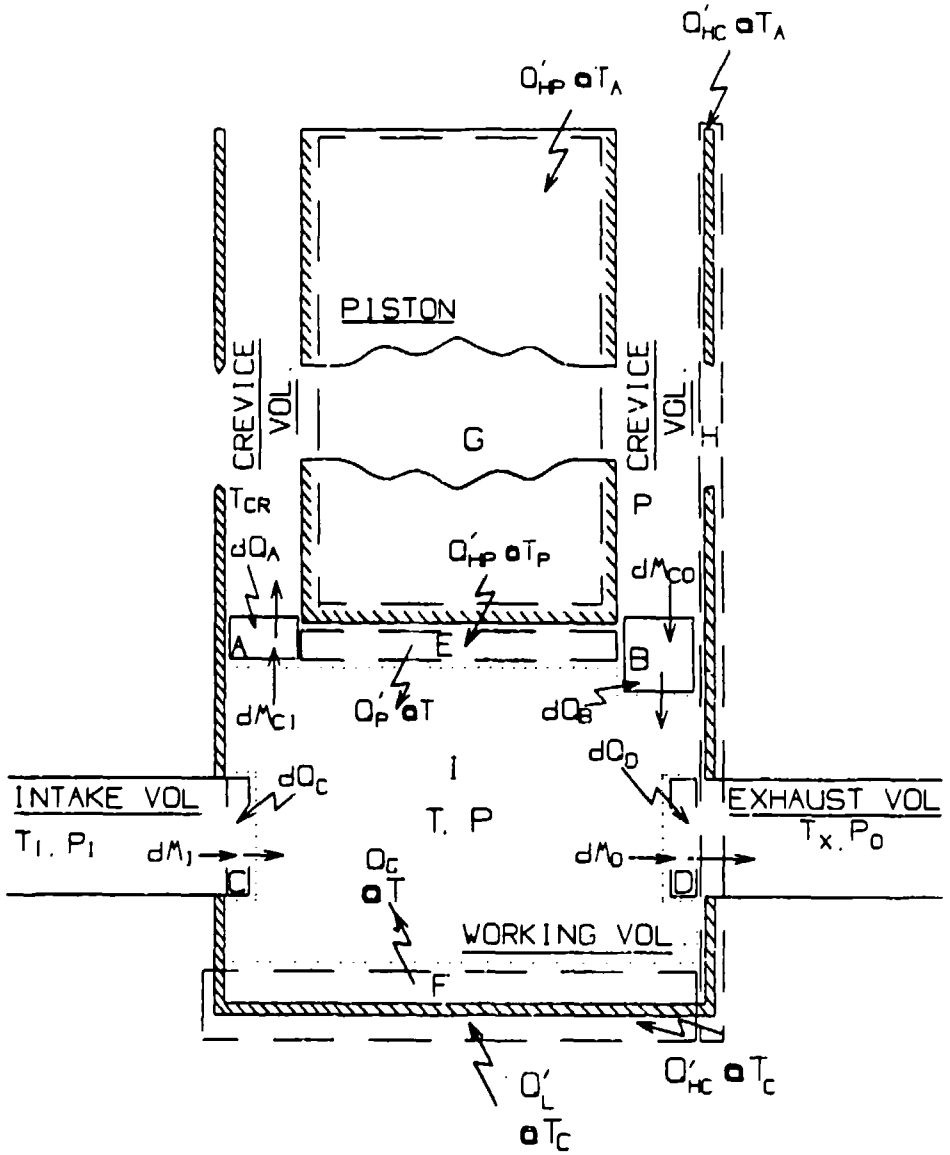

Fig. 2. Sub-divided control volumes in expander

to mass and energy crossing the boundaries of the expander. Control Volume I contains the working volume gas, which is at a uniform but unsteady temperature (T) and pressure (P).

HEAT TRANSFER LOSSES

The generated entropy associated with heat transfer from the piston crown and cylinder head is evaluated in the control volumes E and F. One side of each control volume is at the constant crown or head temperature and the other is the time varying working volume temperature. On average, Q'_C is equal to $Q'_{HC} + Q'_L$ and Q'_P is equal to Q'_{HP}. The rate of entropy generation due to heat transfer from the crown and the head to the gas is

$$S'_{heat\,trans} = \frac{1}{\tau} \oint \frac{Q'}{T}\, dt - \frac{Q'_{HC} + Q'_L}{T_C} - \frac{Q'_{HP}}{T_P}. \tag{6}$$

INTAKE AND EXHAUST MIXING LOSSES

The intake and exhaust mixing losses are evaluated in the control volumes (C and D) at the exit of the intake valve and the entrance of the exhaust valve. The generated entropy is the change in the entropy of the gas from entering to exiting the control volume minus the entropy input associated with heat transfer. For example, during the intake process, gas enters the control volume C at T_I and exits at the time varying expander temperature T. The gas experiences a heat interaction with the working volume to reach T. In addition to the temperature difference, a pressure difference exists across the control volumes. The equation for the average entropy generation rate due to mixing losses during intake is

$$S'_{intake} = \frac{1}{\tau} \oint \left[c_p \left(\ln\left(\frac{T}{T_I}\right) - \frac{T - T_I}{T} \right) - R \ln\left(\frac{P}{P_I}\right) \right] M'_I\, dt. \tag{7}$$

The equation describing the entropy generation for the exhaust control volume (D) is similar to that for the intake control volume except for the net heat transfer term. The cyclic integral of the heat transfer term ($\delta Q_D = \oint (T - T_X)\, dt$) is zero, because T_X is the mass-averaged value of the working volume temperature during the exhaust process. The average entropy generation rate due to mixing losses during exhaust is

$$S'_{exhaust} = \frac{1}{\tau} \oint \left(c_p \ln\left(\frac{T_X}{T}\right) - R \ln\left(\frac{P_O}{P}\right) \right) M'_O\, dt. \tag{8}$$

CREVICE MIXING LOSSES

The mixing losses are evaluated separately for flow into and out of the crevice volume. The control volumes, A and B, are at the entrance to the crevice volume. For flow into the crevice, gas enters the control volume at the time varying work volume temperature, T, and exits at the constant crevice temperature T_{CO}. Flow out of the crevice enters control volume B at T_{CO} and exits at T. The change in entropy is due only to the temperature change, as the pressures in the crevice and working volumes are assumed equal in this analysis.

Although control volumes A and B are treated as completely separate, they occupy the same space. The differential mass terms for flow into the crevice, dM_{CI}, and flow out of the crevice, dM_{CO}, are either positive or zero, so only one of the control volumes is considered at a time. Gas flows into the control volume during the blow-in portion of the intake and during recompression. The gas flows out of the crevice volume during expansion and the blow-down portion of the exhaust.

The entropy generation due to flow into the crevice is evaluated in control volume A.

$$dS_A = c_p \left(\ln\left(\frac{T_{CO}}{T}\right) - \frac{(T_{CO} - T)}{T_{CO}} \right) \delta M_{CI}. \tag{9}$$

Since T_{CO} is the mass-averaged temperature of the gas that flows into the crevice during one cycle, the cyclic integral of dS_A is zero.

The energy and entropy equations are similar for flow into the working volume from the crevice volume except that T_{CO} is not equal to the average of T during the flow out of the crevice.

$$dS_B = c_p \left(\ln\left(\frac{T}{T_{CO}}\right) - \frac{(T - T_{CO})}{T} \right) \delta M_{CO}. \tag{10}$$

Integrating equation 10 over one cycle and dividing by the cycle period (τ) gives the average rate of entropy generation for the crevice mixing losses.

$$S'_{crevice} = \frac{c_p}{\tau} \oint \left(\ln\left(\frac{T}{T_{CO}}\right) - \frac{T - T_{CO}}{T} \right) M'_{CO}\, dt \tag{11}$$

HEAT LEAK LOSSES

This analysis of the expander calculated a conduction heat leak down the piston, a separate heat leak down the cylinder walls that included the shuttle heat leak.[3] These heat leaks were considered to enter the expander at ambient temperature. The piston heat leak enters the working volume at the piston crown temperature, T_P, while the cylinder leak enters at the cylinder head temperature, T_C. The piston control volume, G, contains the entire piston. The generated entropy is the

difference between the entropy that enters at T_A and that which leaves at T_P and T_C. The cylinder control volume, H, contains the cylinder walls beginning at the warm flange and ending where the cylinder walls join cylinder head. The equation for generated entropy in G and H due to heat leaks is

$$S'_{heat\ leak} = \frac{Q'_{HP}(T_A - T_P)}{T_A T_P} + \frac{Q'_{HC}(T_A - T_C)}{T_A T_C}. \tag{12}$$

It can be shown that the sum of these equations equals the generated entropy equation for the complete expander. An entropy balance of I, which is zero over one cycle, can be added to the above equations to cancel the integral values and thus show algebraically that they sum to equal the expander equation which is in terms of average flows.

INPUTS

To reduce the number of inputs, the simulation was non-dimensionalized. The thermal inputs are the pressure ratio (P_I/P_O), the non-dimensional temperature difference in the pre-cooling heat exchanger ($\Delta T_{HE}/T_C$), the ambient temperature (T_A/T_C), and the specific heat ratio of the working gas. The non-dimensional speed of the piston is defined as $\tau^* = (\tau\,\alpha)/B^2$. The valve timing is the cross-sectional flow area divided by the valve maximum flow area ($A_I(t)/A_{IM}$ and $A_O(t)/A_{OM}$). Figure 3 plots a typical valve timing for the valves and the typical sinusoidal variation of the volume. ($V(t)/B^3$). The various expander dimensions such as the stroke length, fin height, piston/cylinder crevice gap size, piston length, etc, are non-dimensionalized by the cylinder bore.

SOLUTION ALGORITHM

The Simnon simulation software integrates the set of differential equations derived from the governing equations over one piston cycle for each iteration. The exhaust temperature, the crevice outflow temperature, the initial pressure, temperature and mass are updated each iteration. The algorithm iterates on the piston crown temperature, searching for the temperature that will satisfy the piston-energy-balance. Convergence is reached when the energy change of the piston crown during one cycle is less than 1% of the piston heat leak per cycle.

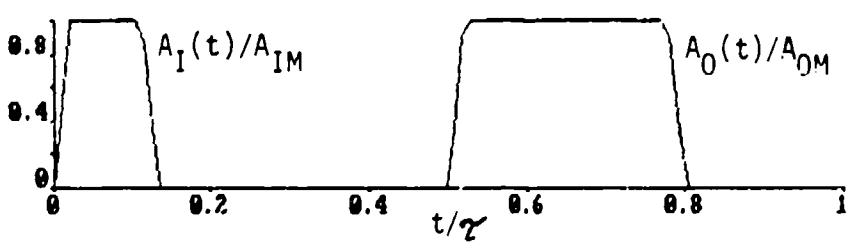

Fig. 3. Simulation valve timing input

NEAR-ISOTHERMAL EXPANDER

The computer simulation was used to optimize the design of an experimental near-isothermal expander. The expander is the subject of an experiment to demonstrate the feasibility of the expander for a cryocooler operating at liquid-nitrogen temperature. The simulation will also provide a better understanding of the expansion process in this new isothermal device, where the heat transfer from the gas to the expander is large.

Figure 4 presents an assembly drawing of the expander including a nitrogen recondenser that supplies the load, actuated valves that control the flow and a

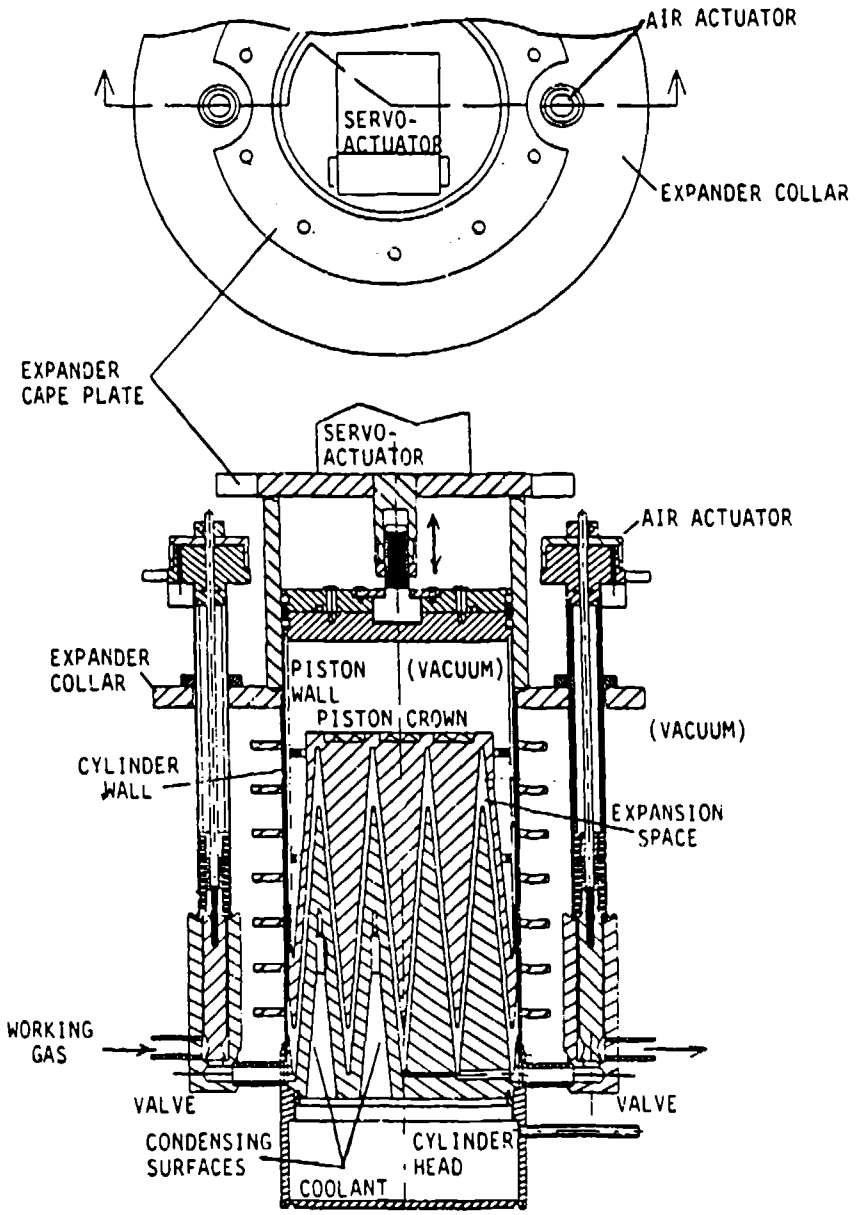

Fig. 4. Expander assembly drawing

hydraulic servo-actuator to control the motion of the expander. Tapered conical fins, machined from brass, provide the necessary surface area and conductivity to the load to assure good isothermal performance. The nitrogen in the recondenser is reboiled to maintain the liquid at a constant level. The piston is sealed at the warm end. The experiment is scaled to produce approximately 650 watts of cooling at 77 K.

The expander is the critical component of a proposed new cryocooler configuration (Figure 5). The proposed cyrocooler consists of an ambient-temperature, high-pressure-ratio compressor, a counter-flow heat exchanger, surge volumes and the near-isothermal expander. The working gas is helium which retains ideal gas properties down below the liquid-nitrogen operating temperature.

This new cooler promises efficiency, reliability and manufacturability. The high-pressure ratio requires a small gas flow rate which allows a small heat exchanger employing reasonable temperature differences for heat transfer. The near-isothermal expansion avoids large temperature differences between the expanding gas and the load. The near-isothermal expander requires low speed and a short stroke. This allows a long-life mechanism with low surface velocities. Contacting gas seals may be designed with adequate life. However, the slow speed and small hydraulic diameter of the isothermal expander requires a larger diameter expander. The extended surfaces on the piston crown and cylinder head serve to reduce the size of the expander.

OPTIMIZATION OF EXPANDER DIMENSIONS

Many of the dimensions and operating conditions of the expander such as the pressure levels and the minimum stroke distance were fixed by the available equipment or the limits of machining. Reasonable values were selected for other inputs, such as ΔT_{HE} as they were unknown. A Nusselt number of 8 is assumed for the intake and exhaust processes as they resemble flow between parallel plates.

Several of the expander's dimensions were optimized including fin size, blow-down pressure, recompression pressure, speed and and stroke length, by a series of parametric computer simulations that varied the operating conditions and critical

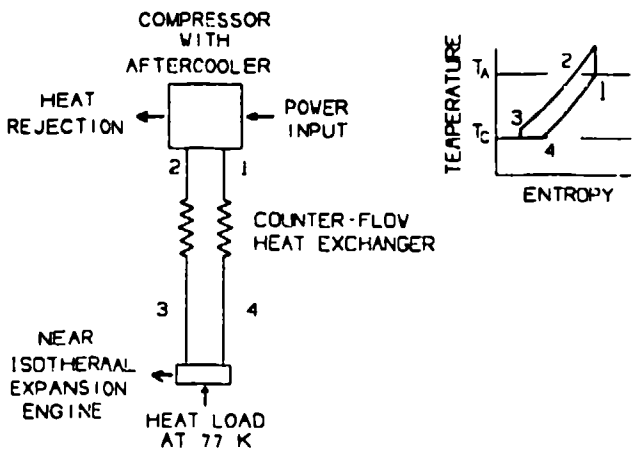

Fig. 5. Cryocooler Configuration

expander dimensions. The resulting design dimensions and operating parameters are

$$Bore = 19.1\,\text{cm}, \quad Fin\,Angle = 5°, \quad Fin\,Height = 25.4\,\text{cm},$$

$$Piston\,Length = 27.9\,\text{cm}, \quad A_{IM} = A_{OM} = 1.3\,\text{cm}^2 \quad Stroke = 2.4\,\text{cm}, \quad \tau = 0.49\,\text{s}.$$

$$P_R = 8.25\,\text{atm}, \quad P_B = 3.3\,\text{atm}, \quad P_I = 16.5\,\text{atm}, \quad P_O = 1.65\,\text{atm},$$

The bore and the displaced volume rate of the expander are limited by the servo-actuator. The stroke length and cycle period, which determine the volume rate, were selected to maximize the cooling capacity of the expander. The range of considered stroke and period had little effect on the efficiency. The valve timing was selected so that the recompression pressure P_R and the blow-down pressure P_B maximized cooling capacity at reasonable efficiencies.

The effect of the fin angles, from 2.5° to 10°, on the performance of the expander is plotted in Figure 6. The expander efficiency is the predicted cooling over the maximum cooling if the gas had been isothermally and reversibly expanded without heat leaks. The $Cooling/Cycle$ is the predicted cooling normalized by $P_M\,B^3$ where P_M is the mean pressure. The $Sgen/Cycle$ is entropy generation per cycle normalized by $P_M\,B^3/T_C$.

A smaller fin angle results in more surface area and thus a more isothermal expander. The expander efficiency decreases and the capacity increases at higher fin angles. The $S'_{heattrans}$ increases quickly with the fin angle and soon dominates the other losses which also increase with the fin angle. A 5° fin angle was chosen because it is a good trade-off between cooling rate and efficiency. At angles smaller than 5°, the capacity drops off and the efficiency increases only slightly. A 5° fin angle also seems to be about the smallest angle that could be reasonably machined.

The computer simulation predicts that this experimental expander will achieve good efficiency and good capacity. The predicted parameters for the expander are:

Expander Isothermal Efficiency: 60%

Expander Cooling Rate: 640 watts.

The distribution of generated entropy in the experimental expander is predicted to be 45% due to heat transfer to the helium gas, 27% due to exhaust, 20% due to intake, 6% due to heat leaks and 2% due to crevice flows.

SUMMARY AND CONCLUSIONS

A computer simulation of valved reciprocating expanders has been developed that models the flow, expansion and heat transfer processes. The simulation includes entropy generation equations that quantify the various loss mechanisms in an expander. The design of a near-isothermal expander was optimized through parametric studies using the computer simulation model.

This simulation is a first step in applying Lee's and Kornhauser's work on heat transfer in reciprocating volumes to all valved reciprocating devices. The next step is modifying the model to accommodate high Peclet number devices, where heat

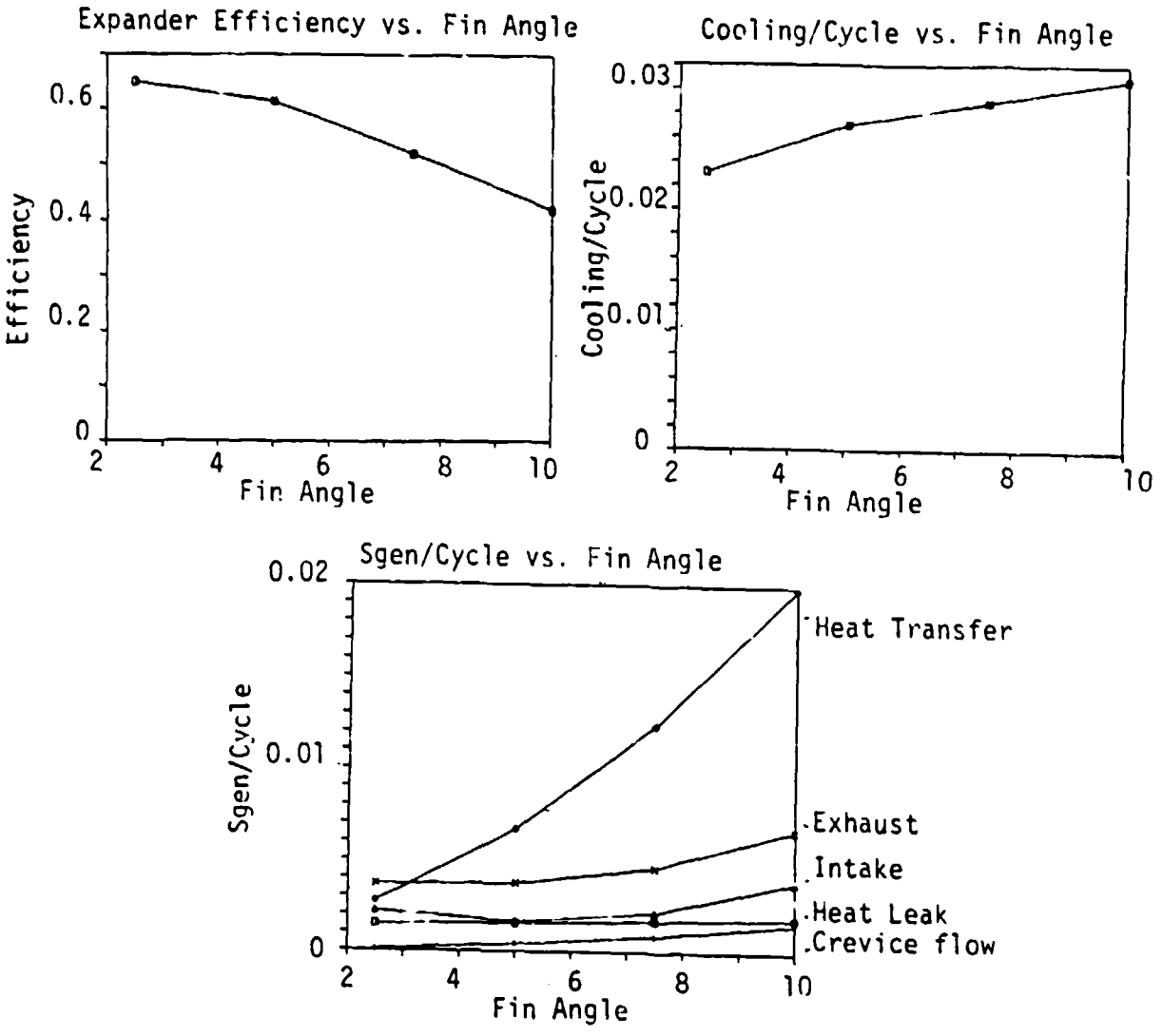

Fig. 6. Performance vs. Fin Angle

transfer is both a function of ΔT and dT/dt. The entropy generation equations will be unchanged.

ACKNOWLEDGEMENTS

This work is supported by the International Business Machines Corp. This publication is based on a thesis to be submitted in February 1991 by M.G. Norris in partial fulfillment of requirements for the degree of Master of Science in Mechanical Engineering at the Massachusetts Institute of Technology.

REFERENCES

1. K. Lee, "A Simplistic Model of Cyclic Heat Transfer Phenomena in Closed Spaces," Proceedings of the 18^{th} Intersociety Energy Conversion Engineering Conference, (1983), p. 720-723.

2. A.A. Kornhauser,"Gas-Wall Heat Transfer During Compression and Expansion", Sc.D. Thesis, MIT, (1989).

3. F.J. Zimmerman, and R.C. Longsworth, "Shuttle Heat Transfer", Advances in Cryogenic Engineering, Vol 16, Plenum Press, (1971) p.342-351.

LIST OF SYMBOLS

The prime ($'$) indicates a derivative with respect to time that may vary with time. The δ refers to a differential amount of the valve.

B	Bore of cylinder
E'	Rate of change of energy in the expander
M'	Rate of change of mass in the expander
Nu	Nusselt number
P	Expander pressure
Q'	Total Heat transfer rate to the expander
T	Expander gas temperature
$V(t)$	Expander volume as an input function of time

Subscripted Variables

A_C	Cylinder head and exposed walls area
$A_I(t)$	Inlet valve cross-sectional area, input function of time
$A_O(t)$	Outlet valve cross-sectional area, input function of time
A_{IM}	Maximum inlet valve cross-sectional area
A_{OM}	Maximum outlet valve cross-sectional area
A_P	Piston head area
C_d	Flow resitriction coefficient
c_p	Specific heat at constant pressure
c_v	Specific heat at constant volume
D_h	Hydraulic diameter = $4\ V(t)/(A_C + A_P)$
H	Height of the fins
h	Heat transfer coefficient
k_g	Thermal conductivity of the gas
L_P	Piston length
L_S	Stroke length
M'_C	Rate of change of the piston/cylinder crevice mass

M'_{CI}	Rate of mass flow into the piston/cylinder crevice
M'_{CO}	Rate of mass flow out of the piston/cylinder crevice
M'_I	Inlet valve mass flow rate
M'_O	Outlet valve mass flow rate
P_B	Blow-down pressure
P_I	Expander inlet pressure
P_O	Expander low pressure
P_R	Recompression pressure
Q'_{HC}	Heat leak rate to the expander through cylinder walls
Q'_{HP}	Heat leak rate to the expander through piston walls
Q'_L	Heat transfer rate from the load to the expander
T_A	Ambient temperature
T_C	Cylinder head temperature
T_{CO}	Mass averaged temperature of the gas that flows into the piston/cylinder crevice volume
T_{CR}	Temperature of the piston/cylinder crevice gas
ΔT_{HE}	Temperature difference across the heat exchanger
T_I	Expander inlet temperature
T_P	Piston crown temperature
T_X	Mass averaged temperature of the exhaust
V_C	Piston/cylinder crevice volume

Greek Symbols

α	Thermal diffusivity
ρ	Density
τ	Expander cycle period
θ	Slope of the fins

DEVELOPMENT OF A He II GAP HEAT SWITCH FOR A 2K TO 10K ADR

Ali Kashani and Ben P. M. Helvensteijn
Sterling Federal Systems
Palo Alto, CA 94303

Randall A. Wilcox
Trans-Bay Electronics
Richmond, CA 94804

ABSTRACT

A 2K He II gap heat switch has been developed as a component of a 2-10K ADR. The heat switch consists of He II channels inserted into axial holes in the paramagnetic pill (GGG) maintaining a small gap with the GGG. To make the thermal contact between the GGG and the 2K He II channels the gap is filled with helium gas condensing at 2K. The flow of helium in and out of the gap is accomplished with an activated carbon adsorption pump. A prototype heat switch, with a gap size of 0.009cm, has been tested. The on conductance to off conductance ratio for the prototype is on the order of 5000. In the on mode and with a 14.3mW of power on the heat switch the temperature gradient across the switch is 35mK. In the off mode an 8K temperature gradient across the switch corresponds to a 0.25mW heat leak. It is concluded that this heat switch design meets the conductance requirements of the ADR.

INTRODUCTION

An adiabatic demagnetization refrigerator (ADR) is currently under development at NASA-Ames Research Center to operate between 2K and 10K and is to provide 0.1W of cooling at 2K.[1] The ADR is intended to be used in cooling of the Large Deployable Reflector (LDR). The LDR is a space-borne array of reflectors for space infrared astronomy in the next century. The principle behind an ADR is the magnetic ordering of a paramagnetic material at low temperatures and/or high magnetic fields. The magnetic ordering of the paramagnet which occurs when magnetized isothermally causes a drop in its entropy. During this process heat is exchanged with and rejected to a 10K heat sink. The reverse process, isothermal demagnetization at 2K, results in an increase in the entropy of the material. The heat required to increase the entropy is supplied by the load (e.g., the LDR).

The magnetic material selected for operating in the 2-10K temperature range is Gadolinium Gallium Garnet (GGG). During the magnetic cycling of the GGG pill it is necessary to make and break the thermal link from the GGG to the 2K load and the 10K heat sink. Contact to the cold end is made by means of a He II heat switch. At the hot end, a helium gas heat switch is employed. The efficiency of the refrigeration cycle is greatly affected by the performances of the heat switches. The on and off conductances and the switching times of the heat switches, in large, determine the efficiency of the refrigeration cycle.

The present paper focuses on the 2K He II heat switch. First, a description of the design of the heat switch is given. Next, the problems faced in implementing this design in the actual refrigerator is discussed. Finally, some of the test results performed on a 2K heat switch prototype are presented.

2K He II HEAT SWITCH

A unique heat switch concept has been developed for the 2K heat switch. The design incorporates a He II gap heat switch taking advantage of the high thermal conductivity of He II. The switch operates such that it conducts heat, from the load to the GGG, when the gap is filled with He II and insulates when it is under vacuum. Because of the high heat transfer rate from the load to the GGG (0.1W) the more conventional helium gas gap heat switch concept is not practical. This method would require a very large heat transfer surface area due to the low thermal conductivity of helium gas at 2K.

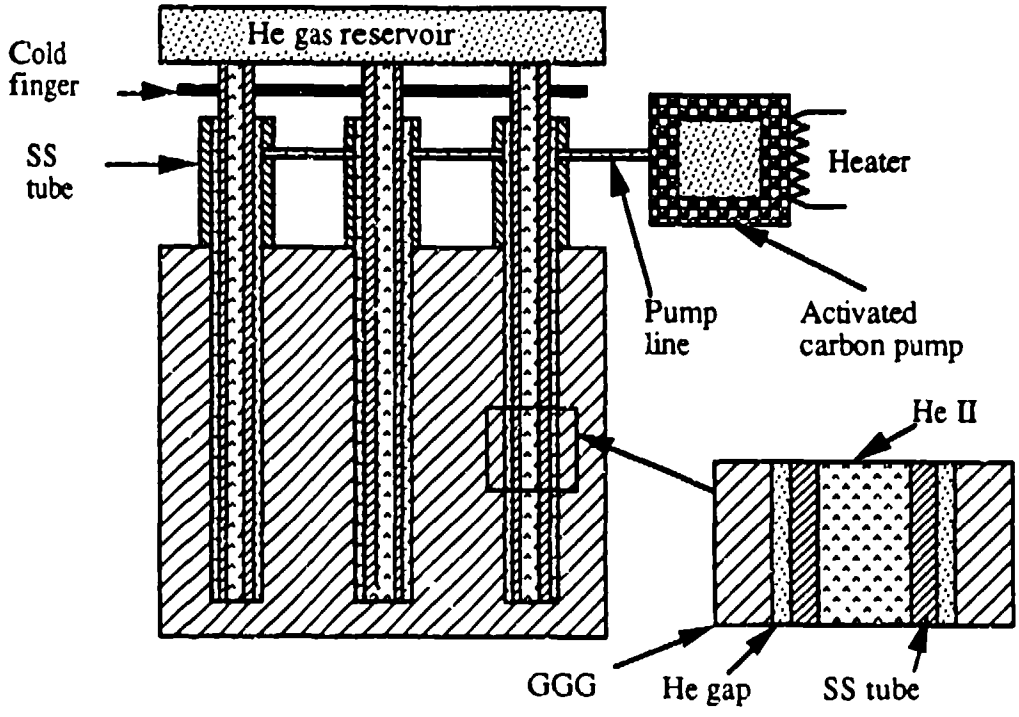

Fig. 1. Schematic of the He II heat switch.

The He II heat switch is made internal to the GGG pill (Fig. 1). In order to limit temperature differences in the GGG this arrangement is vital since the 2K thermal conductivity of GGG is quite low. The thermal conductivity of GGG decreases from 200W/m-K at 10K to only 3W/m-K at 2K.[2] By distributing the heat switch throughout the pill, the thermal conduction path is shortened and the temperature differences in the GGG are reduced approximately by a factor of three. Seven blind holes, 0.23cm in diameter, will be drilled through the GGG pill in a hexagonal pattern. The depth of the holes will be 11cm. A thin-wall stainless steel tube, pluged at one end, will be placed inside each hole. The tubes will contain He II at 2K throughout the ADR cycle and will provide the major thermal link between the 2K heat source and the GGG pill. A He II gap heat switch surrounds each stainless steel tube with the gap width being 0.003cm.

The two stage thermal contact, consisting of He II tubes and gaps, between the load and the GGG pill is a necessary compromise between thermal conduction in the on mode and the latent heat. In order to keep the temperature drop in the He II tubes low, the total cross section of the He II column in the GGG pill needs to exceed $0.15cm^2$. The thermal conduction taking place over a distance of 20cm brings the liquid helium volume up to $3cm^3$. If all this liquid would be condensed, the latent heat load on the GGG pill would correspond to more than half of the available cooling. This is greatly reduced by dividing the thermal conduction path into permanent He II tubes and the heat switches, i.e., He II gaps.

In order to minimize the heat leak from the GGG to the He II filled stainless steel tubes in the off mode, the tubes will be made to protrude over 5cm out of the holes in the GGG. A 5 cm-long thin-wall SS support tube having an internal diameter of 0.23cm will be placed over each of the He II tubes, bonded to the GGG at one end and welded to the He II tube at the other end. This tube will be the main conduction path between the GGG pill and the He II tube in the off mode. The increased thermal conduction path between the tubes and the GGG reduces the heat leak to the He II tubes, substantially. The estimated heat leak from the GGG when at 10K, to the 2K He II tubes is on the order of 2mW.

Before the 2K refrigeration takes place, the He II gap heat switch is thermally shorted condensing helium gas into the gap. After the refrigeration step, the thermal contact is broken by removal of the liquid in the gap. Both the supply and removal of the helium is accomplished by means of an activated carbon pump (ACP). When cooled down the ACP adsorbs helium; when heated it desorbs the gas.

A He II gap heat switch concept has been recently tested.[3] In the tests the ACP is cooled down by means of a thin copper wire connected to an external cold reservoir. The cooldown rate is low because of the small size of the copper wire resulting in a long switching off time. The wire is kept thin to limit the heat leak to the external reservoir in the on mode in which the ACP is heated. The rate of warm up is largely determined by the ACP heater power. The on switching time, in these tests, has been under one minute.

In the model proposed here, the copper connection to the external 10K reservoir is replaced by a helium gas heat switch. To this purpose, a small carbon pump (CP) is placed in the vacuum space surrounding the ACP and is allowed to adsorb a small quantity of helium. When the CP is hot, it desorbes the helium gas which thermally shorts the ACP to the cold reservoir. The ACP is thermally isolated by vacuum when the CP is cold. The on/off thermal conduction ratio of the helium gas switch guarantees rapid switching of the ACP between adsorption and desorption.

The 2K heat switch including its ACP is contructed as a closed system containing the required amount of helium at room temperature. The system is charged with helium gas at 300K. The ACP consists of a cylindrical reservoir with the activated carbon glued to its inner surface. The volume of the reservoir is significantly larger than that needed to enclose

the activated carbon in order to reduce the initial fill pressure. To optimize the pump parameters according to the gap size a computer program has been generated which can be used to find the activated carbon mass, the reservoir volume and the energy required to liberate the gas when the 2K heat switch is turned on. The program is employed to optimize the pump size by varying different parameters such as the initial gas pressure and/or the activated carbon temperature during desorption. The adsorption temperature of the pump is assumed to be 10K, i.e., the cryocooler temperature. The model is based on a helium mass balance for the helium contained in the reservoir, the ACP and the gap.

The He II filled stainless steel tubes are connected to a helium gas reservoir. Once the GGG pill becomes cold the gas condenses into the tubes. The gas reservoir is added so that the initial pressure at room temperature at which the tubes are filled, need not be very high. For an initial helium gas pressure of 10atm the volume of the gas reservoir has to be about $500cm^3$. The gas in the reservoir is first cooled down to 10K by the cryocooler and is then cooled to 2K and condensed in the tubes requiring about 50J of cooling by the GGG pill.

The total temperature drop in the different parts of the 2K heat switch is estimated to be 27mK. This is the temperature drop between the 2K heat load and the GGG surface at the He II gap. The different contributions to this temperature drop are listed below:

- The temperature drop over the He II filled tube: 4mK.

- The temperature drop due to Kapitza resistance between He II and the inside wall of the SS tube: 7mK.

- The temperature drop in the 0.25mm-thick-wall SS tube: 6mK.

- The temperature drop due to Kapitza resistance between He II and the outer wall of the SS tube: 5mK.

- The temperature drop due to Kapitza resistance between He II and the GGG: 5mK.

In the above calculations a Kapitza conductance of $4W/m^2$-K has been assumed between the He II and the solid materials.

HEAT SWITCH IMPLEMENTATION

In incorporating the He II heat switch, described above, into the ADR some technical problems are encountered. The foremost problem is in making the hermetic seals between the stainless steel support tubes and the GGG. Two possible approaches to this problem have been conceived. The first approach involves bonding the SS tubes to the GGG by means of an epoxy. This approach has proven to be nontrivial, since SS contracts more than GGG when cooled down to 2K. To overcome this problem a titanium insert could be epoxied to the GGG pill and then welded to the stainless steel tube. Titanium has the closest thermal contraction of any metal to that of the GGG. Welding titanium to stianless steel poses another problem. Laser welds between thin-wall stainless steel and titanium tubes have been performed and shown to be very brittle. A possible remedy to this problem would be to use a buffer material such as vanadium between the SS and the titanium. Laser welding of titanium-vanadium-SS joints are currently being performed to test such a possibility.

The other approach to sealing the SS support tubes to the GGG would be in metalizing the GGG and welding the SS tubes to the metailized GGG. As a first test of this technique a sample GGG piece was sputtered with gold. The bond between the deposited gold and the GGG was very weak, rendering gold unsuitable for this purpose. Titanium or nickel are

two other possible candidates for metallizing the GGG which will be tested. An alternative to direct sputtering of a metalic layer onto the GGG would be to deposit a layer of a material such safire onto GGG and sputter a metalic layer over the layer of safire. Depositing GGG with safire has been performed successfully in the past.[4]

Another problem in assembling the heat switch is centering the SS tubes when inserted into the holes in the GGG. This can be accomplished by placing some small-diameter glass beads inside the gap to prevent the SS tubes from direct contact with the GGG. This technique has been used in building a prototype 2K heat switch.

A different problem has to do with acquiring the optimum activated carbon material for the ACP, since the switching times of the heat switch are directly related to the adsorption quality of the carbon. There is very little data in the literature on the adsorption of helium by the activated carbons available commercially. Thus, an effort has been undertaken to test the helium adsorption of various activated carbons, presently available.[5]

HEAT SWITCH PROTOTYPE

To test the on and off conductances of the heat switch design described above, a prototype of such a system has been built and recently tested. A schematic of this prototype heat switch is shown in Fig. 2. The prototype is comprised of an 11.25cm long brass cylinder (load), representing the GGG, with a 10.6cm-deep blind hole drilled through its center. The hole is 0.23cm in diameter. A 0.21cm-OD SS tube (He II tube) pluged at one end, is inserted into the hole. The gap between the outer surface of the tube and the inner surface of the hole is maintained by placing a small number of glass beads along the length of the tube. The thermal link between the He II tube and the brass load is made by a 0.23cm-ID SS tube (support tube) which is 5cm long. The support tube is soldered to the brass load at one end and to the He II tube at the other end.

An activated carbon pump (ACP) is connected to the He II gap via a SS capillary tube. The activated carbon used in the ACP is courtesy of Barnebey-Cheney (type PE). Because the adsorption characteristics of this carbon is not known its amount required for the testing of the heat switch prototype was estimated based on the available data on other activated carbons.[6] Based on this, the volume of the ACP is made to be $14cm^3$ and the mass of the activated carbon glued to its inner surface is 1g. The ACP is initially filled with gaseous helium to 5atm pressure at room temperature. A thermal link between the ACP and the bath was made by a copper rod to conduct the heat of desorption.

Three 56-Ohm Allen-Bradley carbon resistance thermometers were glued at different locations along the heat switch. The first thermometer is placed on the brass load near its joint with the SS support tube. The second one is placed on the SS support tube below the pressure port, i.e., where the capillary fill tube is connected to the gap. The third thermometer is located where the He II tube and the SS support tube are soldered together. A similar thermometer is also mounted on the ACP for monitoring its temperature. Manganin-wire-heaters are wound around the brass load and the ACP to control their temperatures. The heat switch assembly is placed inside a vacuum can. The He II tube is open to the He II bath through a hole in the top flange of the vacuum can. This allows the inner tube to be filled with He II and remain at the bath temperature during the tests.

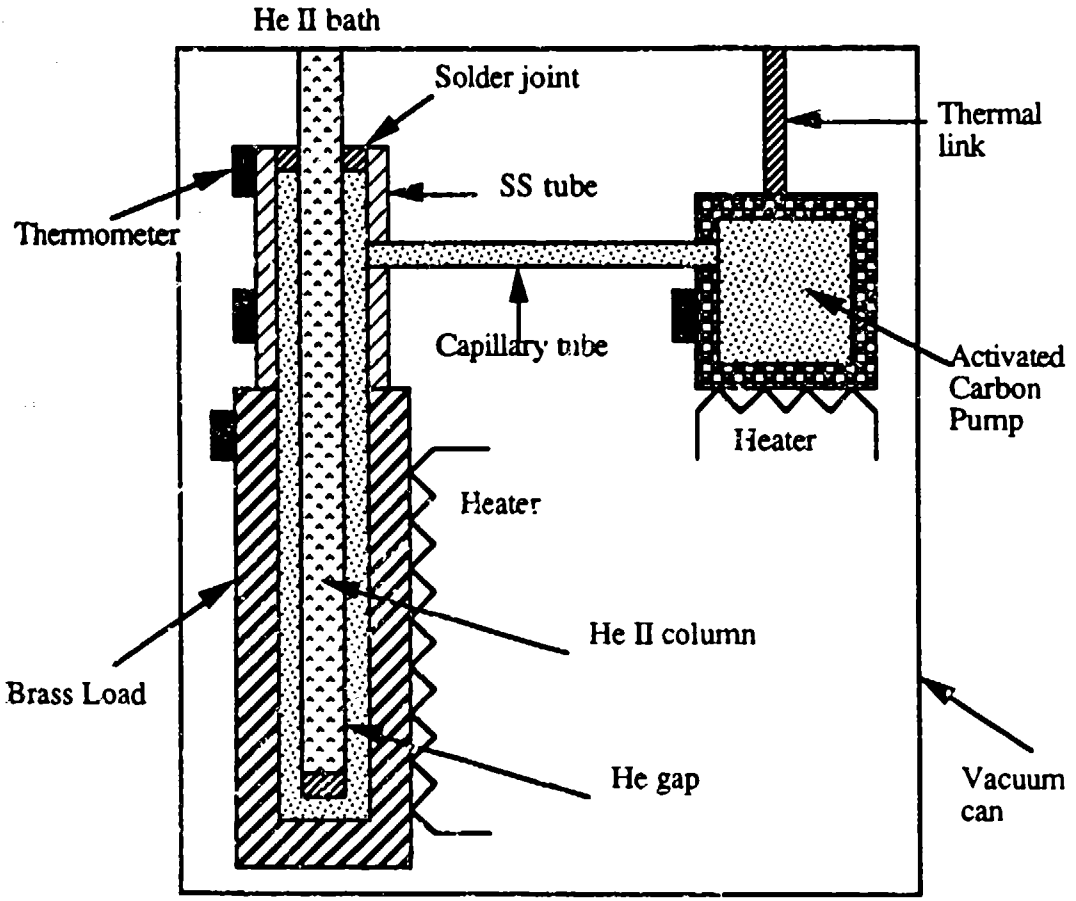

Fig. 2. Schematic of the He II heat switch prototype

TEST RESULTS

The heat switch prototype is tested both in the off and the on modes. To obtain the off conductance it is first tested without any helium gas present in the switch at 2K. The off conductance is obtained for different load heater powers while its temperature is monitored. The heater power on the load is increased until the load thermometer is just above 10K. This provides a measure of the heat leak rate form the 10K-GGG to the He II tubes in the off mode. The off conductance measured in this test is quite close to the conduction of the stainless steel tube in this temperature range. This is an indication that there is no significant thermal contact between the load and the He II tube, except through the SS support tube.

Next, the switch is charged to 5 atm and tested for its on conductance at 2K. The switch conductance in the on mode, at a given load power, is obtained after the ACP is turned on by being heated. For a given load power the temperature of the load decreases as the temperature of the ACP is increased due to more helium gas being condensed in the gap. At a certain ACP temperature and for a set load power a sharp drop is observed in the temperature of the load. As an example, when 14.3 mW is applied to the load, its

temperature decreases from 2.16K to 2.05K when the ACP temperature is about 24K. At this time the load thermometer and the middle thermometer on the heat switch indicate the same temperature value. This is an indication that the switch is full. Further increase in the temperature of the ACP raises the load temperature due to thermal conduction through the helium gas in the capillary tube.

The on and off conductances of the heat switch are plotted in Fig. 3. The on to off conductance ratio at the same load power (0.25mW) is nearly 5000. In the on mode when there is 14.3mW on the load the temperature difference across the heat switch is about 35mK. This load power represents the heat flow rate through a single heat switch as required by the ADR. The temperature difference obtained from this test is close to the calculated temperature drop of 27mK.

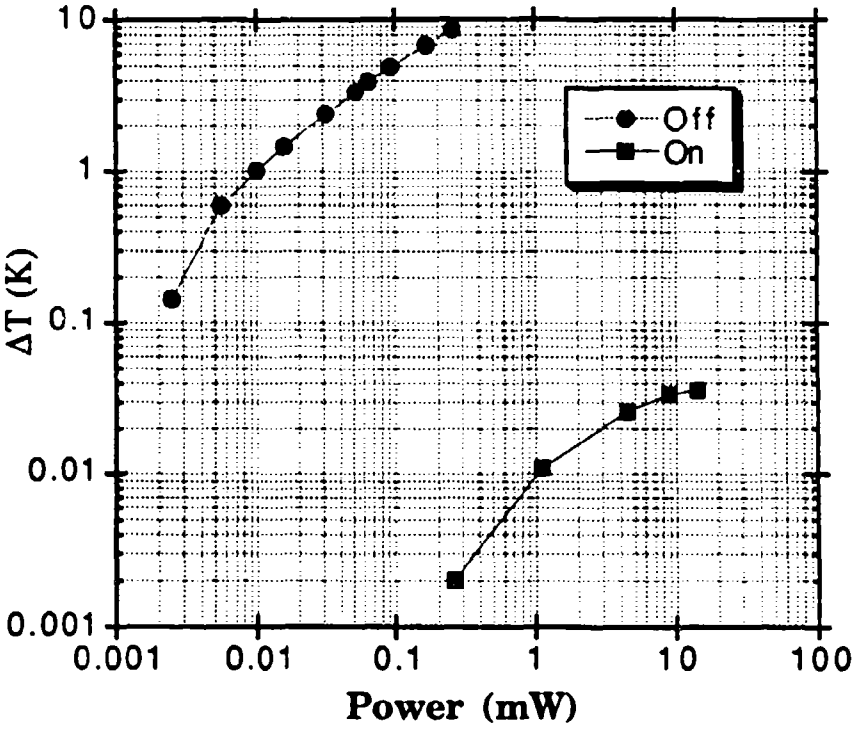

Fig. 3. Temperature drop across the heat switch vs. power input.

The protoype heat switch has not been optimized for its on and off switching times. Its on switching time is less than a minute. The off time, however, is on the order of several minutes. This is mostly due to the long capillary tube connecting the pump to the gap. This time can be reduced by increasing the pumping conductance of this tube.

CONCLUSIONS

The results of the tests performed on the He II heat switch prototype indicate the feasibility of incorporating this design into the 2-10K ADR. The on and off conductances of such a heat switch are close to their predicted values. Further work is required to make the switching times of the heat switch fast enough for the ADR.

REFERENCES

1. B.P.M Helvensteijn and A. Kashani, " Conceptual Design of a 0.1W Magnetic Refrigerator for Operation Between 10K and 2K," Adv. Cryo. Engn., Vol. 35 (1989).
2. T.F. Connolly and E.D. Copenhaver, " Bibliography of Magnetic Materials and Tabulation of Magnetic Transition Temperatures," ORNL-RMIC-7 (1970).
3. J.P. Torre and G. Chanin, " A Heat Switch for Liquid Helium Temperatures," Rev. Sci. Inst., Vol. 55(2), (1984).
4. Private communications with W. Bircik of TRW.
5. B.P.M Helvensteijn, A. Kashani and R.A. Wilcox, "Activated Carbon Test Assembly," Preseneted at ICCC (1990).
6. I.Vazquez, et. al., " Helium Adsorption on Activated Carbons at Temperatures Between 4K and 76K," Adv. Cryo. Engn., Vol. 33 (1988).

Paper presented at Sixth Intl. Cryocooler Conf.
Plymouth, Mass., Oct. 1990

MICRO AND NANNO CRYOCOOLERS: SPECULATION ON FUTURE DEVELOPMENT

Graham Walker and Edward R. Bingham
Department of Mechanical Engineering
University of Calgary
Alberta, Canada, T2N 1N4

ABSTRACT

Modern electronics combines the arts of photolithography with silicon chemical technology and advanced automatic manufacturing techniques to the large scale, low cost production of increasingly sophisticated and miniaturized integrated circuits. Using the same technology a new field, called microdynamics, has developed. Microdynamics, the science, technology and design of moving micromechanical devices uses silicon as the principal material of fabrication for a broad range of inexpensive batch-fabricated devices primarily associated with-micro-processors.

Contemporaneously the science of low temperature electronics is developing, carrying with it the demand for miniaturized cryogenic cooling systems of modest cost, high reliability with low power, low weight and small size requirements.

This paper explores the potential application of microdynamic technology to the field of micro or nanno cryocoolers and speculates on some possible developments and applications.

INTRODUCTION

In the 1950's the arts of photolithography and silicon chemical technology were combined to develop integrated circuit technology. This combination was unusually productive and resulted in circuits of ever-increasing complexity revolutionising the whole basis of electronic systems. Combination with advanced automatic manufacturing techniques has resulted in high volume, low cost production.

Silicon has emerged as an unusually versatile material being increasingly employed in a variety of new commercial products not only for its well established electronic properties but also because of its advantageous mechanical properties. Peterson[1] published the classic paper on silicon as a mechanical material reviewing the mechanical characteristics and micromechanical processing techniques as well as applications both electronic and non-electronic.

MICRODYNAMICS

The technology derived from integrated chip processes when applied to the science and design of moving micromechanical devices and mechanisms has come to be known as 'microdynamics'. Muller[2] recently reviewed this field describing how polycrystalline silicon and silicon nitride can be applied as mechanical materials. Microstructures in these materials are freed from the substrate by etching a sacrificial layer of silicon dioxide. This technique has allowed the development of electrostatically driven resonant bridges, rotating and sliding structures, gears, springs and micromotors.

Some concept of the scale of microdynamic structures may be gained by reference to Figure 1, after Muller[2], comparing an electrostatically driven micromotor (having a rotor diameter of 0.1 mm) with the blonde human hair lying in the forefront of the picture.

COLD ELECTRONICS

Contemporaneously with the above developments the science and technology of low-temperature electronics both semiconductor and superconductor including combinations of the two has proceeded apace. Kirschman[3] has provided an excellent overview of this new field. The first international conference on low temperature electronics was held recently (Edelsack *et al*[4]).

Refrigeration to 80 K or below is required for all low temperature electronic systems. The cooling capacity required ranges from kilowatts of cooling at 80 K (recondensing the nitrogen vapour boiling from liquid nitrogen cooled supercomputers) to microwatts of cooling for the miniature silicon chips of simple systems. It is with this latter requirement that this paper is primarily concerned.

MINIATURE CRYOCOOLERS

Miniature cryocoolers have been the subject of intense research and

development effort over the past forty years. This has been directed primarily to provide cooling at 80 K for the infrared systems used in missile guidance and night vision equipment, initially an exclusively military requirement and, now, to an increasing extent, a variety of civil applications.

The three systems which have passed into general use following intense, competitive research are:

a) a dewar flask filled with liquid nitrogen which evaporates. This system is extremely reliable and quiet with a relatively low cost, is light in weight, with a small volume. Its 'life' between refills with liquid nitrogen is limited (a few hours) but often this is sufficient for many of the applications.

b) a Linde-Hampson cryocooler wherein compressed gas is expanded through an isenthalpic Joule-Thomson nozzle following precooling in a recuperative heat exchanger. In the open cycle version the gas is derived from high pressure storage of very clean gas in storage bottles. 'Closed cycle' versions are also made with multiple stage compressors to supply the high pressure gas for expansion.

c) mechanical cryocoolers operating on a closed regenerative Stirling cycle with compression and expansion of the working fluid at different temperature levels.

Many versions of the above three systems are in series production for primarily military but also civil applications. Walker[5] has recently reviewed the present status of development in the two latter types of cryocooler. The Stirling systems sometimes called miniature electric cryocoolers are generally understood to be some variation of the 1 to 0.2 watt (at 80 K) integral and split refrigerator built to a US Army, Air Force or Navy specification. Four models of these 'common' cryocoolers are in production at the rate of thousands a month.

More recently a new generation of smaller lower capacity cryocoolers have been developed, typified by the Inframetrics cooler[6]. These consume 3 to 5 watts of power and produce 5 to 15 milliwatts of refrigeration at 80 K. The low input power requirements have two significant advantages. They provide the possibility of hand-held, battery powered, infrared equipment operating for eight hours or so before the batteries need to be replaced. Further the low power input simplifies the cooling problem. The cooler can simply be thermally coupled to the equipment frame at the heat dissipated by natural convective cooling from the frame.

These newer coolers are simply scaled down versions, about a third the size

and weight and about a tenth the power input of the common coolers that have been in production for well over a decade. Further reductions in size, weight and power are anticipated to as little as 1 watt of power input[6].

Perhaps these future superminiaturised cryocoolers represent the lower limits of size and power input feasible by conventional, albeit advanced manufacturing methods. Yet even these small machines would appear as 'heavy engineering' to watchmakers. Wristwatches are a high volume, low cost item of very high reliability, and are incredibly compact with low power input. It is likely that very advantageous designs for superminiaturised cryocoolers could be developed by application of watchmaking technology.

Alternative concepts for high volume, low cost throw-away cryocoolers have been examined. These include the 'radio-tube' multiple-expansion Stirling cryocooler shown in Figure 2 with a superconducting or other cold electronic chip mounted at the tip of the third expansion stage. This incorporated a linear electric drive and was intended for 'plugging-in' to ambient temperature circuits. The development of high temperature superconducting electronics requiring refrigeration to only 80 K or so allowed for substantial simplification of the unit to a single stage of expansion. However no solution was evident to the problem of magnetic interference from the linear driver and so this project has been set aside.

Alternative concepts have been examined for superminiaturised cryocoolers with a diaphragm compressor activated hydraulically as shown in Figure 3. This effectively eliminates the problem of electro-magnetic emissions for the electrically driven hydraulic pump can be located remote from the site of the electronic unit. A similar pneumatic drive system is possible and, moreover, multiple expansion units can be energised from a single large pump or compressor drive unit. This provides relatively simple distributed cryogenic 'spot' cooling to a virtually unlimited number of sites, for example the 30 or so cryogenic sensors anticipated on the Earth Observation Satellite.

The resurgence of development effort and achievement with the orifice-pulse tube[7] provides the opportunity to simplify the design and dispense with the reciprocating displacer shown in Figure 3.

The superminiaturised pulse tube regenerative cryocooler with a diaphragm compressor appears to be among the most promising of the future machines. It lends itself readily to large scale low cost production and appears suitable for use in a wide range of refrigeration capacity. It can be made in single stage or multiple stages of expansion.

MICROCOOLERS

There is no well established widely accepted nomenclature to distinguish between miniature, superminiature, and microminiature cryocoolers. Here we shall reserve the term microminiature to systems so small as to be beyond the practical limitation of feasible manufacture. The ultimate reduction in size may qualify the unit to be called a nanno cryocooler in line with the terminology adopted by some of the microdynamics fraternity.

Since micro and nanno cryocoolers would be used most likely with electronic chips it is at least worthwhile to examine how the technologies of silicon processing developed for electronic systems might be adapted to mass produced, low cost, reliable cryocoolers.

The pioneer of this field is of course William Little, Professor of Physics at Stanford University and founder of MMR Inc. (MicroMiniature Refrigerators) of Mountain View California. Little[8] recognised the value of microcryocoolers over a decade ago and also the technical infeasibility of scaling down the existing Joule-Thomson cryocoolers. He developed a novel planar photolithographic method of fabrication using established silicon processing techniques. In this endeavour he was brilliantly successful, both technically and commercially. Several thousand 'Little' cryocoolers are now presently in use world wide.

The potential inherent in these developments was dramatically enhanced by the discovery that expansion of certain gas mixtures can improve the effectiveness of Joule-Thomson refrigerators many times compared with pure gases. The mixtures can be expanded at very substantially reduced pressures thus relieving both the high pressure compressor problem and the clogging of heat exchangers and expansion nozzles by condensed contaminant.

Little has also pioneered the development of integrated cryogenic electronic packages, for example, a miniature hybrid system containing a microminiature refrigerator combined with a superconducting device for use on an ambient temperature circuit board.

It is likely that microminiature refrigerators of the Little *genre* will continue to find increasing and diverse applications in the future.

ALTERNATIVE MICROCRYOCOOLERS

Other forms of mechanical cryocoolers may be possible that are different to the Little microcoolers discussed above. It is thought likely these alternatives

will include machines of the Stirling variety. This view arises simply because history shows that, after 40 years of competitive development and evaluation, of miniature cryocoolers for military infrared systems Stirling cryocoolers of one form or another emerged as the preferred choice. Stirling cryocoolers have no valves and are smaller, cheaper, faster and more efficient than the competitive Gifford-McMahon, Vuilleumier, Claude, Linde-Hampson and Brayton systems. It is likely this trend will continue into the micro and nanno cryocooler range.

It is also thought possible that many of the same techniques and processes described by Peterson[1] and Muller[2] could be adapted for Stirling cryocooler production.

Consider for example the device shown in Figure 4, reproduced from Muller[2] and described by him as a linear vibrating plate with interleaved comb structures for electrostatic drive and sense. The beams holding the structure to the substrate are 50 μm in length'.

Comparing this with present miniature Stirling cryocoolers, say the Oxford cryocooler[9] it is easy to see some common elements. For example the interleaved electrostatic comb structures correspond to the electro-magnetic drive motors of the Stirling machine. Similarly the folded beams supporting the moveable plate correspond to the flexure supports or suspension springs found in the Oxford cooler and the many variations this machine has spawned. The use of flexure supports (or folded beams) combines the possibility for small but relatively unrestrained motion in the horizontal axial direction with rigid support in the transverse (radial) direction. This exactly fulfils the requirements of the interleaved electrostatic comb structures or the close tolerance, no rubbing seals found in contemporary cryocoolers.

In his classic paper Peterson[1] discusses a variety of micromechanical processing techniques for the production of thin silicon or metallic membranes with circumferential support (diaphragms) using dopant dependent chemical etching, and electrochemical etching, thin film deposition, metal plating and epitaxial growth.

It requires little imagination for the combination of these thin diaphragms and appropriate compression chambers with the interleaved comb structures and flexure type support described above to achieve the compressor part of a Stirling system.

Other alternatives include the possibility of driving the diaphragm using a modified loudspeaker coil as in the thermoacoustic engines now in development[7].

Petersen also discusses:

'.... single crystal silicon with a dense network of very fine holes or channels from much less than 1 μm to several micrometers in diameter preferentially orientated in the direction of current flow. The thickness of the layer can be anywhere from micrometers up to many mils. Porous silicon, as it is called, has a number of interesting properties. Its average density decreases with increasing applied current density to as low as 10 percent of normal silicon. Since it is so porous gases readily diffuse into the structure ....'

To a student of Stirling machines this reads remarkably like a description of the regenerative matrix necessary to Stirling cryocooler operation.

The pulse tube cryocooler is essentially a Stirling cryocooler with one of the two reciprocating elements (the displacer or expansion piston) removed. It is not known at this time whether or not the pulse tube cryocooler can be scaled down to microminiature size but there appears to be no intrinsic or fundamental physical limit to the scaling process.

CONCLUSIONS

It appears all the necessary ingredients, processes and techniques for the realisation of microminiature Stirling type cryocoolers is at hand. Future developments in this exciting technology are eagerly awaited.

ACKNOWLEDGEMENTS

Research on Stirling cryocoolers at the University of Calgary is supported by the National Science and Engineering Research Council of Canada and by the Department of Energy, Mines and Resources, Government of Canada.

REFERENCES

1. Peterson, K.E., "Silicon as a Mechanical Material", Proc. IEEE, Vol. 70, No. 5, pp. 420-457, May (1982).

2. Muller, R.S., "Microdynamics", Jnl. of Sensors and Actuators", A21-23, 1-8, Elsevier Sequoia, Netherlands (1990).

3. Kirschman, R., "Low Temperature Electronics", IEEE Circuits and Devices Magazine, Vol. 6, No. 2, pp. 12-24, March (1990).

4. Edelsack, E. *et al*, Proc. First Intl. Conf. on Low Temperature Electronics (to be published in Cryogenics, Butterworths Scientific Pubs., Guildford, U.K., late 1990).

5. Walker, G., "Miniature Refrigerators for Cryogenic Sensors and Cold Electronics", (1989).

6. Stetson, N., Foreword II to Walker, (1989).

7. Radebaugh, R., "A Review of Pulse-Tube Refrigeration", Adv. in Cryogenic Eng. (Ed. R.W. Fast), Vol. 35A, pp. 1191-1206, Plenum Publishing Corp., New York, N.Y. (1990).

8. Little, W.A., "Microminiature Refrigerators for Joule-Thomson Cooling of Electronic Chips and Devices", Adv. in Cryo. Eng. (Ed. R.W. Fast), Vol. 35, pp. 1325-1334, Plenum Publishing Corp., New York, N.Y. (1990).

9. Orlowska, H.H. and Davy, G., "Measurement of Losses in a Stirling Cycle Cooler", Cryogenics, Vol. 27, pp. 645-51, Butterworths Sc. Pubs., Guildford, U.K. (1987).

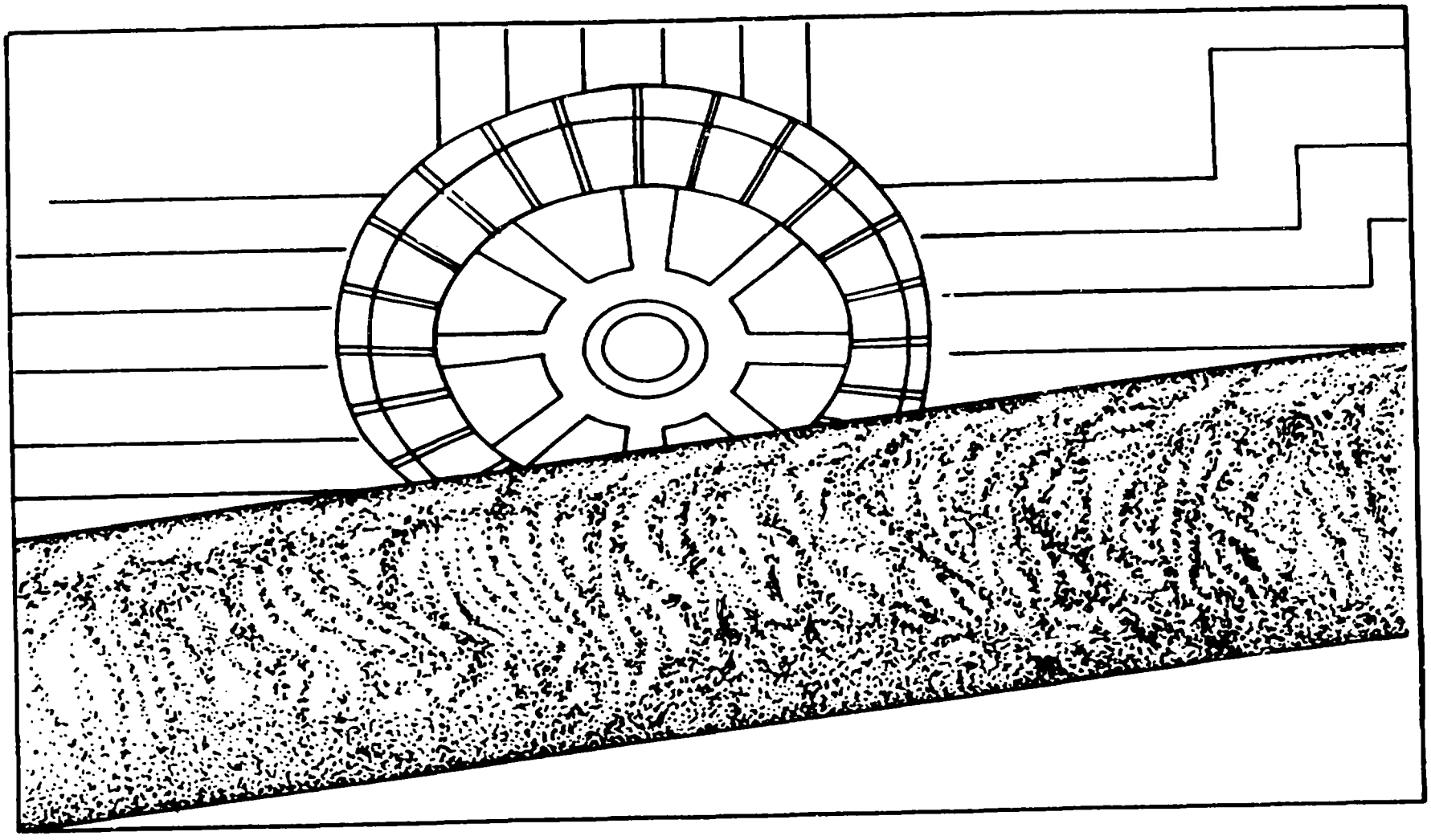

Fig. 1 Comparison of a micromotor with a human hair (after Muller[9]).

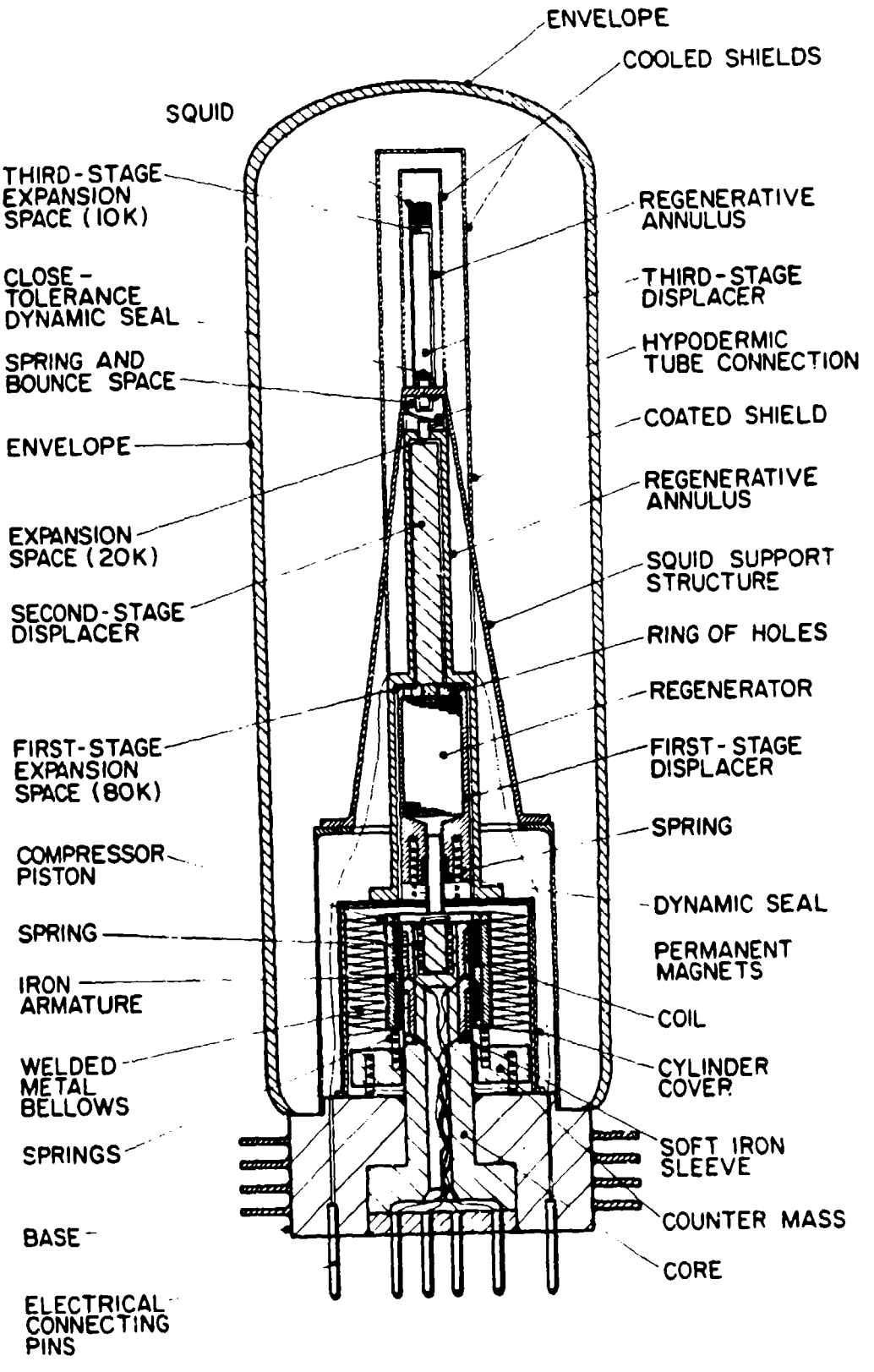

Fig. 2 Concept for throw-away multiple-expansion Stirling cryocooler.

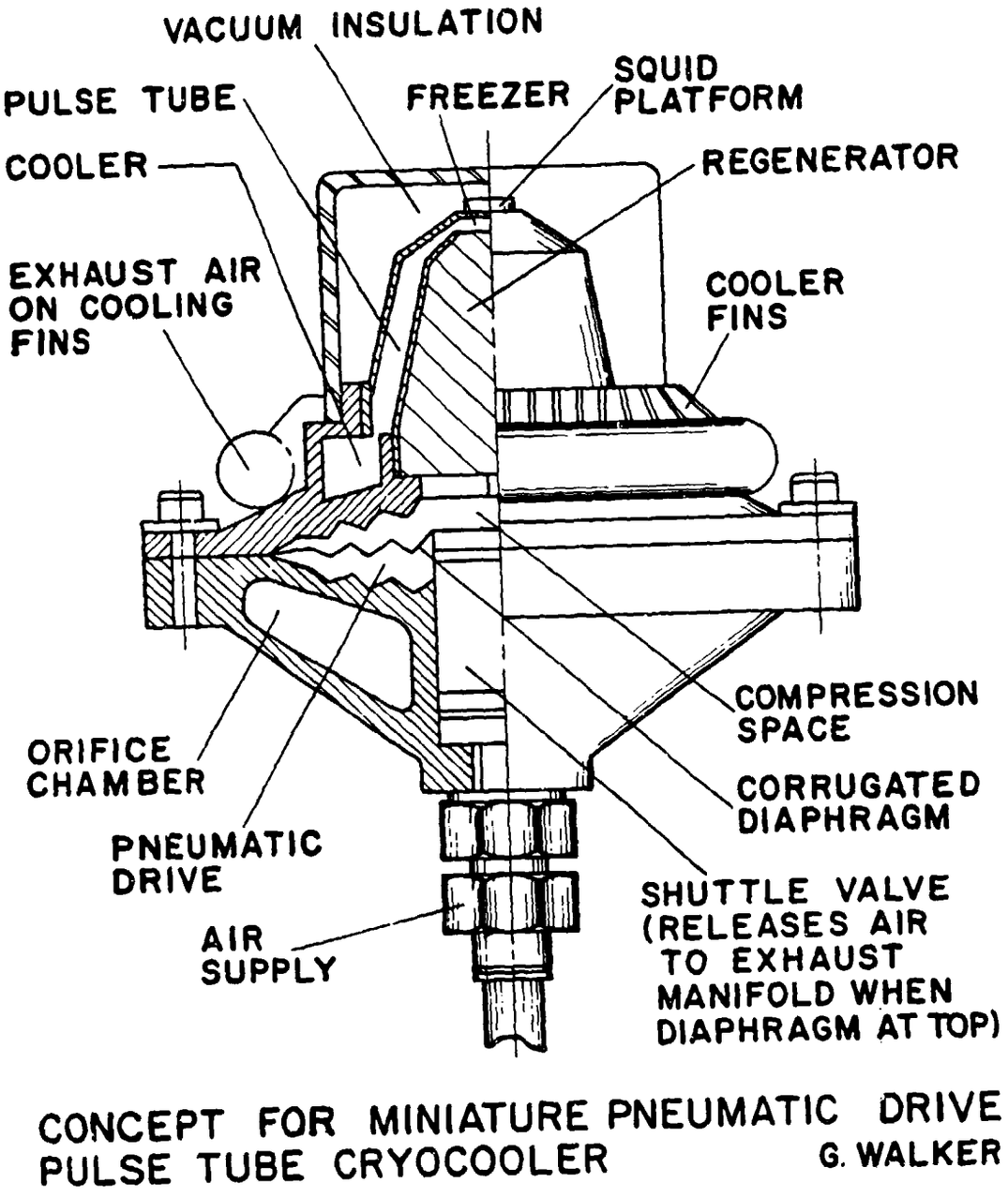

Fig. 3 Concept for hydraulically activated miniature Stirling cryocooler.

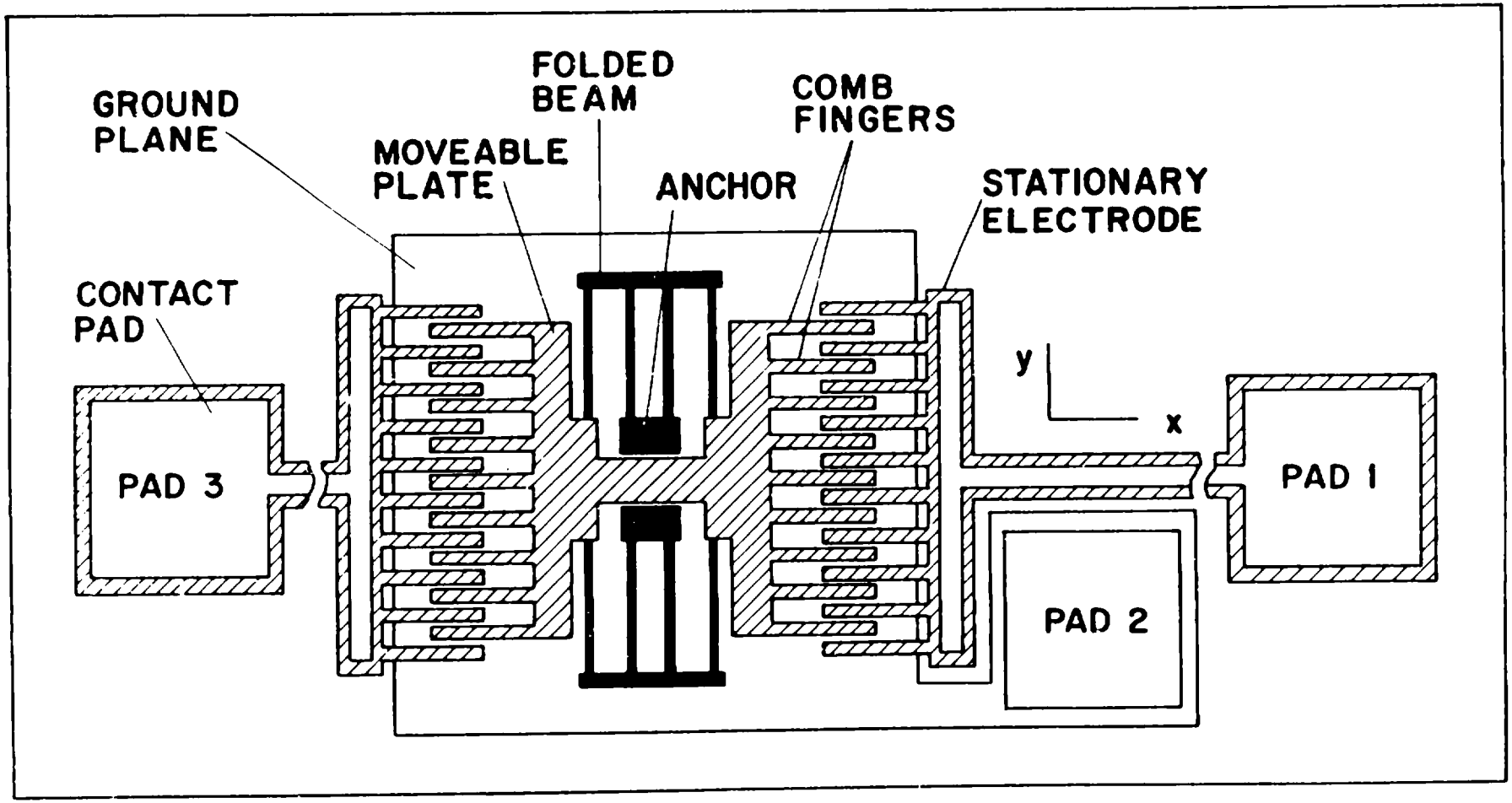

Fig. 4 Linear vibrating plate with interleaved comb structures (after Muller[9]).

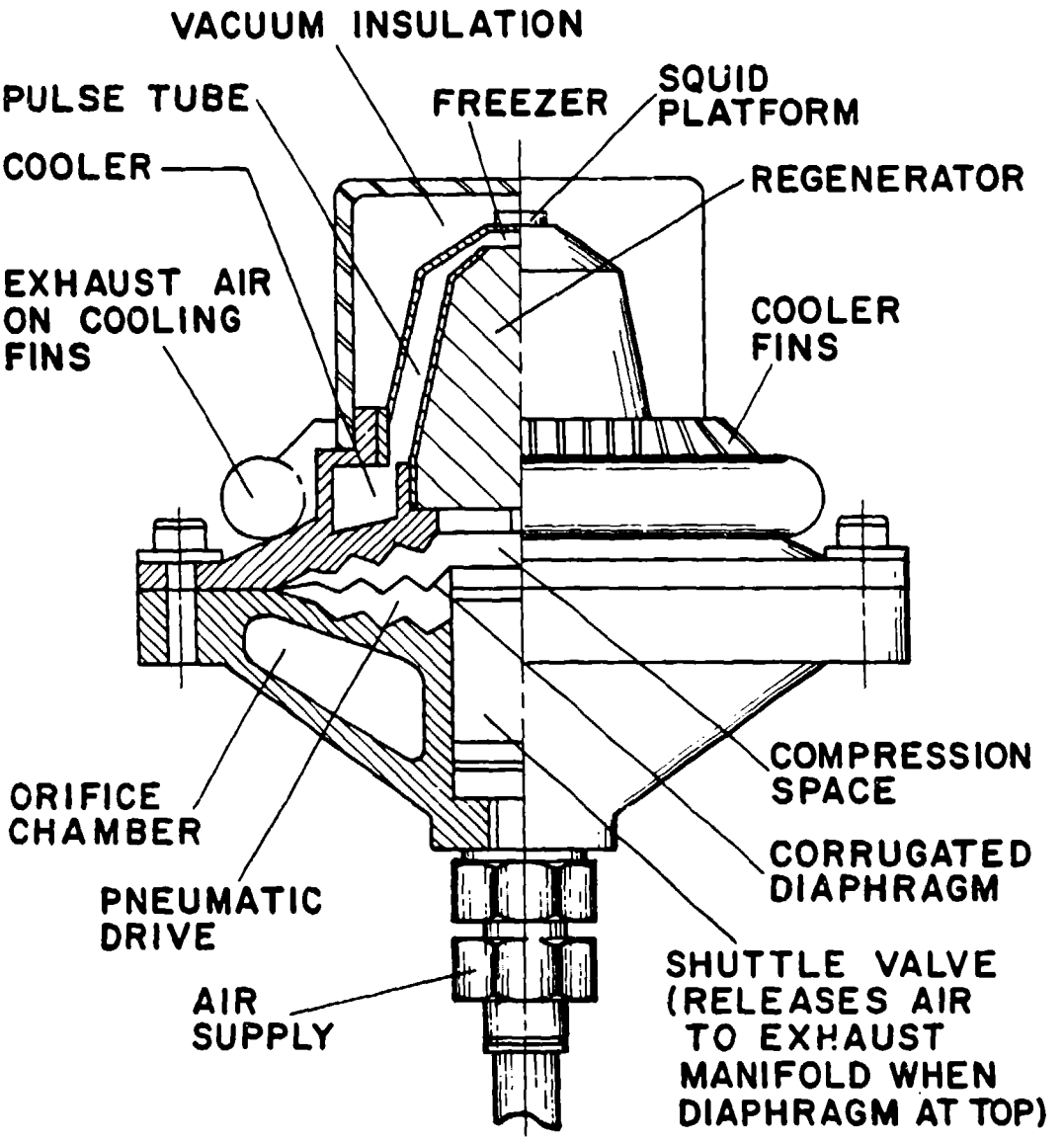

CONCEPT FOR MINIATURE PNEUMATIC DRIVE PULSE TUBE CRYOCOOLER

G. WALKER

INITIAL DISTRIBUTION

DTIC (12 copies)

Stephen Abush
ADP Cryogenics Inc.
1833 Vultee Street
Allentown PA 18103
215–791–6700

Robert Ackermann
General Electric Corp. Res. & Dev.
P.O. Box 8, Bldg. K–1, EP–123
Schenectady NY 12301
518–387–6730

Frank S. Adams
TSA
2401 Bristol Court S.W.
Olympia WA 98502
206–984–1677

Sol Aisenberg
Raytheon New Product Center
63 Second Avenue
Burlington MA 01803
617–270–2300

Les Albiol
Air Force
P.O. Box 92960
Los Angeles CA 90009
213–363–6878

John A. Alvarez
Perkin-Elmer
2771 North Garey Avenue
Pomona CA 91767
714–593–3581

Tamirisa R. Apparao
Penn State University
Dept of Mechanical Engineering
University Park PA 16802
814–863–4652

Louis F. Aprigliano
David Taylor Research Center
Code 2812
Annapolis MD 21402–5067
301–267–2484

M.D. Atrey
Department of Mechanical Engineering
Indian Institute of Technology, Powai
Bombay– 400 076, India

Zdnenek F. Backovsky (Stan)
Rockwell International Corp.
P.O. Box 3644
Seal Beach CA 90740
213–797–3759

James R. Baker
David Taylor Research Center
Code 2712
Annapolis MD 21402–5067
301–267–2634

Michael Balister
National Radio Astronomy Observatory
2015 Ivy Road
Charlottesville VA 22903
804–296–0365

Dr. John A. Barclay
Astronautics Corporation of America
5800 Cottage Grove Road
Madison WI 53716–1387
608–221–9001

Steven Bard
JPL
MS 157–102
Pasadena CA 91109
818–354–4487

Martin Bareiss
AEG, Aktiengesellschaft
Theresienstr. 2
Germany Heilbronn
017131/6212–81

Edward L. Bartlett, Jr.
General Dynamics
234 Broadway
Norwich CT 06360
203–433–2214

William H. Baumgart
Hughes Aircraft Co.
2000 El Segundo Blvd.
El Segundo CA 90245
213–636–0912

Bill Baumgret
Hughes Aircraft
P.O. Box 902, EO/ESI/A290
El Segundo CA 90245

Luc Bauwens
Mitchell/Stirling Machines/Sys, Inc.
2550 Ninth Street
Berkeley CA 94710
415–845–2528

Trevor P. Benson
Dowty Weapon Systems
Site 25, Cheltenham Road East
England GL2 90N
011–44–452–714–382

David M. Berchowitz
Sunpower, Inc.
6 Byard Street
Athens OH 45711
614–594–2221

Robert E. Bernert, Sr.
3 Pleasant Street
Thermax, Inc.
S. Dartmouth MA 02748
508–999–1231

Peter K. Bertsch
CTI-Cryogenics
266 Second Avenue
Waltham MA 02254
617–622–5389

David P. Bloomfield
Analytic Power Corporation
123 South Street
Boston MA 02111
617–542–6352

Glenn E. Bonney
APD Cryogenics Inc.
1833 Vultee Street
Allentown PA 18103
215–791–6740

John D. Bowes
Ford Aerospace
3825 Fabian Way
Palo Alto CA 94303
415–852–6869

Douglas A. Bowker
Private Consultant
P.O. Box 13506, Sinoville 0129
Pretoria SA
27–12–572547

Peter E. Bradley
NIST
325 Broadway/M.S. 583.30
Boulder CO 80303
303–497–3465

Thomas W. Bradshaw
Rutherford Appleton Laboratory
Chilton, Didcot Oxon OX11 OQX
U.K.
(0) 235 821900 x6149

G.W. Brassell
Nuclear Filter Technology, Inc.
409 Corporate Circle
Golden CO 80401
303–278–1888

R. Warren Breckenridge
Arthur D. Little, Inc.
20 Acorn Park
Cambridge MA 02140
617–864–5700 x5870

Jeffrey A. Bruning
Consultant, Nichols Research Corp.
Rt. 1, Box 692
Leasburg MO 65535
314–245–6670

Warren Buckles
Superconductivity, Inc.
P.O.Box 56704
Madison WI 53705
608–831–3700 x112

Stan Buller
R.G. Hansen & Associates
631 Chapala Street
Santa Barbara CA 93101
805–564–3388

Connie Burke
WRDC/FIVP
Wright-Patterson AFB OH 45433
513–255–4853

William W. Burt
TRW Space & Technology Group
One Space Park (R1/1126)
Redondo Beach CA 90278
213–814–0411

Robert Buzerak
Loral Aeronutronic Corp.
Ford Road
Newport Beach CA 92658
714–720–4966

Steven R. Carolus
Carelton Technologies Inc.
10 Cogham Drive
Orchard Park NY 14127
716–662–0006 x283

Constantin Carpetis
German Aerospace Research Est. (DLR)
Pfaffenwaldring 38–40
D–7000 Stuttgart–80 Germany
(0711) 6862–427

Stephen H. Castles
NASA/GSFC
Code 713
Greenbelt MD 20771
301–286–5405

James N. Chafe
David Taylor Research Center
Code 2712
Annapolis, MD 21402–5067
301–267–2149

Chung-Kin Chan
One Space Park R1/1126
TRW Space and Technology Center
Redondo Beach CA 90278
213–813–9414

Dr. Fang Chen
Oak Ridge National Laboratory
P.O. Box 2008
Oak Ridge TN 37831–6070
615–574–0712

William E. Chen
General Electric Company
3001 W. Radio Drive
Florence SC 29501
803–678–9222

Yeu-Ching Chen
The Perkin-Elmer Corporation
2771 N. Garey Avenue
Pomona CA 91767
714–593–3581 x4719

James E. Chenoweth
Air Force Wright Aeronautical Labs
AFWAL/FIEC WRDC/FIVP
Wright Patterson AFB OH 45433–6533
513–255–4853

Jean-Claude Christeler
Balzers
8 Sagamore Park Road
Hudson NH 03051
603–889–6888

Y.K. Chuah, Manager
Industrial Technology Research Inst
Bldg. 64, 195, sec. 4., Chung Hsin Rd.
Chutung, Taiwan 31015
886–35–916279

F.J. Cogswell
Boreas, Inc.
175–U New Boston Street
Woburn MA 01801
617–937–9080

Richard M. Colgate
Colgate Thermodynamics
14 Nassau Street
Princeton NJ 08542
609–921–8770

Marc B. Connally
Air Force Astronautics Lab.
AL/RKLB
Edwards AFB CA 93523
805–275–5327

Peter Coyle
Loral Fairchild Systems
9 East Haddon Avenue
Oaklyn NJ 01807
609–858–1361

J. Alan Crunkleton
Boreas, Inc.
175–U New Boston Street
Woburn MA 01801
617–937–9080

Mr. Jeffrey D. Dalton
Naval Weapons Ctr
Commander, Code 36213
China Lake CA 93555–0001
619–939–1694

Marc David
Cryophysics
9 Rue Dallery
Jouy-En-Josas France 78350
33–1–39–56–00–66

Lt. Col. Thomas M. Davis
Air Force Space Technology Center
AFSTC/SW
Kirtland AFB NM 87117
505–846–6243

Anthony J. Degregoria
Astronautics Corp. of America
5800 Cottage Grove Road
Madison WI 53716
608–221–9001

Ronald den Heijer
Koch Cryogenics International B.V.
Achtseweg Noord 5, Building AQ
Acht, The Netherlands 5651 CG
+31–40–766425

Peter C. Dent
Lake Shore Cryotronics, Inc.
64 East Walnut Street
Westerville OH 43081
614–891–2243

F. David Doty, President
Doty Scientific Inc.
600 Clemson Road
Columbia SC 29223
803–788–6497

Lionel R. Duband
University of California, Berkeley
Department of Physics
Berkeley CA 94720
415–642–3618

Stephen B. Dunn
AFSTC/SWS
Kirtland AFB NM 87117
505–846–5803

Allen L. DeForrest
Hughes-Santa Barbara Research
75 Coromar Drive/Bldg. 32/M.S. 28
Goleta CA 93117
805–562–7220

James Eastwood
Allied-Signal Aerospace Company
2525 West 190th Street
Torrance CA 90509
213–512–3361

David B. Eisenhaure
Satcon Technology Corporation
12 Emily Street
Cambridge MA 02139
617–661–0540

Donald M. Ernst
DTX
780 Eden Road
Lancaster PA 17601
717–569–6551

Ralph Fenn
Satcon
12 Emily Street
Cambridge MA 02139
617–661–0540 x271

Michael D. Fennell
Energy Science Laboratories
6888 Nancy Ridge Drive
San Diego CA 92121
619–552–2035

Rod Fernandez
Ball Aerospace Systems Group
P.O. Box 1062
Boulder CO 80308–1062
303/939–6784

James H. Firkins
RSRE Mod. P.E.
St Andrews Road, Malvern
WORCS, MR14 3PS England
0684 894630

Marvin L. Firmin
The Aerospace Corporation
P.O. Box 9045
Albuquerque NM 87119
505–846–7062

Frank B. Fisk
AFSTC/SWS
Kirtland AFB NM 87117
505–846–5803

Terry N. Fleener
Ball-Electro Optics Cryo Div.
P.O. Box 1062
Boulder CO 80306
303–939–4413

Dr. Thomas M. Flynn
Ball Aerospace
P.O. Box 1062–M.S RA/3
Boulder CO 8030
203–939–4787

Don Formiller
Hughes Aircraft Company
3100 W. Lomita Blvd. P.O. Box 2999
Torrance CA 90509–2999
213–517–6204

Paul B. Forney
Lockheed Missiles & Space
3251 Hanover St.
Palo Alto CA 94304
415–424–2121

Howard Fraser
United Technologies Carrier
P.O. Box 4803
Syracuse NY 13221
315–432–3452

Kelly P. Gaffney
USAF
Space Technology Center
Kirtland AFB, NM 87117
505–846–9752

John M. Gary
NIST
325 Broadway, Mail Code 719
Boulder CO 80303–3328
303–497–3369

David Gedeon
Gedeon Associates
16922 South Canaan Road
Athens OH 45701
614–592–5166

R. Andrew Gerrick
McDonnell Douglas Space Systems
5301 Bolsa Avenue
Huntington Beach CA 92647
714–896–4391

Peter E. Gifford
Cryomech, Inc.
1630 Erie Boulevard East
Syracuse NY 13210
315–475–9692

George Giggey
Raytheon Corporation
55 Barefoot Road
Northboro MA 01532
508–393–7300

David Glaister
Aerospace Corporation
P.O. Box 92957–M.S. M4908
Los Angeles CA 90009
213–336–6716

Charles D. Glenn
Glenn Company
1610 Manton Court
Campbell CA 95008
408–378–0570

Kimberly Godshalk
Tektronix
P.O. Box 500–M.S. 50–324
Beavertown OR 97077
502–627–5244

Lt. Col. Craig Golart
WRDC/FIVP
4049 Meridell Drive
Beavercreek OH 45430–2060
513–255–4063

Harald Gotthardt
Leybold AG
Bonner Strasse 498
5000 Cologne, 51 Germany
221–347–1010

Geoffery F. Green
Code 2712
David Taylor Research Center
Annapolis MD 21402–5067
301–267–3632

Kenneth E. Green
Loral Infrared & Imaging Systems
2 Forbes Road
Lexington MA 02173
617–863–3528

Youfan Gu
Univ of Colorado/Dept of Chem Engr
Campus Box 424
Boulder CO 80309
303–492–7680

Dr. Wilfred Gully
Hughes Aircraft Company
2999 W. Lomita Blvd.
Torrance CA 90505
213–517–5664

Marvin E. Gunn, Jr.
U.S. Department of Energy
1000 Independence Ave, SW, CE–232
Washington, DC 20585
202–586–5377

Ulrich Haefner
Leybold AG
Bonner Strasse 49[illegible]
5000 Cologne, 51 Germany
221–3471203

Mark Hanes
Hughes Aircraft
3100 Lomita Blvd.
Torrance CA 90505
213–517–6771

George M. Harpole
TRW R1/1022
One Space Park
Redondo Beach CA 90278
213–812–0397

John T. Harvell
CTI-Cryogenics
266 Second Avenue
Waltham MA 02254
617–622–5314

George C. Haverly
General Electric Astro Space
(M4018) 230 Goddard Blvd.
King of Prussia PA 13406
215–354–3775

Ben P. Helvensteijn
Sterling Federal Systems
1121 San Antonio Rd.
Palo Alto CA 94303
415–604–6521

John B. Hendricks
Alabama Cryogenic Engineering Inc.
P.O. Box 2470
Huntsville AL 35804
205–536–8629

Edward L. Hershberg
Tektronix
P.O. Box 500, M.S. 50–324
Beaverton OR 97077
503–627–1593

Dr. John Hess
The Hebrew University of Jerusalem
706 N. 6th Avenue
Tuscon AZ 85705
602–624–2243

Yu Hiresaki
Suzuki Shokan Company, Ltd.
2–8–52 Yoshinodai
Kwagoe, Saitama, Japan 350
0492–25–7551

Ryochi Hirosi
Kobe Steel Ltd.
MIT NW–14 2508, 170 Albany St.
Cambridge MA 02139
617–253–4161

Bill J. Horsley
Ball Aerospace
P.O. Box 1062
Boulder CO 80306
303–939–6673

Prof. B.J. Huang
National Taiwan University
Dept. of Mechanical Engineering
Taipei, Taiwan 10764
02–363–0231 x2410

Charles A. Hull
GE Aerospace
French Road
Utica NY 13503
315–793–6382

Takashi Inaguchi
Central Research Lab/Mitsubishi Elec.
1–1, Tsukaguchi-Honmachi 8-Chome
Amagasaki, Hyogo, 661 Japan
06–497–7126

Donald Isaac
Lockheed Missiles and Space Co.
Research Lab/Dept. 92–40, Bldg. 205
Palo Alto CA 94304–1191
415–424–3350

Tim James, Ph.D.
STI
460 Ward Drive
Santa Barbara CA 93111–2310
805–683–7646

Dennis J. Jas...
Astronautics Corp of America
Tech Center–5800 Cottage Grove Rd.
Madison WI 53716
608–221–9001

Sangkwon Jeong
MIT
77 Massachusetts Ave/Bldg. 41–208
Cambridge MA 02139
617–253–2273

Christopher I. Jewell
European Space Agency
P.O. Box 299, A.G. Noerdwijk
The Netherlands
(01719) 84309

Bradley Q. Johnson
Analytic Power Corp.
123 South Street
Boston MA 02111
617–542–6352

Dean L. Johnson
Jet Propulsion Laboratory
4800 Oak Grove Drive/M.S. 238–737
Pasadena CA 91109
818–354–1641

Bryan G. Jones
British Aerospace
FC 740, P.O. Box 5
Filton, Bristol BS127QW England
0272–368378

David A. Jones
The Aerospace Corporation
P.O. Box 92957, M/S M6–210
Los Angeles, CA 90009–2957
213–416–7183

Howard W. Jones
Mechanical Technologies Ltd.
968 Albany–Shaker Road
Latham NY 12110
518–785–2118

Peter F. Jones
The Aerospace Corporation
P.O. Box 9045
Albuquerque NM 87119
505–844–9969

Chad Joshi
American Superconductor Corp.
149 Grove Street
Watertown MA 02172
617–923–1122

Frank J. Kadi
Leybold Vacuum Products, Inc.
5700 Mellon Road
Export PA 15632
412–325–6547

Yoon-Myung Kang
Daikin Industries, Ltd.
3 Miyukigaoka
Tsukuba, Ibaraki, 305 Japan
298–58–5001

Ali Kashani
Sterling Federal Systems
NASA-Ames Research Ctr./M.S. 244–10
Moffett Field CA 94035
415–604–3663

Masakuni Kawada
Electrotechnical Laboratory
1–1–4, Umezono, Tsukuba-Shi
Ibaraki, 305 Japan
0298–58–5701

Thomas G. Kawecki
Naval Research Lab Code 8241
4555 Overlook Avenue
Washington DC 20375–5000
202–767–2851

Peter J. Kerney
CTI-Cryogenics
266 Second Avenue
Waltham MA 02254
617–622–5391

Chi Shing Keung
Philips Laboratories
345 Scarborough Road
Briarcliff Manor NY 10510
914–945–6124

Katsunari Kikuchi
Sumitomo Heavy Industries, Ltd.
1 Kanda Mitoshiro-Cho, Chiyoda-Ku
Tokyo 101
03–233–9595

Glenn E. Kinard
Air Products & Chemicals, Inc.
7201 Hamilton Blvd.
Allentown PA 18195–1501
215–481–7902

Kenneth A. King
American Superconductor Corp.
149 Grove Street
Watertown MA 02172
617–923–1122

Peter Kittel
NASA
M.S. 244–10 Ames
Moffett Field CA 94035
415–604–4297

Richard Konian
IBM
Dept. A75, Bldg. 701, P.O. Box 950
Poughkeepsie NY 12602
914–435–1347

Stephen F. Kral
Astronautics Tech. Center
5800 Cottage Grove Rd.
Madison WI 53716
608–221–9001

George A. Kuhr
Hughes Aircraft
P.O. Box 902
El Segundo CA 90245
213–616–8926

Robert R. Lambert
General Electric Company
P.O. Box 915
Blue Bell PA 19422
215–354–7501

William N. Lawless
Ceramphysics, Inc.
921 Eastwind Drive/Suite 110
Westerville OH 43081
614–882–2231

David P. Laycock
RSRE Mod Pe
St. Andrews Road, Malvern
WORCS WR14 3PS England
0684 89–4936

Dr. Otto C. Ledford
Advanced Technology
222 N. Sepulveda Blvd., Suite 1310
El Segundo CA 90245
213–640–1050

Jeffrey H. Lee
Ball Aerospace
P.O. Box 1062, M.S. RA–3
Boulder CO 80306
303–939–5457

Daniel Lehrfeld
Magnavox Electro-Optical Systems
46 Industrial Avenue
Mahwah NJ 07430
201–529–1700

Robert M. Lerner
MIT Lincoln Lab
244 Wood Street
Lexington MA 02173–9108
617–981–2678

James M. Lester
Ball Aerospace Systems Division
P.O. Box 1062
Boulder CO 80306
303–939–4452

Robert Levenduski
Ball Aerospace Systems Group
P.O. Box 1062
Boulder CO 80308–1062
303–939–4194

James R. Lhota
The Aerospace Corp.
P.O. Box 92957 M2/248
Los Angeles CA 90009
213–336–5298

Anthony G. Liepert
Boreas, Inc.
175–U New Boston Street
Woburn MA 01801
617–937–9080

Dr. William A. Little
MMR Technologies Inc.
1400 North Shoreline Blvd/Suite A–5
Mountain View CA 99043
415–962–9620

Ralph C. Longsworth
APD Cryogenics Inc.
1833 Vultee Street
Allentown PA 18103
215–791–6708

Chi Wun Lu
Taiwan University, Mechanical Eng.
National Taiwan University
Taiwan, R.O.C.

Jill Ludwigsen
Nichols Research Corp.
2201 Buena Vista SE, Suite 203
Albuquerque NM 87106
505–843–7364

James F. Maguire
Applied Eng. Technologies Ltd.
10 Tower Office Park, Suite 420
Woburn MA 01801
617–932–3221

Frithjof N. Mastrup
Hughes Aircraft Co.
2000 E. El Segundo Blvd/P.O. Box 902
El Segundo CA 90245
213–616–9647

Yoichi Matsubara
Nihon University
Atomic Energy Research Institute
Funabashi Chiba, 274 Japan
0474–69–5374

Ben-Zion Maytal
Univ. of Wisconsin-Madison
1500 Johnson Dr., Bldg. 811
Madison WI 53706
608–263–2141

Frank E. McCrea
Varian Associates
3560 Bassett Street
Santa Clara CA 95054–2704
408–496–2270

Kathleen M. McDermott
NIST
325 Broadway, MS 583.3
Boulder CO 80303
303–497–3952

James P. McGuire
NASA
Goddard Space Flight Center
Huntsville AL 20771
301–286–9170

Edward R. McLaughlin
Smithsonian Institute
60 Garden Street
Cambridge MA 02142
617–495–7362

Henry Meehan
Magnavox
46 Industrial Way
Mahwah NJ 07430
201–529–1700

Franc Megujar
Institut "Zoran Rant"
Kidriceva 66A
Skofja Loka, Yugoslavia
064–631–251

Gorken Melikian
United Technologies Research Ctr.
411 Silver Lane
E. Hartford CT 06108
203–727–7554

Janice Meredith
Lucas Aerospace
Shaftmoor Lane, Hall Green
Birmingham, B28 8SW, U.K.
011–21–707–7111

Grant Milbouer
Magnavox
46 Industrial Avenue
Mahwah NJ 07430–0615
201–529–1700

John Lester Miller
Martin Marietta
P.O. Box 179, M/S L8030
Denver CO 80201
303–971–6945

Archer Mitchell
Westinghouse Electric
10706 Eastwood Avenue
Silver Spring MD 20901
301–765–7232

Matthew Mitchell
Mitchell Stirling Machines Systems
2550 Ninth Street, Suite 207B
Berkeley CA 94710
415–845–2528

Raymond Moore
Koch Process Systems
20 Walkup Drive
Westboro MA 01581
508–898 -0374

Timothy P. Moran
Astronautics Lab. RKLB
Edwards AFB CA 93523
805–275–5610

William C. Mulroney
Inst. for Defense Analysis
1801 N. Beauregard St.
Alexandria VA 22311
703–578–2746

Dwight M. Munk
ICI Advanced Materials
Wilmington DE 19897
302–886–3858

Hiroshi Nagano
Toyama University
3190 Gofuku Toyama 930
Toyko, Japan
0764–41–1271

Charles S.Naiman
Ice, Inc.
160 Lancaster Terrace
Brookline MA 02146
617–277–4184

Hideki Nakagome
Toshiba Corporation
4–1 Ukishima-Cho
Kawasaki-Ku, 210 Japan
044–288–8019

Ram Narayan
Magnavox
46 Industrial Avenue
Mahwah NJ 07430
201–529–1700

Rob E. Nast
Loral Fairchild Imaging Sensors
1801 McCarthy Blvd.
Milpitas CA 95035
408–433–2534

Theodore C. Nast
Lockheed Research Laboratory
3251 Hanover St./MS 92–40 Bldg. 205
Palo Alto CA 94304-1187
415–424–2401

Neno T. Nenov
UCIG-Linde
P.O. Box 44
Tonawanda NY 14150
716–879–2738

Martin Nisenoff
Naval Research Laboratory
4555 Overlook Rd., S.W. Code 6850.1
Washington DC 20375–5000
202–767–3099

Robert H. Norman
Allied-Signal Aerospace, Air Research
Los Angeles Division
2525 W. 190th Street, P.O. Box 2960
Torrance CA 90509
213–512–3343

Michael G. Norris
MIT
77 Massachusetts Ave/Rm 41–203
Cambridge MA 02139
617–253–2237

Dr. Takenori Numazawa
National Research Inst. for Metals
NW14–2508, MIT/FBNML
Cambridge MA 02139
617–253–4185

Rodney L. Oonk
Ball Aerospace Systems
P.O. Box 1062
Boulder CO 80306
303–939–4449

Anna H. Orlowska
Rutherford Appleton Laboratory
Chilton, Didcot Onon OX11OQX
U.K.
(0) 235 821900 x5717

Andrew P. Owen
Kollmorgen EOD
18 Bradco St.
Keene NH 03431
603–357–2582

Dr. Gottfried Pahler
AEG Aktiengesellschaft
Nachtsichtkomponenten Postfach 1134
D–7100 Heilbronn, Germany
7131/621299

Keith M. Parker
General Electric Company
3001 W. Radio Drive/P.O. Box F–23
Florence SC 29501
803–664–1650

Hsien-Sheng Pei (Jason)
Digital Equipment Corporation
30 Forbes Rd./M.S. NR05/J2
Northboro MA 01532
508–351–4913

Laurence B. Penswick
Stirling Technology Co.
2952 George Washington Way
Richland WA 99352
509–375–4000

Glen G. Pfleiderer
Intermagnetics General Corporation
8 Robin Drive
Voorheesville NY 12186
518–765–2006

John R. Phillips
Harvey Mudd College, Eng. Clinic
260 E. Foothill Blvd.
Claremont CA 91711
714–621–8020

Michael J. Pickett
Koch Process Systems, Inc.
20 Walkup Drive
Westborough MA 01581–5003
508–898–0369

Richard L. Plambeck
University of California
Radio Astronomy Lab
Berkeley CA 94720
415–642–3441

David L. Potts
JSA International
1100 Massachusetts Ave.
Cambridge MA 02138
617–876–3838

Jerry W. Prentice
General Pneumatics Corporation
7662 E. Gray Rd, Suite 107
Western Research Center
Scottsdale AZ 85260
602–998–1856

Kenneth D. Price
Hughes Aircraft
2000 E. El Segundo Blvd.
El Segundo CA 90245
213–616–6863

Robert E. Priest
LLNL
7000 East Ave./P.O. Box 808, L–287
Livermore CA 94550
415–422–8677

Nachman Pundak
Ricor Ltd.
En Harod (IHUD)
Israel 18960
972–6–531703

Jeff R. Raab
TRW S&TG
One Space Park/M.S. 01/2070F
Redondo Beach CA 90278
213–814–0405

Dr. Ray Radebaugh
NIST
325 Broadway
Boulder CO 80303
303–497–3710

John F. Rasmussen
Lorel Infrared & Imaging Systems
2 Forbes Road
Lexington MA 02173
617–863–4543

Wayne C. Rawlins
NIST
325 Broadway/M.S. 583.3
Boulder CO 80303
303–497–5251

Peter Riggle
Stirling Technology Company
2952 George Washington Way
Richland WA 99352
509–375–4000

Dr. James C. Riple, P.E.
Airesearch Los Angeles Division
2525 W. 190th Street, P.O. Box 2960
Torrance CA 90504–6099
213–512–4586

Pat R. Roach
NASA Ames Research Center
MS 244–10
Moffett Field CA 94035
415–604–3191

Gerald F. Robertson
Carrier Corporation
Carrier Parkway/P.O. Box 4808
Syracuse NY 13221
315–432–6287

George Robinson
19 Hemlock Lane
Acton MA 01720
508–263–4643

Ronald G. Ross
Jet Propulsion Laboratory
4800 Oak Grove Dr./M.S. 157–102
Pasadena CA 91109
818–354–9349

Robert T. Ruggeri
Boeing Aerospace & Electronics
P.O. Box 3999
Seattle WA 98124
206–773–8438

Carl J. Russo
American Semiconductor Corp.
149 Grove Street
Watertown MA 02172
617–923–1122

Samuel Russo
Hughes Aircraft Company
Bldg E55/M.S. 6232/P.O. Box 902
El Segundo CA 90245
213–616–9651

Roger D. Scarlotti
Ball Aerospace Systems Group
P.O. Box 1062
Boulder CO 80308–1062
303–939–5319

Richard L. Schapker
S2 Corporation
134 Farnum Street
N. Andover MA 01845
508–689–3973

Steve Schnurer
GE Medical Systems
3001 W. Radio Dr./P.O. Box F–23
Florence SC 29501
803–664–1648

James Gary Seyster
Allied-Signal
2525 W. 190th Street
Torrance CA 90509
213–512–2098

Julia I. Sheldon
Aerojet Electronic Systems
1100 W. Hollyvale St./P.O. Box 296
Azusa CA 91702
818–812–1624

Neil I. Sherman
Aerojet Electrosystems
1100 W. Hollyvale St./P.O. Box 296
Azusa CA 91072
818–812–2698

William R. Shields
Janis Research, Inc.
2 Jewel Drive
Wilmington MA 01887
508–657–8750

Robert Shull
NIST
Bldg. 223, Room B150
Gaithersburg MD 20899
301–975–6035

Bill G. Simmons
Stirling Technology Company
2952 George Washington Way
Richland WA 99352
509–375–4000

Herbert Sixsmith
Creare, Inc.
P.O. Box 71
Hanover NH 03755
603–643–3800

Matthew M. Skertic
Hughes Aircraft Co.
8433 Fallbrook Ave./Bldg. 270/M.S. 071
Canoga Park CA 91304
818–702–1566

Scot A. Slimon
General Dynamics
2 Oslo Street
Mystic CT 06355
203–433–2217

Joseph L. Smith, Jr.
MIT
77 Massachusetts Ave./Rm 41–204
Cambridge MA 02139
617–253–2296

Leroy M. Sparr
NASA/GSFC
Code 713.4
Greenbelt MD 20771
301–286–3811

W. Dodd Stacy
Creare Inc.
P.O. Box 71
Hanover NH 03755
603–643–3800

Walter F. Stewart
Los Alamos National Lab
P.O. Box 1663/M.S. J576
Los Alamos NM 87545
505–665–1416

George Straubs
Dowty Weapon Systems
Sully Road/P.O. Box 5000
Sterling VA 22170
703–450–8296

Michael Superczynski
David Taylor Research Center
Code 2712
Annapolis MD 21402–5067
301–267–2149

Dr. Greg W. Swift
Los Alamos National Lab
P.O. Box 1663/M.S. K764
Los Alamos NM 87545
505–665–0640

Walter L. Swift
Creare, Inc.
P.O. Box 71
Hanover NH 03755
603–643–3800

John A. Talbourdet
Loral Infrared & Imaging Systems
2 Forbes Road
Lexington MA 02173
617–863–3107

John Taylor
Polyflex Airtech/England U.K.
36, Cheltenham Trade Park, Arle Rd.
Cheltenham Glos GL51 8LZ
011–44–242–228878

Silas Teigland
Litton ILSD
2734 Hickory Grove, P.O. Box 4508
Davenport, IA 52808
319–383–6215

Ray Tervo
Clifton Precision
P.O. Box 4508
Davenport IA 52808–4508
319–383–6396

Niranjan Thatte
University of California, Berkeley
601 Campbell Hall
Berkeley CA 94720
415–643–6425

Peter J. Thomas
AFSTC/SWS
Kirtland AFB NM 87117
505–846–5803

Klaus Timmerhaus
University of Colorado/Chem. Engrg.
Campus Box 424
Boulder CO 80903
303–492–7680

Jesse D. Timmons
Bionetics Corporation
NASA Headquarters Code SED
Washington DC 20543
202–453–1750

Russell C. Tipton
Forma Scientific
Millcreek Road, P.O. Box 649
Marietta OH 45750
614–374–1863

Sasaki Toshiaki
Missho Iwai American Corp.
One Cambridge Center
Cambridge MA 02142
617–577–7260

Martin C. Trively
CECOM/NVEOL
Attn: AMSEL–RD–STD–ICT
Ft. Belvoir VA 22060–5677
703–664–1345

Emanuel Tward
TRW Space and Technology Inc.
R1/1126, One Space Park
Redondo Beach CA 90278
213–814–0409

Costas C. Tzemos
CVI Incorporated
P.O. Box 2138
Columbus OH 43216
614–876–7381

Javier A. Valenzuela
Creare Inc.
Etna Road, P.O. Box 71
Hanover NH 03755
603–643–3800

Joseph P. Wachter
Ford Aerospace
3825 Fabian Way, MS/G79
Palo Alto CA 94303
415–852–5631

Philipp Wagner
Wagner Systems (PTY) Ltd.
P.O. Box 117, Plumstead 7800
South Africa
021–758011

Warren D. Waldron
Mechanical Technology Inc.
968 Albany Shaker Road
Latham NY 12110
518–785–2299

Graham Walker
University of Calgary
2500 University Drive N.S,
Calgary, Alberta, Canada T2N 1N4
403–220–5772

David A. Wallace
Stirling Technology Company
2952 George Washington Way
Richland WA 99352
509–375–4000

Joseph D. Walters
David Taylor Research Center
Code 2712
Annapolis MD 21402–5067
301–267–3632

Robert E. Warren
Hughes Aircraft Co.
P.O. Box 902 EO/EO1/C173
El Segundo CA 90245
213–616–9530

Alan Weeks
CTI-Cryogenics Inc.
266 Second Avenue
Waltham MA 02254–9171
617–622–5384

Harold Weinstock
AFSOR/NE
Bolling Air Force Base
Washington DC 20332–6448
202–767–4934

Ron White
Air Force Wright Aeronautical Labs
WRDC/FIVEA
Wright Patterson AFB OH 45433–6553
513–255–6078

Richard J. Williams
Aerojet Electronic Systems Div.
1100 W. Hollyvale St./P.O. Box 296
Azusa CA 91702
818–812–1864

William E. Wyche
AFSTC/SWS
Kirtland AFB NM 87117
505–846–5803

Ran Yaron
31 Mass. Ave.
Boston MA 02115
617–247–2019

Steven Glenn Zylstra
General Pneumatics Corporation
7662 E. Gray Road, Suite 107
Scottsdale AZ 88260
602–998–1856

REPORT DOCUMENTATION PAGE

Form Approved
OMB No. 0704-0188

1. AGENCY USE ONLY (Leave blank)	2. REPORT DATE	3. REPORT TYPE AND DATES COVERED
	January 1991	Conference proceedings

4. TITLE AND SUBTITLE

Proceedings of the Sixth International Cryocoolers Conference

5. FUNDING NUMBERS

6. AUTHOR(S)

Geoffrey Green and Margaret Knox, Editors

7. PERFORMING ORGANIZATION NAME(S) AND ADDRESS(ES)

David Taylor Research Center
Annapolis, Maryland
21402–5067

8. PERFORMING ORGANIZATION REPORT NUMBER

DTRC–91/002

9. SPONSORING / MONITORING AGENCY NAME(S) AND ADDRESS(ES)

10. SPONSORING / MONITORING AGENCY REPORT NUMBER

11. SUPPLEMENTARY NOTES

12a. DISTRIBUTION / AVAILABILITY STATEMENT

Approved for public release; distribution is unlimited.

12b. DISTRIBUTION CODE

13. ABSTRACT *(Maximum 200 words)*

This document contains the proceedings of the Sixth International Cryocoolers Conference, held October 25–26, 1990, in Plymouth, Massachusetts. About 260 people attended, representing many government and private laboratories (both foreign and domestic) as well as numerous universities and industrial companies. Fifty–four papers were presented.

The speakers described advances in many areas of cryocooler technology, mostly in the temperature range below 80 K. Topics included advanced regenerators, pulse tube and sorption coolers, and Stirling, Joule–Thomson, magnetic, and hybrid coolers. The discussions also covered a broad range of applications and component technologies.

14. SUBJECT TERMS	15. NUMBER OF PAGES
Cryocoolers, cryogenics, cryopumps, Gifford-McMahon coolers, helium, infrared detectors, Joule-Thomson coolers, magnetic coolers, pulse tube coolers, rare earths, refrigeration, regenerators, sorption coolers, space coolers, Stirling coolers, superconductors.	16. PRICE CODE

17. SECURITY CLASSIFICATION OF REPORT	18. SECURITY CLASSIFICATION OF THIS PAGE	19. SECURITY CLASSIFICATION OF ABSTRACT	20. LIMITATION OF ABSTRACT